DOI: 10.15774/PPKE.BTK.2024.021

Thesis

PhD

Ola Bilal

Diagnosis and Analysis of Monument Deterioration Classification and Investigation

Study Case: The Medieval Fortifications of Syria/ Crac Des Chevaliers/

Doctoral School of History

The Head of the Doctoral School: Dr. Sándor Őze DSc, professor

Supervisor: Dr. Rozgonyi-Boissinot NiKoletta PhD

Pázmány Péter Catholic University

Faculty of Humanities and Social Sciences

Budapest, 2023

DOI: 10.15774/PPKE.BTK.2024.021

Acknowledgements

I would liKe to express my gratitude to everyone who helped to achieving this worK.

First and foremost, I would liKe to thanK and acKnowledge my supervisor (Dr. Rozgonyi-Boissinot NiKoletta) for maKing this worK possible. Her advice, consultation, and guidance have made me scientifically better at what I do. She was very generous to me, and I appreciate all of her help.

I want to convey my appreciation to the faculty of humanities and social sciences at Pázmány Péter Catholic University for accepting me as one of its PhD candidates. I appreciate the scholarship from the Tempus Public Foundation that allow me to study in Hungary.

I would liKe to express my sincere thanKs to the Department of Engineering Geology and Geotechnics at Budapest University of Technology and Economics for providing their laboratory, the essential equipment, and the materials required to carry out this worK. ThanK you to all of the technicians and staff at the university, especially Dr. KopecsKó Katalin, ViKtoria RónaKy, and EriKa Csányi. Special thanKs to Professor AKos TöröK, head of Department of Engineering Geology and Geotechnics, for his assistance and consultation.

Many thanKs to the Hungarian mission worKing in Syria, specially professor Balázs Major who gave the opportunity to worK with them and provided the inspiration for my research topic. I want to thanK Mr. Zsolt Vagner, who was the head of Hungarian mission worKing at Syria at Crac des Chevaliers castle, for his help and introducing me to Budapest University of Technology and Economics professors.

I would liKe to thanK my entire family for encouraging me to start this mission and for their moral support throughout.

ThanK you to all of my colleagues at the Directorate-General of Antiquities and Museums/ DGAM in Syria, especially Eng. Edmond Alejji and Eng. Hazem Hanna, for their contributions to the completion of this worK. I would liKe to thanK all of the employees and worKers at Crac des Chevaliers castle for their hard worK during those difficult years in Syria. Their dedication to the castle is greatly admired, so thanK you for their efforts.

I want to express my gratitude to my colleague Eng. Ahmad Alboush for lending me lots of his valuable time to finish the field investigation. He did not hesitate to offer me any assistance I

DOI: 10.15774/PPKE.BTK.2024.021

needed to complete this project. Sincere appreciation to him for being a main contributor to this worK and allowing me to generously benefit from his expertise.

Finally, I would liKe to thanKs my colleagues Alina Vattai and BenedeK Lógó for their generous assistance and warm care they provided me.

DOI: 10.15774/PPKE.BTK.2024.021

Table of Contents

DOI: 10.15774/PPKE.BTK.2024.021

DOI: 10.15774/PPKE.BTK.2024.021

1. Introduction and objectives

DOI: 10.15774/PPKE.BTK.2024.021

1.1 Introduction:

Crac des Chevaliers is a significant crusader castle in the Middle East. This historical structure was built during the medieval period in the 11th century and was later expanded with additional structures in the 13th century. The castle is the most unique and well-preserved medieval fortress in the world. It is a formidable Gothic castle with a small Romanesque chapel, numerous residence and military facilities, and various motifs and decorations carved on the stones. However, in the 13th century, the Mamluks added their own towers in the purpose of enhancing the defensive role of the crusader castle, demonstrating the ingenuity of Islamic military architecture craftsmen.

Such a fundamental and wonderful castle attracts many historians and archaeologists across the world to study it. On the other hand, very few studies on conservation status of the castle has been published. Furthermore, the restoration projects in the castle were limited to the rebuilding of some parts or the isolation of the roof, which facilitates and secures visitor tours. Regardless of the destruction that occurred in the castle during the recent Syrian war, the castle contains numerous stone decay and deterioration cases that must not be ignored. Those cases should be studied precisely when preparing the conservation plan.

According to that, this study concerns with the diagnosis of weathering types at the castle and the investigation of its stone properties, which can form the basis for conservation plan of the castle.

Panel 1 depicts the research plan of this study, which includes two main investigations in-situ and in the laboratory. This research begins with gathering the necessary data about the building site and its conditions, such as meteorological data, climate characteristics, and geological and environmental settings. One of the important data that is investigated is restoration history of the castle. The in-situ and field investigations are divided into several steps. First, the identified stone deterioration cases are classified into various categories [the most serious issues are mechanical (impact) damage, microorganism colonization, salt efflorescence, discoloration, cracks, graffiti, splitting, erosion, and encrustation]. Then, identifying building stone based on the various lithotypes to which it belongs, along with a macroscopic description of those lithotypes. By the naked eye investigation, the castle was built mainly by carbonate stone in addition to the use of basalt stone in some buildings. This study focuses on examining carbonate stones because they are less resistant to weathering than basalt. By the field investigation, the carbonate stones are categorized into four lithotypes as follows: 1)

DOI: 10.15774/PPKE.BTK.2024.021

homogenous porous stones (HPS); 2) homogenous dense stones (HDS); 3) laminated stones (LS); 4) newly built stones (NBS). Finally, the field investigation is completed by using non-destructive techniques that are useful for determining the properties of many stones in situ while causing no damage to any part of this valuable building. One of these techniques is deterioration mapping, which helps to provide a general overview of the distribution of stone decay cases; how they spread and prevail according to the direction of the façade; and it is useful to know which decay cases dominate in the castle. In this study, the deterioration mapping is performed on the external south façade of the building (46), as well as on the external east and north façades of the building (36). The results of the deterioration mapping of three external facades with different directions (south, east, and north facades) show that the orientation of the façade is a key factor in the presence of some distinct deterioration types. The discoloration with orange is a characteristic stone deterioration type that is found in the south and east external facades. However, the grey microorganisms colonization is dominated in north and west facades. The red-orange microorganisms colonization can be found in the north façade in shaded moisturized areas.

Rilem tube is also used as one of the non-destructive techniques. By that tool can figure out how the deterioration type and its intensity can affect the wettability property of the stone. In addition, it helps to estimate to what extent can the weathering crust protect the stone from the wind-driven rain. In this study, the different kinds of lithotypes as well as several decayed stone surfaces, are examined by this technique. The results show that the water absorption behaviour depends on the stone condition, its orientation, and its location. The stone condition includes the stone deterioration type (salt efflorescence, biological colonisation, or affected by mechanical shock); its spread (e.g., whether the biological colonisation covers the stone surface totally or partially); and its intensity on the surface (e.g., the thickness of salt crust or the biological colonisation). The location means in which course and story of the building, the tested stone is built. Blocks located on the ground floor are usually exposed to rising damp (through capillary absorption from the ground). It can reduce the water absorption behaviour by the Rilem tube if the pores of the stone are full of water from the ground. Schmidt was also used in this study to determine the compressive strength of the different lithotypes with several stone decay cases. Schmidt hammer is used to test the same stones that were tested by Rilem tube. The results showed that the rebound value of the tested stones ranged between 25 and 48. The lithotype of the tested stones have no significant effect on rebound value of the stone. However, the type of deterioration has a significant impact on reducing the compressive

DOI: 10.15774/PPKE.BTK.2024.021

strength of the tested stone, particularly when these stones are fragmented or have eroded surfaces.

It is critical to collect stone samples from the castle for laboratory analysis. Ten stone core samples (S1, S2, S3, S4, S5, S6, S7, S8, S9, S10) are collected from the castle, where the number and location are limited to administration recommendations and technical issues. According to administration recommendations, only a limited number of stone cores should be collected, with a preference for cores from fallen stones. The technical issues stems from a lack of electricity and the requirement to use an electricity generator that cannot be moved around the entire castle. As a result, stone coring is limited to a few locations. These stone cores belong to different building periods of the castle. Those buildings periods are mainly the First Frankish period (at the beginning of the 12th century), the Second Frankish period (from the beginning to the half of the 13th century), and finally the Mamluk building period (around 1271). As a result, the cores S1, S2, S5, S6, and S7 most likely belong to the second Frankish period, while S8 was taken from a building dated to the first Frankish period. S3, S4, S9, and S10 are cores taken from fallen stones, so determining their building period is approximate based on their locations where they have been found fallen. According to that, S3 and S4 might belong to the second Frankish period, while S9 and S10 to the Mamluk one.

Furthermore, many stone deposits and weathering powder were collected to be analysed. Panels 2A, 2B, and 2C depict the locations of the in-situ investigation and sampling sites with their probable historical period they were used in.

The physical, mechanical, petrographic, and chemical properties of the stone cores are determined in the laboratory. Many tests are carried out on the stone specimens, including water absorption under atmospheric conditions and drying under different conditions. The petrographic analysis of the stone cores reveals that the stones belong to the three main groups of lithotypes: 1) S1 and S9 are micro bioclast packstones 2) S5 is a micro bioclast wackstone 3) S2, S3, S4, S7, S8, and S10 are microcrystalline dolomite stone. S1 and S9 have the lowest open porosity (around 14%v/v on average) and their tensile strength is about 6 Mpa, however the open porosity of the microcrystalline dolomite stones is about 28%v/v-on average, their tensile strength ranges between 1.5-4 Mpa. The open porosity of S5 is 27.8%V/v, however its tensile strength differs largely between the crust and the sound part, 2.8 and 6.8 Mpa respectively.

DOI: 10.15774/PPKE.BTK.2024.021

The drying test in this study is performed to examine the drying behaviour of the specimens under three different conditions. The first group is dried at 25°C in the oven, which provides air circulation during the heating (these specimens are not covered). The remaining two groups of samples are dried at room temperature. The second group of specimens is sealed with Epoxy-resin on all sides except the top side, whereas the other group is left to dry without being covered. The drying test results showed that the micro bioclast packstone (S1 and S9) exhibit high effective drying behaviour because they have the lowest open porosity and less pore connectivity. S4, S8, and S10 have the highest amount of closed pores, around 4 v/v %. S4 has moderate drying behaviour (moderate water retention capacity), but S8 and S10 have fast drying behaviour because of their good pores connectivity and the presence of macropores. S2, S3, and S7 have the lowest closed pores (0.9; 0.3, and 0.7 v/v %, respectively) and approximately similar open porosity. S3 exhibits the highest water retention capacity, while S7 showed moderate capacity. The water vapour permeability test is crucial based on the results of the Rilem tube test, which determines the weathering crust ability to prevent or reduce capillary absorption of rainwater, i.e., whether this crust plays a protective role or not. The water vapour permeability of the stone cores is calculated for both fresh and crust specimens. This test is critical in determining how the weathering crust affected water vapour permeability of the stone. And whether this crust should be removed in conservation practice or preserved due to its water vapour permeability limit, which prevents condensation areas from forming inside the stone. The results of this test reveal that S2 has the lowest water vapour resistant factor value, while S4 and S10 come in second order. S3, S7, and S8 have moderate vapour resistant factor values. S1 and S9 have the highest value of vapour resistant factors. The crust affects significantly the water vapour permeability of the stones, where the extent of that effect is more related to type of crust and less to the thickness of the crust. The water vapour permeability of the crust of S1, S2, S3, S8, and S9 is less than the water vapour permeability of the sound specimens of at most 20%. Thus, the crust of those specimens can be preserved from water vapour permeability criteria and when there is no other harmful effect of the crust on the stone. The crusts of S4, S7 and S10 reduce the water vapour permeability to around 50% compared to the sound specimens. Such crusts are recommended to be removed from the conservation point of view.

To assess the durability of the stone specimens, a salt aging test with several salts is completed. The salt solutions are chosen based on the salt content of the powder and deposit specimens. Four salt solutions are chosen, two of which are simple salts (NaCL and KNO_3) and two of

DOI: 10.15774/PPKE.BTK.2024.021

which are hydrated salts (Na_2SO_4 and $MgSO_4$). The specimens in this study reveal different type of weathering according to the type of salt solution, where Na_2SO_4 and $MgSO_4$ are the most aggressive to the specimens comparing to the other two salt solutions. On the other hand the specimens show different durability degrees against salt solution aging test. Thus, the difference in the porosity and its connectivity is reflected in the difference in the resistance of the specimens. The more compact stones are less susceptible to damage than the more porous ones. S1 and S9 and are the most durable stones against the salt ageing test of different salt solutions. S4, S8, and S10 are durable against the salt ageing test because of the high value of closed pores they have. S2, S3, and S7 exhibit less durability against different salt solutions comparing to other specimens, because they have less close porosity.

DOI: 10.15774/PPKE.BTK.2024.021

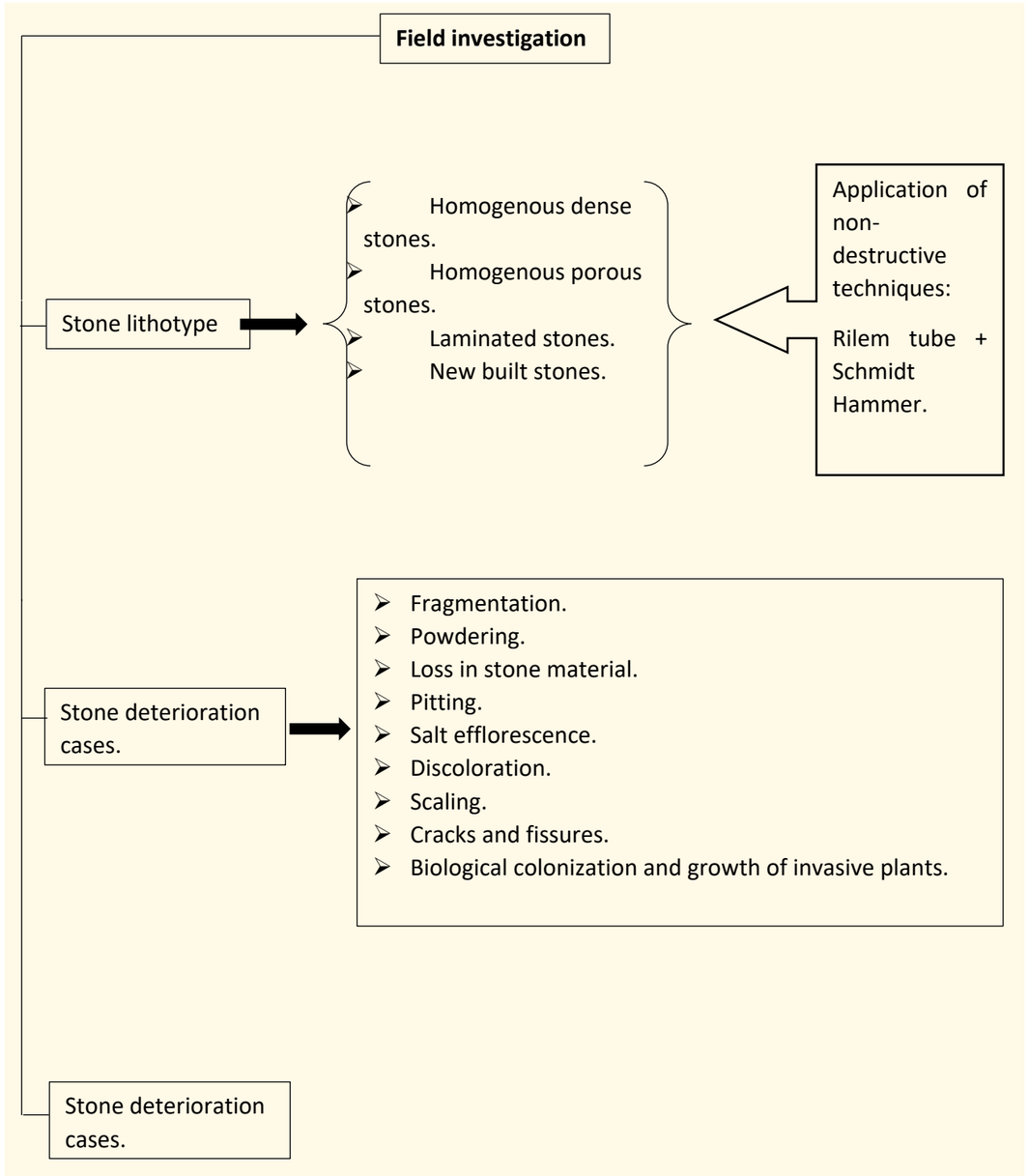

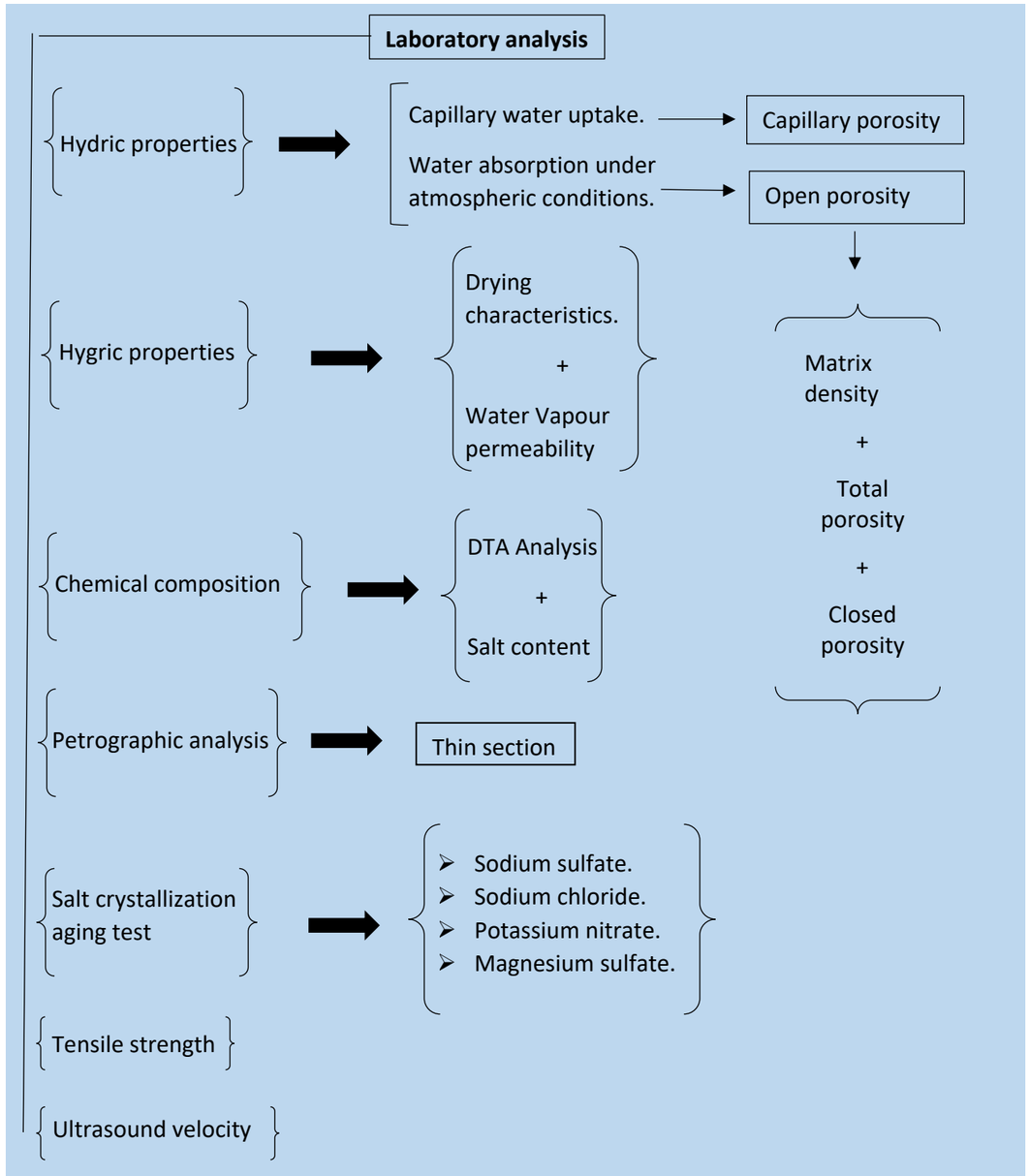

Panel 1 The detailed steps of both field and laboratory investigations that are fulfilled to achieve the objectives of this study

DOI: 10.15774/PPKE.BTK.2024.021

Specimen number in the plan	Specimen name	Building period
1	B9	-
2	B10	-
3	B11	-
4	S8	F1
5	B7	-
6	S1	F2

Specimen number in the plan	Specimen name	Building period
7	B5	-
8	B2	-
9	S3	F2(?)
10	S2	F2
11	S9	M(?)
12	S10	M(?)

Specimen number in the plan	Specimen name	Building period
1	HDS_0	F2
2	HPS_0_2	F2
3	HDS_D_4	F2
4	HPS_MC	F2
5	HPS_0_1	F2
6	NBS_0_1	F1

Specimen number in the plan	Specimen name	Building period
7	HDS_D_2	F1
8	HDS_D_3	F1
9	HDS_FMC	M
10	HDS_MC_6	M

F1: The first Frankish building period/ F2: The second Frankish building period/ M: The Mamluk building period.

Panel 2 A The locations of the in-situ investigation as well as sampling places-level 3

DOI: 10.15774/PPKE.BTK.2024.021

Specimen number in the plan	Specimen name	Building period
1	S4	F2 (?)
2	B6	-
3	S5	F2
4	S7	F2
5	S6	F2
6	B3	-

Specimen number in the plan	Specimen name
7	B4
8	B8
9	B1

Specimen number in the plan	Specimen name	Building period
1	LS_D	F2
2	NBS_D/ NBS_MC	1954
3	HDS_MC_4	F1
4	HDS_DS	F2
5	HDS_S	F2
6	HPS_S	F2

Specimen number in the plan	Specimen name	Building period
7	LS_S_1	F2
8	LS_MC_3	F2
9	LS_S_2	F2
10	LS_MC_1	F2
11	HDS_MC_5	F2
12	HDS_E	F2

Specimen number in the plan	Specimen name	Building period
13	HDS_EF	F2

F1: The first Frankish building period/ F2: The second Frankish building period/ M: The Mamluk building period.

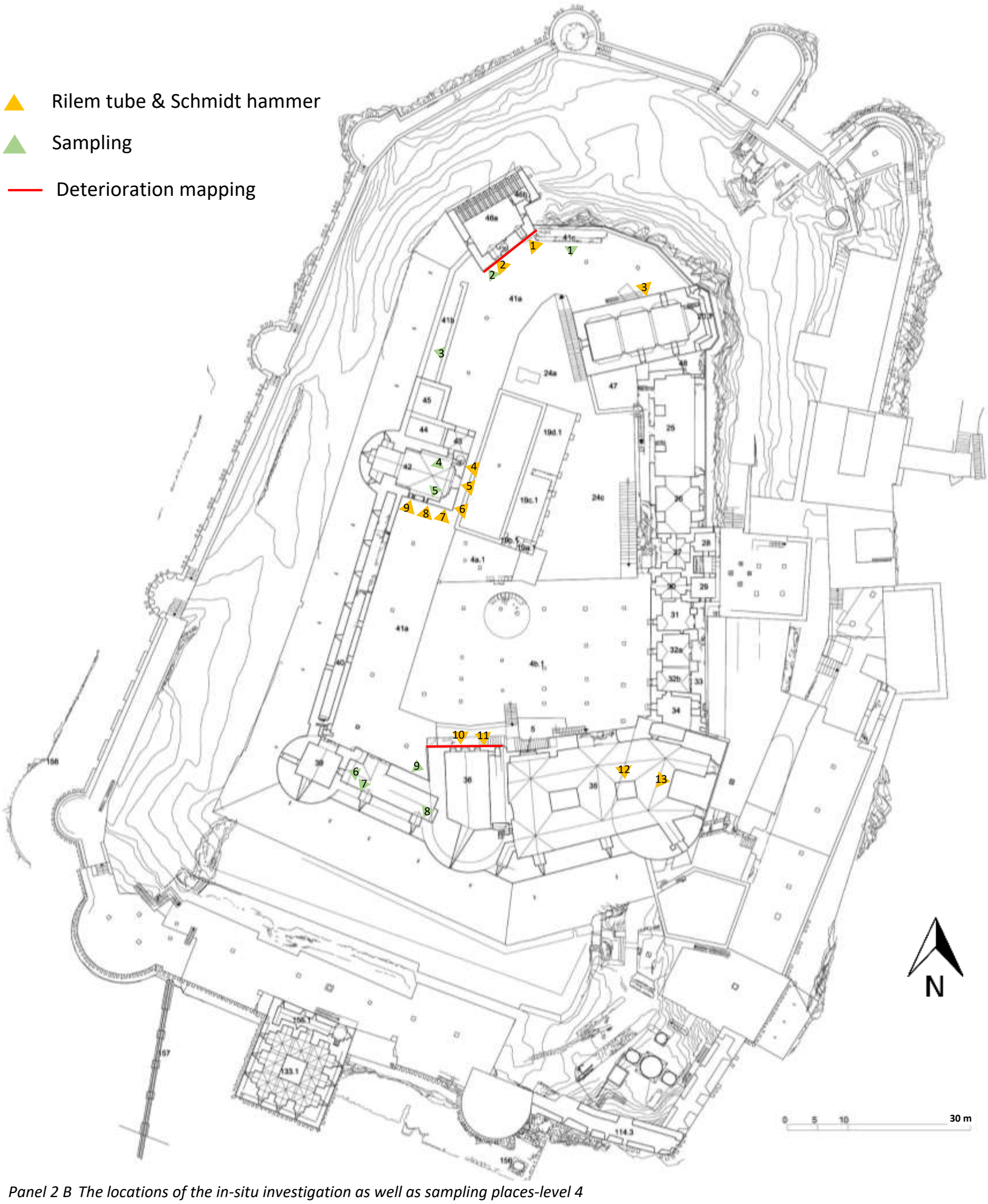

Panel 2 B The locations of the in-situ investigation as well as sampling places-level 4

Specimen number in the plan	Specimen name	Building period
1	HPS_D	F2
2	HDS_D_1	F2
3	LS_MC_2	F2
4	HDS_MC_3	F2
5	LS_DS	F2
6	NBS_S	2004

Specimen number in the plan	Specimen name	Building period
7	HDS_MC_1	F2
8	HDS_MC_2	F2
9	NBS_0_2	2002

F2: The second Frankish building period

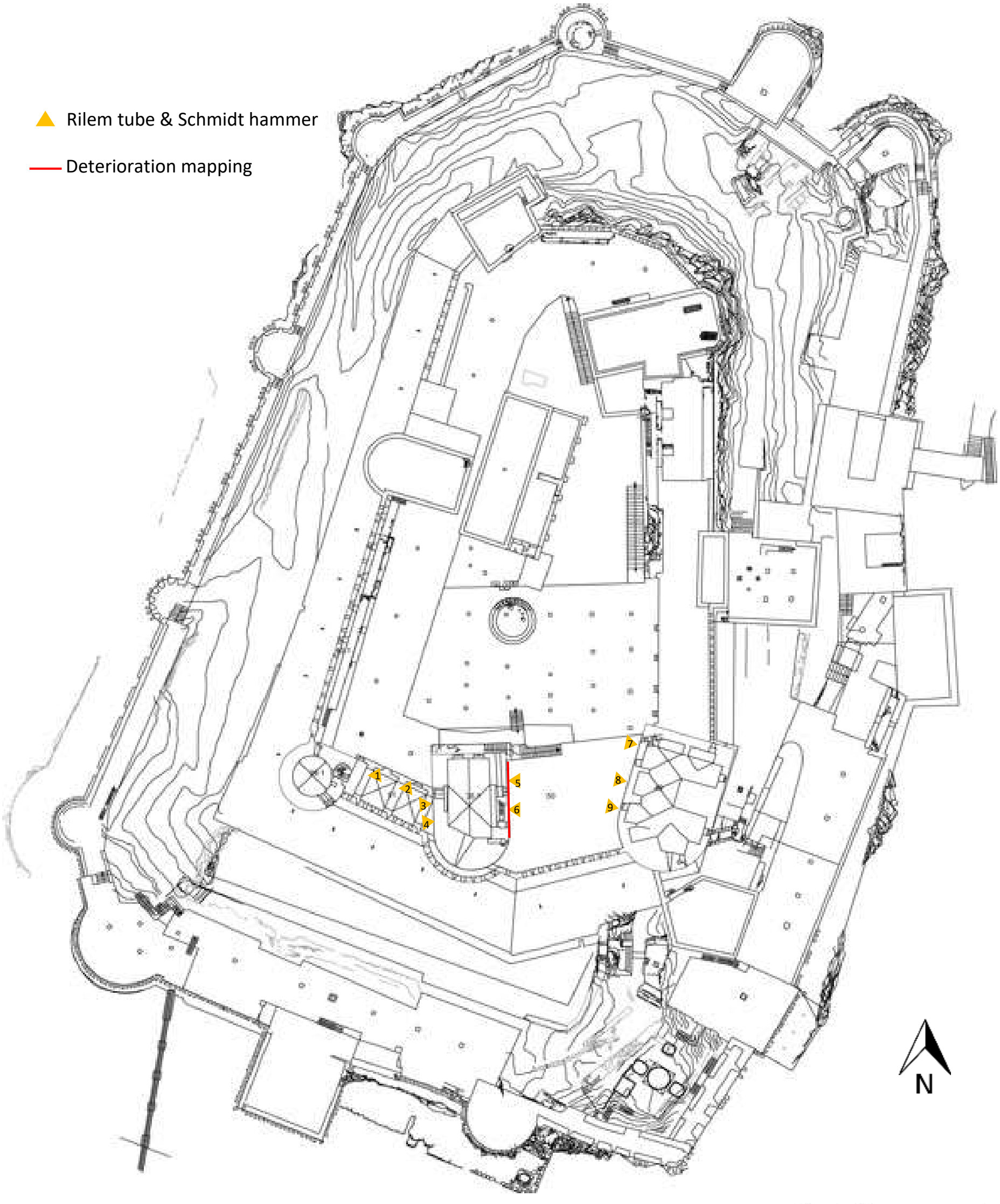

Panel 2 C The locations of the in-situ investigation as well as sampling places-level 5

DOI: 10.15774/PPKE.BTK.2024.021

1.2 Objectives:

The primary goal of this research is to investigate the state of conservation of Crac des Chevaliers castle by completing the following tasks:

- Identify the most common types of deterioration and how they spread at the castle.
- How does the type of deterioration affect some stone properties measured in situ using non-destructive techniques? (Rilem tube penetration test and Schmidt hammer).
- Determine the stone properties (petrographic, chemical, physical, and mechanical properties) of some castle core stone samples.
- Investigating the behaviour of stone samples under various drying conditions, as drying is an important property that determines the weathering susceptibility of stone blocks.
- Investigating the behaviour of stone samples in salt aging tests. The stones are subjected to salt solutions of NaCl, Na_2SO_4, KNO_3, and $MgSO_4$.
- What effect does the weathering crust have on water vapour permeability? Determine whether the weathering crust can serve as a protective coat from a conservation standpoint.

Achieving the previous points creates a database of the current conservation status of the castle. This database can be used to create a sustainable conservation plan for the castle.

DOI: 10.15774/PPKE.BTK.2024.021

2. Literature summary

DOI: 10.15774/PPKE.BTK.2024.021

2.1 The restoration plan of historical buildings

The durability of a historical building is always linked to various agents in which many alterations can damage the building stones physically, chemically, or biologically [1]. Understanding these agents needs a broad and precise study of the building since it was established. This study relies on a vast database of information based on research in both the field and literature to evaluate the conservation status of the building and select the appropriate restoration method when necessary.

A complex process should be worked on using standard methods and keeping pace with the development of diagnostic techniques that play an essential role in ensuring the sustainability of heritage buildings and monuments [2]. Vast amounts of data are required to be collected to define the restoration approach. Fitzner & Heinrichs (2001) produced a systemic approach to the sustainable conservation of historical buildings [3]. That systemic approach consists of three main steps: 1) anamnesis 2) diagnosis 3) therapeutic procedures (Figure 2.1).

1- Anamnesis involves the building identification, geographical location and the surrounding

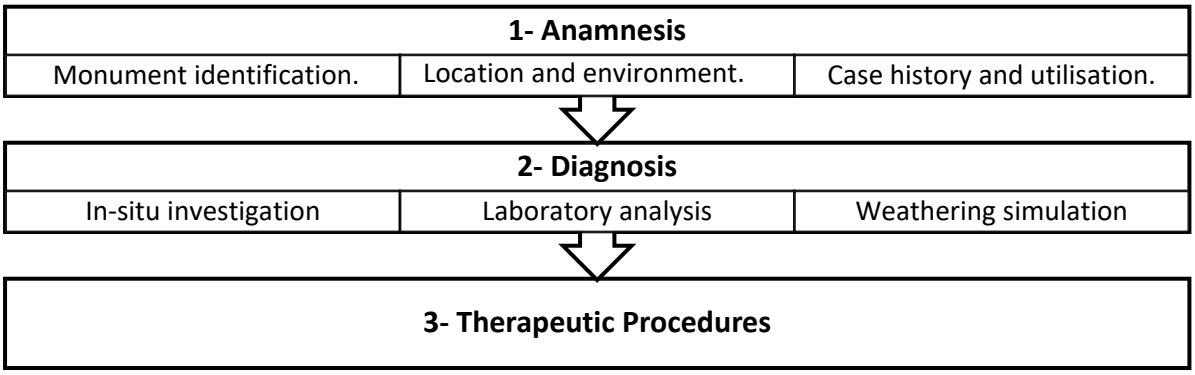

Figure 2. 1 The systemic approach to a sustainable conservation of historical buildings (updated from (Fitzner & Heinrichs, 2001)).

environment, and case history and utilization.

Building identification implies the name of the building and its dimensions, the owner of the property, and the authority responsible for it.

Geographical location and the surrounding environment describe the location of the building and its conditions. It contains a collection of meteorological data components of the

[1] Oscar Buj and Josep Gisbert, "Influence of Pore Morphology on the Durability of Sedimentary Building Stones from Aragon (Spain) Subjected to Standard Salt Decay Tests," *Environmental Earth Sciences* 61/7 (2010): 1327–36.

[2] Clifford A Price and Eric Doehne, "Stone Conservation: An Overview of Current Research," (2011):29.

[3] Bernd Fitzner and Kurt Heinrichs, 'Damage Diagnosis on Stone Monuments— Weathering Forms, Damage Categories, and Damage Indices' in Understanding and Managing Stone Decay, Proceeding of the International Conference Stone Weathering and Atmospheric Pollution, eds. Heather Viles, Richard Přikryl (Prague,2001) 11-56.

DOI: 10.15774/PPKE.BTK.2024.021

location (temperature variations, relative humidity, amount of precipitation, sunshine duration, wind speed, wind direction, and amount of snowfall) are considered as essential factors in inducing damage to the stone. Relative humidity, temperature variation, and precipitation are critically important in controlling the growth of ice or salt crystals hygric and hydric swelling, which all result in physical stress in the stone structure [4]. The amount of precipitation has an essential role in the chemical dissolution rate, which leads to the gradual recession of the stone surface [5]. Other chemical damage and biological attacks on the stone also contribute to environmental conditions such as rain and air quality as well as the rate of air pollution. Defining the natural disasters such as earthquakes, damages caused by human activities like wars, fires, etc. is also essential data that should be known at this step.

Case history and utilization contains studying the historical background that includes the construction development over time, the former modifications, the rebuilding and the restoration work, what was the function of the building during history until now [6].

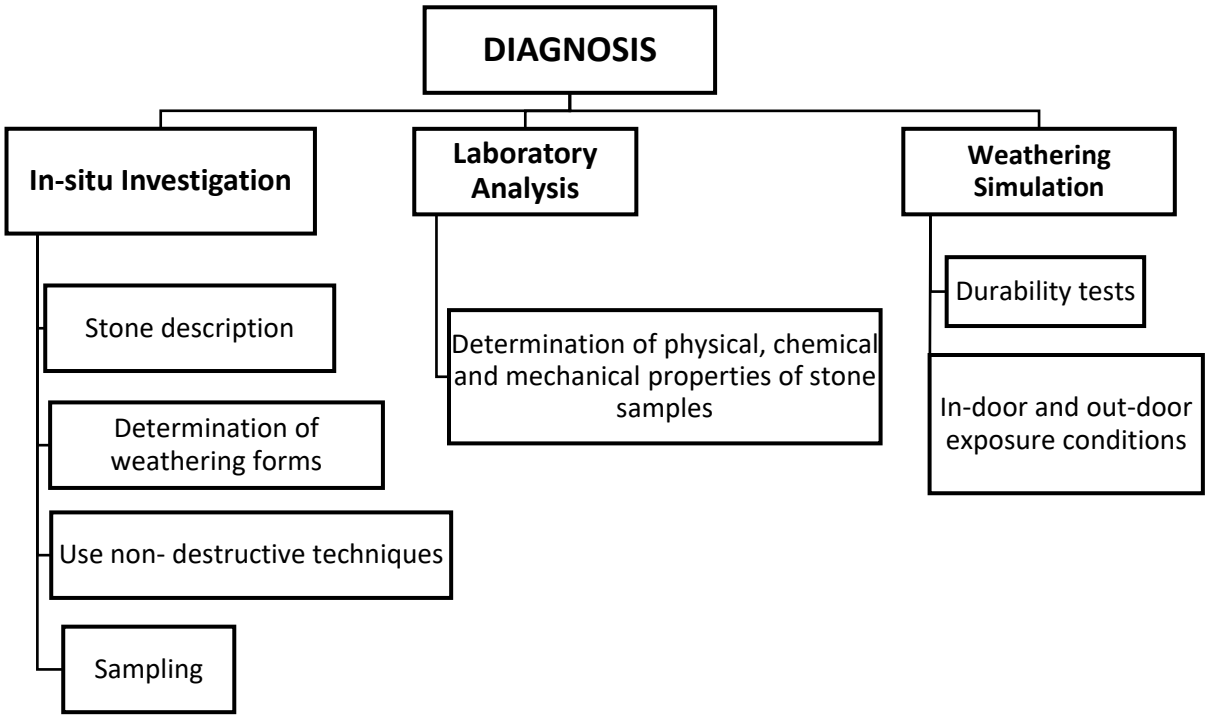

Figure 2. 2 Diagnosis step for the sustainable conservation of historical buildings

[4] Michael Steiger, A Elena Charola, and Katja Sterflinger, "Weathering and Deterioration," in Stone in Architecture (2011), 227–316.

[5] Malcolm Ross, Elaine S McGee, and Daphne R Ross, "Chemical and Mineralogical Effects of Acid Deposition on Shelburne Marble and Salem Limestone Test Samples Placed at Four NAPAP Weather-Monitoring Sites," *American Mineralogist* 74/3–4 (1989): 367–83.

[6] Bernd Fitzner, "Damage Diagnosis on Stone Monuments-in Situ Investigation and Laboratory Studies," in Proceedings of the International Symposium of the Conservation of the Bangudae Petroglyph, vol. 7 (2002), 29–71.

DOI: 10.15774/PPKE.BTK.2024.021

2- Diagnosis: this step includes three sub-steps: 1) in-situ investigation 2) laboratory analysis 3) weathering simulation (see Figure 2.2).

2-1 In-situ investigation is subdivided into:

i. Stone description is the visual description of the building stones, which are recognized at the site by the naked eye, i.e., their type, color, pores, observed distinct particles at the surface, texture, etc.

ii. Determination of weathering forms and stone deterioration cases observed by the field investigation [7] (Delegou et al., 2019). This step also depends on the eye human ability to recognize the decay cases that found in various scales. Viles et al.(1997) divides the weathering scales into nanoscale, microscale, mesoscale and macroscale [8]. Nanoscale is less than 1 mm and is related to the changes in stone properties that cannot be diagnosed in-situ without laboratory analysis. Microscale is less than 1 cm, which involves loss in stone material, change of the porosity, or discoloration, etc. Mesoscale is between 1 cm to 1 m and includes the weathering forms related to surface damage. Macroscale is greater than 1 m, it is related to structural stability across the whole façade. Many methods can be followed to classify the weathering forms, such as Fitzner and Heinrichs method (more details can be found in [9]) or following the "ICOMOS-ISCS: Illustrated glossary on stone deterioration patterns" [10]. The latter recommendation is used in this study.

iii. Use of non-destructive techniques to determine the stone properties [11]. Recently many techniques can be applied directly to the building stone such as Rilem tube (to test the capillary water absorption of the stone), Schmidt hammer (to test the strength property of the stone), ultrasonic wave measurement (to evaluate the degree of weathering), deterioration mapping, etc. These techniques are used to assess the deterioration degree

[7] Ekaterini T Delegou et al., "A Multidisciplinary Approach for Historic Buildings Diagnosis: The Case Study of the Kaisariani Monastery," *Heritage* 2/2 (2019): 1211–32.

[8] H A Viles et al., "What Is the State of Our Knowledge of the Mechanisms of Deterioration and How Good Are Our Estimates of Rates of Deterioration?," in *Saving Our Architectural Heritage. Conservation of Historic Stone Structures*, 1997, 95–112.

[9] Fitzner & Heinrichs (2001).

Bernd Fitzner and Kurt Heinrichs, 'Damage Diagnosis on Stone Monuments— Weathering Forms, Damage Categories, and Damage Indices' in Understanding and Managing Stone Decay, Proceeding of the International Conference Stone Weathering and Atmospheric Pollution, eds. Heather Viles, Richard Přikryl (Prague,2001) 11-56.

[10] Véronique Vergès-Belmin, *ICOMOS-ISCS: Illustrated Glossary on Stone Deterioration Patterns= Glosario Ilustrado de Formas de Deterioro de La Piedra*, vol. 15 (2011).

[11] ADEmilia Vasanelli et al., "Non-Destructive Techniques to Assess Mechanical and Physical Properties of Soft Calcarenitic Stones," *Procedia Chemistry* 8 (2013): 35–44.

DOI: 10.15774/PPKE.BTK.2024.021

[12] or evaluate the treatment or restoration work [13]. In this study, Rilem tube, Schmidt hammer and deterioration mapping are used as non-destructive techniques. Rilem tube is invented to evaluate the capillary uptake of rainwater carried and directed by the wind. The pressure of 100 mm height of the water column is equivalent to the wind pressure of approx. 160 km/h by rain [14]. When the tube is applied to the stone and filled with water, the stone is exposed to water pressure that causes water penetration. However, when the water level decreases by the time (as the result of absorption, the stone will expose to a decreasing water pressure. Balakrishna et al. (2013) emphasizes that the difference in water pressure simulates the actual condition of the building in which it is not exposed to a constant wind speed [15]. In that context, the Rilem tube is usually used to measure the water absorption of building material in situ [16] . It is also considered as an effective tool to assess the efficiency and durability of the treatment of stone blocks, where the measurements are usually taken before and after the treatment [17].

Deterioration mapping is an in-situ investigation that relates to determining noticeable stone weathering at the mesoscale (cm-m) [18]. It includes various types of decay forms which were surveyed precisely on a given façade by photogrammetry technique. It is a useful non-destructive technique that is utilized for the documentation of several historical buildings and monument sites [19]. It helps to categorize the weathering forms

[12] Silvana Fais et al., "An Innovative Methodology for the Non-Destructive Diagnosis of Architectural Elements of Ancient Historical Buildings," *Scientific Reports* 8/1 (2018): 1–11.
[13] Richard A Livingston, "Nondestructive Testing of Historic Structures," in *Science and Technology in Historic Preservation* (2000), 97–120.
[14] Delphine Vandevoorde et al., "Contact Sponge Method: Performance of a Promising Tool for Measuring the Initial Water Absorption," *Journal of Cultural Heritage* 10/1 (2009): 41–47.
[15] M N Balakrishna et al., "Determination of Flow Rate of Water in Concrete by Rilem Tube Method," International Journal of Structural and Civil Engineering Research 2/4 (2013): 98–109.
[16] W Wedekind et al., "First Investigations of the Weathering and Deterioration of Rock Cut Monuments in Myra, Lycia (Turkey)," Science and Art: A Future for Stone (2016) 197.
Roel Hendrickx, "Using the Karsten Tube to Estimate Water Transport Parameters of Porous Building Materials," *Materials and Structures* 46/8 (2013): 1309–20.
[17] Rob P J Van Hees et al., "Evaluation of the Performance of Surface Treatments for the Conservation of Brick Masonry," in *8th= Eighth International Congress on Deterioration and Conservation of Stone, Berlin, 30 Sept.-4 Oct. 1996: Proceedings* (1996)1695–1715.
R Duarte et al., "Variability of In-Situ Testing in Wall Coating Systems-Karsten Tube and Moisture Meter Techniques," *Journal of Building Engineering* 27 (2020): 100998.
[18] Fitzner and Heinrichs, "Damage Diagnosis at Stone Monuments-Weathering Forms, Damage Categories and Damage Indices."
[19] Xavier Brunetaud et al., "Application of Digital Techniques in Monument Preservation," *European Journal of Environmental and Civil Engineering* 16/5 (2012): 543–56.
Elisavet Tsilimantou et al., "GIS and BIM as Integrated Digital Environments for Modeling and Monitoring of Historic Buildings," *Applied Sciences* 10/3 (2020): 1078.

DOI: 10.15774/PPKE.BTK.2024.021

and calculate the areas they spread on a given surface [20]. It can be used to locate the intervention areas in a given building [21]. Although this technique helps to understand the decay mechanisms, it is insufficient to analyze them unless it is used with other weathering analytical techniques (laboratory analysis, environmental measurements, using other non-destructive techniques) [22]. As such, it is a link between the data that is provided by the field and the laboratory [23].

Schmidt hammer is used for the determination of surface hardness in historical buildings. It is utilized to achieve at least two goals; either to predict the strength property of the stone [24] or to assess the stone weathering state [25]. There are two types of hammers according to their impact energy. The first type is called 'N', the classic Schmidt hammer, with the impact energy of 2.207 J, which is essentially used in concrete structures. The other type is called 'L' with a lower impact energy of 0.735 J, which is suitable for stones and bricks [26]. The principle work of the hammer is based on the theory that states "The rebound of an elastic mass from a surface corresponds to the hardness of this surface"[27]. The mass is started moving in the hammer with a spring (constant force) and thrown onto the stone surface. The rebound of this mass from the rock surface is measured. The value read on the scale is the rebound value . Barton & Choubey (1977) believe that many factors affect the accuracy rebound value. These factors are the orientation of the measured surface (vertical or horizontal), dimension, and moisture of the tested sample [28]. Several studies have been conducted to indirectly

Danae Phaedra Pocobelli et al., "Building Information Models for Monitoring and Simulation Data in Heritage Buildings," in *International Archives of the Photogrammetry, Remote Sensing and Spatial Information Sciences-ISPRS Archives*, 42 (2018) 909–16.

[20] Efstathios Adamopoulos and Fulvio Rinaudo, "Combining Multiband Imaging, Photogrammetric Techniques, and FOSS GIS for Affordable Degradation Mapping of Stone Monuments," *Buildings* 11/7 (2021): 304.

[21] Supriya Mahesh Patil, A K Kasthurba, and Mahesh V Patil, "Characterization and Assessment of Stone Deterioration on Heritage Buildings," *Case Studies in Construction Materials* 15 (2021): e00696.

[22] Efstathios Adamopoulos, "Learning-Based Classification of Multispectral Images for Deterioration Mapping of Historic Structures," Journal of Building Pathology and Rehabilitation 6/1 (2021): 1–15.

[23] José Delgado Rodrigues, "Defining, Mapping and Assessing Deterioration Patterns in Stone Conservation Projects," *Journal of Cultural Heritage* 16/3 (2015): 267–75.

[24] O Katz, Z Reches, and J-C Roegiers, "Evaluation of Mechanical Rock Properties Using a Schmidt Hammer," *International Journal of Rock Mechanics and Mining Sciences* 37/4 (2000): 723–28.

[25] Ákos Török, "Surface Strength and Mineralogy of Weathering Crusts on Limestone Buildings in Budapest," *Building and Environment* 38/9–10 (2003): 1185–92.

[26] Adnan Aydin and Arindam Basu, "The Schmidt Hammer in Rock Material Characterization," *Engineering Geology* 81/1 (2005): 1–14.

[27] Magdalini Theodoridou and Ákos Török, "In Situ Investigation of Stone Heritage Sites for Conservation Purposes: A Case Study of the Székesfehérvár Ruin Garden in Hungary," *Progress in Earth and Planetary Science* 6/1 (2019): 1–14.

[28] Nick Barton and Vishnu Choubey, "The Shear Strength of Rock Joints in Theory and Practice," Rock Mechanics 10/1 (1977): 1–54.

DOI: 10.15774/PPKE.BTK.2024.021

calculate the uniaxial compressive strength of the rock from the rebound value by defining empirical correlations between two values like [29]. Many researchers concentrated on the reliability of those empirical correlations in estimating the uniaxial compressive strength of the rocks, and they find a high correlation between these parameters [30].

iv. Sampling [31]: After the field investigation and observation of the building material as well as the stone decay types, many samples should be taken from the site to characterize the building material and the stone deterioration cases.

2-2 Laboratory analysis: at the laboratory, the stone samples are analyzed to determine their physical, chemical, and mechanical properties. Many tests can be carried out to define these properties such as mineralogical composition by using (X-ray diffraction analysis or differential thermal analysis that both can be coupled with thin section investigation techniques to produce photos of the minerals and stone texture), matrix and bulk density, open and total porosity, tensile and compressive strength, water absorption, water vapor permeability, etc.

2-3 Weathering simulation: weathering simulation means testifying the resistance of building material at the laboratory under extremely weathering conditions. Many tests can be included under weathering simulation such as salt aging, freeze- thaw cycles test, wet-dry cycles, heat-cool cycles, etc.

3- Therapeutic procedures include various work types according to the stone deterioration the building has. These procedures might be rebuilding or replacing the missing stones, restoration of damaged stones, rejoining between the stone blocks, reinforcing and supporting the weak parts, cleaning the stone surfaces, removing the salt crust, etc.

[29] Don Uel Deere and R P Miller, "Engineering Classification and Index Properties for Intact Rock" (1966):101
Ali M Rajabi, Alireza Hosseini, and Alireza Heidari, "The New Empirical Formula to Estimate the Uniaxial Compressive Strength of Limestone; North of Saveh a Case Study," *Journal of Engineering Geology* 11/3 (2017): 159.

[30] I S Buyuksagis and R M Goktan, "The Effect of Schmidt Hammer Type on Uniaxial Compressive Strength Prediction of Rock," *International Journal of Rock Mechanics and Mining Sciences* 2/44 (2007): 299–307.
Ali Abd Elhakam Aliabdo, "Reliability of Using Nondestructive Tests to Estimate Compressive Strength of Building Stones and Bricks," *Alexandria Engineering Journal* 51/3 (2012): 193–203.
I A Oyediran and E J Foghi, "Petrography and Strength Properties of Some Southwestern Nigeria Precambrian Rocks," *Journal of Mining and Geology* 54/2 (2018): 87–98.

[31] José E Meroño et al., "Recognition of Materials and Damage on Historical Buildings Using Digital Image Classification," *South African Journal of Science* 111/1–2 (2015): 1–9.

DOI: 10.15774/PPKE.BTK.2024.021

2.2 Overview of some common deterioration types

2.2.1 Salt crystallization

The contamination of porous building material with salts is widespread. Salts found in stone structures can originate from different sources. Salts can be initially present inside the stone structure if they have been brought from the marine environment [32]. The salts can enter the stone from an external source such as deicing salts [33], sea spray effect [34], or rising ground damp [35] that carries salts from the soil. Salts may result when the stone reacts with inorganic material, as the reaction between the stone material and air pollution components [36]. Some inappropriate conservation treatments lead to salts accumulation on a stone surface (e.g., cement mortar or cement plaster). The use of cement mortars on or between the stone blocks contributes to salts contaminations, such as calcium sulfates and sodium salts, which result from the interaction between Portland cement and water [37]. The most common salts that are frequently found in stone blocks are chlorides (NaCl, KCl), sulfates (Na_2SO_4, $MgSO_4$), carbonates ($CaCO_3$, $MgCO_3$), and nitrate salts (KNO_3, $NaNO_3$) [38].

When salts dissolve in water and form a salt solution, they can enter and move through the stone structure. Water vapor and liquid water (rainwater and rising damp) are water phases that can produce salt solutions. Inside the stone, salts will either crystallize or dissolve into salt solution, depending on the ambient conditions. When the water content of the salt solution decreases due to evaporation, the concentration of the salt solution rises until it reaches equilibrium. As more water evaporates, the salts begin to crystallize and form either a simple salt (such as NaCl and KNO_3) or a hydrated salt (such as the hydrated forms of magnesium

[32] Karlien Torfs et al., "The Cathedral of Bari, Italy: Evaluation of Environmental Effects on Stone Decay Phenomena," *Studies in Conservation* 42/4 (1997): 193–206.
[33] A Elena Charola, Bénédicte Rousset, and Christine Bläuer, "Deicing Salts: An Overview," in *Proceedings of the 4th International Conference on Salt Weathering of Buildings and Stone Sculptures SWBSS 2017* (2017):16-23.
[34] Fulvio Zezza and Fabio Macrì, "Marine Aerosol and Stone Decay," *Science of the Total Environment* 167/1–3 (1995): 123–43.
[35] JMPQ Delgado et al., "Salt Damage and Rising Damp Treatment in Building Structures," Advances in Materials Science and Engineering 2016 (2016):1-13.
[36] Beatriz Menéndez, "Estimators of the Impact of Climate Change in Salt Weathering of Cultural Heritage," *Geosciences* 8/11 (2018): 401.
[37] M Apostolopoulou et al., "Compatible Mortars for the Sustainable Conservation of Stone in Masonries," in *Advanced Materials for the Conservation of Stone* (2018), 97–123.
[38] Matthieu Angeli, "Multiscale Study of Stone Decay by Salt Crystallization in Porous Networks" (Doctoral dissertation, Université de Cergy Pontoise) (2007):10.

DOI: 10.15774/PPKE.BTK.2024.021

sulfate $MgSO_4.7H_2O$, $MgSO_4.6H_2O$, $MgSO_4.H_2O$) [39]. Those salts can be dissolved by rainwater or rising damp and form a salt solution again.

Salt is a hygroscopic material, i.e. it can absorb water vapor from the environment [40] (M Steiger, 2003). Each saturated salt solution has a specific deliquescence relative humidity (DRH) depending on the temperature. If the relative humidity of air exceeds the DRH of salt, the salt absorbs more water vapor from the air and gradually dissolves into the salt solution. When the relative humidity falls, the concentration of the salt solution rises. The salt solution becomes saturated when the relative humidity equals DRH. However, once the relative humidity falls further, the salt begins to form the solid phase (crystallization). At ambient relative humidity equals DRH of the salt, three phases can be recognized inside the pores, saturated salt solution, solid salt minerals, and water vapor [41]. Therefore, the salts with very low DRH are called soluble salts, and they can rarely be found in the solid phase. While the salts with very high

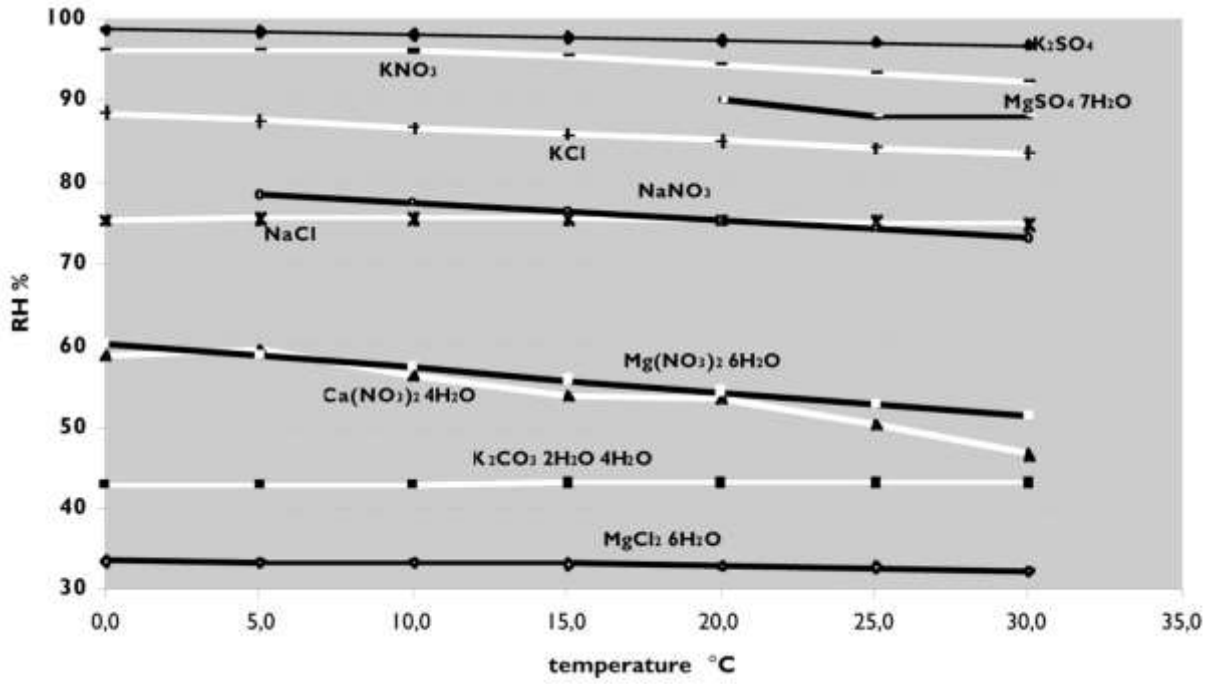

Figure 2. 3 The DRH values of the most common salts that can be found in stone masonry (taken from [Borrelli and Urland 1999])

DRH are called insoluble salts, and they hardly dissolve in water. Figure 2.3 shows the most common salts found in masonry with their DRH values [42].

[39] A Elena Charola and Christine Bläuer, "Salts in Masonry: An Overview of the Problem," *Restoration of Buildings and Monuments* 21/4–6 (2015): 119–35.
[40] M Steiger, "Salts and Crusts," *The Effects of Air Pollution on the Built Environment* (2003) 133–81.
[41] Michael Steiger, A Elena Charola, and Katja Sterflinger (2011):275.
[42] Ernesto Borrelli and Andrea Urland, *ARC Laboratory Handbook: Salts*, (1999):5.

DOI: 10.15774/PPKE.BTK.2024.021

A single salt is not usually found inside a stone structure; instead, a mixture of salts is present. Therefore, there is a range of DRH in the salt mixture rather than one DRH of a single salt case. For example, the DRH of a saturated solution of NaCl is 75.3% and 91.4% for Na_2SO_4 at 25°C. However, when these salts are mixed, the DRH of the mixture ranges between 74.5% and 80% [43].

The type of ions present in the salts mixture influences the solubility of these salts. If both salts have an ion in common (such as sodium chloride and sodium sulfate), the solubility will decrease [44]. Vice versa is true; if they do not have an ion in common (such as sodium chloride and calcium sulfate), the solubility of both salts will increase [45] (Charola, 2000).

Deteriorative role of salts:

Physical stresses derived from salts can result from two main causes: crystallization pressure and hydration pressure.

When the relative humidity of the air is equal to the deliquescence relative humidity of the salt, a saturation salt solution is established. When the relative humidity drops further, the concentration of the salt increases, and supersaturated solution forms. Once the supersaturation is present, the crystallization process is pronounced. Two types of salt crystals can be found, anhydrous and hydrated. Both exert stresses induced by the crystallization pressure, whereas hydrated salts exert additional pressure, so-called hydration pressure resulting from the volume increase of the hydrated crystals. The crystallization pressure depends on both the temperature and the supersaturation degree, whereas the hydration pressure is related to the temperature and the relative humidity [46].

- Crystallization pressure

The growing of salt crystals inside a pore can exert stress on the pore wall. The repulsive forces between the salt crystal and the pore walls generate this pressure where both interfaces are separated by a supersaturated film [47].

[43] Charola and Bläuer (2015): 119–35.
[44] Peter AYOGU, Matthew Ezugwu, and Fabian Eze, "Principle of Common-Ion Effect and Its Application in Chemistry: A Review.," Journal of Chemistry Letters 1/2 (2020): 77–83.
[45] A Elena Charola, "Salts in the Deterioration of Porous Materials: An Overview," *Journal of the American Institute for Conservation* 39/3 (2000): 327–43.
[46] Frederic Gladstone Bell, *Engineering Geology* (2007).
[47] J. Desarnaud, D. Bonn, and N. Shahidzadeh, "The Pressure Induced by Salt Crystallization in Confinement," *Scientific Reports* 6 (2016): 1–8.

DOI: 10.15774/PPKE.BTK.2024.021

The crystal and stone mineral will repel each other if the energy of the solid/ solid interface is larger than the energy of the sum of solid/ liquid interfaces (the stone mineral with the solution film and the salt crystal with the solution film) [48]. The repelling forces are called disjoining pressure or crystallization pressure [49]. The disjoining pressure contributes to the presence of the solution film that is considered a source of ions that attach to the salt crystal leading to further growth. As long as the solution film exists, more ions will participate in the further growth of salt crystals and apply stresses to the pore wall [50]. The salt crystal will continue growing and exerting pressure until it fills all the pore space. The crystallization pressure will eliminate where there is no solution between the salt crystal and the pore walls. The crystallization pressure can be calculated by the following equation [51]:

$$P = \frac{R*T}{V_m} * ln \frac{C}{C_0}; \ [MPa] \qquad \text{Equation 1}$$

where R is the ideal gas constant [MPa .cm^3. mol^{-1}. K^{-1}], T is the temperature [K], V_m is molar volume of the salt [$cm^3.mol^{-1}$], $\frac{C}{C_0}$ is the supersaturation degree [-].

The damage induced by salt crystallization depends on the crystal shape, supersaturation degree, pore size distribution, and the presence of salt mixtures [52]. La Russa et al. (2013) test two different limestone lithotypes under the crystallization/ solution cycles of sodium sulfate and study the effect of crystallization pressure [53]. The results demonstrate that high crystallization pressure and small pore sizes contribute to more damage to the stone. The heterogeneity of pore size distribution generates several different stressed areas within the stone structure, which leads to more decay.

- Hydration pressure

[48] Hannelore Derluyn et al., "Crystallization of Hydrated and Anhydrous Salts in Porous Limestone Resolved by Synchrotron X-Ray Microtomography," *Nuclear Instruments and Methods in Physics Research, Section B: Beam Interactions with Materials and Atoms* 324 (2014): 102–12.

[49] Jason Houck and George W Scherer, "Controlling Stress from Salt Crystallization," *Fracture and Failure of Natural Building Stones*, 1 (2006): 299–312.

[50] Michael Steiger, "Crystal Growth in Porous Materials - I: The Crystallization Pressure of Large Crystals," *Journal of Crystal Growth* 282/3–4 (2005): 455–69.

[51] Encarnación Ruiz-Agudo, Carlos Rodriguez-Navarro, and Eduardo Sebastián-Pardo, "Sodium Sulfate Crystallization in the Presence of Phosphonates: Implications in Ornamental Stone Conservation," *Crystal Growth & Design* 6/7 (2006): 1575–83.

[52] Serena Andreotti et al., "New Polymer-Based Treatments for the Prevention of Damage by Salt Crystallization in Stone," *Materials and Structures/Materiaux et Constructions* 52/1 (2019): 1–28.

[53] Mauro Francesco La Russa et al., "Study of the Effects of Salt Crystallization on Degradation of Limestone Rocks," Periodico Di Mineralogia 82/1 (2013): 113–27.

DOI: 10.15774/PPKE.BTK.2024.021

Some salts can pick up water molecules to merge with the salt crystal, i.e., the water molecules change the lattice of the salt crystal. Each hydrated salt transforms to a higher hydrated form at a specific temperature when the relative humidity of the air is above the DRH of the less hydrated form of the same salt. Conversely, the lower hydrated form of the salt can be presented if the relative humidity of the air decreases under the DRH of the higher hydrated form of that salt. The most common hydrated salts found in stone blocks are $MgSO_4.7H_2O$ and $Na_2SO_4.10H_2O$, where the latter is the most deteriorative one [54].

Magnesium sulfate can be found in three solid phases depending on the temperature and relative humidity. These are epsomite ($MgSO_4.7H_2O$), hexahydrite ($MgSO_4.6H_2O$), and kieserite ($MgSO_4.H_2O$). Hexahydrite hydrates to epsomite at 24.85◦C and between 50-55% RH [55] (Figure 2.4). However, the DRH of all these phases is high, ranging between 85-95%, and above it, the solution is found in the pores (see Figure 2.4).

Na_2SO_4 can be found as anhydrous salt (thenardite), where it can crystallize at a temperature above 32.4 C°. Under this temperature, it will hydrate to $Na_2SO_4.10H_2O$ (mirabilite) according to the relative humidity. $Na_2SO_4.10H_2O$ will dehydrate to Na_2SO_4 below 32.4 C° depending on the relative humidity (see Figure 2.5)

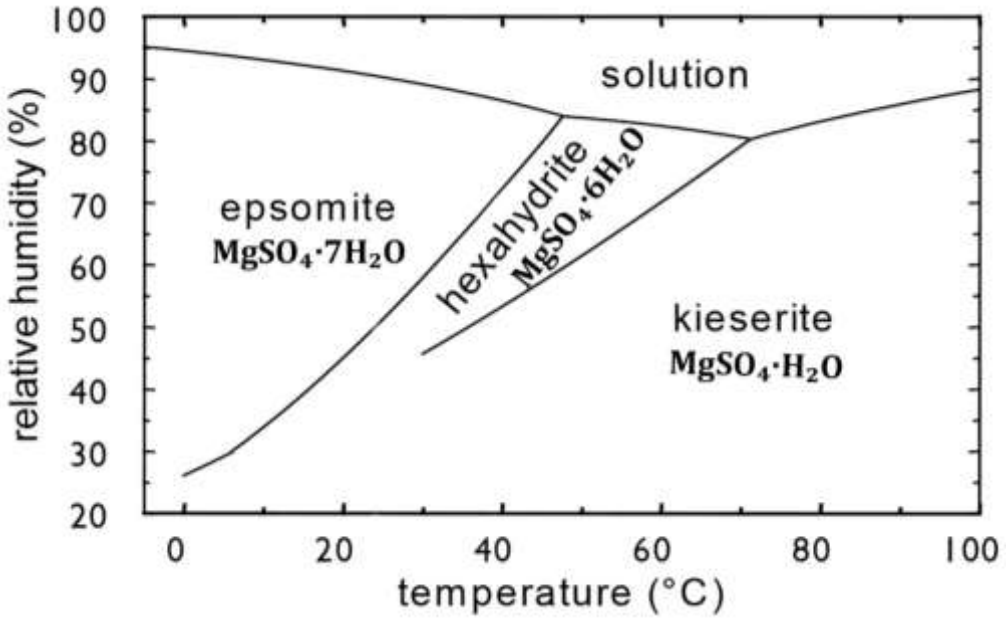

Figure 2. 4 Phase diagram of magnesium sulfate salts as a function of relative humidity and temperature (updated from [Gülker et al. 2007])

[54] E Doehne, C Selwitz, and D Carson, "The Damage Mechanism of Sodium Sulfate in Porous Stone," in *Proceed. of the SALTeXPERT Meeting*, (2002), 27–146.

[55] David T. Vaniman et al., "Magnesium Sulphate Salts and the History of Water on Mars," *Nature* 431/7009 (2004): 663–65.

DOI: 10.15774/PPKE.BTK.2024.021

The hydration process leads to the increased molecular volume of the salt and the expansion causes a "hydration pressure" [56]. The hydrated salts are more deteriorative than anhydrous ones. Ġelik & Aygün (2019) compare the effect of sodium chloride solution (anhydrous salt) and sodium sulfate solution (hydrated salt) on Tufus stones [57]. They observe that sodium sulfate performs more damage to the stone specimen and this damage most likely contributes to the hydration ability of that salt. Although the volume expansion of hydrated salts may increase stone deterioration more than simple salts. Rodriguez-Navarro et al. (2000) suggest that this belief should be reconsidered [58]. They realize that crystallization of $Na_2 SO_4$ induces damage, and the hydration pressure does not exist under their experimental conditions. They confirm that environmental conditions (relative humidity and temperature) define whether crystallization or hydration pressure exists and which of them will induce damage to the stone.

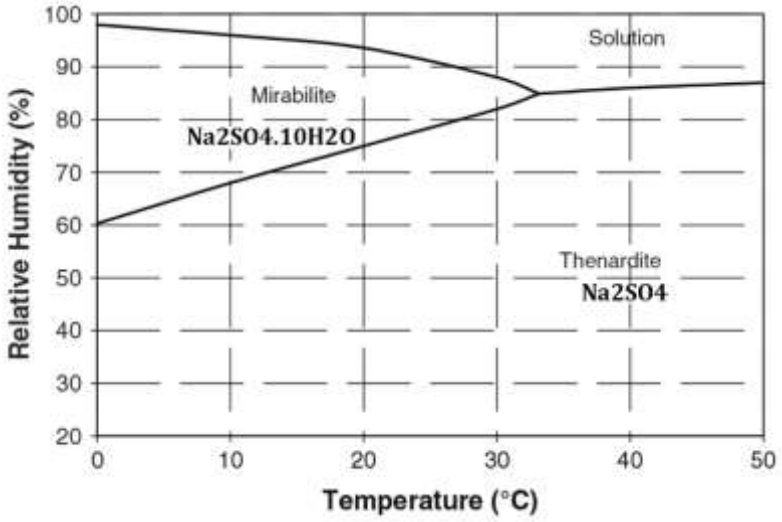

Figure 2. 5 Phase diagram of Sodium sulfate salt as a function of relative humidity and temperature (updated from [Bassuoni and Nehdi 2009])

Efflorescence of salts and their mobility

Efflorescence of salt is present when the evaporation of salt solution occurs on the stone surface. That leads to salt accumulation on the surface without inducing any damage to the stone structure; rather, it can be an aesthetic problem. When the evaporation front moves beneath the surface, crystallization occurs under the surface, called sub-efflorescence. Sub-

[56] S Pombo Fernandez, "Factors Influencing Salt-Induced Weathering of Building Sandstone," (1999) ((Doctoral dissertation):31.

[57] Mustafa Yavuz Çelik and Ahmet Aygün, "The Effect of Salt Crystallization on Degradation of Volcanic Building Stones by Sodium Sulfates and Sodium Chlorides," Bulletin of Engineering Geology and the Environment 78/5 (2019): 3509–29.

[58] Carlos Rodriguez-Navarro, Eric Doehne, and Eduardo Sebastian, "How Does Sodium Sulfate Crystallize? Implications for the Decay and Testing of Building Materials," Cement and Concrete Research 30/10 (2000): 1527–34.

DOI: 10.15774/PPKE.BTK.2024.021

efflorescence will exert stress and damage the stone structure due to the high crystallization pressure. The sub- efflorescence occurs when the evaporation rate is faster than the flow rate of salt solution that moves towards the stone surface. Therefore, the evaporation front is moved inside the stone. Many factors control whether salts will cause efflorescence or sub-efflorescence such as salt solution properties (viscosity and density), environmental conditions (relative humidity and temperature), and porosity of the stone (pore sizes and their distribution). The presence of well-connected micropores with a large surface area promotes rapid evaporation [59]. Those factors also will control the water circulation within the stone, i.e., the wet-dry cycles that lead to crystallization- solution cycles of the salt within the pores.

Salt solution uptake in the stone depends on the viscosity and density of the salt solution. Capillary absorption of the salt solution slows down by increasing the viscosity of the solution [60]. In that case, the evaporation rate will be faster than the capillary absorption resulting in sub-effloresces of the salt. NaCl has low viscosity; however, $MgSO_4$ and Na_2SO_4 have a higher viscosity [61]. Therefore, the latter two salts induce more damage than NaCl that effloresces on the surface. Open porosity, especially the capillary one (less than 5μm), controls the salt solution absorption and determines the extent of damage induced by salt crystallization [62]. Stone with smaller pores will experience a higher crystallization pressure than large ones [63]. Salt crystallization in smaller pores will cause the enlargement of these pores [64].

The presence of salt solution in a part of a building is highly affected by its location. The salt solution can be formed by water if this part is exposed directly to rainfall, rising damp or is in a sheltered area, where the relative humidity and temperature are the critical factors in forming a salt solution. Salts are subjected to capillary transport in their solutions, i.e., salts are mobile through the porous material. The mobility of salts is highly related to their DRH because the salt with a high DRH will crystalize at first, and these salts cannot move. In contrast, the salts with lower DRH can move within the building and further away from their first origin. That

[59] Carlos Rodriguez-Navarro and Eric Doehne, "Salt Weathering: Influence of Evaporation Rate, Supersaturation and Crystallization Pattern," *Earth Surface Processes and Landforms* 24/2–3 (1999): 191–209.

[60] E Ruiz-Agudo et al., "The Role of Saline Solution Properties on Porous Limestone Salt Weathering by Magnesium and Sodium Sulfates," *Environmental Geology* 52/2 (2007): 269–81.

[61] Céline Thomachot-Schneider et al., "Thermal Response of Building Stones Contaminated with Salts," *Construction and Building Materials* 226 (2019): 331–44.

[62] Swe Yu and Chiaki T. Oguchi, "Role of Pore Size Distribution in Salt Uptake, Damage, and Predicting Salt Susceptibility of Eight Types of Japanese Building Stones," *Engineering Geology* 115/3–4 (2010): 226–36.

[63] D. Benavente et al., "Role of Pore Structure in Salt Crystallisation in Unsaturated Porous Stone," *Journal of Crystal Growth* 260/3–4 (2004): 532–44.

[64] Simona Scrivano and Laura Gaggero, "An Experimental Investigation into the Salt-Weathering Susceptibility of Building Limestones," *Rock Mechanics and Rock Engineering* 53/12 (2020): 5329–43.

DOI: 10.15774/PPKE.BTK.2024.021

can be indicated by the moistened areas in a building at high elevations far from the effect of rising dampness. Therefore, salt accumulates in those areas and attract water vapor by their hygroscopicity, making a moistened area. The presence of salts will decrease the evaporation rate and modify the wettability of the surface [65].

The type of presented salt (hydrated or anhydrous), the location of their accumulation (efflorescence on the surface or sub-surface), and the DRH of the salts may imply a variety of alterations within the stone structure. Sato & Hattanji (2018) use two sandstones and a tuff. Each specimen is immersed in a salt solution of NaCl, Na_2SO_4, and $MgSO_4$ (both are hydrated salts) [66]. The specimens experience cycles of crystallization-deliquescence under relative humidity fluctuation. Because of the low DRH value of NaCl, it crystallizes and starts to absorb water vapor making a moisturized stone surface. Na_2SO_4 crystallizes at the surface in its hydrated form $Na_2SO_4.10H_2O$, which hinders water circulation within the stone because the pores are blocked by the expansion volume of $Na_2SO_4.10H_2O$ (whose DRH value is very high). $MgSO_4$ develops sub-efflorescence of $MgSO_4.7H_2O$ and induces damage to the stone specimens. From this experiment, under the relative humidity variations, salts can alter the stone depending on their type and the ambient conditions. Salim et al. (2020) study the crystallization of NaCl on a hydrophobic surface at 70°C [67]. They realize that NaCl crystals create tiny legs that lift the crystals from the stone surface. As such, the salt crystals formed on the stone surface fall down through a process called "self–cleaning". Vazquez et al. (2018) study the effect of temperature on the crystallization of KNO_3 [68]. They recognize that salt creep phenomena occur at low temperatures, where KNO_3 effloresces and is widely spread. However, at high temperatures, the salt efflorescence becomes thicker, and more concentrated which is also related to the stone properties. Dei et al. (1999) investigate the effect of KNO_3 crystallization on different stone lithotypes [69]. They confirm that the deteriorative role of that salt is to accumulate in the pores and clog them up resulting in reducing the porosity of the tested stones.

[65] Mina Bergstad and Nima Shokri, "Evaporation of NaCl Solution from Porous Media with Mixed Wettability," *Geophysical Research Letters* 43/9 (2016): 4426–32.
[66] Masato Sato and Tsuyoshi Hattanji, "A Laboratory Experiment on Salt Weathering by Humidity Change: Salt Damage Induced by Deliquescence and Hydration," Progress in Earth and Planetary Science 5/1 (2018) : 1-10.
[67] Herish Salim et al., "Self-Lifting NaCl Crystals," Journal of Physical Chemistry Letters 11/17 (2020): 7388–93.
[68] Patricia Vazquez, Lucas Sartor, and Céline Thomachot-Schneider, "Influence of Substrate and Temperature on the Crystallization of KNO3 Droplets Studied by Infrared Thermography," Progress in Earth and Planetary Science 5/1 (2018): 1-10.
[69] Luigi Dei et al., "Growth of Crystal Phases in Porous Media," Langmuir 15/26 (1999): 8915–22.

DOI: 10.15774/PPKE.BTK.2024.021

2.2.2 Microorganisms and stone biodeterioration:

Biodeterioration of stone is a worldwide issue that our heritage buildings challenge. Many studies and researches have been conducted to investigate microbial colonization and detect the microorganisms species dwelling on stone surfaces in historic buildings [70]. Various microorganisms commonly colonize the stone surface, causing numerous changes to the stone structure. Understanding biogenic activity of microorganisms and their sequence of presence requires knowing their classification based on energy and carbon sources. From a biological view, the terminology of microorganism types depends on their metabolism, energy, and carbon sources [71]. If the microorganism obtains the energy from light, the prefix "photo" is used in the term; however, if it obtains energy from inorganic chemical substances, the prefix "chemo" is used. When it comes to a carbon source, if the microorganism utilizes CO_2, the prefix "auto" is used in the term; however, if it obtains carbon from organic material, the prefix "hetero" is used, see Figure 2.6. The different types of microorganisms found in stone, their metabolism types, and the products of their metabolism process are exhibited in Table 2.1 (updated from Wakefield & Jones (1998)[72]). The microorganisms that dwell on the stone surface are epilithic; however, others that colonize and grow in

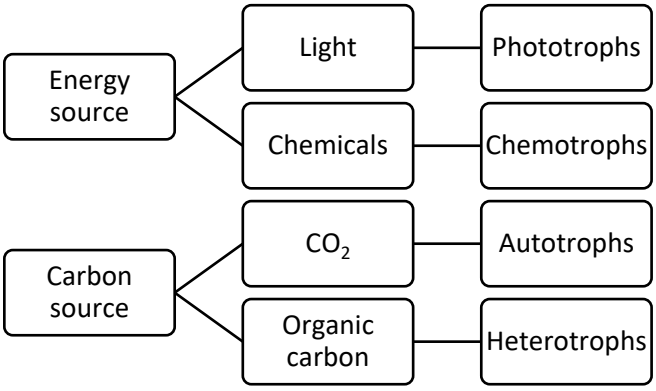

Figure 2. 6 The terminology of microorganisms according to their carbon and energy source

[70] Peter M. Gaylarde and Christine C. Gaylarde, "Algae and Cyanobacteria on Painted Buildings in Latin America," International Biodeterioration and Biodegradation 46/2 (2000): 93–97.
Luisa Tomaselli et al., "Biodiversity of Photosynthetic Micro-Organisms Dwelling on Stone Monuments," International Biodeterioration and Biodegradation 46/3 (2000): 251–58.
W. S. González-Gómez et al., "Calcium Oxalates in Biofilms on Limestone Walls of Maya Buildings in Chichén Itzá, Mexico," Environmental Earth Sciences 77/6 (2018): 1–12.
Ana Catarina Pinheiro et al., "Limestone Biodeterioration: A Review on the Portuguese Cultural Heritage Scenario," Journal of Cultural Heritage 36 (2019): 275–85.
Christine C. Gaylarde et al., "Microbial Biofilms on the Sandstone Monuments of the Angkor Wat Complex, Cambodia," Current Microbiology 64/2 (2012): 85–92.

[71] Lawrence K Wang et al., Environmental Biotechnology, Springer Science & Business Media 10 (2010).
[72] Rachael D Wakefield and Melanie S Jones, "An Introduction to Stone Colonizing Micro-Organisms and Biodeterioration of Building Stone," Quarterly Journal of Engineering Geology and Hydrogeology 31/4 (1998): 301–13.

DOI: 10.15774/PPKE.BTK.2024.021

existing cavities or pores are called endolithic [73].

The stone biodeterioration can be caused by the activities of phototrophs (cyanobacteria, algae, and lichen); heterotrophs (fungi, heterotrophic filamentous bacteria (Actinomyces));

Table 2. 1 Types of microorganisms and their various metabolism updated from (Wakefield and Jones 1998)

Type of metabolism	Type of organism	Energy source	Carbon source	Products
Chemoautotrophy (Chemolithotrophy)	Sulphur- oxidizing bacteria	$H_2S + O_2$ (from sulfur reducers)	CO_2	H_2O + S + C (S output supports growth of other S oxidizers)
		$S+O_2+ H_2O$ (from sulphur oxidizers)	CO_2	H_2SO_4+C (acidification of environment)
	Iron-oxidizing bacteria	$Fe^{2+} + O_2 + H_2O$ (from solution)	CO_2	$Fe^{3+} + OH^-$ (loss of iron, iron may stain)
	Nitrifying bacteria	NH_3+O_2 (from atmosphere or denitrifying bacteria)	CO_2	$HNO_2+ H_2O$+C (acidification of environment)
		HNO_2+O_2 (from atmosphere or denitrifying bacteria)	CO_2	HNO_3 +C
Chemoheterotrophy (heterotrophy) aerobic	Bacteria/fungi/actinomycetes	$O_2+CH_2O+ H_2O$	CH_2O	$CO_2 + H_2O$ + C (CO_2 form H_2CO_3 and precipitate CO_3, C represents organic acids, mucilage and other chelating agents)
Photoautotrophy (aerobic)	Algae and cyanobacteria	$CO_2 + H_2O$ + light	CO_2	O_2+C (cellular components like CH_2O, or mucilage, organic acids and other chelating agents
		$CO_2+ CH_2O+ H_2O$ (dark)	CH_2O	CO_2+H_2O+C

[73] F. Pique M. Cicardi, C. Corti, O. Savadori, "Endolithic Microorganisms in Carbonatic Rocks and Conservations Problems," in *Monument Future : Decay and Conservation of Stone: Proceedings of the 14th IInternational Congress on the Deterioration and Conservation of Stone*, ed. Siegfried Siegesmund Bernhard Middendorf (2020), 516–66.

DOI: 10.15774/PPKE.BTK.2024.021

chemolithotrophs (sulphur bacteria, nitrifying bacteria, iron-oxidizing bacteria); and higher plants.

Phototrophs (Cyanobacteria and algae) are the pioneered that dwell on the stone surface depending upon water availability. They produce organic materials and extracellular polymeric substances (EPS), which form a biofilm. Through the photosynthesis, this biofilm helps them adhere to the stone surface and is considered as a suitable environment for heterotrophs microorganisms (fungi and bacteria) to flourish. As a result, the entire community develops

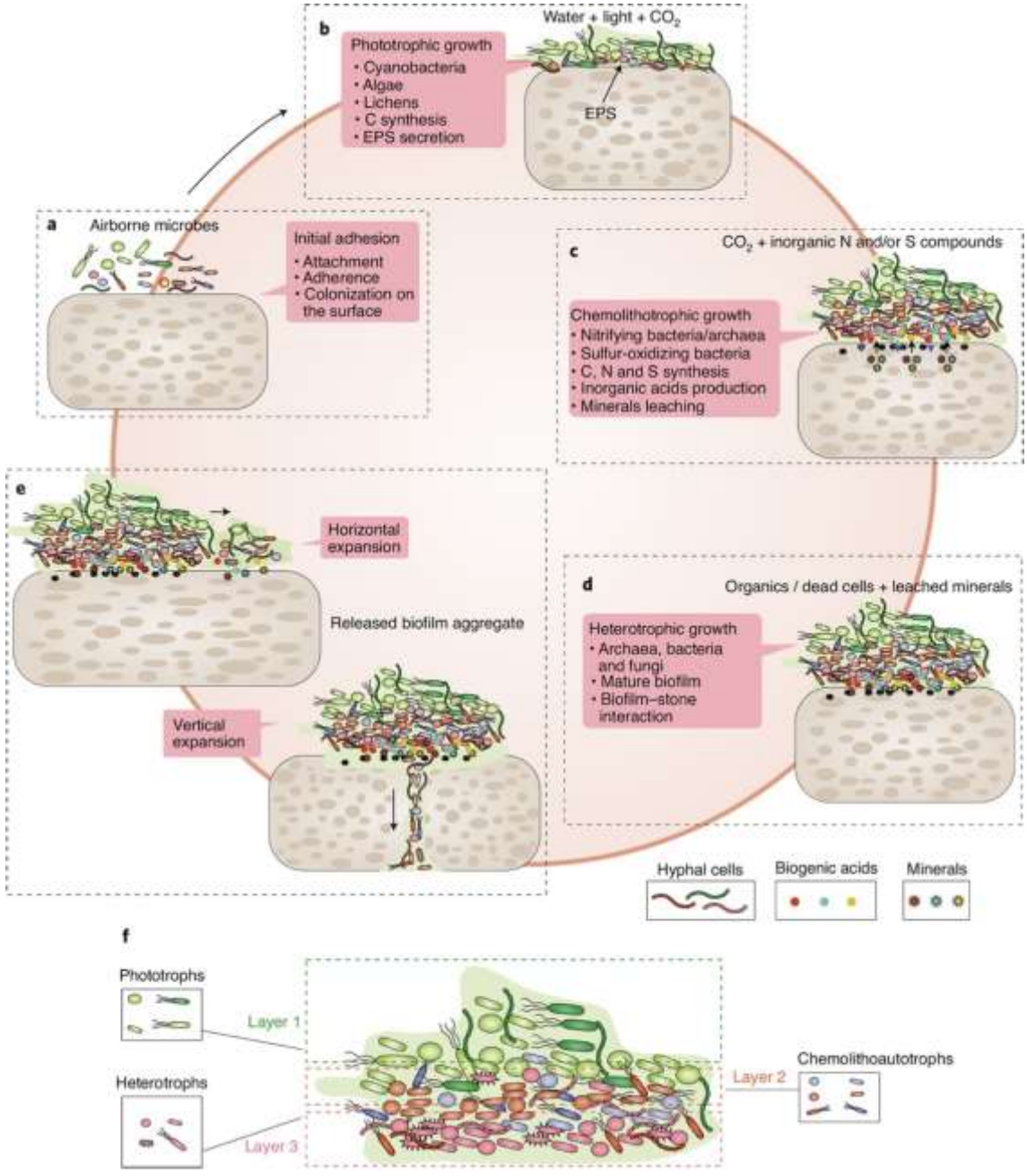

Figure 2. 7 The succession colonization of different type of microorganisms on the stone surface, the figure is taken from Liu et al. (2020)

DOI: 10.15774/PPKE.BTK.2024.021

into a complex biofilm of various species, algae lichens, fungi, and bacteria [74]. The succession of different microorganisms and the development of the biofilm on the stone surface are exhibited in Figure 2.7. All these species extract EPS to form the biofilm that acts interactive medium between the stone surface and the microorganisms. These microorganisms build the biofilm to protect themselves from desiccation, osmotic stress, temperature, solar radiation stresses, toxic air pollutants, and biocidal treatments [75].

Although EPS plays a deteriorative role in the stone surface by chelating process, it can also protect the stone surface from environmental conditions [76]. The biofilm can transform into a patina and cause more coloration to the stone surface because they contain dust, ash, dirt, pollen, etc. [77]. EPS can induce mechanical stress within the stone structure by its swelling and contraction due to moisture sorption [78]. The biofilm leads to alterations in porosity, permeability, evaporation properties of the stone [79], wettability of minerals [80], and capillary water uptake [81]. It buffers the temperature variations, reducing the thermal stress inside the stone [82].

The role of microorganisms in biodeterioration:

- Heterotrophs and biodeterioration:

Fungi are heterotrophic aerobic microorganisms that can be epilithic or endolithic stone dwellers [83]. The fungal species commonly found in the stones include filamentous fungi

[74] Patrick D Martino, "What about Biofilms on the Surface of Stone Monuments?," in *The Open Conference Proceedings Journal*, 7 (2016):14-28.

[75] H A Viles et al., "What Is the State of Our Knowledge of the Mechanisms of Deterioration and How Good Are Our Estimates of Rates of Deterioration?," in Saving Our Architectural Heritage. Conservation of Historic Stone Structures, 1997, 95–112.

76 Davide Gulotta et al., "Biofilm Colonization of Metamorphic Lithotypes of a Renaissance Cathedral Exposed to Urban Atmosphere," Science of The Total Environment 639 (2018): 1480–90.

77 A Kemmling et al., "Biofilms and Extracellular Matrices on Geomaterials," Environmental Geology 46/3 (2004): 429–35.

78 Elżbieta Stanaszek-Tomal, "Environmental Factors Causing the Development of Microorganisms on the Surfaces of National Cultural Monuments Made of Mineral Building Materials," Coatings 10/12 (2020): 1203.

79 Ji-Dong Gu and Yoko Katayama, "Microbiota and Biochemical Processes Involved in Biodeterioration of Cultural Heritage and Protection," Microorganisms in the Deterioration and Preservation of Cultural Heritage, (2021), 37-58.

[80] Mahvash Karimi et al., "Investigating Wettability Alteration during MEOR Process, a Micro/Macro Scale Analysis," *Colloids and Surfaces B: Biointerfaces* 95 (2012): 129–36.

[81] Thomas Warscheid and Hans Leisen, "Microbiological Studies on Stone Deterioration and Development of Conservation Measures at Angkor Wat," in Biocolonization of Stone: Control and Preventive Methods, Proceedings from the MCI Workshop Series, vol. 2 (2011), 1–18.

[82] Stephen McCabe et al., "Building Sandstone Surface Modification by Biofilm and Iron Precipitation: Emerging Block-scale Heterogeneity and System Response," Earth Surface Processes and Landforms 40/1 (2015): 112–22.

[83] Frank H Gleason et al., "The Roles of Endolithic Fungi in Bioerosion and Disease in Marine Ecosystems. I. General Concepts," Mycology 8/3 (2017): 205–15.

DOI: 10.15774/PPKE.BTK.2024.021

(ubiquitous hyphomycetes and coelomycetes) and microcolony fungi (black yeasts and meristematic fungi)[84].

Fungi can induce physical and chemical changes in the stone matrix. The growing of fungal hyphae is the most mechanical deteriorative role. The hyphae can penetrate the stone and cause considerable stress in its structure by excreting a force called "turgor pressure". Turgor pressure is a hydrostatic pressure that helps the hyphae to penetrate and reach the nutrient within the stone [85]. This pressure can reach 8 MPa [86]. The hyphae penetration leads to the cracking of the stone matrix [87].

Fungi produce inorganic and organic acids (oxalic, lactic, and gluconic) that play a fundamental role in biodeterioration. The organic acids act as chelating agents [88] and leach many calcium, silicon, iron, manganese, or magnesium [89]. De la Torre et al. (1992) investigate the metabolism effect of fungi on sandstone, granite, and limestone [90]. They find the organic acids released by fungi (oxalic, lactic, and gluconic) lead to form many of insoluble salts such as calcium, magnesium, and ferric oxalate as well as calcium citrates which confirms the chelating ability of those organic acids. On the other hand, fungi contribute to the precipitation of secondary calcite during their life and death, which involves in hardening of the stone matrix [91]. Fungi metabolism produces oxalic acid, which dissolves the calcite minerals, resulting in the

[84] Stefanie Scheerer, Microbial Biodeterioration of Outdoor Stone Monuments: Assessment Methods and Control Strategies (2008):44.
[85] Thomas Dornieden and Anna A Gorbushina, "New Methods to Study the Detrimental Effects of Poikilotroph Microcolonial Micromycetes (PMM) on Building Materials," in Proceedings of the 9th International Congress on Deterioration and Conservation of Stone (2000), 461–68.
[86] Richard J Howard et al., "Penetration of Hard Substrates by a Fungus Employing Enormous Turgor Pressures," Proceedings of the National Academy of Sciences 88/24 (1991): 11281–84.
[87] Xiaobo Liu et al., "Microbial Deterioration and Sustainable Conservation of Stone Monuments and Buildings," Nature Sustainability 3/12 (2020): 991–1004.
[88] E P Burford, M Fomina, and G M Gadd, "Fungal Involvement in Bioweathering and Biotransformation of Rocks and Minerals," Mineralogical Magazine 67/6 (2003): 1127–55.
Nadège Liaud et al., "Exploring Fungal Biodiversity: Organic Acid Production by 66 Strains of Filamentous Fungi," Fungal Biology and Biotechnology 1/1 (2014): 1–10.
[89] P S Griffin, Norman Indictor, and Robert J Koestler, "The Biodeterioration of Stone: A Review of Deterioration Mechanisms, Conservation Case Histories, and Treatment," International Biodeterioration 28/1–4 (1991): 187–207.
[90] Ma de la Torre et al., "Biochemical Mechanisms of Stone Alteration Carried out by Filamentous Fungi Living in Monuments," Biogeochemistry 19/3 (1992): 129–47.
[91] E P Verrecchia, J-L Dumont, and K E Rolko, "Do Fungi Building Limestones Exist in Semi-Arid Regions?," *The Science of Nature* 77/12 (1990): 584–86.
Euan P Burford, Stephen Hillier, and Geoffrey M Gadd, "Biomineralization of Fungal Hyphae with Calcite (CaCO3) and Calcium Oxalate Mono-and Dihydrate in Carboniferous Limestone Microcosms," Geomicrobiology Journal 23/8 (2006): 599–611.
Saskia Bindschedler, Guillaume Cailleau, and Eric Verrecchia, "Role of Fungi in the Biomineralization of Calcite," Minerals 6/2 (2016): 41.

DOI: 10.15774/PPKE.BTK.2024.021

formation of calcium oxalates and enrichment of the stone with free carbonate anions. These free carbonate anions will react somewhere with calcium in the stone and form calcium carbonate as a secondary precipitant. When fungi decompose within the stone, the calcium oxalates will be oxidized by the bacteria and converted to calcium carbonate as a form of secondary precipitation [92]. Fungi can contribute to the chromatic alteration of stone surfaces as the darkening of the stone surface by the presence of black fungi [93]. Besides, fungi can be responsible for the blackening of gypsum in urban environments [94]. The melanin within their cell, particularly black yeasts and meristematic fungi, is responsible for the black stains [95]. Melanin plays a fundamental role in protecting the fungi from diverse factors such as solar radiation (UV light), oxidant-mediated damages, temperature extremes, hydrolytic enzymes, heavy metal toxicity, and resistance to antifungal agents [96].

The heterotroph bacteria commonly found in the biofilms of colonized stone are Actinomyces (filamentous bacteria) [97]. They play a fundamental role in enhancing biodeterioration. These bacteria are highly tolerant to salt and they live on the stone surface with the presence of salts, which increase the deterioration [98]. The mechanical role of Actinomyces hyphae is similar to fungi hyphae [99]. Their hyphae can penetrate the fissures and fill the pores that apply pressure

[92] Geoffrey M Gadd, "Fungal Production of Citric and Oxalic Acid: Importance in Metal Speciation, Physiology and Biogeochemical Processes," Advances in Microbial Physiology 41 (1999): 47–92.

[93] Iba Patrizia Santo et al., "Black on White: Microbial Growth Darkens the External Marble of Florence Cathedral," Applied Sciences 11/13 (2021): 6163.

A A Gorbushina et al., "Role of Black Fungi in Color Change and Biodeterioration of Antique Marbles," Geomicrobiology Journal 11/3–4 (1993): 205–21.

[94] M Bekker et al., "Quantifying Discoloration Caused by the Indoor Fungus Penicillium Rubens on Building Material at Controlled Humidity," Building and Environment 90 (2015): 60–70.

[95] Francesca Cappitelli et al., "Synthetic Consolidants Attacked by Melanin-Producing Fungi: Case Study of the Biodeterioration of Milan (Italy) Cathedral Marble Treated with Acrylics," Applied and Environmental Microbiology 73/1 (2007): 271–77.

[96] Tatiana A Belozerskaya, Natalya N Gessler, and Andrey A Aver'yanov, "Melanin Pigments of Fungi," Fungal Metabolites 2017 (2017): 263–91.

Sandra R Pombeiro-Sponchiado et al., "Production of Melanin Pigment by Fungi and Its Biotechnological Applications," Melanin, 2017, 47–75.

Nakarin Suwannarach et al., "Characterization of Melanin and Optimal Conditions for Pigment Production by an Endophytic Fungus, Spissiomyces Endophytica SDBR-CMU319," PLoS One 14/9 (2019): e0222187.

[97] Th Dornieden, A A Gorbushina, and W E Krumbein, "Biodecay of Cultural Heritage as a Space/Time-Related Ecological Situation—an Evaluation of a Series of Studies," International Biodeterioration & Biodegradation 46/4 (2000): 261–70.

Maria Saarela et al., "Heterotrophic Microorganisms in Air and Biofilm Samples from Roman Catacombs, with Special Emphasis on Actinobacteria and Fungi," International Biodeterioration & Biodegradation 54/1 (2004): 27–37.

[98] Hesham Abdulla et al., "Characterisation of Actinomycetes Isolated from Ancient Stone and Their Potential for Deterioration," Pol J Microbiol 57/3 (2008): 213–20.

[99] Laurenz Schröer et al., "The Capabilities of Bacteria and Archaea to Alter Natural Building Stones–A Review," *International Biodeterioration & Biodegradation* 165 (2021): 105329.

DOI: 10.15774/PPKE.BTK.2024.021

inside the stone structure [100]. Actinomyces take part in the discoloration of the stone to dark color (ranging from brown to black) because of the melanin pigment in their cells [101].

- Phototrophs and biodeterioration:

Cyanobacteria and algae are microorganisms that live on the stone surface in which moisture and enough light are available. They produce their nutrition by the photosynthesis process, so the presence of light is a key factor for flourishing the epilithic or endolithic cyanobacteria [102]. However, they are more tolerant to the lack of light than algae; therefore, they can be found deeper in the stone and the internal walls [103]. The color of cyanobacteria is various such as green, red, orange, blue, blue-green, yellow, and yellow-red. The photosynthetic pigments in their cells are responsible for those colors [104]. The photosynthetic pigments present in algae make them appear in various colors from green, red to black. However, algae and cyanobacteria exhibit a high response to the environment, their color (pigments content) depends on the environmental conditions surrounding them such as availability of nutrition, and temperature [105]. For example, some species produce brown pigments to protect themselves from UV sunlight on external facades exposed to high temperatures from the sun [106]. Cyanobacteria and algae can produce green biofilm in high humid areas; however, in low humidity areas, the biofilm appears in a less green color [107].

Cyanobacteria and algae contribute to biophysical and biochemical deterioration of the stone they colonized. The biogeochemical process includes the release of organic acids such as lactic, oxalic, succinic, acetic, glycolic, and pyruvic [108] that cause etching and dissolution of calcite

[100] Agnes Mihajlovski et al., "An Overview of Techniques for the Characterization and Quantification of Microbial Colonization on Stone Monuments," Annals of Microbiology 65/3 (2015): 1243–55.
[101] Giulia Caneva et al., Plant Biology for Cultural Heritage: Biodeterioration and Conservation (2008):70.
[102] Patrizia Albertano, "Cyanobacterial Biofilms in Monuments and Caves," in Ecology of Cyanobacteria II (2012), 317–43.
[103] Franco Palla and Giovanna Barresi, *Biotechnology and Conservation of Cultural Heritage* (2017):7.
Wan-Loy Chu, Shao-Yang Tneh, and Stephen Ambu, "A Survey of Airborne Algae and Cyanobacteria within the Indoor Environment of an Office Building in Kuala Lumpur, Malaysia," *Grana* 52/3 (2013): 207–20.
[104] Dinesh Kumar Saini, Sunil Pabbi, and Pratyoosh Shukla, "Cyanobacterial Pigments: Perspectives and Biotechnological Approaches," Food and Chemical Toxicology 120 (2018): 616–24.
[105] Hikaru Endo et al., "Interactive Effects of Nutrient Availability, Temperature, and Irradiance on Photosynthetic Pigments and Color of the Brown Alga Undaria Pinnatifida," *Journal of Applied Phycology* 29/3 (2017): 1683–93.
[106] Christine C Gaylarde, "Influence of Environment on Microbial Colonization of Historic Stone Buildings with Emphasis on Cyanobacteria," Heritage 3/4 (2020): 1469–82.
[107] Akiko Ogawa et al., "Microbial Communities on Painted Wet and Dry External Surfaces of a Historic Fortress in Niteroi, Brazil," International Biodeterioration & Biodegradation 123 (2017): 164–73.
B O Ortega-Morales et al., "Orientation Affects Trentepohlia-Dominated Biofilms on Mayan Monuments of the Rio Bec Style," *International Biodeterioration & Biodegradation* 84 (2013): 351–56.
[108] Jagjit Singh, *Building Mycology: Management of Decay and Health in Buildings* (2006):221.

DOI: 10.15774/PPKE.BTK.2024.021

and precipitation of calcium carbonate [109]. Aerobic microorganisms produce carbon dioxide by their respiration, which is in turn converted to carbonic acids (by the presence of water) that lead to acidic erosion in the stone [110]. Cyanobacteria and algae cells are surrounded by mucilage cover that plays an important role in water retention within the cell during the desiccation period and can absorb moisture [111]. This mucilage cover is highly affected by the presence of water, where it exhibits considerable swelling and shrinkage by wetting and drying cycles [112]. The shrinkage and swelling of mucilage cover lead to loosening mineral grains and fatigue in the stone structure [113]. As discussed before, cyanobacteria and algae are the first colonizers of the stone. The development and enrichment of their biofilm by their metabolism products will support the establishment of the heterotrophic microorganisms that will increase the deterioration rate of the stone [114].

Lichens are composite microorganisms in which a symbiotic relationship between mycobiont (fungi) and photobiont (algae or cyanobacteria) exists [115]. The photobiont provides carbon to the mycobiont by photosynthesis and protects it from light exposure [116]. The lichens that live on rocks are known as "Saxicolous lichens". They can be epilithic or endolithic [117]. They are very sensitive to air pollution, especially sulphur dioxide [118], and cannot grow in polluted areas.

[109] M S Jones, R D Wakefield, and G Forsyth, "A Study of Biologically Decayed Sandstone with Respect to Ca and Its Distribution," in *Proceedings of the 9th International Congress on Deterioration and Conservation of Stone* (2000), 473–81.

[110] Maria Filomena Macedo et al., "Biodiversity of Cyanobacteria and Green Algae on Monuments in the Mediterranean Basin: An Overview," *Microbiology* 155/11 (2009): 3476–90.

[111] Sanjeeva Nayaka, Kiran Toppo, and Sushma Verma, "Adaptation in Algae to Environmental Stress and Ecological Conditions," in *Plant Adaptation Strategies in Changing Environment* (2017), 103–15.

[112] Federico Rossi and Roberto De Philippis, "Role of Cyanobacterial Exopolysaccharides in Phototrophic Biofilms and in Complex Microbial Mats," *Life* 5/2 (2015): 1218–38.
Francisca Sánchez-Antón and Antonia D Asencio-Martínez, "Participation of Cyanophyceae in the Biodeterioration of the Stones of the Santo Domingo College in Orihuela, Alicante (SE Spain)," *Algological Studies*, 2007, 95–108.

[113] S Leite Magalhães and M A Sequeira Braga, "Biological Colonization Features on a Granite Monument from Braga (NW, Portugal)," in Proceedings of the 9th International Congress on Deterioration and Conservation of Stone (2000), 521–29.

[114] P Albertano et al., "Polysaccharides as a Key Step in Stone Bio-Erosion," in Proceedings of the 9th International Congress on Deterioration and Conservation of Stone (2000), 425–32.

[115] Gamze AKBULUT and Atila YILDIZ, "An Overview to Lichens: The Nutrient Composition of Some Species," Kafkas Üniversitesi Fen Bilimleri Enstitüsü Dergisi 3/2 (2010): 79–86.

[116] ADGeoffrey Gadd, "Fungi and Their Role in the Biosphere," in Encyclopedia of Ecology (2008), 1709–17.

[117] Frank Bungartz and Laurence A J Garvie, "Anatomy of the Endolithic Sonoran Desert Lichen Verrucaria Rubrocincta Breuss: Implications for Biodeterioration and Biomineralization," The Lichenologist 36/1 (2004): 55–73.

[118] Franc Batič, "Bioindication of Sulphur Dioxide Pollution with Lichens," in *Protocols in Lichenology* (2002), 483–503.
M R D Seaward, "Lichens and Sulphur Dioxide Air Pollution: Field Studies," *Environmental Reviews* 1/2 (July 1, 1993): 73–91.

DOI: 10.15774/PPKE.BTK.2024.021

Lichen species are different from each other by the concentrations of pollutants that affect their growth [119]. Their growth is used to estimate the air quality of a particular area [120].

The biodeterioration role of lichens is the same as that of fungi, algae, and cyanobacteria. The photobiont part produces carbonic acid due to its respiration, which can dissolve the carbonate stones. As a result of fungal hyphae penetration of the lichen, micro fractures and fissures can be produced within the stone structure. The mycobiont produces organic acids such as oxalic, lactic, and gluconic that acts as chelating agents for the stone minerals. Oxalic acid is one of the most frequently reported acids in stone decay because it reacts with the calcium in the stone to form calcium oxalate [121]. Not only calcium oxalate is the new-formed mineral that is detected due to oxalic acid by lichen. Manganese, ferric, copper, and magnesium oxalate can be recognized according to the stone composition [122]. Because calcium oxalate is 10 times less soluble than calcite, the formation of calcium oxalate gives rise to the potential protective role of lichens for stone surfaces [123]. The calcium oxalate can protect the stone from atmospheric weathering regardless of its undesirable aesthetic appearance on the stone surface [124]. However, not all species of rock-dwelled lichens have this feature because the biomineralization is related to metabolic products of the mycobiont of the lichen [125]. In their experiment, they approve that

[119] T H Nash, "Lichen Sensitivity to Air Pollution," in *Lichen Biology*, ed. I I I Nash Thomas H., 2nd ed. (Cambridge, 2008), 299–314.

[120] Marcelo Enrique Conti and Gaetano Cecchetti, "Biological Monitoring: Lichens as Bioindicators of Air Pollution Assessment—a Review," Environmental Pollution 114/3 (2001): 471–92.

[121] González-Gómez et al., "Calcium Oxalates in Biofilms on Limestone Walls of Maya Buildings in Chichén Itzá, Mexico." ,77 (2018): 1-12.

Annalaura Casanova Municchia et al., "Evaluation of the Biodeterioration Activity of Lichens in the Cave Church of Üzümlü (Cappadocia, Turkey)," *International Biodeterioration & Biodegradation* 127 (2018): 160–69.

Carmen Ascaso, "Lichens on Rock Substrates: Observation of the Biomineralization Processes," *Bibliotheca Lichenologica*75 (2000): 127-135.

Products in Four Lichen Species Growing on Sandstone in Western Norway," *The Lichenologist* 34/5 (2002): 429–40.

[122] Paola Adamo and Pietro Violante, "Weathering of Rocks and Neogenesis of Minerals Associated with Lichen Activity," *Applied Clay Science* 16/5–6 (2000): 229–56.

Ornella Salvadori and Annalaura C Municchia, "The Role of Fungi and Lichens in the Biodeterioration of Stone Monuments," in *The Open Conference Proceedings Journal*, 7 (2016).

[123] Annalaura Casanova Municchia et al., "Evaluation of the Biodeterioration Activity of Lichens in the Cave Church of Üzümlü (Cappadocia, Turkey)," *International Biodeterioration & Biodegradation* 127 (2018): 160–69.

[124] Alessandra Bonazza et al., "Oxalate Patinas on Stone Monuments in the Venetian Lagoon: Characterization and Origin," *International Journal of Architectural Heritage* 9/5 (2015): 542–52.

Daniela Pinna, "Biofilms and Lichens on Stone Monuments: Do They Damage or Protect?," *Frontiers in Microbiology* 5 (2014): 133.

[125] Virginia Souza-Egipsy et al., "Chemical and Ultrastructural Features of the Lichen-Volcanic/Sedimentary Rock Interface in a Semiarid Region (Almeria, Spain)," The Lichenologist 34/2 (2002): 155–67.

DOI: 10.15774/PPKE.BTK.2024.021

lichens retain water in the hyphae, which helps in reducing the thermal stresses in the limestone surface compared with a stone without lichens [126].

- Chemolithotrophs and biodeterioration:

Chemolithotrophs use inorganic materials such as sulphur, ammonium, and iron (Fe^{+2}) as a source of energy [127]. Sulphur, nitrifying, and iron oxidizer bacteria are the chemolithotrophs bacteria that participate in stone biodeterioration. Sulphur bacteria are usually found in urban and industrial areas [128], because there is abundant sulphur in the atmosphere. They can produce sulphuric acid that is aggressive to carbonate stones [129] and causes serious erosion [130]. Sulphuric acid reacts with calcite and forms gypsum [131]. Nitrifying bacteria use ammonium released by the decomposition of organic mass within the stone, or presented in the atmosphere as a source of energy [132]. They can oxidize the ammonia and convert it to nitrate [133]. The deteriorative role of nitrifying bacteria is the enrichment of the stone with nitrate [134] as well as forming acidic attacks by nitric acid that is formed during the oxidizing process of ammonium [135]. The nitrate is well-recognized on the stone surface, and it is characterized by high hygroscopicity so it can

[126] N E A Carter and H A Viles, "Experimental Investigations into the Interactions between Moisture, Rock Surface Temperatures and an Epilithic Lichen Cover in the Bioprotection of Limestone," Building and Environment 38/9–10 (2003): 1225–34.

[127] Elham Kazemi et al., "Chemolithotroph Bacteria: From Biology to Application in Medical Sciences," *Crescent Journal of Medical and Biological Sciences* 8/2 (2021):81-89.

[128] Sophia Papida, William Murphy, and Eric May, "The Use of Sound Velocity Determination for the Non-Destructive Estimation of Physical and Microbial Weathering of Limestones and Dolomites," in Proceedings of the 9th International Congress on Deterioration and Conservation of Stone (2000), 609–17.

[129] Xianshu Li et al., "Enumeration of Sulfur-Oxidizing Microorganisms on Deteriorating Stone of the Angkor Monuments, Cambodia," *Microbes and Environments*, 23/4 (2008):293-8.

[130] Elisabetta Zanardini et al., "Nutrient Cycling Potential within Microbial Communities on Culturally Important Stoneworks," *Environmental Microbiology Reports* 11/2 (2019): 147–54.

[131] Christopher J McNamara and Ralph Mitchell, "Microbial Deterioration of Historic Stone," Frontiers in Ecology and the Environment 3/8 (2005): 445–51.

Giancarlo Ranalli et al., "The Use of Microorganisms for the Removal of Sulphates on Artistic Stoneworks," International Biodeterioration & Biodegradation 40/2–4 (1997): 255–61.

[132] Ji-Dong Gu and Yoko Katayama, "Microbiota and Biochemical Processes Involved in Biodeterioration of Cultural Heritage and Protection," *Microorganisms in the Deterioration and Preservation of Cultural Heritage*, (2021):37.

[133] Reiner Mansch and Eberhard Bock, "Biodeterioration of Natural Stone with Special Reference to Nitrifying Bacteria," *Biodegradation* 9/1 (1998): 47–64.

[134] Xiaobo Liu et al., "Microbial Deterioration and Sustainable Conservation of Stone Monuments and Buildings," Nature Sustainability 3/12 (2020): 991–1004.

[135] M Bartolini and M Monte, "Chemiolithotrophic Bacteria on Stone Monuments: Cultural Methods Set Up," in Proceedings of the 9th International Congress on Deterioration and Conservation of Stone (2000), 453–60.

Han Meng, Yoko Katayama, and Ji-Dong Gu, "More Wide Occurrence and Dominance of Ammonia-Oxidizing Archaea than Bacteria at Three Angkor Sandstone Temples of Bayon, Phnom Krom and Wat Athvea in Cambodia," International Biodeterioration & Biodegradation 117 (2017): 78–88.

DOI: 10.15774/PPKE.BTK.2024.021

retain moisture on the stone surface at low humidity [136]. The nitrifying and sulphur bacteria in urban areas facilitate the fixation of atmospheric pollutants on the stone surface and consequently increase the rate of deterioration [137]. Iron oxidizing bacteria utilize Fe^{+2} to obtain energy for their metabolism [138]. In the stone minerals bearing Fe^{+2}, iron-oxidizing bacteria can oxidize Fe^{+2} to Fe^{+3}, which then reacts with oxygen to form iron oxide (Fe_2O_3) that chromatically alters the stone surface [139].

- Higher plants

Higher plants or vascular plants have distinguished roots, stems, and leaves. The growth of higher plants in historic buildings and monuments is very common and forms a challenging issue in many buildings [140]. The climatic conditions (temperature, rainfall, etc.), light, and nutrition (organic nutrition from decomposed microorganisms or inorganic nutrition that is available in the stone) are key factors controlling the growth of higher plants in historic buildings [141]. The conservation state of the building plays a crucial role in facilitating the growth of higher plants [142]. Higher plants can induce damage by biophysical and biochemical

[136] Brenda J Little and Jason S Lee, Microbiologically Influenced Corrosion, in *International Materials Reviews*, 59 (2009).
Xinghua Ding et al., "Microbiome and Nitrate Removal Processes by Microorganisms on the Ancient Preah Vihear Temple of Cambodia Revealed by Metagenomics and N-15 Isotope Analyses," Applied Microbiology and Biotechnology 104/22 (2020): 9823–37.
[137] C Balland-Bolou-Bi et al., "Effect of Microorganism Activities in a Polluted Area on the Alteration of Limestone Used in Historical Buildings," SCIENCE AND ART: A FUTURE FOR STONE (2016):25.
[138] David Emerson, "The Role of Iron-Oxidizing Bacteria in Biocorrosion: A Review," Biofouling 34/9 (2018): 989–1000.
[139] Horst Czichos, Tetsuya Saito, and Leslie E Smith, *Springer Handbook of Metrology and Testing* (2011):816.
Wolfgang E Krumbein, "Patina and Cultural Heritage–a Geomicrobiologist's Perspective," Cult Herit Res a Pan-European Chall (2003): 39–47.
[140] Zohreh Hosseini et al., "Substrate Preferences of Ruderal Plants in Colonizing Stone Monuments of the Pasargadae World Heritage Site, Iran," Sustainability 13/16 (2021): 9381.
Chan Hee Lee et al., "Deterioration Assessment and Conservation of a Heavily Degraded Korean Stone Buddha from the Ninth Century," Studies in Conservation 51/4 (2006): 305–16.
M Dalimi et al., "Vegetations as Biodeterioration Agents on Archaeological Stones: Comparative Study of Plant Species Found on the Walls of Some Moroccan Historical Monuments," 3 (2014):193-204.
Meriem Benharbit Et Al., "Checklist And Role Of Vegetation In The Deterioration Of Archaeological Sites Contribution To The Knowledge Of The Plants Of Chellah (Rabat, Morocco)," Plant Cell Biotechnology And Molecular Biology (2021): 124–40.
J S Bhargav, R C Mishra, and C R Das, "Environmental Deterioration of Stone Monuments of Bhubaneswar, the Temple City of India," Studies in Conservation 44/1 (1999): 1–11.
[141] Selvam Vinodh Kumar et al., "ERADICATION OF VEGETAL GROWTH AND SYSTEMATIC SCIENTIFIC CONSERVATION APPROACH OF BALLALESHWAR TEMPLE, TRIMBAKESHWAR (INDIA).," *International Journal of Conservation Science* 7/3 (2016): 615-626
[142] Marcello Lisci, Michela Monte, and Ettore Pacini, "Lichens and Higher Plants on Stone: A Review," *International Biodeterioration & Biodegradation* 51/1 (2003): 1–17.

DOI: 10.15774/PPKE.BTK.2024.021

processes [143]. The biophysical process is caused by the growth of the root and trunk inside the wall. Their continuous growth and expansion exert pressure on the surrounding areas [144] . Roots typically follow the least resistant areas in the wall (joints, fissures, or cracks), which gradually reduces the cohesion inside the wall [145]. The biochemical role of higher plants involves the dissolution and chelating of cations from the stone. The acidic tips of the root keep a layer of hydrogen ions (H^+) which in turn can be exchanged with metal cations in the stone, where these cations are important nutrition for the plant [146]. The roots of plants exert several substances that are aggressive to the stone such as amino acids, sugars, organic acids, and enzymes [147]. The respiration process of plants also causes acidic dissolution by carbonic acid that reacts with calcium and magnesium carbonate, which are insoluble, and soluble calcium and magnesium bicarbonate will be formed [148].

2.3 Weathering factors

2.3.1 Water as a promoting deterioration factor

Water can be found inside stone pores as liquid or vapor depending upon both the ambient conditions and the intrinsic properties of the stone. The interaction between stone, ambient conditions, and water phase outlines the durability of the stone blocks [149] as well as its damage susceptibility to frost action [150], salt weathering [151], or microorganisms colonization [152]. The presence of liquid water inside stone blocks can be from different sources such as rain, leakage

[143] Jamila Dahmani et al., "Vascular Plants Census Linked to the Biodeterioration Process of the Portuguese City of Mazagan in El Jadida, Morocco," *Journal of King Saud University-Science* 32/1 (2020): 682–89.
[144] G Caneva et al., "Tree Roots and Damages in the Jewish Catacombs of Villa Torlonia (Roma)," *Journal of Cultural Heritage* 10/1 (2009): 53–62.
Christopher Overbeke, "Do Trees Really Cause so Much Damage to Property?," *Journal of Building Appraisal* 3/4 (2008): 247–58.
[145] Elisabetta Princi, *Handbook of Polymers in Stone Conservation* (2014):108.
[146] A K Mishra, Kamal K Jain, and K L Garg, "Role of Higher Plants in the Deterioration of Historic Buildings," *Science of the Total Environment* 167/1–3 (1995): 375–92.
[147] M T Almeida, T Mouga, and P Barracosa, "The Weathering Ability of Higher Plants. The Case of Ailanthus Altissima (Miller) Swingle," International Biodeterioration & Biodegradation 33/4 (1994): 333–43.
[148] Riccardo Motti and Adriano Stinca, "Analysis of the Biodeteriogenic Vascular Flora at the Royal Palace of Portici in Southern Italy," International Biodeterioration & Biodegradation 65/8 (2011): 1256–65.
[149] G Cultrone et al., "Influence of Pore System Characteristics on Limestone Vulnerability: A Laboratory Study," *Environmental Geology* 54/6 (2008): 1271–81.
[150] Martin Ondrasik and Peter P Hudec, "Freezing Expansion and Thermodynamics of Pore Water in Rock Deterioration," in *CD Proceedings of 9-Th IAEG Congress, Durban, South Africa* (2002):443-451.
[151] Carlos Alves et al., "Limestones under Salt Decay Tests: Assessment of Pore Network-Dependent Durability Predictors," *Environmental Earth Sciences* 63/7 (2011): 1511–27.
[152] Cézar A Crispim and C C Gaylarde, "Cyanobacteria and Biodeterioration of Cultural Heritage: A Review," *Microbial Ecology* 49/1 (2005): 1–9.

DOI: 10.15774/PPKE.BTK.2024.021

from roof or gutters nearby the stone, or liquid water generated from the condensation of water vapor within pores. The liquid water can enter the stone by capillary force, so the liquid water moves inside the stone by its capillary pores network [153]. Besides capillary force, liquid water moves through the pore system under other forces such as diffusion, osmosis, and heat difference [154].

Water vapor can enter and move within stone pores and adsorb to their wall. However, different processes cause the movement or presence of water vapor inside the pores. When the temperature of the stone surface or pore walls is lower than the dew point of the ambient air, the water molecules in the air adhere to the pore wall [155]. On the other hand, the material can attract water vapor that is present in the air in a process that is so-called hygroscopicity [156]. That results in the adsorption of water vapor molecules on the material surface even though the temperature of the material is higher than the dew point of the ambient air. Water vapor transports inside the pores from the region with high water vapor pressure to the other with low water vapor pressure, which causes the evaporation in the former region and condensation in the latter [157].

Water moves inside the stone throughout its interconnected pores (effective pores) and that movement is dependent upon the pore size [158]. The pore size affects the thermodynamic properties of the water presented inside that pores; i.e. water vapor pressure, freezing point, etc. [159]. Therefore, the water transport mechanism varies according to pore sizes. The water inside the large pores (more than 0.1 μm) is subjected to the atmospheric conditions (e.g. water freezes at 0 ^{o}C), however, the water in smaller pores (less than 0.1 μm) is subjected to different thermodynamic conditions (e.g. water needs very low temperature to freeze) [160]. Charola and Wendler (2015) classify the water transport mechanism inside stone pores according to the

[153] Delgado et al., "Salt Damage and Rising Damp Treatment in Building Structures." Advances in Materials Science and Engineering 2016 (2016):1-13.
[154] Giorgio Torraca, "Porous Building Materials: Materials Science for Architectural Conservation," (1982):11-12.
[155] V Cammalleri, E G Lyon, and S Gumpertz, "Condensation in the Building Envelope: Expectation and Realities," *Proceedings of" SSPC* (2003):210–19.
[156] Xingyi Zhou et al., "Atmospheric Water Harvesting: A Review of Material and Structural Designs," *ACS Materials Letters* 2/7 (2020): 671–84.
[157] Torraca, "Porous Building Materials: Materials Science for Architectural Conservation.":13
[158] Bahman Ghiassi and Paulo B Lourenço, *Long-Term Performance and Durability of Masonry Structures: Degradation Mechanisms, Health Monitoring and Service Life Design* (2018):72.
[159] Martin Ondrášik and Miloslav Kopecký, "Rock Pore Structure as Main Reason of Rock Deterioration," *Studia Geotechnica et Mechanica* 36/1 (2014): 79–88.
[160] Steiger, Charola, and Sterflinger, "Weathering and Deterioration."

DOI: 10.15774/PPKE.BTK.2024.021

pore size [161]. In the pores and cavities with a size of more than 1 mm, there is free water flow, however, the capillary water absorption (water is subjected to suction forces) occurs in pores with sizes between 1 mm and 1 μm in diameter. The water vapor adsorption and surface diffusion usually take place in pores with size smaller than 1 μm. The capillary condensation occurs in the pores with a size of less than 0.1 μm, however water vapor diffusion takes place in pores with a diameter of more than 0.1 μm, see Table 2.2.

Water transport mechanisms within the pore system highly depend on the pore size distribution more than the total porosity [162].

The stone pores respond to the variation in the relative humidity of the ambient by condensation of water vapor molecules to their pore walls. Starting from the dried phase of stone material, the condensation process with the increase of relative humidity can be divided into six stages in which the water transport mechanism varies depending upon the pore sizes and the amount of the adsorbed water [163]. In the first stage (the dry phase), all water vapor molecules penetrating the pores are adsorbed on the pore walls; so there is no transport in this stage (Figure 2.8a). The water vapor molecules continue to adsorb on the pore walls until they form water film (sorbate layer) that covers the pore wall (Figure 2.8b). That water film consists of one or more layers of water molecules according to the relative humidity of the ambient. Pore

Table 2. 2Water transport mechanisms inside the stone block according to its pores sizes (updated from (Charola & Wendler, 2015))

$\phi > 1$ mm	1 mm $>\phi>$ 1 μm	1 μm $>\phi>$ 0.1 μm	$\phi <$ 0.1 μm
Liquid water flow	Capillary absorption	water vapor adsorption and surface diffusion	
Water vapor diffusion			Capillary condensation

space in this stage is permeable for water vapor. By increasing the relative humidity, the bottle neck pores (a smaller pore connected to a large one) are filled with liquid water due to capillary condensation. However, the large pores are full of air, water vapor, and the water film on its walls (Figure 2.8c). In this stage, the water film in a large pore is so thin that water vapor

[161] A Elena Charola and Eberhard Wendler, "An Overview of the Water-Porous Building Materials Interactions," Restoration of Buildings and Monuments 21/2–3 (2015): 55–65.
[162] Buj and Gisbert, "Influence of Pore Morphology on the Durability of Sedimentary Building Stones from Aragon (Spain) Subjected to Standard Salt Decay Tests." *Environmental Earth Sciences* 61(2010): 1327-1336.
Luciana Randazzo et al., "Pore Structure and Water Transfer in Pietra d'Aspra Limestone: A Neutronographic Study," Applied Sciences 10/19 (2020): 6745.
[163] Peter Lutz, *Lehrbuch Der Bauphysik: Schall Wärme Feuchte Licht Brand Klima* (2013):177.

DOI: 10.15774/PPKE.BTK.2024.021

diffusion can only occur. However, liquid water transport is accomplished in the bottle neck pores. In the following stage, the thickness of the water film has increased to an extent that liquid water transport occurs in large pores (Figure 2.8d). In this stage, the liquid water transport rate is significantly higher than vapor diffusion. By increasing the water inside the large pores, an unsaturated flow has developed inside those pores, where air bubbles are still trapped (Figure 2.8e). When relative humidity rises more, the pore space of large pores fills with water, so a saturated flow develops in this stage (Figure 2.8f). Under normal conditions, liquid water cannot flow in fine pores of less than 0.2 μm in diameter because the thickness of the adsorbed water film in those pores is more than 0.1 μm [164]. The changing in temperature and relative humidity causes cycles of condensation – evaporation inside stone pores. Those cycles can be expressed by a so-called adsorption isotherm, representing the amount of the adsorbed water versus relative humidity. The adsorption isotherm curve consists of two branches that form together with a hysteresis loop, see Figure 2.9. D Camuffo (2014) divides that loop into four stages according to the relative humidity (Figure 2.9). At low relative humidity (Stage AB) all the pores of the material have been covered with water film (see Figure 2.8b) [165]. When the relative humidity of the ambient increases, the pores are gradually filled with bulk water (see Figure 2.9 lower branch of BC). At very high relative humidity (Stage CD), all the internal pores are filled with water except for some large pores, especially the external ones, that are still empty. In the case of salts on the stone surface, the hygroscopicity of the salts attracts more water vapor molecules that bring about condensation and liquid water formation on the external surface (see the final

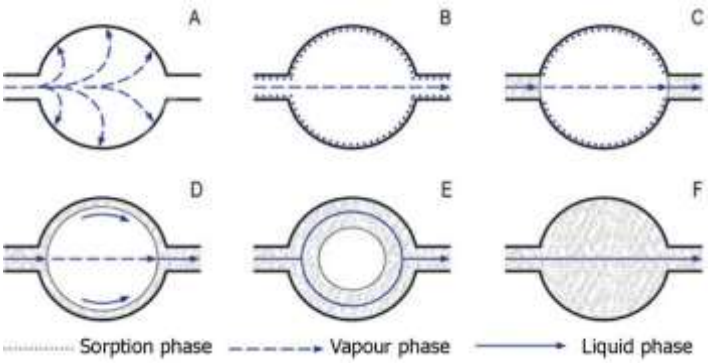

Figure 2. 8 Schematic representation of progressive water retention in a building material pore with increasing water content (updated from (Lutz, 2013))

[164] Li Dejian et al., "Analysis of Microscopic Pore Structures of Rocks before and after Water Absorption," *Mining Science and Technology (China)* 21/2 (2011): 287–93.
[165] D Camuffo, "Microclimate Studies for Cultural Heritage: Conservation, Restoration and Maintenance of Indoor and Outdoor Monuments" (2014).

DOI: 10.15774/PPKE.BTK.2024.021

stage DE in Figure 2.9). The final rise of DE can also occur when the temperature drops lower than the dew point, then condensation of water vapor occurs on the external surface. When the relative humidity decreases, desorption occurs in ED and DC branches. By continuing to lower relative humidity, evaporation occurs inside the pores (The higher branch of CB). The evaporation from the internal pores is related to the sizes of those pores as well as their connectivity, and the presence of small and large pores (large pores with smaller radius entrances) that are connected causes the formation of hysteresis effect in the porous material. As mentioned before, the response of pores to the relative humidity is not the same in the pore system, rather it is related to the pore size. Camuffo (1984) emphasizes the hysteresis effect that exists in the case of a pore with radius r_s is connected with a smaller pore with radius r_o, see Figure 2.10a [166]. In that case, the large pore remains empty by the increase of the relative humidity until it reaches the critical relative humidity RH(r_s), at which point condensation begins inside the larger pore at RH(rs) and higher. In the case of evaporation, the larger pore remains filled with water by decreasing the relative humidity until it reaches the critical relative humidity RH(r_o), at which point evaporation starts inside the smaller pore at RH(r_o) and lower. In the case of a pore with radius, r_s is connected with a larger pore with radius r or facing the external environment (Figure 2.10b), the hysteresis effect does not exist. In that case, the smaller pore remains empty except for the water film on its walls until the relative humidity becomes higher than the critical relative humidity RH(r_s). That process is reversible where the evaporation starts when the relative humidity reaches below RH(r_s).

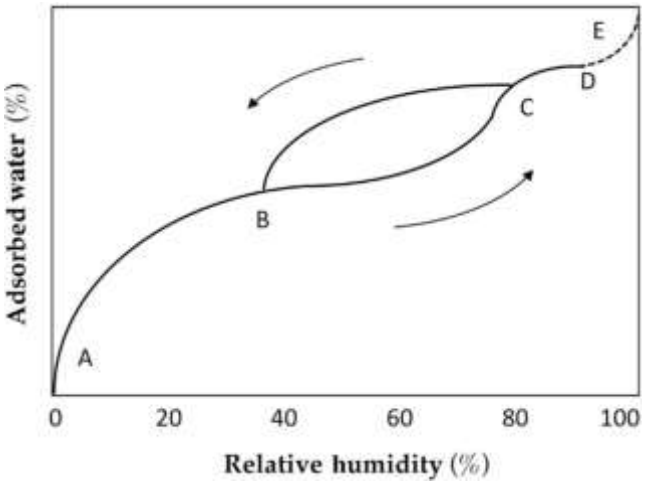

Figure 2. 9 The sorption isotherm of a building material (updated from (D Camuffo, 2014))

The understanding of the building materials structure (porosity, pore size distribution, mineralogical compositions), as well as the water (vapor or liquid) circulation within their pores, define the durability and quality criteria to be used for different purposes (coating material, building walls, flooring tiles, etc.) [167]. At the laboratory scale, many tests are

[166] Dario Camuffo, "Condensation-Evaporation Cycles in Pore and Capillary Systems According to the Kelvin Model," Water, Air, and Soil Pollution 21/1 (1984): 151–59.
[167] P Vázquez et al., "Evaluation of the Petrophysical Properties of Sedimentary Building Stones in Order to Establish Quality Criteria," *Construction and Building Materials* 41 (2013): 868–78.

DOI: 10.15774/PPKE.BTK.2024.021

generally used to determine water (vapor or liquid) circulation within building materials such as capillary water uptake, water absorption under atmospheric conditions, drying, and water vapor permeability tests [168].

When natural stone is exposed to rain fall or rising damp from the ground, water enters the stone blocks through its capillary pores by the effect of capillary forces. In that case, the amount of pore water attributes to the connectivity of the capillary pores and how their connectivity facilitates the water movement by the mean of tortuosity of the pores [169]. Many studies have concluded that capillary water uptake is greatly related to open porosity and pore size distribution (in the capillary pore range) [170]. Ġelik & Kaçmaz (2016) examine the capillarity of two types of tuff stones [171]. They realize that the tuff type with a pore size distribution between 0.01-100 µm exhibits a faster capillary water uptake and a higher capillary water uptake coefficient than the other tuff type with a pore size distribution between 0.01-4 µm. When Sengun et al. (2014) study 118 lithotypes of metamorphic, igneous, and sedimentary stones, they find that the capillary water uptake coefficient had a linear relationship with a bulk density as well as open and total porosity [172].

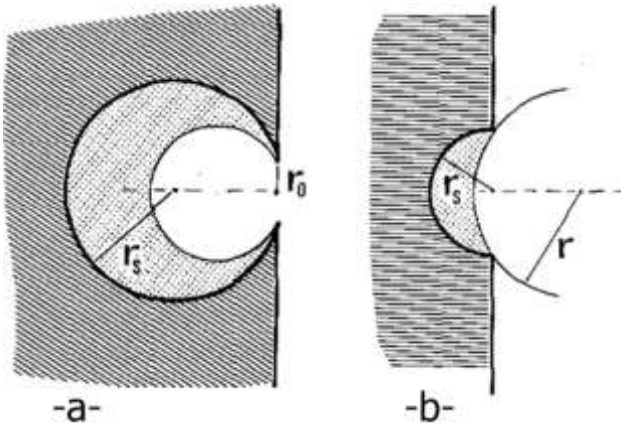

Figure 2. 10 The connectivity between large pores and small pores that can be found in stone structures (updated from (Dario Camuffo, 1984))

Tim De Kock et al., "Rock Fabric Heterogeneity and Its Influence on the Petrophysical Properties of a Building Limestone: Lede Stone (Belgium) as an Example," Engineering Geology 216 (2017): 31–41.

[168] There are also another tests, however, this study concentrates on the mentioned tests.

[169] H Dong, P Gao, and G Ye, "Characterization and Comparison of Capillary Pore Structures of Digital Cement Pastes," *Materials and Structures* 50/2 (2017): 1–12.

[170] Vázquez et al., "Evaluation of the Petrophysical Properties of Sedimentary Building Stones in Order to Establish Quality Criteria." *Construction and Building Materials* 41 (2013): 868-878.

De Kock et al., "Rock Fabric Heterogeneity and Its Influence on the Petrophysical Properties of a Building Limestone: Lede Stone (Belgium) as an Example." *Engineering Geology* 216 (2017): 31-41.

Yue Zhang, Yunmeng Zhang, and Jizhong Huang, "Experimental Study on Capillary Water Absorption of Sandstones from Different Grotto Heritage Sites in China," *Heritage Science* 10/1 (2022): 1–17.

Gioacchino F Andriani and Nicola Walsh, "Petrophysical and Mechanical Properties of Soft and Porous Building Rocks Used in Apulian Monuments (South Italy)," *Geological Society, London, Special Publications* 333/1 (2010): 129–41.

[171] Mustafa Yavuz Çelik and Ahmet Uğur Kaçmaz, "The Investigation of Static and Dynamic Capillary by Water Absorption in Porous Building Stones under Normal and Salty Water Conditions," *Environmental Earth Sciences* 75/4 (2016): 1–19.

[172] N Sengun et al., "Investigation of the Relationships between Capillary Water Absorption Coefficients and Other Rock Properties of Some Natural Stones, V," *Global Stone Congress* (2014): 22–25.

DOI: 10.15774/PPKE.BTK.2024.021

In the test of water absorption under atmospheric conditions of the natural stone, the stone is immersed. That causes the gradual filling of all open pores in the stone by water until it reaches the saturation degree. The water absorption under atmospheric conditions indirectly measures the open (effective) pores and their connectivity. Therefore, the stone with higher open porosity and well-connected pores absorbs more water. Karaca (2010) examines water absorption of different lithotypes of natural stones [173]. He argues that chemical composition affects water absorption and realizes that water absorption value increases when magnesium oxide content increases.

Water in the stone pores alters some of its properties, such as P-wave velocity. Generally, P-wave velocity correlates with the stone porosity by negative relationship and with the bulk density (dry and wet phases) by positive one [174]. However, the presence of water within the pore system affects the ultrasound velocity, which may decrease, increase or both trend together (decrease then increase) compared to the dried phase. In some studies, the primary ultrasound velocity increases with the increase of saturation degree of the stone [175]. At the same time, other investigations reveal reverse results, where the primary ultrasound velocity decreases with the increase of water content (water saturation degree) [176]. Some investigations reveal that the primary ultrasound velocity exhibits a decreasing trend at first by low water saturation degree, then the trend changes at a

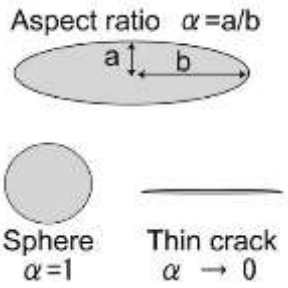

Figure 2. 11 Pore aspect ratio (Tsuji et al., 2008)

[173] Zeki Karaca, "Water Absorption and Dehydration of Natural Stones versus Time," Construction and Building Materials 24/5 (2010): 786–90.

[174] Ann Bourgès, "Holistic Correlation of Physical and Mechanical Properties of Selected Natural Stones for Assessing Durability and Weathering in the Natural Environment." (2006):19.
CENGİZ Kurtulus, S Cakir, and AHMET Yoğurtcuoğlu, "Ultrasound Study of Limestone Rock Physical and Mechanical Properties.," *Soil Mechanics & Foundation Engineering* 52/6 (2016): 348-54.
Rahmouni Abdelaali et al., "Prediction of Porosity and Density of Calcarenite Rocks from P-Wave Velocity Measurements," *International Journal of Geosciences* 4 (2013): 1292-99.

[175] Ma Doreen Esplana Candelaria et al., "Effects of Saturation Levels on the Ultrasonic Pulse Velocities and Mechanical Properties of Concrete," *Materials* 14/1 (2020): 152.
Mohamed A Kassab and Andreas Weller, "Study on P-Wave and S-Wave Velocity in Dry and Wet Sandstones of Tushka Region, Egypt," *Egyptian Journal of Petroleum* 24/1 (2015): 1–11.

[176] Kurtulus, Cakir, and Yoğurtcuoğlu, "Ultrasound Study of Limestone Rock Physical and Mechanical Properties." *Soil Mechanics & Foundation Engineering* 52/6 (2016): 348-354.
Siddharth Garia et al., "A Comprehensive Analysis on the Relationships between Elastic Wave Velocities and Petrophysical Properties of Sedimentary Rocks Based on Laboratory Measurements," *Journal of Petroleum Exploration and Production Technology* 9/3 (2019): 1869–81.
Hasan Karakul and Resat Ulusay, "Empirical Correlations for Predicting Strength Properties of Rocks from P-Wave Velocity under Different Degrees of Saturation," *Rock Mechanics and Rock Engineering* 46/5 (2013): 981–99.

DOI: 10.15774/PPKE.BTK.2024.021

certain saturation degree [177]. The effect of water saturation on the primary ultrasound velocity is related to many factors such as porosity and mineralogical composition [178]. Baechle et al. (2009) argue that the decreasing or increasing of ultrasound velocity by water saturation is attributed to wet bulk density and pore-saturated compressibility or stiffness [179]. As such, water in pores increases the bulk density of the stone. However, when water within the pore space leads to form stiff layers (i.e. decrease the compressibility of the pore space), the ultrasound velocity will increase; otherwise, it will decrease. Once ultrasound wave passes within stone structure, the latter experiences a compression increase. That compression leads to an increase in pore pressure that resists the compression wave and by this way the stiffness of rock increases [180]. Pore geometry or what is so-called pore aspect ratio (see Figure 2.11) plays an important role in increasing the pore-saturated stiffness [181]. Wang et al. (2011) find that spherical pores with a high aspect ratio are stiffer than oblate pores in the presence of water [182]. Therefore, the rock or stone with pores with a high aspect ratio more than those with a lower value, its ultrasound velocity is predicted to increase by the presence of liquid.

The presence of clay minerals influences the primary ultrasound velocity in saturated stone; where some studies on sandstone confirm that the velocity decreases with the increase of clay content [183].

2.3.2 Drying characteristics

When water enters a stone structure, it forms a medium that accelerates its deterioration. The drying process is important in porous materials because it removes water from the stone

[177] Thaqibul Fikri Niyartama and Umar Fauzi, "Influence of Water Saturation on Ultrasonic P-Wave Velocity in Weakly Compacted Sandstone," in *Journal of Physics: Conference Series*, 795 (2017):12012.

[178] Nisar Ahmed, Perveiz Khalid, and Abdul Waheed Anwar, "Rock Physics Modeling to Assess the Impact of Spatial Distribution Pattern of Pore Fluid and Clay Contents on Acoustic Signatures of Partially-Saturated Reservoirs," *Acta Geodaetica et Geophysica* 51/1 (2016): 1–13.

[179] Gregor T Baechle et al., "Changes in Dynamic Shear Moduli of Carbonate Rocks with Fluid Substitution," Geophysics 74/3 (2009): E135–47.

[180] G Mavko, T Mukerji, and J Dvorkin, "The Rock Physics Handbook: Tools for Seismic Analysis of Porous Media". Cambridge University Press, Cambridge (2009):273.

[181] Fagen Pei et al., "Experimental Study of the Relationship between Fluid Density and Saturation and Sonic Wave Velocity of Rock Samples from the WXS Depression, South China Sea," *Petroleum Science* 8/1 (2011): 43–48.

Takeshi Tsuji et al., "Effective Stress and Pore Pressure in the Nankai Accretionary Prism off the Muroto Peninsula, Southwestern Japan," *Journal of Geophysical Research: Solid Earth* 113/B11 (2008).

[182] Haiyang Wang et al., "The Influence of Pore Structure on P-& S-Wave Velocities in Complex Carbonate Reservoirs with Secondary Storage Space," *Petroleum Science* 8/4 (2011): 394–405.

[183] De-hua Han, Amos Nur, and Dale Morgan, "Effects of Porosity and Clay Content on Wave Velocities in Sandstones," *Geophysics* 51/11 (1986): 2093–2107.

Theodoros Klimentos, "The Effects of Porosity-Permeability-Clay Content on the Velocity of Compressional Waves," *Geophysics* 56/12 (1991): 1930–39.

DOI: 10.15774/PPKE.BTK.2024.021

structure. The drying rate is more appropriate when discussing a building stone that has been exposed to environmental factors. The stones that dry faster have a lower chance of salt crystallization, biological colonization, etc. Removing water from the stone structure in form of water vapor is known as the drying process. When the relative humidity of the ambient air is less than 100%, evaporation occurs on the stone surface [184]. The drying behaviour of the stone is determined by its intrinsic properties (water absorption and its distribution within the stone structure, porosity, amount of capillary pores, connectivity of the pores) as well as the environmental conditions (relative humidity, temperature, and airflow velocity) [185].

The typical drying curve of a stone block is shown in Figure 2.12. Initially, the free water on the surface evaporates (Stage I) [186]. The rapid diagonal stage (Stage II) occurs due to capillary action when water moves inside the stone to its surface [187]. When the majority of the water has evaporated, this stage is completed. The slow horizontal stage (Stage III) is the final stage, in

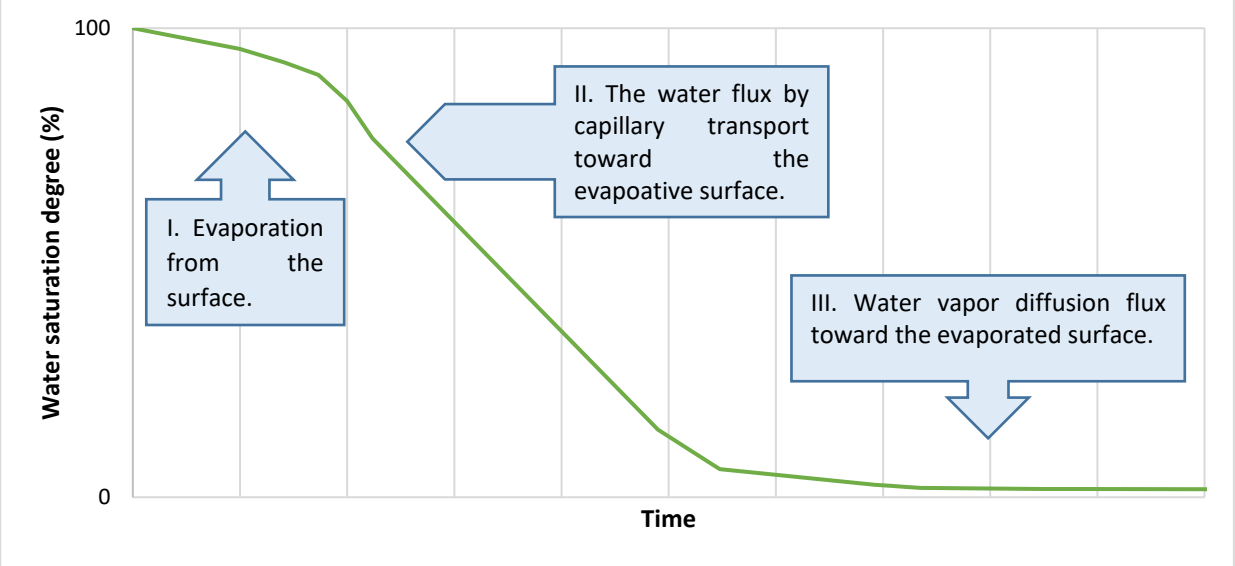

Figure 2. 12 The typical drying curve of a natural stone as a function of water saturation degree by time

[184] Torraca, "Porous Building Materials: Materials Science for Architectural Conservation.":14

[185] Maria Cláudia de Freitas Salomão, Elton Bauer, and Claudio de Souza Kazmierczak, "Drying Parameters of Rendering Mortars," *Ambiente Construído* 18 (2018): 7–19.
Gregor A Scheffler and Rudolf Plagge, "Introduction of a Drying Coefficient for Building Materials," *ASHRAE Transactions* 116/pt 2 (2010):2.

[186] C Franzen and P W Mirwald, "Moisture Content of Natural Stone: Static and Dynamic Equilibrium with Atmospheric Humidity," *Environmental Geology* 46/3 (2004): 391–401.

[187] B Sena da Fonseca et al., "Non-Destructive and on Site Method to Assess the Air-Permeability in Dimension Stones and Its Relationship with Other Transport-Related Properties," *Materials and Structures* 48/11 (2015): 3795–3809.
Christopher Hall and William D Hoff, *Water Transport in Brick, Stone and Concrete*, CRC Press (2021):188.

DOI: 10.15774/PPKE.BTK.2024.021

which water diffusion is the dominant mechanism of water transport [188]. This stage will continue until the water vapor pressure inside the stone structure equates to the atmospheric water vapor pressure.

Garrabrants & Kosson (2003) produce an approach to how the different phases of water transport (liquid and vapor) inside the stone pores could be present during the drying stages [189]. In stage I, the relative humidity of the stone surface is 100%. The evaporation occurs at the surface because the relative humidity of the stone surface is higher than the ambient environment. At the end of this stage, the stone transitions from bulk saturation to capillary saturation [190]. The dominant water phase in this stage is liquid, see Figure 2.13a. In stage II, the capillary pores are completely saturated at the start. During this stage, liquid capillary

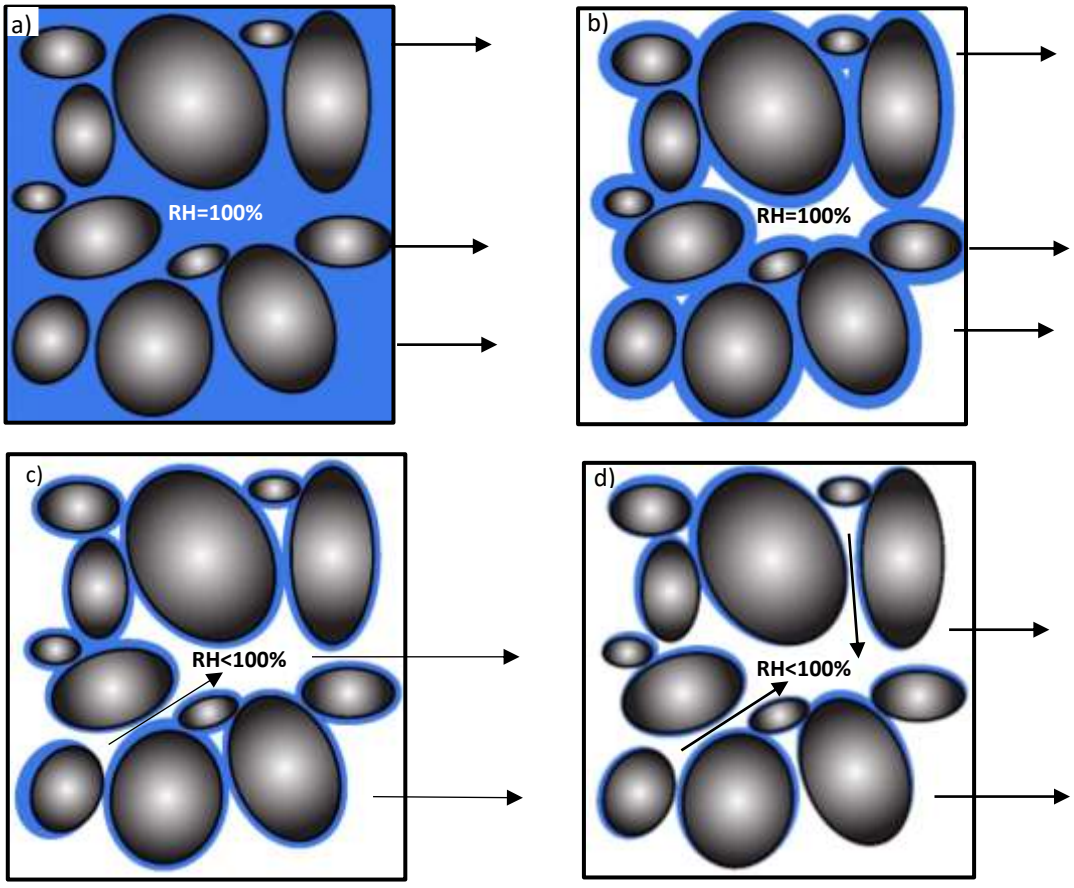

Figure 2. 13 Liquid water and water vapor transport during the drying stages of stone block (updated from Garrabrants & Kosson (2003))

transport is the primary mode of water transport. As the drying process continues, the degree of capillary saturation decreases until liquid transport becomes discontinuous, see Figure 2.13b.

[188] Siegesmund and Snethlage, *Stone in Architecture: Properties, Durability*.
[189] Andrew C Garrabrants and David S Kosson, "Modeling Moisture Transport from a Portland Cement-Based Material during Storage in Reactive and Inert Atmospheres," Drying Technology 21/5 (2003): 775–805.
[190] J R Anold et al., "Moisture Transport Review" (2009): VI-9.

DOI: 10.15774/PPKE.BTK.2024.021

In stage III, there is no liquid water in the pores, and the saturation degree of the material reaches insular saturation. Water vapor diffusion is the dominant mechanism in this stage, see Figure 2.13c. McAllister et al. (2016) find that the pore size distribution is the dominant factor controlling the transition period between stages II and III [191].

When the saturation degree falls below insular saturation, water vapor diffuses from the pore walls until the material is fully dry, see Figure 2.13d.

Stage II is highly affected by ambient conditions such as relative humidity, temperature, and airflow velocity, according to Hall et al. (1984) experiment [192]. They find that the rate of stage II increases significantly by temperature as well as airflow speed and decreases by increasing relative humidity. They do not find any effect on the relative humidity degree in stage III. On the other hand, the porosity of the stone is a critical factor. The amount of water that occupies the pores increases as the porosity of the stone increases. Because of that concept, the drying period will increase, as confirmed by Karaca (2010)[193]. Different lithotypes (sedimentary, igneous, and metamorphic stones) are dried in this research. As a result, it is found that the more porous is the stone, the longer is the drying period. However, Ozcelik & Ozguven (2014) investigate the drying behavior of 12 different lithotypes of natural stones at 70°C [194]. They realize that Stage II is rapid by increasing the open porosity of the stone, regardless of the amount of water inside the stone. On the other hand, Bourgès (2006) emphasizes that the pore size distribution has a crucial effect on the drying process, where the small pores can slow down the drying behavior [195]. The smaller pores can store the water for longer and cause a slow drying behavior; however, the larger pores have the reverse effect. The evaporation occurs first in the pores with large radii as they are under the effect of atmospheric pressure [196].

2.3.3 Water vapor permeability

Water vapor permeability is a material property that determines the amount of water vapor that can pass through the stone under pressure difference between the two stone sides. The water

[191] Daniel McAllister et al., "Evaporative Moisture Loss from Heterogeneous Stone: Material-Environment Interactions during Drying," Geomorphology 273 (2016): 308–322.
[192] C Hall, W D Hoff, and M R Nixon, "Water Movement in Porous Building Materials—VI. Evaporation and Drying in Brick and Block Materials," Building and Environment 19/1 (1984): 13–20.
[193] Karaca, "Water Absorption and Dehydration of Natural Stones versus Time."
[194] Y Ozcelik and A Ozguven, "Water Absorption and Drying Features of Different Natural Building Stones," Construction and Building Materials 63 (2014): 257–270.
[195] Ann Bourgès, "Holistic Correlation of Physical and Mechanical Properties of Selected Natural Stones for Assessing Durability and Weathering in the Natural Environment." (2006).
[196] Garrabrants and Kosson, "Modeling Moisture Transport from a Portland Cement-Based Material during Storage in Reactive and Inert Atmospheres." *Drying Technology* 21/5 (2003): 775-805.

DOI: 10.15774/PPKE.BTK.2024.021

vapor moves from a region of higher pressure to lower pressure [197]. It is the rate of the transmitted water vapor through a unit area of flat material of unit thickness, which is determined by the difference in vapor pressure between two surfaces at a given temperature and relative humidity [198]. In building practice, the water vapor diffusion resistance factor is commonly used to describe the measurement of water vapor diffusion. It is the ratio of the water vapor diffusion coefficient of the air and building material [199]. Water vapor diffusion is the second most important water transport in porous materials after capillary water uptake [200]. The water vapor diffusion resistance factor is one of the most significant criteria to consider when selecting appropriate building materials, such as replacing stones in historic buildings [201]; or application of coating material to make hydrophobic surfaces [202]. The ability of building material to transport and store water vapor influences its durability [203]. Because of that, it is essential to measure this property for hydrophobic materials applied to the stone surfaces for conservation purposes. Hydrophobic material should prevent liquid water (rain) from entering the stone and allow the water vapor to move from the inside to the outside of the stone to avoid any build-up of moisture (condensation) inside the structure [204]. The formation of condensation zones inside the structure reduces the durability of the stone especially when freeze-thaw cycles occur. Due to freezing, the expansion of water volume will induce considerable stresses, resulting in cracks and fissures [205]. When it comes to assessing the validity use of coating

[197] Phalguni Mukhopadhyaya et al., "Correlation between Water Vapour and Air Permeability of Building Materials: Experimental Observations," *JAI* 8/3 (2011): 1–14.

[198] Phalguni Mukhopadhyaya et al., "Water Vapor Transmission Measurement and Significance of Corrections," *Heat-Air-Moisture Transport: Measurements on Building Materials* 4/1495 (2007): 21.

[199] Hartwig M Künzel, "Simultaneous Heat and Moisture Transport in Building Components," *One-and Two-Dimensional Calculation Using Simple Parameters. IRB-Verlag Stuttgart* 65 (1995):15.

[200] Joerg Ruedrich, Dirk Kirchner, and Siegfried Siegesmund, "Physical Weathering of Building Stones Induced by Freeze–Thaw Action: A Laboratory Long-Term Study," *Environmental Earth Sciences* 63/7 (2011): 1573–86.

[201] Birte Graue, Siegfried Siegesmund, and B Middendorf, "Quality Assessment of Replacement Stones for the Cologne Cathedral: Mineralogical and Petrophysical Requirements," *Environmental Earth Sciences* 63/7 (2011): 1799–1822.

[202] Giorgio Pia et al., "Coating's Influence on Water Vapour Permeability of Porous Stones Typically Used in Cultural Heritage of Mediterranean Area: Experimental Tests and Model Controlling Procedure," *Progress in Organic Coatings* 102 (2017): 239–46.

Zaixin Xie et al., "Nano-Materials Enhanced Protectants for Natural Stone Surfaces," *Heritage Science* 9/1 (2021): 1–13.

Emilia Vasanelli et al., "Stone Consolidation with SiO2 Nanoparticles: Effects on a High Porosity Limestone," *Construction and Building Materials* 219 (2019): 154–63.

[203] Martin Keppert et al., "Water Vapor Diffusion and Adsorption of Sandstones: Influence of Rock Texture and Composition," *Advances in Materials Science and Engineering* 2016 (2016):1-7.

[204] J Drchalová et al., "Evaluation of Water Resistance and Diffusion Properties of Paint Materials," *Acta Polytechnica* 41/1 (2001).

Price and Doehne, "Stone Conservation: An Overview of Current Research."

[205] Piotr Narloch, Wojciech Piątkiewicz, and Barbara Pietruszka, "The Effect of Cement Addition on Water Vapour Resistance Factor of Rammed Earth," *Materials* 14/9 (2021): 2249.

DOI: 10.15774/PPKE.BTK.2024.021

material in conservation practice, the water vapor permeability of the coated surface is allowed to be equal or less 20% than of the uncoated (untreated) surface [206].

Water vapor permeability of the material is related to environmental conditions such as relative humidity and temperature as well as intrinsic properties of the material such as porosity characterizations. Many research has been conducted regarding the effect of relative humidity and temperature on water vapor permeability. In the case of hygroscopic material, such as stones, the water vapor permeability increases by increasing the relative humidity gradient [207]. The effect of temperature is still debatable because it is not clear yet. In another experiment on fibreboard and gypsum board, the water vapor permeability does not affect by the increase in the temperature [208]. Other research concludes that the temperature affects water vapor permeability depending on the relative humidity. Doty et. al (1946) find that the water vapor permeability of plywood and medium density fiber increased by the increase of temperature when relative humidity is more than 60%; however, the effect of the temperature is negligible when the relative humidity is less than 60% [209]. On the other hand, Galbraith et al. (2000) emphasize that the effect of temperature depending on relative humidity does not apply to all porous materials [210]. They study the water vapor permeability of the plasterboard and phenolic foam. They find that water vapor permeability of these materials does not increase by raising the temperature even though at high relative humidity. Nenadálová et al.(2016) study the effect of temperature and relative humidity on the water vapor diffusion resistance factor of different mortars (different compositions) [211]. They conclude that the determination of the dominant

[206] Rolf Snethlage and Katja Sterflinger, "Stone Conservation," in *Stone in Architecture* (2011), 411–544.
Mariateresa Lettieri and Maurizio Masieri, "Performances and Coating Morphology of a Siloxane-Based Hydrophobic Product Applied in Different Concentrations on a Highly Porous Stone," *Coatings* 6/4 (2016): 60.
[207] Mukhopadhyaya et al., "Water Vapor Transmission Measurement and Significance of Corrections." *Heat-Air-Moisture Transport: Measurements on Building Materials* 4/1495 (2007): 21.
MARYSUSAN Couturier and CRAIG Boucher, "Dynamic Water Vapor Permeance of Building Materials and the Benefits to Buildings," in *Proceedings of the 26th RCI International Convention and Trades Show, Reno, NV, USA*, 29 (2011):13-20.
[208] Phalguni Mukhopadhyaya, M Kumar Kumaran, and John Lackey, "Use of the Modified Cup Method to Determine Temperature Dependency of Water Vapor Transmission Properties of Building Materials," *Journal of Testing and Evaluation* 33/5 (2005): 316.
[209] Paul M Doty, W H Aiken, and H Mark, "Temperature Dependence of Water Vapor Permeability," Industrial & Engineering Chemistry 38/8 (1946): 788–791.
[210] G H Galbraith, J S Guo, and R C McLean, "The Effect of Temperature on the Moisture Permeability of Building Materials," Building Research & Information 28/4 (2000): 245–259.

[211] Šárka Nenadálová et al., "Laboratory Verification of Water Vapour Permeability of Plaster Compositions," Procedia Engineering 151 (2016): 50–57.

DOI: 10.15774/PPKE.BTK.2024.021

factor influencing the vapor permeability is not simple and it differs according to the composition.

Porosity characterization effect on water vapor permeability also attract many researchers. Togkalidou et al.(2013) study the relationship between the water vapor permeability with microstructure parameters of limestones and clay bricks [212]. They find that vapor permeability has a poor correlation with total porosity and mean pore radii and a good correlation with pore size distribution. In their experiment on six stones of different lithotypes (limestone, sandstone, dolostone, and travertine), Vázquez et al.(2013) find that water vapor permeability increases by the increase of open porosity and pore size [213]. However, the results of another study on sandstones reveal that water vapor diffusion resistance is mainly related to total porosity [214]; on the other hand, Stück et al. (2011) highlight that the water vapor diffusion resistance factor is affected by the pore size distribution [215].

[212] Timokleia Togkalidou et al., "Correlation of Water Vapor Permeability with Microstructure Characteristics of Building Materials Using Robust Chemometrics," Transport in Porous Media 99/2 (2013): 273–295.
[213] P Vázquez et al., "Evaluation of the Petrophysical Properties of Sedimentary Building Stones in Order to Establish Quality Criteria," Construction and Building Materials 41 (2013): 868–878.
[214] Keppert et al., "Water Vapor Diffusion and Adsorption of Sandstones: Influence of Rock Texture and Composition." *Advances in Materials Science and Engineering* 2016 (2016):1-7.
[215] Heidrun Stück, Siegfried Siegesmund, and Jörg Rüdrich, "Weathering Behaviour and Construction Suitability of Dimension Stones from the Drei Gleichen Area (Thuringia, Germany)," Environmental Earth Sciences 63/7 (2011): 1763–86.

DOI: 10.15774/PPKE.BTK.2024.021

3. The Investigated castle

DOI: 10.15774/PPKE.BTK.2024.021

3.1 Geographical and geological settings:

The Crac des Chevaliers is located in the northwest of Syria, between latitude 34.76° north and 36.29° longitude east. It is situated on a hill that rises about 660 m above sea level and it is approx. 35 km away from the Syrian coast. The castle region is a rural area, where al-Ḥuṣn town bounds the castle from north and east (the town is situated on an average level of approximately 570 m), see Figure 3.1 and Figure 3.2.

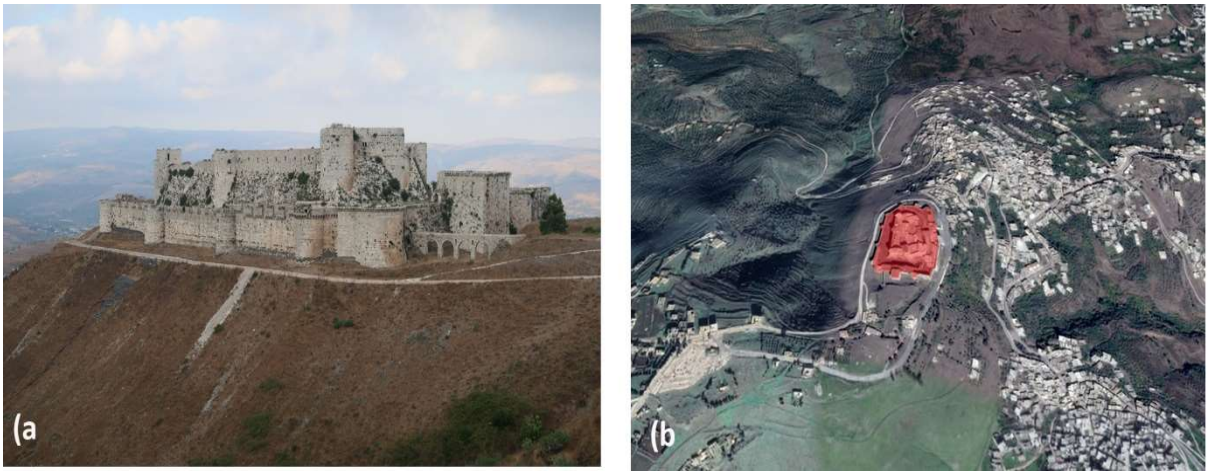

Figure 3. 1 a) General view of the castle. b) Satellite photo of the castle surroundings

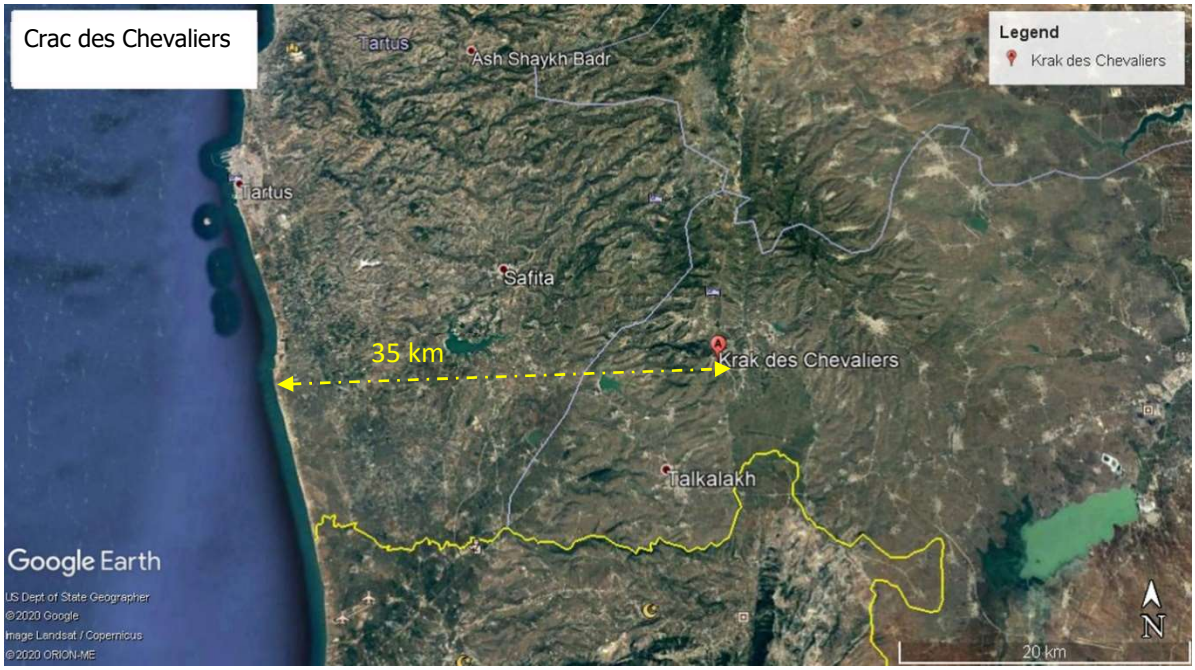

Figure 3. 2 A print screen taken from Google Earth demonstrates the distance of the sightline between the castle and the coast

DOI: 10.15774/PPKE.BTK.2024.021

The castle was built from dolomite, limestone, and basalt on a basilic and clay foundation. The different stone types, which were recognized in the castle, attribute to the geological setting of the location. The Neogene basalt is dominated in the eastern region that surrounds the castle

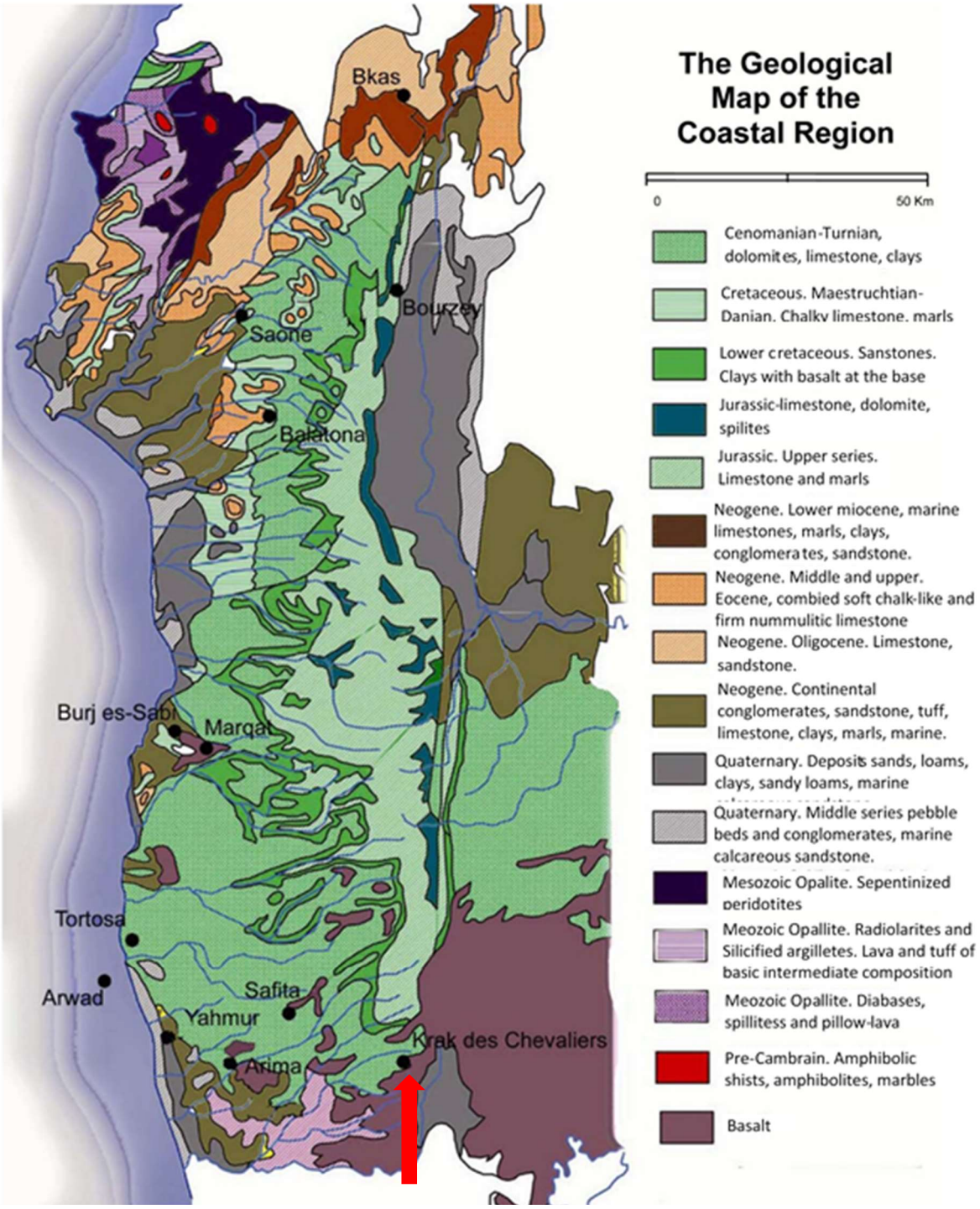

Figure 3. 3 The geological map of the Syrian coastal region. The red arrow refers to castle location on the map (The map was updated from (Al-Khateeb, 2008)

DOI: 10.15774/PPKE.BTK.2024.021

(Homs city) [216], and it extends under the Cenomanian-Turonian (late cretaceous) to the west [217], see Figure 3.3. Cenomanian-Turonian mainly consists of well-bedded limestone, marls with chert nodules and massive dolomitized limestone [218].

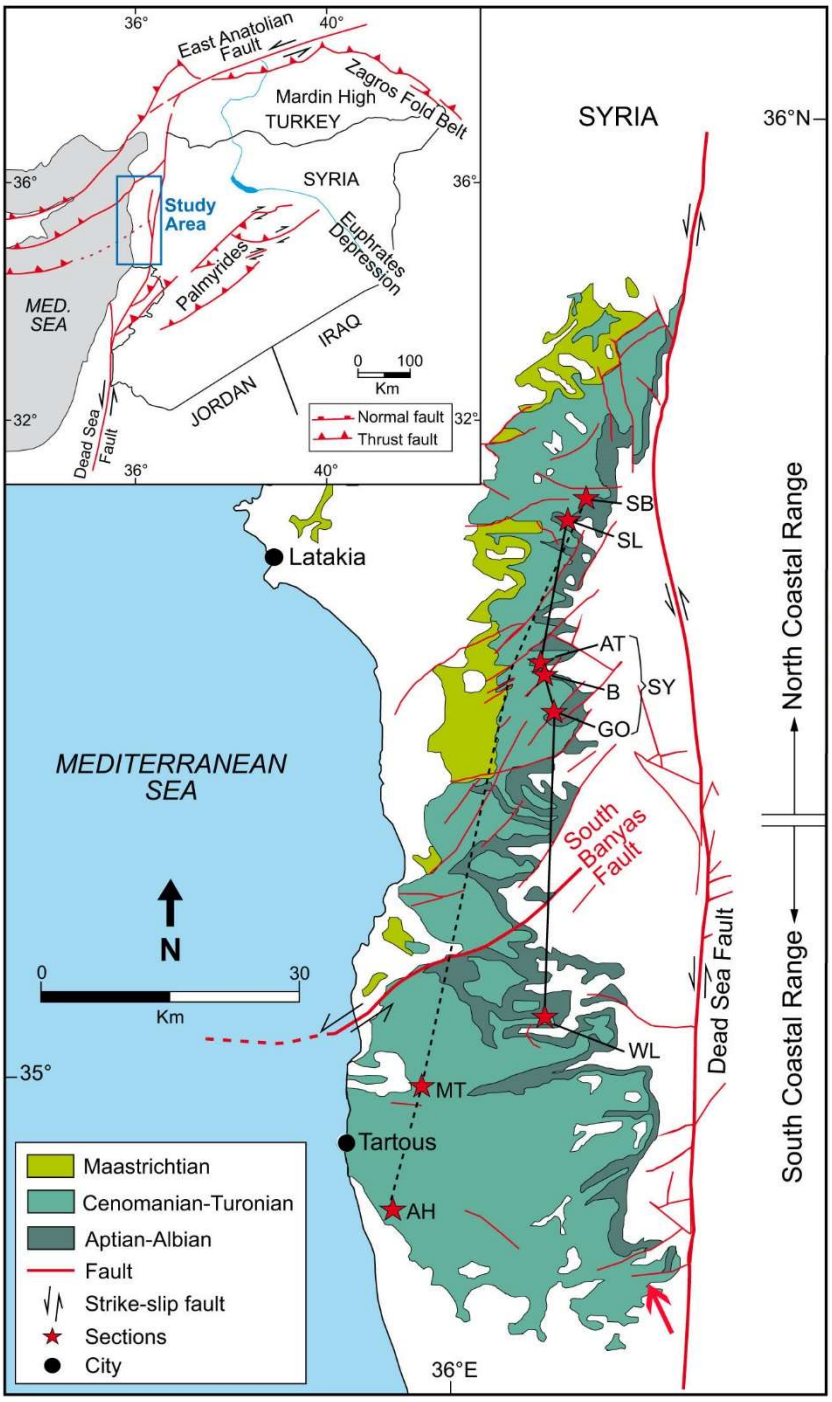

Figure 3. 4 A geological map of the Syrian coast region shows the seismic faults that surround the region. The dead sea fault is close to Crac des Chevaliers castle where the pink arrow refers. This map is updated from Ghanem & Kuss (2013)

DOI: 10.15774/PPKE.BTK.2024.021

The western and northern borders of Syria are nearby active boundaries, and these are the Anatolian-Arabia collision zone in the north and the Dead Sea fault in the west[219] see Figure 3.4; (the castle location is closed to the dead sea fault). That coastal region, including the castle site, is an active seismic zone, with many moderate earthquakes (5< Ms <6) recorded along the Dead Sea fault system over the last century [220].

The castle was built from stones that were brought from the nearby quarries in the region. There is one group of quarries 5 km to the west of the site which the literature identified as the main quarrying site for the castle. One of these quarries is Magharat Qadda [221]; which is located in a valley west of the castle, see Figure 3.5.

Figure 3. 5 The Magharat Qadda quarry that the Crac stones were brought from. (photo B. Major)

[216] Youssef Jubaili, Rashad Al-Hant, and Musa Issa, "Radio Spectrometric Survey of Un-Surved Areas in Syria", *Atomic Energy Commission*, AECS-G/RSS--477 (2002):17.

[217] Eyas Al-Khateeb, "Masonry Structures at the Crusader Castles in Syria: Building Material, Building Technique, Damage and Conservation Methodology," (2008):21.

[218] Hussam Ghanem and Jochen Kuss, "Stratigraphic Control of the Aptian–Early Turonian Sequences of the Levant Platform, Coastal Range, Northwest Syria," *GeoArabia* 18/4 (2013): 85–132.

[219] [219] Eric Barrier, Louai Machhour, and Marc Blaizot, "Petroleum Systems of Syria,"in Petroleum Systems of the Tethyan Region (2014): 335-378.

[220] Mohamed Reda Sbeinati, Ryad Darawcheh, and Mikhail Mouty, "The Historical Earthquakes of Syria: An Analysis of Large and Moderate Earthquakes from 1365 BC to 1900 AD," *Annals of Geophysics* 3/48 (2005): 374-435.

[221] Balázs Major, *Medieval Rural Settlements in the Syrian Coastal Region (12th and 13th Centuries)* (2016):41.

DOI: 10.15774/PPKE.BTK.2024.021

3.2 Meteorological data and environmental conditions:

According to Köppen's classification, the castle region is characterized by a Mediterranean dry, hot summers climate (CSA) [222]. The summers are warm to hot- dry (the amount of precipitation around 3mm), and the winters are mild- wet (the amount of precipitation is 160 mm, and the monthly average temperature in winter is 11◦C) [223].

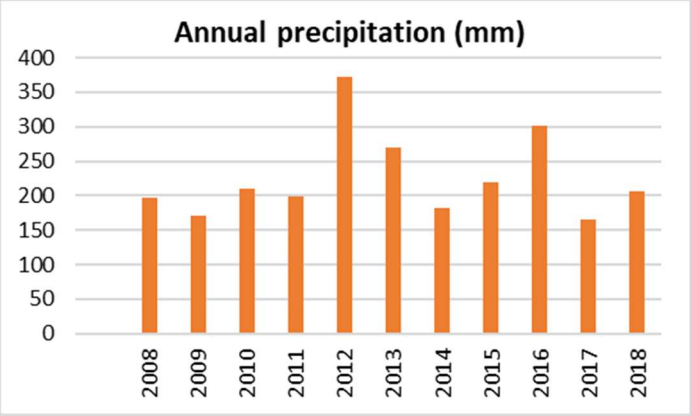

Figure 3. 7 The average of annual precipitation

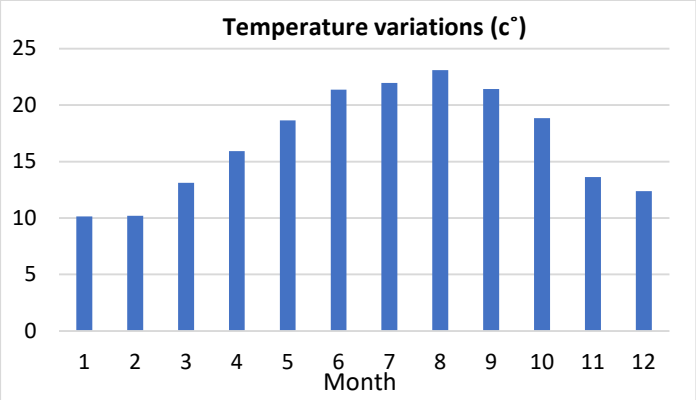

Figure 3. 6 The average of monthly temperature variations

For a better and more detailed investigation of the climate, meteorological data were collected for 20 years (from 1998 to 2018). It included daily and hourly data of precipitation amounts, snowfall, temperature variations, relative humidity, wind speed and direction, and sunshine duration. Because there is no weather station in the castle, the meteorological data have been obtained from the Meteoblue website [224]. The website collects the measured data from the weather stations of the country to produce a model.

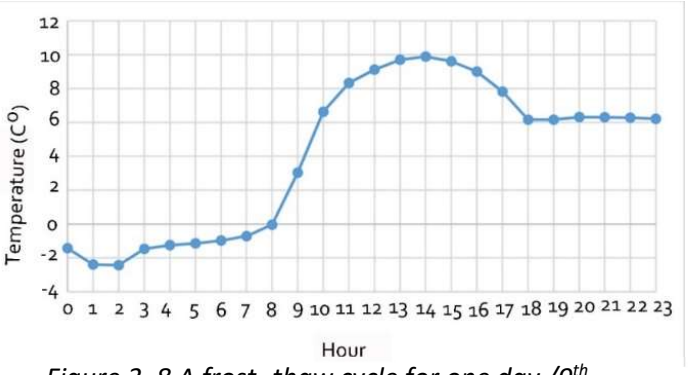

Figure 3. 8 A frost- thaw cycle for one day /9th December 2013

[222] Murray C Peel, Brian L Finlayson, and Thomas A McMahon, "Updated World Map of the Köppen-Geiger Climate Classification," *Hydrology and Earth System Sciences* 11/5 (2007): 1633–44.
[223] Ghaleb Faour, Yousef Meslmani, and Abbas Fayad, *Climate-Change Atlas of Syria*, (2010). DOI: 10.13140/RG.2.2.26562.17601
[224] "Https://Www.Meteoblue.Com/En/Weather/Archive/Histogram/34.760N36.290E," n.d.

DOI: 10.15774/PPKE.BTK.2024.021

The average annual precipitation in the castle is around 230 mm. The monthly average relative humidity of this region can vary from around 60- to 70% according to the season, see Figure 3.6 and Figure 3.10.

The average monthly temperature is 11◦C in winter and 23 ◦C in summer, see Figure 3.7.

Figure 3. 9 The crystal icicles at the castle, taken in February 2020

Nevertheless, the temperature at this site may drop to a freezing point in wintertime. Consequently, the stones in the castle are exposed to a maximum of one frost-thaw cycle per winter day, and crystal icicles can spawn on the arches in the castle see Figure 3.8 and Figure 3.9.

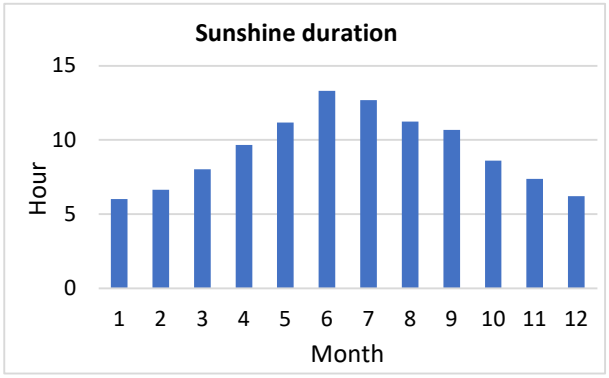

Figure 3. 10 The monthly average of sunshine duration

By observing the hourly temperature per winter day, it can be concluded that the frost lasts for more than one hour and then the thaw happens for only once (see appendix7). Therefore, it can be said that the total number of frost-thaw cycles per winter is equal to the number of freezing days (see Table 3.2).

Solar radiation plays an important role in the alteration of stone blocks so it should be considered. The average sunshine duration in summer is 13 and 6 hours per day in winter, see Figure 3.11.

The wind direction changes according to the season. In spring and summer (i.e., from April to September), the prevailing wind direction is west or southwest, see Figure 3.12. Whereas in winter and autumn (i.e., from January to March and from October to December), the wind usually blows alternately between the west direction

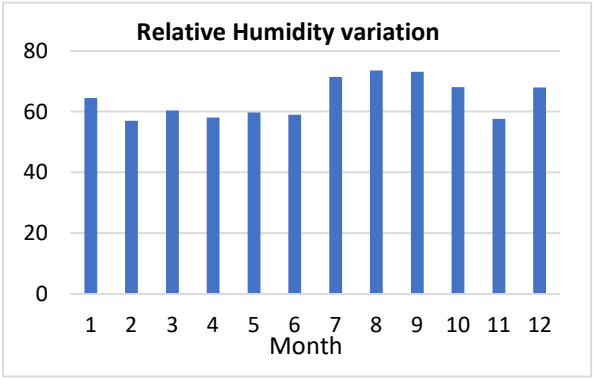

Figure 3. 11 The monthly average of relative humidity

DOI: 10.15774/PPKE.BTK.2024.021

(it can be west or southwest) and the east direction (it can be east, southeast, or northeast), see Figure 3. 13.

The most dominated speed of the western, southern west, and east wind is 20- 40 km/h with frequencies around 250, 400, and 80 occurrences respectively. Whereas the wind speed, especially in west and southwest directions, can reach a higher value (40- 50 km/h or even to 50- 60 km/h in some years) but in fewer frequencies (around 35 occurrences). The high-speed wind (50- 60 km/h) can rarely blow from the east direction with little frequency (about 4 occurrences per year).

As mentioned above, the meteorological data was taken from the Meteoblue website. The wind speed values of the castle, which were taken from the website, are relatively small values compared to the region of the castle, which is located on a high hill that is not separated from the sea by any other higher hills or mountains. The website took the wind value from the nearest wind station to the castle (which is in this case Homs city).

Due to the fact that there is a relationship between wind speed and the level in which the higher level the greater values of wind speed. As well as there is a considerable level difference between Homs city and the castle location (around 170 m). The wind values of the website need to be modified to represent the actual wind speed in the castle region. There is an equation that represented the relationship between the level of two locations and the wind speed in each.

Figure 3. 13 The wind rose of the wind direction from April to September in the castle region

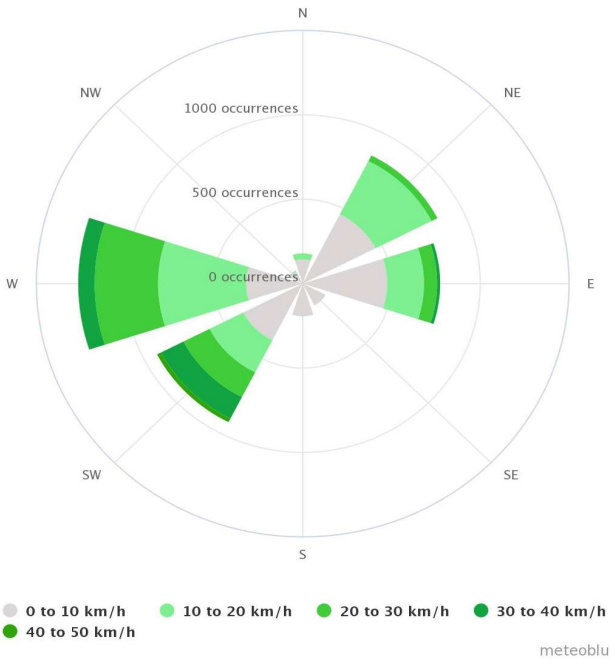

Figure 3. 12 The wind rose of the wind direction from October to April in the castle region

DOI: 10.15774/PPKE.BTK.2024.021

Therefore, if the wind speed and the level of one location are known, the wind speed of another location can be known by knowing its level also as follows:

$V_2 = V_1 * [\ln(h_2/a_2)] / [\ln(h_1/a_1)]$ [225] Equation 2

Where a2 and a1 are roughness lengths in the current wind direction (which is a characteristic value of the location whether it is a city with high buildings or not, if it is a rural area with high trees or not, etc.). In our study case, a1=0.6 (Large towns with high buildings) and a2=0.03 (Open agricultural land without fences and hedges; maybe some far apart buildings and very gentle hills) [226]. h1 and h2 are the levels of each location. V1 is the known wind speed of one location, and V2 is the wind speed that needs to be calculated for the other location.

The wind speed of the castle region was modified according to that equation by taking into account the level of Homs city (500m above sea level), the castle level (670 m above the sea level) considering the wind speed values, which are taken from the website, are related to Homs city (i.e. V1 values in the equation). By using the mentioned parameters in equation 2, the modified wind speed at the castle can be calculated as:

$V_2 = 1.5 * V_1$ Equation 3

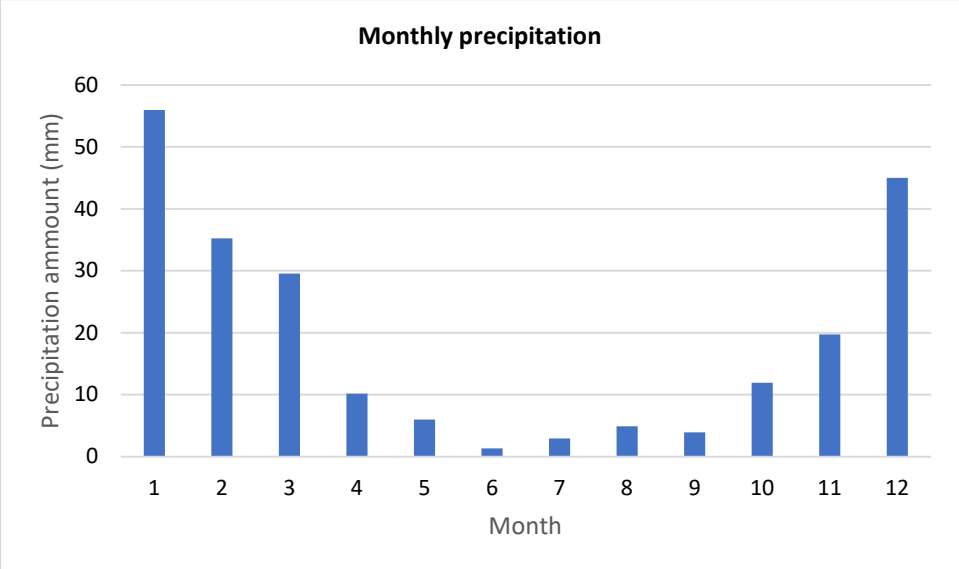

Figure 3. 14 The average of monthly precipitation

[225] O A Jaramillo and M A Borja, "Wind Speed Analysis in La Ventosa, Mexico: A Bimodal Probability Distribution Case," *Renewable Energy* 29/10 (2004): 1613–30.

[226] Dalila Khalfa et al., "Comparative Study of Wind Speed Extrapolation Methods for Sites with Different Roughness," *International Journal of Power and Energy Conversion* 9/3 (2018): 205–27.

DOI: 10.15774/PPKE.BTK.2024.021

Table 3. 1The amount of precipitation and the rainy days according to wind direction at the castle region

Year	The precipitation amount with **western** wind	The number of rainy days with **western** wind	The precipitation amount with **eastern** wind	The number of rainy days with **eastern** wind
	(mm)	(day)	(mm)	(day)
2008	167.6	49	23	9
2009	130.5	45	40.9	19
2010	142.8	49	65.2	11
2011	159	51	39.5	15
2012	300	55	62	17
2013	142.4	55	94.3	13
2014	126	51	55.4	18
2015	147.2	49	69.6	12
2016	248.5	49	42.6	10
2017	126.3	66	38.4	18
2018	157.8	66	49.6	18

Table 3. 2 The number of freezing days and the corresponding relative humidity at the castle for 20 years

Year	The number of freezing days (The number of frost thaw cycles)	Relative humidity between 60-75%	Relative humidity above 75%
2018	-	-	-
2017	12	2	10
2016	11	-	6
2015	10	1	7
2014	5	1	3
2013	16	3	10
2012	14	2	11
2011	6	1	5
2010	5	2	3
2009	6	2	3
2008	27	5	10
2007	7	-	1
2006	8	-	6
2005	13	1	11
2004	12	-	12
2003	14	1	11
2002	10	3	5
2001	3	-	2
2000	7	3	4
1999	6	-	3

DOI: 10.15774/PPKE.BTK.2024.021

By using t equation 2 the average wind speed in the castle region ranges between 60-70 km/h (if the wind speed on the website is 40-45 km/h is used).

The rainstorm, which usually happens in winter, co-occurs in both directions (west and east). But the probability of a rainstorm with western wind and the greatest amount of rain is extremely high compared with the east direction (see table 3.1) and Figure 3.14.

The observation of the daily minimum temperatures, especially ones below 0°C during the winter months, and the relative humidity underlines the presence of frost in the pores of stones. When the relative humidity value rises, the condensation of water vapor in the pores increases. However, when relative humidity reaches its critical values, the water vapor in the pores will be transformed into liquid water [227]. Therefore, the presence of the liquid water, when the

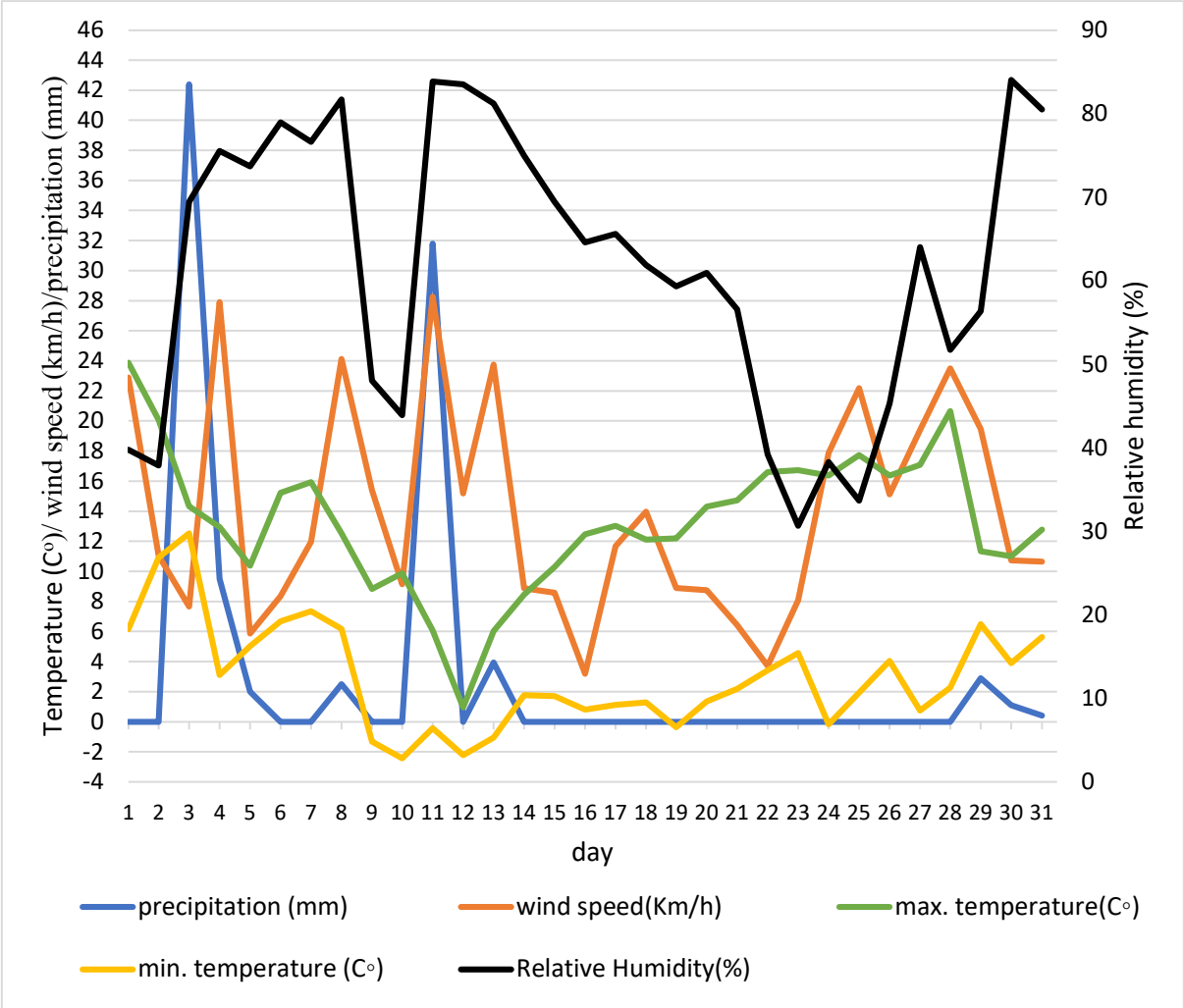

Figure 3. 15The weather condition at the castle in December 2013. The wind speed vaues in ths chart did not modified according to Eqation 3

[227] Peter Lutz, *Lehrbuch Der Bauphysik: Schall Wärme Feuchte Licht Brand Klima* (2013):177.

DOI: 10.15774/PPKE.BTK.2024.021

temperature is below the freezing point, will freeze. This phenomenon can apply additional stresses to stone blocks, especially the pores that are full of water, and there is no space to accommodate the ice crystal volume. Franzen & Mirwald (2004) emphasized that the critical relative humidity is above 75-80%, and there is a threshold of relative humidity (60-75%) at which a mixture of water and water vapor forms [228].

This process is influenced not only by the temperature and relative humidity but also by the pore system (pore size and its distribution). The number of freezing daily in some years with relative humidity values and minimum temperatures are shown in Table 3.2. The number of freezing days with relative humidity above 75% is high and, therefore, the frost phenomena effects on the stones cannot be neglected in this region. The meteorological data is one of the key factors, which control the stone deterioration process. Precipitation, wind speed, min. and max. temperatures during the December month in 2013 are demonstrated in Figure 3.15. This chart illustrates that every rainy storm co-occurs with high-speed wind blows, which can facilitate water passage within the stone surface. In other words, the capillary absorption of the stones, which are located in the western facades, will increase. Because the rainstorm, which is characterized by plentiful rain amount and high wind speed, usually comes from the western

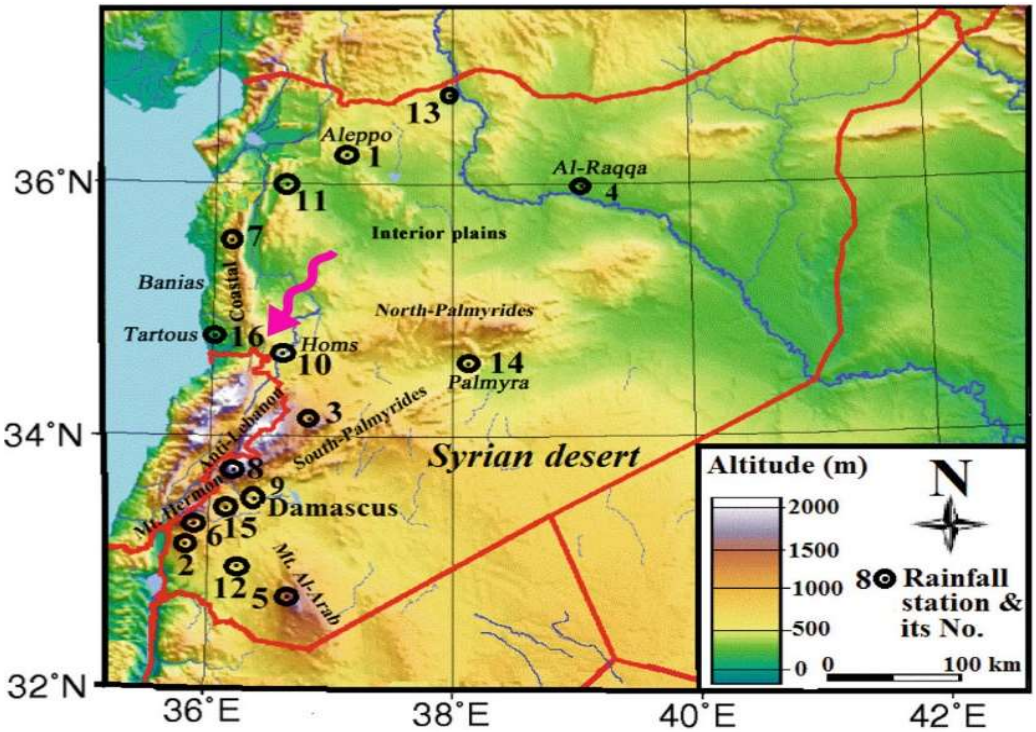

Figure 3. 16 The distribution of rain stations. The pink arrow refers to the castle location (This map was updated from (Kattan, 2020)

[228] C Franzen and P W Mirwald, "Moisture Content of Natural Stone: Static and Dynamic Equilibrium with Atmospheric Humidity," Environmental Geology 46/3 (2004): 391–401.

DOI: 10.15774/PPKE.BTK.2024.021

or southwestern direction. It is obvious from the chart that the stones suffered from freezing damage between 9-14th of this month, especially since the relative humidity exceeds 75%.
It is a vital issue to know the rain quality in the castle region. It can give an essential clue in the interpretation of some deterioration phenomena and the sort of deposits on the stone surface. The chemical ions in the rainwater would indicate the extent and the source of the pollution in the region. Besides, how the sea and its marine salts can affect the stones by knowing the contribution of the marine salts in the rainwater. The data of the rainwater quality have been concluded from a study done by Kattan (2020) [229]. He studied the rainwater of 16 stations spread all over Syria, see Figure 3.16. As mentioned above, Crac des Chevaliers is

Table 3. 3 The concentrations of the major ions in the rainwater samples that were collected from the stations surrounded the castle (the measurements were taken from Kattan (2020)

station	PH	Electrical conductivity EC	[NH4]+	[Na]+	[K]+	[Mg]+2	[Ca]+2	[Cl]-	[So4]-2	[NO3]-	[HCO3]-	Total dissolved salts TDS	Total marine salts TMS
		µS/cm	mg/L										(%TDS)
Bab-Janeh(7)	6.04	75.6	___	3.2	1.8	2.8	9.3	7.6	4	8.5	37.3	74.5	18%
Homs(10)	6.98	139.4	0.14	5	1.1	3.3	16.9	9.8	15.7	6.9	43	101.9	16%
Idleb(11)	6.9	84.1	0.13	1.6	0.5	2.1	11.2	3.8	6.9	3.6	34.5	64.4	11%
Tartous(16)	6.63	146.2	0.11	13.9	0.9	3.6	10.1	25.6	9.1	4.3	27.8	94.5	42%

located on a high hill between a major city (Homs) and the coast. To obtain the rainwater quality of the castle, the conditions of the castle site were taken into account with some of the stations measured: stations in Homs (number 1) and Tartous (number 16) represents the coastal condition; Bab Janeh (number 7) represents a mountainous region near the coast; and Idleb (number 11) represents a mountainous area that has approximately the distance from the coastline as the castle location, see Table 3.3. The largest concentrations of sodium and

Table 3. 4 The approximate rain quality at Crac des Chevaliers region, calculated from the average of the four stations demonstrated in Table 3.3

station	PH	Electrical conductivity EC	[NH4]+	[Na]+	[K]+	[Mg]+2	[Ca]+2	[Cl]-	[So4]-2	[NO3]-	[HCO3]-	Total dissolved salts TDS	Total marine salts TMS
		µS/cm	mg/L										(%TDS)
The approximate rain quality at Crac des Chevaliers region	6.64	111.3	0.1	5.9	1.1	3.0	11.9	11.7	8.9	5.8	35.7	83.8	22%

[229] Zuhair Kattan, "Factors Affecting the Chemical Composition of Precipitation in Syria," *Environmental Science and Pollution Research* 27/22 (2020): 28408–28.

DOI: 10.15774/PPKE.BTK.2024.021

chloride ions were found in Tartous city, because it is a coastal city. However, Homs, as a major city, had the highest amount of nitrate, sulfate and hydro carbonate ions (Table 3.3).

The average of these four stations was used to determine the rain quality of the Crac des Chevaliers region (Table 3.4).

`3.3 Building of the castle and its restoration history

Crac des Chevaliers is a uniquely well-preserved medieval fortress. It was already existing in the first half of the 11th century and its recently visible elements were mostly developed from the 1170s onward until the beginning of the 14th century [230]. This castle is a diverse structure with a Crusader concentric fortress of the most formidable power, and the later Mamluk towers, outstanding examples of Islamic architecture [231].

When it comes to describing the significance of the castle, it is wise to explain the importance of its location. Crac des Chevaliers dominates the gap of Homs, through which the Orontes Valley at the height of Homs connects with the coastal plain of Tripoli and Ṭarṭūs. The Mediterranean coastal plain and the Orontes Valley have always constituted two long fertile bands separated by well-defined mountain ranges. The initial builders of the castle chose to establish the fortification on a rounded north-south spur with fairly steep sides.

The building process of the castle had been developed by the time basically upon its developing defensive role as well as its increasing status as the most influential leadership center in the region. The first mention about the castle was when the prince of Homs strengthened the site to accomdate the garrison of Kurds in 1031 [232].

It was a simple fort that transformed during a century into one of the most powerful Christian castles in the Levant. The importance of the castle started when the Crusaders occupied it in 1099 and 1110 then the Hospitaller knights settled there in 1142 [233].

In 1099 Crusaders took the fortress under the leadership of Raymond of saint Gilles [234]. The military and political situation of the frankish states quickly deteriorated in the 1130s. In 1142

[230] John Zimmer et al., *Krak Des Chevaliers in Syrien: Archäologie Und Bauforschung 2003 Bis 2007* (2011):277-279.

[231] Jean Mesqui and Maxime Goepp, *Le Crac Des Chevaliers: Histoire et Architecture* (2018):9.

[232] D J Cathcart King, "The Taking of Le Krak Des Chevaliers in 1271," *Antiquity* 23/90 (1949): 83–92.
Mahmoud Ahmed Darwish, "Architectural Elements in Krak Des Chevaliers in Homs -Syria (Analytical Study)," *International Journal of Innovation and Applied Studies ISSN* 18/1 (2016): 2028–9324.

[233] Balázs Major, *Medieval Rural Settlements in the Syrian Coastal Region (12th and 13th Centuries)* (2016):33.

[234] Mesqui and Goepp, *Le Crac Des Chevaliers: Histoire et Architecture*:17.

DOI: 10.15774/PPKE.BTK.2024.021

the count of Tripoli asked military help from the Hospitaller knights [235], where they got in turn fortification/ place to fortify themselves in several places. One of these fortifications was Crac castle around which the Hopsitallers created an independent seigneury endowed with an economically viable territory. Crac remained for one hundered and thirty nine years the advanced point of the Frankish possessions towards the east and the valley of Orontes. Crac des Chevaliers was one of the important fortresses to confront the raids of Zengi and his son Nūr al-Dīn and finally his successor Ṣalāḥ al-Dīn.

The crusader building can be classified into three stages:

1- after a period of many earthquakes, which ended by in the half of 1170, the castle was rebuilt [236]. The earthquake in 1170 was at 9th intensity which was believed to have destroyed

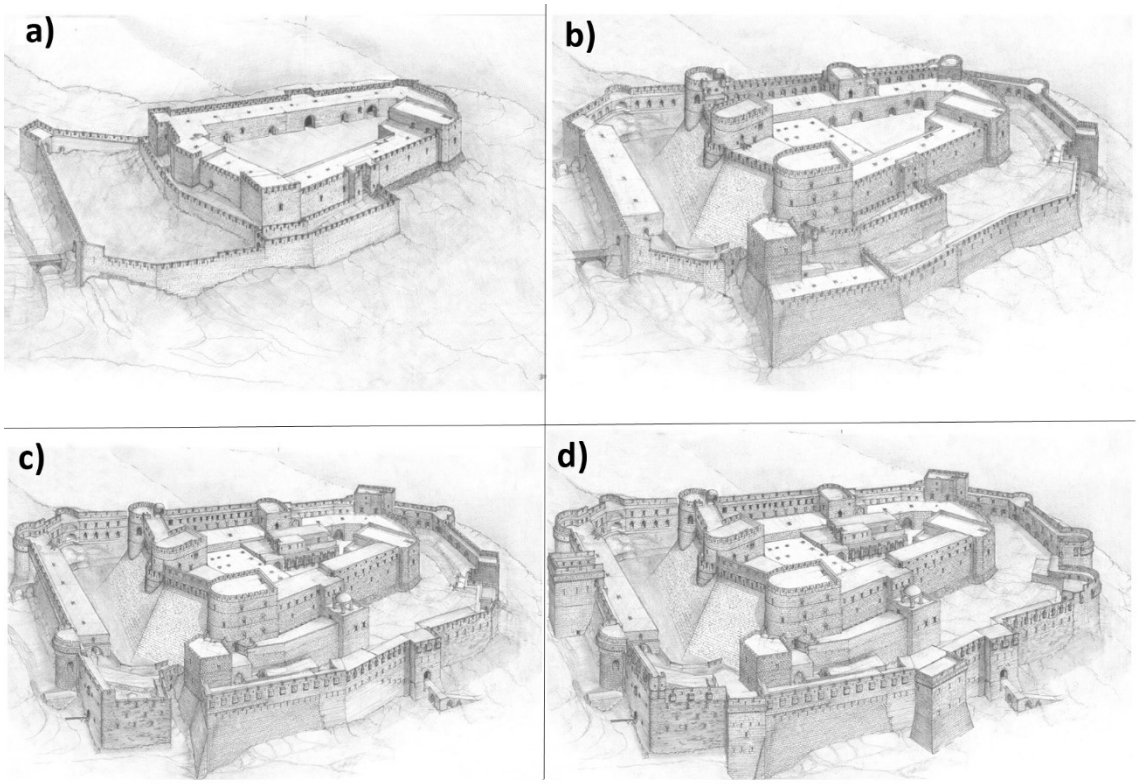

Figure 3. 17 Building phases of Crac des Chevaliers, Drawn by (Zimmer et al., 2011)

the castle so the effect of the earthquake was considerable and probably leading to a total reconstruction of the fortress. The new castle had a polygonal shape with some projecting rectangular towers, in addition to a moat located in the south to protect the castle, see

[235] Andrew D Buck, "The Military Orders and the Principality of Antioch: A Help or a Hindrance?," (2019): 285-295.

[236] David Nicolle, *Crusader Castles in the Holy Land 1192-1302*, vol. 32 (2005) :15.
Jean Mesqui, "L´architecture D´une Forteresse Hors Du Commum," in *Le Crac Des Chevaliers : Chroniques d'un Rêve de Pierre*, ed. Jean Hofman and Emmanuel Pénicaut (Paris, 2018):19–32.

DOI: 10.15774/PPKE.BTK.2024.021

Figure 3.17a. In 1180 after Saladin having secured his hold on Damascus and Bosra, went to raid the count of Tripoly. The Hosiptallers in Crac stood fearful in their castle "Crac", so they preffered to protect their fortress. The battle of Ḥittīn in 1187, when Saladin claimed the victory over Franks, dramatically changed the situation of the Latin states only confirming the imbalance between them and Sultan Salaḥ al- Din. After his victory, Salaḥ al- Din failed in taking Crac castle.

2- After the destructive earthquakes in 1202 [237], a new approach to rebuilding began, where the construction of a one-level fortress style was changed. These alterations came in response to the growing importance of the site. The new castle included the outer rampart surrounding the old fortress, rounded towers on the south side above the old castle, sectors for accommodation and leadership. In addition, the defenses were reinforced with the construction of a glacis attached to the south and west side of the old castle, which contained a defensive corridor equipped with arrow slits [238], see Figure 3.17. Starting in the early 13th century, Crac served as a base for military expeditions launched by the Hospitallers against the Muslim fortresses in the Orontes Valley [239].

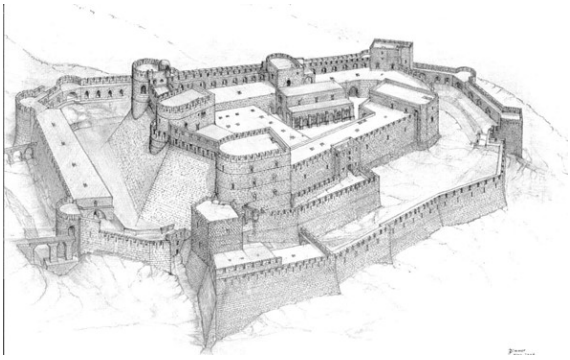

Figure 3. 18 Crac des Chevaliers in 1260, drawn by (Zimmer et al., 2011)

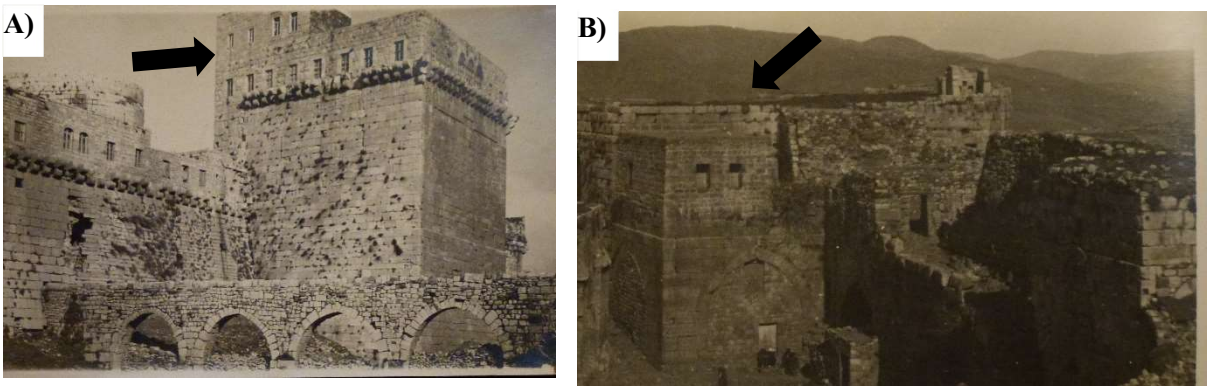

Figure 3. 19 The black arrows refer to the buildings that were added by the locals in the castle. A) a view of the external east façade of Building (133). B) a view of the external south façade of Building (22) [photos from the Paul Deschamps archive]

[237] Adrian Boas, *Archaeology of the Military Orders: A Survey of the Urban Centres, Rural Settlements and Castles of the Military Orders in the Latin East (c. 1120-1291)* (2006):40.
[238] Bengt Kristian Molin, "The Role of Castles in the Political and Military History of the Crusader States and the Levant 1187 to 1380" (1995):45.
[239] Mesqui and Goepp, *Le Crac Des Chevaliers: Histoire et Architecture*:30.

DOI: 10.15774/PPKE.BTK.2024.021

3- the last Crusader period of the building period was related to the middle of the thirteen century, 1240 [240]. The most important added building in this period was the gothic hall inside the old castle, see Figure 3.18.

The seventh Crusade had a consequence heavy with implications, which was the establishment of a new power replacing the decadent Ayyubid regime, with the Mamluk Sultanate who reigned over the East from 1250-1517. There were no raids made by Mamluks before Sultan Bībars seized power in 1260. Bībars was known for his determination to expel the Christians from the Middle East, so he started to bring them down to the Frankish positions one after other. The Frankish fortress Margat and Crac remained the last places in the hands of Hospitallers.

There were two periods of the building during the Mamluks era, the first one in Al Ẓāhir Bībars'period in 1270 and the other one during the Qalāūūn era in 1310 [241], see Figure 3.17d. In 1271 Bībars (Al Ẓāhir Bībars) sieged the castle with his army [242]. After taking the castle Bībars ordered to start the restoration work in the castle. Although the Mamluks did not radically change the construction of the Crusader castle, they repaired the damage caused by

Figure 3. 20 The restoration work of the Building (103) in 2006

their siege and added their distinctive character to the military architecture, see Figure 3.17c. They rebuilt the gate tower (130), tower (135), and the gate tower (120), and all of these towers had inscriptions commemorating the restoration work and the glory of Bībars. There were also

[240] Donald Hill, *A History of Engineering in Classical and Medieval Times* (2013):173.
[241] Mesqui, "L´architecture D´une Forteresse Hors Du Commum.":20.
[242] Jaroslav Folda et al., "Crusader Frescoes at Crac Des Chevaliers and Marqab Castle," *Dumbarton Oaks Papers* 36/1982 (1982): 177.

DOI: 10.15774/PPKE.BTK.2024.021

other rebuilding work during Bībars era without inscription commemorated them. In 1289 Qalāūūn orderd to build a square tower (tower 133) with an inscription commemorating it. During the Mamluk period in 1302 the castle was hit by a very violent hailstorm which caused the falling of the upper part of curtain wall 10-17a. That curtain wall was rebuilt with an inscription to the glory of the reigning Sultan al-Malik al-Naṣir Muḥammad.

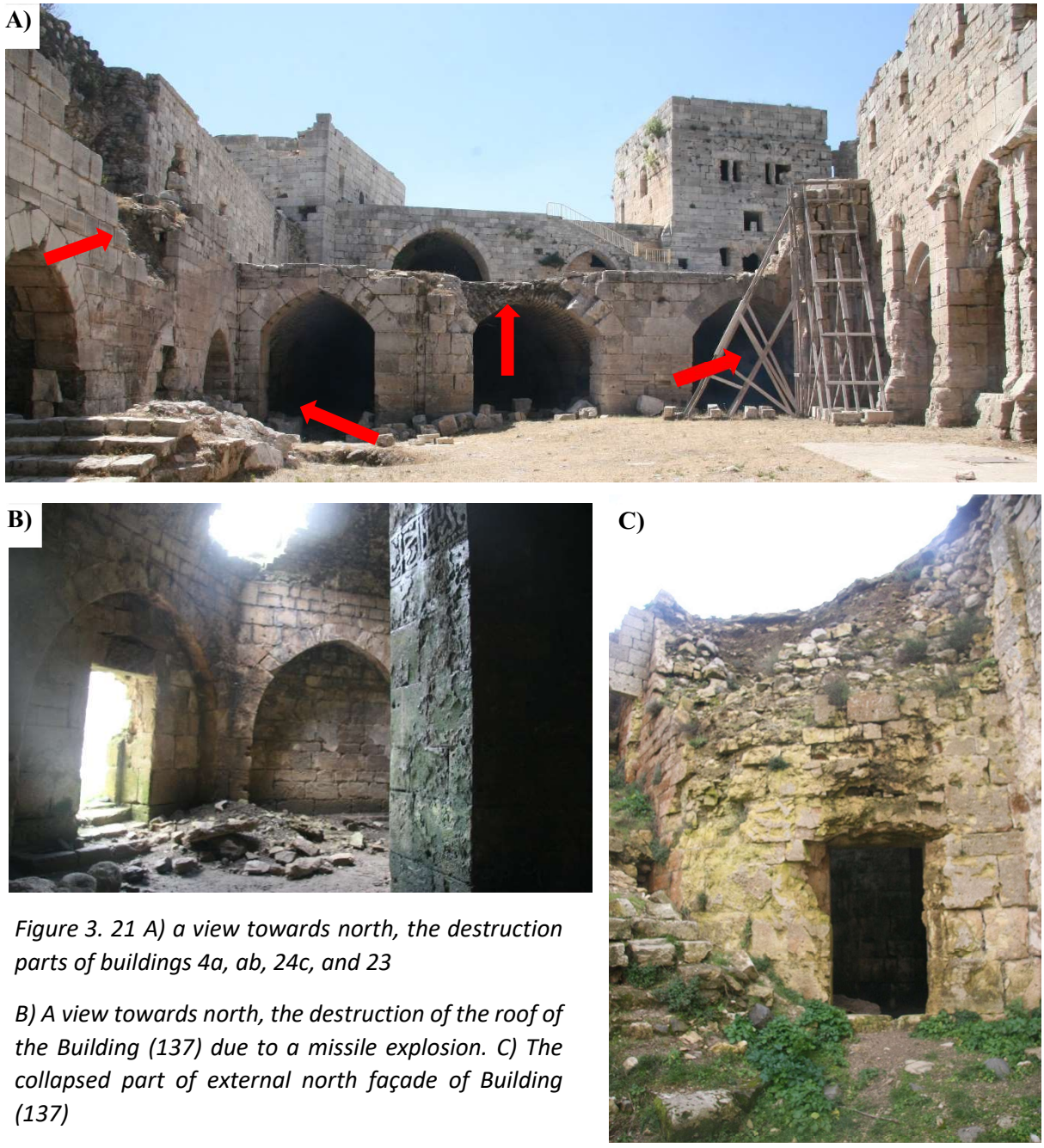

Figure 3. 21 A) a view towards north, the destruction parts of buildings 4a, ab, 24c, and 23

B) A view towards north, the destruction of the roof of the Building (137) due to a missile explosion. C) The collapsed part of external north façade of Building (137)

DOI: 10.15774/PPKE.BTK.2024.021

Later, during the Ottoman period, the castle lost its defensive role, and from 1860 it turned into a small village inhabited by the local population [243], see Figure 3.19.

In the French Mandate period, the castle was evacuated from local people [244]. It was subject to restoration by the French government in 1931 [245] where the relatively recent additions by local inhabitants were removed. The French excuted serious restoration and rebuilding works, such as the rebuilding of the collapsed part of the southeast facade of Building (103) in 1930.

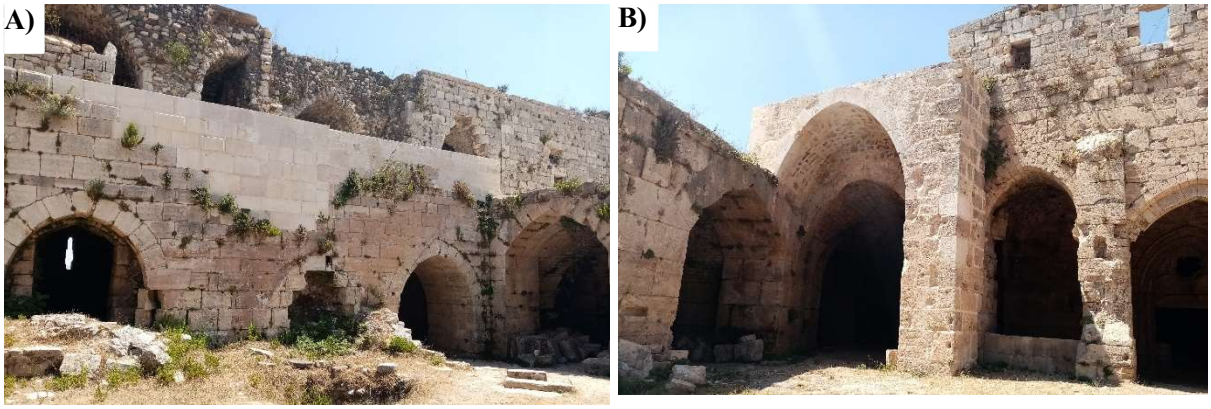

Figure 3. 22 A) The rebuilt parts of Building (23) that were completed in 2021. B) The rebuilding parts of Building (4a) that were completed in 2021

Following the evacuation of the French, the Directorate General of Antiquities and Museums (DGAM) in Syria took over the castle in 1949. DGAM began the restoration work in the castle in 1950, and until now, DGAM has accomplished several restoration and rebuilding work in the castle. In 1952, the missing parts of the west external facade of Building (36) in its second story were rebuilt by using stones and cement mortar. Some consolidation work was also carried out on the eastern facade of the Building (19). Many decoration parts in that facade were reinforced using cement and iron bars. Between 1951 and 1954, the eastern edge of the southern external facade of Building (46) was also rebuilt. That edge had previously been rebuilt between 1935 and 1936. In 2004, the external eastern facade of Building (36) was also restored by rebuilding some new stones and refilling the joints between the stones at the northern part and waterproofing its roof. In 2006 as part of the restoration work was a massive rebuilding of the curtain wall attached to the Building (103) from the north, see Figure 3.20. The waterproofing of the buildings was also carried out by the DGAM from 2003-to 2006.

[243] Teofil Retfalvi, "Burials in Crac Des Chevaliers Excavated in 2017," in *Bridge of Civilizations: The Near East and Europe c. 1100–1300*, ed. Peter Edbury, Denys Pringle, and Balazs Major (2019):79-88.
[244] Millar Burrows, "Palestinian and Syrian Archaeology in 1931," *Bulletin of the American Schools of Oriental Research* 45/1 (1932): 20–32.
[245] W F Albright, "Archaeological Exploration and Excavation in Palestine and Syria, 1935," *American Journal of Archaeology* 40/1 (1936): 154–67.

DOI: 10.15774/PPKE.BTK.2024.021

Between 2012 and 2014, the castle was highly affected by the recent war in Syria. The castle has been exposed to missiles, bullets, and bombs that caused various degrees of destruction in many different parts of the castle Figures 3.21.

Between 2017 and 2018, the waterproofing of the Building (20) and replacement of some damaged stones were accomplished. From 2020 till now, the rebuilding of destructive parts took place in many different buildings such as Building (36), Building (23), Building (4a), etc., see Figure 3.22.

The evaluation of the Crac des chevaliers as a military garrison

The permanent garrison was estimated about 430 men and 400 mounts, in addition to other number of people with different positions. The population present in the site of Crac usually reached a thousand people [246].

The castle was established to contain around 50-100 brothers, 50 knights and 30 sergents. To this workforce was added two other categories of combatants, Turcoples and crossbowmen [247]. Turcopoles were mostly Oriental Christian mercenaries, and their numbers varied depending on the resources available to the castellan and the Order during peacetime. Crossbowmen were foot soldiers equipped not only with crossbows but also likely spears and swords. Additionally, some individuals were responsible for managing religious affairs, while others were involved in various trades to ensure that the large garrison had access to provisions, arms, and necessary supplies for daily life. The castle also housed craftsmen who were tasked with fortifying the site. There was another population within the fortress comprising prisoners who were used for labor-intensive tasks.

Architectural development during the Frankish and Mamluk periods

This description is presented according to Jean Mesqui and Maxime Goepp analysis [248]. They divided the castle into two parts the upper castle and the outer enclosure around the upper one.

1. The outer enclosure is divided into seven sectors, see Figure 3.23.

Sector 1: It is constitutes an advanced defence of the enterance access to the castle, intended to protect the entrance through gate 102 in the lower courtyard of the barracks in the southeast.

[246] Mesqui and Goepp, *Le Crac Des Chevaliers: Histoire et Architecture*:40.
[247] Mesqui and Goepp:40.
[248] Mesqui and Goepp: 102-381.

DOI: 10.15774/PPKE.BTK.2024.021

The construction of this advanced defence during the Frankish period was part of an overall programme to extend the area of the castle towards the east, with the goal of improving the defence of the escarpment that forms the castle base. A gate tower leaning against the cliff and a powerful rectangular tower joining the enclosure of the lower barracks courtyard were part of the new access fortification. The ramp rose open between the two under the fire of a series of arrow slits served from a vaulted corridor at the top of the curtain crowing the escarpments. This sector was not built in a single campaign, but it had a high level of internal coherence and externality in its interactions with neighbouring elements. It can be dated between 1250 and 1270. Because the elevations of the towers had to be rebuilt, the sector was heavily shelled by

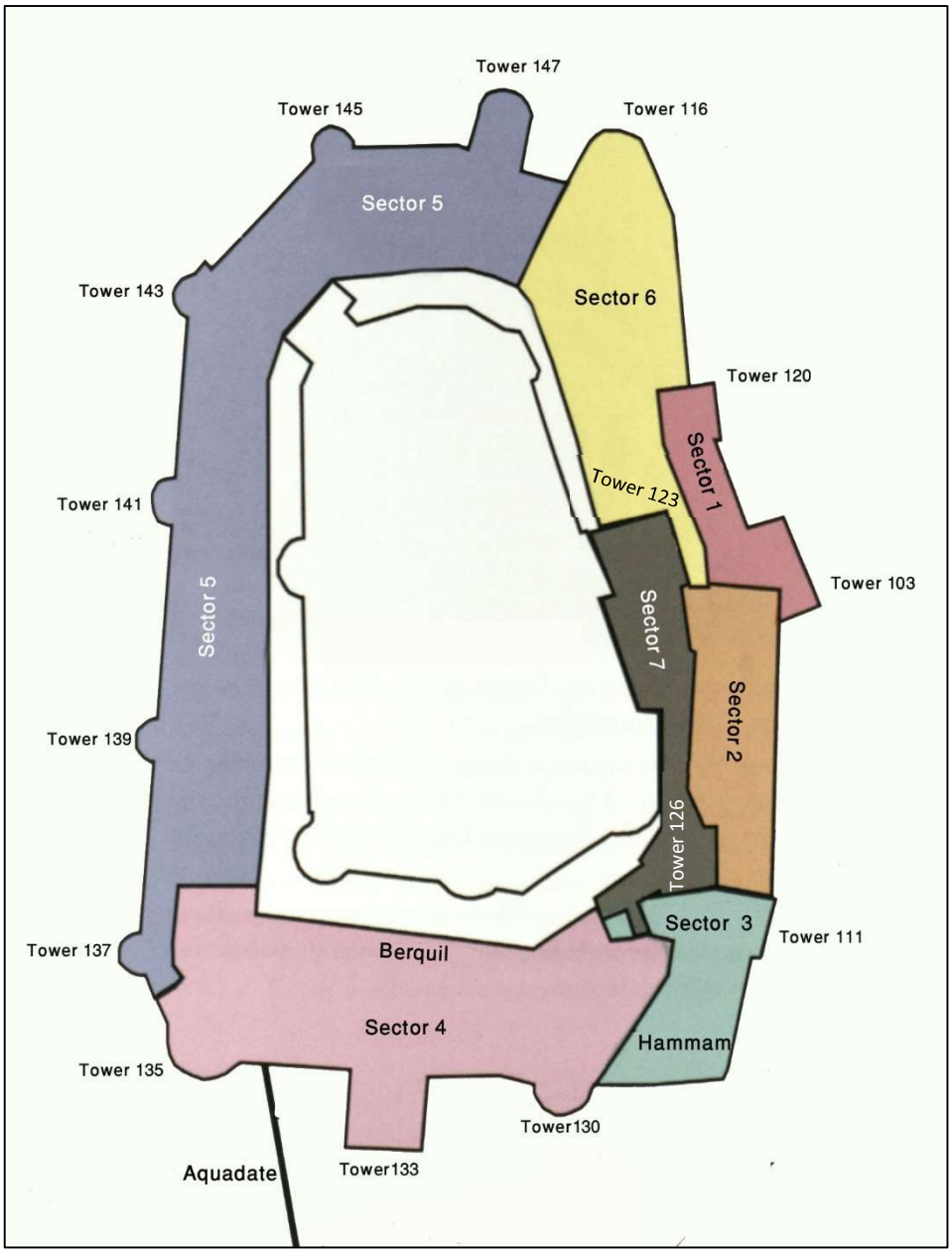

Figure 3. 23 The outer enclosure of the castle with its seven sectors. The plan was updated from [Mesqui and Goepp (2018)]

DOI: 10.15774/PPKE.BTK.2024.021

Bībars troops' artillery during the final siege. The complex was rebuilt and significantly raised, but it was not unitary. The Ottoman houses were removed from the castle during the French Mandate as part of the castle preservation programme; however, the houses above towers 103 and 120 were preserved.

Sector 2: The enclosure of sector 2 was constructed to gain useful surface area on the slopes east of the upper castle, with the dual goal of controlling the ramp further downstream and allowing for the installation of stables. This building is thought to have been completed around the time of the original construction (probably in the last third of the tenth century). That sector has changed significantly since the Frankish period. Significant changes occurred in the area during the Mamluk period, most likely as a result of the siege destruction.

Sector 3: It was originally completed outside the fortress, consisting of escarpments to the east, beneath the enclosure of the tower courtyard of the southern stables (see Figure 3.23). During the Frankish period occupation, an enclosure with extremely thick walls was built on this side to protect the easily accessible flanks, and this was done concurrently with the construction of the north of tower 120. That sector appears to have been unaffected by the siege. It was built to be large enough to accommodate a dual devensive and residential programme of high architectural quality. The Mamluk builders took advantage of the sectors' favourable altimetric situation to build the *Ḥammām* (bath) there. Tower 111, in addition to the Hamam, played an important role. Despite being obviously defensive in the first place, with hits arrow slits and its continous machicolation, it hosted a dignitary apartment on its upper floor (possibly for the residence of an Amir).

Sector 4: It is the southern courtyard of the castle. It is probably in its present plan from the first Frankish period at the end of the 12th century. There were many building periods can be recognised in this sector:

I. First Frankish period: The bailey's enclosure was originally a moderate-thickness basalt wall with a door leaves without projection near its south-eastern corner. To begin the western enclosure, a curtain was launched to the west, but it was not completed during the first Frankish period.
II. Second and third Frankish periods: During the second period, a very long vaulted stable was built between the southern enclosure and the moat, see Figure 3.23. The construction of the building was linked to a section of the glacis that covered the

DOI: 10.15774/PPKE.BTK.2024.021

southern counterscarp of the glacis. At the same time, the southern curtain wall was reinforced with external glacis.

III. Last Frankish period: The weakness of the defence of this sector promoted the Hospitallers to build the enclosure of sector 3 to the south- east, intended to effectively cover of the eastern flanks of the fortress.

IV. First Mamluk period: Following the siege, the southwest corner was most likely damaged; the construction site of a large circular tower equipped with a rectangular apartment block was launched at the expense of the stable with the dual goal of strengthening the area and providing a residence for the officer in charge of the stable. At the same time, an aqueduct was built. A semi-rectangular tower was glued in front of the door and inserted into the glacis on the other side, to the east. The glacis of the old curtain wall was restored in their western half, and the entire structure was topped by a double-level machicolation gallery that ran from tower 130 to tower 135.

V. Second Mamluk period: In 1285, an enormous sequare tower solid was built over two thirds of its height right in the middle of the curtain wall 130-135 which had no significant flanking at this point.

Sector 5: The way that the western and northern approaches to the rocky promontory that supports the higher castle were originally laid out is extremely difficult to restore. It is possible that the promontory was once surrounded on this side by a kind of flat area 20 to 30 m wide that expanded and slanted towards the north. Such a layout can still be seen south of the castle, at the base of the spur.

The enclosure of the western barbican of the castle was built in the middle of the 13th century according to the Frankish terminology of the Holy Land. This large building site was connected to the beginning of the south-eastern basalt wall, and it featured a moated wall flanked by five circular towers and a large rectangular tower, as well as a double summit gallery superimposing a vaulted corridor with breteches and a crenellated walkway, the first example of such development at the Crac. The rectangular tower to the north overlooked the preserved old moat. The upper castle was equipped with western glacis, thus the west face of the castle appeared in the middle of the 13th century.

The enclosure of the barbican itself was only marginally modified during the Mamluk period, and it was only in the southwest that major restoration was undertaken, with the reconstruction of the top of tower 137 as well as the top of the neighbouring curtain wall.

DOI: 10.15774/PPKE.BTK.2024.021

Sector 6: The lower enclosure and tower 116 were not added much later including new areas to accommodate the defenders, at the same time the enclosure of sector 3 was built. However, towers 103 and 120, as well as the large eastern ramp, were most likely built later.

Sector 7: The higher castle was built on a rounded triangle eminence, with its extremities bordered by escarpment to the west and east. The only access to the castle's upper platform was chosen roughly in the middle of the eastern face, most likely for topographical reasons. To reach it from the meeting point between the two access routes, the southern access via the barnyard of the large southern stable and the eastern access via large eastern ramp, a ramp was constructed

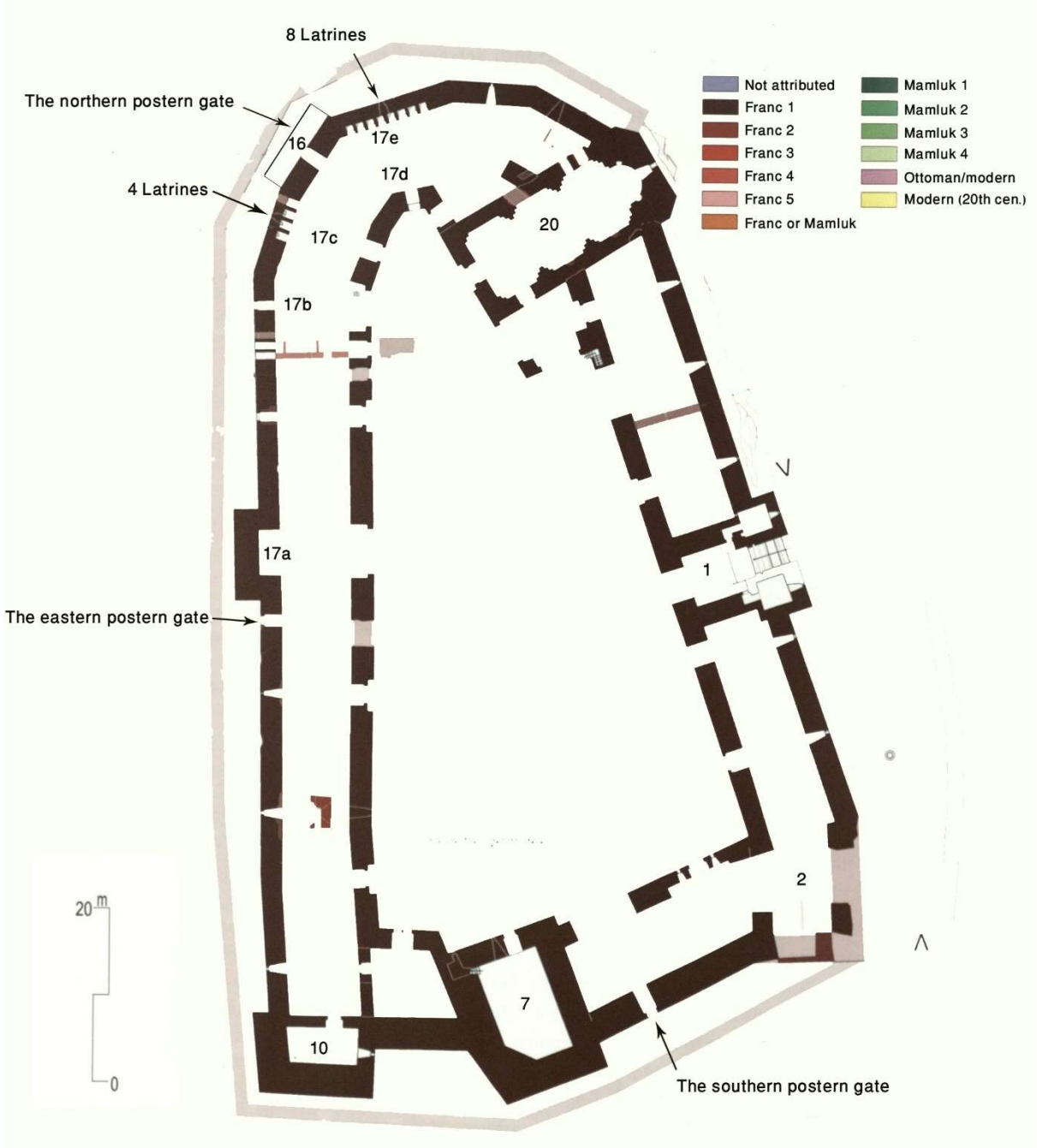

Figure 3. 24 The first Frankish building period of the upper castle

DOI: 10.15774/PPKE.BTK.2024.021

along the upper east escarpment. It forms sector 7 with its two terminal gate towers, the so-called Lion's gate to the south (tower 126) and *Miḥrāb* tower to the north (tower 123). The lion gate (tower 126), a major access point to the upper castle, is an evocative location for two reasons. The first is that its facing is made of large tabular bosses reminiscent of the outstanding ancient construction; the second is the presence of two recumbent lion sculptures dominating the south-east entrance.

2. The upper castle

The upper castle occupies the upper part of the rounded spur, which, like its rocky base, serves as a foundation for the fortification. All sectors of the Crac have a generally triangular plan. The mounted complex visible today is the result of three main mediaeval buildings combining two Frankish and one Mamluk phase.

- The Frankish construction campaigns

The first Frankish phase

The castle was designed in the first period as a subtriangle polygon bounded by seven irregularly arranged flanks (see Figure 3.24). Figure 3.24 depicts all of the buildings that can be dated to the first Frankish campaign. The plan depicted an enclosure with an external rectangular facing of limestone with tabulated bosses and an internally smooth facing with some exceptions. The vaults were constructed with rubble stones atop two courses of cut stones.

With the possible exception of the towers on the south front, this programme was essentially limited to ground-floor spaces. At the terrace level, as well as the tower levels, parapets surrounded the entire enclosure. These parapets (1.8 m high; 0.6 m wide) were made of limestone. Tower gate (1) with a vaulted hall on the ground floor on the east side with numerous arrow slits to primarily protect the gate. The chapel (20) has two main gates, one to the west and another to the south. The 120 m curved hall (17) was provided by 8-span latrines to the north and 4-span latrines to the west, as shown in Figure 3.24.

Paul Deschamps [249] considered that the first building campaign was undertaken in the 1140s after the Hospitallers had taken the position of the site, however in 1170 the work of Hospitallers was limited to the reconstruction of the chapel (20). Thomas Biller argued that the

[249] Paul Deschamps, "Les Châteaux Des Croisés En Terre Sainte/1. Le Crac Des Chevaliers Album," *Les Châteaux Des Croisés En Terre Sainte* 19 (1934): 275-277.

DOI: 10.15774/PPKE.BTK.2024.021

entire castle was completely rebuilt after the earthquake of 1170 [250]. Jean Mesqui suggested that the first building could be presented before 1170, so the building that can be dated to around 1170 was rebuilt with respect to the preexisting building at the begging of the 12th century [251].

The second Frankish Phase

It seems that the main goal of the Frankish construction campaign of the inner castle was to improve the defenses of the castle. The enhancement of the defensive role was obvious by providing the inner castle with a dressed stone glacis covering the rocky base of the previous

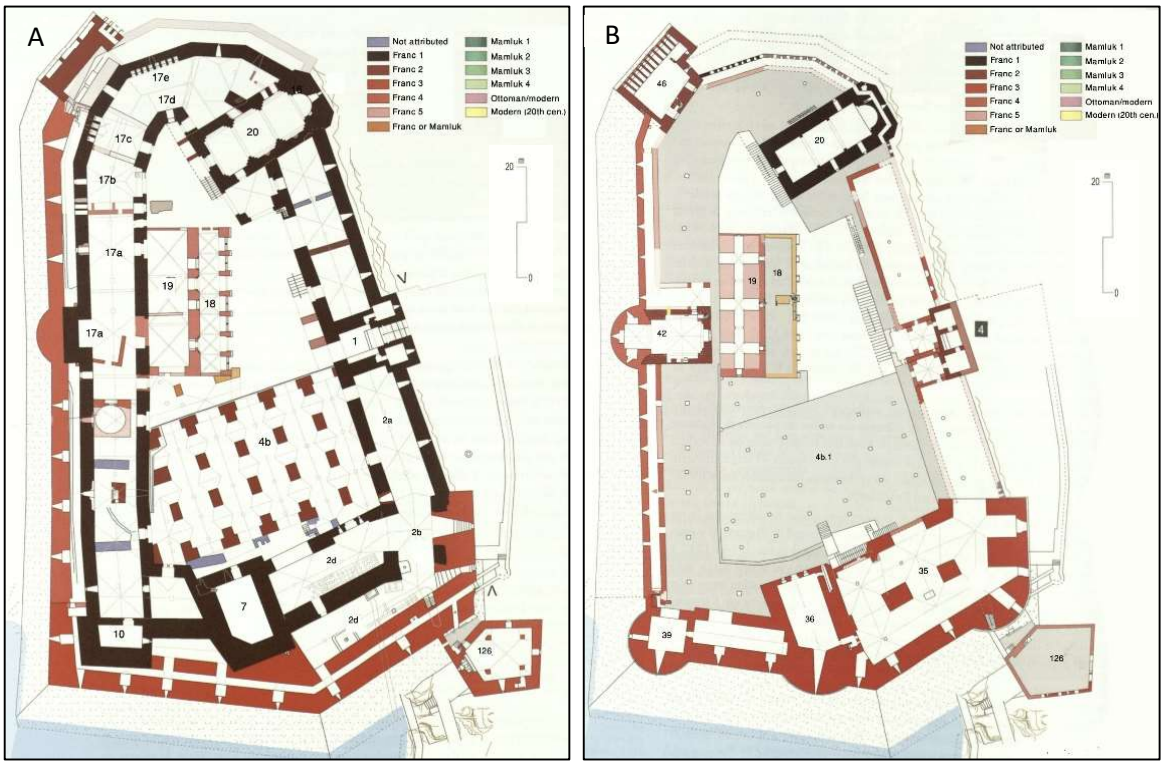

Figure 3. 25 The second Frankish building period of the upper castle. A) the ground floor. B) the first floor

building, absorbing the ground floor of the latter in an enormous mass of masonry from which powerful rounded towers emerged toward outside (tower 10, 7, and 2) the whole was furnished with several of several levels of arched allowing a more active defense of the building than before. The construction phase did not concern the east and north front of the castle.

During this campaign, a series of vaulted galleries (see Figure 3.25) were built on the castle's south and west sides to solve the defence problem on these sides. Those new galleries also

[250] Thomas Biller, "Die Johanniterburg Belvoir Am Jordan. Zum Frühen Burgenbau Der Ritterorden Im Heiligen Land," *Architectura: Zeitschrift Für Geschichte Der Baukunst* 19 (1989): 105–36.
[251] Mesqui and Goepp, *Le Crac Des Chevaliers: Histoire et Architecture*:313.

DOI: 10.15774/PPKE.BTK.2024.021

served another purpose, collecting wastewater and runoff water towards the northwest and the latrines complex.

- The Mamluk construction campigns

The siege of 1271 had little effect on the upper castle. Its state did not justify major defensive additions, as was done in the lower enclosure, as shown in Figure 3.26. However, the uppermost defences were strengthened on the most vulnerable fronts, and work was done in the interior to adapt the Hospitallers' fortress to the use of the Mamluk garrison and governor; however, those works are poorly documented because they were frequently the victims of the Ottoman village's expansion in the 1890s.

Figure 3. 26 The Mamluk building period of the upper castle. A) the ground floor. B) the first floor

DOI: 10.15774/PPKE.BTK.2024.021

4- In situ investigation:

DOI: 10.15774/PPKE.BTK.2024.021

4.1 In-situ stone classification

The castle was built mainly of carbonate stones (limestone, dolomitic limestone, and dolomite [252]. It is challenging to distinguish these stone types on the site, so they are called carbonate stones by collective name. In addition to carbonate stones, basalt stones were used to build of some buildings and they appear also in the foundation of some buildings in the outer castle

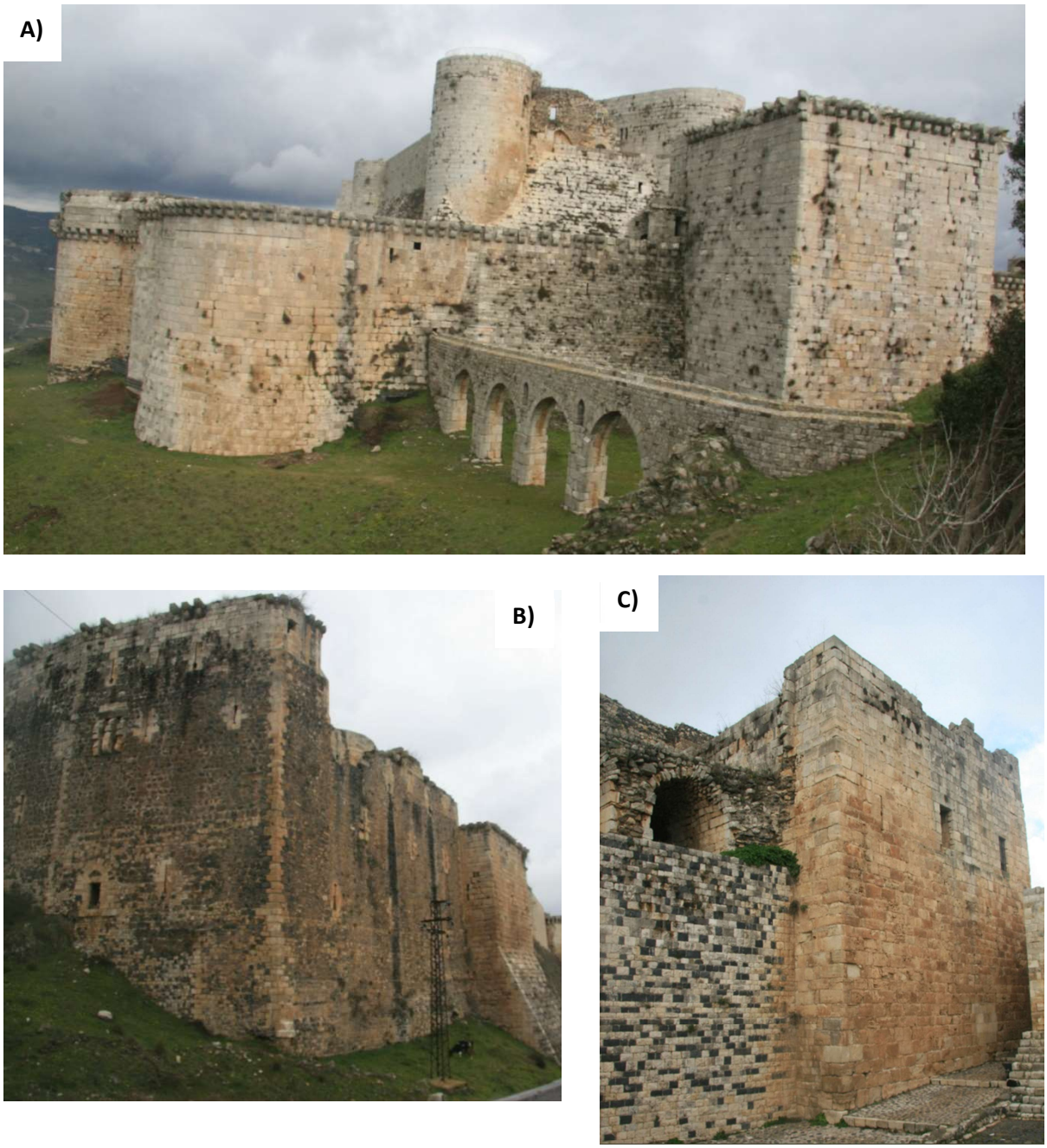

Figure 4.1. 1 A) The majority building stones are carbonate (The southern west corner of the castle). B) The southern east corner of the castle was mainly built by basalt stones. C) Some basalt stones were used in building of some parts inside the inner castle

[252] Eyas Al-Khateeb, "Masonry Structures at the Crusader Castles in Syria: Building Material, Building Technique, Damage and Conservation Methodology," (2008):22.

DOI: 10.15774/PPKE.BTK.2024.021

(Figure 4.1.1). As a response to build a prestigious halls containing many types of ornaments, carbonate stones were the best choice to be carved. As a result, the percentage of the carbonate stones used in the building stages of the castle was much more than the basalt stones (Figure 4.1.2).

Figure 4.1. 2 Some stone ornaments that are found in the castle

This study focuses on carbonate stones, because they are more borne to deterioration and less resistant to weathering than basalt. By the field investigation, the carbonate stones are categorized into four lithotypes as follows: 1) homogenous porous stones (HPS); 2) homogenous dense stones (HDS); 3) laminated stones (LS); 4) newly built stones (NBS). HPS is a homogenous carbonate stone with visible porosity, where the size of its pores ranges from

Figure 4.1. 3 The lithotypes of carbonate stones used in Crac des Chevaliers

DOI: 10.15774/PPKE.BTK.2024.021

0.5 mm to 2 cm. HDS is a homogenous dense stone whose porosity is not visible to the naked eye. LS is a laminated carbonate stone where the sedimentary layers appear clearly on its surface with 10-20 cm in height. In some laminated stones, big flint particles can be found parallel to the sedimentary layers; and the size of the flint particles ranges from 3 to 10 cm (Figure 4.1.3). NBS are the stones brought to the castle from nearby quarries for restoration work. These newly built stones were rebuilt during the restoration work between 2002 and 2006. HDS and LS are more common at the castle compared with HPS. The percentage of newly built stone is very low.

4.2 Decay types

Due to the long construction phase of the castle, carbonate stone blocks with different porosity and structural properties were built together. This variety in pore structure imposes a different moisture content, decay types, salt crystallization, and biological colonization on the stone surface. The diagnostic research has been begun with the classification of stone deterioration cases based on the proposals of [253] and defined the most serious issues that are: mechanical (impact) damage, microorganisms colonization, salt efflorescence, discoloration, cracks, graffiti, splitting, erosion, and encrustation.

1. Mechanical (impact) damage

Stone blocks have been damaged as a result of the recent armed conflict in Syria. These stones have varying degrees of destruction. Demolished and fragmented stone blocks (partially or entirely) cannot be restored and must be replaced instead, see Figure 4.2.1 & Appendix 1_Figure 1. The size of every single fragment from the stone ranges 0.5-10 cm in width and 1-10 cm in depth. However, the direct bullets left powdering areas on the stone surface, see Figure 4.2.2 & Appendix 1_Figure 2. The diameter of the hole, caused by the bullet, is around 15 cm while its depth is around 5 cm from the stone surface. Missile fragmentation leads to a loss in stone material with a thickness of about 0.5 – 1.5 cm and flaking parts with a thickness ranging from submillimeter to

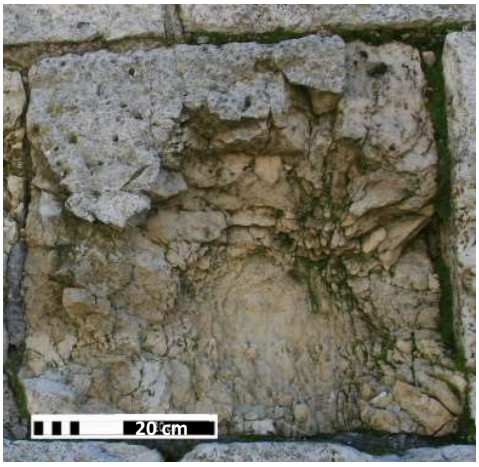

Figure 4. 2. 1 Fragmentation case

[253] Vergès-Belmin (2011)

DOI: 10.15774/PPKE.BTK.2024.021

1-5 millimeters (Figure 4.2.3 & Appendix 1_Figure 3). The stones exposed to direct bullets are still restorable in most cases. The pitted
and rough surfaces of the outer façades from the shots represent a favorable environment for the flourishing of various species of microorganism colonization.

Figure 4. 2. 2 Powdering case in stone

Figure 4. 2. 3 Loss in stone material case in stone exposed to missiles fragmentation

2. Microorganisms colonization

Colonization of microorganisms is very common on both the external and internal walls. The ambient environment of the castle is favourable for flourishing many kinds of microorganisms. The following three main types of biological colonization are the most characteristic species in the castle: grey, red-orange, and green microorganisms. The presence of grey microorganisms gives a grey appearance to the stone surfaces (Figure 4.2.6 & Appendix 1_Figure 6). They are concentrated on the west and north external façades, where the moisturized stones can be dried in summertime leading to the drying of the microorganisms

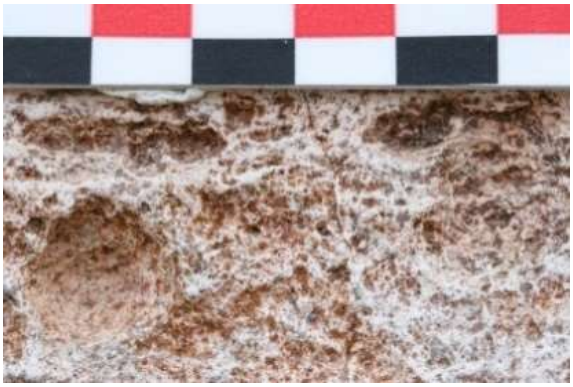

Figure 4. 2. 5 Red- orange microorganism colonization

Figure 4. 2. 4 Green microorganism colonization

DOI: 10.15774/PPKE.BTK.2024.021

on them. They are also present in south and east façades on shaded areas by plants. The thickness of the colonization is very thin (not visible to the naked eye) in most cases.

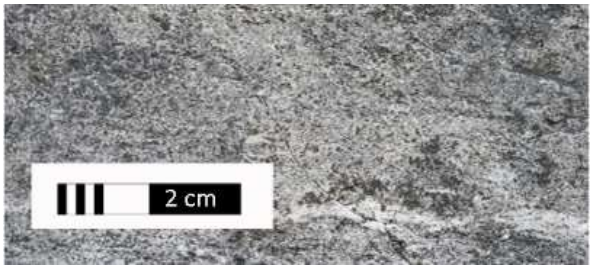

Figure 4. 2. 6 Grey microorganism colonization

The red-orange microorganisms are concentrated on an external damped stone surface that does not receive a high rate of sunlight. They are widespread, even in summertime, in the external north façades of the castle in the areas with continuous moisture (see Figure 4.2.5 & Appendix 1_Figure 7). The colonization has a very thin layer on the stone surface, their thickness is not identifiable by the naked eye.

Figure 4. 2. 7 The microorganism colonization on third pillar from west of the first northern row of Pillar of Building (4) (east face)

The green microorganisms are presented in the internal façades that always have enough moisture to flourish. Many of the castle towers suffer from water infiltration in the walls that mainly occurrs as a side effect of the bombing and leads to the dense presence of green microorganisms on the inner walls, see Figure 4.2.4 & Appendix 1_Figure 5. The colonization also occurs on the outdoor stones affected by bullets and missiles fragmentations (specifically in the powdering and fragmented areas). Their thickness varies on the stone surface from a moisturized green layer with no thickness to a 1cm thick layer on some stones.

Figure 4. 2. 8 The microorganism colonization on the second pillar from west of the first northern row of Pillar of Building (4) (east face)

Two other species flourish only at Building (4) on the first northern pillars. This building was exposed to bombing shots and this area is suffering from heavy water infiltration on the pillars. The first can be found on the east face of the third pillar from the west of the first northern row of the Pillar of Building (4). (the same location as the B2 sample, see Appendix 3). The colonization is coloured orange, green, and black. It forms a thin layer with a thickness of less than 0.5 mm, and that layer is peeled off

DOI: 10.15774/PPKE.BTK.2024.021

from the stone surface in some areas, with a small amount of stone material attached to it. (Figure 4.2.7 & Appendix 1_Figure 8). The second one can be found on the east face of the second pillar from west of the first northern row of Pillar of Building (4) (the same location as the B5 sample, see Appendix 3). That colonization is brown and has the appearance of moistened sand (Figure 4.2.8 & Appendix 1_Figure 9).

Figure 4. 2. 9 Black and white microorganism colonization on the outermost west edge of the south external façade of Building (46)

Black and white microorganisms flourish on the external southern façade of the Building (46). They vertically grow at the western edge of the façade. They heavily colonize that section in a thickness of around 1-3 mm (Figure 4.2.9 & Appendix 1_Figure 10).

The presence of higher plants in the castle is widespread and is considered one of the serious issues that challenge the conservation state of the stones there. The invasive plants include the growth of shrubs and herbaceous species. The shrubs and trees influence the stability of the whole wall and threaten the entire structure of the building (see Figure 4.2.11 & Appendix 1_Figure 4). The herbaceous

Figure 4. 2. 11 Herbaceous species grow in the joints between the stone blocks

Figure 4. 2. 10 shrub that grows on the east corner of Building (39). The red arrow refers to massive crack caused by the plant

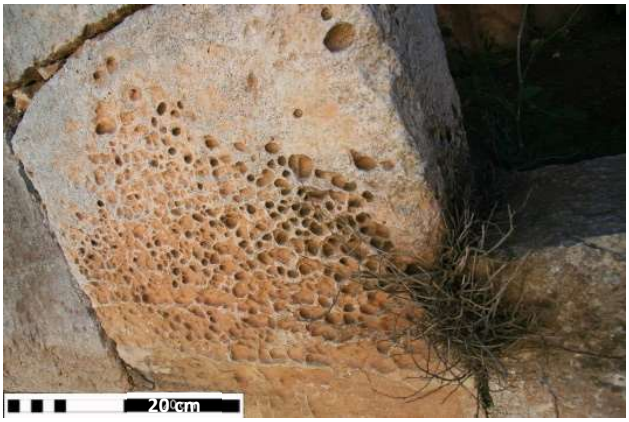

Figure 4. 2. 12 A Pitting case

DOI: 10.15774/PPKE.BTK.2024.021

species are widespread between stone joints or even inside the cracks (see Figure 4.2.10 & Appendix 1_Figure 4). The role of invasive plants in stone deterioration is not only a physical aspect. The growing plants exercise additional stresses on their surrounding masonry by the continuous growth of their stems and roots. The invasive plants contribute to the chemical deterioration of the stone surface through their respiration process resulting in acidic erosion in the form of pitting, see Figure 4.2.12 & Appendix 1_Figure 14. The thickness of the eroded area on the stone surface ranges from less than 0.5 mm - 0.5 cm. Whereas, the circle shape of this erosion has a diameter range of 1 mm -1 cm.

3. Salt efflorescence

Salt efflorescence and sub-efflorescence are not only presented on the ground floor level because of rising damp but also at the level of the upper floors where that salt appears in light thickness, see Figure 4.2.13 & Appendix 1_Figure 11. One of the sources of salts is the air-bearing sea salts. The castle is located around 35 km away from the coast.

Figure 4. 2. 14 Salt efflorescence on a stone surface located in the first floor. The salt source is from sea spray effect

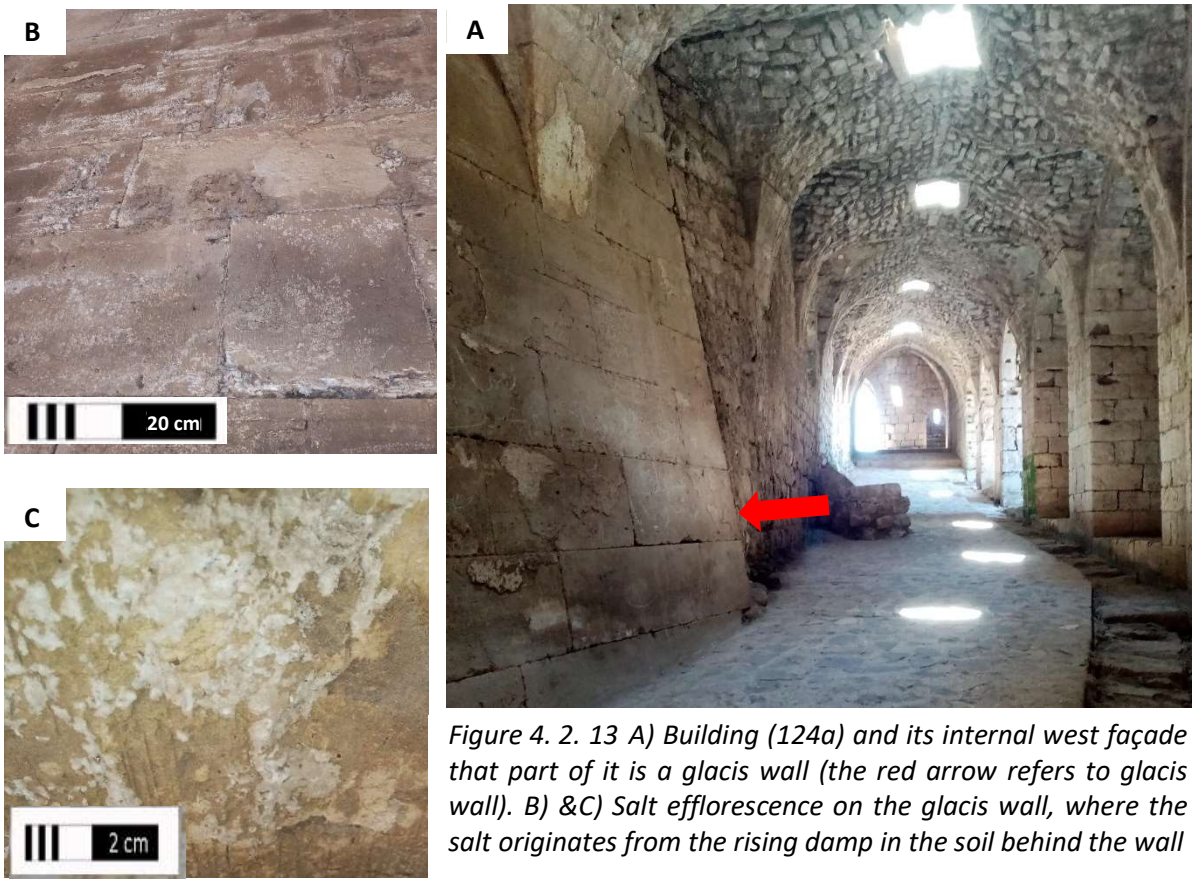

Figure 4. 2. 13 A) Building (124a) and its internal west façade that part of it is a glacis wall (the red arrow refers to glacis wall). B) &C) Salt efflorescence on the glacis wall, where the salt originates from the rising damp in the soil behind the wall

DOI: 10.15774/PPKE.BTK.2024.021

Salts can be seen on the stone surfaces exposed to rising damp from the soil, such as the stones located near the ground or glacis walls that retain soil behind it, such as in Building (124a) (see Figure 4.2.14).

4. Discolouration

The discolouration with the orange of both east and south façades is a characteristic feature of the castle, see Figure 4.2.15 & Appendix 1_Figure 13. This colour is most likely caused by sunlight whose radiation hits these façades all day. In contrast, the shaded area (e.g.by higher plants) at these façades does not have this discolouration. Furthermore, this colouration co-

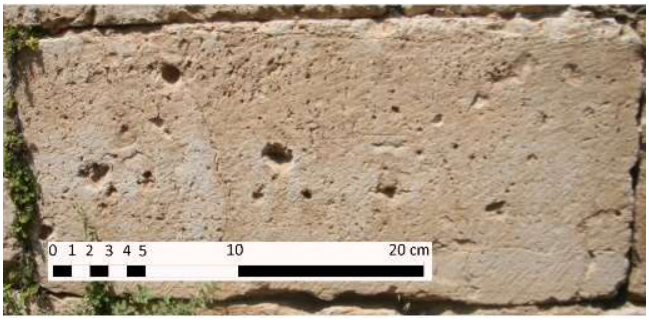

Figure 4. 2. 16 Discolouration with orange

Figure 4. 2. 15 Discolouration with orange together with scaling part and salt sub-efflorescence

occurs by scaling with some traces of salt sub-efflorescence in some parts of the stone. The thickness of the exfoliated layer on the stone surface is about 0.5 cm, see Figure 4.2.16 & Appendix 1_Figure 12.

5. Cracks

Cracks of different types can be also found at the castle. The first type of crack is a fracture that divides the stone into two parts. The thickness of the fracture ranges from 0-2 cm (Figure 4.2.17 & Appendix 1_Figure 16).

Figure 4. 2. 17 A fracture in the middle of the stone

DOI: 10.15774/PPKE.BTK.2024.021

Star crack is a network of cracks that originate from one point. That point is created by mechanical damage that might be resulted from the bombing effect or the growth of higher

Figure 4. 2. 18 A star crack

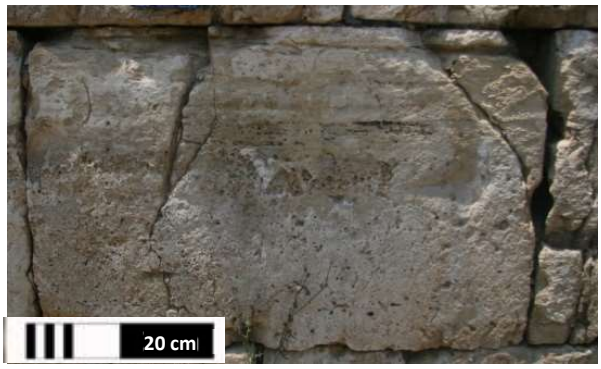

Figure 4. 2. 19 Hair cracks

plants (Figure 4.2.18 & Appendix 1_Figure 17). Hair and minor cracks can also be found on some stones in the castle. The bombing effect does not cause those cracks, however many of them existed before the war. The sizes range from 0.5 mm to 2 cm and they do not cause separation of the stone parts (Figure 4.2.19 & Appendix 1_Figure 18).

6. Graffiti

Graffiti is widespread on the stones at the castle, where paint marker pen or sharp tools were used for writing (see, Figure 4.2.20 & Appendix 1_Figure 20).

Figure 4. 2. 20 A) Graffiti by using paint. B) Graffiti by using sharp tool

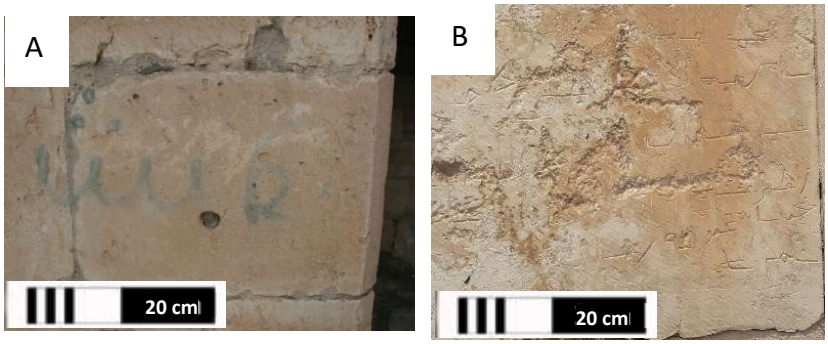

7. Specific deterioration cases in specific buildings

Specific deterioration cases are only found in certain buildings in the castle, as follows:

- Building (35) at the castle is characterized by two typical deterioration cases: On the inner façades, all the stones were eroded or eroded and split. The eroded surfaces are smooth, and the stones have rounded corners. The eroded

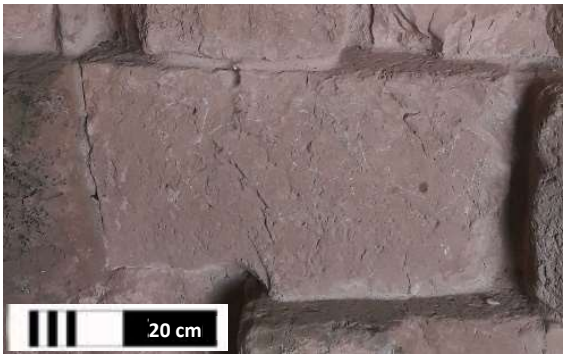

Figure 4. 2. 21 Eroded surface in Building (35)

DOI: 10.15774/PPKE.BTK.2024.021

stones lost around 1 mm-1 cm from their surface (see Figure 4.2.21 & Appendix 1_Figure 15). That building also contains stones with splitting parts that are fragmented and weakly attached to the mother stone. The sizes of splitting parts are variable (between 2- 10 cm in depth and 1-15 cm in width).

Figure 4. 2. 22 Splitting in Building (35)

In some stones, splitting parts appear in white and grey colours (see, Figure 4.2.22 & Appendix 1_Figure 19).

- In both Building (19) and Building (23), some sheltered stones were exposed to bullet or missile fragments. On the damaged areas of these stones an orange material deposits weakly on the stone surface (see, Figure 4.2.23 & Appendix 1_Figure 21).

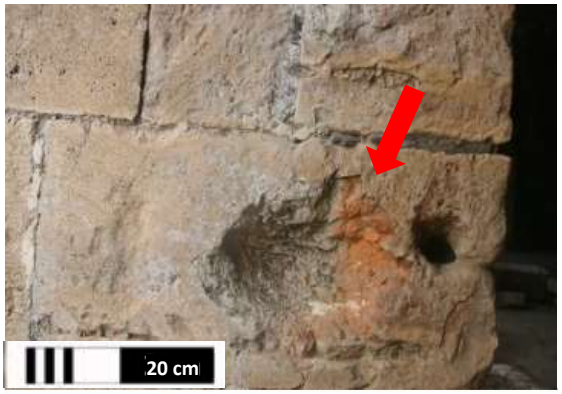

Figure 4. 2. 23 Deposition of orange material on the damaged parts by bullet at Building (19)

- On the northern and eastern internal façades of Building (38), rounded material deposits heavily on the stone surfaces (encrustation). This framboidal crust adheres to the stone firmly. Each round is 2-5 mm in diameter. (see, Figure 4.2.24 & Appendix 1_Figure 22).

Figure 4. 2. 24 Framboidal encrustation case in Building (38)

4.3 The use of non-destructive techniques

4.3.1 Methods

4.3.1.1 Rilem tube penetration test

The water absorption behaviour of the stones is frequently influenced by the stone type and by many factors such as the weathering degree of the stone, the presence of salts, or biological colonisation. Water uptake capacity is a vital feature, because water is considered a key factor in weathering phenomena. Rilem tube measurements are performed to determine the water absorption ability of the stones as a function of the lithotypes and the current weathering state.

DOI: 10.15774/PPKE.BTK.2024.021

In this study, a tube with a diameter of 1.17 cm and a length of 15 cm is used. The diameter of the circle that is fixed to the stone surface is 2.58 cm (Figure 4.3.1). The tube is graduated from 0-15 cm in mm scale.

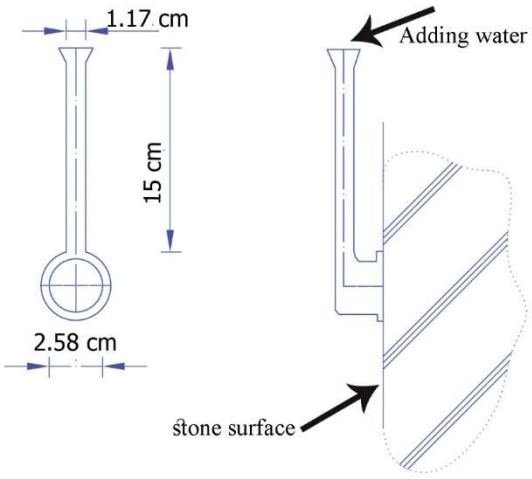

Figure 4. 3. 1 The application of Rilem tube on the stone surface

After fixing the tube to the stone surface with plasticine, it is filled with water. Once the water begins to drop inside the tube, the stone absorbs the water. To know the absorption speed, the time and the amount of absorbed water are measured.

The amount of absorbed water per area is calculated depending on the time as follows:

Q= q/A [cm3/cm2] Equation 4

where A[cm2] is the area of the circle that is applied to the stone surface (in this measurement $A = \frac{\pi \cdot 2.58^2}{4}$ [cm2]); and q: The amount of water in each 1 cm inside the tube [cm3].

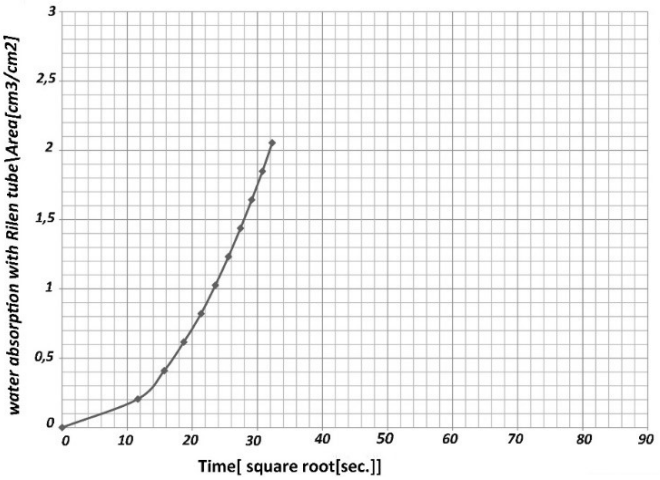

Figure 4. 3. 2 The standard absorption curve. This curve represents the absorption rate as the result of the variation of the absorbed water per area by the square root time

The absorption rate curve is drawn by using two parameters: (Q) the amount of absorbed water per area and the square root of the consumed time (Figure 4.3.2). That absorption curve is independent of the diameter of the tube and is usually used in academic research because it deals with the amount of water per area by time. The tube is filled once only in each test, so the water pressure applied by the water column inside the tube decreased over time. As a result, the stone is not exposed to constant water pressure.

DOI: 10.15774/PPKE.BTK.2024.021

4.3.1.2 Deterioration mapping

Deterioration mapping includes various decay forms that are surveyed precisely on a given façade by the photogrammetry technique. The photogrammetry technique, which is used in this investigation, consists of several steps to fulfil. At first, 5-6 surveying points are fixed to the defined façade; and those points are measured by a topographical total station (Sokkia power set 1030R3). Then the façade with its survey points is photographed by the camera. To use this photo in its geometrical scale, the photo is rectified, depending on the surveying points measured before, by using Perspective Rectifier software (version: 3.3.37894.23). That software allows exporting the rectified scaled photo to the AutoCAD software (version: 0.49.0.0 AutoCAD 2018) to draw the weathering forms on it.

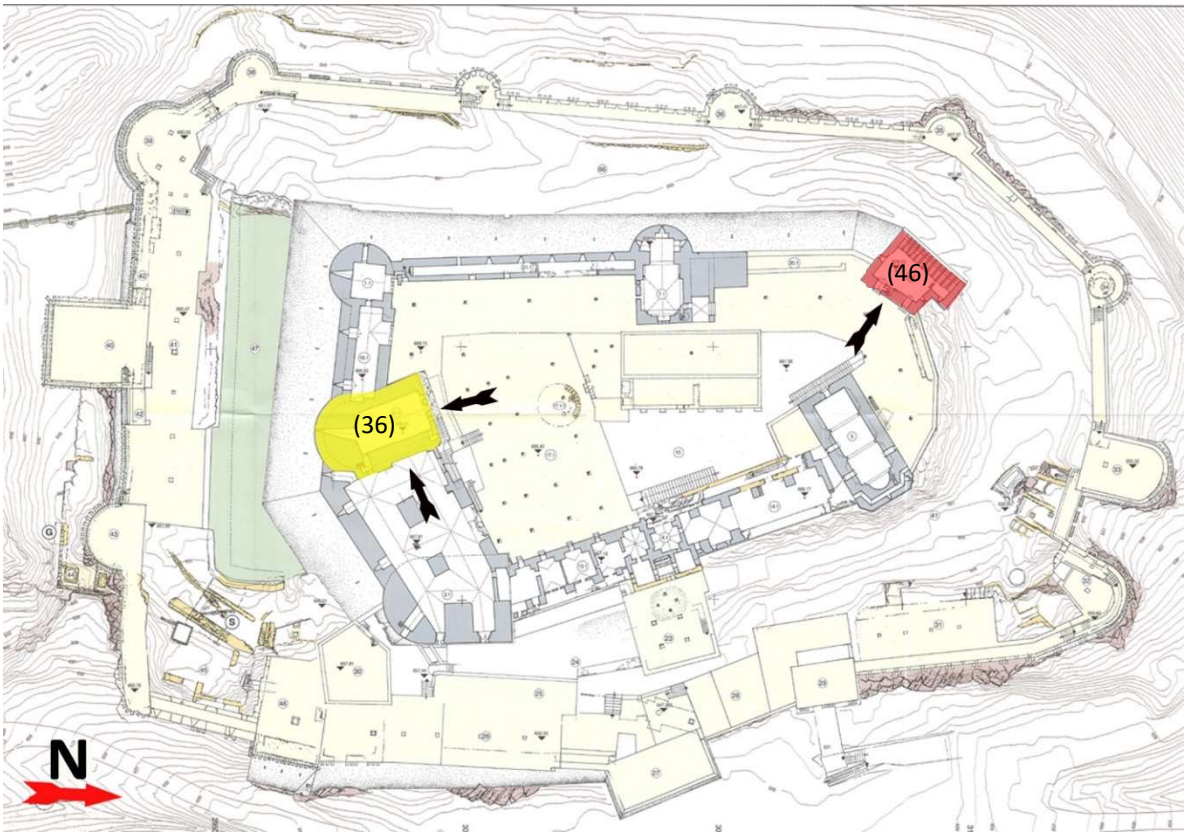

Figure 4. 3.3 The towers with the mapped facades in Crac des Chevaliers: The building (46) is highlighted with red and the building (36) with yellow

The deterioration mapping is performed on the external south façade of the building (46), as well as on the external east and north façades of the building (36), see Figure 4.3.3. These three façades are chosen based on the following criteria: i) the different directions of each one, which imposes several deterioration cases; ii) the accessibility of each façade for easy identification of the deterioration types to the naked eye; iii) the inclusivity and variety of the types of

DOI: 10.15774/PPKE.BTK.2024.021

deterioration at the three façades, which can represent the weathering occurrences of the stones at the Crac des Chevaliers in general.

4.3.1.3 Schmidt hammer

Because of the value of the historical building, determining the compressive strength with the uniaxial compressive strength test in the laboratory is impossible. As a result, a non-destructive technique, the Schmidt hammer rebound tester, is chosen to assess compressive strength. A fundamental priority is preserving the tested stones from any possible harmful effect, so a low-impact energy hammer is utilised. The Schmidt hammer which is applied in this investigation is the "VSYIQI" HT-75 brick rebound hammer, see Figure 4.3.4

The specifications of the hammer[254]:

- Impact energy: 0.735 J.
- Rebound hammer stroke: 75 mm.
- Rebound pole: 15 mm.
- Static friction between pointer slider and shaft: 0.4-0.6 N.
- Size: ϕ 60*280 mm.
- Net weight ≈ 1 KG.

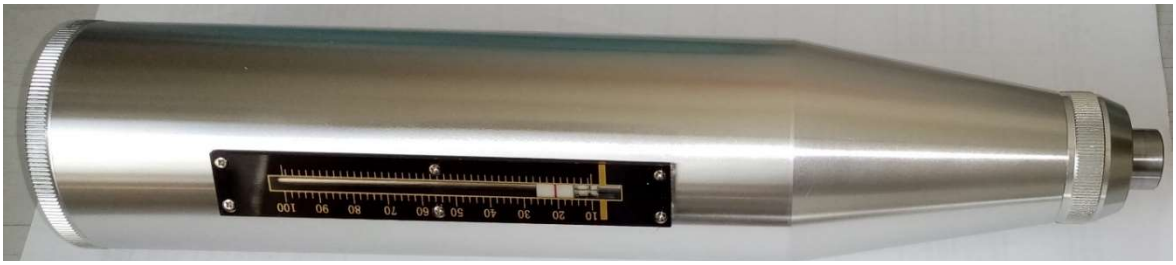

Figure 4. 3. 4 "VSYIQI" HT-75 brick rebound hammer

In lots of former research works, the Proseq rebound hammer was used. The rebound values of the VSYIQI hammer are compared with the Proseq hammer and converted after drawing the correlation curve between the rebound values of the two hammers. To achieve that, a L- type Proseq hammer and the VSYIQI- HT-75 hammer are used to measure three different strengths (at a steel anvil and on two different limestones (Hungarian travertine from Süttő and Jurassic limestone from Siklós). The relationship between the rebound value of two hammers is

[254] Manual user book of "VTSYIQI" Schmidt hammer.

DOI: 10.15774/PPKE.BTK.2024.021

exhibited in Figure 4.3.5. From that relationship the calibrated rebound values of tested stones are obtained in this study.

Many different points are chosen to be measured horizontally by the hammer in each stone tested. The measuring points are evenly distributed on the stone surface (the stone surface is divided into rows and each row contained many measured points with equal distances). As a result, the rebound values are measured at least on 20 points of each tested stone. Statistical calculation is needed to conclude the rebound number in each tested stone. The statistical study is completed with the use of "PASW Statistics 18" software. Outlier values are determined and omitted, and the average as well as standard deviation are also calculated. The outlier values are usually either very low readings (presence of hidden cracks or fissures) or very high readings (visible flint particles on the stone surface or hidden ones under the surface). The stones, which are tested by Rilem tube, are also tested with a Schmidt hammer. The locations of the tested stones are exhibited in Table (Appendix 2). However, the results of the statistical study of the measurement are shown in Table 4.3.7.

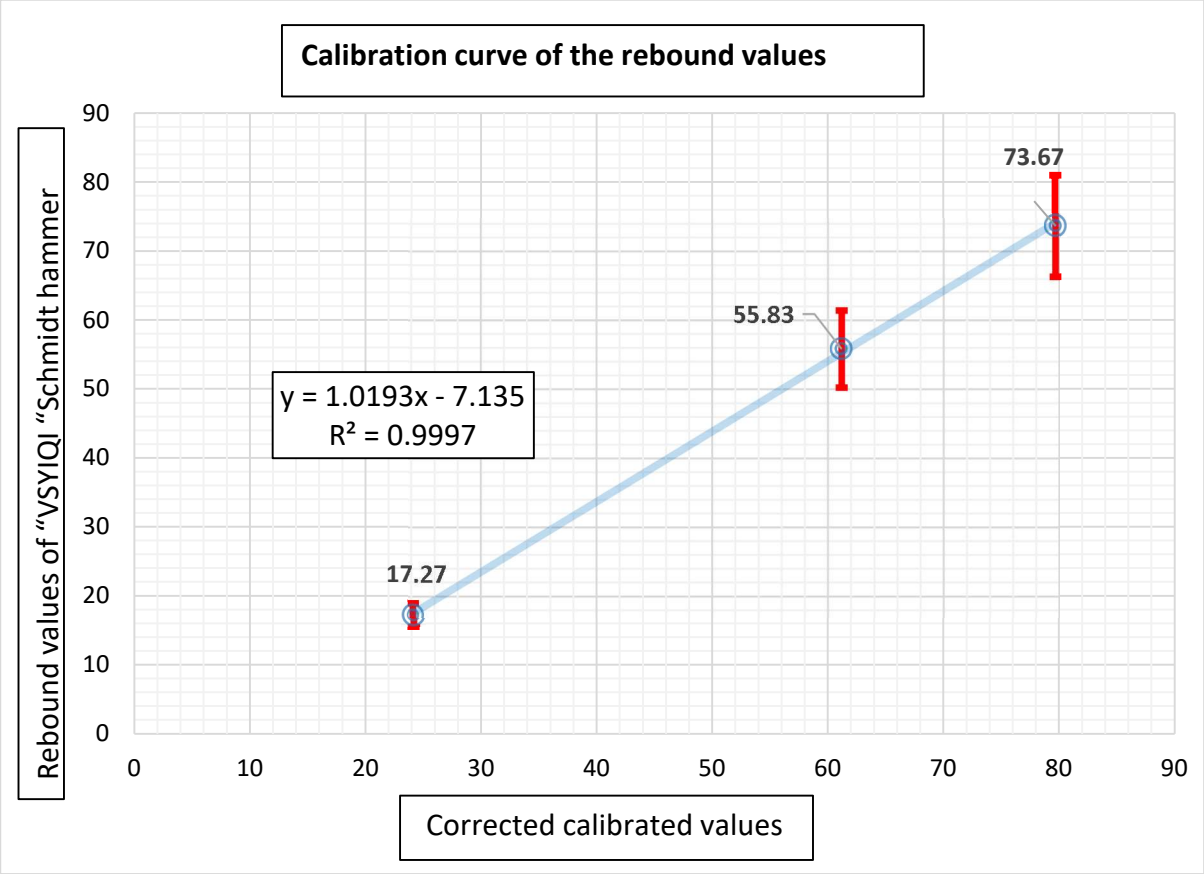

Figure 4. 3.5 The correlation curve of rebound values of the VSYIQI Schmidt hammer

DOI: 10.15774/PPKE.BTK.2024.021

4.3.2 Results and discussion

4.3.2.1 Rilem tube penetration test

The different kinds of lithotypes [laminated stones (LS), homogenous dense stone (HDS), homogenous porous stone (HPS), and new built stones (NBS)], as well as several decayed stone surfaces, are examined by this technique. The results of the tested surfaces with General documentation of the tested stones with Rilem tube, their location at the castle, orientation, lithotype, absorption behaviour, and stone deterioration type is shown in Table 4.3.1, Table 4.3.2, and Appendix 2.

The water absorption behaviour depends on the stone condition, its orientation and its location. The stone condition includes the stone deterioration type (salt efflorescence, biological colonisation, or affected by mechanical shock); its spread (e.g. whether the biological colonisation covers the stone surface totally or partially); and its intensity on the surface (e.g. the thickness of salt crust or the biological colonisation). The location means in which course

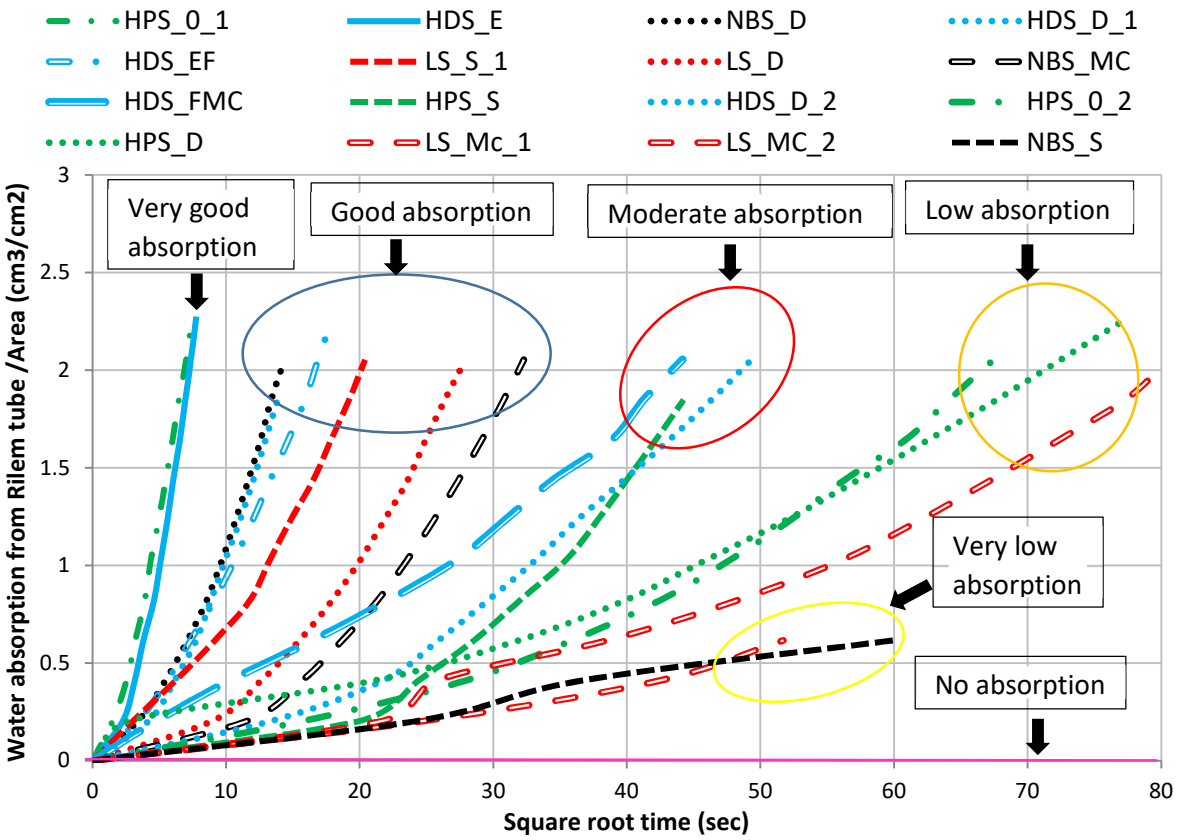

Figure 4. 3. 6 The absorption diagram of the tested stones by Rilem tube at Crac des chevaliers. In this chart the line colour refers to a stone lithotype, however the line type refers to a stone decay type. In the case of two stones with the same lithotype and same stone decay such as (LS_MC_1& LS_MC_2); (HPS_0_1 & HPS_0_2); and (HDS_D_1 & HDS_D_2), the first curve corresponds to the lower number in the names of the two similar stones

DOI: 10.15774/PPKE.BTK.2024.021

Table 4. 3. 1 The tested stones with the Rilem tube (with location, orientation and absorption behaviour) (The order of the tested stones in the table are according to the decreasing water absorption behaviour order as exhibited in Figure 4.3.6)

Name	Lithotype	Orientation	Location	Deterioration type	Absorption behavior
HPS_0_1	HPS	Inside a building	Ground floor- 3rd row.	-	Very good absorption
HDS_E	HDS	Inside a building	First floor- 3rd row.	Eroded surface.	Very good absorption
NBS_D	NBS	South	First floor- 3rd row.	Discolouration with orange	Good absorption
NBS_MC	NBS	South	First floor- 3rd row.	Black and white microorganisms colonization	Firstly very low then good absorption
HDS_D_1	HDS	South	second floor- 1st row.	Discolouration with orange	Good absorption
HDS_EF	HDS	Inside a building	First floor- 3rd row.	Eroded and fragmented surface	Good absorption
LS_S_1	LS	South	First floor- 2nd row.	Salt efflorescence	Good absorption
LS_D	LS	South	First floor- 3rd row.	Discolouration with orange	Good absorption
HDS_FMC	HDS	North	Ground floor- 3rd row.	Fragmented stone + red- orange microorganisms colonization	Moderate absorption
HPS_S	HPS	South	First floor- 3rd row.	Salt efflorescence	Firstly very low then moderate absorption
HDS_D_2	HDS	East	Ground floor- 4th row.	Discolouration with orange	Moderate absorption
HPS_0_2	HPS	North	Ground floor- 3rd row.	-	Low absorption
HPS_D	HPS	South	Second floor -5th row.	Discolouration with orange	Firstly very good then low absorption
LS_MC_1	LS	North	First floor- 3rd row.	Grey microorganisms colonization	Firstly very low then low absorption
LS_MC_2	LS	West	Second floor-2nd row.	Grey microorganisms colonization	Very low absorption
NBS_S	NBS	East	Second floor-2nd row.	Salt efflorescence	Very low absorption

DOI: 10.15774/PPKE.BTK.2024.021

Table 4. 3. 2 The tested stones with the Rilem tube with their location at the castle, their orientation, and their absorption behaviour (The order of the tested stones in the table are according to their lithotypes)

Name	Lithotype	Orientation	Location	Deterioration type	Absorption behavior
NBS_0_1	NBS	East	Ground floor -4th row	_	No absorption
NBS_0_2	NBS	West	Second floor -3rd row	_	No absorption
HDS_0	HDS	north	Ground floor -1st row	-	No absorption
HDS_DS	HDS	East	First floor- 2nd row	Discolouration with orange+ Salt efflorescence	No absorption
HDS_D_3	HDS	East	Ground floor -4th row	Discolouration with orange-brown	No absorption
HDS_D_4	HDS	North	Ground floor -1st row	Discolouration with brown	No absorption
HDS_MC_1	HDS	West	Second floor -2nd row	Grey microorganisms colonisation	No absorption
HDS_MC_2	HDS	West	Second floor -3rd row	Grey microorganisms colonisation	No absorption
HDS_MC_3	HDS	West	Second floor -3rd row	Grey microorganisms colonisation	No absorption
HDS_MC_4	HDS	North	First floor- 2nd row	Grey microorganisms colonisation	No absorption
HDS_MC_5	HDS	North	First floor -1st row	Red - orange microorganisms colonisation	No absorption
HDS_MC_6	HDS	Inside a building	Ground floor -5th row	Green microorganisms colonisation	No absorption
HDS_S	HDS	East	First floor- 2nd row	Salt efflorescence	No absorption
LS_MC_3	LS	South	First floor -4th row.	Grey microorganisms colonisation	No absorption
LS_S_2	LS	South	First floor- 2nd row	Salt efflorescence	No absorption
LS_DS	LS	East	Second floor -2nd row	Discolouration with orange + Salt efflorescence	No absorption
HPS_MC	HPS	North	Ground floor- 2nd row	Red - orange microorganisms colonisation	No absorption

DOI: 10.15774/PPKE.BTK.2024.021

and story of the building, the tested stone is built. Blocks located on the ground floor are usually exposed to rising damp (through capillary absorption from the ground). It can reduce the water absorption behaviour by the Rilem tube if the pores of the stone are full of water from the

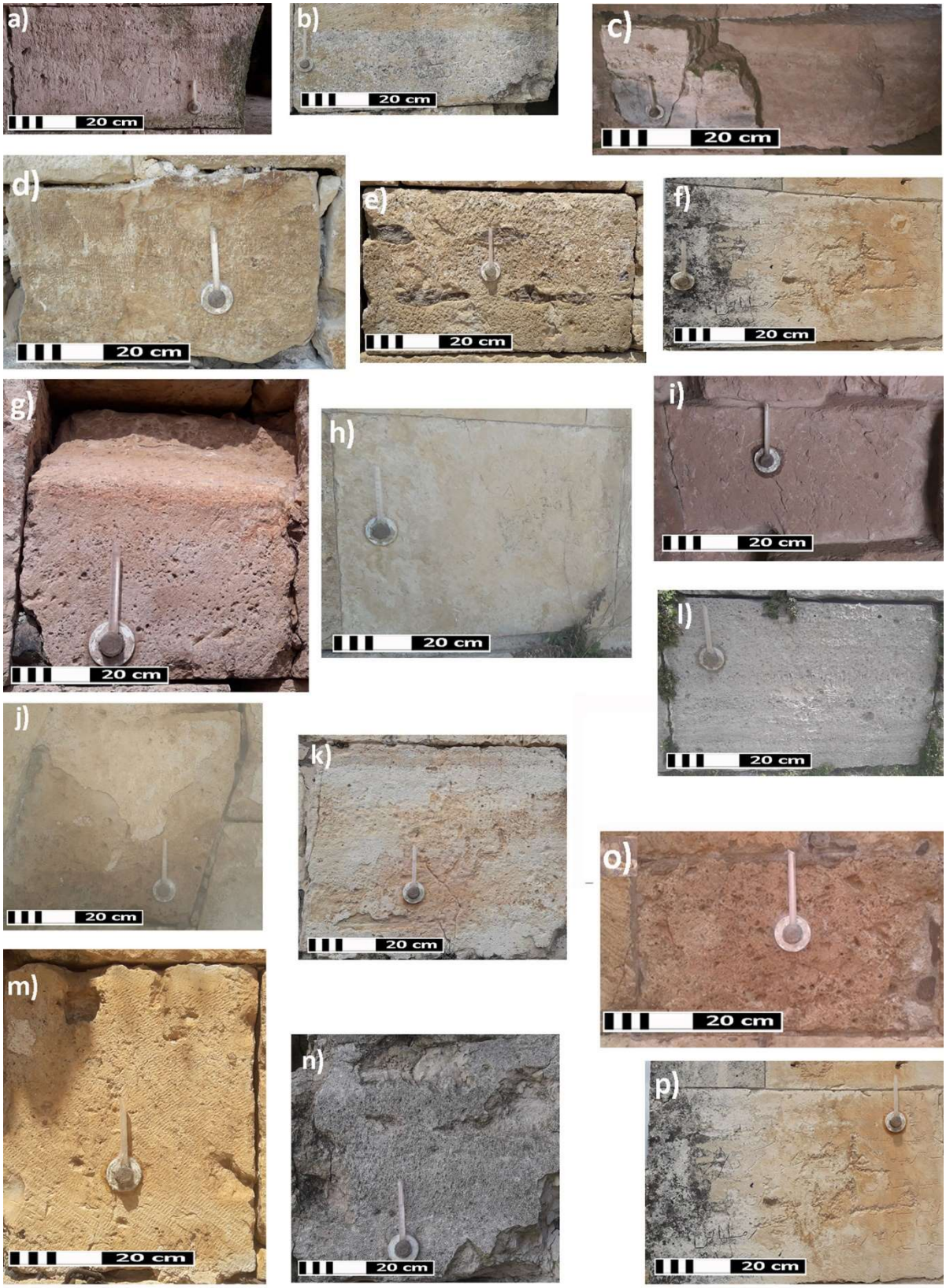

Figure 4. 3. 7 The stones that absorb water at the castle

DOI: 10.15774/PPKE.BTK.2024.021

ground. different absorption behaviour are collected and classified. This classification is a local one, and it expresses the relative differences in water absorption of Crac des Chevaliers stones.

The stones reveale different degrees of absorption ranging from non-absorption or neglected absorption to a rapid one, see Figure 4.3.6.

Even though HPS_0_1 and HDS_E belong to different lithotypes, they have very good and identical absorption behaviour. They are both located in sheltered places inside buildings, and there is nothing covered their surfaces. HPS_0_1 is a homogenous porous stone whose surface does not have any distinct deterioration, see (Figure 4.3.6 &Figure 4.3.7a). HDS_E is a homogenous dense stone, whose surface is eroded, and many fissures appear on it (Figure 4.3.6, curve 2 & Figure 4. 3.7i).

The common factor between the stones, which reveal good absorption behaviour, is that all of these stones, except HDS_EF, are oriented towards the south. Both NBS_D and NBS_MC are linked to the same stone, a new one built by a restoration work in 1954. The stone is located in the 3rd row of the external south facade (at the first floor) of the building (46).

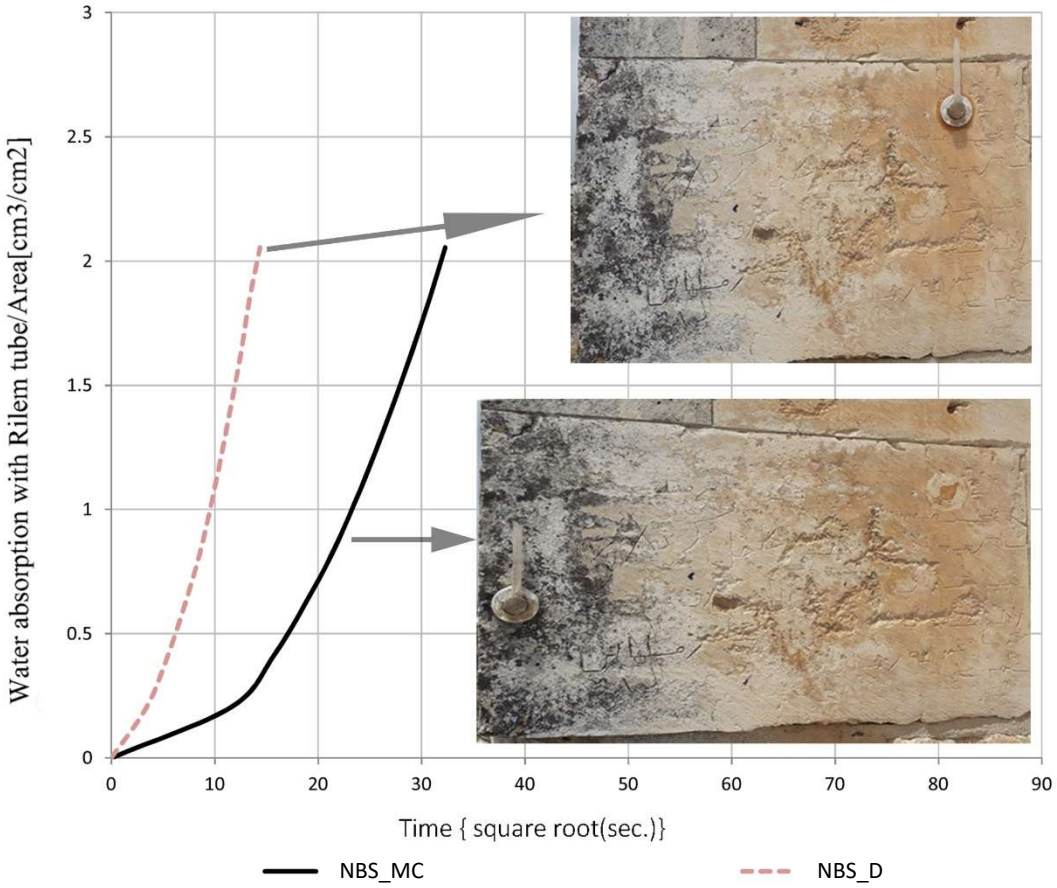

Figure 4. 3.8 A comparison between two-absorption behaviours of a stone that has two different kind of stone deterioration. NBS_D represents the discolouration part. NBS_MC shows the presence of black and white microorganisms on the stone surface

DOI: 10.15774/PPKE.BTK.2024.021

This stone is characterised by discolouration with orange in one part and an accumulation of black and white microorganisms in the other part (Figure 4.3.7f & Figure 4.3.7p). NBS_D curve represents the water absorption curve of the discoloured area, whereas the NBS_MC curve represents the water absorption curve of the microbial colonised part.

The water absorption of the colonised part starts with low absorption and then it becomes good behaviour, see Figure 4.3.8. The low absorption corresponds to the first centimetre of water inside the tube. The high water pressure at the beginning opens the passage to the later water, therefore, the absorption enhances from low to good. Comparing the curves of the two stone halves with different deterioration show that the absorption behaviour of the discoloured part is better than the microbial one. As such, the microbial colonisation reduces the absorption ability of this stone (Figure 4.3.8).

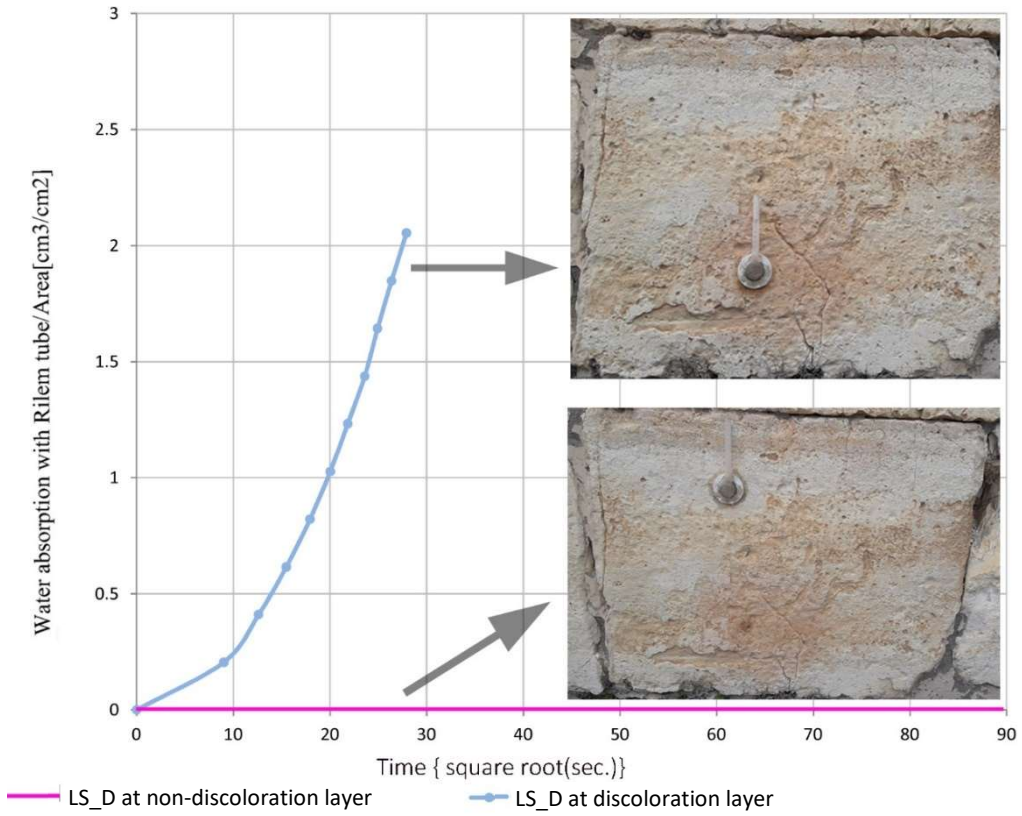

Figure 4. 3. 9 A comparison between two-absorption behaviours of a stone that has two different kind of stone deterioration. The white layer has no absorption behaviour that is represented by pink line. The orange discolouration of the same stone has good absorption behaviour, and it is represented by LS_D

DOI: 10.15774/PPKE.BTK.2024.021

HDS_D_1 is a homogenous dense stone whose surface is discoloured by orange, see Figure 4.3.7m. It demonstrates a good absorption behaviour, and its absorption curve is identical to the absorption curve of NBS_D, see Figure 4.3.6. HDS_EF is a fragmented homogenous dense stone with an eroded surface (Figure 4.3.7c). This stone, like HDS_E, is located inside Building (35), and both stones

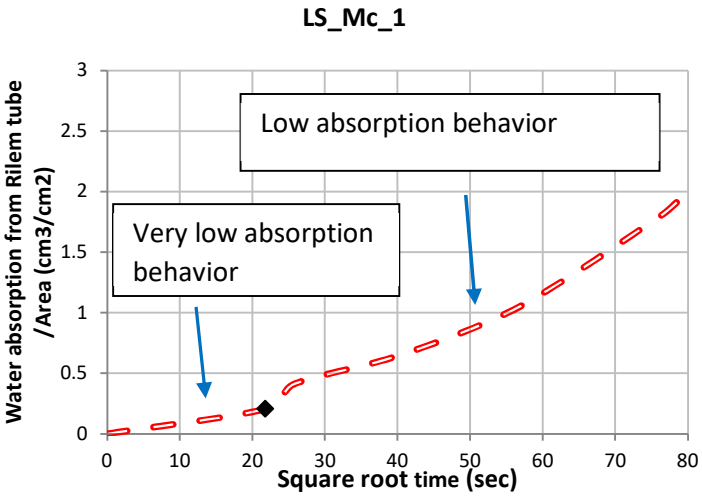

Figure 4. 3. 10 The absorption curve of LS_MC_1 stone. The black dot on the curve corresponds to the first cubic centimetre the stone absorbed

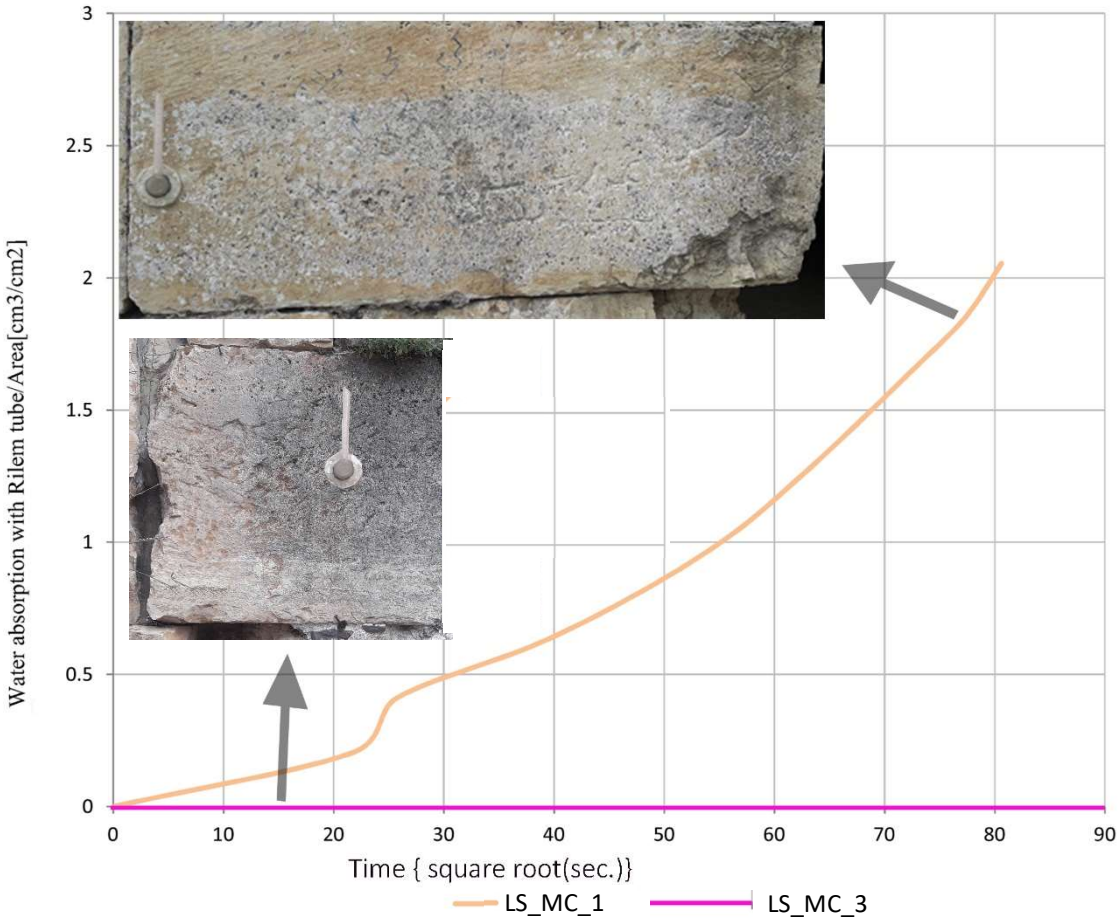

Figure 4. 3. 11 Water absorption with Rilem tube on two laminated stones with grey microorganisms. Pink line - LS_MC_3 (no absorption, stone located at the external south façade of Building 42); Orange line – LS_MC_1 (low absorption, stone located at the north external façade of Building (36))

DOI: 10.15774/PPKE.BTK.2024.021

have eroded surfaces; however, the absorption rate of HDS_E is higher than the one of HDS_EF, see Figure 4.3.6.

LS_D is a laminated stone that has discolourated layers with orange. So it has white and orange layers (Figure 4.3.7k). The white layers of the stone have macropores, whereas the orange layers (discolouration) do not have any visible pores. This stone reveals two different absorption behaviours, where two experiments are carried out at the white layers and show non-absorption behaviour. On the other hand, the orange discolouration demonstrates good absorption (Figure 4.3.6). Consequently, the white-coloured layer leads to no absorption behaviour (Figure 4.3.9).

The water absorption of the surfaces colonised with microorganisms show the effects of those biofilms on the water wettability of the stone surface. The stones colonised with grey microorganisms reveal low or no absorption. Consequently, these grey microorganisms form a waterproof layer that affects the water absorption at various degrees depending on its thickness. The laminated stones LS_MC_1 and LS_MC_2 are located at the north (first floor-

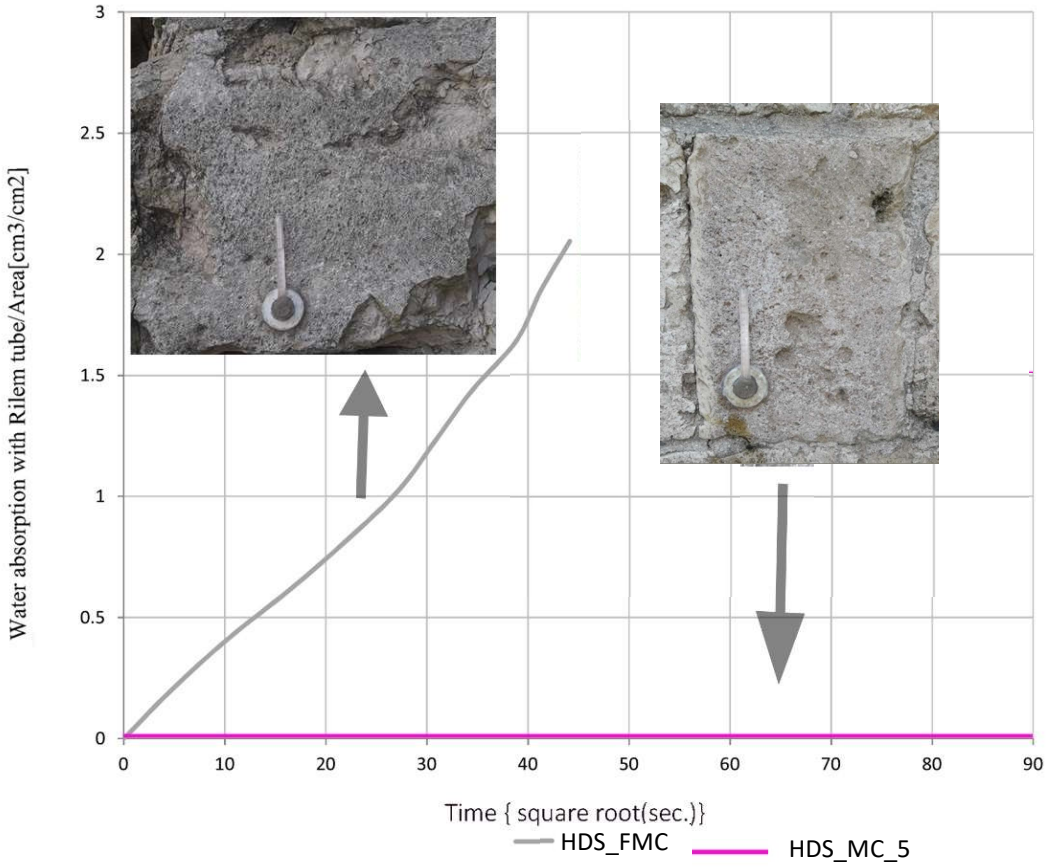

Figure 4. 3. 12 Water absorption with Rilem tube on two homogenous dense stones with red –orange microorganisms. Pink line - HDS _MC_5 (no absorption, stone located at the external north façade of Building 36); grey line – HDS_FMC (moderate absorption, stone located at the north external façade of Building (137.1))

DOI: 10.15774/PPKE.BTK.2024.021

3rd row) and west external façade (second floor- 2nd row) of Building (36), respectively. They are colonised by grey microorganisms (Figure 4.3.7b and Figure 4.3.7l), and both reveal at the beginning very low absorption. The wettability of LS_MC_1 changes a few minutes later. Once the stone absorbs the first cubic centimetre of water from the tube, it changes to low absorption (Figure 4.3.10).

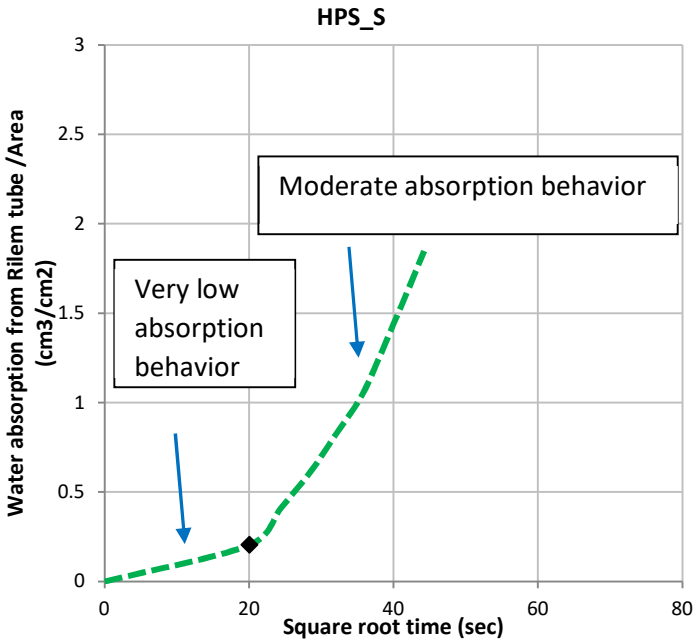

Figure 4. 3.13 Water absorption with Rilem tube of HPS_S. The black dot on the curve corresponds to the first cubic centimetre absorbed water

This change cannot be recognizable on the stone block LS_MC_2 (Figure 4.3.6). The different absorption behaviour between two stones colonised by grey microorganisms is

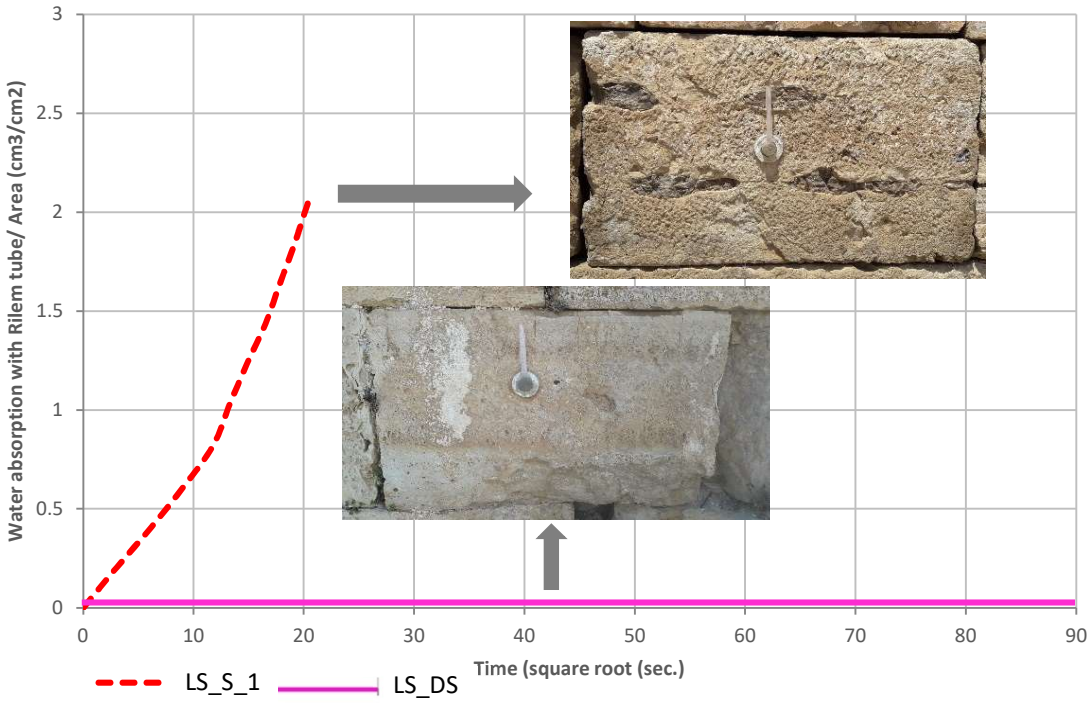

Figure 4. 3.14 Water absorption with Rilem tube on two laminated stones with salts efflorescence on their surfaces. Red line - LS_S_1 (good absorption behaviour; stone located in the external east façade of Building 42). The Pink line- LS_DS (no absorption behaviour; stone located in the external east façade of Building (36)

DOI: 10.15774/PPKE.BTK.2024.021

shown in Figure 4.3.11. They both have grey microorganisms on their surface. The first one is located in the north external façade of Building (36) and reveals low and very low absorption behaviours (LS_MC_1). However, the other one is located in a south external façade of the Building (42) and has no absorption (LS_MC_3).

Another example of the microbial colonisation effect on water absorption is the presence of red-orange microorganisms on the stone surfaces. HDS_FMC is a homogenous dense stone covered with that kind of microorganism. This stone is located on the north façade of the Building (137.1). This building is exposed to bombing shots, so the stone is fragmented (Figure 4.3.7n). The mechanical shock, which affected the stone, creates micro-cracks on the stone surface. In most cases, microcracks in the stone structure increase the interconnected porosity and thus facilitate the water penetration into the pores. Despite the microcracks, this stone demonstrates moderate absorption because it is colonised with red-orange microorganisms that protected the surface against water (Figure 4.3.6). While red-orange microorganisms colonisation on the non-cracked stone surface leads to no water absorption such as in HDS_MC_5. Therefore, when the stone, which colonized by red-orange microoganisms, is exp osed to mechanical shots, the behaviour changes from no absorption to moderate see Figure 4.3.12.

The salt efflorescences also changes the water absorption property of the stones. The homogenous porous stone with salt efflorescence on the surface (HPS_S, Figure 4.3.7g) is located at the external east façade of Building (42) and has a very low water absorption at the beginning of the measurement (ca. 7 min). However, the water absorption increases (moderate absorption) after the stone absorbs the first cubic centimetre of water from the tube (Figure 4.3.13). The salts reduce the water movement from the tube to inside the stone in the beginning.

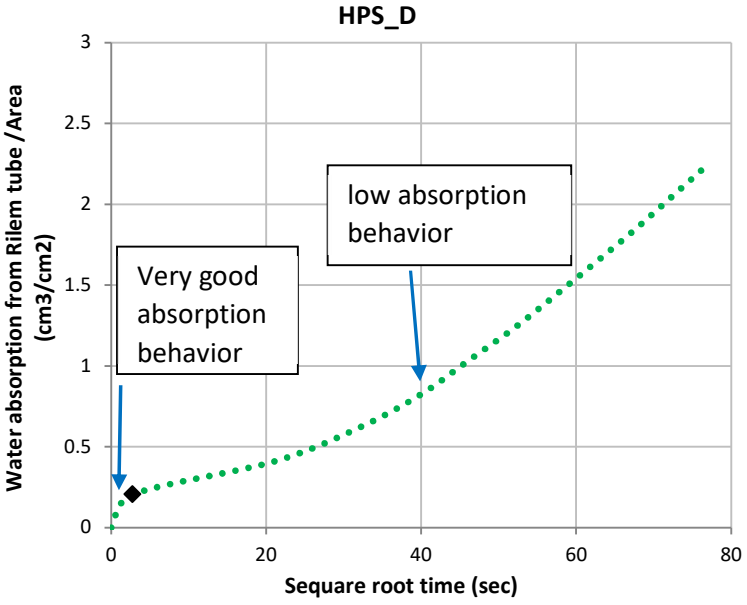

Figure 4. 3. 15 The absorption curve of HPS_D stone. The black dot on the curve corresponds to the first centimetre the stone absorbed

DOI: 10.15774/PPKE.BTK.2024.021

LS_S_1 is a laminated stone with salt efflorescence on its surface (Figure 4.3.7e). That stone is located on the external east façade of Building (42). The absorption behaviour of this stone is good even though the presence of salt on its surface (Figure 4.3.6). Where the borders areas between flint particles and the stone might create weak points and micro-fissures that facilitate the water movement. NBS_S is a new stone built during the renovation work in 2004. That stone is located in the external east façade of Building (36). Its surface is exfoliated with salt efflorescence (Figure 4.3.7h) and demonstrates very low absorption behaviour (Figure 4.3.6). Figure 4.3.14 shows the different absorption behaviours of two laminated stones that have salt efflorescence on their surfaces. The first stone is located in the external east facade of the Building (42) and it shows a good absorption (represented in LS_S_1), whereas the other one reveals no water absorption. It is located in the external east façade of Building (36), and it is discolourated with orange and has salt efflorescence on it (LS_DS).

HDS_D_2 is one of the stones that belonged to the moderate absorption group (Figure 4.3.6). This stone is oriented to the east at an external façade of Building (42), and it had yellow-orange discolouration (Figure 4.3.7d).

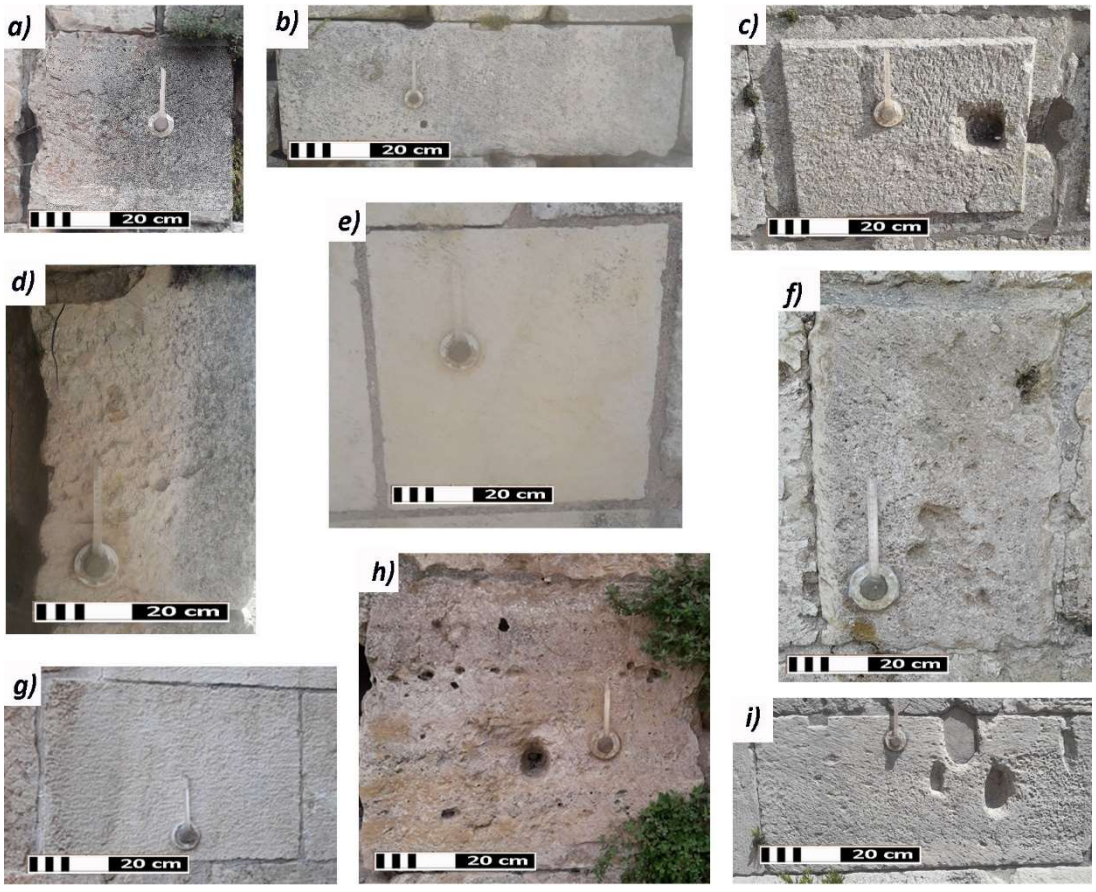

Figure 4. 3. 16 The stones that have no absorption behaviour at Crac des chevaliers (I)

DOI: 10.15774/PPKE.BTK.2024.021

Both HPS_0_2 and HPS_D are included in the low absorption group (Figure 4.3.6), and they are both homogenous porous stones in the external façades of the Building (19). HPS_0_2 is located in the north direction (at the ground floor- 3rd row), and it does not have a distinct deterioration on its surface (Figure 4.3.70). While HPS_D is oriented to the south (at second floor -5th row), and its surface is discolourated with orange (Figure 4.3.7j). The absorption behaviour of HPS_D is very good for the first cubic centimetre of absorbed water, and then it becomes low absorption (Figure 4.3.15). The first cubic centimeter of absorbed water dramatically fills the open pores near the surface (ca.8 minutes). Because of the low interconnectivity of the pores, the water cannot be absorbed deeply.

Many causes prevented the stone blocks from absorbing water through the Rilem tube at the castle. These causes include salt efflorescence, accumulation of grey microorganisms, presence of red-orange microorganisms colonisation, the case of new stone, or the presence of water in the stone (rising damp from the ground or water infiltration from the roof). The following figures (Figures 4.3.16 and Figure 4.3.17) contain the stones with no absorption.

Two new stones, built during the renovation work in 2002, do not have any distinct deterioration type on their surface and do not absorb water. The first measured stone is NBS_0_1, located in the external east façade of Building (151) (Figure 4.3.16g), the other one is NBS_0_2, located in the external west façade of Building (49) (Figure 4.3.16e).

Several stones that are colonised with grey microorganisms do not exhibit any absorption behaviour independent from their lithotype: LS_MC_3 is located in the external south façade of Building (42) and a higher plant above shaded it (Figure 4.3.16a). This shaded stone is the preferred place for accumulating grey microorganisms that appeared in black-grey on the stone surface and made it non-absorbent. HDS_MC_1 has in addition to the microorganisms a few fissures on the surface, and it is placed in the external west façade of the Building (49) (Figure 4.3.16b). On the same façade, HDS_MC_2 is located on a jamb door. This stone is vertically divided into two parts, grey microorganisms colonised the external one, and the other part had no visible stone decay (Figure 4.3.16d). The absorption test of both the sound and the colonised parts reveals no absorption. HDS_MC_3 and HDS_MC_4 are located on the external west façade of Building (36) and on the external north façade of the building (20), respectively (Figure 4.3.16i and Figure 4.3.16c). They both exibit no absorption behaviour.

The existence of orange-red microorganisms on some tested stone surfaces also contributs to the non-absorption behaviour (such as HDS_MC_5 and HPS_MC). HDS_MC_5 is placed

DOI: 10.15774/PPKE.BTK.2024.021

on the external north façade of Building (36) (Figure 4.3.16f), and the location of HPS_MC is on the north external façade of Building (14) (Figure 4.3.16h).

Salt efflorescence on the surface blocks the water uptake as in the case of LS_S_2 (Figure 4.3.17h) and HDS_S (Figure 4. 3.17c). Stones with salt efflorescence and an orange discolouration do not absorb water too such as HDS_DS on the external east façade of Building (42) (Figure 4. 3.17f) and LS_DS on the external east façade of Building (36) (Figure 4.3.17g).

Three tested stones by the Rilem tube revealed no absorption behaviour because they are damped enough to make their pores full of water, so they cannot absorb any additional water. That moisture at the castle can be generated from two different sources, either rising damp from the ground or water infiltration from the defected roofs. Two tested stones are affected by rising damp and do not absorb water from the Rilem tube: HDS_o with no distinct deterioration type on its surface (Figure 4. 3.17a) is located on the external east façade of Building (18) in the 4th row. That building is a ground-floor one, and the stone is placed around one meter from the ground. That level is affected by rising damp from the ground.

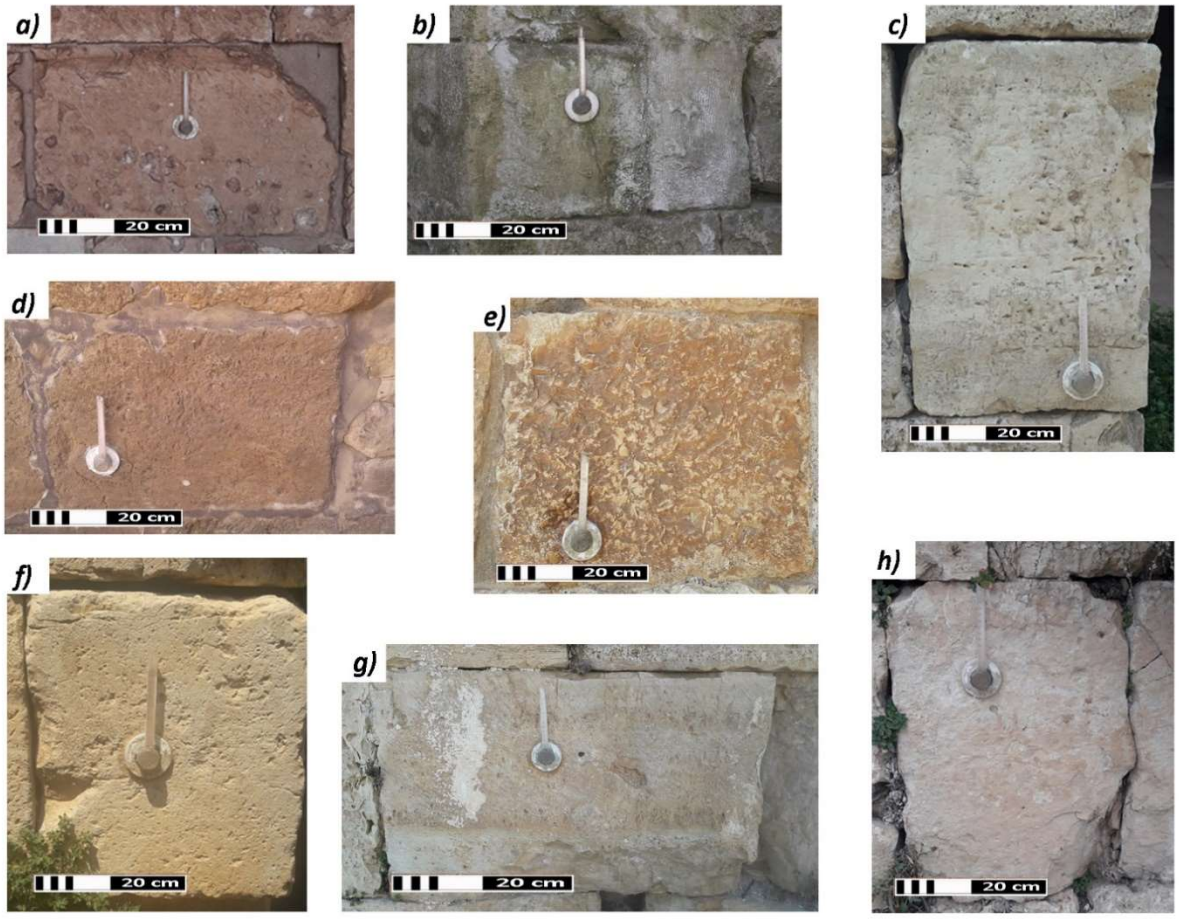

Figure 4. 3. 17 The stones that have no absorption behaviour at Crac des chevaliers (II)

DOI: 10.15774/PPKE.BTK.2024.021

The other stone (HDS_D_3) is located in the same building but at the north external façade (the first row appears on the ground surface). It has brown discolouration and some fissures on its surface (Figure 4. 3.17d). That stone is highly affected by rising damp, and the dampness can consistently be recognized on the stone surface even in the summertime. HDS_MC_6 is located on the middle pillar inside the building (137.1). That pillar sufferes from water infiltration from the defected roof above it and is colonised by green microorganisms (Figure 4. 3.17b). It reveals no absorption because it is always moistured from the infiltrated water. The last tested stone, which demonstrates no absorption, appears in Figure 4. 3.17e. It is a homogenous dense stone with an orange-brown discolouration on its surface (HDS_D_3). This stone is located in the external east façade of Building (151).

To conclude, all the stones with discolouration with orange (especially at south facades), and the stones inside buildings (there is no layer on its surface), have revealed either a very good absorption or a good one. Whereas the stones with microorganisms on their surface, either the red-orange or grey microorganisms, have demonstrated low to very low absorption behaviour or even no absorption, particularly those located on north and west façades. The presence of salts plays an important role in the alteration of the absorption behaviour of the stone. Depending on the thickness of the salt, especially in the east and south façades, the stones have shown either moderate, very low, or no absorption. Two stones, one covered with microorganism colonisation and the other with salt efflorescence, the water uptake of which increases after consuming the first cubic centimetre of water inside the tube (i.e. when the water pressure is high). In that case, the high water pressure can open a path within the salt or the microorganisms colonisation, so the absorption behaviour increases later. On the contrary, the water absorption is slower in a stone discolourated with orange (HPS_D). In the last case, the absorbed water probably fills the open pores dramatically in a defined depth; and when the water pressure decreases, the water cannot be absorbed deeply. The last case could also be explained by a less porous layer under the surface, which might decrease the water absorption. The row number of the stone, especially in the ground-floor buildings, which is affected by rising damp, is essential in determining the absorption behaviour. Where the stone most probably does not absorb any water if it is saturated with rising damp from the ground.

DOI: 10.15774/PPKE.BTK.2024.021

4.3.2.2 Schmidt hammer

Several stones with 4 lithotypes (HPS, HDS, LS, and NBS) and different stone deterioration cases are measured. The first measured stone group belongs to the homogenous porous stone lithotype (HPS) with different deterioration cases (no decay, salt efflorescence, discolouration, and microorganism colonisation, Table 4.3. 3). The rebound value of the non- damaged HPS stones (HPS_0_1 and HPS_0_2) is 30.1 and 32.6, respectively (Figure 4.3. 18 and Table 4.3. 3). The stone with salt efflorescence on its surface (HPS_S; Figure 4.3.7g) has a 10% higher rebound value of 34.5. The discolouration is one of the most often deterioration cases on the homogenous porous stones with the rebound value of 33.6 (HPS_D; Figure 4.3.7j). The highest surface hardness is for the homogenous porous stone colonised by microorganisms (HPS_MC). That stone has red-orange microorganism colonisation on its surface (Figure 4.3.16h), and its rebound value is 20% higher (38.4) than that of the non-decayed surface (Table 4.3. 3).

Table 4. 3. 3 The tested homogenous porous stones (HPS) and their rebound values

Lithotype	Name	Stone deterioration case	Rebound value
Homogenous porous stone (HPS)	HPS_0_1	no	30.1
	HPS_0_2	no	32.6
	HPS_S	Salt efflorescence	34.5
	HPS_D	Discolouration	33.6
	HPS_MC	Microorganisms colonization	38.4

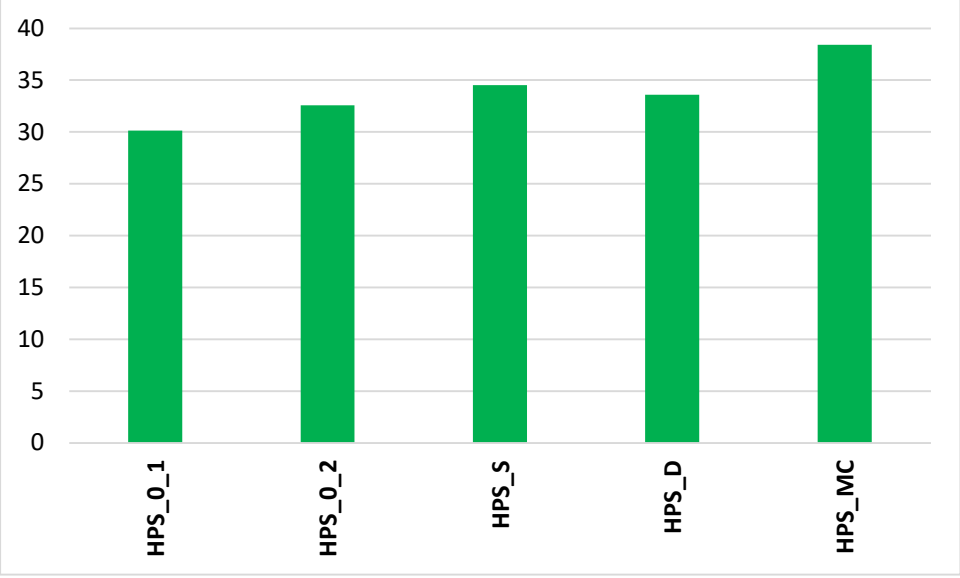

Figure 4. 3. 18 The rebound values of the homogenous porous stones (HPS)

DOI: 10.15774/PPKE.BTK.2024.021

On the homogenous dense stones lithotype (HDS), various stone decay types are recognized and measured. This causes the rebound values to be in a wide range (Table 4.3. 4 and Figure 4.3. 19). The non-damaged stone (HDS_0; Figure 4. 3.17a) shows a rebound value of 39.5 (Table 4.3. 4). Four stones with discolouration are present in this group of lithotype. HDS_D_1 is a homogenous dense stone with discolouration and an orange surface (Figure 4.3.7m). The rebound value of this stone is 36.4. Another homogenous dense stone with brown discolouration (HDS_D_2; Figure 4.3.7d), whose rebound value is 32.6 (Table 4.3.

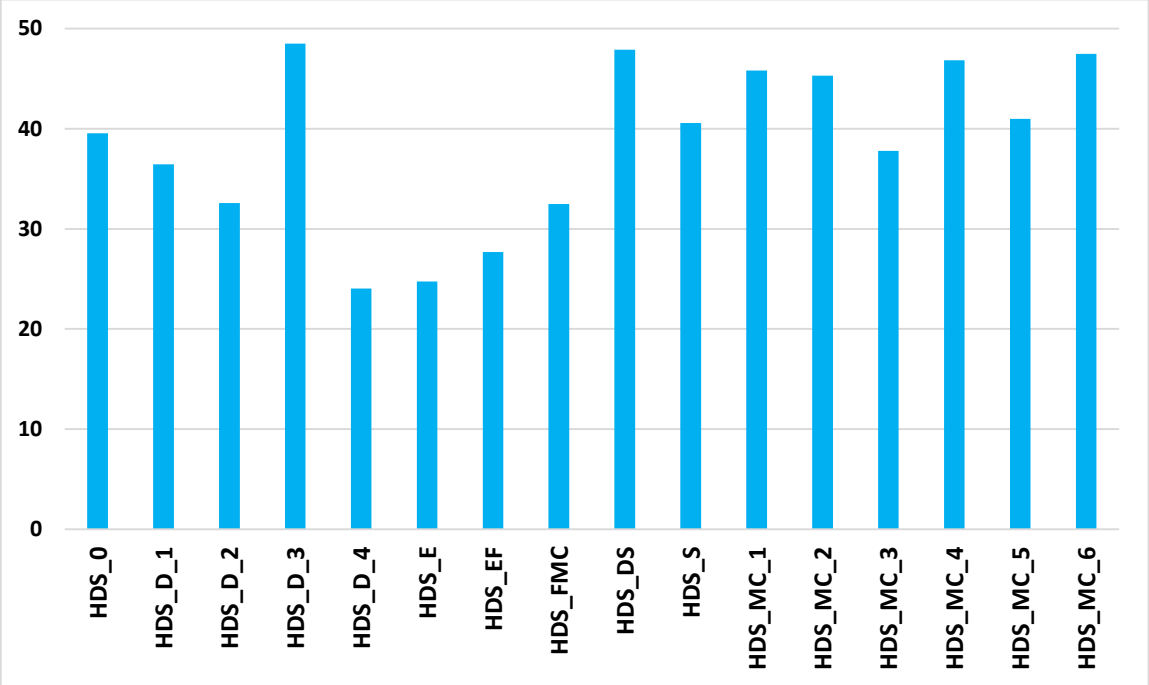

Figure 4. 3.19 The rebound values of the homogenous dense stones (HDS)

4). HDS_D_3 is also a homogenous dense stone with brown-orange discolouration (Figure 4.3.17e), and its rebound value is 48.5. This stone has a rough surface with protrusions and dips. When the pole of the hammer strikes a protrusion, the rebound value is high. When the pole strikes a point in the dip part, the pole does not touch completely the stone surface (because the diameter of the pole is greater than the width of the dip part) and thus the rebound value is low. This explains why the standard deviation of this stone is so high (8.9) when compared to other stones (see Table 4.3.7). The last measured homogenous dense stone with brown discolouration is HDS_D_4 (Figure 4.3.17d). This stone has some fissures on its surface

DOI: 10.15774/PPKE.BTK.2024.021

and its rebound value is the lowest value among all measured stones (24). Two stones with erosion on their surface and low rebound values are investigated. On the surface of HDS_E fissures are observable (Figure 4. 3.7i), and its rebound value is (24.7). HDS_EF is also fragmented and eroded homogenous dense stone (Figure 4.3.7c) and its rebound value is close to HDS_E (27.7, Table 4.3. 4). The stone exposed to mechanical shock due to bombing so it has fragmented parts, and its surface is colonised by grey microorganisms (HDS_ FMC; Figure 4.3.7c) and has a little higher rebound value than the previous stones (32.5). When compared to other tested stones, this stone has the highest standard deviation (10.8), see Table 4.3.7. The mechanical shots cause some weak points in the stones (micro-cracks and fragmented parts). The rebound value of these weak parts will be very low compared to the rest of the stone. As a result, the difference in rebound value results in a high standard deviation value. There is a stone that has discolouration and salt efflorescence on its surface (HDS_DS; Figure 4. 3.17f), and its rebound value is 47.9. HDS_S is a homogenous dense stone with salt efflorescence on its surface (Figure 4. 3.17c), its rebound

Table 4. 3. 4 The tested homogenous dense stones and their rebound values

Lithotype	Name	Stone deterioration case	Rebound value
Homogenous dense stone (HDS)	HDS_0	no	39.5
	HDS_D_1	Discolouration	36.4
	HDS_D_2	Discolouration	32.6
	HDS_D_3	Discolouration	48.5
	HDS_D_4	Discolouration	24.0
	HDS_E	Eroded surface	24.7
	HDS_EF	Fragmented and eroded surface	27.7
	HDS_FMC	Fragmented and microorganisms colonization	32.5
	HDS_DS	discolouration and Salt efflorescence	47.9
	HDS_S	Salt efflorescence	40.6
	HDS_MC_1	Microorganisms colonization	45.8
	HDS_MC_2	Microorganisms colonization	45.3
	HDS_MC_3	Microorganisms colonization	37.8
	HDS_MC_4	Microorganisms colonization	46.8
	HDS_MC_5	Microorganisms colonization	41.0
	HDS_MC_6	Microorganisms colonization.	47.5

DOI: 10.15774/PPKE.BTK.2024.021

value is 40.6. Six homogenous dense stones with microorganism colonisation are also tested. HDS_MC_1, HDS_MC_2, HDS_MC_3, and HDS_MC_4 are colonised by grey microorganisms (Figure 4.3.16b, Figure 4.3.16d, Figure 4.3.16c, and Figure 4.3.16i). The rebound values of HDS_MC_1, HDS_MC_2, and HDS_MC_4 are close (45.8, 45.3, and 46.8, respectively), however, the rebound value of HDS_MC_3 is a little lower, compared to the previous stones, and it is 37.8. HDS_MC_5 is a homogenous dense stone with red-orange microorganism colonisation on its surface

Table 4. 3. 5 The tested laminated stones and their rebound values

Lithotype	Name	Stone deterioration case	Rebound value
Laminated stone (LS)	LS_S_1	Salt efflorescence	34.9
	LS_S_2	Salt efflorescence	42.5
	LS_D	Discolouration	42.2
	LS_DS	Discolouration and Salt efflorescence	44.5
	LS_MC_1	Microorganisms colonization	41.3
	LS_MC_2	Microorganisms colonization	44.4
	LS_MC_3	Microorganisms colonization	43.6

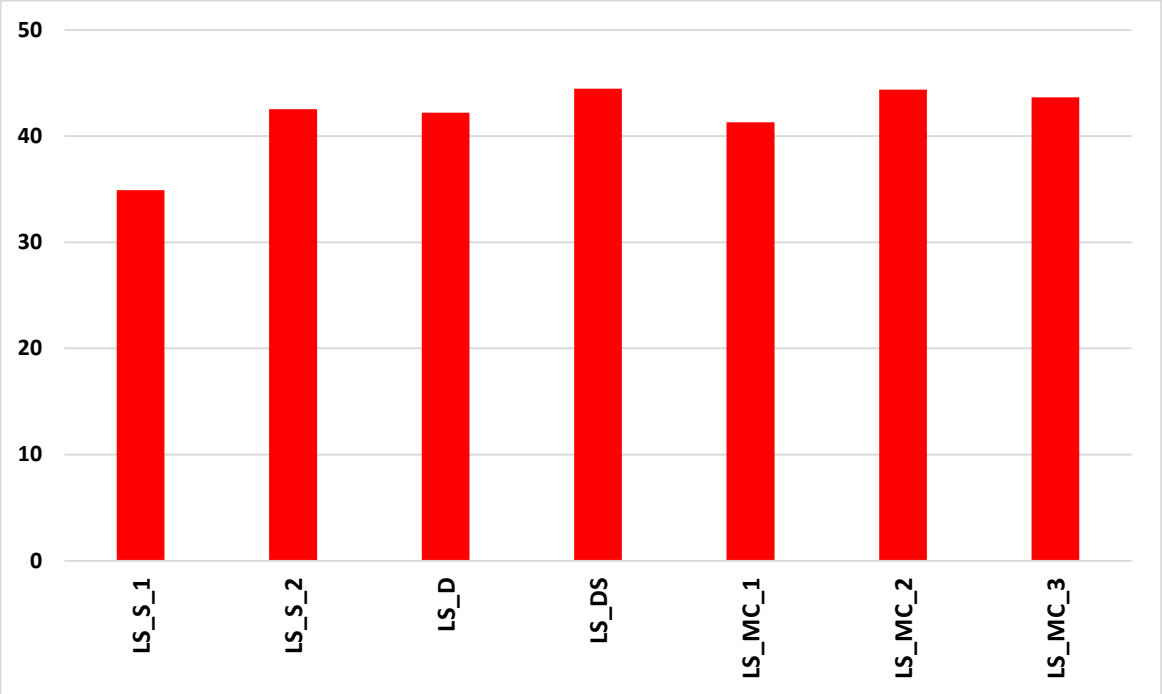

Figure 4. 3. 20 The rebound values of the laminated stones (LS)

DOI: 10.15774/PPKE.BTK.2024.021

(Figure 4.3.16f). The rebound value of this stone is 41. HDS_MC_6 is a homogenous dense stone with green microorganism colonisation on its surface and is exposed to water infiltration (Figure 4. 3.17b). The rebound value of that stone is 47.5.

The rebound values in the group of laminated stones are close to each other even though they have different deterioration cases (Table 4.3. 5). There is no laminated stone that does not have deterioration, because of that we do not have measurements on these stones. The smallest surface strength from this group belongs to a laminated stone with salt efflorescence on its surface (LS_S_1, Figure 4.3.7e), and its rebound value is 34.9 (Figure 4.3.20). However, another stone with the same deterioration (LS_S_2) has a slightly higher result, which is (around 18%) 42.5 (Figure 4.3.17h). The rebound value of the laminated stone with discolouration and salt efflorescence (LS_DS; Figure 4.3.17g) is 44.5 (Figure 4.3.20) which is a little higher than of the laminated stone just

Table 4. 3. 6 The tested new built stones and their rebound values

Lithotype	Name	Stone deterioration case	Rebound value
NBS	NBS_D & NBS_MC	Discolouration and Microorganisms colonization	42.4
	NBS_S	Salt efflorescence	40.5
	NBS_0_1	No	38.1
	NBS_0_2	No	42.6

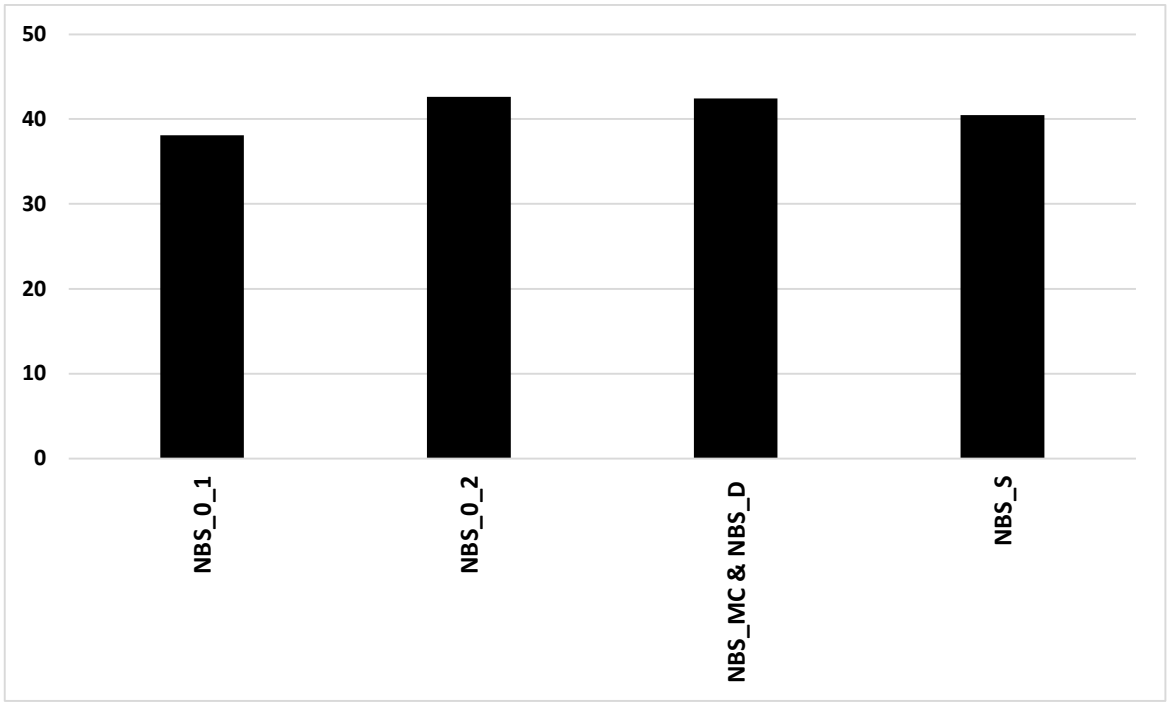

Figure 4. 3.21 The rebound values of the new built stones (NBS)

DOI: 10.15774/PPKE.BTK.2024.021

with discolouration on its surface (LS_D; Figure 4.3.7k) (its rebound value is 42.2). The surface strength of those colonized with different microorganisms is very similar: LS_MC_1 is colonized with red-orange microorganisms, and LS_MC_2 and LS_MC_3 are colonized

Table 4. 3. 7 The number of measurement in each tested stone and the result of the statistical study of the measurements

Name	Lithotype	Number of measurements	Rebound value			
			Min. value	Max. value	Average	Standard deviation
HPS_0_1	HPS	29	21.4	37.7	30.1	3.8
HPS_0_2		23	25.4	41.8	32.6	3.7
HPS_S		14	33.6	38.7	34.5	5.6
HPS_D		32	23.4	49.0	33.6	6.5
HPS_MC		28	25.4	52.1	38.4	6.8
HDS_0	HDS	33	27.5	48.0	39.5	5.4
HDS_D_1		27	27.5	48.0	36.4	4.9
HDS_D_2		29	24.4	45.9	32.6	4.8
HDS_D_3		31	31.5	64.5	48.5	8.9
HDS_D_4		25	17.4	33.6	24.0	4.2
HDS_E		19	19.4	31.5	24.7	4
HDS_EF		27	18.8	39.7	27.7	5.4
HDS_FMC		20	16.8	48.0	32.5	10.8
HDS_DS		23	41.8	52.1	47.9	2.4
HDS_S		28	28.5	49.0	40.6	1.6
HDS_MC_1		38	39.7	56.2	45.8	4.0
HDS_MC_2		23	37.7	56.2	45.3	4.8
HDS_MC_3		31	27.4	50.0	37.8	4.9
HDS_MC_4		31	41.8	52.1	46.8	2.7
HDS_MC_5		29	27.5	50.0	41.0	6.1
HDS_MC_6		29	34.1	56.3	47.5	5.9
LS_S_1	LS	42	25.4	46.9	34.9	4.6
LS_S_2		29	33.6	50.0	42.5	4.3
LS_D		42	35.6	54.2	42.2	4.4
LS_DS		30	31.5	59.3	44.5	5.5
LS_MC_1		43	27.5	56.2	41.3	5.3
LS_MC_2		40	31.5	56.2	44.4	5.2
LS_MC_3		38	35.6	54.2	43.6	3.9
NBS_0_1	NBS	26	33.6	45.9	38.1	3.4
NBS_0_2		23	35.6	53.1	42.6	4.9
NBS_MC & NBS_D		28	33.6	50.0	42.4	4.6
NBS_S		29	31.5	51.1	40.5	4.4

DOI: 10.15774/PPKE.BTK.2024.021

with grey microorganisms. Their rebound values are 41.3, 44.4, and 43.6, respectively (Figure 4.3.20).

There are several new built stones (NBS), with various deterioration cases, which are also tested by Schmidt hammer, see Table 4.3.6. The rebound values of the newly built stones are similar, see Figure 4.3.21. NBS_0_1 and NBS_0_2 do not have any distinct deterioration cases, and their rebound values are close (38.1 and 42.6, respectively) (Figure 4.3.21). NBS_D and NBS_MC belong to the same newly built stone that has discolouration and microorganism colonisation on its surface. Its rebound value is 42.4 (Figure 4.3.7p). NBS_S is another newly built stone that has salt efflorescence on its surface and its rebound value is 40.5 (Figure 4.3.7h).

4.3.2.3. Deterioration mapp

- **External south façade of Building (46)**

Building (46) is located on the northwest corner of the internal castle on the first floor, see Figure 4.3.3. This building consists of one large room whose area is around 117m², its height is about 6.5 m and the thickness of the wall is about 2.3 m. The area of the mapped southern façade is around 110 m² (approx.9*12 m). The entire facade is built of carbonate stone blocks, the height of which is 50-70 cm. The whole façade is built of carbonate stone blocks whose range of 50-70 cm; with exception of the last two stone rows on the top that define the border of the roof and their height is between 25-30 cm. The width of each stone block is variable (30-170 cm), see Figure 4.3.22.

The western section of the façade, whose area is around 14 m², is rebuilt by the reconstruction works in 1954 with new stones [255], see Figure 4.3.23 and Figure 4.3.24. There is a vertical stone canal, that drains the rainwater from the roof to the floor below (in front of the façade), which is located around 4.6 m from the eastern edge of the façade, see Figure 4.3.22.

The mapping of the external south façade of Building (46) reveals different kinds of stone decay, see Figure 4.3.25. Figure 4.3.26 shows the percentage of each stone decay type in relation to the total area of the façade, with the total percentage of damaged stones of 70.13%. The first and the most dominating case is discolouration by orange colour with a quantity of 33%. It is concentrated in the middle part of the sunlight exposed southeastern façade. The

[255] Jean Mesqui and Maxime Goepp, *Le Crac Des Chevaliers: Histoire et Architecture* (2018).

DOI: 10.15774/PPKE.BTK.2024.021

orange-coloured zone is separated into two parts by the presence of microorganism

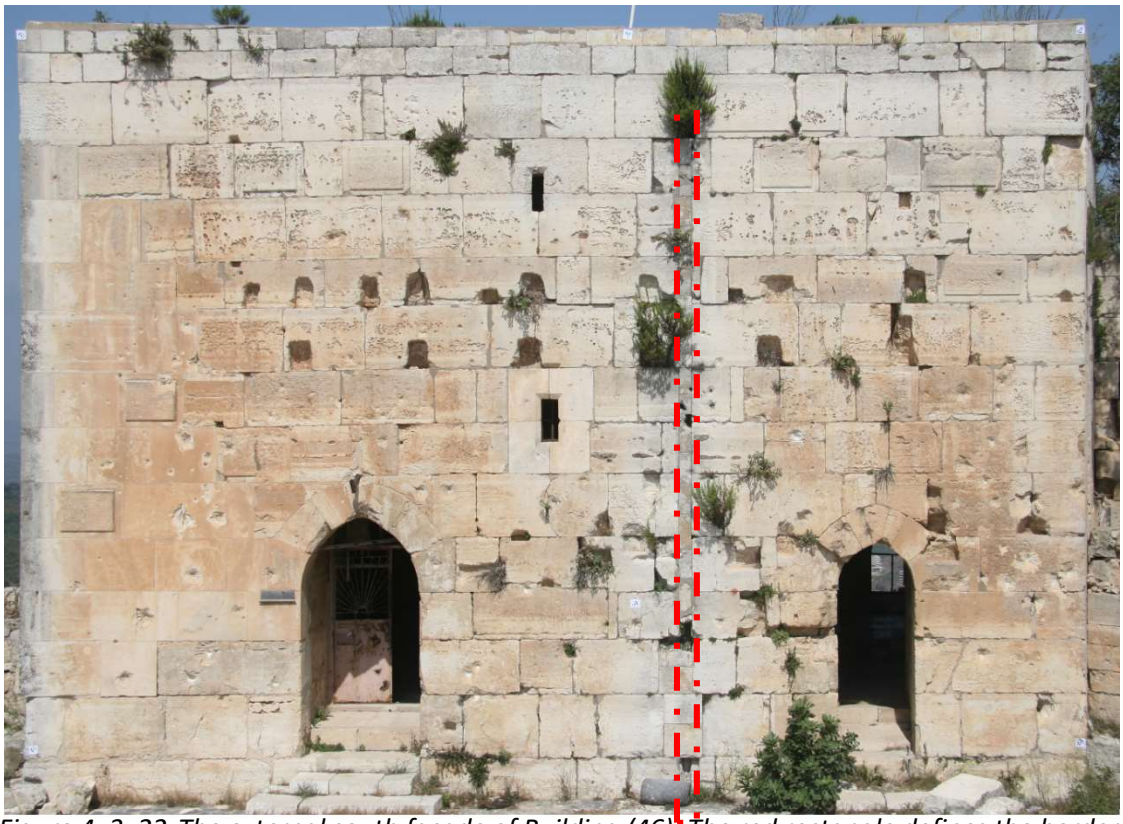

Figure 4. 3. 22 The external south façade of Building (46). The red rectangle defines the border of a vertical canal that drains down the rainwater from the roof to the floor level of the building

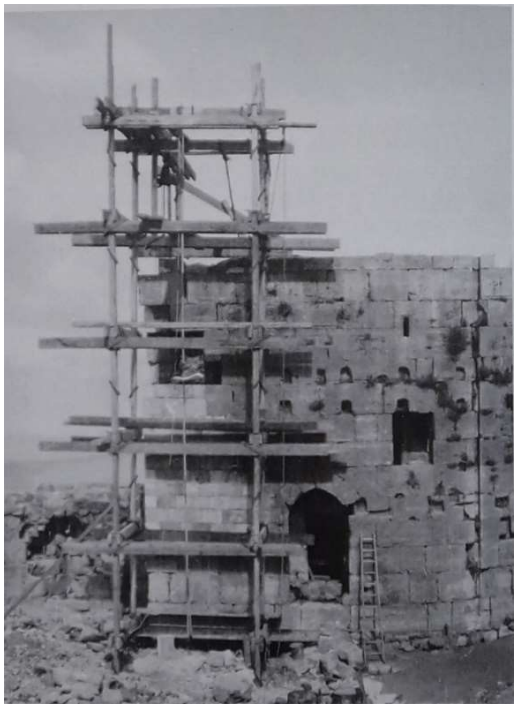

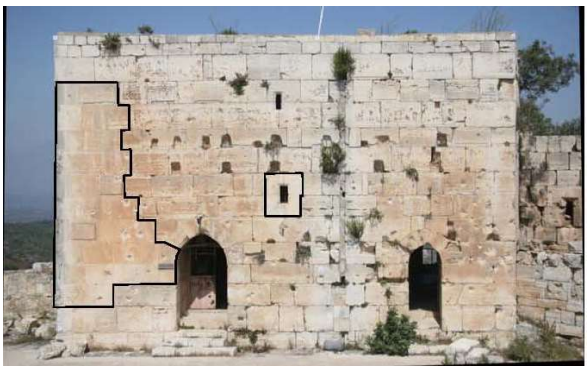

Figure 4. 3. 23 The external south façade of Building (46). The black polylines define the reconstructed section in 1954

Figure 4. 3. 24 The reconstruction work of the western section of Building (46) in 1954 (The photo is taken from Mesqui and Goepp.

colonisation, forming a grey region. This grey region is located on the vertical stone rainwater canal from the roof to the floor level of the building, see Figure 4.3.22. This section is always wetter than the other parts of the façade, making it a suitable environment for microorganisms

DOI: 10.15774/PPKE.BTK.2024.021

in winter. In the summertime, the façade gets dry, and the dried-out microorganisms stick on the stone surface, giving it a dark appearance. The lower part of this façade is characterised by scaling with an amount of 10%. The orange discolouration probably extended to this part in the past, but it has disappeared due to scaling. This scaling co-occurs with salt crystallization as traces of salts are visible in some parts of the stone surfaces, and with parts that are discoloured with orange.

The upper part of this façade is most likely shaded by higher plants, which explains why there is no orange discolouration at that part. The clear evidence of the growth of plants in that area is the presence of pitting on the stones for 9% of the entire façade. These holes have resulted

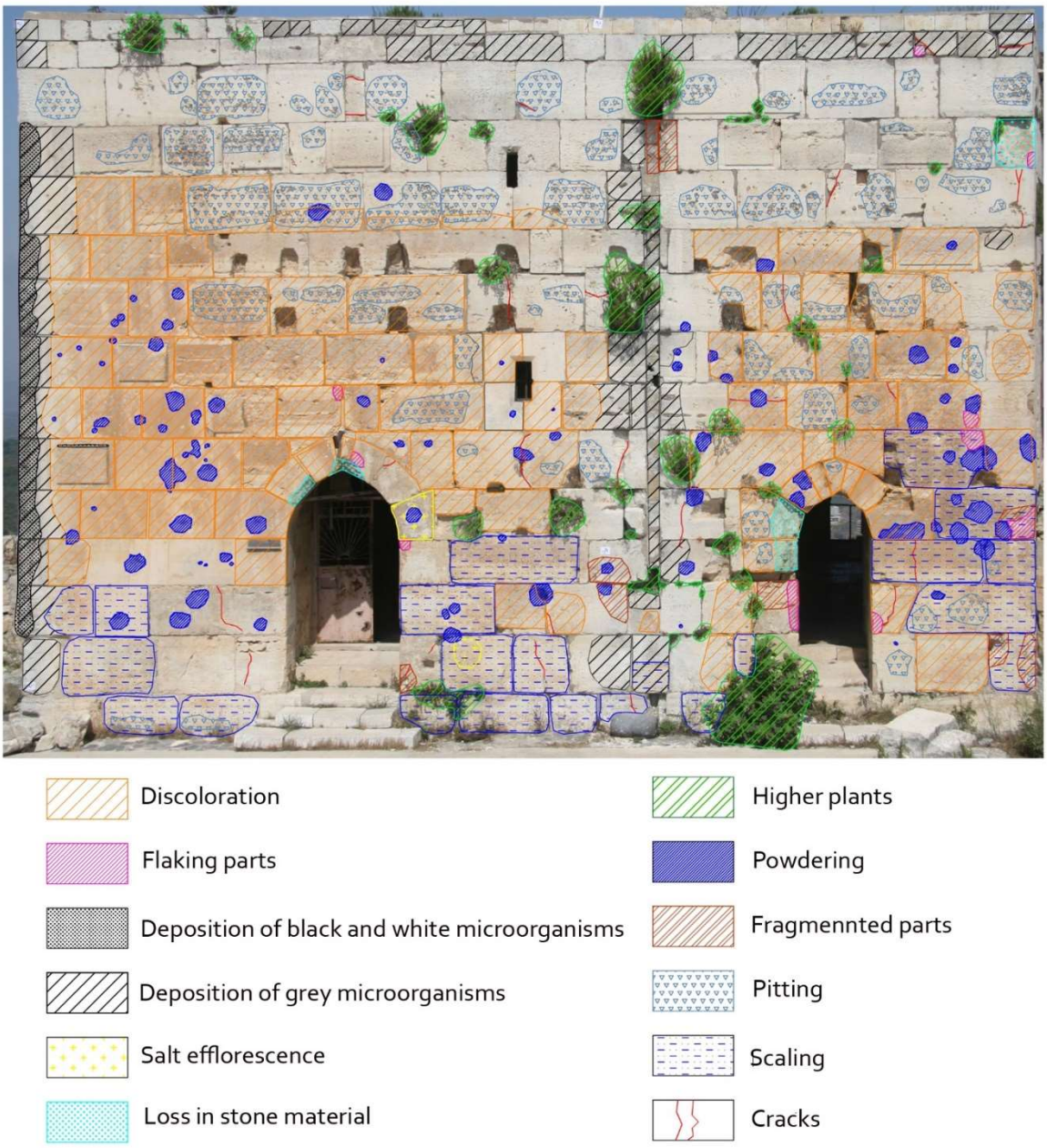

Figure 4. 3.25 The deterioration mapping of the external south facade of the building (46)

DOI: 10.15774/PPKE.BTK.2024.021

from the respiration process of the plants. This produces carbon dioxide that causes acidic dissolution of the carbonate stone in the presence of water. This part is also colonised by the grey microorganisms that give it a grey appearance.

The façade suffers from water infiltration on the western edge during rainy weather. The rainwater runs off on the thickness of the roof border, accumulates at the southwest corner of the roof, and heavily runs off on the western edge of the façade. The abundance of water at that edge leads to flourishing black and white microorganisms that appear in visible thickness up to several millimetres along with the height of the façade (see chapter 4.2/ stone decay types/ Figure 4.2.9). These black and white microorganisms colonise an area of 1.26% of the mapped façade. There is no doubt that this façade is a favourable environment for growing higher plants that can somehow live whenever they find little soil with water and other nutrients and other environmental conditions. The amount of the higher plants is demonstrated in the mapping at this façade of about 4% (Figure 4.3.26).

As a result of the armed conflict in Syria, the stones of this façade are obviously affected by different damage degrees. Some parts are exposed to shooting bullets and missiles fragmentation, which are recognized by making the stone material either smashed and powdered (1.81%) or fragmented (0.87%).

The cracks, loss in stone material and flaking parts, as well as the salt crusts, represent a very low percentage of all other cases in this façade.

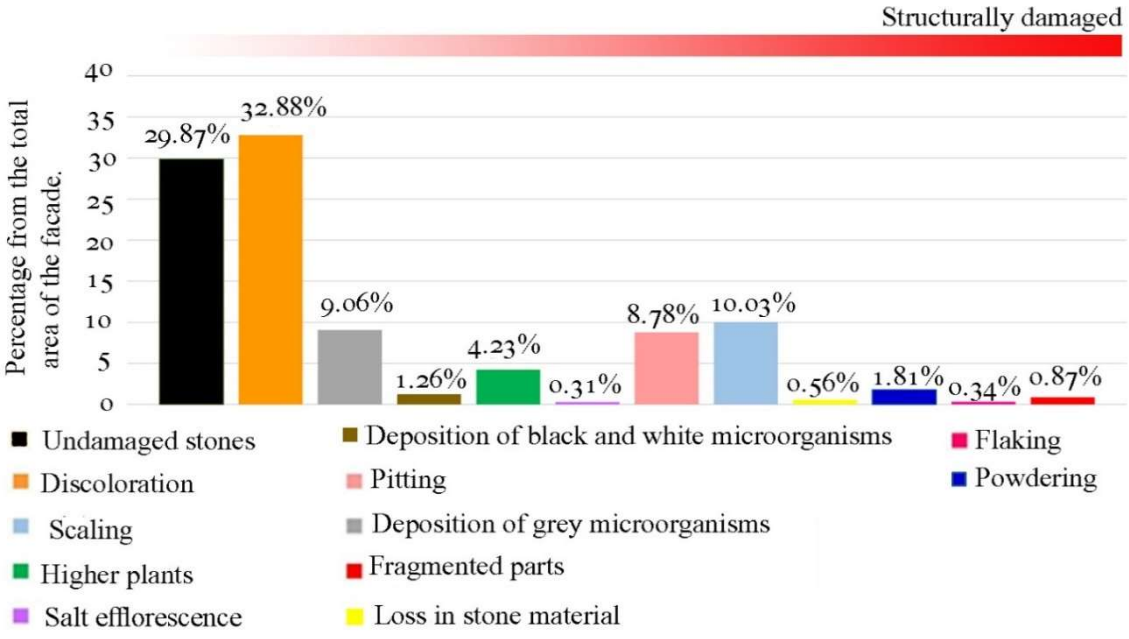

Figure 4. 3. 26 The percentage of each deterioration type at the external south facade of building (46)

DOI: 10.15774/PPKE.BTK.2024.021

- **External east façade of Building (36)**

Building (36) is located on the southern side of the internal castle on the first floor, see Figure 4.3.3. It is a two-storied building whose plan is a semi-rectangular shape with an approximate area of 148 m². This building is bounded directly from the east by Building (35) on the first floor, so it only has an outer east facade on the second floor (Figure 4.3.27). The second floor consists of one vaulted room whose height is approximately 6 m. The last stone row from above forms the roof edge. The mapped area is approximately 175 m². This façade is built of carbonate stone blocks whose height ranges from 50-60 cm, and their width is variable (30- 170 cm). A restoration project for this building is carried out in 2004. That project

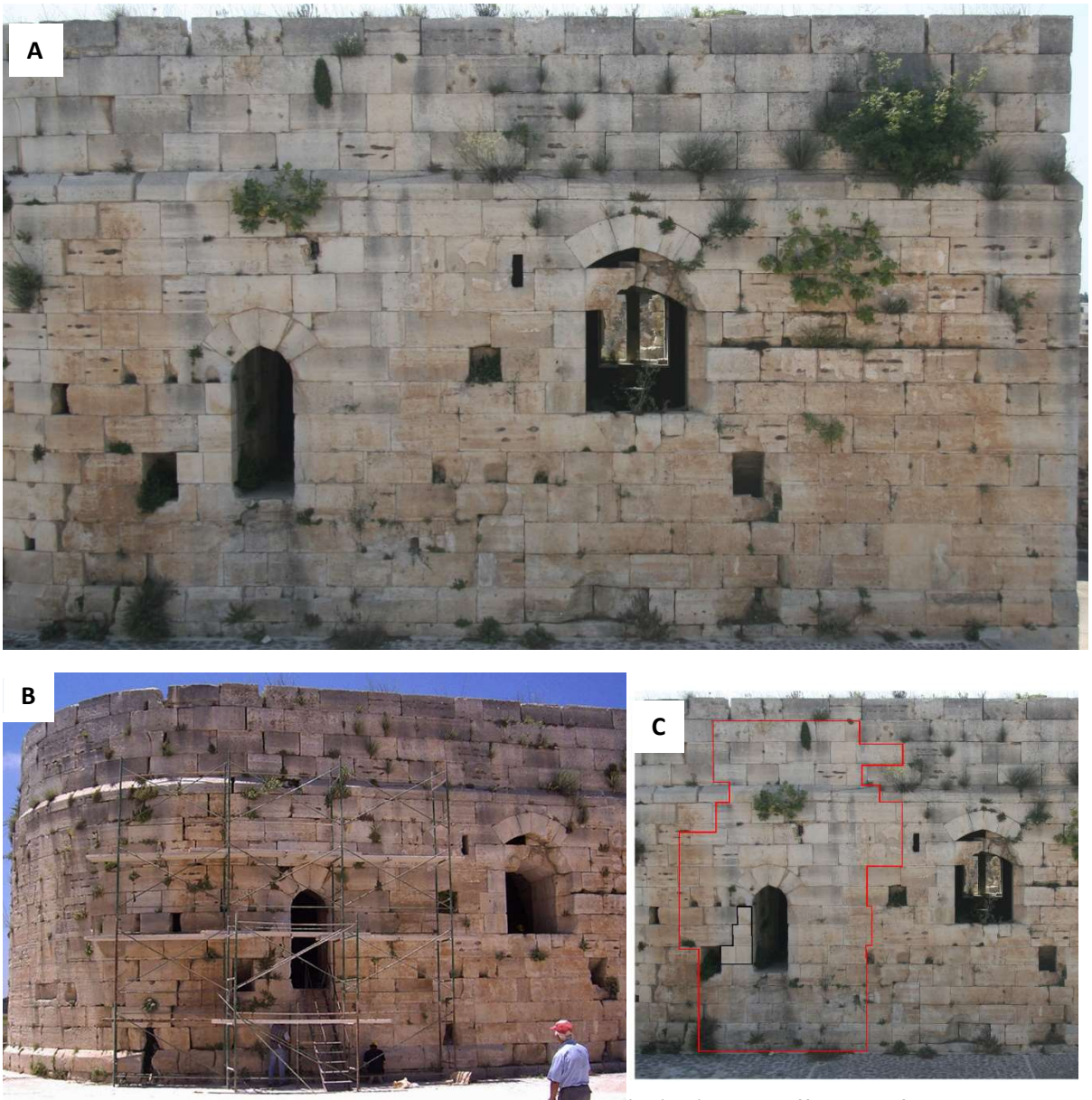

Figure 4. 3. 27 A) The external east façade of Building (36). B) The scaffolding of the restoration project of the facade in 2004. C) The black polyline defines the new stones that are added to the façade and the red poly line represents the area of jointing work

DOI: 10.15774/PPKE.BTK.2024.021

includes the waterproofingof its roof, the rebuilding of an area (1 m²) on its east façade with new stones (see Figure 4.3.27C, the black polyline), and jointing between the stones (see Figure 4.3.27C, the red polyline).

The deterioration mapping of the external east façade of Building (36) demonstrates the same deterioration cases that appear at the external south façade of Building (46) but in different percentages, see Figure 4.3.28 and Figure 4.3.29.

As mentioned above, both the external south and the east façade at the castle have a common stone deterioration case, the discolouration with orange. It is the most dominating case on the facade and affects more than a third of the total surface (37.6%), see Figure 4.2.29. This discolouration is most likely attributed to sunlight exposure; therefore, it concentrates on the entire façade except for the upper quarter, where the higher plants have been flourishing and shading the stone blocks formerly. The deposition of grey microorganisms (approx. 25.5%) takes a place in areas that are now shaded by higher plants, or, if this is not currently the case, the grey microorganisms are distributed in stones that have pitting on their surfaces. This pitting

Figure 4. 3. 28 The deterioration mapping of the external east facade of the building (36)

DOI: 10.15774/PPKE.BTK.2024.021

is a perfect indicator that the vegetation has previously shaded these stones, and is extends approx. 1.25% of the total area of the facade. The invasive plants that occupy currently a place of about 12.65% are not only herbaceous species but also shrubs. Scaling (scaling percentage is about 8.89%., like on the external south façade of the building (46), co-occurs with the presence of discolouration and salts. The scaling percentage is about 8.89%. The very thin layer of salts whose colour is white, appears clearly on the orange colour but it is not visible on the

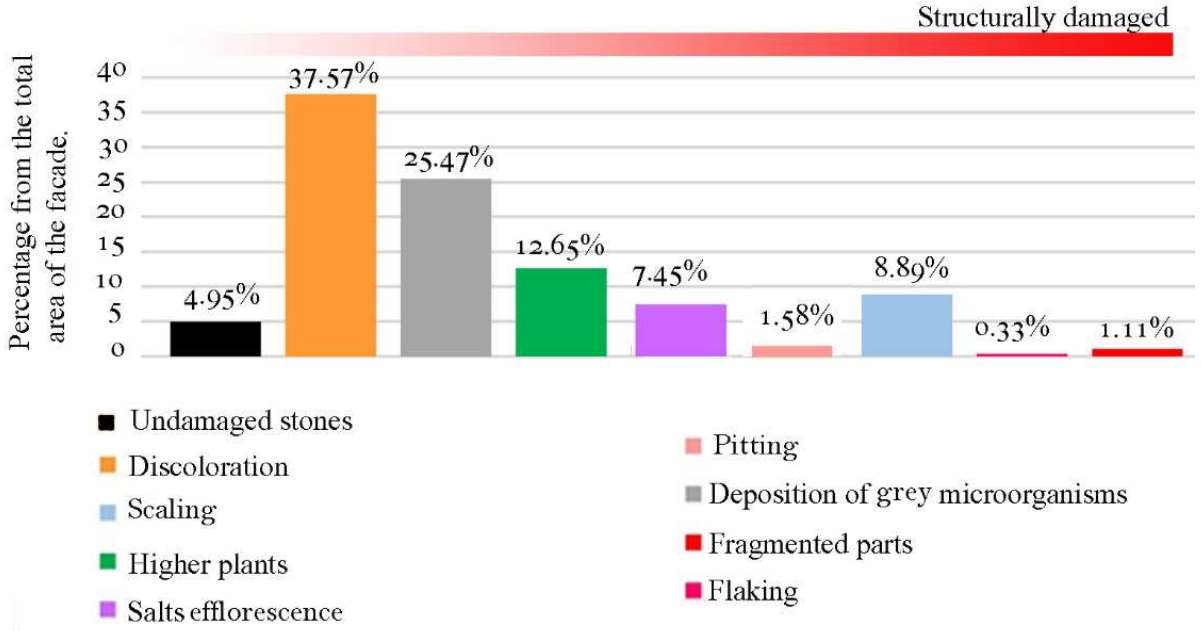

Figure 4.3. 29 The percentage of each deterioration type at the external east facade of building (36)

stones where there is no discolouration, see Figure 4.3.28. The percentage of surfaces with salts efflorescence is around 7.45 %. This phenomenon is concentrated in the lower part of the façade. This façade is not located on the ground floor, where the rising dampness of the soil leads to salt accumulation, however it is located on the second floor. Hence there are two possible salt sources either from the mortar between the stones or from the sea spray effect. Several stones at this façade are replaced in 2004 and inappropriate mortar might have been used resulting in salt accumulation. Finally, the east façade is not highly affected by the recent war; hence, cracks and fragmented, flaking parts resulting from bullet fragmentation represent a very low proportion of the whole façade.

Many results can be conducted by comparing the two façades (the south façade of Building 46 and the east façade of Building 36). Firstly, the percentages of discolouration with orange on both façades are approximately equal; because the south and east directions receive the highest rate of sunlight. That is noticed for all east and south façades at the castle. The deposition of

DOI: 10.15774/PPKE.BTK.2024.021

grey microorganisms on the east façade is higher than on the south one. The percentage of higher plants in the east façade is more than in the south one. Both facades have the same case of salt accumulation on the orange discolouration. Therefore, the source of the salt in both facades is most likely the sea spray effect. On the other hand, the percentage of salts in the east façade is higher than in the south one, because the mortar used in 2004 might form an additional salt source compared to the south façade of the Building (46). The percentages of scaling in both facades are very close to each other.

The interesting issue is that although the proportion of higher plants on the east facade is higher than on the south facade, the percentage of pitting on the south facade has a higher value. That means the percentage of higher plants at the south facade was previously higher than the east one. The two dominant wind directions in the region are west and southwest, and the direction of precipitation is assumed to follow the direction of the wind. The rain hits the stone surface directly on the south facade so that a lot of water is absorbed and plants can generate more carbon dioxide. Finally, this phenomenon causes more pitting on the facade. In contrast, the east façade does not receive water directly, resulting in a low percentage of pitting.

- **External north façade of Building (36):**

The external north façade of Building (36) consists of two stories. The height of the façade is approximately 16 m, while its width is approximately 13 m; and it is built by carbonate stone blocks whose height ranges from 40-to 60 cm with variable width.

Due to the fact that deterioration mapping is a process that depends on the human eye ability, and the whole façade is too high to entirely investigate, the deterioration mapping of this façade has been done to the lower 8 m part, see Figure 4.3.30. This façade is distinguished by the appearance of three major decay forms: deposition of red-orange microorganisms, deposition of grey microorganisms, and discolouration, see Figure 4.3.32. The red-orange microorganisms settle in the mapped area at around 27.8% (see Figure 4.3.33). These microorganisms can be found in the moisturised shaded sections or areas exposed to low sunlight rates. The western curtain walls prevent the wind (Figure 4.3.31, highlighted with red), which comes in both directions (west and southwest), from reaching the lower part, where these microorganisms spread in the mapped part, see Figure 4.3.31 and Figure 4.3.32. Consequently, the proper humidity these microorganisms need always exists even in the summer when the wind cannot dry it. In the upper part of the mapped area (with approximately 40.7%), the deposition of grey microorganisms prevailed. The wind can quickly dry this section without

DOI: 10.15774/PPKE.BTK.2024.021

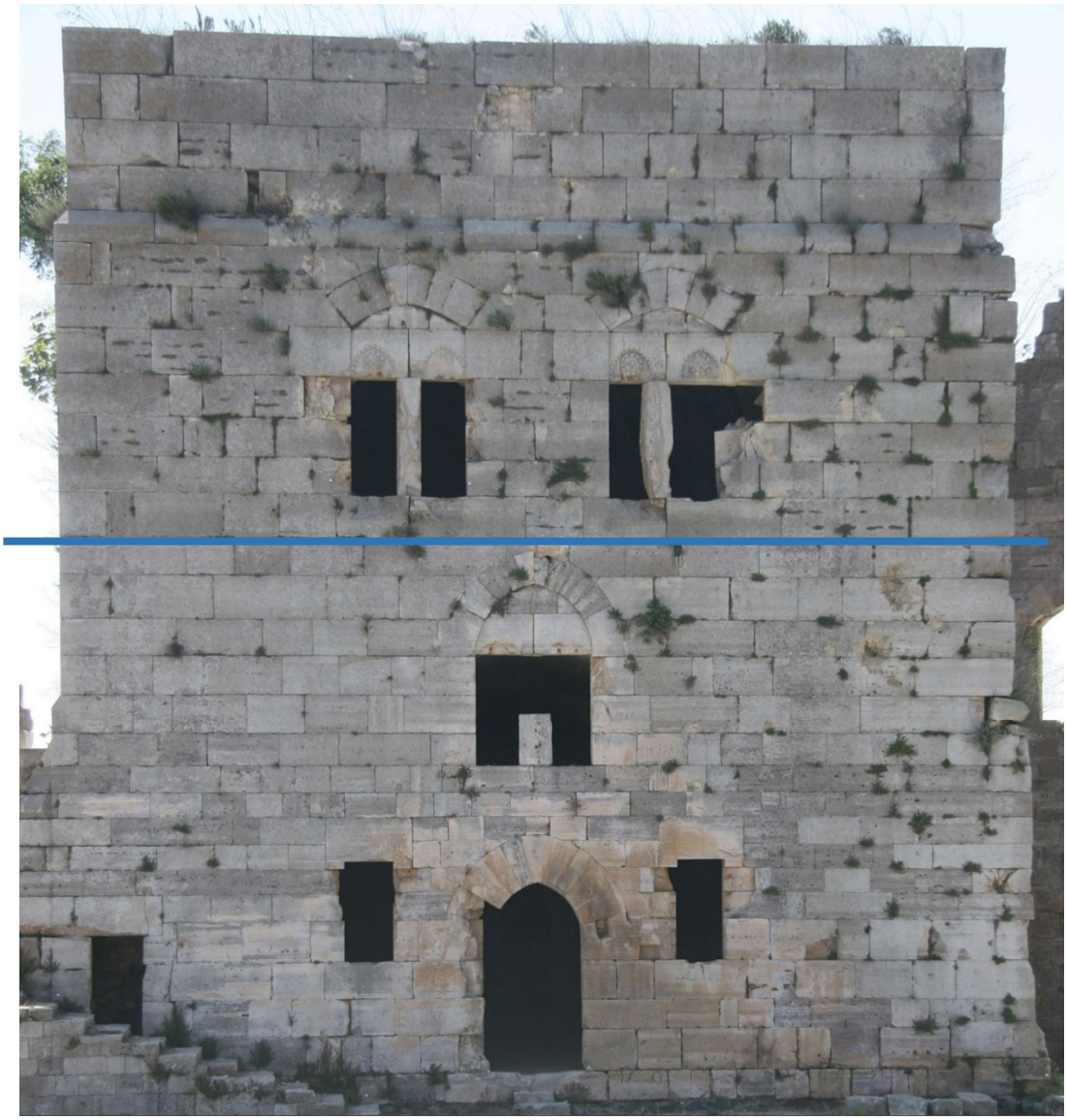

Figure 4. 3. 30 The external north façade of Building (36).The blue line defines the boundary of the lower section that is mapped

any restrictions, which can lead to the drying of any existing microorganisms there. A brown discolouration which concentrates in the middle part of the mapped area in a percentage of 9.6%, see Figure 4.3.33. The brown colour cannot be caused by the sun because the façade is oriented to the north in which it receives indirect sunlight with low energy.

This façade is also affected by the war, where the damaging scale ranges from destroying some parts (the window parts) to the effects of missile fragmentations. The latter resulted in a loss in stone material (1.72%), fragmentation (1.83%), flaking (0.5%), and cracks in some parts. The presence of vegetation (around 2.75%) in this façade is represented by the growth of some

DOI: 10.15774/PPKE.BTK.2024.021

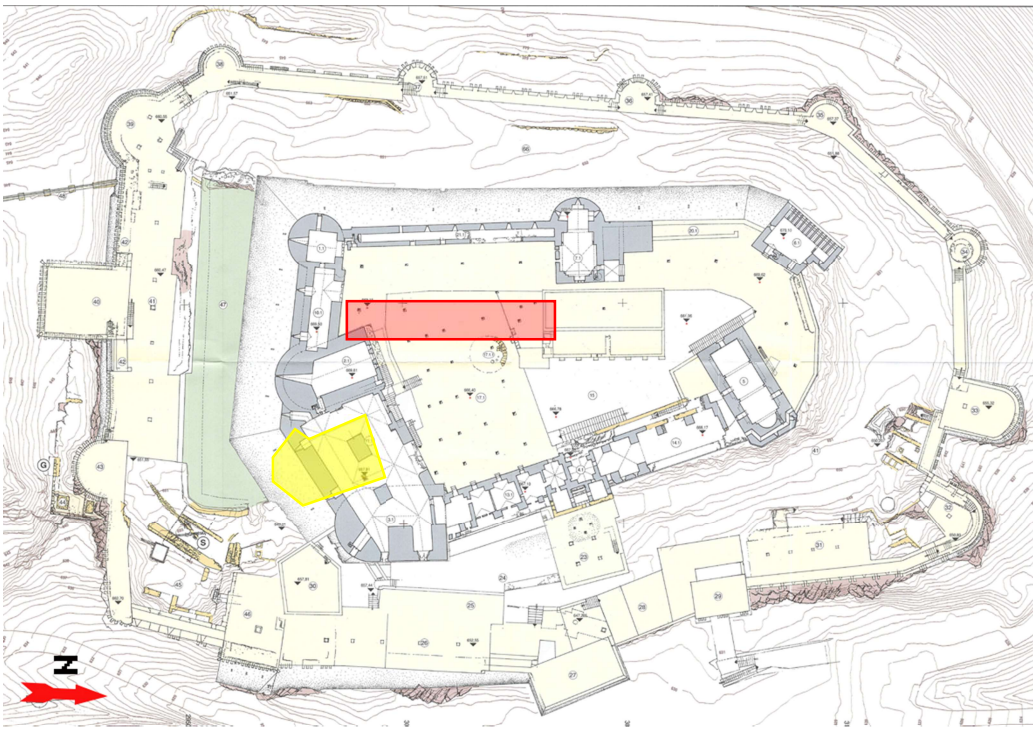

Figure 4. 3. 31 The plan shows the western curtain wall (highlighted with red) which prevent the western and the south-western winds from reaching the lower part of the northern façade of building (36) (highlighted with yellow)

Figure 4. 3. 32 The deterioration mapping of the external north facade of the building (36)

herbaceous species. Since the joints between the stones are very fine, there is not enough space

DOI: 10.15774/PPKE.BTK.2024.021

to grow other vegetation such as shrubs or even trees.

Several observations can be mentioned by comparing this façade with the two previous facades, the southern and eastern facades. The northern façade contains brown discolouration that is quite different from the orange discolouration, which is found on the southern and eastern facades. The salt efflorescence and scaling are presented only on the eastern and southern facades. Even though the percentage of higher plants in the northern façade is 2.75%, no pitted stone surfaces are observed. That is most likely because the vegetation that thrive in that facades are herbaceous species, and every type of them extends at a very small spot on the façade (see Figure 4.3.30 and Figure 4.3.32). The three facades contain grey microorganisms colonisation, however, the red-orange microorganisms colonisation flourish at the northern façade.

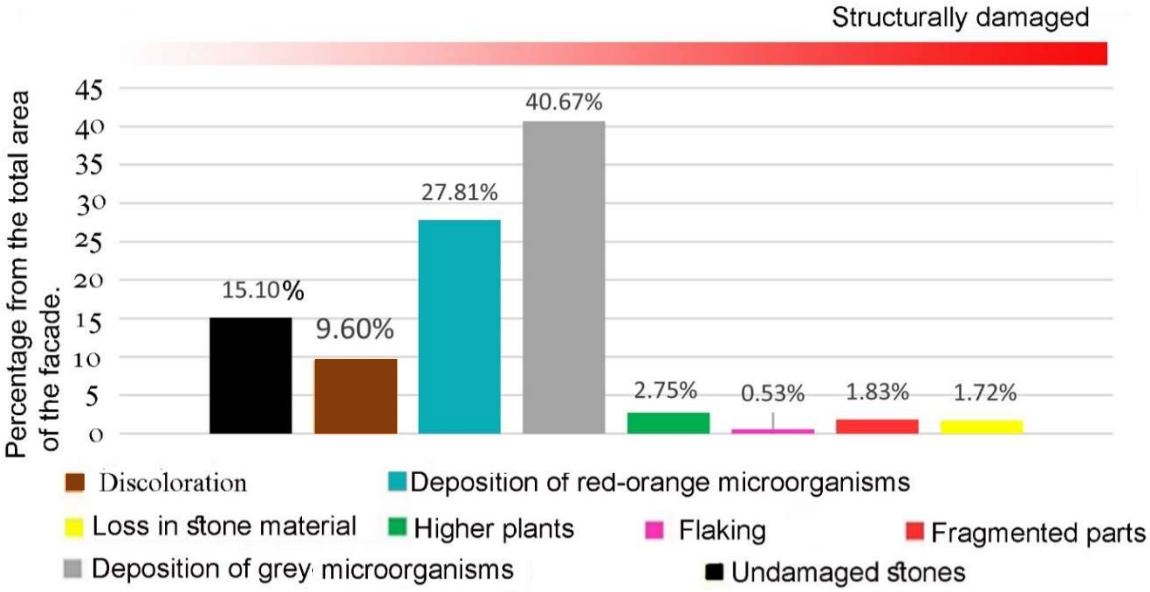

Figure 4. 3. 33 The percentage of each deterioration type at the external north facade of building (36)

4.4 Specimens sampling

The total number of samples collected in situ is 21. The locations of the obtained samples are concentrated on both the ground and first levels of the upper castle. Some samples are taken from indoor stones and others from outdoor stones. The samples are divided into two categories: i) surface deposits (11) and ii) drilled core samples (10). The first sample type is related to the deposited material on the stone surface, whether it is a biological material, stone powder, or stone fragment. Those samples are referred by (B). The biological material is

DOI: 10.15774/PPKE.BTK.2024.021

collected in small boxes by using a small wall scraper tool, or by taking a stone fragment containing this material (in the case of fragmented stone). The stone powder is also collected

Table 4.4. 1 The description of (B) samples

Sample name	Type	Description	Sampling method *	Photo number in Appendix 3
B1	Biological material	Red-orange microorganisms	II	Layout 4
B2	Biological material	Exfoliated biological material	I	Layout 1
B3	Biological material	Green microorganisms	I	Layout 4
B4	Stone powder	Orange exfoliated powder from sound stone	I	Layout 4
B5	Biological material	Orange-brown biological exfoliated material	I	Layout 1
B6	Biological material	Grey microorganisms	I	Layout 5
B7	Stone fragment	Orang material from stone that affected by a direct bullet	II	Layout 1
B8	Stone powder	Rounded brown material (framboidal crust)	I	Layout 5
B9	Stone fragment	Sample from the basement of the inner castle	II	Layout 3
B10	Biological material	Yellow microorganisms	I	Layout 2
B11	Biological material	Green –blue microorganisms	I	Layout 2

* I: Collected material. II: stone fragment

DOI: 10.15774/PPKE.BTK.2024.021

carefully by using a small wall scraper tool. While the stone fragments came from already fragmented stones.

The description of (B) samples is summarized in Table 4.4.1, whereas their locations are demonstrated in Appendix 3 (Layout 1- Layout 5).

Table 4.4. 2 (B) samples photos and where their locations

Sample name	The stone from which the sample is taken from	Photo of sample
B1		
B2		
B3		

DOI: 10.15774/PPKE.BTK.2024.021

Continue Table 4.4. 2

B4		
B5		
B6		

DOI: 10.15774/PPKE.BTK.2024.021

Continue Table 4.4. 2

B7		
B8		
B9		

DOI: 10.15774/PPKE.BTK.2024.021

Continue Table 4.4. 2

B10		
B11		

DOI: 10.15774/PPKE.BTK.2024.021

Table 4.4. 3 The description of the stone core samples(S)

Sample name	Type	Description	Stone condition	The building period of the sample	Photo number in Appendix 3
S1	Carbonate stone	An indoor stone located in a ground floor building. No stone deterioration appears on its surface	Built stone	Second Frankish period	Layout 6
S2	Carbonate stone	An indoor stone located in a ground floor building. There is green algae flourish on its surface	Built stone	Second Frankish period	Layout 6
S3	Carbonate stone	An outdoor stone colonized by orange-red algae. There are many perforations (their depth 0.5-1cm) on its surface	Fallen stone	Second Frankish period (?)	Layout 7
S4	Carbonate stone	An outdoor stone colonised by grey dead microorganisms	Fallen stone	Second Frankish period (?)	Layout 9
S5	Carbonate stone	An outdoor stone located in a building on the first floor in the east direction. The stone is discolored with orange	Built stone	Second Frankish period	Layout 9
S6	Carbonate stone	An indoor stone located in a building on the first floor. No stone deterioration appears on its surface	Built stone	Second Frankish period	Layout 10
S7	Carbonate stone	An indoor stone located in a building on the first floor. No stone deterioration appears on its surface	Built stone	Second Frankish period	Layout 10
S8	Carbonate stone	An outdoor stone located in a building on the ground floor in the north direction. There is brown layer on its surface	Built stone	First Frankish period	Layout 7
S9	Carbonate stone	An outdoor stone is fallen near Building (138). There are green algae on its surface	Fallen stone	Mamluk period (?)	Layout 8
S10	Carbonate stone	An indoor stone is fallen inside Building 137.1 No stone deterioration appears on its surface	Fallen stone	Mamluk period (?)	Layout 8

DOI: 10.15774/PPKE.BTK.2024.021

Core Drill Machine (Hilti DD-106 E). The diameter of the core bit is 2". Carbonate stones are mainly chosen for coring. These stones have the most distinct weathering types. By the primary field survey, the selection of stones to be drilled was determined . Due to the recent war, there are fallen stones from many parts of the castle. Directorate-General of Antiquities & Museums (DGAM)/ Syria recommends the drilling of the cores from fallen stones instead from the stone block in the walls. The total number of stone cores is 10. S6 is not a core sample because it is fragments of flint particles that are underlying under the stone surface, see Layout 9-S6. When the drilling has been started these flint particles resisted the machine from penetrating deeply. Therefore, the drilling in that stone is only ca. 20 cm inside the stone, and the resulted sample is fragments of flint.

The stone cores belong to the stone blocks in the walls that were built during one of the castle's three main construction periods: the first Frankish (F1), the second Frankish (F2), or the Mamluk period (M). The historic period of the fallen stones is predicted based on the construction period of the building from which they most likely fell. The majority of the core dates from the second Frankish period (S1, S2, S5, S6, and S7), with the exception of S8, which dates from the first Frankish period. Four cores are extracted from the fallen stones. S3 and S4 are found near buildings constructed during the second Frankish period, so these stones may also be from that time period. S9 and S10 were discovered in the rubble left by the destroyed part of Building (137), implying that those cores, like Building (137), date from the Mamluk period.

Table 4.4.3 describes the core stones samples (S) . The location of each core on the plan of the castle is demonstrated in Appendix 3 (Layout 6- Layout 10). Each name with an arrow refers to a core taken from a built stone, whereas the name without an arrow refers to the location where a fallen stone is taken from. The characteristics of the stone core samples are exhibited in Table 4.4.4

DOI: 10.15774/PPKE.BTK.2024.021

Table 4.4. 4 The characteristics of the stone core samples

Sample name	Diameter	Length	Notes	Photo
S1	5 cm	35 cm	One fragment	
S2	5 cm	26 cm	Two fragments	
S3	5 cm	28 cm	One fragment	
S4	5 cm	30 cm	One fragment	
S5	5 cm	30 cm	Four fragments	
S6	_	_	The machine only penetrated about 20cm because it is exposed to a large flint particle. The material consisted of stone and flint fragments.	

DOI: 10.15774/PPKE.BTK.2024.021

Continue Table 4.4..4

S7	5 cm	35 cm	One fragment	
S8	5 cm	35 cm	Two fragments	
S9	5 cm	30 cm	Two fragments	
S10	5 cm	32 cm	One fragment	

DOI: 10.15774/PPKE.BTK.2024.021

5. Laboratory investigation

DOI: 10.15774/PPKE.BTK.2024.021

5.1 Methods

5.1.1 Physical and mechanical properties

Many physical properties of the specimens have been calculated such as bulk density, matrix density, open (effective) porosity, closed porosity, total porosity, and ultrasound velocity for both dry and saturation conditions. The effective porosity is conducted from the results of water absorption at atmospheric conditions test as shown in Chapter 5.2.3. The effective capillary porosity is also obtained from the results of the capillary water uptake test as demonstrated in Chapter 5.2.2. The matrix density of the specimens is determined by using a pycnometer. The longitudinal ultrasonic wave velocity (Vp) is measured by the Pundit device with 54 kHz transducers. The physical properties are determined from the non-weathered (sound part) of the stone cores.

As for mechanical properties, the tensile strength is only measured due to the lack of stone material. The Brazilian test is performed on the front parts of the stone cores that contain the weathering crust as well as for the host stones (the non-weathered parts of the stone cores).

To know the texture (mineral types, grain size, sorting, pore size) and the type and diagenesis of the host rock of the specimens, thin sections of the specimens is prepared. The thin section specimens are prepared from front parts of the stone cores in which the petrographic description of the host rock as well as the weathering crust can be obtained.

The mineral composition is distinguished by the thermoanalytical method. The "Derivatograph Q-1500 D" device is used for the thermoanalytical test, and the "Winder V 4.4" software is utilized for obtaining the carbonate content. The mineral compositions are determined by using powdered specimens that are taken from the non-weathered (sound part) of the stone cores.

5.1.2 Capillary water uptake

For determining the water absorption ability of the stone through capillary pores, the capillary water uptake is determined by the MSZ EN 1925: 2000 standard. Before running the experiment, the specimens are dried to a constant weight (m_d) at 70 ±5 °C. Then the specimens are placed on a plastic grid inside a vessel. Water has been poured into the vessel. The specimens are immersed in water to a depth of about 3 mm. The increase in weight is repeatedly measured by the time for each specimen. The amount of water absorption per time, which is called the capillary water absorption coefficient (W_{cap}) is calculated as:

$$W_{cap} = \frac{\Delta m}{\sqrt{t} * A} \ [g/m^2 s^{0.5}]. \qquad \text{Equation 5}$$

DOI: 10.15774/PPKE.BTK.2024.021

Δm is the amount of absorbed water and can be obtained by $\Delta m = (m_i - m_d)$ [g],

m_i is the successive weight during the experiment [g],

m_d is the dry weight [g],

A is the area of the in-water immersed part [m^2],

and t is the absorption time [s].

The capillary penetration height can be calculated by[303] the following equation:

$$B = \frac{Z}{\sqrt{t}} [mm/s^{0.5}]. \quad \text{Equation 6}$$

Z is the height of the rising moisture in the sample [mm].

The water content (by volume percent) that the specimen gains by capillary water absorption is calculated as follow:

$$V_{cap} = \frac{\Delta m}{\rho_w * V_d} * 100 [\%]. \quad \text{Equation 7}$$

V_d is the volume of the specimen [cm^3],

and ρ_w is the density of water (considered as 1g/cm^3).

The maximum value of V_{cap} represents the open capillary porosity of the specimen

5.1.3 Water absorption at atmospheric conditions

Water absorption under atmospheric pressure is determined by following MSZ EN 13755: 2008 standard. The dry weight (m_d) is determined after drying the specimens to a constant weight at 70 ±5 C. Afterwards, the specimens are placed on a plastic grid inside a tank (distance between each other at least 15 mm), and tap water is added so that the specimens are half-immersed at the start time (t_o). One hour later (t_o+60 min.), more water is added until three-quarters of the samples are submerged. After another hour (t_o+120 min.), full immersion occurred, with a water level of 25 mm above the specimens. During the first two hours, the samples are weighed every 10 minutes. The weight interval is one hour from (t_o+120 min.) to (t_o+240 min.). Following that, the weighing is done daily. The experiment is terminated when all specimens reach a constant weight (the saturated mass m_s). The saturated mass is reached after about 4 months of running the experiment.

[303] P Vázquez et al., "Evaluation of the Petrophysical Properties of Sedimentary Building Stones in Order to Establish Quality Criteria," *Construction and Building Materials* 41 (2013): 868–878.

DOI: 10.15774/PPKE.BTK.2024.021

The successive mass (m_i) during the experiment is recorded. The water absorption by mass under atmospheric pressure is calculated as:

$$W_{atm} = \frac{(m_i - m_d)}{m_d} * 100 \ [w/w\%]; \qquad \text{Equation 8}$$

where W_{atm} is the mass percent of absorbed water.

The water absorption by volume under atmospheric pressure is calculated as:

$$V_{atm} = \frac{(m_i - m_d)}{V_d * \rho_w} * 100 \ [v/v\%]; \qquad \text{Equation 9}$$

where: V_d is the volume of the specimen.

(m_i-m_d) is the volume of the absorbed water per time considering the density of water ρ_w (approximately 1 g/cm^3).

The value of V_{atm} at the saturation mass (m_s) represents the percentage of the effective (open) pores.

The water absorption rate was calculated from the inclination of the initial rapid part of the water absorption versus square root of time diagram.

The longitudinal ultrasonic wave velocity is measured several times after measuring the mass by Pundit device with 54 kHz transducers.

5.1.4 Drying characteristics

The drying test in this study is performed after water saturation under atmospheric pressure to examine the drying behaviour of the specimens under three different conditions (Table 5.1.1). Three samples of all stone types are created to complete the tests: each water saturated specimen is cut into three specimens with similar dimensions, one for each group. The first

Table 5.1.1 Drying conditions

	Testing environment	Sealing	Drying temperature
Group 1	Inside the oven	No	Constant at 25°C
Group 2	Laboratory conditions	Yes	varying during the day
Group 3	Laboratory conditions	No	varying during the day

DOI: 10.15774/PPKE.BTK.2024.021

group is dried at 25°C in the oven, which provided air circulation during the heating (Group 1). These specimens are not covered. The remaining two groups of samples are dried at room temperature. The second group of specimens is sealed with Epoxy- resin on all sides except the top side (Group 2), whereas the other group is left to dry without being covered (Group 3).

Group 1 represents the drying behaviour at the laboratory conditions under constant temperature. Group 3 represents the drying behaviour of the stone at the building during the variable temperature of the day. Except for one, all sides of the specimens are covered in Group 2 to allow the water to move toward one surface by drying. The primary goal of sealing is to simulate the drying behaviour of the built-in stone in the wall of a building. Due to humidity and pressure differences inside and on its surface, the water moved toward the unique non-sealed surface.

After reaching the constant mass, the specimens of Groups 1 and 3 are dried out in the oven at 105° C to figure out the residual moisture. The drying mass at the end of the experiment cannot be determined for Group 2 because they cannot be placed inside the oven due to their sealing. The evaporation rate is used to assess the drying behaviour in this case.

During the evaporation process, the weight loss versus time is recorded, and the water content of the specimens in mass per cent (Equation 10) is calculated. The water content as a function of time is plotted.

$$W_{w1} = \frac{(m_i - m_d)}{m_d} * 100 \ \ [w/w\%] \qquad \text{Equation 10}$$

m_i is the successive weight during the experiment [g], and m_d is the dry weight of the specimen[g].

The saturation degree has also been calculated (Equation 11) to show the decreased water content over the drying period for Group 1 and Group 3.

$$S = \frac{W_{w1}}{W_{sat}} * 100 \qquad \text{Equation 11}$$

where W_{w1} [w/w%] is the successive water content by mass per cent during the drying experiment; and W_{sat} [w/w%] is the water content by mass per cent at the saturation (measured by water saturation under atmospheric pressure).

The evaporation rate is calculated as Equation 12 [304]:

[304] I Wasserman and A Bentur, "The Efficiency of Surface Treatments on Enhancement of the Durability of Limestone Cladding Stones," Materials and Structures 38/1 (2005): 99–105.

DOI: 10.15774/PPKE.BTK.2024.021

$$E = \frac{\Delta m}{A * \sqrt{t}} \; [kg/m^2 * h^{0.5}] \qquad \text{Equation 12}$$

$\Delta m = m_s - m_i$; m_s is the saturated mass [kg],

m_i successive mass during the experiment [kg].

A is the area of the unsealed surface [m^2] where evaporation can occur, and t is the time [h].

S2 and S5 are not tested in drying experiment due to lack of stone material of these two specimens. The core sample of both specimens are originally fragmented, where S5 consists of 4 fragments and S2 is broken at the middle into two fragments (Chapter 4.4). Therefore, cutting them in the laboratory to make several tests is not possible always.

5.1.5 Permeability

The test results are primarily intended to achieve two objectives. The first one is to determine the water vapor permeability and the permeability resistance factor of the stones. The second goal is to compare the water vapor permeability of weathered and un-weathered specimens. As such, determining the extent to which the weathered surface modifies the water vapor permeability property.

Two specimens from each core sample are examined to achieve the test goals. One specimen is taken from the backside (the sound part) of the core sample, and it is referred to /R/ in the following text. The other specimen is made from the front side with a crust (the weathered surface of the stone), and it is referred to /C/. The dimensions of the samples are shown in Table 5.1.2.

Table 5.1.2 The dimensions of the specimens for the permeability measurement

Specimen	Area (cm^2)	Thickness (cm)
S1-R	10.05	0.83
S1-C	9.96	1.05
S2-R	8.75	1.12
S2-C	9.10	1.18
S3-R	8.00	1.01
S3-C	8.20	1.28
S4-R	9.15	1.05
S4-C	9.10	1.03
S7-R	19.63	1.02
S7-C	14.20	0.90
S8-R	19.63	1.39
S8-C	8.70	0.83
S9-R	9.45	1.03
S9-C	9.20	1.33
S10-R	10.90	1.33
S10-C	10.20	1.02

The specimens are placed on the top of a transparent plastic jar with 5 cm diameter (the same as the diameter of the core samples) and 3.7 cm height. In the case of specimens with non-circular surfaces, the plastic jar cover is cut to cover the top of the jar (Figure 5.1.1 and Figure5.1.2).

DOI: 10.15774/PPKE.BTK.2024.021

The specimen is glued to the jar, with silicon glue, carefully not to cover any effective evaporation surfaces (the top and the bottom side of the specimen) (Figure5.1.2). Water is injected through a 1 mm thick hole into the jar. The hole is tightly closed once the water is added. Before placing the specimens in the jars, they are dried at 70°C. Each jar is filled with 15 ml of distilled water, with a 1.5 cm air gap between the specimen and the water. The experiment is performed in a climate room with a temperature of 19°C and relative humidity of 60%. The water vapor is transferred due to the relative humidity differences between the inside air (RH 100 %) and the room (RH 60 %). The weight loss of the jar at time intervals is used to calculate the water vapor permeability rate, as shown in equation 13.

$$D=\frac{G*d}{t*A*S*(R_1-R_2)} \ [Kg/(s.m.Pa)] \quad [305] \qquad \text{Equation 13}$$

D is the water vapor permeability rate [Kg/(s.m.Pa)], G is the weight change [kg],

d is the thickness of the specimen [m], t is the time [s], A is the effective area of the specimen [m²], S is the partial pressure of the saturated air at 19°C [Pa], R_1 is the relative humidity inside the jar (100%), and R_2 is the relative humidity at the climate room (60%).

Water vapor diffusion resistance factor is calculated as:

$$\mu=\delta l*\frac{1}{D} \ [-] \quad [306] \qquad \text{Equation 14}$$

δl is the water vapor diffusion coefficient of air at 19°C (kg/Pa. m. s) and can be calculated from equation 15:

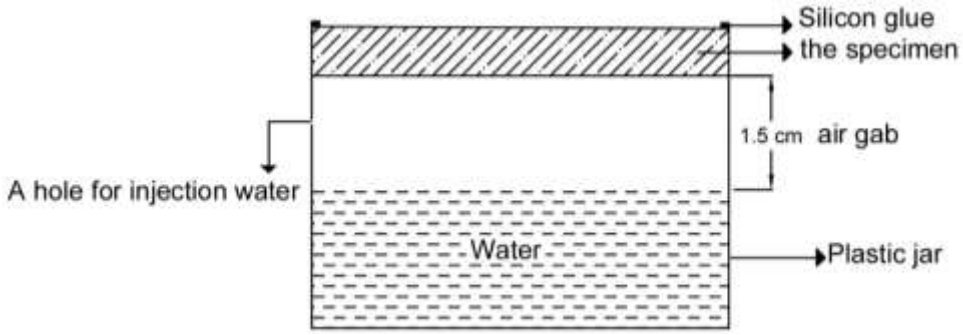

Figure 5.1. 1 Schematic diagram of the measuring equipment of the water vapor permeability measurement

[305] Phalguni Mukhopadhyaya et al., "Water Vapor Transmission Measurement and Significance of Corrections," *Heat-Air-Moisture Transport: Measurements on Building Materials* 4/1495 (2007): 21.
[306] Siegfried Siegesmund and Helmut Dürrast, "Physical and Mechanical Properties of Rocks," in *Stone in Architecture* (2011), 97–225.

DOI: 10.15774/PPKE.BTK.2024.021

$$\delta l = \frac{2*10^{-7}*T^{0.81}}{Pl}\ [kg/Pa.\ m.\ s]$$ [307] Equation 15

T is the test temperature [K], and Pl is the atmospheric pressure [Pa].

The characteristics of each weathering crust sample are summarised in Table 5.1.3.

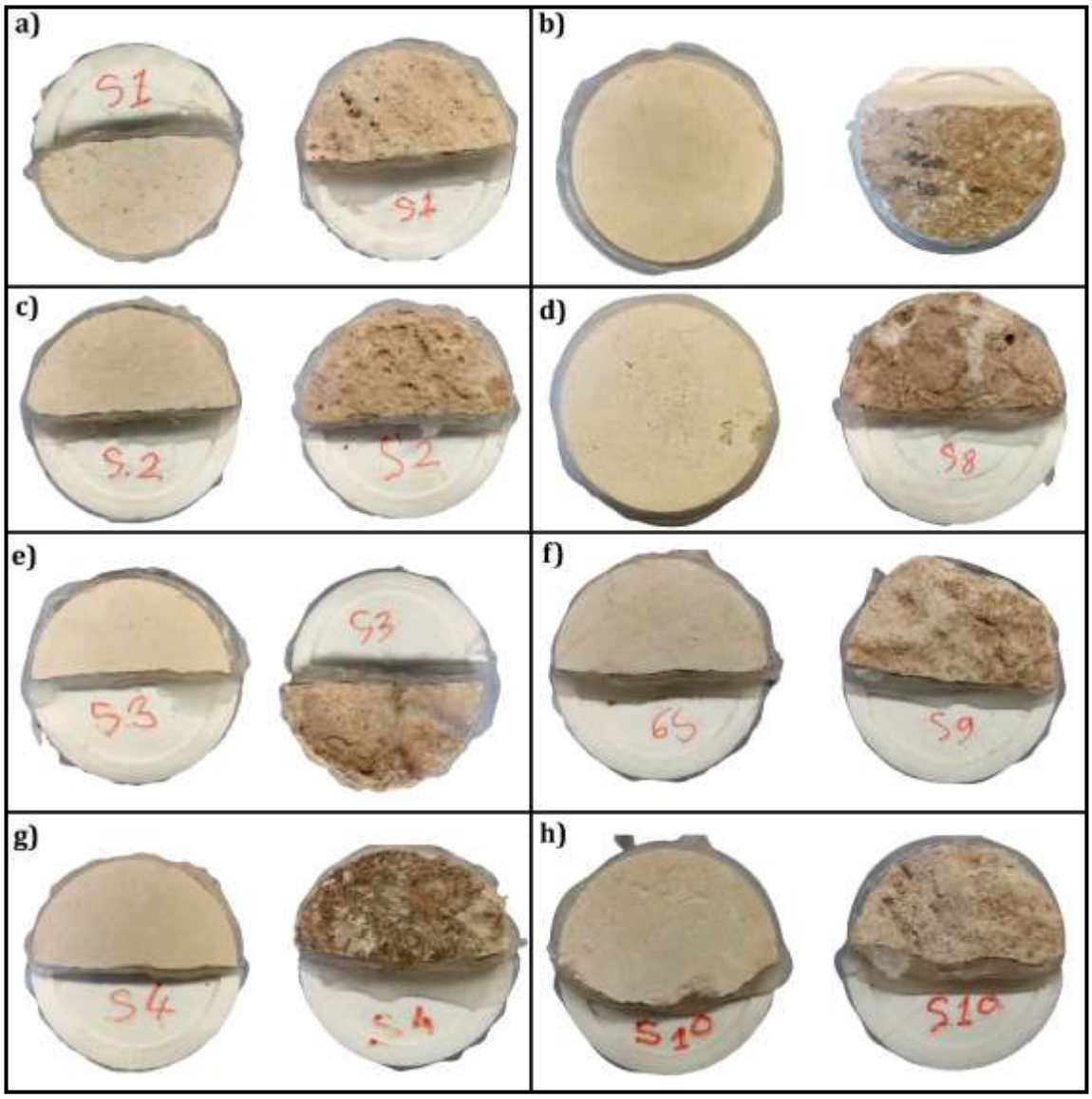

Figure 5.1. 2 The tested specimens for water vapor permeability. In each pair, the left specimen is sound and the right one is from the weathering crust. 2a) S1 specimens; 2b) S7 specimens; 2c) S2 specimens, 2d) S8 specimens; 2e) S3 speciemns; 2f) S9 specimens; 2g) S4 specimen; 2h) S10 specimens

**The green algae are observed on the original stone surface of S2 and S9 before taking the core sample, see Appendix 3/ Layout 6 & Layout 8. Due to the wet coring the water washed out the green algae. Therefore, the green algae did not appear on both S2-C and S9-C, see Figure 5.1.2*

[307] Hartwig M Künzel, "Simultaneous Heat and Moisture Transport in Building Components," *One-and Two-Dimensional Calculation Using Simple Parameters. IRB-Verlag Stuttgart* 65 (1995).

DOI: 10.15774/PPKE.BTK.2024.021

Table 5.1.3 The characteristic description of the weathering crusts (observation by naked eye and under optical microscope by using the thin section method)

Specimen	Macroscopic description	Thin section description	Figure
S1-C	No distinct decay type visually recognized on the surface.	There is a dissolution and recrystallisation of dolomite with tiny crystals on the surface. The thickness of the crust is 0.1mm.	5.1.3/S1
S2-C	Green algae are flourished on the surface *.	The thickness of the crust is about 3 mm. There is a transitional boundary between the crust and the host rock. The crust is more porous than the original rock, where the size of its pores is around 0.5 mm. Recrystallisation of dolomite crystals on the crust causes the disappearance of the microfabric of the original rock.	5.1.3/S2
S3-C	Orange-red algae flourish on the surface.	The crust is slightly micritic and contains organic material that extends to 1.5 mm depth under the surface. The thickness of the crust 1.5mm.	5.1.3/S3
S4-C	Grey microorganisms colonized the surface.	The weathering crust is lower porous than the original stone by about 25%. There is a biological activity associated with pores under the surface. Under the crust, there is a porous zone of about 1.5-2 mm that is more porous than the stone itself.	5.1.3/S4
S7-C	The color of its surface is orange.	Its crust can be divided into four layers: 1) L_1 The outermost layer with a thickness of 0.01-0.04 mm is a brownish organic layer with biological activity. This layer is not continuous. 2) L_2 is a layer under L_1. It is very dense and consists of microcrystalline dolomite crystals with a size of less than 0.005 mm. The thickness of this layer is around 0.1-0.3 mm. 3) L_3 is the layer under L_2. It has a dark grey micritic matrix with the presence of oval micritic forms with a size of 0.005 mm. The thickness of this layer is around 1.5 mm. 4) L_4 is the layer under L_3. It is similar to L_3 but it has a lighter colour and much fewer oval micritic forms. The thickness of this layer is 0.2-0.4 mm as a mean value.	5.1.3/S7
S8-C	A brown layer on the surface.	The thickness of the crust is about 1.25-2 mm. On the crust are observable wind-blown sand grains with 0.03-0.05 mm sizes. The topmost of the crust, with an irregular thickness that ranges between 0.15-0.5 mm has iron staining. Those iron staining give a brownish colour of the crust. Under the crust is a biological activity, that appears in the form of a dark circle with a diameter of 0.02 mm and is surrounded by other circles with a diameter of 0.03 mm (it might be a filamentous part of algae or lichen). Many pores in the crust have a coating with a maximum thickness of 0.03 mm on their walls and might be related to biological activity.	5.1.3/S8
S9-C	Green algae are flourished on the surface*.	There is a dissolution on the surface. The dolomite crystals in the crust are clear without any inclusions; however, there is inclusion-rich dolomite under the crust. The thickness of the crust 0.08-0.12mm.	5.1.3/S9
S10-C	No distinct decay type visually recognized on the surface.	The crust is micritic with very fine crystals. There are tiny crystals on the surface that do not form a uniform crust. There is a cemented zone under the crust of 0.1-0.16mm. The thickness of the crust 0.02-0.1mm.	5.1.3/S10

DOI: 10.15774/PPKE.BTK.2024.021

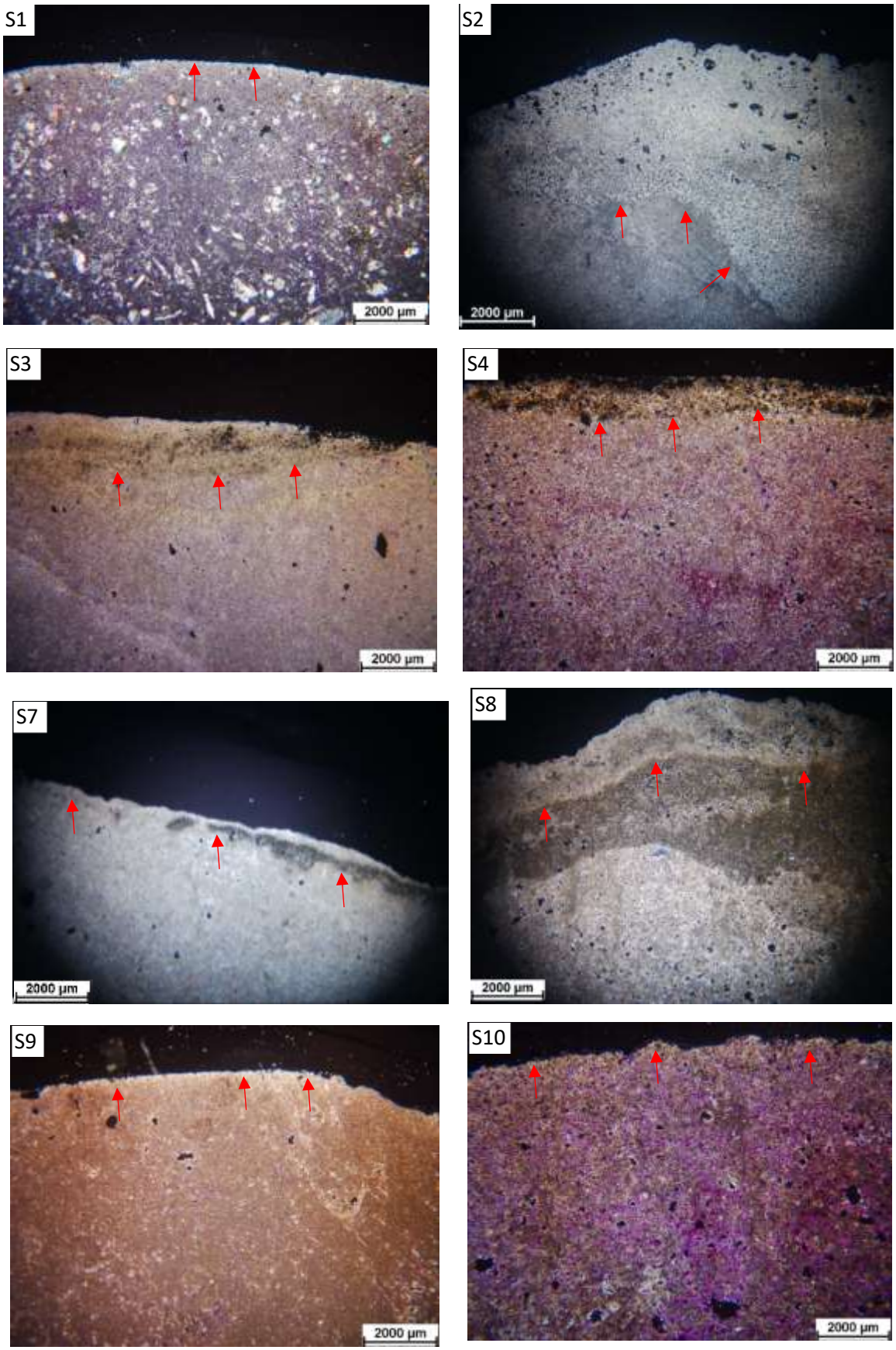

Figure 5.1. 3 Thin section photos of the specimens crusts. The red arrows refer to the boundary of each crust

DOI: 10.15774/PPKE.BTK.2024.021

5.1.6 Salt ageing test

Salt crystallization on the stones surfaces is a common deterioration case in Crac castle; therefore, it is important to assess the resistance of stones against salt ageing. The choosing of salts for the experiment is based on the salts present in the castle. That is achieved by making a salt content test for B samples (mentioned in chapter 4.4) to reveal the existence of chloride, nitrate, nitrite, and sulfate, the most frequent ions found in a salt crust. The gravimetric method is used to calculate sulfate anion content, whereas chloride anion content is determined by Mohr argentometric method. A semi-quantitative method is used for the determination of nitrate anions content. The salt content results of B samples are shown in Table 5.1.4. The most common anions in B samples are chloride and sulfate; however, nitrate is present in some samples. Nitrite anions did not exist in any samples. Based on these results four salts are

Table 5.1.4 The result analysis of PH and anions content (by weight percent) for B samples

Specimen	Weight	pH	Nitrite ion content	Nitrate ion content	Chloride ion content	Sulfate ion content
	g		W%	W%	W%	W%
B1	0,44	7,7	0	in traces	0,52	0,28
B2	0,48	10,0	0	0,10	1,05	0,85
B3	0,29	8,4	0	0	0,43	0,51
B4	0,39	9,1	0	0,332	0,65	49,73
B5	0,36	9,4	0	in traces	0,42	10,82
B7	0,64	9,1	0	0,78	0,75	0,89
B8	1,02	10,1	0	in traces	0,20	0,38
B9	1,17	8,8	0	2,14	1,27	0,22
B10	0,61	8,7	0	0	0,25	1,09
B11	0,52	7,9	0	0	0,29	0,24

selected for the ageing test: sodium chloride (NaCl); sodium sulfate (Na_2SO_4), magnesium sulfate ($MgSO_4$); and potassium nitrate (KNO_3). It is important to study the stones under NaCl solution, as the castle is near the coast and is affected by salt spray [308]. Sulfate salts, Na_2SO_4

[308] Simona Scrivano and Laura Gaggero, "An Experimental Investigation into the Salt-Weathering Susceptibility of Building Limestones," *Rock Mechanics and Rock Engineering* 53/12 (2020): 5329–43.

DOI: 10.15774/PPKE.BTK.2024.021

and $MgSO_4$ are extremely damaging [309], and Na_2SO_4 is considered the most aggressive salts used to assess the durability of the stone in the laboratory [310]. However, KNO_3 is chosen since it is the most famous nitrate salt that can be found in salt crust of stone [311].

The standard for determining the resistance against salt crystallisation of Na_2SO_4 (MSZ EN 12370) is followed. The procedure mentioned in the standard is used for the four salts to compare the behavior of the specimens under different salts and the same conditions. Against the recommendation of the standard (drying temperature of 105°C), 70°C is used as drying temperature in this test. Because 70°C is sufficient to reach the hydrate- non hydrate change for both hydrated salts ($MgSO_4$ and Na_2SO_4) and this temperature is usually used as a drying degree.

The salt ageing test consists of several solution-drying cycles, where each cycle is at least 24 hours long. The specimens are immersed in the salt solution for two hours before placing them in the oven. The oven is set to gradually heat from 20°C to 70°C for ten hours before remaining at 70°C for another ten hours. After that, the specimens are cooled down for two hours at room temperature before being placed back into the salt solution for two hours and starting the next cycle (Figure 5.1.4). The cycle starts by putting the stones in the salt solution and ends at the end of the cooling period. A 2 liters water vessel is put inside the oven to provide high relative humidity inside the oven. The experiment is running during the working day of the week. The measurement cannot be fulfilled daily during the weekends and holidays. Therefore, the cycle duration is more than 24 h during the weekends. The gradual increase of temperature from 20 to 70 °C is the same but the remaining time at 70°C is longer during period of holiday.

14% w/w salt solutions are separately prepared with NaCl, $Na_2SO_4.10H_2O$, KNO_3 and $MgSO_4.7H_2O$ by using distilled water. Before running the experiment, the specimens are dried in the oven at 70°C to reach the constant mass (m_d). By the end of the cooling period of each cycle, the mass of each specimen (m_i) is recorded. Salt crystallisation occurs inside the stone structure because of repeated salt solution-drying cycles. The crystalised salt inside the specimen causes an increase of the specimen mass. However, when the crystalised salt leads to grain loss and degradation of stone, the specimen mass decreases due to salt crystallization

[309] E Ruiz-Agudo et al., "The Role of Saline Solution Properties on Porous Limestone Salt Weathering by Magnesium and Sodium Sulfates," *Environmental Geology* 52/2 (2007): 269–81.
[310] Barbara Lubelli et al., "Towards a More Effective and Reliable Salt Crystallization Test for Porous Building Materials: State of the Art," *Materials and Structures* 51/2 (2018): 1–21.
[311] Joerg Ruedrich and Siegfried Siegesmund, "Salt and Ice Crystallisation in Porous Sandstones," *Environmental Geology* 52/2 (2007): 343–67.

DOI: 10.15774/PPKE.BTK.2024.021

damage. The change in specimen mass in each cycle is calculated as a percentage of the initial dry mass:

$$D_{salt} = \frac{(m_i - m_d)}{m_d} * 100 \ [w/w\%];$$ (MSZ EN 12370: 2000 standard) Equation 16

where; m_i is the successive mass in each salt cycle [g], and m_d is the dry mass [g].

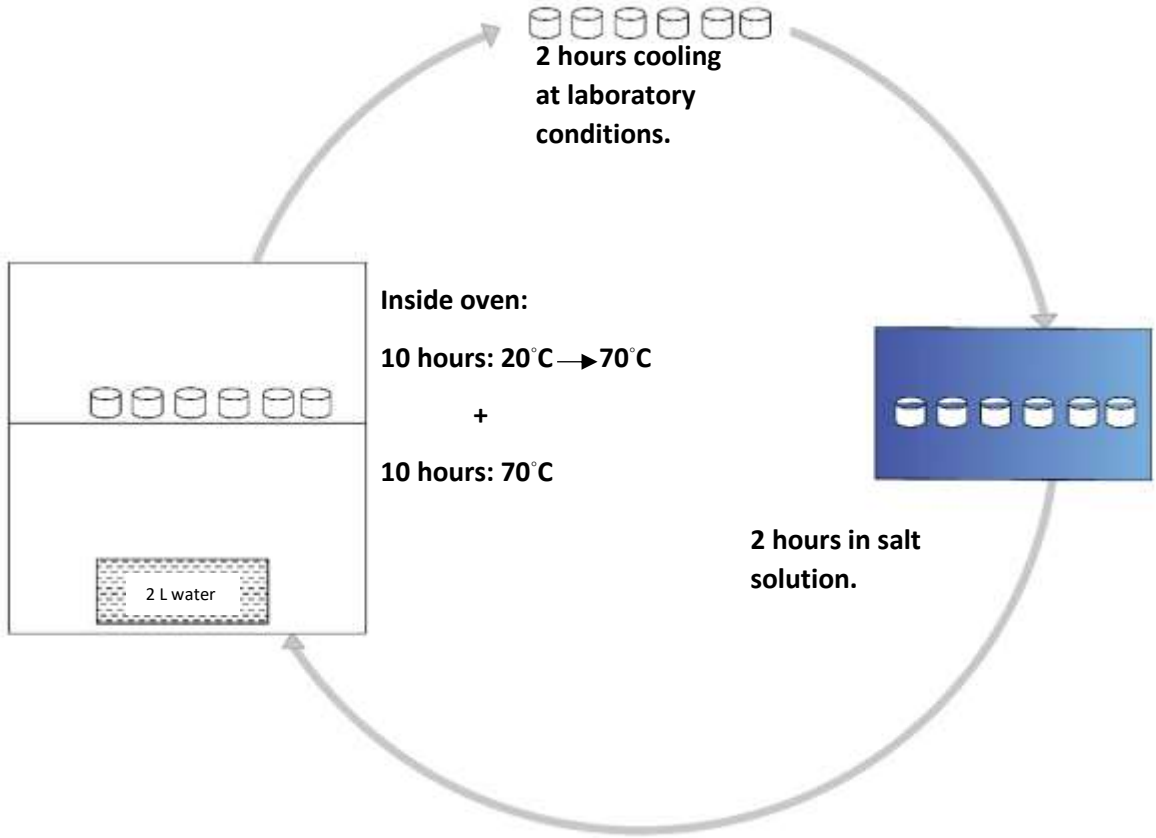

Figure 5.1. 4 A schematic representation of one 24 hours salt cycle

The concentration of the salt solution is controlled by using hydrometers. Therefore, if the concentration of salt solution increased, distilled water is added. If the salt solution concentration decreased, more salt is added to keep the concentration fixed during the test. 50 cycles of NaCl and $Na_2SO_4.10H_2O$, 30 cycles of KNO_3, and 40 cycles of $MgSO_4.7H_2O$ are made.

Four groups of specimens are prepared from the stone cores, and each group is tested under one salt solution. Three groups contained 9 specimens (S1, S2, S3, S4, S5, S7, S8, S9, and S10) and are aged with NaCl, $Na_2SO_4.10H_2O$, and KNO_3 solutions, respectively. The fourth group, which is aged with MgSO4.7H2O solution, contains 7 specimens (S1, S3, S4, S7, S8, S9, and

DOI: 10.15774/PPKE.BTK.2024.021

S10). As such, the aim of this test is to study the behaviour and resistance of different stone types in different salt solutions.

According to our results, the long period cycles affected only the specimens of the simple salts, NaCl & KNO_3, due to their hygroscopicity. The behaviours of these salts under 24 hours-cycle are different from those under a more extended cycle period (more details in the results). However, the behaviour of the hydrated salts remained the same regardless of the period length of the cycle.

5.2 Results and discussion

5.2.1 Specimens properties:

The mechanical and the physical properties are summarized in Table 5.2.2.

As for the host stones, S2 has the lowest value of tensile strength (about 1.58 MPA); S1 and S9 have the highest values (4.83 and 6.56 MPA, respectively); however, the tensile strength of the rest of specimens is close to each other (around 3 MPA in average). The tensile strength of S7 crust part cannot be determined because that part is originally broken when the core is obtained (see 4.4 section). The tensile strength of the crust parts of the specimens are close to the host stones (non- weathered parts) except for S5, see Table 5.2.2. In S5 the tensile strength of the crust is around three times higher than the host stone. The crust part of S5 (around 3-4 cm) is dense, however, the host rock contains many cracks and fissures that make the host rock so weak.

Table 5. 2. 1 The MgoCO3 and CaCO3 content of the specimens as a result of thermoanalytical test

Specimen	$MgCO_3$	$CaCO_3$
	w/w%	w/w%
S1	29.5	67.9
S2	39.5	57.7
S3	39.2	55.6
S4	39.8	56.8
S5	39.6	57.1
S7	40	54.5
S8	38.5	57.8
S9	35.9	52.7
S10	37	59

DOI: 10.15774/PPKE.BTK.2024.021

Table 5. 2. 2 The physical and mechanical properties of the specimens

Specimen				S1	S2	S3	S4	S5	S7	S8	S9	S10
Main lithology (based on HCl tests)				Limestone	Dolomitic limestone	Dolomite	Dolomite	Dolomitic limestone	Calcitic dolomite	Dolomitic limestone	Dolomite	Dolomite
Physical properties			Dry bulk Density	g/cm^3	2.204	1.904	1.933	1.943	2.009	1.949	1.902	2.431	1.977
			Wet bulk density	g/cm^3	2.384	2.192	2.249	2.223	2.274	2.235	2.188	2.542	2.254
			Matrix density	g/cm^3	2.751	2.705	2.841	2.879	2.782	2.757	2.834	2.814	2.889
			Total porosity	% (v/v)	19.9	29.6	32.0	32.5	27.8	29.3	32.9	13.6	31.6
			Total open porosity	% (v/v)	18.0	28.8	31.7	28.1	26.5	28.9	28.8	11.2	27.7
			open capillary porosity	% (v/v)	13.8	23.0	26.5	20.7	21.8	22.8	22.0	7.6	22.0
			Closed porosity	% (v/v)	1.9	0.9	0.3	4.5	1.3	0.4	4.1	2.4	3.9
			Vp/dry	km/s	4.29	2.49	2.92	2.97	3.14	3.28	3.13	4.42	3.47
			Vp/ saturation	km/s	4.35	2.35	2.84	2.60	2.87	2.78	2.82	4.38	3.23
Mechanical properties													
	Tensile strength MPA		Crust		5.52	1.71	2.13	3.98	6.84	—	4.31	6.96	1.38
			Host stone		4.83	1.58	3.52	3.5	2.82	2.9	3.13	6.59	2.45

DOI: 10.15774/PPKE.BTK.2024.021

Petrographic description (thin section technique) and thermoanalytical results (DTA/TG/ DTG):

The DTA/TG/ DTG curves resulted from thermal analysis can be found in Appendix 4.

According to the thin sections of S1, it is a slightly dolomitized and silicified micro bioclastic wackstone (a limestone). It is a well-sorted stone with very fine grain size. It contains limonitic spots, small patches of brownish micrite mottles and fragments with a size of 0.05-0.2 mm. The pores are moldic rounded ones (0.05-1.2 mm), and they are filled with spiritic calcite. Some angular pores with a size of 2.5 mm (about 5%) are filled with calcite. The size of open pores ranges from 0.05 mm to 0.45 mm,

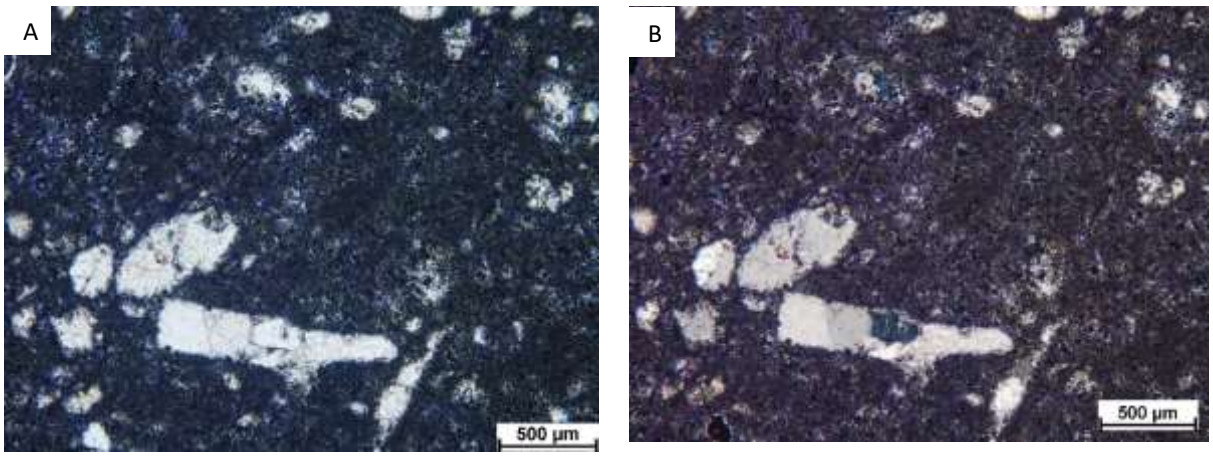

Figure 5. 2. 1 The thin section photos of S1 specimen. 1A) plane polarized 1B) crossed polarized

see Figure 5.2.1. The thermal analysis of S1 shows that this specimen is a limestone and consists of about 30 w/w% $MgCO_3$ and 68 w/w % $CaCO_3$ (Table 5.2.1).

*S2 is a microcrystalline dolomitic limestone with very fine dolomicritic crystals (less than 0.*005 mm) and very few larger crystals with a size of 0.01 mm. The original texture of the

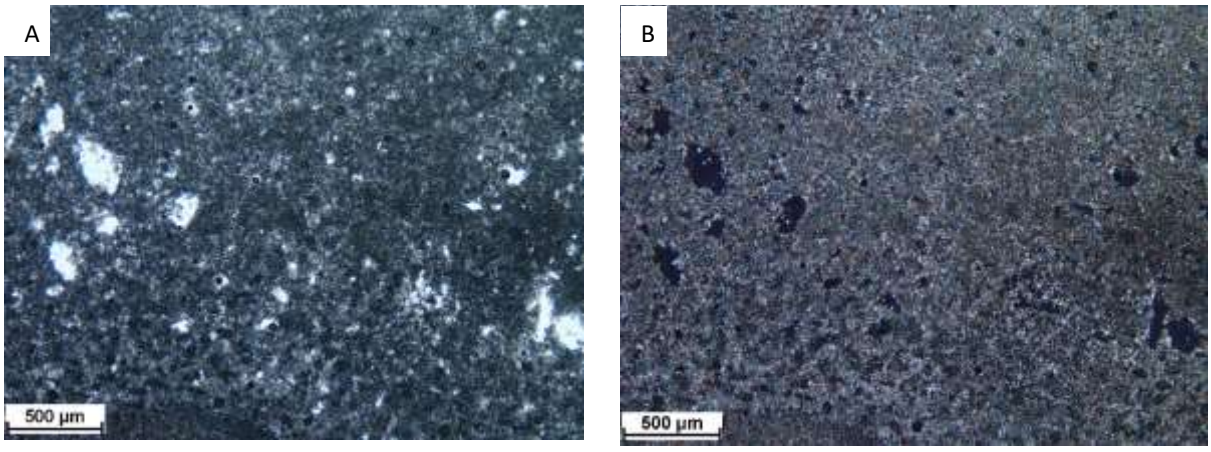

Figure 5. 2. 2 The thin section photos of S2 specimen. 2A) plane polarized. 2B) crossed polarized

DOI: 10.15774/PPKE.BTK.2024.021

stone is oolitic limestone, where the size of ooids is about 0.25 mm with the presence of some peloids. The stone texture and the micro fabric are not uniform. The texture is on the one hand micritic and in other places it is microcrystalline with a crystals size of 0.01 mm. It has bimodal pores; it contains both large and very tiny pores. The size of large pores is around 0.4 mm, and there are dolomite crystals with a size of 0.03 mm on the walls of these pores. The tiny pores are well-connected (Figure 5.2.2). The thermoanalytical results of S2 indicates that it is a dolomite stone with around 40 w/w% $MgCO_3$ and 58 w/w% $CaCO_3$.

As for S3, it is a microcrystalline dolomite stone with very fine dolomitic crystals (with a size of about 0.005 mm). Some shades of former texture appear in the thin section. The stone has many intercrystalline pores (in a micrometre scale) as well as few large ones with a size of 0.1 mm (Figure 5.2.3). It consists of 39 w/w% $MgCO_3$ and 56w/w% $CaCO_3$ (these percentages are very close to S2), see Table 5.2.1.

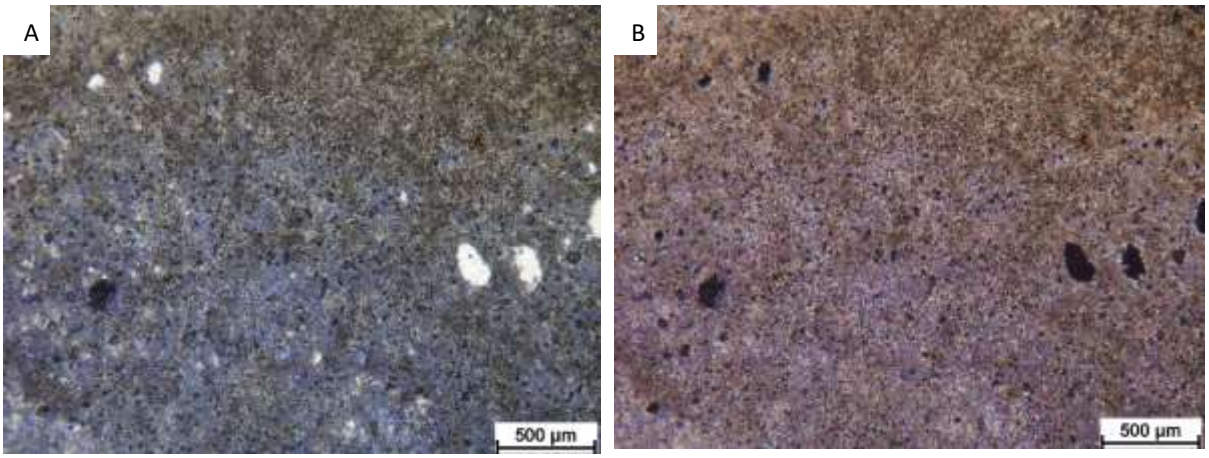

Figure 5. 2. 3 The thin section photos of S3 specimen. 3A) plane polarized. 3B) crossed polarized

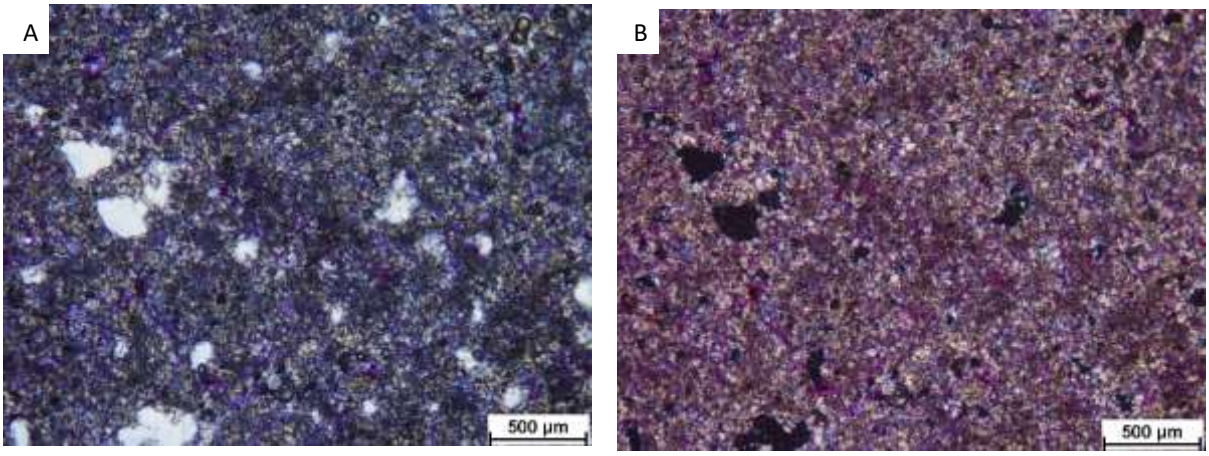

Figure 5. 2. 4 The thin section photos of S4 specimen. 4A) plane polarized. 4B) crossed polarized

DOI: 10.15774/PPKE.BTK.2024.021

S4 is a microcrystalline dolomite stone with equiangular crystals (0.03-0.07 mm). There are ghosts of original texture as well as crystals with clear rims and cloudy cores in its structure. It has bimodal pores, where the size of large pores ranges between 0.3 mm-0.5 mm and the tiny ones are about 0.02 mm (Figure 5.2.4). The thermoanalytical results reveals that this dolomite stone consists of around 40 w/w% $MgCO_3$ and 57 w/w% $CaCO_3$, see Table 5.2.1.

S5 is a micro bioclast packstone (dolomitic limestone). The size of prevailing bioclast crystals of that stone is about 0.07-0.1 mm. It contains very thin shell fragments, and a slight lamentation is also visible with tiny orange-brown limonitic particles (0.01-0.1 mm). A closed crack filled with calcite can be noticed with a thickness of 0.03-0.05 mm. It has very few visible pores with size of 0.2 mm and its tiny pores are not visible under the microscope (Figure 5.2.5). The thermoanalytical results shows that this dolomite stone consists of around 39.6 w/w% $MgCO_3$ and 57.1 w/w% $CaCO_3$.

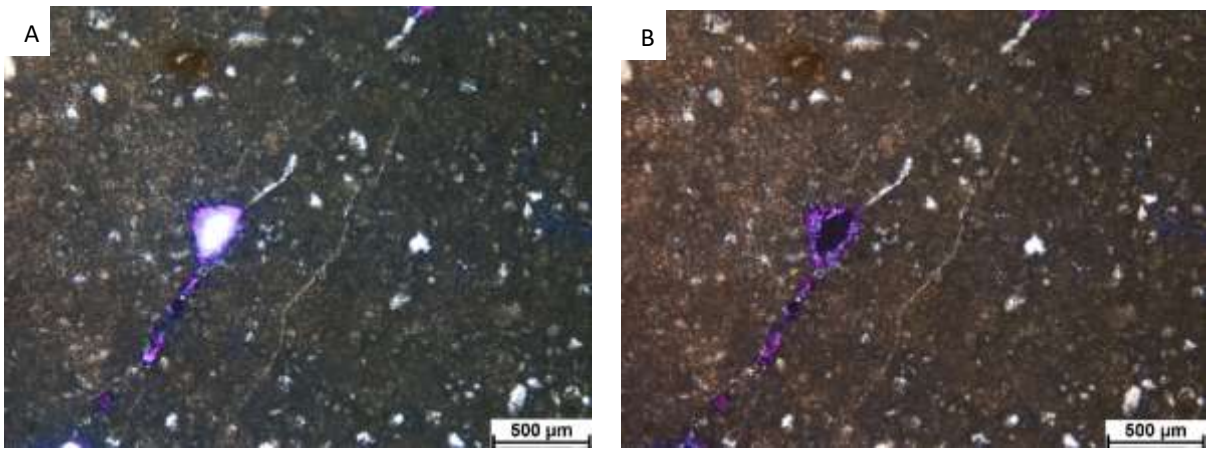

Figure 5. 2. 5 The thin section photos of S5 specimen. 5A) plane polarized. 5B) crossed polarized

As for S7, it is microcrystalline calcitic dolomite with a high recrystallisation rate and about 0.005 mm crystal size. Its texture is homogenous, and the ghosts of the original texture are weakly appearing. The pore size is around 0.2 mm, and it contains a lot of very fine pores (the size of which cannot be defined by the microscope) (Figure 5.2.6). It consists of 40w/w% $MgCO_3$ and 55w/w% $CaCO_3$, according to the thermoanalytical results.

DOI: 10.15774/PPKE.BTK.2024.021

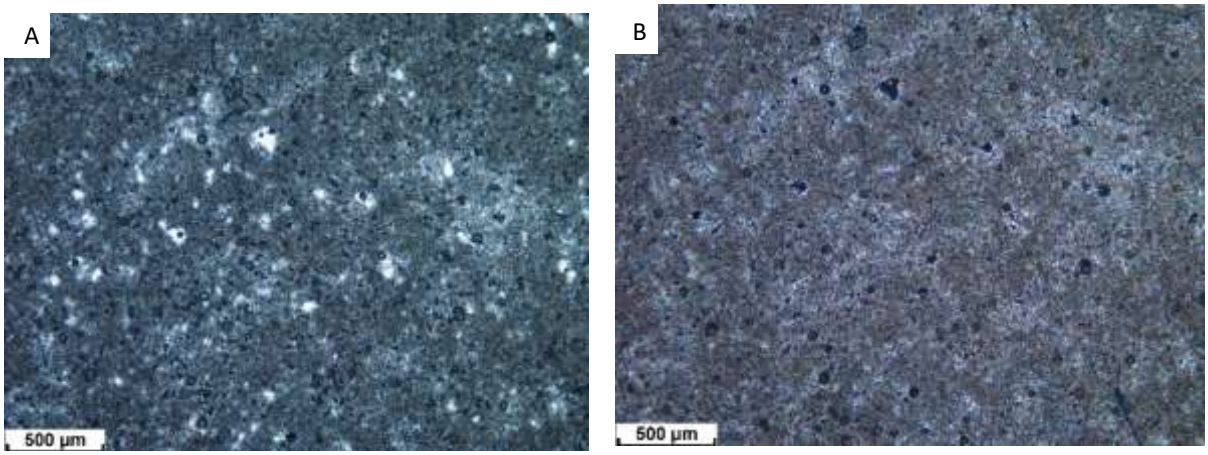

Figure 5. 2. 6 The thin section photos of S7 specimen. 6A) plane polarized. 6B) crossed polarized

S8 is laminated dolomitic limestone with peloids and small intraclasts. The thickness of the lamination is 1.2-2.9 mm. It contains some micritic layers. The size of the dolomicritic crystals is around 0.01-0.002 mm. On the pore walls are observable dolomite crystals with a size of 0.03 mm. The stone has a bimodal pore size where the large pores are about 0.3 mm and the tiny ones range between 0.02-0.05 mm (Figure 5.2.7). The thermoanalytical results reveals that this dolomite stone consists of about 39 w/w% $MgCO_3$ and 58 w/w % $CaCO_3$.

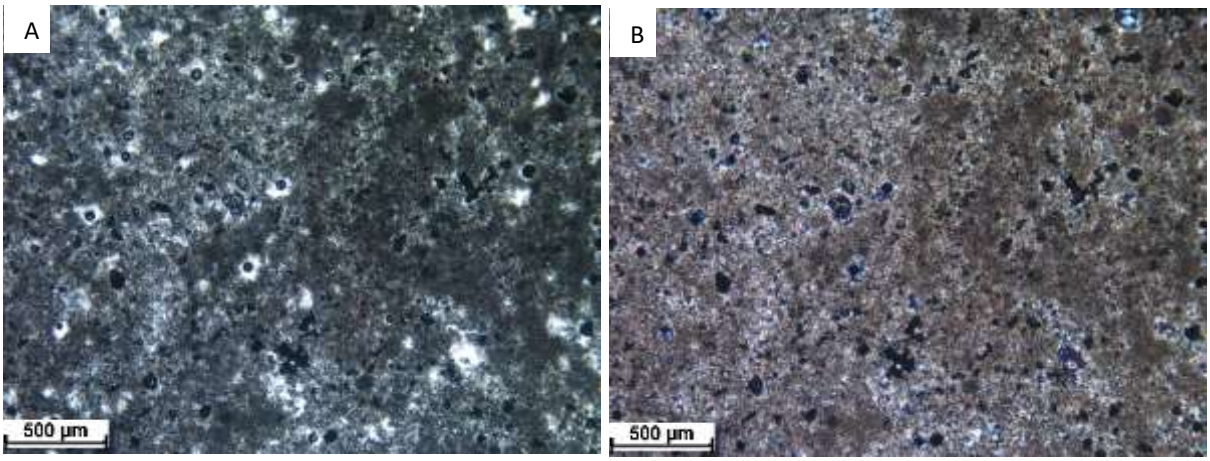

Figure 5. 2. 7 The thin section photos of S8 specimen. 7A) plane polarized. 7B) crossed polarized

S9 is a micro bioclastic wackstone with algal mat and fenestral pores. The stone has bimodal pore size where the size of large pores ranges between 0.4-0.6 mm and the tiny ones are about 0.01 mm. An algal mat appears in the texture, which contains lots of clast fenestral closed pores filled with sparitic calcite. There are ghosts of shell fragments with a size of 0.4-0.6 mm in the texture (Figure 5.2.8). This dolomite stone comprises of around 40 w/w% $MgCO_3$ and 58 w/w % $CaCO_3$.

DOI: 10.15774/PPKE.BTK.2024.021

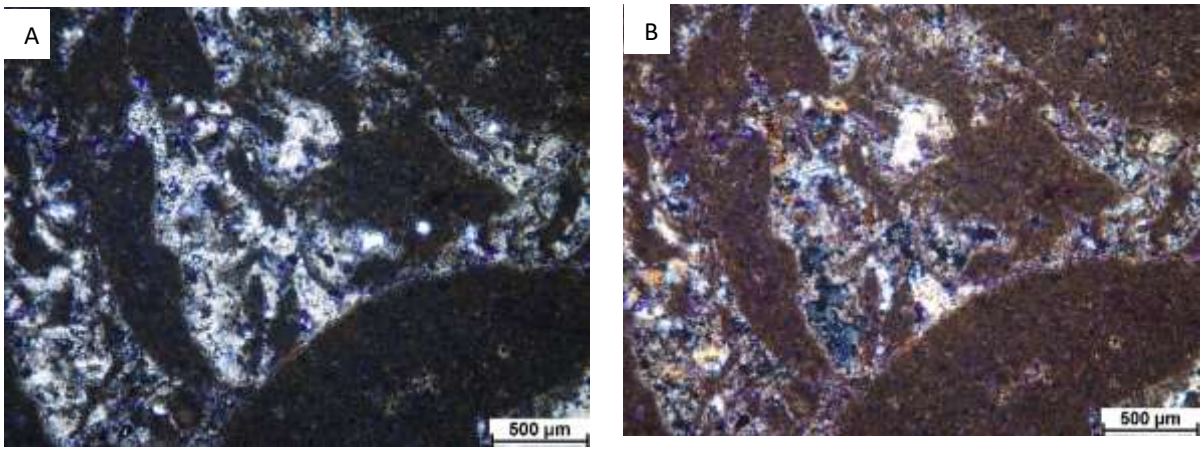

Figure 5. 2. 8 The thin section photos of S9 specimen. 8A) plane polarized. 8B) crossed polarized

S10 is a dolomitic limestone with creamy white calcitic rounded mottles and darker brownish creamy dolomite zones. Its original texture is micritic peloidal wackstone/ packstone (with a particle size of 0.05-0.08 mm). There are few foraminifera fragments (about 0.1 mm). The stone has scattered large pores of 1-2 mm in diameter and plenty of smaller closed pores with a size of 0.1-0.25 mm (Figure 5.2.9). The thermoanalytical results shows that this dolomite stone consists of about 37 w/w% $MgCO_3$ and 59 w/w% $CaCO3$ (Table 5.2.2).

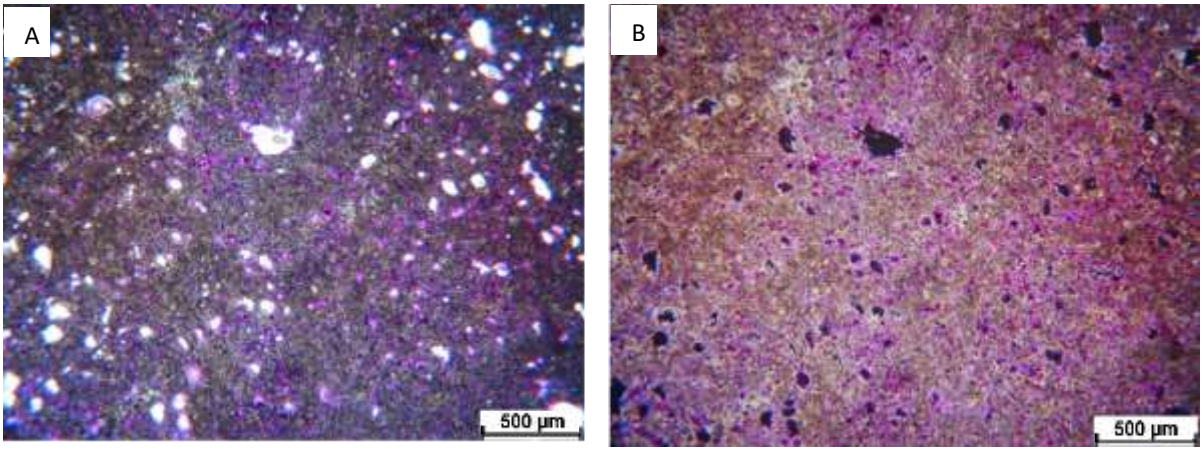

Figure 5. 2. 9 The thin section photos of S10 specimen. 9A) plane polarized. 9B) crossed polarized

5.2.2 Capillary water uptake

The amount of absorbed water per area versus the square root of time in seconds is plotted in Figure 5.2.10, while Figure 5.2.11 shows the capillary water uptake capacity curve by time. All specimens demonstrate capillary water absorption curves with 3 stages. The first stage is linear and expresses the gradual increase of absorbed water that fills the capillary pores over time. The middle stage is slower, short or barely existing as in specimens such S3, S4, S7, S8,

DOI: 10.15774/PPKE.BTK.2024.021

and S10 or relatively long as in S1, S2, S5, and S9. The last stage of the capillary absorption curve represents the saturation condition, the stability one, which is reached when almost all effective capillary pores are filled. The water uptake coefficient can be obtained from the slope of the first linear part of each curve.

Table 5. 2. 3 The Capillary water uptake coefficient, water penetration rate and capillary water capacity of the specimens

Specimen	Capillary water uptake coefficient (W_{cap})	Water penetration rate* (B)	The maximum water content by volume (open capillary porosity) (V_{cap})
	$g/m^2\ s^{0.5}$	$mm/\ s^{0.5}$	v/v%
S1	41.50	0.9	13.83
S2	125.39	1.3	23.00
S3	290.22	1.16	26.46
S4	292.13	1.9	20.67
S5	87.87	0.65	21.84
S7	191.82	1.6	22.78
S8	313.12	2.2	22.04
S9	34.13	0.9	7.59
S10	167.97	1.8	21.98

* This rate is calculated from the first inclination of penetration height per time curve.

S3, S4, and S8 exhibit the highest capillary water uptake coefficient (about 300 $g/m^2\ s^{0.5}$) compared to other specimens (Figure 5.2.10). S7 and S10 have lower capillary water uptake coefficients than S3, S4, and S8 (192 and 170 $g/m^2\ s^{0.5}$), but they are still higher than the rest of the specimens. The

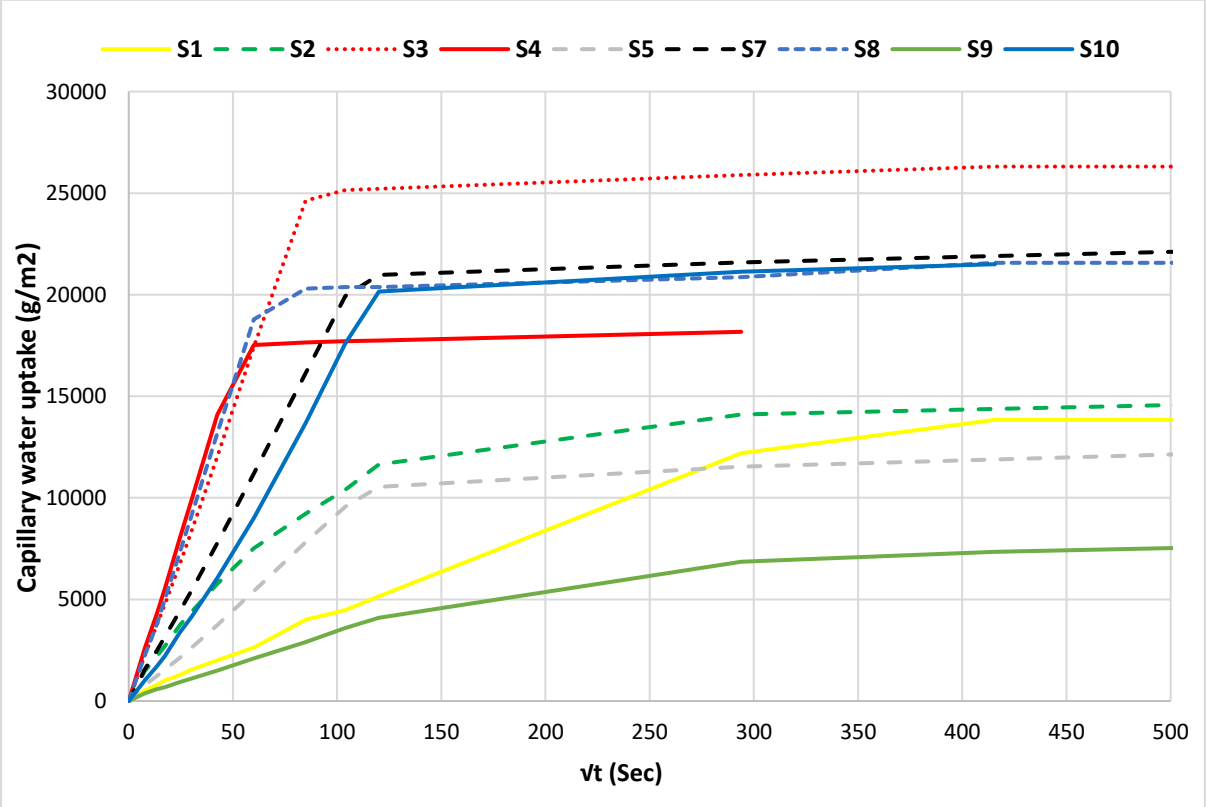

Figure 5. 2. 10 The amount of absorbed water that pass the area due to the capillary force per time

DOI: 10.15774/PPKE.BTK.2024.021

capillary water uptake coefficient of S2 is 125 g/m^2 s$^{0.5}$. However, S1, S5, and S9 have low capillary water uptake coefficients compared with former specimens (Table 5.2.3), and S9 have the lowest value of all specimens (around 34 g/m^{2}s$^{0.5}$). Regarding the maximum capillary water uptake (open capillary porosity), S3 ranks first (26.46 v/v%) compared to other specimens (Figure 5.2.11, Table 5.2.3), implying the highest percentage of effective capillary pores. S2, S4, S5, S7, S8, and S10 have approximately the same open capillary porosity (around 20-23 v/v%). In contrast, S1 and S9 are characterized by low open capillary porosities (13.8 v/v% and 7.6 v/v%, respectively, Figure 5.2.11, Table 5.2.3).

Although S2, S4, S5, S7, S8 and S10 have the same capillary porosity, their capillary water uptake coefficients are different. The capillary pores in S4 and S8 are greatly well-connected, which allow water to pass through, resulting in the rapid absorption uptake and higher capillary water uptake coefficient. The capillary pores in S2 and S5 are poorly connected because they had lower capillary water uptake coefficients. The connectivity of pores in S2 is better than S5 because it has a higher capillary water uptake coefficient.

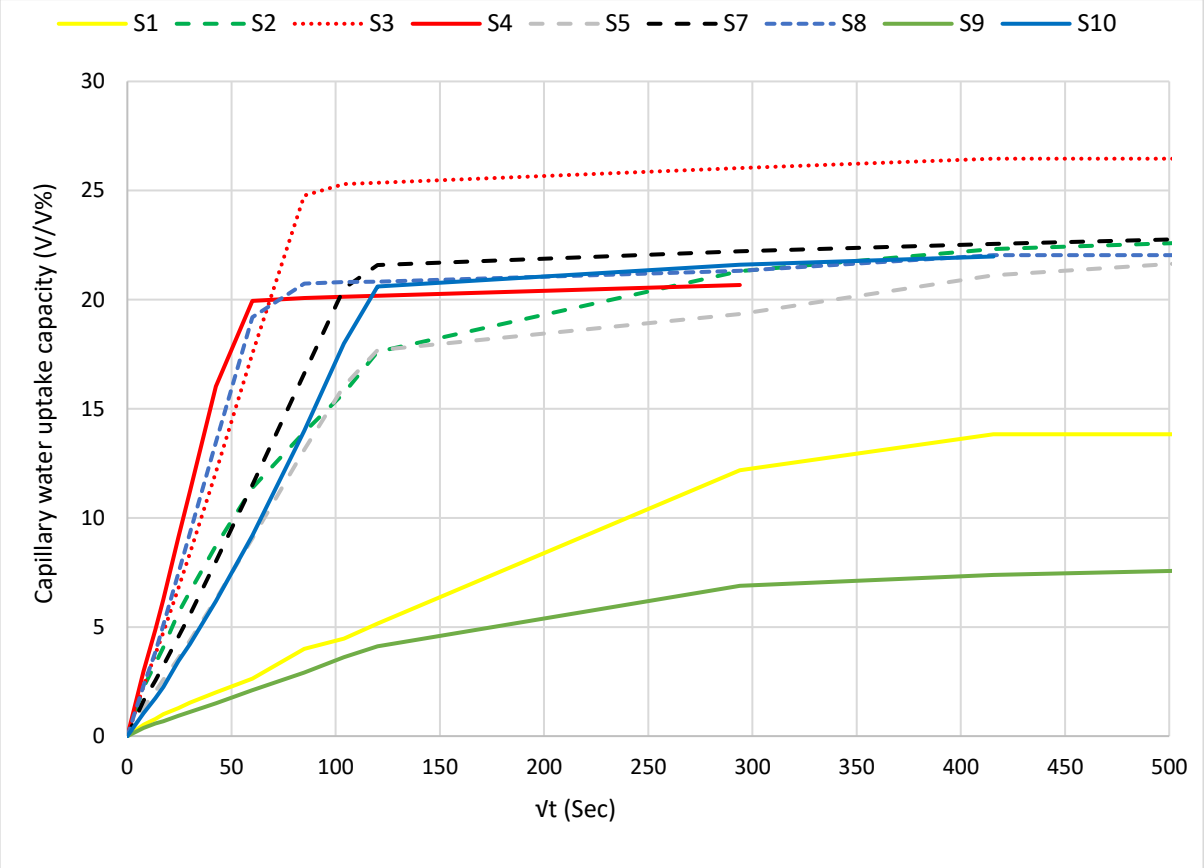

Figure 5. 2. 11 The water content by volume percent per time during the capillary uptake experiment (The maximum value of each curve represents the percentage of capillary effective porosity of the sample)

DOI: 10.15774/PPKE.BTK.2024.021

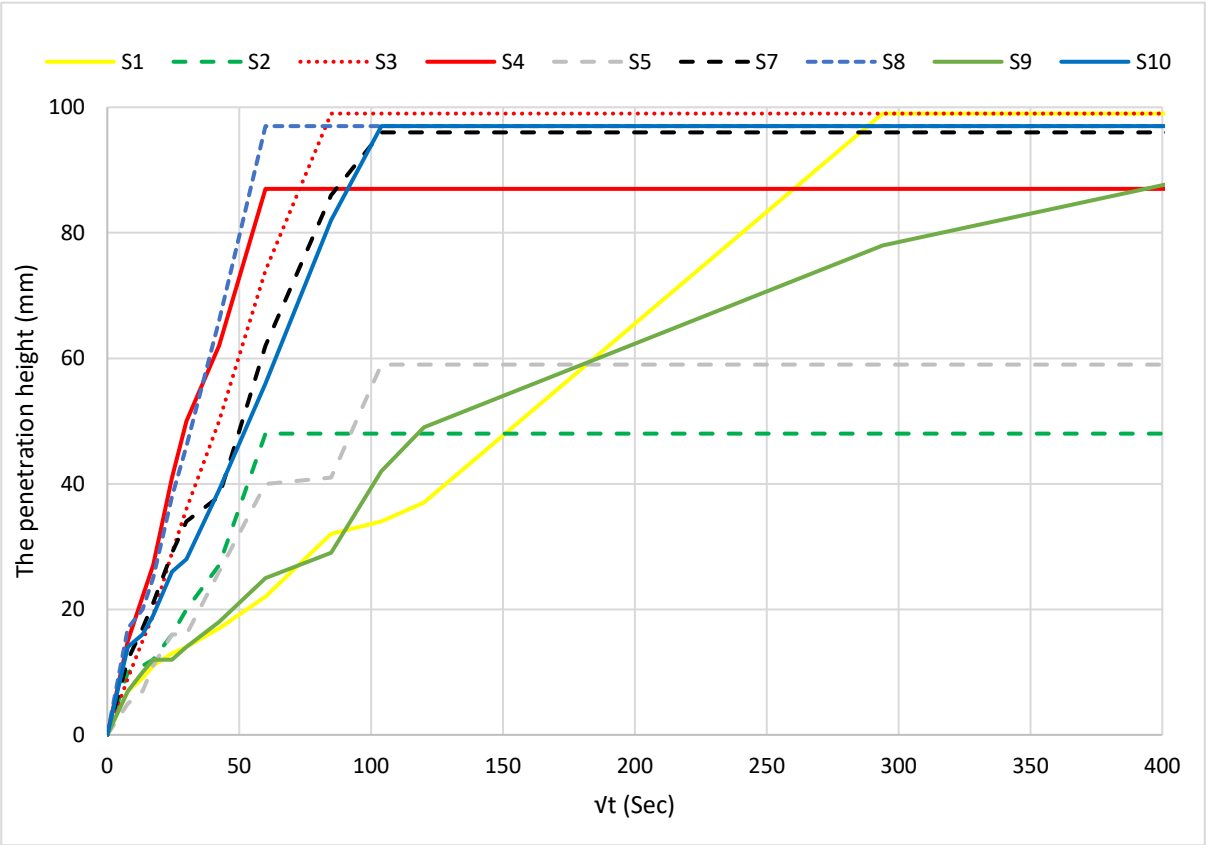

Figure 5. 2. 12 The water penetration height per time

The penetration rate of S8 is greater than that of any other specimen (see Figure 5.2.12). This reflects the good interconnectivity of the effective capillary pores of that specimen. The capillary pores connectivity in S2, S4, S7, S8, and S10 is better than in S3 because they have higher penetration rates than S3 (Figure 5.2.13). The penetration rates of S1, S5 and S9 are the lowest. During the first 6 minutes of the experiment, S5 has the lowest penetration rate, after that its rate increases, and the penetration rates of S9 and S1 become the lowest (see Figure 5.2.13). The water does not reach the top of specimen S9 during the measurement. In S1 and S9, the capillary pores are not well interconnected because they have pores filled with calcite, which reduce the pore connectivity and affect the water transport [312]. The presence of shell fragments (see

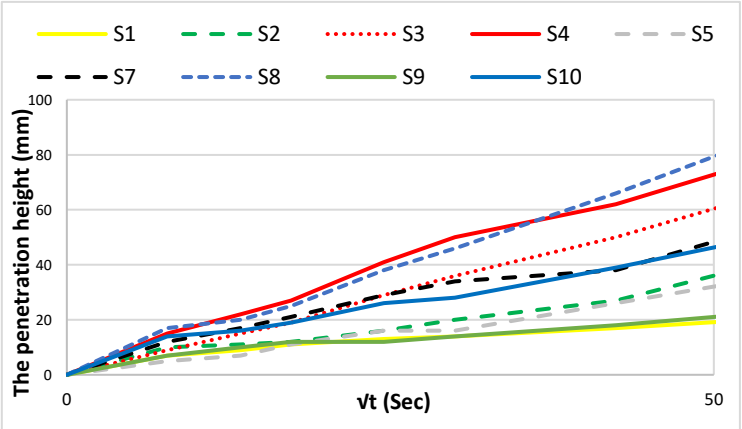

Figure 5. 2. 13 The water penetration height per time during the first 41 minutes

[312] İsmail Dinçer and A Orhan, "Effect of Pore Size Distribution on Capillary Water Absorption Characteristics of Pyroclastic Rock," in *Conference: International Black Sea Mining & Tunnelling Symposium, Trabzon-Turkey*, 2016, 311–18.

DOI: 10.15774/PPKE.BTK.2024.021

thin section description of S5) and the calcite filled some cracks in S5 structure reduce the connectivity between its pores. The poor connectivity of the pores of S5 is also reflected in the penetration curve. The penetration curve of S5 has two stages in which the penetration stopped before the water reached the top of the specimen (see Figure 5.2.12).

5.2.3 Water absorption at atmospheric conditions

The weight incensement due to water absorption by the square root of time is exhibited in Figure 5.2.14. All the specimens have a typical water absorption curve that consists of two stages. The first one is linear, which reflects the absorption rate of the specimen in question, where the water fills the effective pores gradually. The second stage begins when all easily accessible pores are already filled, and the water fills the effective pores by diffusion [313].

The end of the second stage is reached when the weight of the specimen is constant. As such, the percentage of water volume that fills the pores at the stability time expresses the percentage of effective porosity of the specimen, see Figure 5.2.15. The absorption rate is the inclination of the first part of the absorption curve (water content by mass per cent per square root time, Figure 5.2.14). The absorption rate expresses how well the effective pores are connected, with the faster rate indicating better connectivity.

S2 exhibits the highest water absorption rate (see Table 5.2.4) among the specimens; however, S3, S4, and S8 approximately reveal the same and second-ranked absorption rates, which indicates that those four specimens have a very well-connected effective pores system (Figure 5.2.14). S3 has the highest effective porosity among all specimens, around 32 v/v%. S2, S8 and S4 have a little lower effective porosity of about 28-29 v/v%, see Figure 5.2.15. The absorption rate of S7 is lower than the former specimens (Figure 5.2.14 and Table 5.2.4); however, its effective porosity (29 v/v%) is approximately the same as the former (see Figure 5.2.15), so the effective pores in S7 are not so well connected as in S2, S8 and S4.

S5 and S10 have the same water absorption rate, and the characteristics of pores connectivity are the same and lower than the former specimens. However, the effective porosities of those two specimens are different (26.5 v/v% and 28 v/v%, respectively).

[313] Oscar Buj and Josep Gisbert, "Influence of Pore Morphology on the Durability of Sedimentary Building Stones from Aragon (Spain) Subjected to Standard Salt Decay Tests," *Environmental Earth Sciences* 61/7 (2010): 1327–36.

DOI: 10.15774/PPKE.BTK.2024.021

S1 and S9 have smaller percentages of effective pores, because they are the densest stones among the specimens. Therefore, they absorb less water, and their absorption rates are lower.

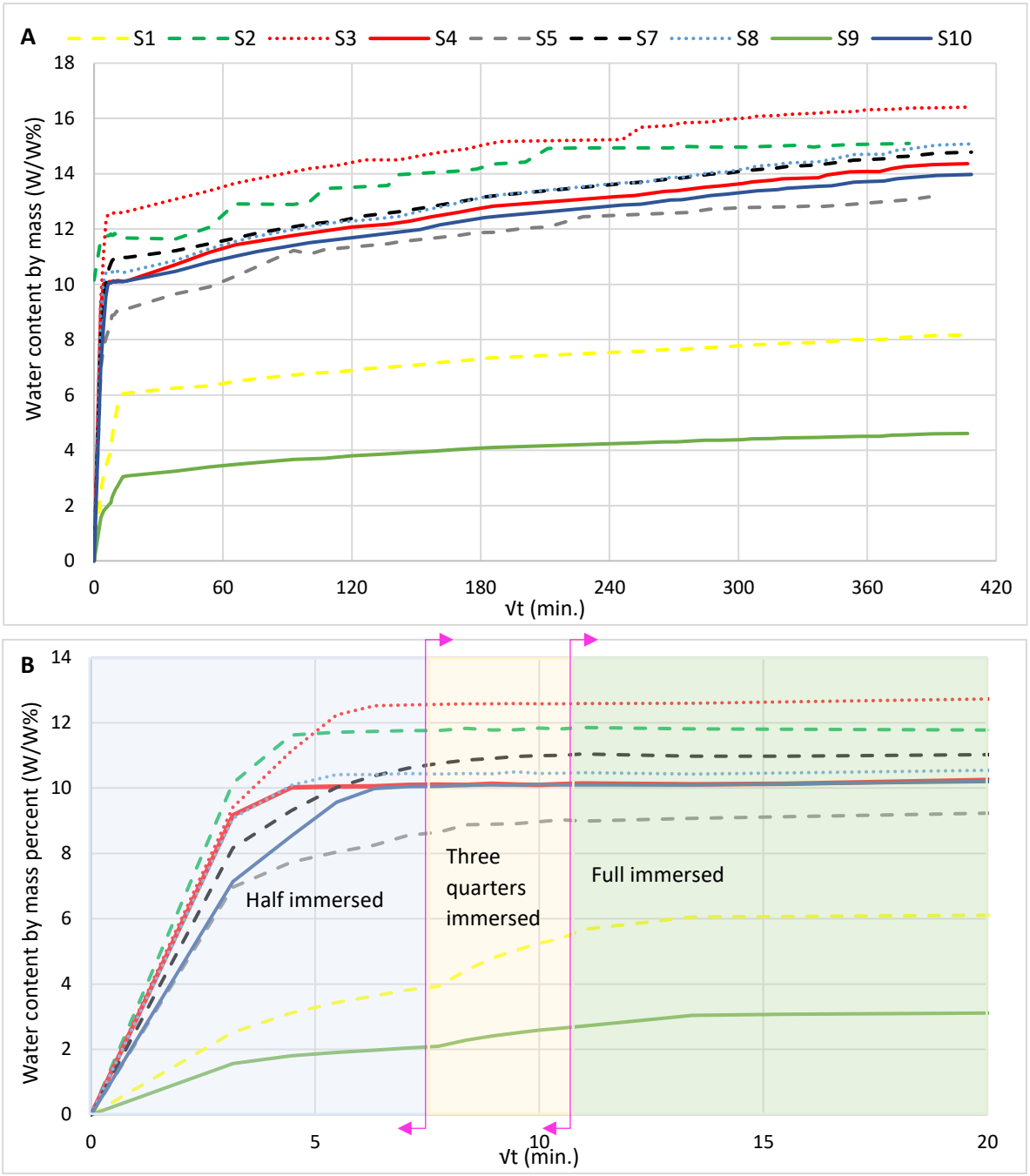

Figure 5. 2. 14 A) Water content (mass percent) by the square root of time during water absorption under atmospheric conditions. B) Water content (mass percent) by the square root of time during water absorption under atmospheric conditions at the first 400 minutes of the experiment

S1 has a higher effective porosity (18 v/v%) than S9 (11 v/v%) and its pores are well-connected compared with S9.

DOI: 10.15774/PPKE.BTK.2024.021

Because of the partial immersion during the first two hours of the experiment, capillary absorption is essential, and the capillary pores are primarily full during that period. For all specimens, the contribution of capillary pores to total absorption is remarkable. Specifically, the rapid linear part of the absorption curve has been completed during partial immersion (except for S1 and S9), as shown in Table 5.2.4. S2, S4 and S8 need 20 minutes (half-immersed) to complete the linear part of the absorption curve and they reach 77 %, 63.5 % and 68.8 % of their water content, respectively. S2 achieves a higher saturation degree by the end of the linear part than S4 and S8 because it has a higher percentage of effective capillary pores, and its pores are more well connected than S4 and S8 (higher absorption rate). S3 consumes 30 minutes to complete its linear part where it completes 76% of its water content. S2 and S3 achieve the same water saturation degree by the end of the linear part (see Table 5.2.4); however, S2 needs less time to complete it than S3. As a result, the effective pores of S2 are more well connected than S3.

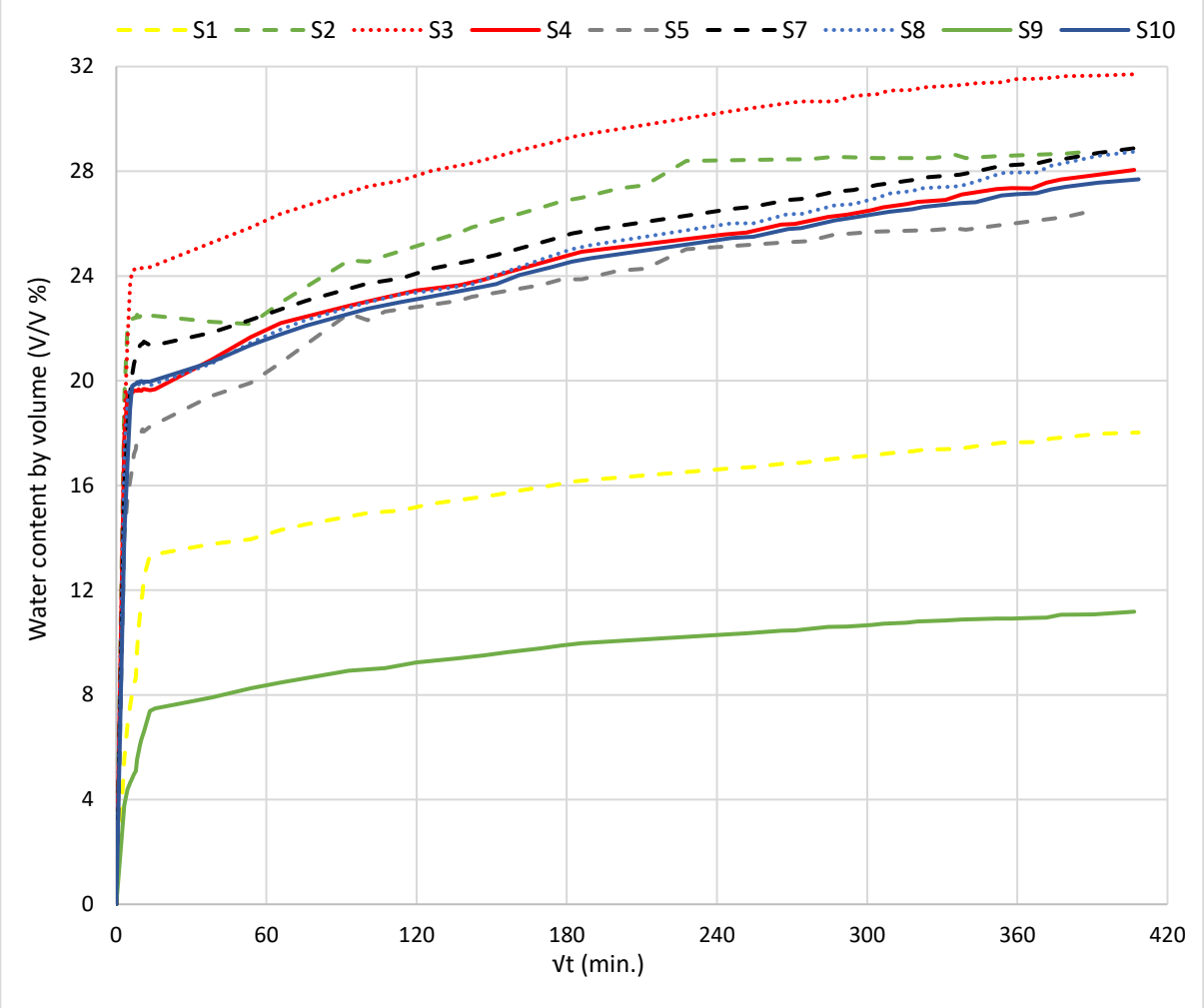

Figure 5. 2. 15 Water content (volume percent) by the square root of time during water absorption under atmospheric conditions

DOI: 10.15774/PPKE.BTK.2024.021

S7 and S10 achieve approximately the same saturation degree at the first period of 40 minutes (around 73.5% and 71%, respectively, see Table 5.2.4), and they both have approximately the same percentage of effective capillary pores to total effective pores. However, the absorption rate of S7 is higher than S10. That indicates that the effective pore connectivity in S7 is better than in S10.

S5 needs a longer time (50 minutes) to complete the linear part of the absorption curve and a lower saturation degree (59%) at this time compared to the previous specimens. Therefore, the

Table 5. 2.4 The effective porosity and the absorption rate during Water absorption at atmospheric conditions

Specimen.	Time consumed to complete the rapid linear part of absorption curve.	Immersion height.	The ratio between water content at the end of the rapid linear part of the absorption curve and water content at saturation	Absorption rate	Effective porosity	Capillary effective porosity/ Total effective porosity
S1	3 hours	Totally immersed	74 %	0.698 (w/w%)* $min^{-0.5}$	18% (v/v)	76.8 %
S2	20 minutes	Half-immersed	77 %	3.212 (w/w%)* $min^{-0.5}$	28.8% (v/v)	80%
S3	30 minutes	Half-immersed	76 %	2.978 (w/w%)* $min^{-0.5}$	31.7% (v/v)	83%
S4	20 minutes	Half-immersed	63.5 %	2.978 (w/w%)* $min^{-0.5}$	28% (v/v)	73.7%
S5	50 minutes	Half-immersed	59 %	2.206 (w/w%)* $min^{-0.5}$	26.5% (v/v)	82.5%
S7	40 minutes	Half-immersed	73.5 %	2.585 (w/w%)* $min^{-0.5}$	28.9% (v/v)	78.8%
S8	20 minutes	Half-immersed	68.8 %	2.873 (w/w%)* $min^{-0.5}$	28.8% (v/v)	76.6%
S9	3 hours	Totally immersed	66 %	0.494 (w/w%)* $min^{-0.5}$	11.2% (v/v)	67.8%
S10	40 minutes	Half-immersed	71 %	2.259 (w/w%)* $min^{-0.5}$	27.7% (v/v)	79.4%

effective pores of S5 are less connected than the former specimens. The pores in S1 and S9 are not well connected, and they need 3 hours to complete the linear part of the absorption curve.

-Ultrasound velocity during water saturation:

DOI: 10.15774/PPKE.BTK.2024.021

The relationship between ultrasound velocity and bulk density (dry and full saturated) of the specimens is a positive linear one with a correlation coefficient of 0.87 and 0.83 for dry and full saturated phases, respectively (see Figure 5.2.16). Figure 5.2.16 obviously demonstrates that the increase of bulk density (due to water saturation) leads to the increase of the inclination of the correlation line between bulk density and ultrasound velocity at the saturation phase. The relationship between ultrasound velocity of the primary wave (p- wave velocity) versus saturation degree for the tested stones is exhibited in Figure 5.2.17 and Figure 5.2.18.

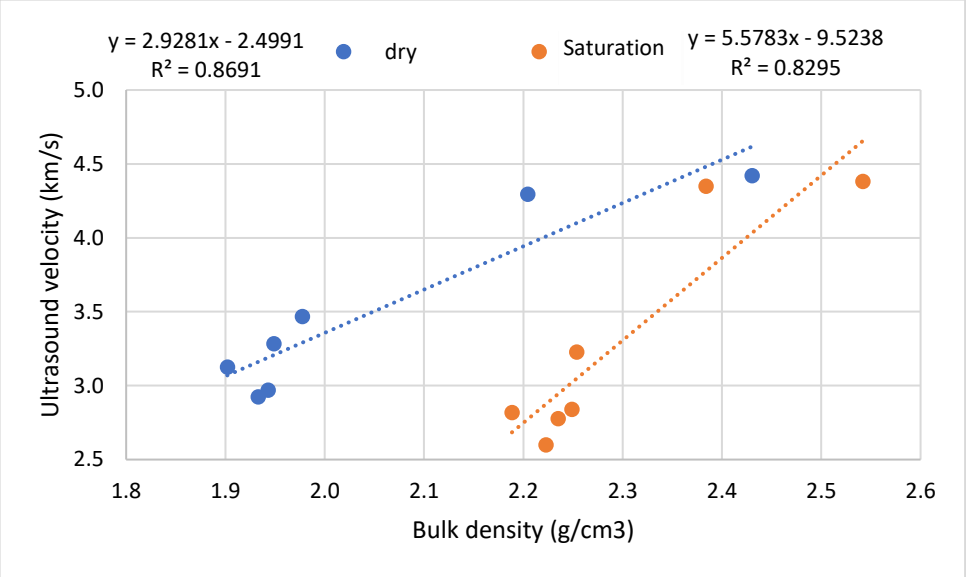

Figure 5. 2. 16 Primary ultrasound velocity vs dry and wet bulk density of the specimens

The relationship between ultrasound velocity and the saturation degree of the specimens shows two different characteristics. For some samples S2, S5, S8 and S10, it is a decrease trend during the complete saturation. However in others, the relationship has a decrease trend until a specific saturation level of the sample, and after that, the trend becomes an increase one (S1, S3, S4, S7 and S9).

The P-wave velocity in S2, S5, S8, and S10 correlates with the saturation degree with a negative linear correlation. As for S2, a negative relationship between P-wave velocity and water saturation is presented with a correlation coefficient of 0.54. The ultrasound velocity in dried condition is 2.49 km/s, and it decreases to 2.37 km/s by a saturation degree of 68%. After that, the velocity continues to drop while the specimen absorbes more water until it reaches about 2.33 km/s at 100% saturation degree (see Figure 5.2.17).

DOI: 10.15774/PPKE.BTK.2024.021

The ultrasound velocity in S5 decreases with the increase of the saturation degree of the specimen, and it correlates to a linear regression by a 0.64 correlation coefficient. The velocity decreases from 3.14 km/s (dry phase) to 2.87 km/h at 100% saturation degree (see Figure 5.2.18). In S8, a negative and moderate relationship is present between the ultrasound velocity and the saturation degree. The relationship between the two parameters correlate by a 0.54 correlation coefficient. After 10 minutes of being half-immersed with water, the saturation degree of the specimen reaches 60%. During that period, the velocity remarkably decreases from 3.15 to 2.84 km/s. Between 60% and the full saturation state, the velocity trend exhibites modest changes, where the velocity fluctuates between 2.84 and 2.8 km/s (see Figure 5.2.18). The relationship between water saturation and P-wave velocity in S10 is a negative linear correlation, where the two parameters exhibit a good correlation as the correlation coefficient is 0.68. In the first 10 minutes of half immersion, the specimen is saturated of about 50% which leades to the decrease of P-wave velocity from 3.47 km/s at drying phase to 3.22 km/s (Figure 5.2.18). The velocity trend continues to decrease as the degree of saturation increases

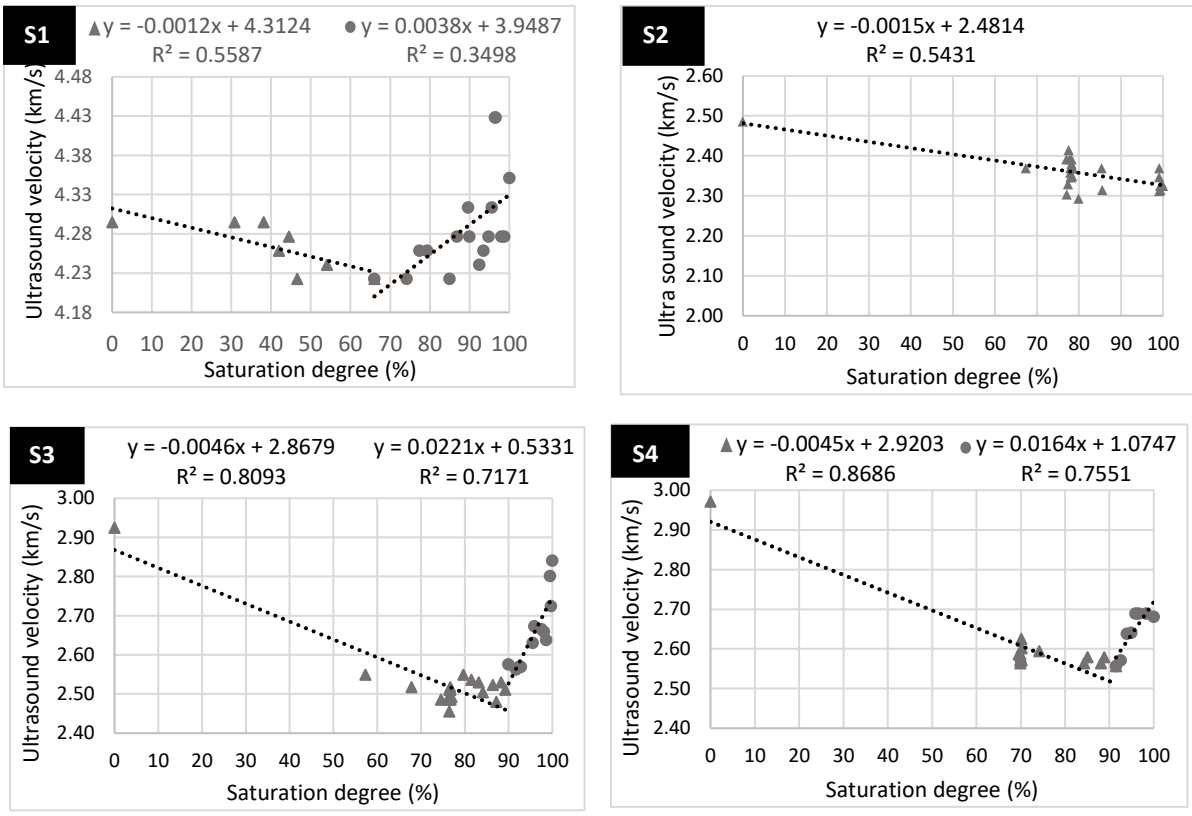

Figure 5. 2. 17 Primary ultrasound velocity vs saturation degree during the water uptake under atmospheric conditions experiment

from 50 to 95%. Above 95%, the velocity shows a slight rise, reaching 3.23 km/s at 100% saturation.

DOI: 10.15774/PPKE.BTK.2024.021

As for S1, S3, S4, S7 and S9, the P-wave velocity decreases at first with the increase of saturation degree then the trend changes and the P-wave velocity increases with an increase of saturation degree until the full saturation. The p-wave velocity in S1 decreases from 4.29 km/s (dry phase) to 4.22 km/s at 66% saturation degree with a negative linear correlation (correlation coefficient of 0.56). After that, the velocity gradually increases and it is about 4.35 km/s at 100 % saturation (positive linear correlation with a correlation coefficient of 0.35, see Figure 5.2.17). In S3, the relationship between P-wave velocity and saturation degree can be divided into two linear parts (for the first part correlation coefficient of 0.81 and for the second one correlation coefficient of 0.71). The first linear part has a downward trend in which the

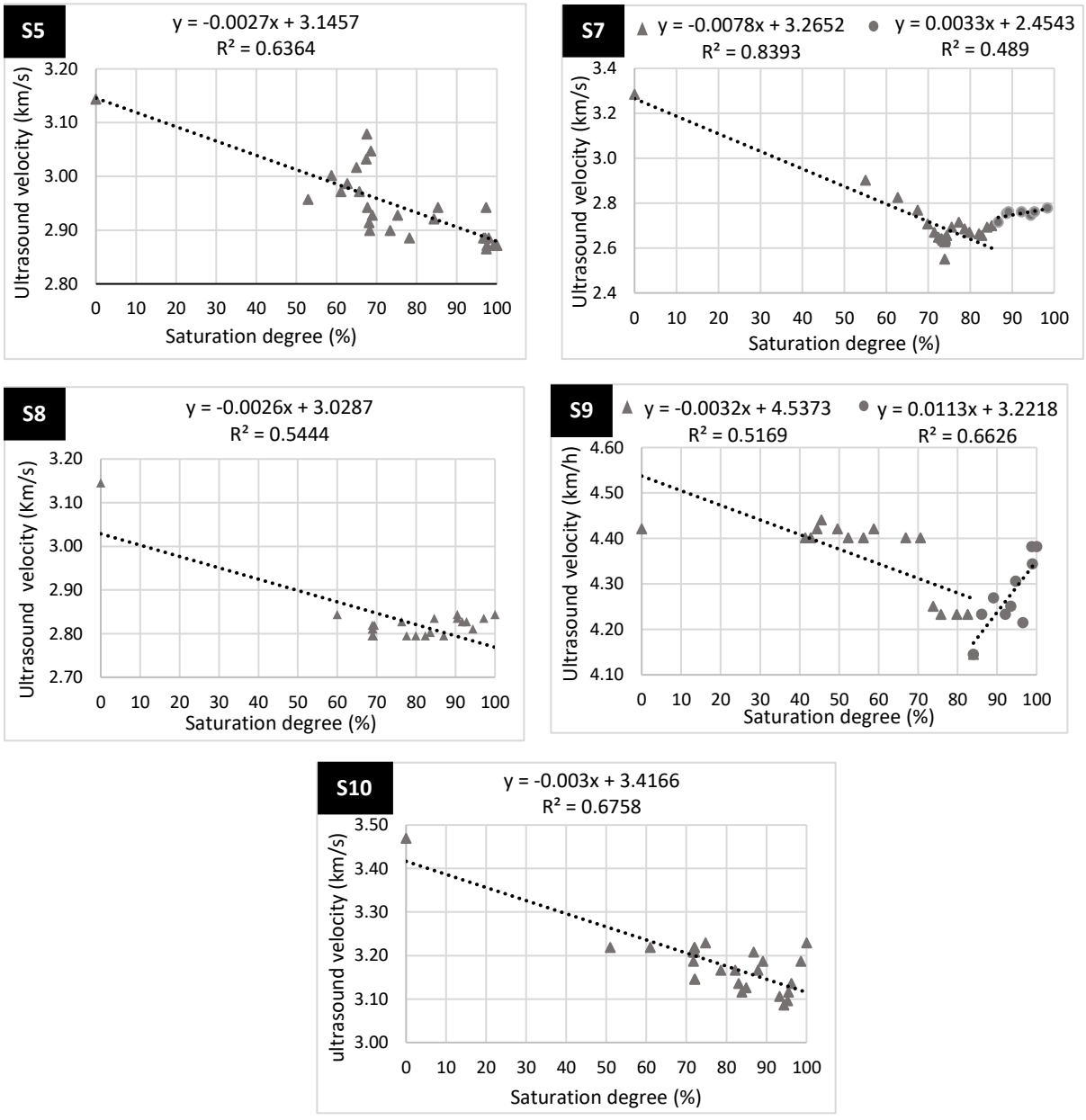

Figure 5. 2. 18 Primary ultrasound velocity vs saturation degree during the water uptake under atmospheric conditions experiment

DOI: 10.15774/PPKE.BTK.2024.021

velocity dramatically drops from 2.9 km/s at the dry phase to around 2.53 km/s at 90 % saturation. During the first 10 minutes, the velocity rapidly decreases to 2.55 km/s, where the saturation degree is about 57%. By increasing the water content inside the stone from 90% to 100%, the velocity has a reverse trend where it gradually increases until it reached 2.8 km/h at 100% saturation (see Figure 5.2.17). The P-wave velocity and water saturation in S_4 are correlated by negative linear correlation with 0.87 correlation coefficient (Figure 5.2.17) from the drying phase until the saturation degree of the specimen reaches around 90%. The velocity rapidly decreases when the specimen starts to absorb water. The velocity drops from 2.97 km/s to 2.56 km/s at 90% saturation degree. After that, the velocity exhibits a reverse trend, where it gradually increases until it reaches 2.68 km/s when the specimen becomes fully saturated. The relationship between saturation degree and ultrasound velocity in S_7 can be divided into two linear parts. The first is a decrease trend with a correlation coefficient of 0.84. The velocity declines from 3.28 to around 2.7 km/s when the water saturation of the specimen changes from 0 to 85%. After that, the velocity shows an increase trend between 85% to 100% water saturation with a correlation coefficient of 0.49. When water saturation exceeds 85%, the velocity gradually increases from about 2.7 km/s until it reaches 2.78 km/s when the specimen is fully saturated with water. The ultrasound velocity in this specimen has a great response to the variation of water saturation degree. During the half-immersion period of S_9 (the specimen begins to absorb water and the saturation divertes from 0 to 70%), the velocity fluctuates around 4.4 km/s. The velocity plummets from 4.4 to 4.21 km/s when the saturation degree rises from 70% to about 80% , where the velocity fluctuates around 4.21 km/s until the saturation degree reaches approximately 85%. The velocity trend exhibits a gradual increase between 95% to 100% saturation until the velocity reaches 4.38 km/s. The P- wave velocity and saturation degree in that stage are correlated by a positive linear correlation with 0.66 correlation coefficient.

In all specimens, the ultrasound velocity decreases with the increase of the saturation degree. However, the relationship between ultrasound velocity and bulk density in dry and full saturated conditions is positive with a correlation coefficient of 0.87 and 0.83, respectively (see Figure 5.2.16). The increase of the wet bulk density does not affect the ultrasound velocity while the water fills the pores. Studying the pore shape and pore size distribution, as mentioned in the literature, is more effective in giving more explanations about the behaviour of ultrasound velocity versus saturation degree.

DOI: 10.15774/PPKE.BTK.2024.021

5.2.4 Drying characteristics

The drying process is divided into two stages distinguished by the water transfer mechanism from the stone structure to the outside. Due to capillary action, the rapid diagonal stage occurs when water moves from inside the stone to the surface [314]. This stage accomplishes when most of the water has been evapourated. The second stage is the slow horizontal stage, in which water diffusion is the dominant mechanism of water transport [315]. This stage lasts until the water vapour pressure inside the stone structure equates with atmospheric water vapour pressure. All the specimens in the three groups undergo drying at these distinct stages.

Due to the constant temperature and air circulation during the experiment, the drying process for Group 1 (inside oven) is rapid. During the first hour, all the specimens have approximately the same evapouration rate (ca. 0.5 $kg/m^2h^{0.5}$), so they lose the equal water amount distributed on their surfaces (Figure 5.2.20 and Table 5.2.6). The specimens S3, S4, S7, S8, and S10, have

Table 5. 2.5 The properties of group 1 and group3 of specimens

	Specimen	Saturation weight	Dry weight	Water content at saturation	Vp (Saturation)	Vp (Dry)
		(g)	(g)	(w/w%)	(km/s)	(km/s)
Inside the oven at 25°C (Group 1)	S1	114.77	105.80	8.48	4.62	3.76
	S3	110.53	94.75	16.65	2.90	2.93
	S4	106.87	92.78	15.19	2.29	2.64
	S7	107.09	92.43	15.86	2.59	2.88
	S8	101.25	86.88	16.54	3.07	2.86
	S9	129.83	124.91	3.91	4.89	4.53
	S10	99.54	84.95	17.17	2.87	3.04
Unsealed specimens (Group 3)	S1	88.21	81.42	8.34	4.05	3.96
	S3	78.61	67.38	16.67	2.78	2.36
	S4	48.30	41.88	15.33	3.54	2.87
	S7	75.45	64.94	16.18	2.88	3.37
	S8	76.31	66.02	15.59	3.04	3.42
	S9	95.70	91.23	4.90	4.87	2.19
	S10	82.78	73.98	11.90	3.08	3.46

[314] B Sena da Fonseca et al., "Non-Destructive and on Site Method to Assess the Air-Permeability in Dimension Stones and Its Relationship with Other Transport-Related Properties," *Materials and Structures* 48/11 (2015): 3795–3809.

[315] Siegfried Siegesmund and Rolf Snethlage, *Stone in Architecture: Properties, Durability* (2011).

DOI: 10.15774/PPKE.BTK.2024.021

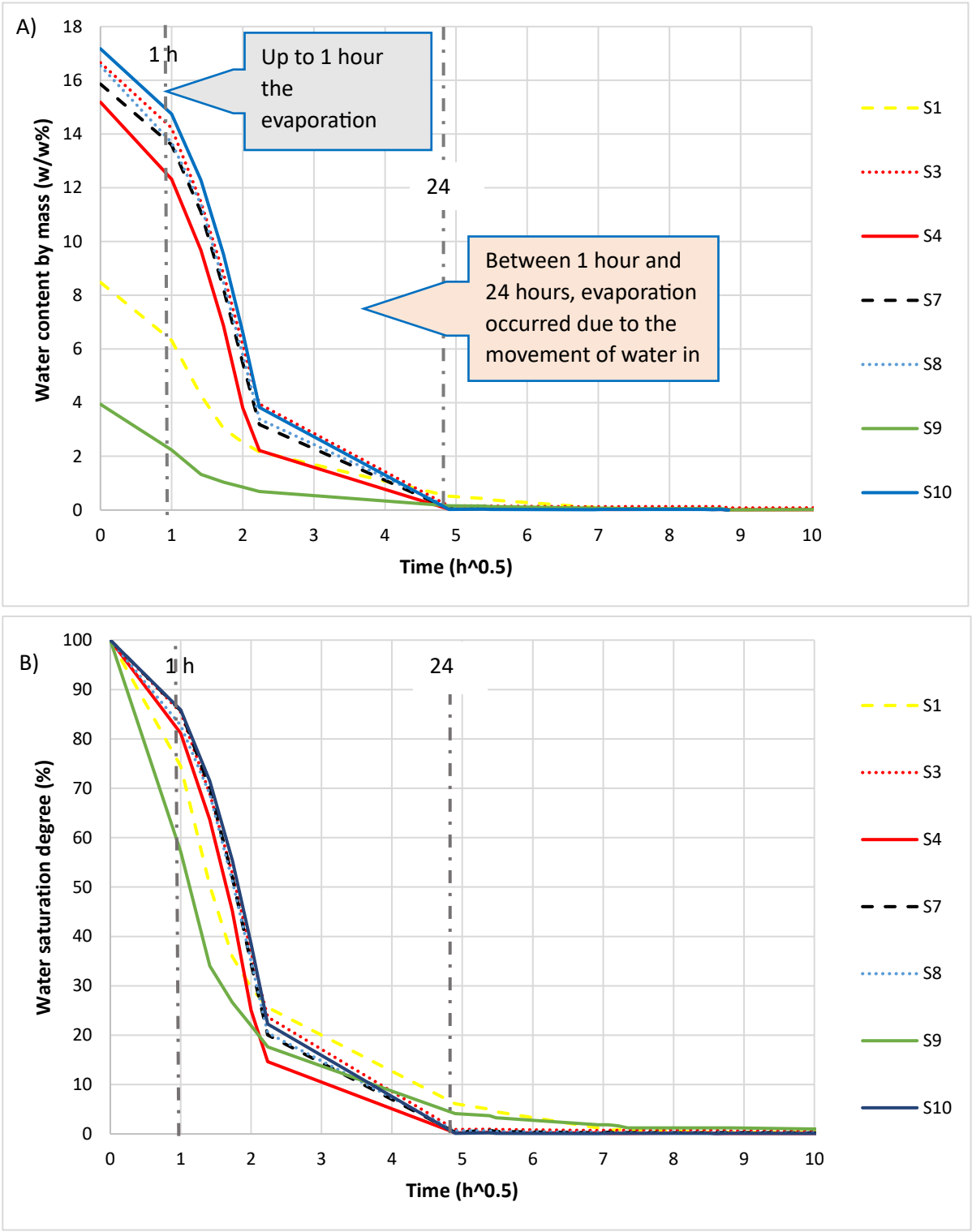

Figure 5. 2. 19 A) The water content by mass vs.time for the Group 1 specimens during the drying process. B) water saturation degree for Group 1 specimens during the drying process

lost 15-20% of their water content. S1 and S9 have lost a larger proportion of their water content, 25% and 40%, respectively (Figure 5.2.19).

DOI: 10.15774/PPKE.BTK.2024.021

All the specimens lose most of their water content during the first 24 hours. The remaining saturation degree is mainly 0.1-1%, except S1 and S9, which still have 6.13% and 4.10%, respectively (Figure 5.2.19). Therefore, the connectivity of capillary pores plays a significant role in affecting the evapouration rate. Between 1 hour to 5 hours, the evapouration rate of specimens increases (Figure 5.2.20), where S3, S4, S7, S8, and S10 exhibit the same high evapouration rate (1.6-1.7 kg/m^{2}h$^{0.5}$). The capillary pores connectivity of the specimens S3, S4, and S8 are similar because they have the same capillary water uptake coefficient. However, capillary water uptake coefficients of S7 and S10 are a little lower than S3, S4 and S8, but good connected capillary pores still characterize them. The well capillary pores connectivity of S3, S4, S7, S8, and S10 cause the same evapouration rate by constant temperature. The evapouration rate of S1 increases to 0.9 kg/m^2 h$^{0.5}$ during the period of 1 to 5 h. After 5 h to 24 h, the specimens tend to decrease their evapouration rate until they reach the constant weight. The evapouration rate in the densest lithotype (S9) is 0.5 kg/m^{2}h$^{0.5}$

*Table 5. 2. 6 The evaporation rate (E in kg/m^2*h$^{0.5}$) of Group 1*

Sample	0-1h	1-2h	2-5h	5-24h
S1	0.51	0.9	0.9	0.15
S3	0.45	1.76	1.76	0.3
S4	0.59	1.69	1.69	0.17
S7	0.46	1.72	1.72	0.24
S8	0.55	1.62	1.62	0.24
S9	0.50	0.50	0.2	0.06
S10	0.46	1.71	1.71	0.28

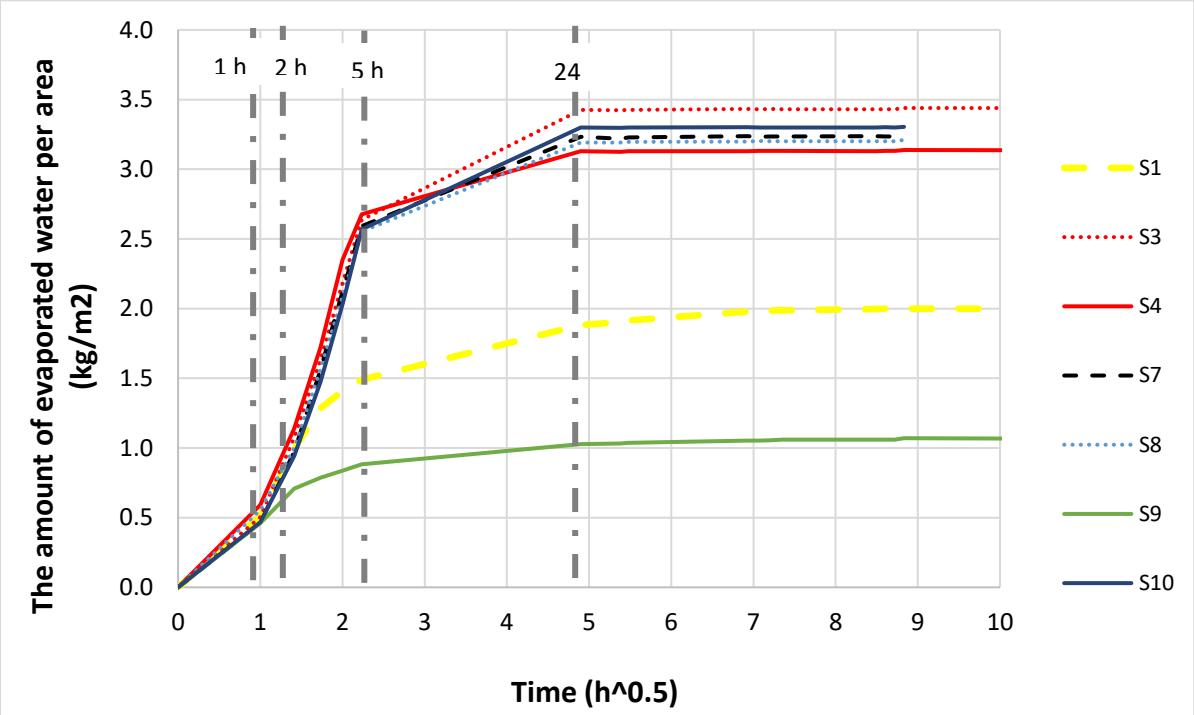

Figure 5. 2. 20 The amount of evaporated water per area by the time for the specimens of Group 1

DOI: 10.15774/PPKE.BTK.2024.021

during the first two hours. It is the lowest rate because it has the lowest amount of capillary pores, afterwards the rate of which decreases until it reaches its constant weight.

*Table 5. 2.7 The evaporation rate (E in kg/m^2*h$^{0.5}$) of Group 3*

Specimen	0- 3 hours	3-24 hours	24-29 hours	29-52 hours
S1	0.052	0.36	0.36	0.1
S3	0.058	0.22	1.3	0.65
S4	0.035	0.25	0.88	0.2
S7	0.052	0.34	1	0.42
S8	0.04	0.41	1.1	0.29
S9	0.064	0.24	0.24	0.03
S10	0.052	0.52	1.12	0.16

All the specimens in Group 3 (unsealed specimens) lose 2-5% of their water content throughout the first three hours (Figure 5.2.21). During that period, the distributed water on the surface of the specimens evapourates. That process is relatively slow, where all specimens exhibit a low evapouration rate (0.03-0.06 kg/m^{2}h$^{0.5}$ (Table 5.2.7, Figure 5.2.22). Twenty-four hours afterwards, the specimens are in different saturation degrees. S9 loses the largest percentage of its water content (its saturation degree is around 13.65%) and is followed by S1 (saturation degree of 21%). S3 loses about 30% of its saturation degree, making it the specimen that loses the least amount of water in the group. However, the rest of the specimens are 45-50 % saturation degree after twenty-four hours (Figure 5.2.21). During that period, the evapouration rate of S10 is the highest among other specimens with 0.5 kg/m^{2}h$^{0.5}$. S8 also exhibits a relatively high evapouration rate with 0.41 kg/m^2 h$^{0.5}$. S1 and S7 have approximately the same evapouration rate of around 0.35 kg/m^2 h$^{0.5}$. While S3, S4, and S9 have the lowest evapouration value of around 0.2 kg/m^2 h$^{0.5}$ during 3-24 hours.

However, between 24 and 29 hours, the evapouration rate of S3, S4, S7, S8, and S10 increases compared to the former period (Figure 5.2.22 and Table 5.2.7). That period includes the daytimes hours in which the temperature degree is in the laboratory higher than the previous period, 3-24 h (nighttime hours). Moreover, during the daytime hours, there is usually air movement in the laboratory due to the working people there. The changing conditions result in higher evapouration rates between 24 and 29h.

These specimens (S3, S4, S7, S8, and S10) have different saturation degrees. S3 exhibits the highest water retention capacity, with a water saturation of 45% (Figure 5.2.21), and S4 has the lowest saturation degree among these specimens. The evapouration rates of S1 and S9 do not change between 24-29 hours, and they have relatively low saturation degrees with 12% and 6%. All specimens have lost most of their water content within 52 hours (their saturation

DOI: 10.15774/PPKE.BTK.2024.021

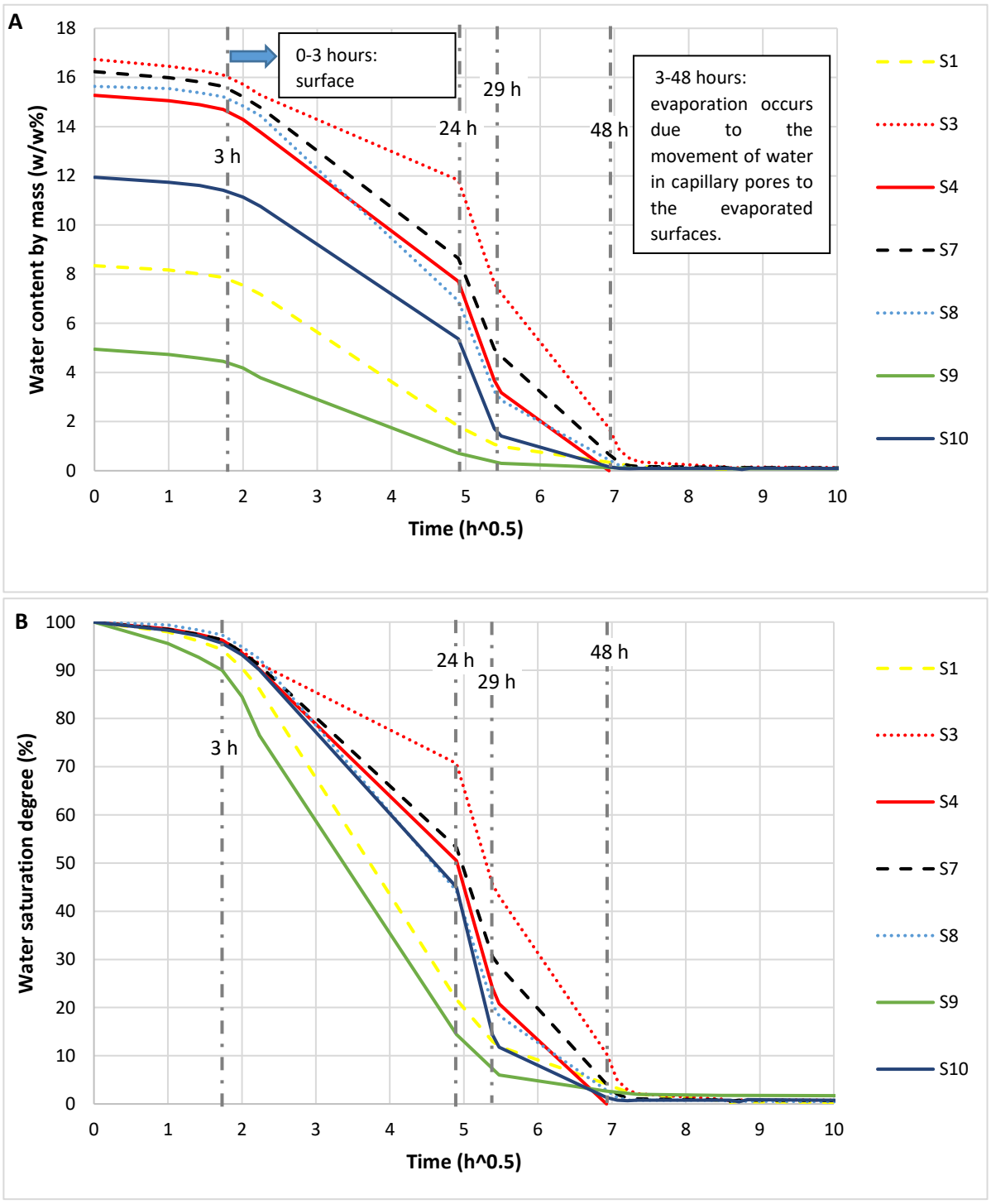

Figure 5. 2. 21 A) The water content by mass vs. time for the Group 3 specimens during the drying process. B) water saturation degree for Group 3 specimens during the drying process

degrees are 1-4%), except for S3, which has a saturation degree of 10%. As a result, the evapouration rate during 29-52 h is relatively slow, especially S1, S9 and S10, because the specimens have lost more than 85% of their water content before. The evapouration rate of all the specimens after 52 hours significantly decreases until they reach their constant mass (see Figure 5.2.22).

DOI: 10.15774/PPKE.BTK.2024.021

The experiment period of Group 2 (sealed specimens) lasts 35 days until the masses of the specimens are constant for three successive measurements. However, the amount of evapourated water per area by the time is created till 100 hours (Figure 5.2.23) to compare the evapouration rates of the three groups. The specimens in Group 2 exhibit approximately the same evapouration rate by the first three hours (0.107-0.199). The specimens have different

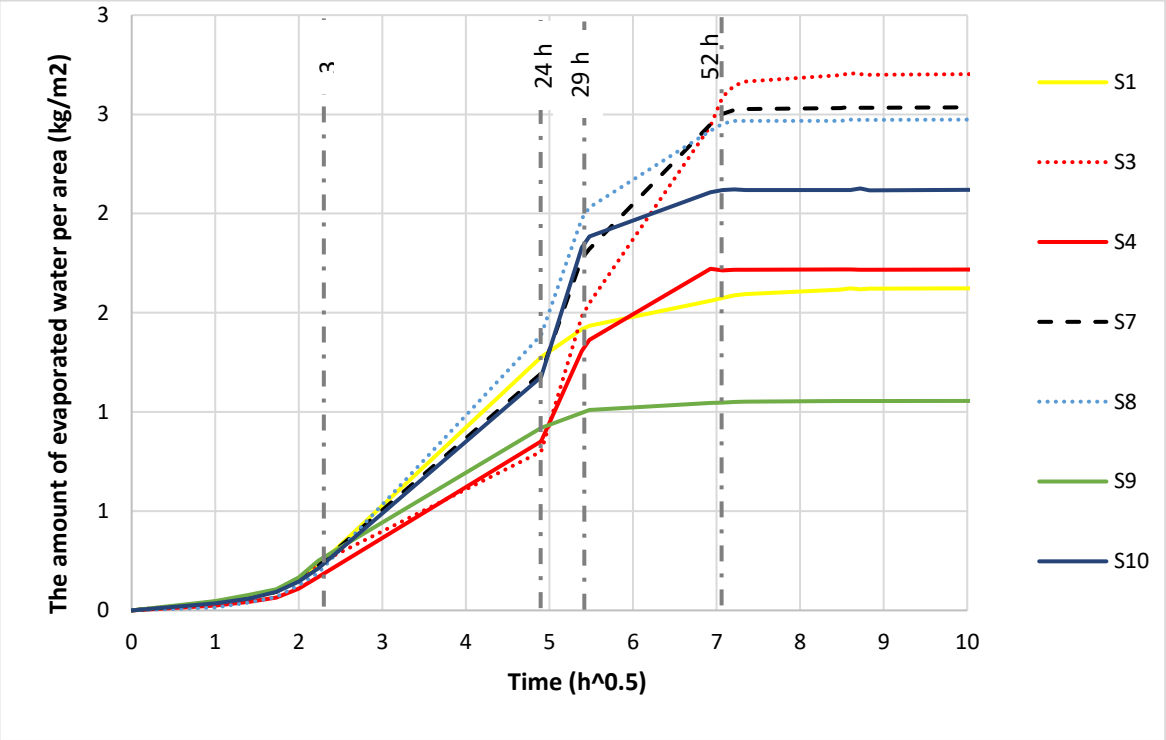

Figure 5. 2. 22 The amount of evaporated water per area by the time for the specimens of Group 3

evapouration rates after that period and until 48 hours (Table 5.2.8). S10 exhibits the highest evapouration rate after 3 hours (Figure 5.2.23). At the same time, S8 is ranked second with a 0.987 kg/m^2 h$^{0.5}$ evapouration rate. S10 and S8 also reach their constant mass faster than the rest of the specimens.

S3 and S7 have approximately the same evapouration rate of about 0.86 kg/m^{2}h$^{0.5}$, while S4 has a lower rate, around 0.7 kg/m^{2}h$^{0.5}$. S1 and S9 have the lowest value of evapouration rate among the specimens. After 48 hours, the evapouration rate of the specimens S1, S8, S9 and S10 decreases until they reach the constant mass. On the contrary, S3, S4 and

*Table 5. 2.8 The evaporation rate (E in kg/m^2*h$^{0.5}$) of Group 2*

Specimen	until 3 hours	3-48 hours	48-78 hours
S1	0.121	0.495	0.48
S3	0.174	0.856	1.35
S4	0.129	0.733	1.22
S7	0.143	0.878	1.35
S8	0.199	0.978	0.48
S9	0.107	0.370	0.23
S10	0.196	1.118	0.25

DOI: 10.15774/PPKE.BTK.2024.021

S7 specimens the evapouration rate of which increases between 48 to 78 hours (Table 5.2.8), so these specimens need more time to dry in this group.

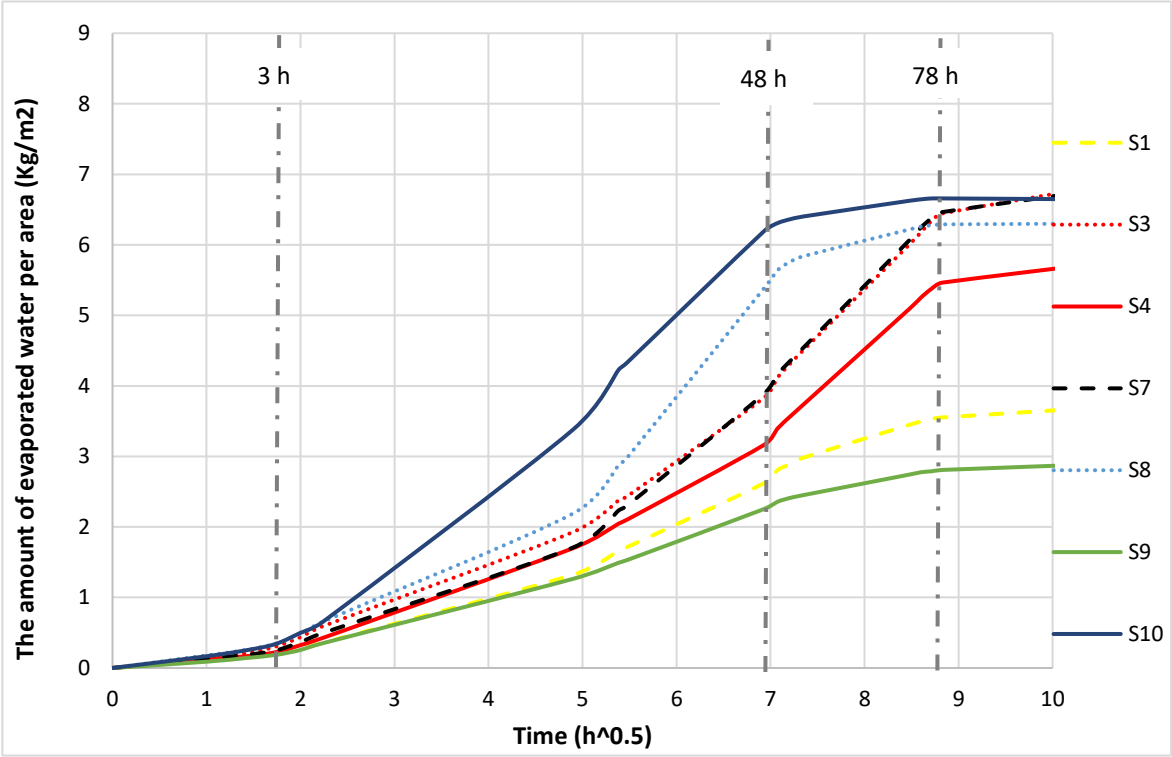

Figure 5. 2. 23 The amount of evaporated water per area by the time for the specimens of Group 2

When the evapouration rates of the three groups are compared, Group 1 (inside the oven) has the fastest rate of evapouration. During the first three hours (surface evapouration), Group 3 (unsealed specimens) has the lower rate than Group 2 (sealed specimens).

Unlike Groups 2 and 3, the specimens inside the oven (Group 1), specifically S3, S4, S7, S8, and S10, show no difference in evapouration rate. S10 has the fastest rate in Group 2 and Group 3 before reaching its constant mass. Its scattered large macro pores of size 1 -2 mm are most attributable to this, as the water dries first from these large pores.

The constant temperature in Group 1 allows a fast drying with roughly the same drying rates for all porous samples. The change in room temperature during the day is reflected most significant in Group 3 (unsealed samples) and less in Group 2 (sealed samples) by alternately larger and smaller evapouration rate, which is slower than the evapouration rate in Group 1. In Group 3, the evapouration rate is more rapid and the specimens reach their constant stage faster than in Group 2 during the capillary water mechanism (3-52 hours).

DOI: 10.15774/PPKE.BTK.2024.021

Regarding the drying behaviour of the specimens in the three groups, S9 is the most effective specimen, exhibiting the lowest water retention capacity and faster drying. Compared to other specimens, S3 demonstrates greater water retention capacity in Group 1 and Group 3 than in Group 2. The drying features of S7 and S4 are moderate compared to other specimens, and their relative order do not change in each group.

To conclude, S1 and S9 have the most effective drying behaviour because of their lowest porosity and poor-connected pore system. Regarding the specimens with higher porosity (S3, S4, S7, S8, and S10), the drying behaviours of S10 and S8 are fast because of their high percentage of big pores (250-500 μm, as thin section reveals) and well-connected pore system. However, S3 exhibits the highest water retention capacity as it has a high percentage of tiny capillary pores, and most of its pores are open. As much as the pore is tiny, the water thin layer strongly attaches to its pore walls by hydrostatic forces. Therefore, the stone reveals high water retention capacity if it has a high percentage of tiny pores, as in S3. In big pores, water accumulates in many layers, and the layers that are far from the pore wall can be easily removed by evapouration, i.e., dry rapidly as in S8 and S10.

5.2.5 Permeability

The water vapour permeability rates of the sound specimens vary, resulting in different values of water vapour resistance factors (Table 5.2.9). The non-weathered specimen of S2 (S2-R) has the lowest water vapour diffusion resistance factor of 5.2, giving it the highest water vapour permeability rate of the sound specimens (Figure 5.2. 24). Compared to the sound specimen (S2-R), the crust specimen of S2 (S2-C) reduces the water vapour permeability rate by about 15% (Table 5.2.9). The water vapour diffusion resistance factor of S2-C is 6.07 [-]. The S4 sound specimen (S4- R) has a relatively high water vapour permeability rate with a water vapour diffusion resistance factor of 7.6 [-]. In contrast, the crust (S4-C) decreases the water vapour permeability rate of the S4 specimen by 61 % compared to the S4 sound specimen. The weathering crust of S4 composes of grey microorganisms flourished on the stone surface. According to thin section analysis, the porosity is ca. 25% lower than that of the sound stone, and the biological activity is associated with pores beneath the surface. Compared to sound specimens, the low porosity of the crust increases the water vapour diffusion resistance factor to 12.4 [-] (Figure 5.2.26).

The sound specimen of S10 (S10-R) has a relatively high-water vapour permeability rate and low water vapour diffusion resistance factor of 8.3 [-]. The crust reduces the water vapour permeability rate of the specimen by 50% compared to the sound specimen (S10-R)

DOI: 10.15774/PPKE.BTK.2024.021

(Table 5.2.9). This crusted specimen (S10-C) is micritic, with fine crystals and has an irregular thickness of about 0.02 -0.1 mm. Beneath the micritic crust, there is a cemented zone with 0.1-0.16 mm thickness. The cemented zone in the crust most likely attributes to minimizing the water vapour permeability rate of (S10-C) to the half.

The sound S_3 (S_3-R) specimen has a relatively high water vapour permeability rate and a water vapour diffusion resistance factor of around 10 [-] (Table 5.2.9). The crust on the S_3 specimen (S_3-C) reduces the water vapour permeability rate by 10%. Although the micritic crust in this specimen (S_3-C) is around 1.5 mm in thick and contained organic material on its surface, the crust appears to have a minor effect on the water vapour rate.

S_1 (S_1-R) has a moderate water vapour permeability rate than other sound specimens (Figure 5.2.25). The water vapour diffusion resistance factor of this specimen is 18.3 [-]. The crust of this specimen (S_1-C) has little effect on the water vapour permeability of the stone, reducing it by only 3% (Table 5.2.9& Figure 5.2.26). The crust of this specimen, which has been slightly

Table 5. 2.9 The water vapour diffusion resistant factor and the water vapour permeability rate of sound and crusted specimens

Specimen	Water vapour diffusion resistant factor (μ)		The ratio of water vapour diffusion resistant factor between the sound specimens and the crust specimens.	Water vapour permeability rate (D)		The ratio of water vapour permeability rate between the sound specimens and the crust specimens.
	[-]			[Kg/(s.m.Pa)]		
	Sound (R)	Crust (C)	R/C	Sound (R)	Crust (C)	R/C
S1	18.4	19	0.97	1.066E-11	1E-11	1.03
S2	5.2	6.1	0.85	3.806E-11	3.2E-11	1.18
S3	10	11.3	0.89	1.964E-11	1.7E-11	1.13
S4	7.6	12.4	0.61	2.577E-11	1.6E-11	1.64
S7	13.1	22.1	0.59	1.493E-11	8.9E-12	1.68
S8	15	16.1	0.93	1.311E-11	1.2E-11	1.08
S9	25.8	30.6	0.83	7.6E-12	6.415E-12	1.2
S10	8.3	15.4	0.54	2.353E-11	1.3E-11	1.85

DOI: 10.15774/PPKE.BTK.2024.021

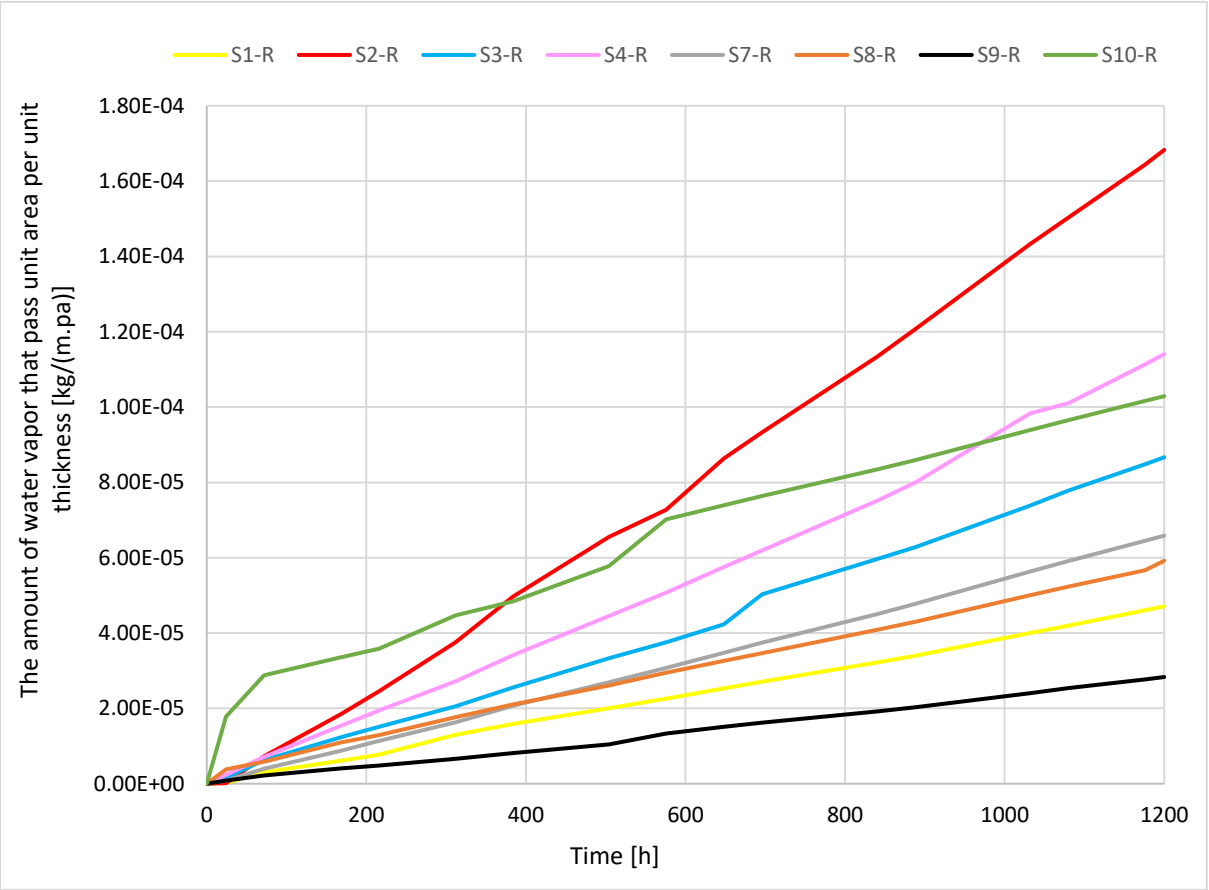

Figure 5. 2. 24 The amount of water vapor that pass unit area per unit thickness by the time for the sound specimens

dissolved, is only 0.1 mm thick, and dolomite crystals have recrystallized on its surface. Compared to other sound specimens, the S7 specimen (S7-R) has a moderate water vapour permeability rate (Figure 5.2.24). The water vapour diffusion resistance factor of the specimen is 13.13[-]. The crust of S7 (S7-C) reduces the permeability rate by about 40%, the water vapour diffusion resistance factor of S7-C is roughly 22 [-] (Figure 5.2.26). One of the sound specimens that reveals a moderate water vapour permeability rate is S8-R. S8-R has a water vapour diffusion resistance factor of 15 [-]. The crust has a minor effect on the water vapour permeability (S8-C), decreasing the water vapour permeability rate by about 7% (Table 5.2.9). Compared to other sound specimens, the S9-R has the lowest permeability rate (Figure 5.2.24). This stone type has the lowest porosity of any of the sound specimens. The water vapour permeability rate of the crust specimen (S9-C) is 17% lower than the sound specimen (S9-R) (Table 5.2.9& Figure 5.2.26). This crust is about 0.08-0.12 mm thick, and clear dolomite crystals characterise it. The inclusion-rich dolomite crystals dominate the sound part of the stone.

DOI: 10.15774/PPKE.BTK.2024.021

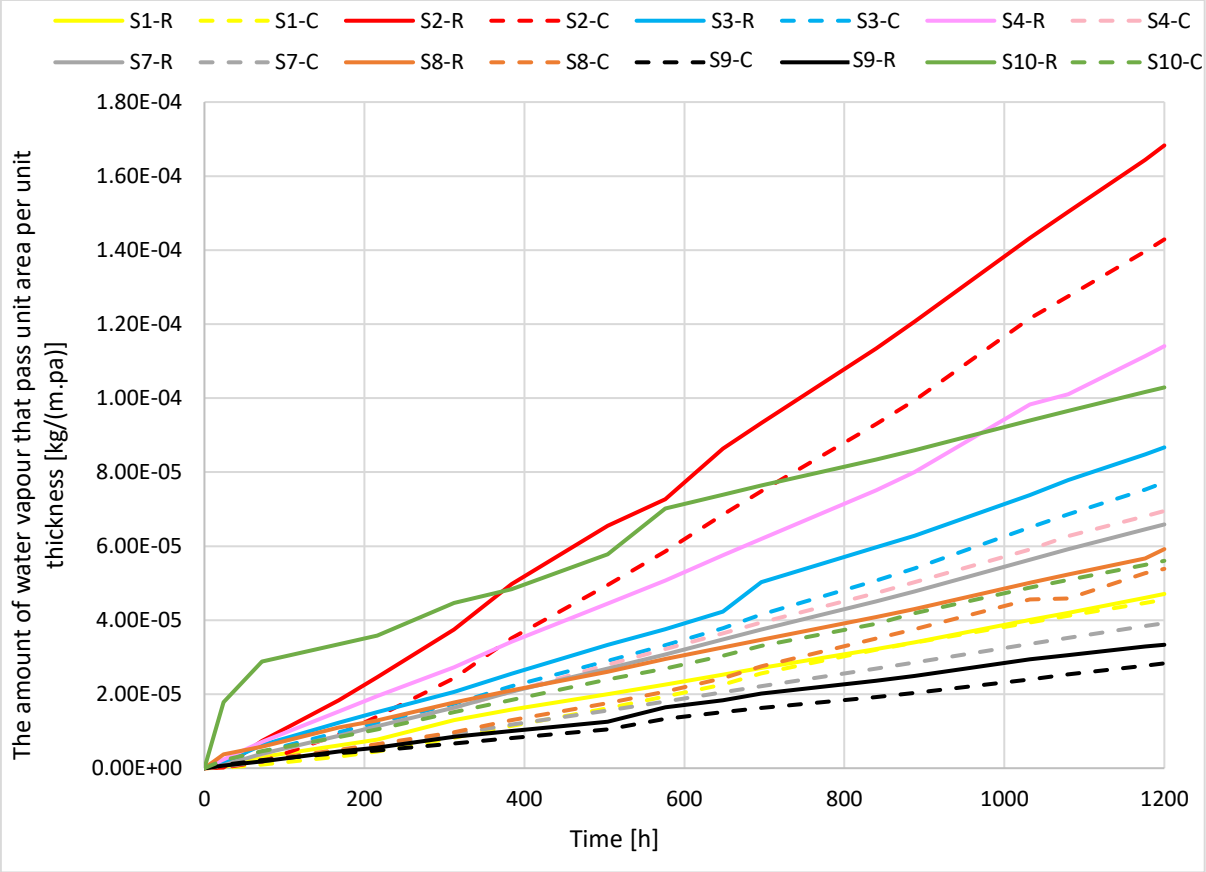

Figure 5. 2. 25 The amount of water vapor that pass unit area per unit thickness by the time for the sound specimens and the specimens with crust

The weathering crusts of S1, S3 and S8 modify the water vapour resistance factor a little (less than 20%). However, the crust of S4, S7, and S10 reduces the water vapour diffusion resistant factor to 50% compared to the original stones. Therefore, the water vapour is trapped longer inside such stones with these crusts. Although the weathered surface always has multiple effects on the alteration of the properties of the original stone, these effects are not always negative, and this weathered surface may not have a significant effect on some properties. The Rilem tube tests performed on-site are used to assess how the weathering crust has changed the water penetration of wind-driven rain. The extent to which the crusts can modify the water vapour movement through the stone (from inside to outside) is also investigated in the laboratory. In other words, if the crust minimizes or prevents water penetration by the Rilem tube and simultaneously allows the stone to breathe (the crust is permeable to water vapour), then the crust is considered as a natural conservative agent regarding these two criteria. For instance, the same crusts of S2, S3, S4, and S9 are examined in situ by Rilem tube. However, comparing the results of water penetration with water vapour permeability would highlight some positive and negative effects of the crust on the stone.

DOI: 10.15774/PPKE.BTK.2024.021

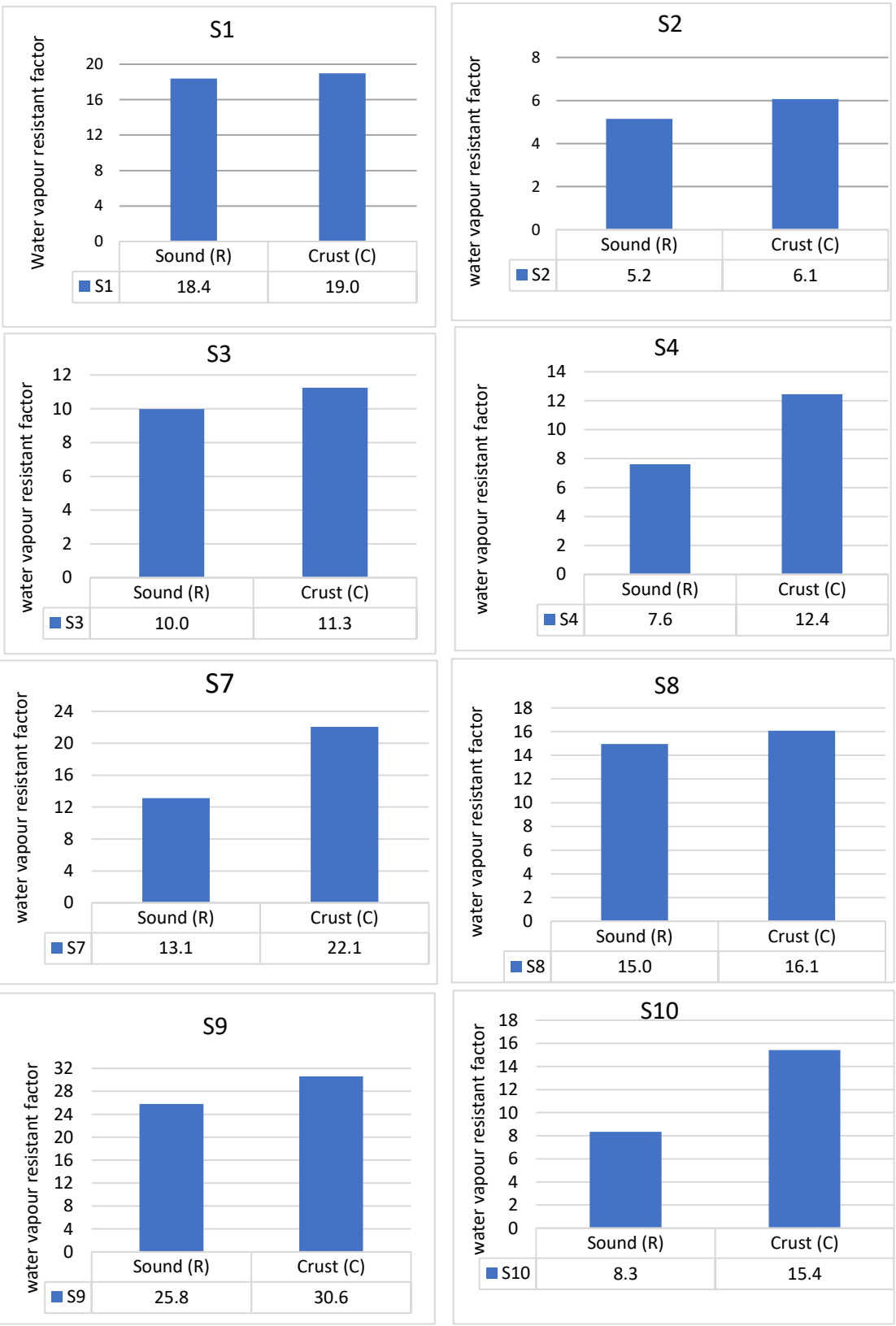

Figure 5. 2. 26 The water vapour resistance factor of the sound and crusted specimens

The presence of red-orange microorganisms in the weathering crust of S_3 prevents water penetration by the Rilem tube. However, the presence of these microorganisms on the S_3-C

DOI: 10.15774/PPKE.BTK.2024.021

has little effect on the water vapour permeability. As a result, this type of crust could be considered as a protective layer from liquid water. Grey microorganisms thrived on the surface of S4 reduce the water vapour permeability to 50%. These microorganisms cause low water penetration or prevent water penetration from the Rilem tube. Although this crust serves as a protective layer for the stone from liquid water, the reduced ability of water vapour permeability may have negative consequences. This crust slows the movement of water vapour, which could lead to water vapour trapping inside the stone, increasing the risk of deterioration. In the case of rising dampness, the negative effects may be enhanced significantly. Because of the low-rate drying behaviour of the crust, water may accumulate inside the stone, probably leading to further deterioration. The stones that are colonised by green algae at the castle are challenging to be tested by Rilem tube because the ability of water retention of these algae on the stone surface makes it highly damp. The tube cannot be fixed on these surfaces (S2 and S9). Their crusts have a slight effect on the water vapour permeability rate. However, the role of this type of crust in either protecting the stone surface or not is unknown. The water penetration by the Rilem tube is fast for S1. The crust (S1-C) does not significantly affect the water vapour diffusion resistance factor. As much as the water penetrates in the stone, the crust does not hinder the movement of water vapour (it can be dry without significant restrictions). The crust in S1 has a minor effect on altering the properties of the stone, such water vapour permeability, drying, and water penetration.

5.2.6 Salt ageing test

1- Sodium sulfate ($Na_2SO_4.10H_2O$)

There are two crystallisation phases of sodium sulfate Na_2SO_4 (Thenardite) and $Na_2SO_4.10H_2O$ (Mirabilite). Sodium sulfate usually precipitates from solution at a temperature below 32.4˚C and at high relative humidity (above 60%) in the form of $Na_2SO_4.10H_2O$ (Mirabilite). Above 32.4˚C and according to the relative humidity, sodium sulfate crystallises as Na_2SO_4 (Thenardite) or will go into solution (see the phase diagram of Na_2SO_4 in Chapter 2.2.1). According to the test conditions, the rate of temperature increase is 5°C/h from 20 to 70˚C, which means the temperature degree in the oven will be under 32.4˚C during the first two hours. Thus, the specimens are in temperature above 32.4˚C during the remaining 8 hours. As such the crystallisation of Mirabilite might occur during the first two hours inside the oven because of the high relative humidity and the temperature (below 32.4˚C). However, the specimens mainly experience the crystallisation of Thenardite during the remaining period inside the oven. When the specimens are put in the salt solution, Na_2SO_4 underwent hydration to form

DOI: 10.15774/PPKE.BTK.2024.021

$Na_2SO_4.10H_2O$. Therefore, the specimen suffer from two types of pressures: i) hydration pressure when Na_2SO_4 (present inside pores) transforms to $Na_2SO_4.10H_2O$ inside the solution, ii) crystallisation pressure of Na_2SO_4.

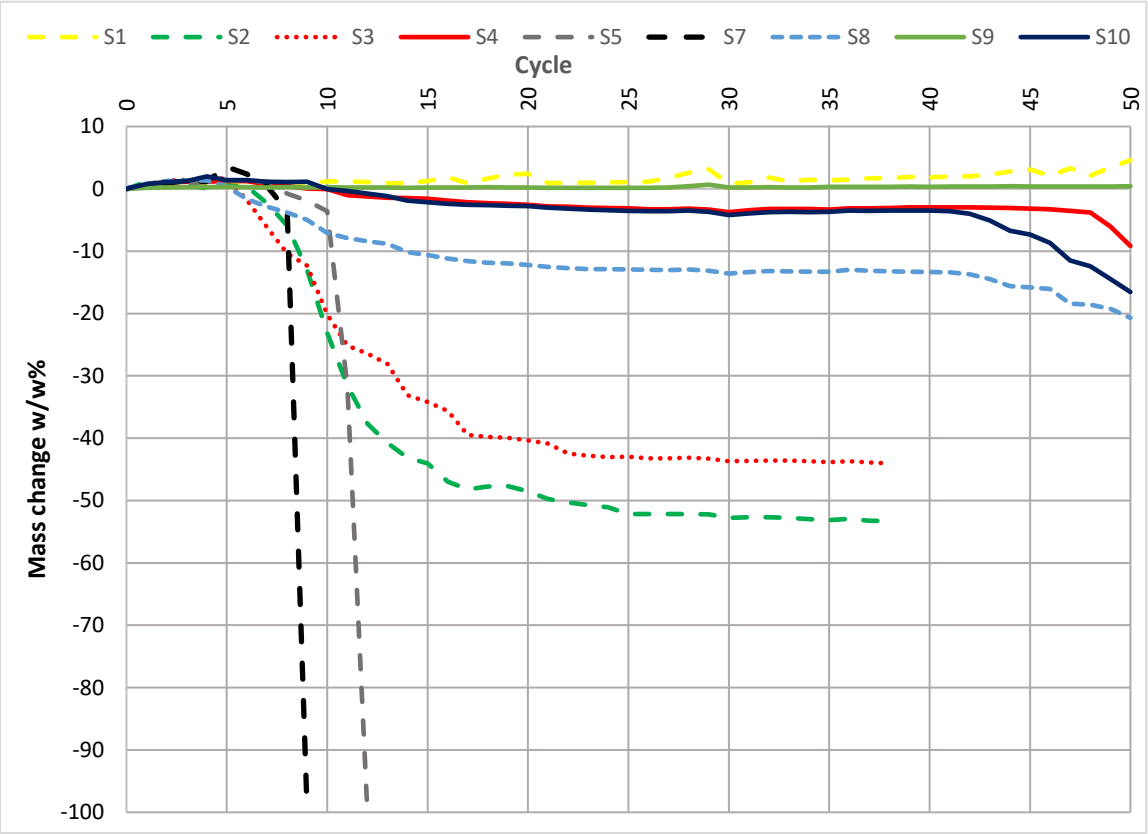

Figure 5. 2. 27 The mass change as a percentage from the initial dry mass of the specimens in Sodium sulfate solution

The specimens under $Na_2SO_4.10H_2O$ reveal various degrees of resistance and damage behaviour during the test cycles (see Figure 5.2.27). S1 and S9 are the most resistant specimens and do not exhibit loss mass during the test. S9 is the most resistant specimen during the test. Due to its low open porosity (around 11 v/v%), its mass barely increases around 0.4 w/w% by the end of the test. The mass of the salt crystals in its pores is very small and it does not lose

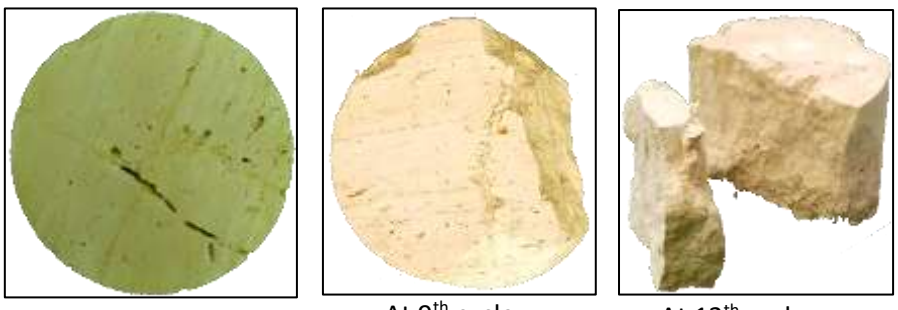

Figure 5. 2. 28 S5 specimen under sodium sulfate salt solution

DOI: 10.15774/PPKE.BTK.2024.021

any material. Although the mass of the specimen increases, the ultrasound velocity shows a decrease trend, see Figure 5.2.31. The crystallisation-solution cycles induce some fissures and voids inside the stone, leading to a decrease in the ultrasound velocity of the specimen. However, the specimen is resistant enough to not show any loss in stone material.

S1 exhibits high resistance where its mass slightly increases about 5 w/w% by the end of the test without any loss of its material. The ultrasound velocity increases during the experiment, where the velocity rises from 3 km/s which higher than at the drying phase to around 4 km/s at the 50th cycle, see Figure 5.2.31. The density of the specimen increases due to the salt formation without inducing any damage or cracks propagation inside the specimen.

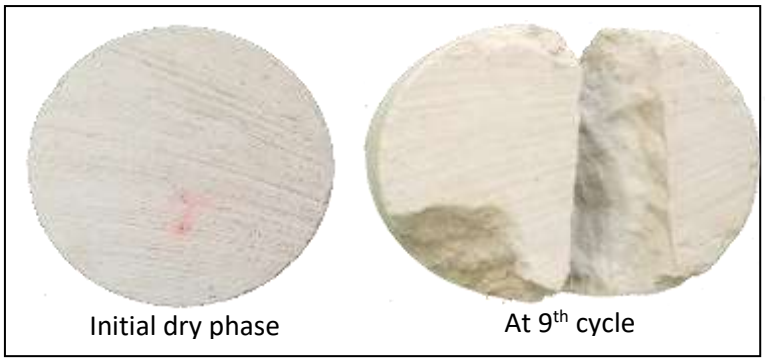

Figure 5. 2. 29 S7 specimen under sodium sulfate salt solution

S7 and S5 exhibit a rupture in stone material resulted in breaking the specimen into half at 8th and 10th cycle, respectively, see Figure 5.2.27. The ultrasound velocity in S5 does not highly change before breaking. This specimen has already a crack that causes the rupture in stone material at the 10th cycle, see Figure 5.2.28. However, the ultrasound of S7 decreases from 3.5 km/s at 5th cycle to 2.5 km/s at 7th cycle, see Figure 5.2.31. That indicates a crack creation inside the stone leading to break the specimen into half in the 8th cycle, see Figure 5.2. 29.

S2 and S3 show different behaviours than the former specimens. As they both have a high percentage of open porosity (29 w/w% and 32 w/w%, respectively), they experience a granular disintegration and thus a gradual loss in stone material. They start to show these weathering

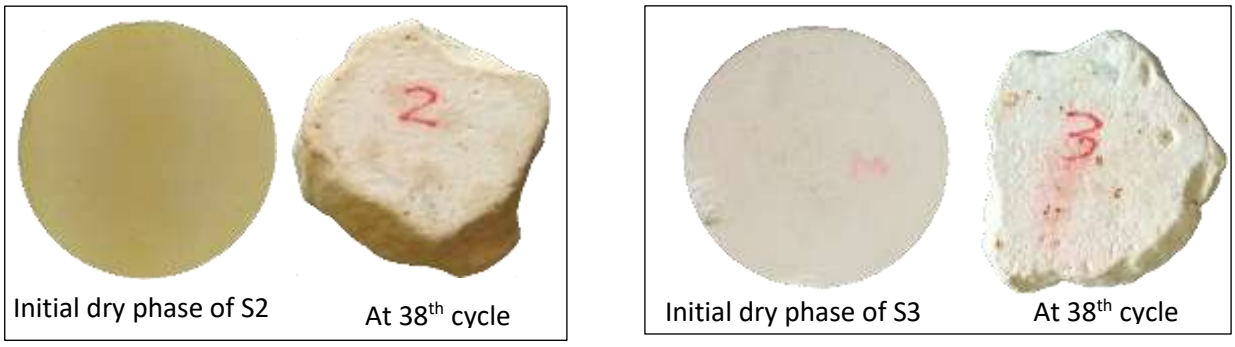

Figure 5. 2. 30 S2 and S3 specimens under sodium sulfate salt solution

DOI: 10.15774/PPKE.BTK.2024.021

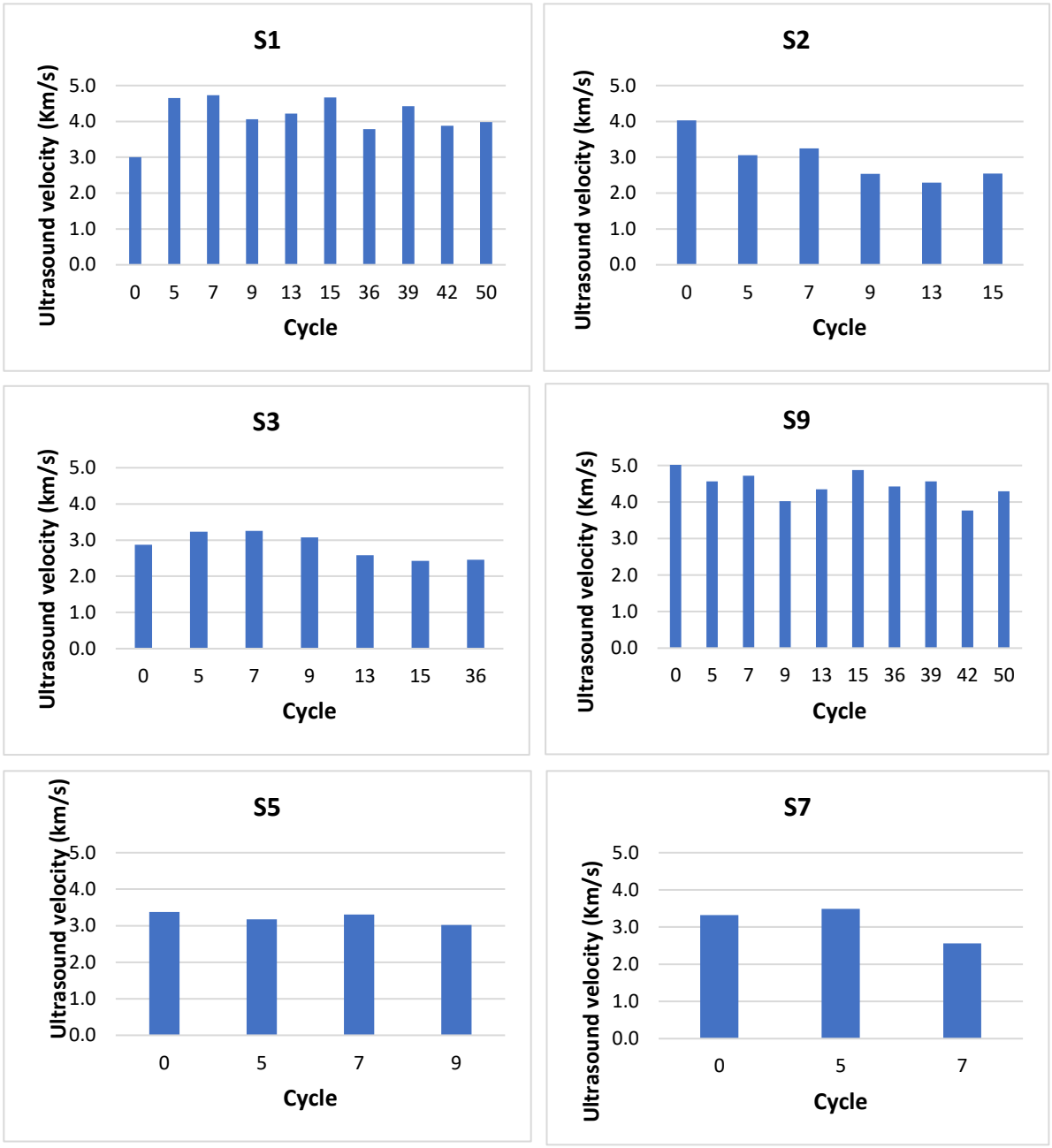

Figure 5. 2. 31 Ultrasound velocity per Na_2SO_4 salt solution-drying cycle

patterns from the 5th cycle and continue it until 25th and 22nd with losses of 52 w/w % and 42.5 w/w %, respectively, see Figure 5.2. 27. After that they show a very slight mass loss until the 38th cycle. So, they lose around 53 w/w % and 44 w/w % of their initial mass by 38th cycle, respectively (see Figure 5.2.30). These specimens are excluded from the test by the 38th cycle. The granular disintegration in S2 causes the irregular shape of the top and bottom of the specimen and the unfeasibility of the ultrasound measurements after the 15th salt cycle. The ultrasound velocity decreases from about 3.5 km/s (dry) to around 2.5 km/s (15th cycle, Figure 5.2. 31). The ultrasound velocity of S3 exhibits a slight increase until the 7th cycle, and

DOI: 10.15774/PPKE.BTK.2024.021

then a decrease under the value of the dried condition (see Figure 5.2.31). The ultrasound velocity at 38th cycle is 2.46 km/s that is lower than in the drying phase, 2.87 km/s.

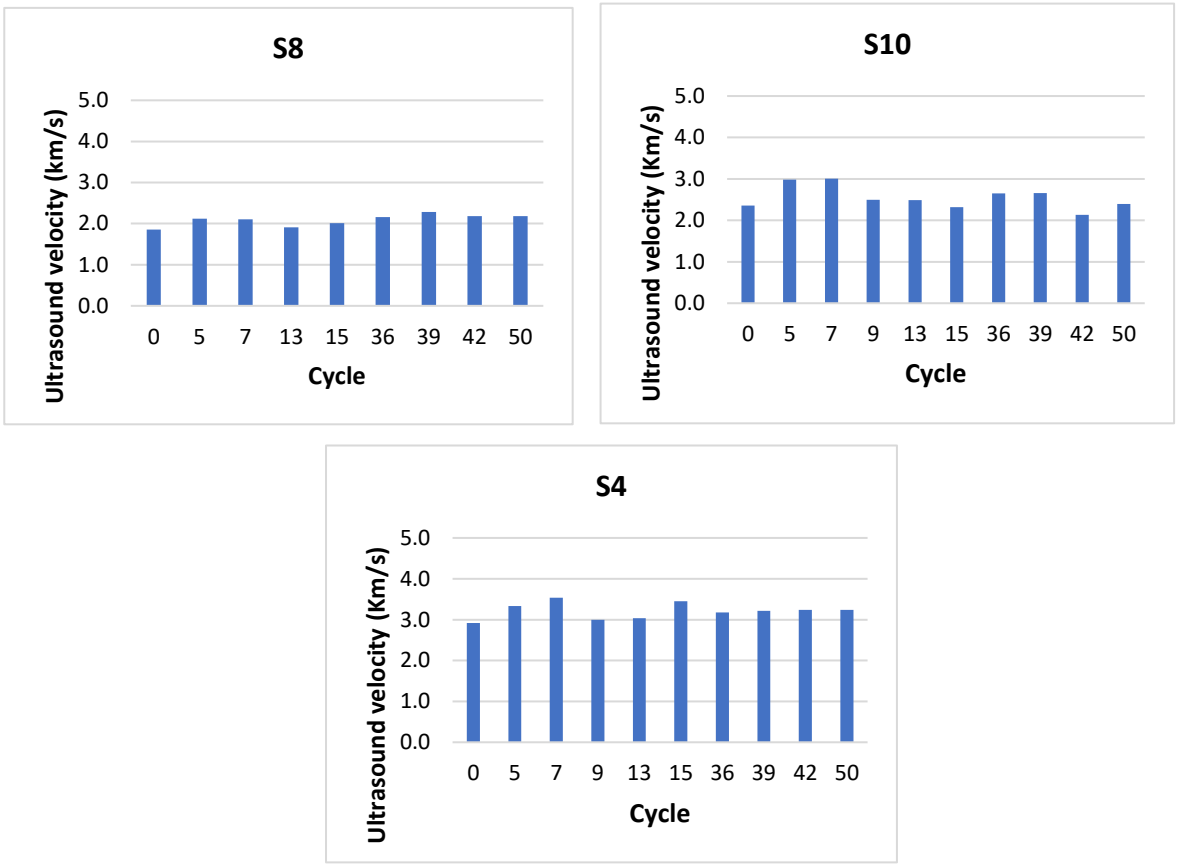

Figure 5. 2. 32 Ultrasound velocity per NaSO4 salt solution-drying cycle

S4, S8, and S10 have approximately the same resistance behaviour, where they show little loss in their material during the test. S8 shows little material loss from the 5th to 21st cycles, where it lost about 12.7%. Afterwards, the specimen experiences a quiet stagnation period, 22nd - 41st, and then it demonstrates a gradual loss until it loses 20 % of its initial mass by the end of 50th cycles (see Figure 5.2.27). This specimen exhibits modest resistance as it has a relatively high percentage of closed pores 4.13 v/v%. The ultrasound velocity of this specimen shows an increase trend. Even though the loss in stone material between 42nd - 50th cycles, the velocity has been barely changed compared with the former cycles, see Figure 5.2.32. The salt crystals that fill the pores spaces cause the increase of the density which is reflected in increasing ultrasound velocity.

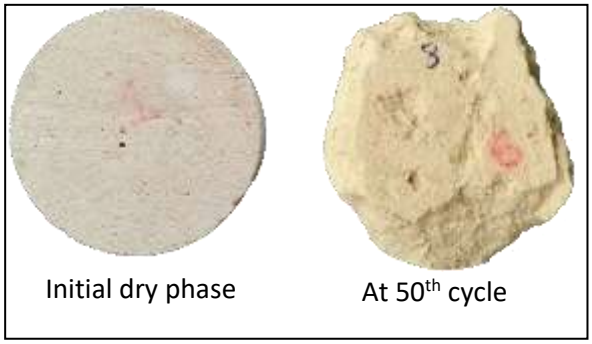

Figure 5. 2. 33 S8 specimen under sodium sulfate salt solution

DOI: 10.15774/PPKE.BTK.2024.021

Even though S10 has approximately similar properties (closed pores and total open pores) of S8, it is more resistant than S8. S10 exhibits the same loss-mass trend of S8; however, in the last eight cycles, the loss from the initial mass in S10 rapidly increases and reaches nearly the mass loss of S8. By the end of the 50th cycle, the specimen loses 16.6 % of its initial mass (Figure 5.2.27). The ultrasound velocity increases from 2.36 km/s (at drying phase) to 3 km/s (at 5th and 7th cycles). After that, the velocity fluctuates between 2.5 and 2.4 km/s. The ultrasound velocity at the end of the experiment and in the drying phase is approximately the same (around 2.4 km/s, see Figure 5.2.32). The salt crystallisation in this specimen does not induce any voids or fissures inside the stone; instead, the salt crystals fill the pores which case an increase of specimen density.

S4 has the highest percentage of closed pores (about 4.5v/v%); therefore, it is quite resistant. It starts to lose its material from the 11th cycle, and the mass loss is about 3 w/w % in average during the following cycles. In the last two cycles, the mass loss plunges until it reaches 9 w/w% by the end of the experiment. The ultrasound velocity of this specimen exhibits an increase trend that reveals the resistance of the specimen. The velocity at the 50th cycle (3.24 km/s) is higher than in the dry phase (2.9 km/s), see Figure 5.2.32.

2- Sodium chloride (NaCL)

The effect of NaCL crystallisation on the specimen is not aggressive as much as Na_2SO_4; however, some specimens are damaged during the experiment. The specimens experience salt efflorescence on its surface during the experiment (when the specimens are exposed to gradual temperature inside the oven). However, when the specimens are kept inside the oven at 70˚C for longer time (during the weekends), the salt crystals weakly adhere on the stone surface and they fall down from the specimen surface. [316] study the crystallisation of NaCL on hydrophobic surface at 70˚C. They realize that NaCL crystals create tiny legs that lift the crystals from the stone surface. As such, the salt crystals will grow on the first crystal that has tiny legs. That will make the salt crystals formed on the stone surface to fall down by a process “self – cleaning” according to the authors. In our experiment, we find that the specimens gain mass during the working day (24 hours salt cycle shown in Figure 5.1.4); and on the weekends (longer time at 70˚C temperature) the specimens lose mass. The specimens experience “self –

[316] Salim et al. (2020)

DOI: 10.15774/PPKE.BTK.2024.021

cleaning" process during the weekends. Therefore, the curve of mass change of the specimens under NaCL salt has a wavy- shape curve, see Figure 5.2.34.

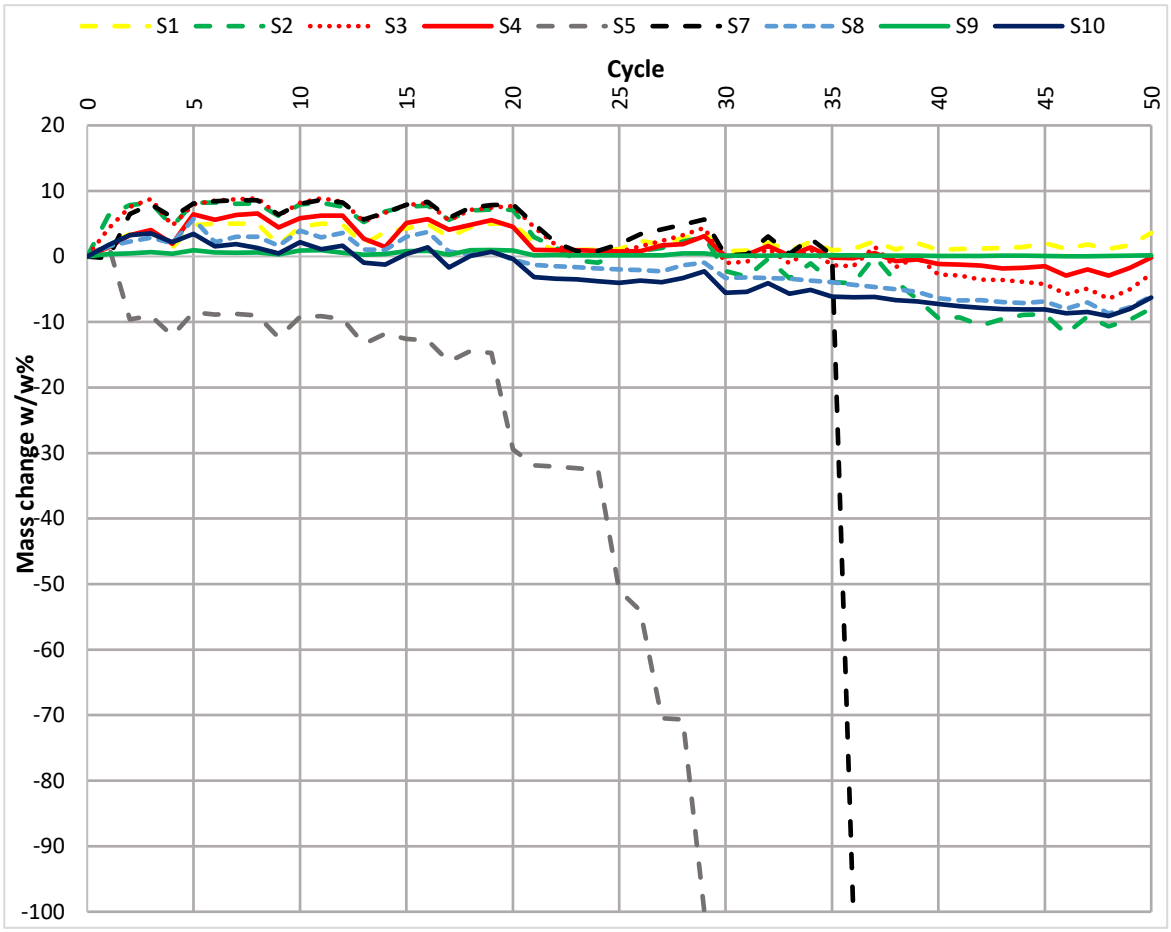

Figure 5. 2. 34 The mass change as a percentage from the initial dry mass of the specimens in Sodium chloride solution

S1 and S9 show the same resistance behaviour so they are highly resistant and do not exhibit any material loss. S9 is the most resistant specimen; it gains very slight mass during the experiment around 0.15 w/w% by the end of 50th cycle, see Figure 5.2.34. The salt heavily accumulates on its surface (Figure 5.2.35). The ultrasound velocity of this specimen does not

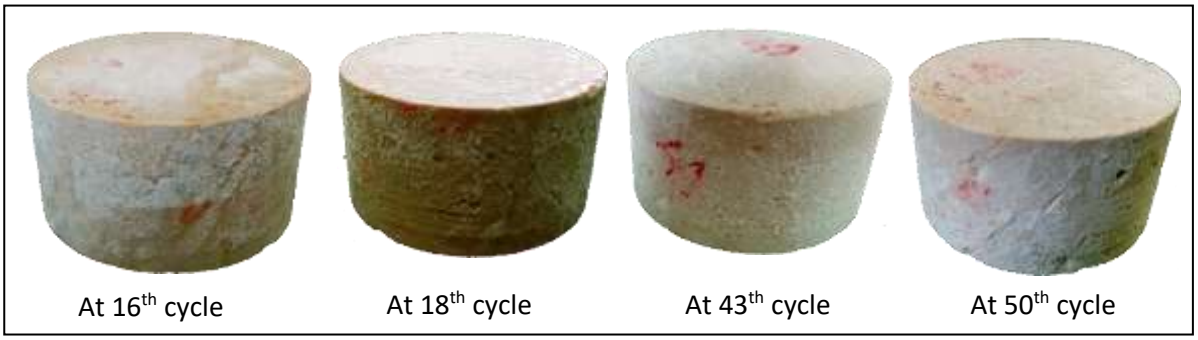

Figure 5. 2. 35 S9 specimen under sodium chloride salt solution

DOI: 10.15774/PPKE.BTK.2024.021

show high changes. The velocity oscillates between 4.6 and 5.5 km/s during the experiment (see Figure 5.2.39).

S1 is the second- ranked resistant specimen, where the mass of the specimen increases during the experiment until it reaches 3.6 w/w % at 50th cycle (see Figure 5.2.34). The salt barely accumulates on its surface; however, it most likely presents within its internal pores. The ultrasound velocity of the specimen exhibits slight changes during the experiment; it fluctuates between 4 and 4.6 km/s (see Figure 5.2.39). That indicates the small amount of salt that created inside the pores does not develop any changes inside the stone.

As for S3, and S4, they have similar behaviour where they start to lose their material from the 30th cycle, where they lose less than 2 % from their initial masses at the end of the test. S3 starts to lose its material from the 30th cycle, but it is a shy loss of around 1 w/w% until the 39th cycle. Afterwards, the mass of the specimen gradually decreases until the loss from initial mass reaches 6% at the 50th cycle. The ultrasound velocity shows a decrease trend, where the velocity drops from 3.35 km/s at dry phase to 2.5 km/s at the 50th cycle. The ultrasound velocity of S3 decreases even though the increase of its mass that indicates cracks propagation inside the stone structure. In addition, the surface of this specimen erodes in the form of pitting that progressively develops during the experiment (see Figure 5.2.36).

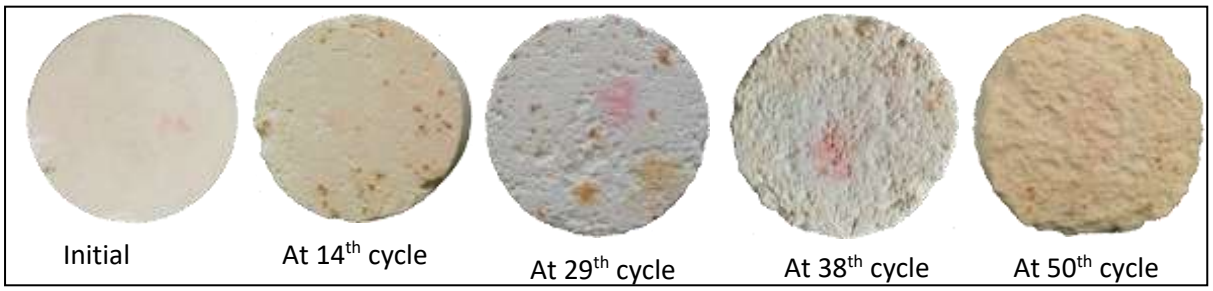

Figure 5. 2. 36 S3 specimen under sodium chloride salt solution

S4 is also a resistant specimen against this salt. The mass of the specimen gradually increases until the increase reaches 4 % at the 30th cycle. After that, the mass of the specimen decreases, but it is still higher than the initial mass until the 34th cycle. From the 35th cycle, the specimen starts to lose its material where the mass of specimen drops 3 % from the initial mass at the 50th cycle, see Figure 5.2.34. When salt crystals start to fill the specimen pores the ultrasound velocity increases specially in the 5th and 7th cycles. After that, the velocity exhibits a slight decrease trend until the end of the experiment. The velocity of the dry phase is 2.84 km/s, which is slightly higher than the velocity of 50th cycle (2.36 km/s), see Figure 5.2.39.

DOI: 10.15774/PPKE.BTK.2024.021

S5 and S7 specimens exhibit a rupture in stone material during the test. S5 is the only specimen that does not have a mass increase; rather, it dramatically loses its mass from the first cycle. This specimen originally has fissures and cracks that rapidly develop into loss in stone material (see Figure 5.2.38). The specimen is excluded from the experiment when it loses around 85 % from its initial mass at the 29th cycle. The ultrasound velocity exhibits a decreasing trend, where the velocity drops from 4 km/s (at dry phase) to 2.8 km/s at 15th cycle, see Figure 5.2.39. Due to massive material loss in this specimen, the ultrasound measurement cannot be fulfilled after the 15th cycle. Until 35th cycle, S7 demonstrates a gradual increase in its mass. The specimen in cycle 36 suddenly exhibits a rupture in stone material and it breaks into half, see Figure 5.2.37. The salt does not accumulate highly on its surface and the specimen does not experience massively pitted surface during the experiment. The ultrasound velocity of this specimen shows a decrease trend even though the increasing mass of the specimen, see Figure 5.2.39. The decreasing velocity during the experiment indicates creation of voids and fissures within the stone structure. Because of crystallisation pressure, theses fissures and voids

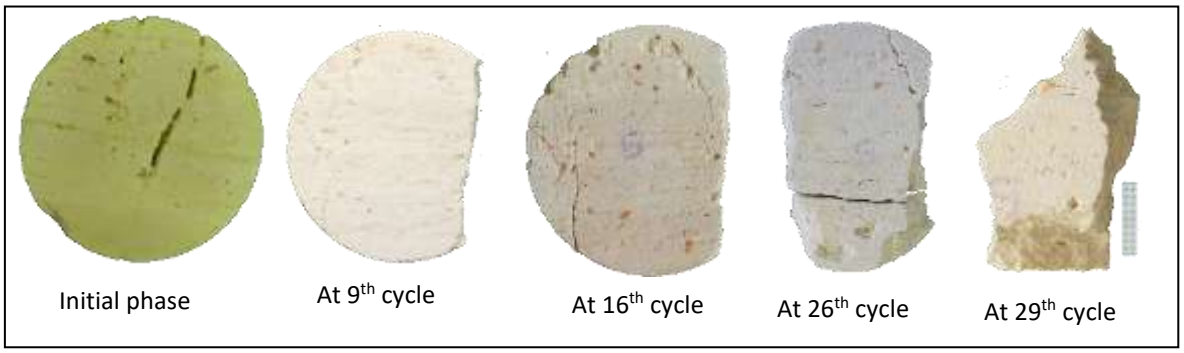

Figure 5. 2. 37 S5 specimen under sodium chloride salt solution

lead to rupture in stone material.

As for S2, S8, and S10, they exhibit similar resistance, where they lose around 6 % from their initial masses by the end of the test. S2 gains mass during the first the 20th cycles, then it starts to lose its material. At the 18th cycle, a crack creates on its top side, which developed into fragmentation and loss in stone material at the 40th cycle; where the specimen loses about 9% from its initial mass (see Figure 5.2.34). After that, the specimen oscillates around this percentage of mass loss until the

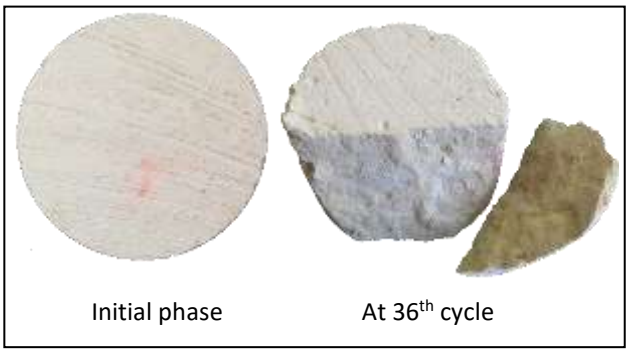

Figure 5. 2. 38 S7 specimen under sodium chloride salt solution

DOI: 10.15774/PPKE.BTK.2024.021

end of the experiment. The ultrasound velocity of this specimen exhibits a decrease trend, where the velocity plunges approximately to the half after 5th cycle. It is around 3.9 km/s at the drying phase then it declines to 2.4 km/s, where it fluctuates around 2 km/s until the end of the experiment (see Figure 5.2.39). Even though the mass of the specimen increases, the velocity decreases. That can be interpreted with new voids or fissures within the stone structure caused

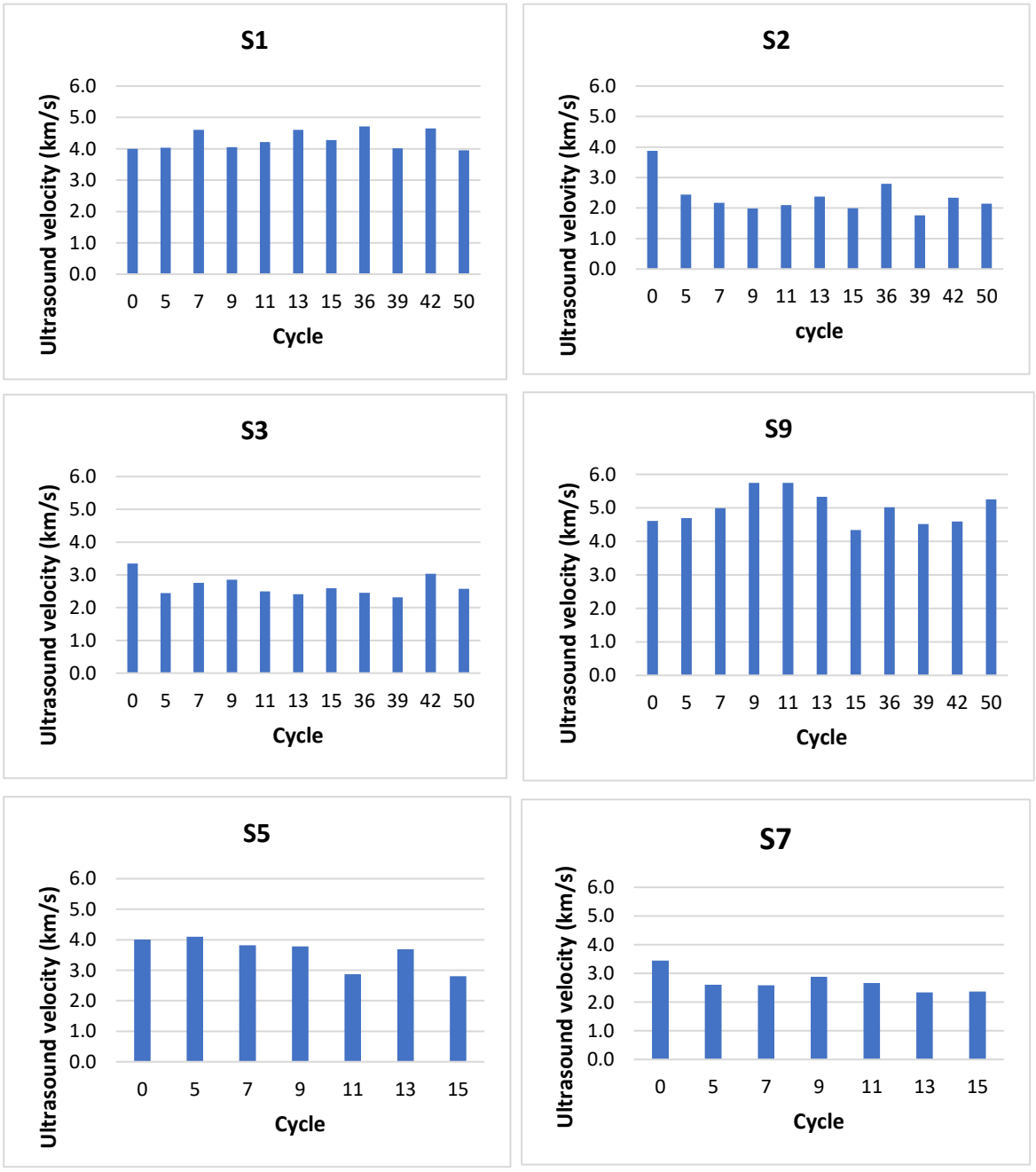

Figure 5. 2. 39 Ultrasound velocity of the specimens per NaCl salt solution-drying cycle

DOI: 10.15774/PPKE.BTK.2024.021

by the crystallisation pressure. By monitoring the weathering of the stone surface, it is obvious that the surface gradually erodes as a form of pitting (see Figure 5.2.40). S8, that has a high percentage of closed pores, is relatively resistant during the experiment. The mass of the specimen slightly increases until the 19th cycle (around 0.8 w/w %). After that, the mass of the specimen starts to decrease in small percentage. By the end of the 50th cycle the mass of the specimen drops around 8% from the initial mass, see Figure 5.2.34. The ultrasound velocity exhibits decreasing trend; however, the velocity slightly decreases from 2.5 km/s (dry phase) to 2 km/s at 50th cycle, see Figure 5.2.41. The surface of stone also exhibits pitting erosion that develops progressively during the experiment. S10 approximately reveals similar resistance degree as S8, because they approximately have the same open and closed porosity. The mass of S10 increases until the 19th cycle, and then it starts to lose its

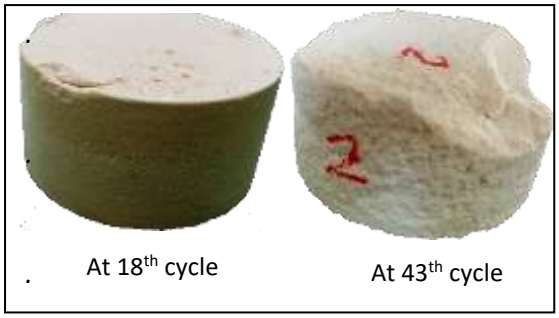

Figure 5. 2. 40 S2 specimen under sodium chloride salt solution

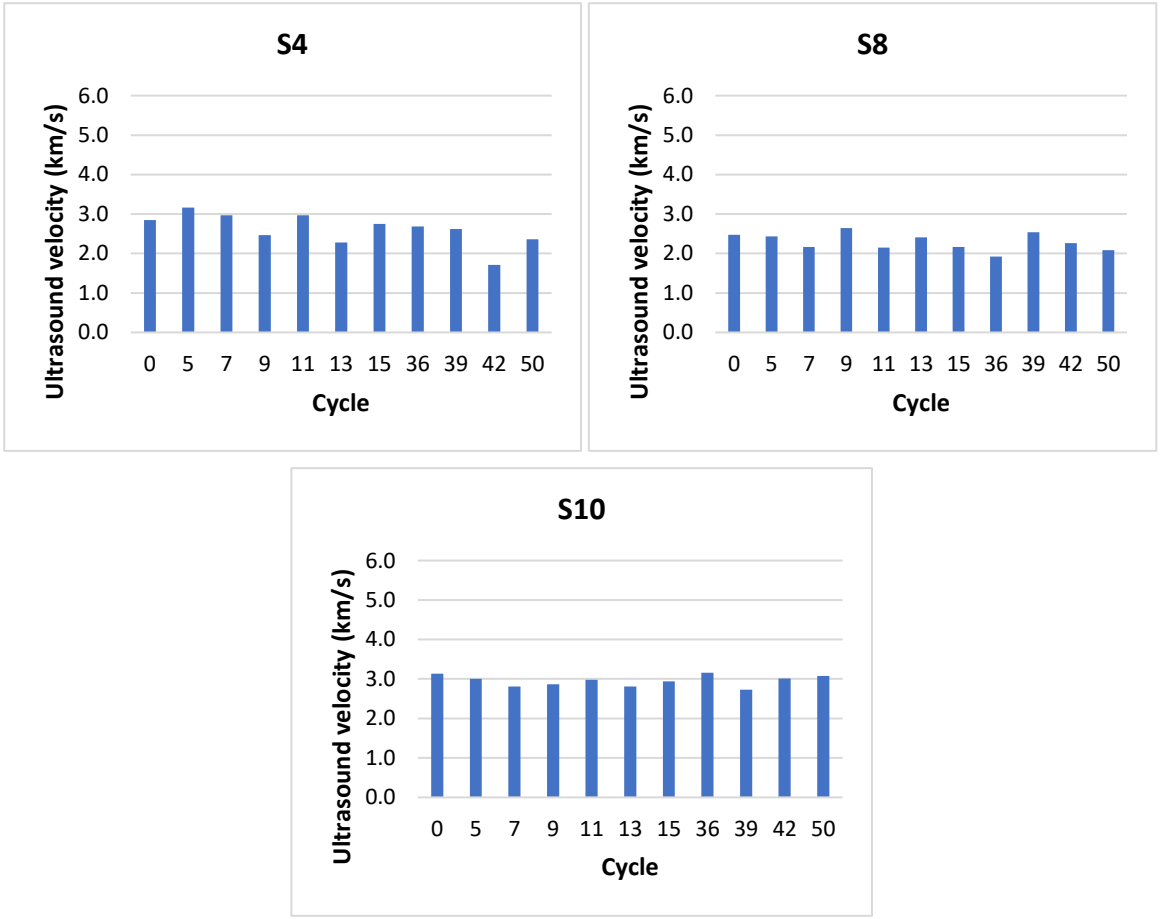

Figure 5. 2. 41 Ultrasound velocity of the specimens per NaCl salt solution-drying cycle

DOI: 10.15774/PPKE.BTK.2024.021

material. By the end of the 50th cycle it loses around 9 % from its initial mass, see Figure 5.2.34. The ultrasound velocity of this specimen remains steady and barely changes; where the velocity is 3.13 km/s at dry phase and it is 3.08 km/s at the end of the experiment, see Figure 5.2.41. Like S2 and S8, S10 also exhibit highly pitted surface during the experiment.

3- Potassium nitrate (KNO_3)

KNO_3 is a simple salt that does not have a hydrated form. It is low soluble salt and can crystalize at high humidity degrees, up to 90% at 20˚C and up to 75% at 75˚C (see phase diagram of KNO_3 in Chapter 2.2.1). At low temperatures, salt creep phenomena occurs where KNO_3 salt widely accumulates and spreads, however, at high temperature the salt efflorescence becomes thicker and concentrated, and that also relates to stone properties [317]. The main deteriorative role of this salt is reported to accumulate in the pores and clogging them up [318]. In this experiment conditions, the specimens experience the crystallisation of KNO_3 when they are

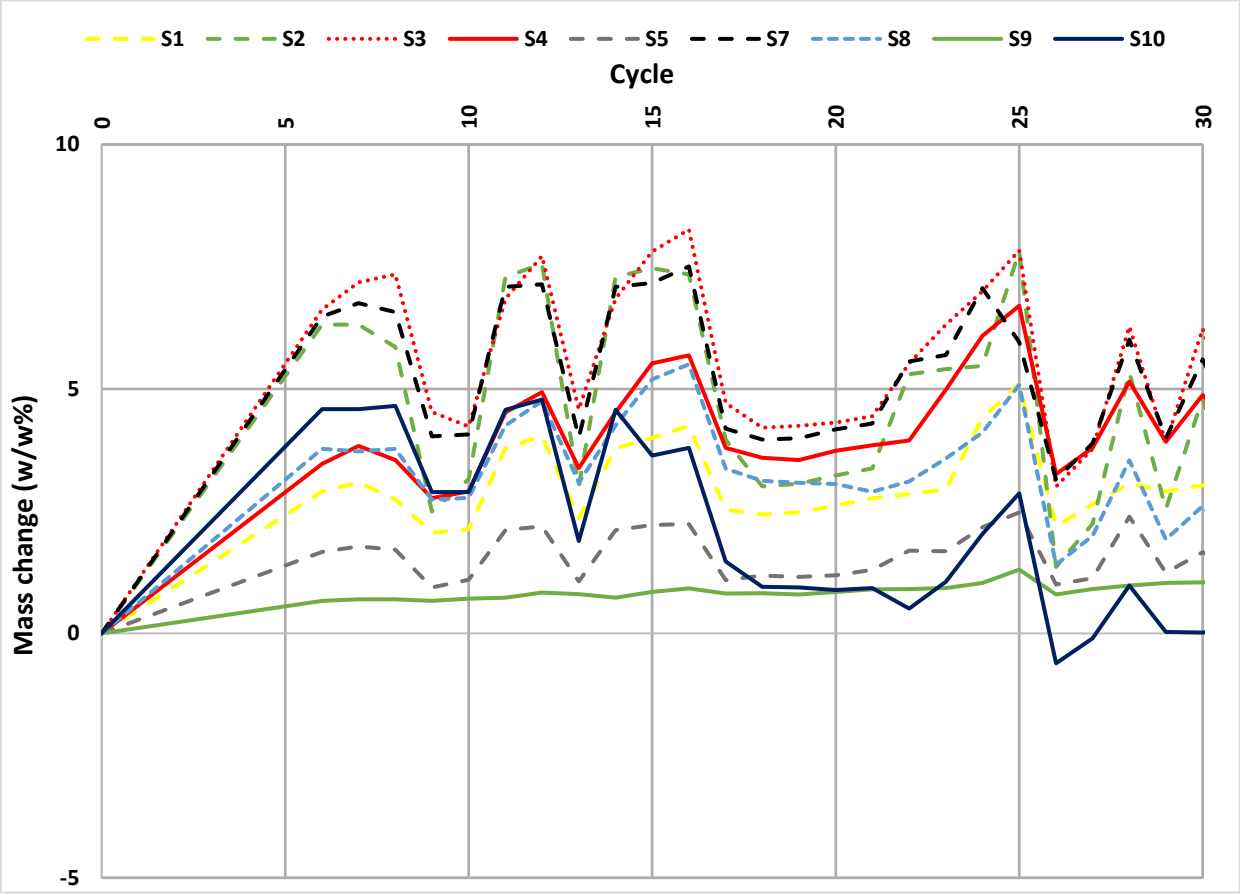

Figure 5. 2.42 The mass change as a percentage from the initial dry mass of the specimens in potassium nitrate solution

[317] Patricia Vazquez, Lucas Sartor, and Céline Thomachot-Schneider, "Influence of Substrate and Temperature on the Crystallization of KNO3 Droplets Studied by Infrared Thermography," *Progress in Earth and Planetary Science* 5/1 (2018).

[318] Luigi Dei et al., "Growth of Crystal Phases in Porous Media," *Langmuir* 15/26 (1999): 8915–22.

DOI: 10.15774/PPKE.BTK.2024.021

inside the oven at 70°C. The salt accumulates on the surfaces of specimens and the loss in stone material is detected at very small percentage. Due to salt accumulation, all the specimens exhibit an increase in their mass. However, the change in mass curve shows increase and decrease trend; but in all cases the mass change is still positive (higher than the dry mass), see Figure 5.2.42. When the salt cycle duration is 24 hours, the mass change curve exhibits increase trend; and when the salt duration cycle is more than 24 hours, the mass change curve exhibits decrease trend. The salt solution needs more time to evapourate from the pores, and that is achieved during a long period cycle. Therefore, the solution evapourates and the mass measured by the end of the cycle includes the mass of the specimen and the mass of crystalized salt. However, during the 24 hour- cycle, the salt solution partially evapourates; so, the

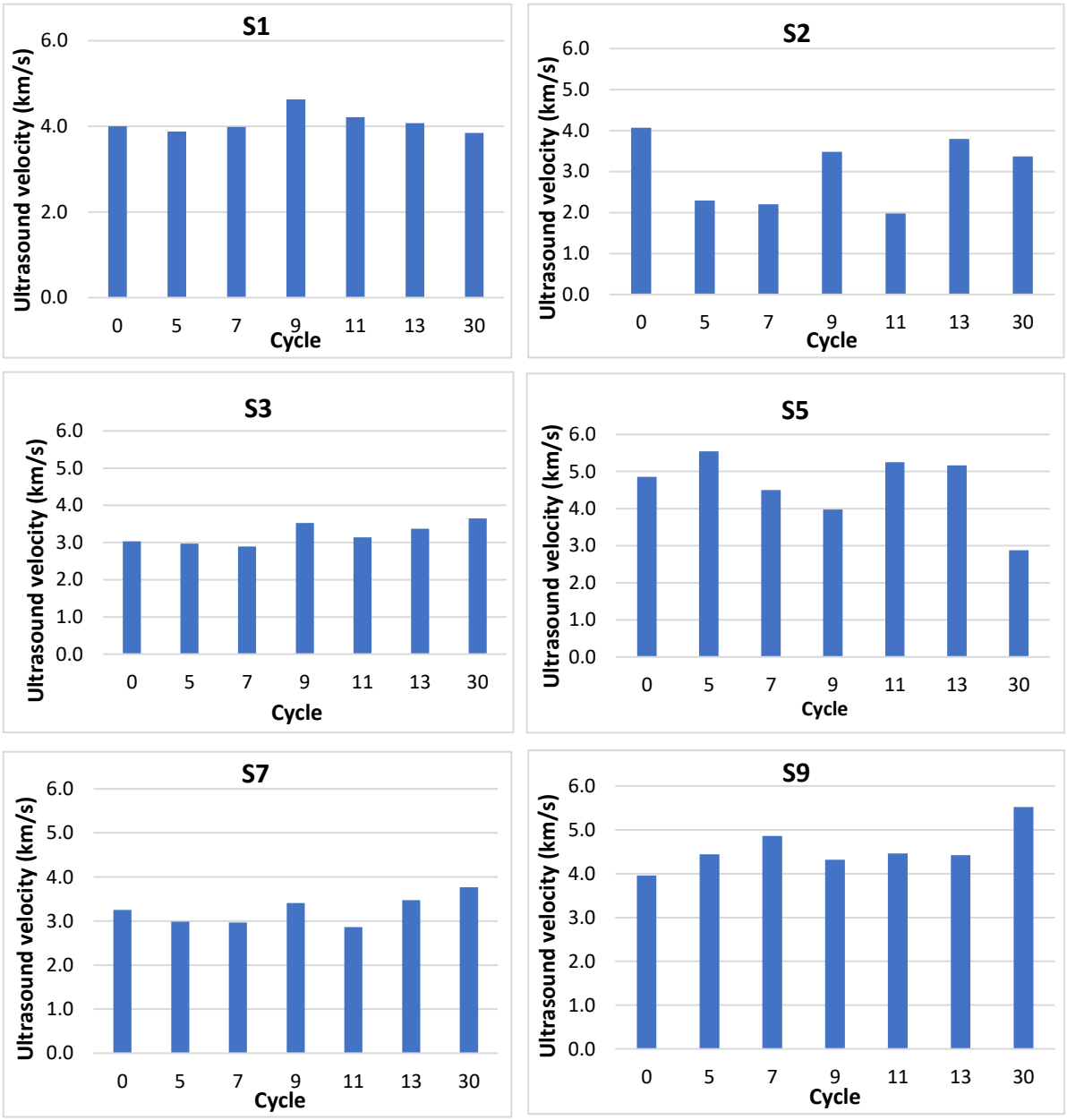

Figure 5. 2. 43 Ultrasound velocity of the specimens per KNO_3 salt solution-drying cycle

DOI: 10.15774/PPKE.BTK.2024.021

measured mass by the end of the cycle contains the mass of specimen, the mass of crystalized salt, and the mass of remaining solution inside the pores. As such, the mass during the short cycle is higher than the long one.

S1 shows an increase in its mass between 2-5 w/w %. The salt is visible and accumulates slightly on its surface. The ultrasound velocity of this specimen approximately remains steady at around 4 km/s (at the drying phase), see Figure 5.2.43. That indicates the stone experiences no changes inside its structure (no fissures or voids as well as no salt crystals accumulate inside). Due to its low porosity, the stone experiences a very low amount of salt crystals within its pores, making it a high resistant stone. The crystallisation of KNO_3 in S2 appears on its surface with a very fine thickness and does not lead to any visible damage. The specimen gains mass due to the salt crystallisation and that increase ranges between 2-8 w/w % during the experiment. The ultrasound velocity of this specimen alternatively increases and decreases. The velocity at drying phase is around 4 km/s, and it decreases to 2.2 km/s at the 5th and the 7th cycles. Afterwards, the velocity increases to 3.5 km/s at the 9th cycle then it decreases to 2 km/s at the 11th cycle. The velocity at the 13th cycle increases to 3.8 km/s, and then it slightly decreases to 3.4 km/s at the 30th cycle, see Figure 5.2.43.

The mass of S3 increases by a percentage of 4-8 w/w % that approximately equal to that of S2. However, a small crack (around 1 mm width) appears on the top of the specimen in the 6th cycle. That crack develops to a flaked part in the 10th cycle and the stone loses from its material after this cycle, see Figure 5.2.44. The salt accumulates in the specimen pore in mass, bigger than the amount of lost stone material. That could be noticed in Figure 5.2.42, the curve of S3 exhibited an increasing trend despite the loss of stone material. The ultrasound velocity of this specimen shows an increase trend; where the velocity rises from 3 km/s at dry phase to 3.64 km/s at the 30th cycle, see Figure 5.2.43. The salt crystals fill the pores of the specimen and do not lead to any damage in the stone structure.

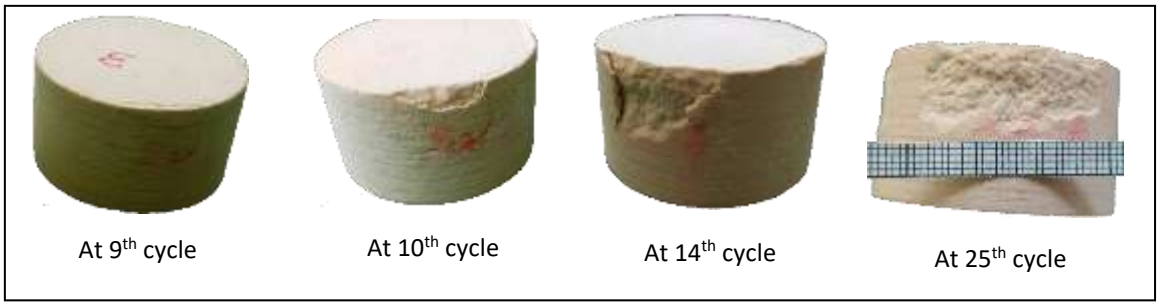

Figure 5. 2. 44 S3 specimen under potassium nitrate salt solution

DOI: 10.15774/PPKE.BTK.2024.021

S4 shows an increase mass trend due to crystallisation of KNO_3, where the mass increases between 2.5-6% of its initial mass. The ultrasound velocity of this specimen slightly decreases from 3.26 km/s at dry phase to 3 km/s at the 5th and the 7th cycles. After that, the velocity increases to 3.47 km/s at the 9th cycle, and then it decreases to 3 km/s at the 11th and the 13th cycles. Finally, the velocity rises to 3.52 km/s at the 30th cycle (see Figure 5.2.46).

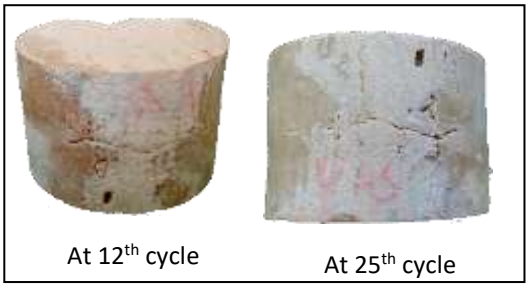

Figure 5. 2. 45 S5 specimen under potassium nitrate salt solution

As for S5, the salt is visible of the specimen surface without inducing any visible damage. Even though the salt accumulates in visible thickness (about 0.5mm) at some parts of S5 surface (see Figure 5.2.45), the mass does not highly increase (Figure 5.2.42). The percentage of gained mass during the experiment ranges 0.9-2 % that is lower than the previous specimens that have approximately the same porosity as this specimen. The ultrasound velocity of this specimen exhibits a decrease trend; where the velocity drops from 4.9 k/h (at drying phase) to 2.9 km/s at the 30th cycle, see Figure 5.2.43. The decrease of the velocity refers to voids and fissures creation inside the stone structure. In S7, the salt crystals appear on the specimen surface in very slight thickness. A small fragmented part is created in the specimens at the 10th cycle, which starts to fall down from the stone from the 11th cycle. Like in S3, even though the loss in stone material the accumulated salt inside the stone in mass higher the percentage of lost material. Therefore, the mass of the specimen exhibits an increase trend, where the specimen gains mass between 4-7 w/w % from the initial mass (see Figure 5.2.42). The ultrasound velocity of this specimen does not show great change during the experiment. The velocity oscillates between 3 km/s and 3.77 km/s (see Figure 5.2.43). S8 also exhibits an accumulation of salt on its surface in slight thickness, however, after the 8th cycle the pores on the surface start to be pitted. The mass of the specimen demonstrates an increasing trend, where the mass exhibits an increase of about 1.5-6 % (see Figure 5.2.42). The ultrasound velocity of this specimen demonstrates a slight increase trend; where the velocity rises from 2.7 km/s (at dry phase) to 3 km/s at the 30th cycle (see Figure 5.2.46). As for S9, which has the lowest porosity among the specimens, the mass of which slightly increases during the experiment. Its mass increases about 1 % of its initial mass, and the salt on its surface is barely visible (see Figure 5.2.42). Due to salt crystallisation inside its pores, the ultrasound velocity of this specimen shows an increase trend. The velocity increased from 4 km/s at dry phase to 5.5 km/s

DOI: 10.15774/PPKE.BTK.2024.021

at the 30th cycle (see Figure 5.2.43). S10 starts to increase its mass by the cycles. However, the specimen contains a weak part that starts to disintegrate and causes loss in stone material after the 6th cycle (see Figure 5.2.46). The amount of accumulated salt inside the pores is higher than the amount of lost stone material until the end of the experiment. However, after the 16th cycle, the amount of lost stone material increases but it is still lower than the amount of accumulated salt. Therefore, the trend of mass change decreases after the 16th cycle until the 30th cycle. The ultrasound velocity of this specimen shows a slight increase (like S8) from 3.4 km/s at dry phase to 3.7 km/s at 30th cycle.

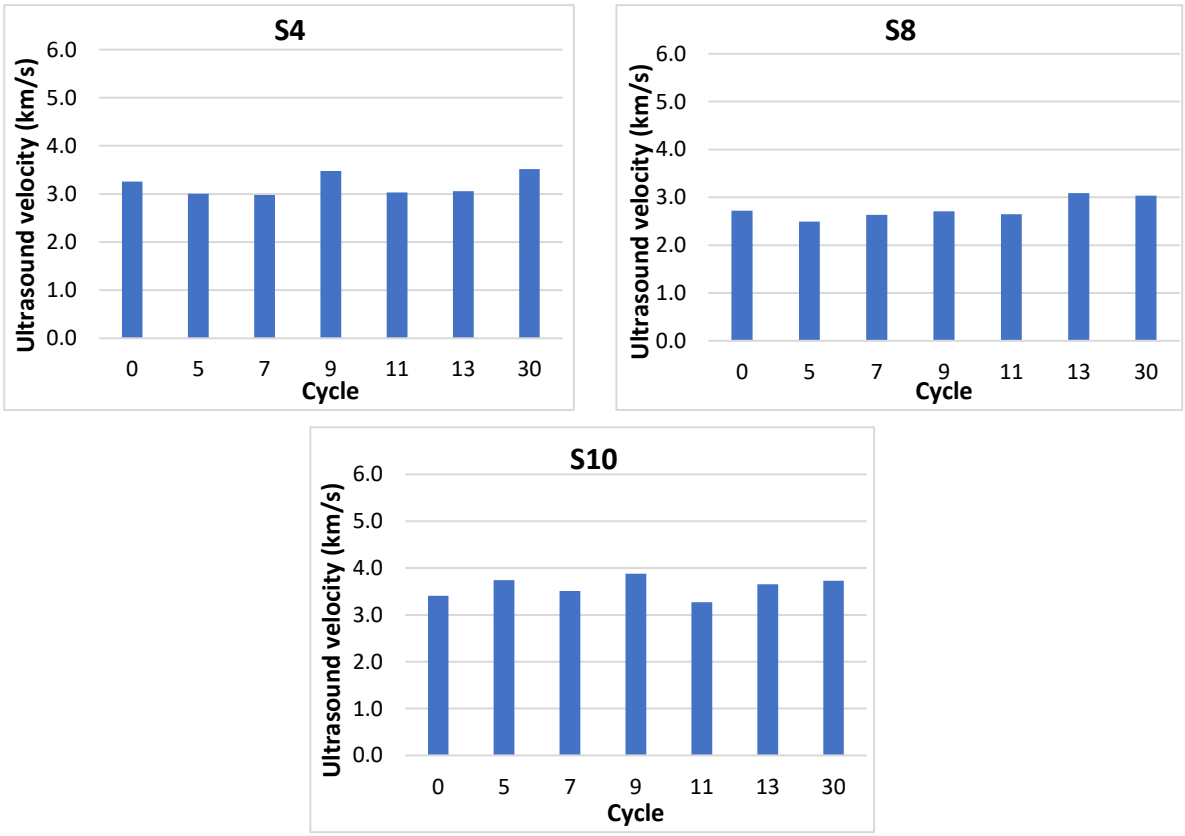

Figure 5. 2. 46 Ultrasound velocity of the specimens per KNO_3 salt solution-drying cycle

4- Magnesium sulfate ($MgSO_4.7H_2O$)

According to the phase diagram of $MgSO_4$, the salt can be found as monohydrate ($MgSO_4.H_2O$), hexahydrate ($MgSO_4.6H_2O$), or Epsomite ($MgSO_4.7H_2O$) depending on the temperature and the relative humidity. In our experiment condition, MgSO4.6H2O will crystallise in the first hours when the water inside the oven still provides proper humidity. When the water gradually evapourates, the humidity decreases and $MgSO_4.6H_2O$ dehydrates and crystalises as $MgSO_4.H_2O$. In the cooling period, the laboratory temperature is above 20°C at which the crystallisation of Epsomite ($MgSO_4.7H_2O$) is not possible, rather $MgSO_4.H_2O$

DOI: 10.15774/PPKE.BTK.2024.021

crystals might be found at the laboratory conditions. The specimens are subjected to the crystallisation pressure of $MgSO_4.6H_2O$ and $MgSO_4.H_2O$ (in the oven and cooling period), as well as to the hydration pressure during the 2 hours of immersion ($MgSO_4.H_2O$ hydrates to $MgSO_4.7H_2O$). The weathering form of this salt is exfoliation and layer detachment from the specimen surface.

S1 and S9 show similar resistance behaviour. The mass change of S1 exhibits an increase trend, where it increases about 3% from the initial mass at the end of the experiment (see Figure 5.2.47). The specimen does not show any weathering form on its surface. The ultrasound velocity of this specimen increases from 3.84 km/s (at dry phase) to 4.84 km/s (at the 40th cycle), see Figure 5.2.48. Salt accumulation inside the pores of the specimen increases its density and the ultrasound velocity as well. The mass of S9 slightly increases during the experiment and it reaches 1.3 % at the end of the experiment, see Figure 5.2.47. This specimen does not show any weathered form. However, very fine salt layer appears on its surface. The ultrasound measurement of this specimen exhibits an increase trend. The velocity rises from

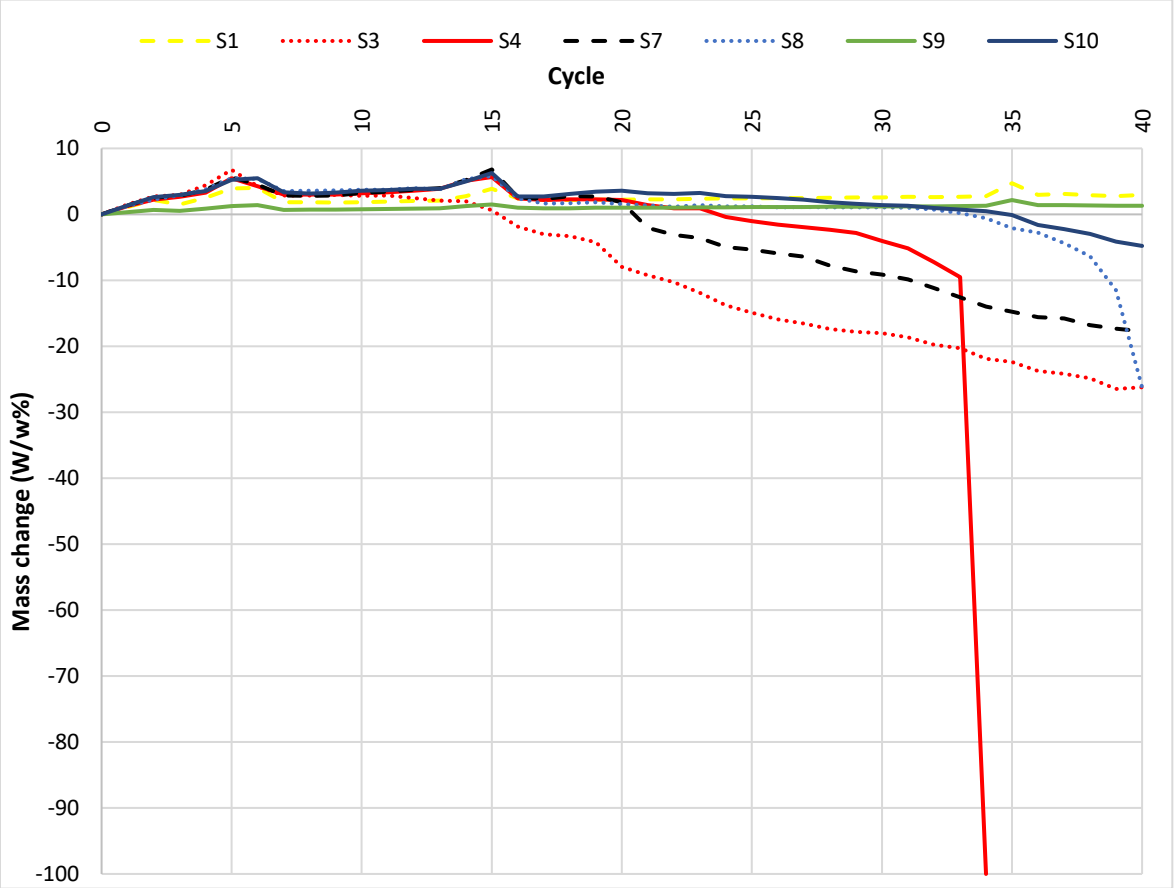

Figure 5. 2. 47 The mass change as a percentage from the initial dry mass of the specimens in magnesium sulfate solution

DOI: 10.15774/PPKE.BTK.2024.021

4.5 km/s (at dry phase) to 5.3 km/s (at the 40th cycle), see Figure 5.2.52. This specimen is the most resistant one compared to other specimens.

S3 and S7 show similar behaviour, where both start to lose their material at the 11th and the 15th cycles (respectively) and they have exfoliated surfaces that progressively develop during the test. They lose around 18 w/w % and 26 w/w % by the end of the test.

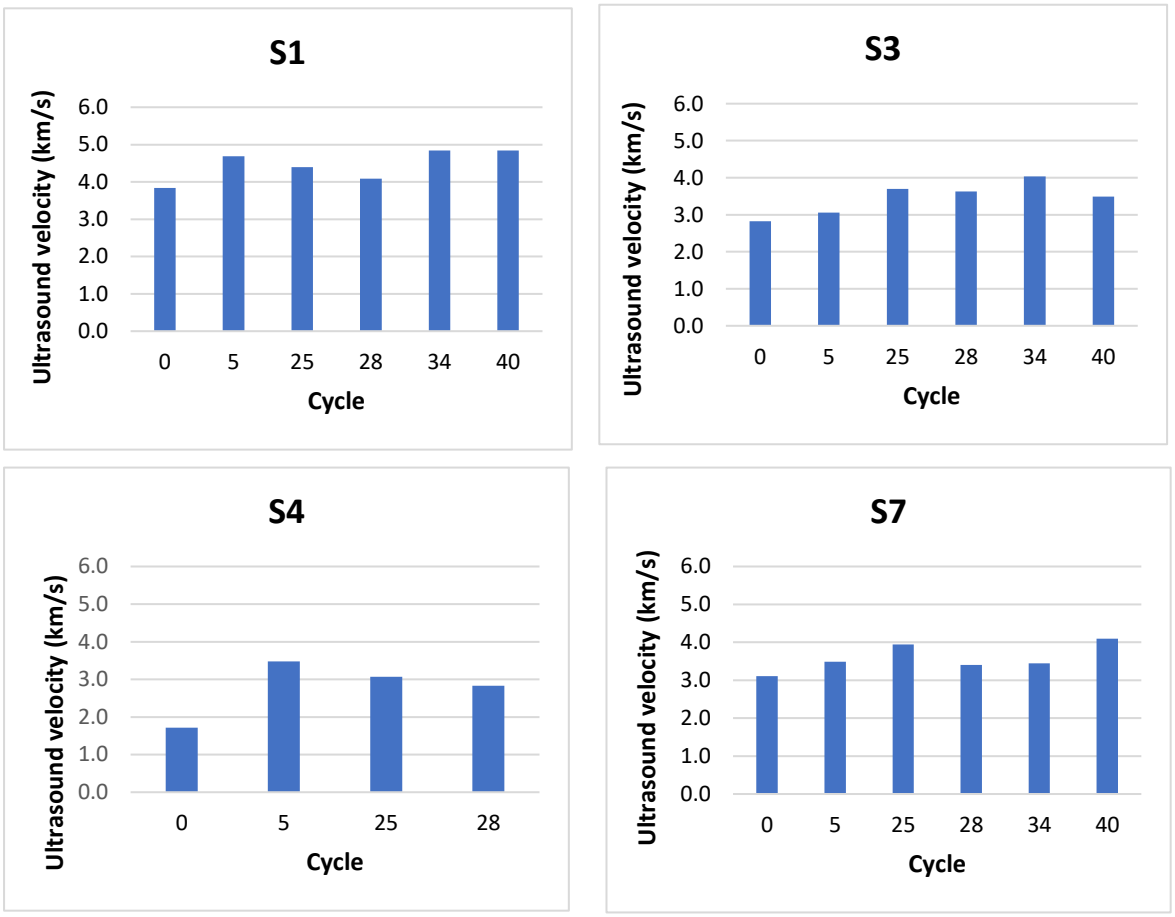

Figure 5. 2. 48 Ultrasound velocity of the specimens per $MgSO_4$ salt solution-drying cycle

The mass of S3 slightly increases up to the 11th cycle, and then the mass dramatically decreases until it reaches 26 % from its initial mass at the end of the experiment (see Figure 5.2.47). This specimen starts to lose its material by making irregular shapes on the stone surface with low percentage mass loss until the 12th cycle. From the 12th cycle upward, very thin layers from the surface start to detach from the specimen until the specimen has uniform surface, see Figure 5.2.49. The ultrasound velocity of the specimen exhibits an increased trend. The velocity slightly rises, even though the material loss, from 2.2 (at dry phase) to 3.49 km/s (at the 40th cycle), see Figure 5.2.48. The salt crystals inside its pores reduce the porosity of the specimen and increase its density, which leads to an increasing velocity. S7 gains mass until 15th cycle where its mass increased around 6 % from its initial mass. After that, the surface of

DOI: 10.15774/PPKE.BTK.2024.021

the specimen starts to weather as a form of exfoliation, and the specimen progressively begins to lose its material as a result. By the end of the 40th cycle, the specimen loses around 18 % from its initial mass, see Figure 5.2.47. The ultrasound velocity of this specimen also exhibits increase trend even though the material loss from 3.1 km/s (at dry phase) to 4.1 km/s (at the 40th cycle), see Figure 5.2.48.

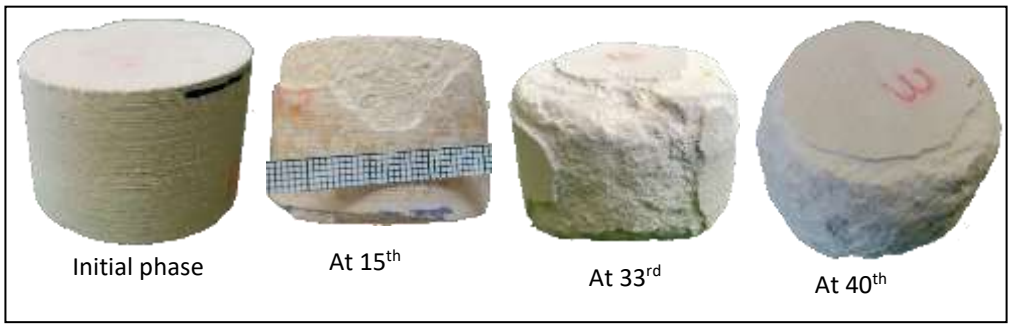

Figure 5. 2. 49 S3 specimen under magnesium sulfate salt solution

S4 has a crack appeared on its surface. This crack expands and develops along the height of the specimen until dividing it into two parts. The surface of the specimen also exhibits edges exfoliation of the top side (where the crack is present) by the 15th cycle (Figure 5.2.50). After that, its surface gradually exfoliates and the loss in its material reaches 10% from its initial mass before it breaks. Even though, the presence of a crack, the ultrasound of the specimen remarkably increases from 1.71 km/s (at dry phase) to 2.83 km/s (at the 28th cycle), see Figure 5.2.48. S8 and S10 have moderate resistant behaviours, compared to other specimens, where they lose around 1.6% and 4.7% from their initial mass.

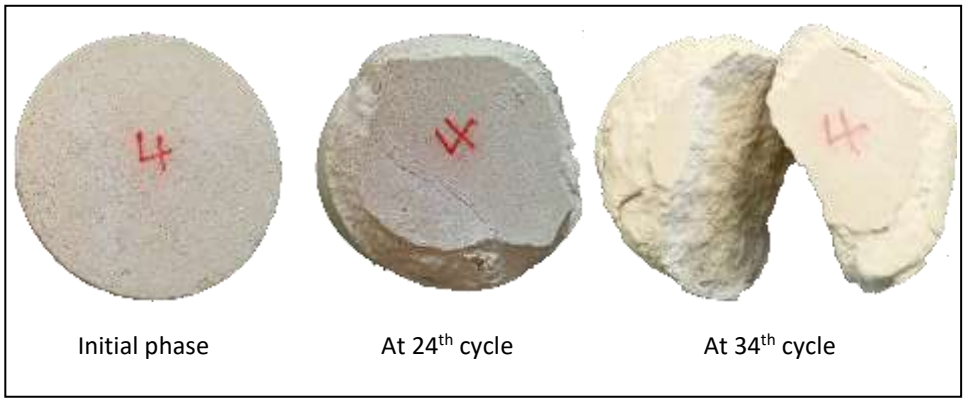

Figure 5. 2. 50 S4 specimen under magnesium sulfate salt solution

S8 exhibits an increase in its mass until the 15th cycle. After that, the edges of its top side start to detach and the surface exfoliates later resulting in a gradual stone material loss by the end of the 36th cycle around 1.6% from its initial mass (see Figure 5.2.47). Between the 37th and the 40th cycle, the mass of the specimen dramatically decreases until it reaches 26% from its

DOI: 10.15774/PPKE.BTK.2024.021

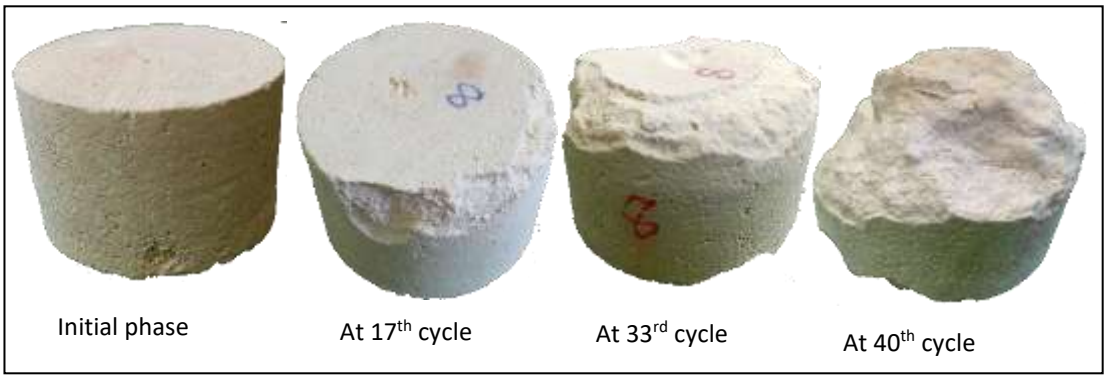

Figure 5. 2. 51 S8 specimen under magnesium sulfate salt solution

initial mass by the end of the 40th cycle, (Figure 5.2.51). The ultrasound velocity increases from 2.7 km/s (at dry phase) to 3.4 km/s (at the 34th cycle), however, the massive material loss leads to reduce the velocity to 2.62 km/s at the 40th cycle, see Figure 5.2.52. The mass of S10 increases until the 15th cycle, and then it decreases until the end of the experiment. The surface weathers as a form of exfoliation and loss in stone material after the 15th cycle. By the end of the 40th cycle, the specimen loses around 4.7% from its initial mass (see Figure 5.2.47). The ultrasound velocity of the specimen increases from 3 km/s (at dry phase) to 3.62 km/s at the 40th cycle, see Figure 5.2.52.

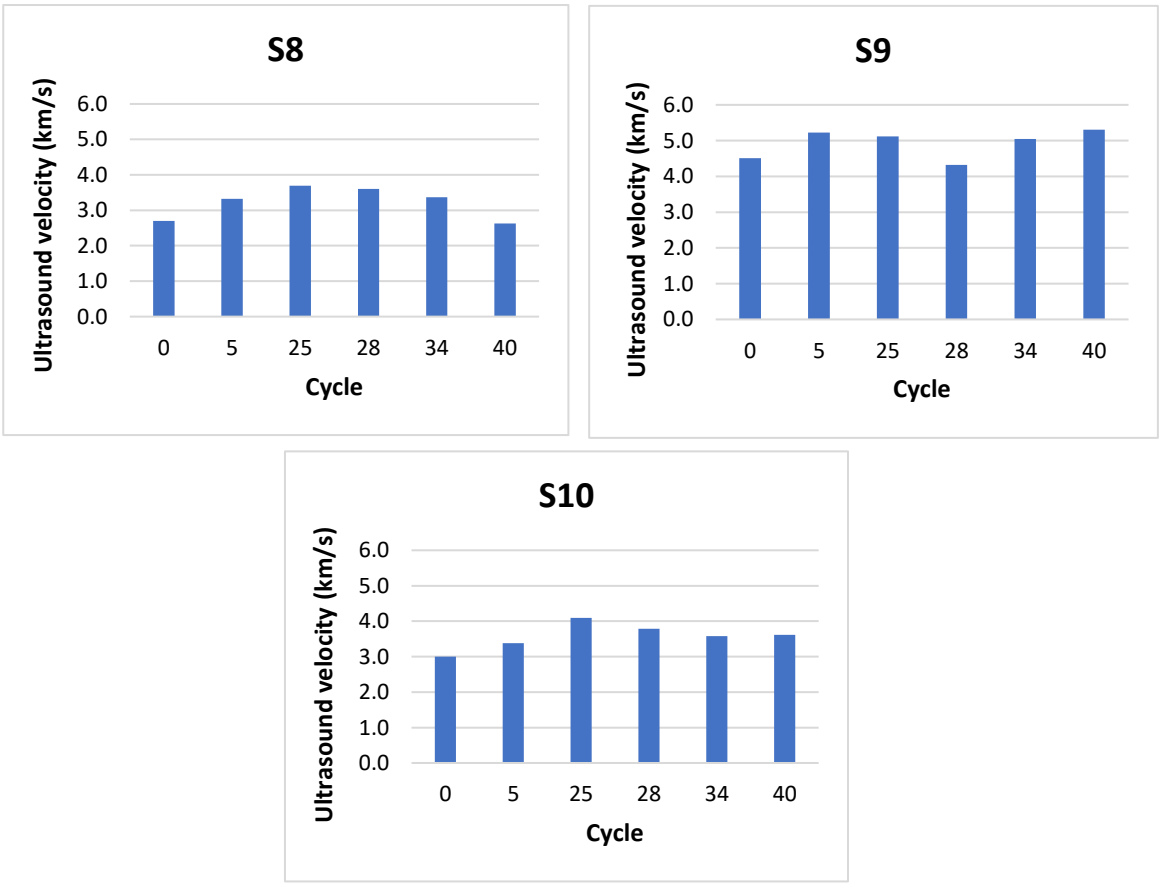

Figure 5. 2. 52 Ultrasound velocity of the specimens per $MgSO_4$ salt solution-drying cycle

DOI: 10.15774/PPKE.BTK.2024.021

6. Conclusion

DOI: 10.15774/PPKE.BTK.2024.021

Crac des Chevaliers is an important medieval monumental building that reflected the wonder of Crusaders military architecture in the East. The Islamic additions to the castle provide an amazing blend of the two cultures.

The preservation of this significant monument necessitates a thorough examination of all factors that may contribute to the site's stone deterioration. These factors are related to the castle's location; its geographical, environmental, and geological settings; building development events; and restoration records. All of these factors have a role in the stone deterioration, and it is challenging to understand the participation of these factors in order to have a sustainable preservation plan .

This study focuses on the stone deterioration cases in Crac the Chevaliers Castle with a detailed investigation of all aspects that might have a role (the geographical, environmental, and geological settings; meteorological data; stone lithotypes; stone decay cases; studying of the stone properties in-situ by using the non- destructive techniques and in the laboratory; and the evaluation of the stone durability). That can give a good database that might be needed when preparing the restoration and rehabilitation plan for the castle.

The location and the environmental conditions of the castle imply that water is the most promoting agent that challenges the historical building and motivates most of its deterioration cases. Water generally promotes the flourishing of many types of microorganism colonization and higher plants that become a serious issue in need of continuous control. Salt crystallization of NaCL that is bearing by the wind from the sea is one of the common deterioration cases at the castle.

Mechanical (impact) damage, microorganisms colonisation, salt efflorescence, discoloration, cracks, graffiti, splitting, erosion, and encrustation are the most serious issues identified in stone deterioration cases. The damaged stones in the castle need more attention regardless of the extent of damage because the shooted parts are a vital environment for growing microorganisms and higher plants that will have their deteriorative role and thus increase the deterioration rate in those stones.

The observations concluded from the deterioration mapping indicate that red-orange and grey microorganisms dominate the external north façades. However, the grey microorganisms can also be found in the external south, west, and east façades. Higher plants prevail on all façades regardless of the direction. Orange discolouration takes place in the external east and south façades, where the common factor is the high rate of solar radiation compared to the other

DOI: 10.15774/PPKE.BTK.2024.021

directions. Thus, this colour might be caused by sun radiation, and this issue needs more investigation. Pitting surfaces are one of the most characteristic cases in the castle, which result from the respiration process of microorganisms and higher plants.

The results of the Rilem tube penetration test reveal that the type of deterioration case can modify the wettability of the stone regardless of its lithotype. The stones with microorganisms on their surface prevent the stone from water absorption and therefore protect it. However, the salt efflorescence can have a protective or semi-protective role from water penetration according to the thickness of the salt. The microorganisms colonization on the damaged stonesurfaces by missiles or bullets cannot prevent the water absorption of those stones, where the results show that such stones have moderate absorption behaviour.

Schmidt hammer was used to test the same stones as Rilem tube. The results showed that the rebound value of the tested stones ranged between 25 and 48. The lithotype of the tested stones had no effect on the stone's rebound value. However, the type of deterioration has a significant impact on reducing the compressive strength of the tested stone, especially when these stones are fragmented or have eroded surfaces.

It was critical to gather stone samples from the castle for laboratory analysis. Ten stone core samples were taken from the castle. The stone cores collected (S1, S2, S3, S4, S5, S6, S7, S8, S9, S10) belonged to different building periods of the castle. As a result, the cores S1, S2, S5, S6, and S7 are most likely from the second Frankish period (from the beginning to the half of the 13th century), while S8 was taken from a building from the first Frankish period (from the beginning of the 12th century). S3, S4, S9, and S10 are cores taken from fallen stones, so determining their building period is based on the locations where they have been found fallen. According to that, S3 and S4 might belong to the second Frankish period, while S9 and S10 to the Mamluk one (around after 1271).

The petrographic analysis of the stone cores reveals that the stones fall into three major lithotype groups: 1) S1 and S9 are packstone microbioclasts. 2) S5 is a wackstone with micro bioclasts. 3) The stones S2, S3, S4, S7, S8, and S10 are microcrystalline dolomite. The open porosity of S1 and S9 stones is the lowest (around 14%v/v on average) and their tensile strength is about 6 Mpa, whereas the open porosity of microcrystalline dolomite stones is about 28%v/v on average and their tensile strength ranges between 1.5-4 Mpa. S5 has an open porosity of 27.8%V/v, but its tensile strength varies greatly between the crust and the sound part, 2.8 and 6.8 Mpa, respectively.

DOI: 10.15774/PPKE.BTK.2024.021

The drying test results showed that the micro bioclast packstone (S1 and S9) exhibit high effective drying behaviour because they have the lowest open porosity and less pore connectivity. S4, S8, and S10 have the highest amount of closed pores, around 4 v/v %. S4 has moderate drying behaviour (moderate water retention capacity), but S8 and S10 have fast drying behaviour because of their good pores connectivity and the presence of macropores. S2, S3, and S7 have the lowest closed pores (0.9; 0.3, and 0.7 v/v %, respectively) and approximately similar open porosity. S3 exhibited the highest water retention capacity, while S7 showed moderate capacity.

Regarding the water vapour permeability of the sound stone specimens, S2 has the lowest water vapour resistant factor value (5 [-]). However, S4 and S10 come in second-order with 7.6 and 8 [-], respectively. S3, S7, and S8 have moderate vapour resistant factor values (10, 13, and 15, respectively). S1 and S9 have the highest value of vapour resistant factors (18 and 26 [-] respectively). The crust affects significantly the water vapour permeability of the stones, where the extent of that effect is more related to type of crust and less to the thickness of the crust. The crust thickness of S1, S2, S3, S8, and S9 ranges from very fine 0.08 to 3 mm, and the water vapour permeability of those specimens is less than the water vapour permeability of the sound specimens of at most 20%. Thus, the crust of those specimens can be preserved from water vapour permeability criteria and when there is no other harmful effect of the crust on the stone. The crusts of S4, S7 and S10 (the crust thickness in S4 and S7 about 2 mm and 0.1 mm in S10) reduce the water vapour permeability to around 50% compared to the sound specimens. Such crusts are recommended to be removed from the conservation point of view. Because those kinds of crust are more likely to cause condensation areas inside the stone, which lead to further deterioration rate of the stone.

The assessment of the durability of the stone specimens was according to the salt aging test with several salt solutions [two simple salts (NaCL and KNO_3) and two of which are hydrated salts (Na_2SO_4 and $MgSO_4$)]. The specimens in this study show varying degrees of weathering depending on the type of salt solution, with Na2SO4 and MgSO4 being the most aggressive to the specimens when compared to the other two salt solutions. On the other hand, the specimens show varying degrees of durability in the salt solution ageing test. As a result, the difference in porosity and connectivity is reflected in the resistance of the specimens. The less porous stones are more prone to damage than the more compact ones. S1 and S9 are the most resistant stones to salt ageing in various salt solutions. Because of their high value of closed pores, S4, S8, and

DOI: 10.15774/PPKE.BTK.2024.021

S10 are resistant to salt ageing. Because they have less close porosity, S2, S3, and S7 have less durability against different salt solutions when compared to other specimens.

To conclude, this precious castle is listed in the world heritage list as one of the most important well preserved Crusader castle in the world, so a sustainable preservation plan forthe castle is a priority. The most urgent step that should be taken is restorating and replacing the damaged parts of the castle. The vegetation and the biocolonisation of the stone surfaces are challenging to control in such a location where the castle is. The removal of the biodeterioration crust from the stone surfaces should be carefully evaluated. Where some of these crusts might have a protective role in hindering or reducing the water penteration inside the stone, as the |Rilem tube penetration and permeability tests reveal, and that should be taken into consideration.

DOI: 10.15774/PPKE.BTK.2024.021

7. New scientific results

DOI: 10.15774/PPKE.BTK.2024.021

I. Water absorption under atmospheric conditions

New scientific result I.1

In my results, the ultrasound velocity vs dry or saturated densities of all specimens exhibit a positive linear relationship. The regression equation between dry density ($X_{1)}$ and ultrasound velocity (Y_1) is [Y_1=2.9X_1-2.5; R^2=0.87]; and the one between saturation density ($X_{2)}$ and ultrasound velocity (Y_2) is [Y_2=5.6X_2-9.5; R^2=0.83]. However, the ultrasound velocity does not always relate to saturation degree by a positive trend, as demonstrated in some studies(Candelaria, Kee, Yee, & Lee, 2020)[317] and (Kassab & Weller, 2015) [318]. My specimens exhibit two different trends in the relationship between ultrasound velocity and saturation degree, the first one is a decreasing trend and the other is decreasing to a certain saturation degree and then it changes to an increasing trend.

In S2, S5, S8, and S10, the relationship between ultrasound velocity and saturation degree is negative in that the velocity decreases with the increase of saturation degree during the water absorption under atmospheric conditions experiment. Those results agree with several studies such as (Kurtulus, Cakir, & Yoğurtcuoğlu, 2016) [319],(Garia, Pal, Ravi, &Nair, 2019) [320], and (Karakul & Ulusay, 2013) [321]. In the other specimens, S1, S3, S4, S7, and S9 the ultrasound velocity decreases with the increase of saturation degree up to 70% saturation degree in S1 and to around 80-90% in S3, S4, S7, and S9. Then they exhibit an increasing trend. The results of the previous specimens agree with the results of Niyartama & Fauzi (2017)study [322].

II. Drying characteristics

New scientific result II.1

[317] Ma Doreen Esplana Candelaria et al., "Effects of Saturation Levels on the Ultrasonic Pulse Velocities and Mechanical Properties of Concrete," *Materials* 14/1 (2020): 152.

[318] Mohamed A Kassab and Andreas Weller, "Study on P-Wave and S-Wave Velocity in Dry and Wet Sandstones of Tushka Region, Egypt," *Egyptian Journal of Petroleum* 24/1 (2015): 1–11.

[319] CENGİZ Kurtulus, S Cakir, and AHMET Yoğurtcuoğlu, "Ultrasound Study of Limestone Rock Physical and Mechanical Properties.," *Soil Mechanics & Foundation Engineering* 52/6 (2016).

[320] Siddharth Garia et al., "A Comprehensive Analysis on the Relationships between Elastic Wave Velocities and Petrophysical Properties of Sedimentary Rocks Based on Laboratory Measurements," *Journal of Petroleum Exploration and Production Technology* 9/3 (2019): 1869–81.

[321] Hasan Karakul and Resat Ulusay, "Empirical Correlations for Predicting Strength Properties of Rocks from P-Wave Velocity under Different Degrees of Saturation," *Rock Mechanics and Rock Engineering* 46/5 (2013): 981–99.

[322] Compacted Sandstone," in Journal of Physics: Conference Series, vol. 795 (2017), 12012.

DOI: 10.15774/PPKE.BTK.2024.021

Ozcelik & Ozguven (2014) argue that the second stage of drying, in which the capillary mechanism is dominated, is more rapid by the increase of open porosity [323]. In my results of Group 1 (drying at fixed temperature), the specimens (S1 and S9 are not included), exhibit the same behaviour (the evaporation rate of which is about 1.72 $kg/m^2*h^{0.5}$ on average) as what Ozcelik & Ozguven (2014) discuss [324]. The specimens S3, S4, S7, S8, and S10 have approximately the same open porosity (around 28v/v% on average) which implies the same drying behaviour (approximately the same evaporation rate).

New scientific result II.2

My results of the drying characteristics Group 3 (non-sealed specimens under room conditions) demonstrate that more porosity implies more prolonged drying period, i.e. ability to retain water inside pores. S3 has the highest porosity (32 v/v% total porosity and 31.7 v/v% open porosity), where it has the low closed pores and high percentage of tiny pores (see thin section description). By the end of the experiment (after 52 h), all the specimens are water saturated between 1-4%, however S3 has 10% saturation degree at the end of that period. As such, my results agree with Karaca (2010) study in which he concludes that the more prolonged drying period belongs to the more porous stone [325].

New scientific result II. 3

Regarding the specimens with higher porosity (S3, S4, S7, S8, and S10), the drying behaviours of S10 and S8 are fast because of their high percentage of big pores (250-500 μm, as the thin section reveals) and well-connected pore system, which lead to more effective drying characteristics compared with other specimens.

New scientific result II.4

In Group 2 (sealed specimens), which simulates the drying behaviour of the stone block in the building, the stage of the capillary water mechanism is delayed due to the evaporation from one surface. However, in Group 3 (with no sealing) that stage starts earlier comparing with Group 2.

III. Water vapour permeability

New scientific result III.1

[323] Y Ozcelik and A Ozguven, "Water Absorption and Drying Features of Different Natural Building Stones," Construction and Building Materials 63 (2014): 257–70.
[324] Ozcelik and Ozguven.
[325] Zeki Karaca, "Water Absorption and Dehydration of Natural Stones versus Time," Construction and Building Materials 24/5 (2010): 786–90.

DOI: 10.15774/PPKE.BTK.2024.021

According to Vázquez et al. (2013) results, the water vapour permeability is related to open porosity [326]. Keppert et al. (2016) study reveals that water vapour permeability increases with the increase of total porosity [327]. My results show that the specimens with approximately the same porosity (28v/v% open porosity and 30v/v% total porosity, in average) /S2, S3, S4, S7, S8, and S10/ have different values of water vapour permeability rate and these values are not close to each other / 3.8 E-11, 1.96 E-11, 2.6 E-11, 1.5 E-11, 1.3 E-11, and 2.45 E-11, respectively/. Thus my results confirm that the open and total porosity is not the key factor that controls the water vapour permeability. Rather it is important to examine the pore size distribution as Stück et.al.(2011) emphasize [328].

New scientific result III.2

In the field of conservation, the recommendation for using coating material is the water vapour permeability of the coating material should be equal to or 20% less than the water vapour permeability of the coated surface [329] [330]. My results demonstrate that in the crusted specimens of S1, S2, S3, S8, and S9 the water vapour permeability of which is 20 % less than the reference specimens(the same stones with no crust) regardless of the thickness of the crust (the crust thickness of these specimen rangesfrom very fine 0.08 to 3 mm). As such the cruts of S1, S2, S3 S8, and S9 can play a protective role from a conservation point of view regardless of the deteriorative role of the crust components. The crusts of S4, S7, and S10 (the crust thickness in S_4 and S_7 about 2 mm and 0.1 mm in S_{10}) reduce the water vapour permeability between 40-45% compared to the water vapour permeability of the reference stones. Therefore, the crusts of S4, S7, and S10 contribute to forming condensation areas inside the stone blocks, which will increase the weathering effect of those crusts.

IV. Salt ageing test

New scientific result IV.1

[326] P Vázquez et al., "Evaluation of the Petrophysical Properties of Sedimentary Building Stones in Order to Establish Quality Criteria," Construction and Building Materials 41 (2013): 868–78.
[327] Martin Keppert et al., "Water Vapor Diffusion and Adsorption of Sandstones: Influence of Rock Texture and Composition," Advances in Materials Science and Engineering 2016 (2016).
[328] Heidrun Stück, Siegfried Siegesmund, and Jörg Rüdrich, "Weathering Behaviour and Construction Suitability of Dimension Stones from the Drei Gleichen Area (Thuringia, Germany)," Environmental Earth Sciences 63/7 (2011): 1763–86.
[329] Rolf Snethlage and Katja Sterflinger, "Stone Conservation," in *Stone in Architecture* (2011), 411–544.
[330] Mariateresa Lettieri and Maurizio Masieri, "Performances and Coating Morphology of a Siloxane-Based Hydrophobic Product Applied in Different Concentrations on a Highly Porous Stone," *Coatings* 6/4 (2016): 60.

DOI: 10.15774/PPKE.BTK.2024.021

In the study of Ruiz-Agudo et al. (2007), the main deterioration pattern of the stone specimens under capillary absorption of sodium sulphate solution is layer detachment from the surface [331]. The stone specimens under the capillary absorption of magnesium sulphate are characterized by the gradual disintegration of the stone material. However, in my experiment, the stone specimens are totally immersed in salt solutions of the same salts; the deterioration patterns are reversed to Ruiz-Agudo et al. (2007) study. My results show that the disintegration of stone material characterizes the specimens immersed in sodium sulphate solution. The specimens immersed in magnesium sulphate exhibited layer detachment.

New scientific result IV.2

My results conclude that the more compact stones are less susceptible to damage than the more porous ones. S1 and S9 are the most resistant specimens under the used salt solutions (sodium sulphate , magnesium sulphate, sodium chloride, and potassium nitrates), where they do not exihibt any weight loss, because they are the less porous stones among the tested stones (the open porosity of them are 18v/v% and 11v/v%). My results agree with the results of some studies such as (Scrivano & Gaggero, 2020)[332] and (Ruedrich & Siegesmund, 2007) [333].

New scientific result IV.3

The results of Yu & Oguchi (2010) [334] and Jamshidi et al. (2013) [335] studies confirm that effective porosity has a significant effect on the amount of the absorbed salt and the induced damage. My results show that specimens with similar or approximate effective porosity have the same amount of absorbed salt solution. However, they do not induce the same damage degree (weight loss percentage). S2, S3, S4, S7, S8, and S10 (50w/w%, 45w/w%, 10 w/w%, 100 w/w %, 20 w/w%, and 15% weight loss under sodium sulphate solution); the

[331] E Ruiz-Agudo et al., "The Role of Saline Solution Properties on Porous Limestone Salt Weathering by Magnesium and Sodium Sulfates," Environmental Geology 52/2 (2007): 269–81.
[332] Simona Scrivano and Laura Gaggero, "An Experimental Investigation into the Salt-Weathering Susceptibility of Building Limestones," *Rock Mechanics and Rock Engineering* 53/12 (2020): 5329–43.
[333] Joerg Ruedrich and Siegfried Siegesmund, "Salt and Ice Crystallisation in Porous Sandstones," *Environmental Geology* 52/2 (2007): 343–67.
[334] Swe Yu and Chiaki T. Oguchi, "Role of Pore Size Distribution in Salt Uptake, Damage, and Predicting Salt Susceptibility of Eight Types of Japanese Building Stones," *Engineering Geology* 115/3–4 (2010): 226–36.
[335] Amin Jamshidi, Mohammad Reza Nikudel, and Mashalah Khamechiyan, "Estimating the Durability of Building Stones against Salt Crystallization: Considering the Physical Properties and Strength Characteristics," Geopersia 3/2 (2013): 35–48.

DOI: 10.15774/PPKE.BTK.2024.021

effective porosity of which around 28v/v% on average, do not exhibit the same degree of resistance. My results show that S4, S8, and S10 are more durable and resistant than the others (S2, S3, and S7) because they have a high percentage of closed porosity (around 4v/v%) compared with S2, S3, and S7 that the closed porosity of which about 0.5v/v% in average.

New scientific result IV.4

The observation of specimen behaviour under the hydrated salt solutions (sodium sulphate and magnesium sulphate) in my experiment reveals that the break down of the specimen (such as S7 and S5 in sodium sulphate solution and S4 in magnesium sulphate) occurs during the immersion period. That observation corresponds to the observation of Yu & Oguchi (2010a) [336], where the authors argue that during the immersion period, the highest crystallization pressure induces as the salt solution is at the greatest degree of supersaturation.

New scientific result IV.5

In my experiment under potassium nitrate solution, the specimens experience salt efflorescence with a visible thickness on the surfaces with no weight loss. My results agree with the results of Vazquez et al. (2018) study, where they realize that the accumulating on the stones surfaces when they dry the specimens at 75°C [337].

New scientific result IV.6

Salim et al. (2020) figured out that the crystallization of sodium chloride at high temperature (70°C) leads to form salt crystals with tiny legs that lift the salt crystals from the stone surface [338]. And after a while, those legs cannot hold the salt crystals, so the salt crystals fall from the stone surface in a process called "self-cleaning". In my experiment, the stone specimens do not experience salt efflorescence, rather visible salt crystals can be seen near the bottom of the specimens inside the tray of the oven after the drying period in each cycle.

[336] Swe Yu and Chiaki T Oguchi, "Is Sodium Sulphate Invariably Effective in Destroying Any Type of Rock?," Geological Society, London, Special Publications 333/1 (2010): 43–58.
[337] Patricia Vazquez, Lucas Sartor, and Céline Thomachot-Schneider, "Influence of Substrate and Temperature on the Crystallization of KNO3 Droplets Studied by Infrared Thermography," Progress in Earth and Planetary Science 5/1 (2018).
[338] Herish Salim et al., "Self-Lifting NaCl Crystals," Journal of Physical Chemistry Letters 11/17 (2020): 7388–93.

DOI: 10.15774/PPKE.BTK.2024.021

New scientific result IV.7

My results of the salt ageing test of different salt solutions reveal that the salt solution are not at the same level of damaging to stone specimens. Potassium nitrates is the less damaging salt, where all specimens show no weight loss. Sodium chloride is a moderate damaging salt where the weight loss ranges between 0 w/w% (S1 and S9) to 8w/w% (for S2); except for S5 and S7 that are broken during the test. Magnesium sulphate has more damaging effect than sodium chloride. The weight loss of the specimens ranges between 0 w/w% (S1 and S9) to 27 w/w% (for S3), except for S4 that is broken during the test. Sodium sulphate is the most damaging salt. S5 and S7 are broken in the very first cycles (12th and 9th cycle out of 50 cycles); however The weight loss of the spcimens ranges between 0 w/w% (S1 and S9) to 50 w/w% (for S2).

V. Rilem tube penetration test

New scientific result V.1

The results of the Rilem tube penetration test demonstrate that the microorganism colonization and presence of salt efflorescence modify the wettability of stone property. The tested stones colonized by colonizations /grey and red-orange microorganisms/ mainly show no absorption behaviour or in some cases very low absorption behaviour. However, the stones previously exposed to mechanical shock (such as missile fragmentation) and colonized by microorganisms exhibit enhanced absorption behaviour (moderate one). As such the microorganism colonizations play a protective role in preventing the capillary water absorption of wind-driven rainwater.

The results of the Rilem tube conducted from salt efflorescence stone show that salt thickness is an important factor. Some stones do not exhibit any absorption behaviour because the water pressure applied from the type is not enough to penetrate the thick salt layer. However, In other tested stones, the absorption behaviour of which changes, where the absorption increases after a while. Firstly, the water pressure inside the tube allows to penetrate (dissolve) the salt layer, then the absorption enhances because the remaining salt cannot obstruct the capillary water absorption.

VI. Deterioration mapping

New scientific result VI.1

The results of the deterioration mapping of three external facades with different directions (south, east, and north facades) show that the orientation of the façade is a key factor in the

DOI: 10.15774/PPKE.BTK.2024.021

presence of some distinct deterioration types. The discoloration with orange is a characteristic stone deterioration type that is found in the south and east external facades. However, the grey microorganisms colonization is dominated in north and west facades. The red-orange microorganisms colonization can be found in the north façade in shaded moisturized areas.

DOI: 10.15774/PPKE.BTK.2024.021

References:

Abdelaali, R., Abderrahim, B., Mohamed, B., Yves, G., Abderrahim, S., Mimoun, H., & Jamal, S. (2013). Prediction of porosity and density of calcarenite rocks from P-wave velocity measurements. *International Journal of Geosciences*, *2013*.

Abdulla, H., May, E., Bahgat, M., & Dewedar, A. (2008). Characterisation of actinomycetes isolated from ancient stone and their potential for deterioration. *Pol J Microbiol*, *57*(3), 213–220.

Adamo, P., & Violante, P. (2000). Weathering of rocks and neogenesis of minerals associated with lichen activity. *Applied Clay Science*, *16*(5–6), 229–256.

Adamopoulos, E. (2021). Learning-based classification of multispectral images for deterioration mapping of historic structures. *Journal of Building Pathology and Rehabilitation*, *6*(1), 1–15.

Adamopoulos, E., & Rinaudo, F. (2021). Combining multiband imaging, photogrammetric techniques, and FOSS GIS for affordable degradation mapping of stone monuments. *Buildings*, *11*(7), 304.

Ahmed, N., Khalid, P., & Anwar, A. W. (2016). Rock physics modeling to assess the impact of spatial distribution pattern of pore fluid and clay contents on acoustic signatures of partially-saturated reservoirs. *Acta Geodaetica et Geophysica*, *51*(1), 1–13.

Akbulut, G., & Yildiz, A. (2010). An overview to lichens: the nutrient composition of some species. *Kafkas Üniversitesi Fen Bilimleri Enstitüsü Dergisi*, *3*(2), 79–86.

Al-Khateeb, E. (2008). *Masonry Structures at the Crusader Castles in Syria: Building Material, Buildingg Technique, Damage and Conservation Methodology*.

Albertano, P, Bruno, L., Bellezza, S., & Paradossi, G. (2000). Polysaccharides as a key step in stone bio-erosion. *Proceedings of the 9th International Congress on Deterioration and Conservation of Stone*, 425–432.

Albertano, Patrizia. (2012). Cyanobacterial biofilms in monuments and caves. In *Ecology of cyanobacteria II* (pp. 317–343). Springer.

Albright, W. F. (1936). Archaeological Exploration and Excavation in Palestine and Syria, 1935. *American Journal of Archaeology*, *40*(1), 154–167.

DOI: 10.15774/PPKE.BTK.2024.021

Aliabdo, A. A. E. (2012). Reliability of using nondestructive tests to estimate compressive strength of building stones and bricks. *Alexandria Engineering Journal*, *51*(3), 193–203.

Almeida, M. T., Mouga, T., & Barracosa, P. (1994). The weathering ability of higher plants. The case of Ailanthus altissima (Miller) Swingle. *International Biodeterioration & Biodegradation*, *33*(4), 333–343.

Alves, C., Figueiredo, C., Maurício, A., Braga, M. A. S., & Aires-Barros, L. (2011). Limestones under salt decay tests: assessment of pore network-dependent durability predictors. *Environmental Earth Sciences*, *63*(7), 1511–1527.

Andreotti, S., Franzoni, E., Ruiz-Agudo, E., Scherer, G. W., Fabbri, P., Sassoni, E., & Rodriguez-Navarro, C. (2019). New polymer-based treatments for the prevention of damage by salt crystallization in stone. *Materials and Structures/Materiaux et Constructions*, *52*(1), 1–28. https://doi.org/10.1617/s11527-018-1309-6

Andriani, G. F., & Walsh, N. (2010). Petrophysical and mechanical properties of soft and porous building rocks used in Apulian monuments (south Italy). *Geological Society, London, Special Publications*, *333*(1), 129–141.

Angeli, M. (2007). *Multiscale study of stone decay by salt crystallization in porous networks*. Université de Cergy Pontoise.

Anold, J. R., Garrabrants, A. C., Samson, E., Flach, G. P., & Langton, C. A. (2009). *Moisture Transport Review*. CBP-TR-2009-002 Cementitous Barriers Partnership Phoenix, AZ, USA.

Apostolopoulou, M., Aggelakopoulou, E., Bakolas, A., & Moropoulou, A. (2018). Compatible mortars for the sustainable conservation of stone in masonries. In *Advanced Materials for the Conservation of Stone* (pp. 97–123). Springer.

Ascaso, C. (2000). *Lichens on rock substrates: observation of the biomineralization processes*.

Aydin, A., & Basu, A. (2005). The Schmidt hammer in rock material characterization. *Engineering Geology*, *81*(1), 1–14.

Ayogu, P., Ezugwu, M., & Eze, F. (2020). Principle of Common-ion Effect and its Application in Chemistry: a Review. *Journal of Chemistry Letters*, *1*(2), 77–83.

DOI: 10.15774/PPKE.BTK.2024.021

Baechle, G. T., Eberli, G. P., Weger, R. J., & Massaferro, J. L. (2009). Changes in dynamic shear moduli of carbonate rocks with fluid substitution. *Geophysics*, *74*(3), E135–E147.

Balakrishna, M. N., Rahman, M. M., Chamberlain, D. A., Mohammad, F., & Evans, R. (2013). Determination of flow rate of water in concrete by Rilem tube method. *International Journal of Structural and Civil Engineering Research*, *2*(4), 98–109.

Balland-Bolou-Bi, C., Saheb, M., Bousserrhine, N., Abbad-Andaloussi, S., Alphonse, V., Nowak, S., Chabas, A., Desboeufs, K., & Verney-Carron, A. (2016). Effect of microorganism activities in a polluted area on the alteration of limestone used in historical buildings. *SCIENCE AND ART: A FUTURE FOR STONE*, 25.

Barrier, E., Machhour, L., & Blaizot, M. (2014). *Petroleum systems of Syria*.

Bartolini, M., & Monte, M. (2000). Chemiolithotrophic bacteria on stone monuments: Cultural methods set up. *Proceedings of the 9th International Congress on Deterioration and Conservation of Stone*, 453–460.

Barton, N., & Choubey, V. (1977). The shear strength of rock joints in theory and practice. *Rock Mechanics*, *10*(1), 1–54.

Batič, F. (2002). Bioindication of sulphur dioxide pollution with lichens. In *Protocols in lichenology* (pp. 483–503). Springer.

Bekker, M., Erich, S. J. F., Hermanns, S. P. M., van Maris, M., Huinink, H. P., & Adan, O. C. G. (2015). Quantifying discoloration caused by the indoor fungus Penicillium rubens on building material at controlled humidity. *Building and Environment*, *90*, 60–70.

Bell, F. G. (2007). *Engineering geology*. Elsevier.

Belozerskaya, T. A., Gessler, N. N., & Aver'yanov, A. A. (2017). Melanin pigments of fungi. *Fungal Metabolites*, *2017*, 263–291.

Benavente, D., García del Cura, M. A., García-Guinea, J., Sánchez-Moral, S., & Ordóñez, S. (2004). Role of pore structure in salt crystallisation in unsaturated porous stone. *Journal of Crystal Growth*, *260*(3–4), 532–544. https://doi.org/10.1016/j.jcrysgro.2003.09.004

Benharbit, M., Dahmani, J., El Harech, M., Cherif, S., Dabghi, A., Belahbib, N., & Ziani, M. (2021). Checklist and role of vegetation in the deterioration of archaeological sites contribution to the knowledge of the plants of chellah (rabat, morocco). *Plant cell*

DOI: 10.15774/PPKE.BTK.2024.021

biotechnology and molecular biology, 124–140.

Bergstad, M., & Shokri, N. (2016). Evaporation of NaCl solution from porous media with mixed wettability. *Geophysical Research Letters*, *43*(9), 4426–4432.

Bhargav, J. S., Mishra, R. C., & Das, C. R. (1999). Environmental deterioration of stone monuments of Bhubaneswar, the temple city of India. *Studies in Conservation*, *44*(1), 1–11.

Bindschedler, S., Cailleau, G., & Verrecchia, E. (2016). Role of fungi in the biomineralization of calcite. *Minerals*, *6*(2), 41.

Bjelland, T., Sæbø, L., & Thorseth, I. H. (2002). The occurrence of biomineralization products in four lichen species growing on sandstone in western Norway. *The Lichenologist*, *34*(5), 429–440.

Boas, A. (2006). *Archaeology of the Military Orders: A Survey of the Urban Centres, Rural Settlements and Castles of the Military Orders in the Latin East (c. 1120-1291)*. Routledge.

Bonazza, A., Natali, C., Ghedini, N., Vaccaro, C., & Sabbioni, C. (2015). Oxalate patinas on stone monuments in the Venetian Lagoon: Characterization and origin. *International Journal of Architectural Heritage*, *9*(5), 542–552.

Bonde, S. (1994). *Fortress-churches of Languedoc: architecture, religion, and conflict in the High Middle Ages*. Cambridge University Press.

Borrelli, E., & Urland, A. (1999). *ARC laboratory handbook: Salts*. https://www.iccrom.org/sites/default/files/ICCROM_14_ARCLabHandbook02_en.pdf

Bourgès, A. (2006). *Holistic correlation of physical and mechanical properties of selected natural stones for assessing durability and weathering in the natural environment.* lmu.

Brunetaud, X., Luca, L. De, Janvier-Badosa, S., Beck, K., & Al-Mukhtar, M. (2012). Application of digital techniques in monument preservation. *European Journal of Environmental and Civil Engineering*, *16*(5), 543–556.

Buj, O., & Gisbert, J. (2010). Influence of pore morphology on the durability of sedimentary building stones from Aragon (Spain) subjected to standard salt decay tests. *Environmental Earth Sciences*, *61*(7), 1327–1336.

DOI: 10.15774/PPKE.BTK.2024.021

Bungartz, F., & Garvie, L. A. J. (2004). Anatomy of the endolithic Sonoran Desert lichen Verrucaria rubrocincta Breuss: implications for biodeterioration and biomineralization. *The Lichenologist*, *36*(1), 55–73.

Burford, E P, Fomina, M., & Gadd, G. M. (2003). Fungal involvement in bioweathering and biotransformation of rocks and minerals. *Mineralogical Magazine*, *67*(6), 1127–1155.

Burford, Euan P, Hillier, S., & Gadd, G. M. (2006). Biomineralization of fungal hyphae with calcite ($CaCO_3$) and calcium oxalate mono-and dihydrate in carboniferous limestone microcosms. *Geomicrobiology Journal*, *23*(8), 599–611.

Burrows, M. (1932). Palestinian and Syrian Archaeology in 1931. *Bulletin of the American Schools of Oriental Research*, *45*(1), 20–32.

Buyuksagis, I. S., & Goktan, R. M. (2007). The effect of Schmidt hammer type on uniaxial compressive strength prediction of rock. *International Journal of Rock Mechanics and Mining Sciences*, *2*(44), 299–307.

C Gaylarde, C. (2020). Influence of environment on microbial colonization of historic stone buildings with emphasis on cyanobacteria. *Heritage*, *3*(4), 1469–1482.

Cammalleri, V., Lyon, E. G., & Gumpertz, S. (2003). Condensation in the building envelope: expectation and realities. *Proceedings of" SSPC*, 210–219.

Camuffo, D. (2014). *Microclimate studies for cultural heritage: conservation, restoration and maintenance of indoor and outdoor monuments*. Elsevier New York.

Camuffo, Dario. (1984). Condensation-evaporation cycles in pore and capillary systems according to the Kelvin model. *Water, Air, and Soil Pollution*, *21*(1), 151–159.

Candelaria, M. D. E., Kee, S.-H., Yee, J.-J., & Lee, J.-W. (2020). Effects of saturation levels on the ultrasonic pulse velocities and mechanical properties of concrete. *Materials*, *14*(1), 152.

Caneva, G, Galotta, G., Cancellieri, L., & Savo, V. (2009). Tree roots and damages in the Jewish catacombs of Villa Torlonia (Roma). *Journal of Cultural Heritage*, *10*(1), 53–62.

Caneva, Giulia, Nugari, M. P., Nugari, M. P., & Salvadori, O. (2008). *Plant biology for cultural heritage: biodeterioration and conservation*. Getty Publications.

Cappitelli, F., Nosanchuk, J. D., Casadevall, A., Toniolo, L., Brusetti, L., Florio, S., Principi,

P., Borin, S., & Sorlini, C. (2007). Synthetic consolidants attacked by melanin-producing fungi: case study of the biodeterioration of Milan (Italy) cathedral marble treated with acrylics. *Applied and Environmental Microbiology*, *73*(1), 271–277.

Carter, N. E. A., & Viles, H. A. (2003). Experimental investigations into the interactions between moisture, rock surface temperatures and an epilithic lichen cover in the bioprotection of limestone. *Building and Environment*, *38*(9–10), 1225–1234.

Ġelik, M. Y., & Aygün, A. (2019). The effect of salt crystallization on degradation of volcanic building stones by sodium sulfates and sodium chlorides. *Bulletin of Engineering Geology and the Environment*, *78*(5), 3509–3529. https://doi.org/10.1007/s10064-018-1354-y

Ġelik, M. Y., & Kaçmaz, A. U. (2016). The investigation of static and dynamic capillary by water absorption in porous building stones under normal and salty water conditions. *Environmental Earth Sciences*, *75*(4), 1–19.

Charola, A. E. (2000). Salts in the deterioration of porous materials: an overview. *Journal of the American Institute for Conservation*, *39*(3), 327–343.

Charola, A. E., & Bläuer, C. (2015). Salts in masonry: an overview of the problem. *Restoration of Buildings and Monuments*, *21*(4–6), 119–135.

Charola, A. E., Rousset, B., & Bläuer, C. (2017). Deicing salts: an overview. *Proceedings of the 4th International Conference on Salt Weathering of Buildings and Stone Sculptures SWBSS 2017*.

Charola, A. E., & Wendler, E. (2015). An overview of the water-porous building materials interactions. *Restoration of Buildings and Monuments*, *21*(2–3), 55–65.

Chu, W.-L., Tneh, S.-Y., & Ambu, S. (2013). A survey of airborne algae and cyanobacteria within the indoor environment of an office building in Kuala Lumpur, Malaysia. *Grana*, *52*(3), 207–220.

Conti, M. E., & Cecchetti, G. (2001). Biological monitoring: lichens as bioindicators of air pollution assessment—a review. *Environmental Pollution*, *114*(3), 471–492.

Couturier, M., & Boucher, C. (2011). Dynamic water vapor permeance of building materials and the benefits to buildings. *Proceedings of the 26th RCI International Convention and Trades Show, Reno, NV, USA*, *29*.

DOI: 10.15774/PPKE.BTK.2024.021

Crispim, C. A., & Gaylarde, C. C. (2005). Cyanobacteria and biodeterioration of cultural heritage: a review. *Microbial Ecology*, *49*(1), 1–9.

Cultrone, G., Russo, L. G., Calabrò, C., Uroševič , M., & Pezzino, A. (2008). Influence of pore system characteristics on limestone vulnerability: a laboratory study. *Environmental Geology*, *54*(6), 1271–1281.

Czichos, H., Saito, T., & Smith, L. E. (2011). *Springer handbook of metrology and testing*. Springer Science & Business Media.

Dahmani, J., Benharbit, M., Fassar, M., Hajila, R., Zidane, L., Magri, N., & Belahbib, N. (2020). Vascular plants census linked to the biodeterioration process of the Portuguese city of Mazagan in El Jadida, Morocco. *Journal of King Saud University-Science*, *32*(1), 682–689.

Dalimi, M., Baghdad, B., Zakarya, D., Taleb, A., & Iñigo, A. C. (2014). *Vegetations as biodeterioration agents on archaeological stones: Comparative study of plant species found on the walls of some Moroccan historical monuments*.

De Kock, T., Turmel, A., Fronteau, G., & Cnudde, V. (2017). Rock fabric heterogeneity and its influence on the petrophysical properties of a building limestone: Lede stone (Belgium) as an example. *Engineering Geology*, *216*, 31–41.

De La Torre, M., Gomez-Alarcon, G., Vizcaino, C., & Garcia, M. (1992). Biochemical mechanisms of stone alteration carried out by filamentous fungi living in monuments. *Biogeochemistry*, *19*(3), 129–147.

Deere, D. U., & Miller, R. P. (1966). *Engineering classification and index properties for intact rock*. Illinois Univ At Urbana Dept Of Civil Engineering.

Dei, L., Mauro, M., Baglioni, P., Manganelli Del Fà, C., & Fratini, F. (1999). Growth of crystal phases in porous media. *Langmuir*, *15*(26), 8915–8922. https://doi.org/10.1021/la981074f

Dejian, L., Guilian, W., Liqiang, H., Peiyu, L., Manchao, H., Guoxing, Y., Qimin, T., & Cheng, C. (2011). Analysis of microscopic pore structures of rocks before and after water absorption. *Mining Science and Technology (China)*, *21*(2), 287–293.

Delegou, E. T., Mourgi, G., Tsilimantou, E., Ioannidis, C., & Moropoulou, A. (2019). A multidisciplinary approach for historic buildings diagnosis: The case study of the

Kaisariani monastery. *Heritage*, *2*(2), 1211–1232.

Delgado, J., Guimarffies, A. S., De Freitas, V. P., Antepara, I., Koč í, V., & Č erný, R. (2016). Salt damage and rising damp treatment in building structures. *Advances in Materials Science and Engineering*, *2016*.

Derluyn, H., Dewanckele, J., Boone, M. N., Cnudde, V., Derome, D., & Carmeliet, J. (2014). Crystallization of hydrated and anhydrous salts in porous limestone resolved by synchrotron X-ray microtomography. *Nuclear Instruments and Methods in Physics Research, Section B: Beam Interactions with Materials and Atoms*, *324*, 102–112. https://doi.org/10.1016/j.nimb.2013.08.065

Desarnaud, J., Bonn, D., & Shahidzadeh, N. (2016). The Pressure induced by salt crystallization in confinement. *Scientific Reports*, *6*, 23–26. https://doi.org/10.1038/srep30856

Dinçer, İ ., & Orhan, A. (2016). Effect of pore size distribution on capillary water absorption characteristics of pyroclastic rock. *Conference: International Black Sea Mining & Tunnelling Symposium, Trabzon-Turkey*, 311–318.

Ding, X., Lan, W., Wu, J., Hong, Y., Li, Y., Ge, Q., Urzì, C., Katayama, Y., & Gu, J.-D. (2020). Microbiome and nitrate removal processes by microorganisms on the ancient Preah Vihear temple of Cambodia revealed by metagenomics and N-15 isotope analyses. *Applied Microbiology and Biotechnology*, *104*(22), 9823–9837.

Doehne, E., Selwitz, C., & Carson, D. (2002). The damage mechanism of sodium sulfate in porous stone. *Proceed. of the SALTeXPERT Meeting*, 27–146.

Dong, H., Gao, P., & Ye, G. (2017). Characterization and comparison of capillary pore structures of digital cement pastes. *Materials and Structures*, *50*(2), 1–12.

Dornieden, Th, Gorbushina, A. A., & Krumbein, W. E. (2000). Biodecay of cultural heritage as a space/time-related ecological situation—an evaluation of a series of studies. *International Biodeterioration & Biodegradation*, *46*(4), 261–270.

Dornieden, Thomas, & Gorbushina, A. A. (2000). New methods to study the detrimental effects of poikilotroph microcolonial micromycetes (PMM) on building materials. *Proceedings of the 9th International Congress on Deterioration and Conservation of Stone*, 461–468.

Doty, P. M., Aiken, W. H., & Mark, H. (1946). Temperature dependence of water vapor permeability. *Industrial & Engineering Chemistry*, *38*(8), 788–791.

Drchalová, J., Podě bradská, J., Madě ra, J., & Č erný, R. (2001). Evaluation of Water Resistance and Diffusion Properties of Paint Materials. *Acta Polytechnica*, *41*(1).

Duarte, R., Flores-Colen, I., de Brito, J., & Hawreen, A. (2020). Variability of in-situ testing in wall coating systems-Karsten tube and moisture meter techniques. *Journal of Building Engineering*, *27*, 100998.

Emerson, D. (2018). The role of iron-oxidizing bacteria in biocorrosion: a review. *Biofouling*, *34*(9), 989–1000.

Endo, H., Okumura, Y., Sato, Y., & Agatsuma, Y. (2017). Interactive effects of nutrient availability, temperature, and irradiance on photosynthetic pigments and color of the brown alga Undaria pinnatifida. *Journal of Applied Phycology*, *29*(3), 1683–1693.

Fais, S., Casula, G., Cuccuru, F., Ligas, P., & Bianchi, M. G. (2018). An innovative methodology for the non-destructive diagnosis of architectural elements of ancient historical buildings. *Scientific Reports*, *8*(1), 1–11.

Faour, G., Meslmani, Y., & Fayad, A. (2010). *Climate-Change Atlas of Syria*. https://doi.org/10.13140/RG.2.2.26562.17601

Fernandez, S. P. (1999). *Factors influencing salt-induced weathering of building sandstone*. 243. http://scholar.google.com/scholar?hl=en&btnG=Search&q=intitle:Factors+influencing+salt-induced+weathering+of+building+sandstone#1%5Cnhttp://hdl.handle.net/10068/646700

Fitzner, B. (2002). Damage diagnosis on stone monuments-in situ investigation and laboratory studies. *Proceedings of the International Symposium of the Conservation of the Bangudae Petroglyph*, *7*, 29–71.

Fitzner, B., & Heinrichs, K. (2001). Damage diagnosis at stone monuments-weathering forms, damage categories and damage indices. *Acta-Universitatis Carolinae Geologica*, *1*, 12–13.

Folda, J., French, P., Conservator, F., & Coupel, P. (1982). Crusader Frescoes at Crac des Chevaliers and Marqab Castle. *Dumbarton Oaks Papers*, *36*(1982), 177.

https://doi.org/10.2307/1291467

Franzen, C., & Mirwald, P. W. (2004). Moisture content of natural stone: static and dynamic equilibrium with atmospheric humidity. *Environmental Geology*, *46*(3), 391–401.

Gadd, G. (2008). Fungi and their role in the biosphere. In *Encyclopedia of ecology* (pp. 1709–1717). Elsevier.

Gadd, G. M. (1999). Fungal production of citric and oxalic acid: importance in metal speciation, physiology and biogeochemical processes. *Advances in Microbial Physiology*, *41*, 47–92.

Galbraith, G. H., Guo, J. S., & McLean, R. C. (2000). The effect of temperature on the moisture permeability of building materials. *Building Research & Information*, *28*(4), 245–259.

Garia, S., Pal, A. K., Ravi, K., & Nair, A. M. (2019). A comprehensive analysis on the relationships between elastic wave velocities and petrophysical properties of sedimentary rocks based on laboratory measurements. *Journal of Petroleum Exploration and Production Technology*, *9*(3), 1869–1881.

Garrabrants, A. C., & Kosson, D. S. (2003). Modeling moisture transport from a Portland cement-based material during storage in reactive and inert atmospheres. *Drying Technology*, *21*(5), 775–805.

Gaylarde, C. C., Rodríguez, C. H., Navarro-Noya, Y. E., & Ortega-Morales, B. O. (2012). Microbial biofilms on the sandstone monuments of the Angkor Wat Complex, Cambodia. *Current Microbiology*, *64*(2), 85–92. https://doi.org/10.1007/s00284-011-0034-y

Gaylarde, P. M., & Gaylarde, C. C. (2000). Algae and cyanobacteria on painted buildings in Latin America. *International Biodeterioration and Biodegradation*, *46*(2), 93–97. https://doi.org/10.1016/S0964-8305(00)00074-3

Ghanem, H., & Kuss, J. (2013). Stratigraphic control of the Aptian–Early Turonian sequences of the Levant Platform, Coastal Range, northwest Syria. *GeoArabia*, *18*(4), 85–132.

Ghiassi, B., & Lourenc□o, P. B. (2018). *Long-term performance and durability of masonry structures: degradation mechanisms, health monitoring and service life design*. Woodhead Publishing.

Gleason, F. H., Gadd, G. M., Pitt, J. I., & Larkum, A. W. D. (2017). The roles of endolithic fungi in bioerosion and disease in marine ecosystems. I. General concepts. *Mycology*, *8*(3), 205–215.

González-Gómez, W. S., Quintana, P., Gómez-Cornelio, S., García-Solis, C., Sierra-Fernandez, A., Ortega-Morales, O., & De la Rosa-García, S. C. (2018). Calcium oxalates in biofilms on limestone walls of Maya buildings in Chichén Itzá, Mexico. *Environmental Earth Sciences*, *77*(6), 1–12. https://doi.org/10.1007/s12665-018-7406-6

Gorbushina, A. A., Krumbein, W. E., Hamman, C. H., Panina, L., Soukharjevski, S., & Wollenzien, U. (1993). Role of black fungi in color change and biodeterioration of antique marbles. *Geomicrobiology Journal*, *11*(3–4), 205–221.

Graue, B., Siegesmund, S., & Middendorf, B. (2011). Quality assessment of replacement stones for the Cologne Cathedral: mineralogical and petrophysical requirements. *Environmental Earth Sciences*, *63*(7), 1799–1822.

Griffin, P. S., Indictor, N., & Koestler, R. J. (1991). The biodeterioration of stone: a review of deterioration mechanisms, conservation case histories, and treatment. *International Biodeterioration*, *28*(1–4), 187–207.

Gu, J.-D., & Katayama, Y. (2021). Microbiota and biochemical processes involved in biodeterioration of cultural heritage and protection. *Microorganisms in the Deterioration and Preservation of Cultural Heritage*, 37.

Gulotta, D., Villa, F., Cappitelli, F., & Toniolo, L. (2018). Biofilm colonization of metamorphic lithotypes of a renaissance cathedral exposed to urban atmosphere. *Science of The Total Environment*, *639*, 1480–1490.

Hall, C, Hoff, W. D., & Nixon, M. R. (1984). Water movement in porous building materials—VI. Evaporation and drying in brick and block materials. *Building and Environment*, *19*(1), 13–20.

Hall, Christopher, & Hoff, W. D. (2021). *Water transport in brick, stone and concrete*. CRC Press.

Han, D., Nur, A., & Morgan, D. (1986). Effects of porosity and clay content on wave velocities in sandstones. *Geophysics*, *51*(11), 2093–2107.

Hendrickx, R. (2013). Using the Karsten tube to estimate water transport parameters of

porous building materials. *Materials and Structures*, *46*(8), 1309–1320.

Hill, D. (2013). *A history of engineering in classical and medieval times*. Routledge.

Hosseini, Z., Zangari, G., Carboni, M., & Caneva, G. (2021). Substrate Preferences of Ruderal Plants in Colonizing Stone Monuments of the Pasargadae World Heritage Site, Iran. *Sustainability*, *13*(16), 9381.

Houck, J., & Scherer, G. W. (2006). Controlling stress from salt crystallization. *Fracture and Failure of Natural Building Stones*, *1*, 299–312. http://dx.doi.org/10.1007/978-1-4020-5077-0_19

Howard, R. J., Ferrari, M. A., Roach, D. H., & Money, N. P. (1991). Penetration of hard substrates by a fungus employing enormous turgor pressures. *Proceedings of the National Academy of Sciences*, *88*(24), 11281–11284.

https://www.meteoblue.com/en/weather/archive/histogram/34.760N36.290E. (n.d.).

Jaramillo, O. A., & Borja, M. A. (2004). Wind speed analysis in La Ventosa, Mexico: a bimodal probability distribution case. *Renewable Energy*, *29*(10), 1613–1630.

Jones, M. S., Wakefield, R. D., & Forsyth, G. (2000). A study of biologically decayed sandstone with respect to Ca and its distribution. *Proceedings of the 9th International Congress on Deterioration and Conservation of Stone*, 473–481.

Jubaili, Y., Al-Hant, R., & Issa, M. (2002). *Radio spectrometric survey of un-surved areas in Syria*.

Karaca, Z. (2010). Water absorption and dehydration of natural stones versus time. *Construction and Building Materials*, *24*(5), 786–790.

Karakul, H., & Ulusay, R. (2013). Empirical correlations for predicting strength properties of rocks from P-wave velocity under different degrees of saturation. *Rock Mechanics and Rock Engineering*, *46*(5), 981–999.

Karimi, M., Mahmoodi, M., Niazi, A., Al-Wahaibi, Y., & Ayatollahi, S. (2012). Investigating wettability alteration during MEOR process, a micro/macro scale analysis. *Colloids and Surfaces B: Biointerfaces*, *95*, 129–136.

Kassab, M. A., & Weller, A. (2015). Study on P-wave and S-wave velocity in dry and wet sandstones of Tushka region, Egypt. *Egyptian Journal of Petroleum*, *24*(1), 1–11.

Kattan, Z. (2020). Factors affecting the chemical composition of precipitation in Syria. *Environmental Science and Pollution Research*, *27*(22), 28408–28428.

Katz, O., Reches, Z., & Roegiers, J.-C. (2000). Evaluation of mechanical rock properties using a Schmidt Hammer. *International Journal of Rock Mechanics and Mining Sciences*, *37*(4), 723–728.

Kazemi, E., Soofiyani, S. R., Ahangari, H., Eyvazi, S., Hejazi, M. S., & Tarhriz, V. (n.d.). Chemolithotroph Bacteria: From Biology to Application in Medical Sciences. *Crescent Journal of Medical and Biological Sciences*, *8*(2).

Kemmling, A., Kämper, M., Flies, C., Schieweck, O., & Hoppert, M. (2004). Biofilms and extracellular matrices on geomaterials. *Environmental Geology*, *46*(3), 429–435.

Keppert, M., Ž umár, J., Č áchová, M., Koň áková, D., Svora, P., Pavlík, Z., Vejmelkova, E., & Č erný, R. (2016). Water vapor diffusion and adsorption of sandstones: influence of rock texture and composition. *Advances in Materials Science and Engineering*, *2016*.

Khalfa, D., Benretem, A., Cheikchouk, N., & Herous, L. (2018). Comparative study of wind speed extrapolation methods for sites with different roughness. *International Journal of Power and Energy Conversion*, *9*(3), 205–227.

King, D. J. C. (1949). The taking of Le Krak des Chevaliers in 1271. *Antiquity*, *23*(90), 83–92.

Klimentos, T. (1991). The effects of porosity-permeability-clay content on the velocity of compressional waves. *Geophysics*, *56*(12), 1930–1939.

Krumbein, W. E. (2003). Patina and cultural heritage–a geomicrobiologist's perspective. *Cult Herit Res a Pan-European Chall*, 39–47.

Kumar, S. V., Waghmare, S. A., Mahajan, N. E., & Sabale, P. D. (2016). Eradication of vegetal growth and systematic scientific conservation approach of ballaleshwar temple, trimbakeshwar (india). *International Journal of Conservation Science*, *7*(3).

Künzel, H. M. (1995). Simultaneous heat and moisture transport in building components. *One-and Two-Dimensional Calculation Using Simple Parameters. IRB-Verlag Stuttgart*, *65*.

Kurtulus, C., Cakir, S., & Yoğ urtcuoğ lu, A. (2016). Ultrasound Study of Limestone Rock

DOI: 10.15774/PPKE.BTK.2024.021

Physical and Mechanical Properties. *Soil Mechanics & Foundation Engineering*, *52*(6).

La Russa, M. F., Ruffolo, S. A., Belfiore, C. M., Aloise, P., Rovella, N., Randazzo, L., Pezzino, A., & Montana, G. (2013). Study of the effects of salt crystallisation on degradation of limestone rocks. *Periodico Di Mineralogia*, *82*(1).

Lee, C. H., Lee, M. S., Kim, Y. T., & Kim, J. (2006). Deterioration assessment and conservation of a heavily degraded Korean Stone Buddha from the ninth century. *Studies in Conservation*, *51*(4), 305–316.

Lettieri, M., & Masieri, M. (2016). Performances and coating morphology of a siloxane-based hydrophobic product applied in different concentrations on a highly porous stone. *Coatings*, *6*(4), 60.

Li, X., Arai, H., Shimoda, I., Kuraishi, H., & Katayama, Y. (2008). Enumeration of sulfur-oxidizing microorganisms on deteriorating stone of the Angkor monuments, Cambodia. *Microbes and Environments*, 809220004.

Liaud, N., Giniés, C., Navarro, D., Fabre, N., Crapart, S., Gimbert, I. H., Levasseur, A., Raouche, S., & Sigoillot, J.-C. (2014). Exploring fungal biodiversity: organic acid production by 66 strains of filamentous fungi. *Fungal Biology and Biotechnology*, *1*(1), 1–10.

Lisci, M., Monte, M., & Pacini, E. (2003). Lichens and higher plants on stone: a review. *International Biodeterioration & Biodegradation*, *51*(1), 1–17.

Little, B. J., & Lee, J. S. (2007). *Microbiologically influenced corrosion* (Vol. 3). John Wiley & Sons.

Liu, X., Koestler, R. J., Warscheid, T., Katayama, Y., & Gu, J.-D. (2020). Microbial deterioration and sustainable conservation of stone monuments and buildings. *Nature Sustainability*, *3*(12), 991–1004.

Livingston, R. A. (2000). Nondestructive testing of historic structures. In *Science and Technology in Historic Preservation* (pp. 97–120). Springer.

Lubelli, B., Cnudde, V., Diaz-Goncalves, T., Franzoni, E., van Hees, R. P. J., Ioannou, I., Menendez, B., Nunes, C., Siedel, H., & Stefanidou, M. (2018). Towards a more effective and reliable salt crystallization test for porous building materials: state of the art. *Materials and Structures*, *51*(2), 1–21.

DOI: 10.15774/PPKE.BTK.2024.021

Lutz, P. (2013). *Lehrbuch der Bauphysik: Schall Wärme Feuchte Licht Brand Klima*. Springer-Verlag.

M. Cicardi, C. Corti, O. Savadori, F. P. (2020). endolithic microorganisms in carbonatic rocks and conservations problems. In S. S. Bernhard Middendorf (Ed.), *Monument future : decay and conservation of stone: Proceedings of the 14th iInternational Congress on the Deterioration and Conservation of Stone* (pp. 516–566). Halle Salle : Mitteldeutscher Verlag.

Macedo, M. F., Miller, A. Z., Dionísio, A., & Saiz-Jimenez, C. (2009). Biodiversity of cyanobacteria and green algae on monuments in the Mediterranean Basin: an overview. *Microbiology*, *155*(11), 3476–3490.

Magalhffies, S. L., & Braga, M. A. S. (2000). Biological colonization features on a granite monument from Braga (NW, Portugal). *Proceedings of the 9th International Congress on Deterioration and Conservation of Stone*, 521–529.

Mansch, R., & Bock, E. (1998). Biodeterioration of natural stone with special reference to nitrifying bacteria. *Biodegradation*, *9*(1), 47–64.

Martino, P. D. (2016). What about biofilms on the surface of stone monuments? *The Open Conference Proceedings Journal*, *7*(1).

Mavko, G., Mukerji, T., & Dvorkin, J. (2009). *The rock physics handbook: Tools for Seismic Analysis of Porous Media. Cambridge University Press, Cambridge, 511 p*.

McAllister, D., Warke, P., McCabe, S., & Gomez-Heras, M. (2016). Evaporative moisture loss from heterogeneous stone: Material-environment interactions during drying. *Geomorphology*, *273*, 308–322.

McCabe, S., McAllister, D., Warke, P. A., & Gomez- Heras, M. (2015). Building sandstone surface modification by biofilm and iron precipitation: emerging block- scale heterogeneity and system response. *Earth Surface Processes and Landforms*, *40*(1), 112–122.

McNamara, C. J., & Mitchell, R. (2005). Microbial deterioration of historic stone. *Frontiers in Ecology and the Environment*, *3*(8), 445–451.

Menéndez, B. (2018). Estimators of the impact of climate change in salt weathering of cultural heritage. *Geosciences*, *8*(11), 401.

Meng, H., Katayama, Y., & Gu, J.-D. (2017). More wide occurrence and dominance of ammonia-oxidizing archaea than bacteria at three Angkor sandstone temples of Bayon, Phnom Krom and Wat Athvea in Cambodia. *International Biodeterioration & Biodegradation*, *117*, 78–88.

Meroño, J. E., Perea, A. J., Aguilera, M. J., & Laguna, A. M. (2015). Recognition of materials and damage on historical buildings using digital image classification. *South African Journal of Science*, *111*(1–2), 1–9.

Mesqui, J. (2018). L´architecture d´une forteresse hors du commum. In J. Hofman & E. Pénicaut (Eds.), *Le Crac des Chevaliers : Chroniques d'un rêve de pierre* (pp. 19–32). Editions Hermann.

Mesqui, J., & Goepp, M. (2018). *Le crac des chevaliers: histoire et architecture*. Académiée des Inscriptions et belles-lettres.

Mihajlovski, A., Seyer, D., Benamara, H., Bousta, F., & Di Martino, P. (2015). An overview of techniques for the characterization and quantification of microbial colonization on stone monuments. *Annals of Microbiology*, *65*(3), 1243–1255.

Mishra, A. K., Jain, K. K., & Garg, K. L. (1995). Role of higher plants in the deterioration of historic buildings. *Science of the Total Environment*, *167*(1–3), 375–392.

Molin, B. K. (1995). *The role of castles in the political and military history of the Crusader States and the Levant 1187 to 1380*. University of Leeds.

Motti, R., & Stinca, A. (2011). Analysis of the biodeteriogenic vascular flora at the Royal Palace of Portici in southern Italy. *International Biodeterioration & Biodegradation*, *65*(8), 1256–1265.

Mukhopadhyaya, P., Batcheller, D., Kumaran, M. K., Lackey, J. C., Van Reenen, D., & Normandin, N. (2011). Correlation between water vapour and air permeability of building materials: experimental observations. *JAI*, *8*(3), 1–14.

Mukhopadhyaya, P., Kumaran, K., Lackey, J., & van Reenen, D. (2007). Water Vapor Transmission Measurement and Signifi cance of Corrections. *Heat-Air-Moisture Transport: Measurements on Building Materials*, *4*(1495), 21.

Mukhopadhyaya, P., Kumaran, M. K., & Lackey, J. (2005). Use of the modified cup method to determine temperature dependency of water vapor transmission properties of building

materials. *Journal of Testing and Evaluation*, *33*(5), 316.

Municchia, A. C., Bartoli, F., Taniguchi, Y., Giordani, P., & Caneva, G. (2018). Evaluation of the biodeterioration activity of lichens in the Cave Church of Üzümlü (Cappadocia, Turkey). *International Biodeterioration & Biodegradation*, *127*, 160–169.

Narloch, P., Pią tkiewicz, W., & Pietruszka, B. (2021). The Effect of Cement Addition on Water Vapour Resistance Factor of Rammed Earth. *Materials*, *14*(9), 2249.

Nash, T. H. (2008). Lichen sensitivity to air pollution. In I. I. I. Nash Thomas H. (Ed.), *Lichen Biology* (2nd ed., pp. 299–314). Cambridge University Press. https://doi.org/DOI: 10.1017/CBO9780511790478.016

Nayaka, S., Toppo, K., & Verma, S. (2017). Adaptation in algae to environmental stress and ecological conditions. In *Plant Adaptation Strategies in Changing Environment* (pp. 103–115). Springer.

Nenadálová, Š., Balík, L., Rydval, M., & Bittner, T. (2016). Laboratory verification of water vapour permeability of plaster compositions. *Procedia Engineering*, *151*, 50–57.

Nicolle, D. (2005). *Crusader Castles in the Holy Land 1192-1302* (Vol. 32). Osprey Publishing.

Niyartama, T. F., & Fauzi, U. (2017). Influence of water saturation on ultrasonic P-wave velocity in weakly compacted sandstone. *Journal of Physics: Conference Series*, *795*(1), 12012.

Ogawa, A., Celikkol-Aydin, S., Gaylarde, C., Baptista-Neto, J. A., & Beech, I. (2017). Microbial communities on painted wet and dry external surfaces of a historic fortress in Niteroi, Brazil. *International Biodeterioration & Biodegradation*, *123*, 164–173.

Ondrasik, M., & Hudec, P. P. (2002). Freezing expansion and thermodynamics of pore water in rock deterioration. *CD Proceedings of 9-Th IAEG Congress, Durban, South Africa*, 443.

Ondrášik, M., & Kopecký, M. (2014). Rock pore structure as main reason of rock deterioration. *Studia Geotechnica et Mechanica*, *36*(1), 79–88.

Ortega-Morales, B. O., Gaylarde, C., Anaya-Hernandez, A., Chan-Bacab, M. J., De la Rosa-García, S. C., Arano-Recio, D., & Montero-M, J. (2013). Orientation affects

Trentepohlia-dominated biofilms on Mayan monuments of the Rio Bec style. *International Biodeterioration & Biodegradation*, *84*, 351–356.

Overbeke, C. (2008). Do trees really cause so much damage to property? *Journal of Building Appraisal*, *3*(4), 247–258.

Oyediran, I. A., & Foghi, E. J. (2018). Petrography and Strength Properties of Some Southwestern Nigeria Precambrian Rocks. *Journal of Mining and Geology*, *54*(2), 87–98.

Ozcelik, Y., & Ozguven, A. (2014). Water absorption and drying features of different natural building stones. *Construction and Building Materials*, *63*, 257–270.

Palla, F., & Barresi, G. (2017). *Biotechnology and conservation of cultural heritage*. Springer.

Papida, S., Murphy, W., & May, E. (2000). The use of sound velocity determination for the non-destructive estimation of physical and microbial weathering of limestones and dolomites. *Proceedings of the 9th International Congress on Deterioration and Conservation of Stone*, 609–617.

Patil, S. M., Kasthurba, A. K., & Patil, M. V. (2021). Characterization and assessment of stone deterioration on Heritage Buildings. *Case Studies in Construction Materials*, *15*, e00696.

Peel, M. C., Finlayson, B. L., & McMahon, T. A. (2007). Updated world map of the Köppen-Geiger climate classification. *Hydrology and Earth System Sciences*, *11*(5), 1633–1644.

Pei, F., Zou, C., He, T., Pan, L., Xiao, K., Shi, G., & Ren, K. (2011). Experimental study of the relationship between fluid density and saturation and sonic wave velocity of rock samples from the WXS Depression, South China Sea. *Petroleum Science*, *8*(1), 43–48.

Pia, G., Corcione, C. E., Striani, R., Casnedi, L., & Sanna, U. (2017). Coating's influence on water vapour permeability of porous stones typically used in cultural heritage of Mediterranean area: Experimental tests and model controlling procedure. *Progress in Organic Coatings*, *102*, 239–246.

Pinheiro, A. C., Mesquita, N., Trovffio, J., Soares, F., Tiago, I., Coelho, C., de Carvalho, H. P., Gil, F., Catarino, L., Piñar, G., & Portugal, A. (2019). Limestone biodeterioration: A review on the Portuguese cultural heritage scenario. *Journal of Cultural Heritage*, *36*,

275–285. https://doi.org/10.1016/j.culher.2018.07.008

Pinna, D. (2014). Biofilms and lichens on stone monuments: do they damage or protect? *Frontiers in Microbiology*, *5*, 133.

Pocobelli, D. P., Boehm, J., Bryan, P., Still, J., & Grau-Bové, J. (2018). Building information models for monitoring and simulation data in heritage buildings. *International Archives of the Photogrammetry, Remote Sensing and Spatial Information Sciences-ISPRS Archives*, *42*(2), 909–916.

Pombeiro-Sponchiado, S. R., Sousa, G. S., Andrade, J. C. R., Lisboa, H. F., & Gonçalves, R. C. R. (2017). Production of melanin pigment by fungi and its biotechnological applications. *Melanin*, 47–75.

Price, C. A., & Doehne, E. (2011). *Stone conservation: an overview of current research*.

Princi, E. (2014). *Handbook of polymers in stone conservation*. Smithers Rapra.

Rajabi, A. M., Hosseini, A., & Heidari, A. (2017). The new empirical formula to estimate the uniaxial compressive strength of limestone; north of saveh a case study. *Journal of Engineering Geology*, *11*(3), 159.

Ranalli, G., Chiavarini, M., Guidetti, V., Marsala, F., Matteini, M., Zanardini, E., & Sorlini, C. (1997). The use of microorganisms for the removal of sulphates on artistic stoneworks. *International Biodeterioration & Biodegradation*, *40*(2–4), 255–261.

Randazzo, L., Paladini, G., Venuti, V., Crupi, V., Ott, F., Montana, G., Ricca, M., Rovella, N., La Russa, M. F., & Majolino, D. (2020). Pore Structure and Water Transfer in Pietra d'Aspra Limestone: A Neutronographic Study. *Applied Sciences*, *10*(19), 6745.

Retfalvi, T. (2019). Burials in Crac des Chevaliers excavated in 2017. In P. Edbury, D. Pringle, & B. Major (Eds.), *Bridge of Civilizations: The Near East and Europe c. 1100–1300*. Archaeopress Publishing Ltd.

Rodrigues, J. D. (2015). Defining, mapping and assessing deterioration patterns in stone conservation projects. *Journal of Cultural Heritage*, *16*(3), 267–275.

Rodriguez-Navarro, C., & Doehne, E. (1999). Salt weathering: Influence of evaporation rate, supersaturation and crystallization pattern. *Earth Surface Processes and Landforms*, *24*(2–3), 191–209. https://doi.org/10.1002/(sici)1096-9837(199903)24:3<191::aid-

esp942>3.0.co;2-g

Rodriguez-Navarro, C., Doehne, E., & Sebastian, E. (2000). How does sodium sulfate crystallize? Implications for the decay and testing of building materials. *Cement and Concrete Research*, *30*(10), 1527–1534. https://doi.org/10.1016/S0008-8846(00)00381-1

Ross, M., McGee, E. S., & Ross, D. R. (1989). Chemical and mineralogical effects of acid deposition on Shelburne Marble and Salem Limestone test samples placed at four NAPAP weather-monitoring sites. *American Mineralogist*, *74*(3–4), 367–383.

Rossi, F., & De Philippis, R. (2015). Role of cyanobacterial exopolysaccharides in phototrophic biofilms and in complex microbial mats. *Life*, *5*(2), 1218–1238.

Ruedrich, J., Kirchner, D., & Siegesmund, S. (2011). Physical weathering of building stones induced by freeze–thaw action: a laboratory long-term study. *Environmental Earth Sciences*, *63*(7), 1573–1586.

Ruedrich, J., & Siegesmund, S. (2007). Salt and ice crystallisation in porous sandstones. *Environmental Geology*, *52*(2), 343–367. https://doi.org/10.1007/s00254-006-0585-6

Ruiz-Agudo, E, Mees, F., Jacobs, P., & Rodriguez-Navarro, C. (2007). The role of saline solution properties on porous limestone salt weathering by magnesium and sodium sulfates. *Environmental Geology*, *52*(2), 269–281.

Ruiz-Agudo, Encarnación, Rodriguez-Navarro, C., & Sebastián-Pardo, E. (2006). Sodium sulfate crystallization in the presence of phosphonates: Implications in ornamental stone conservation. *Crystal Growth & Design*, *6*(7), 1575–1583.

Saarela, M., Alakomi, H.-L., Suihko, M.-L., Maunuksela, L., Raaska, L., & Mattila-Sandholm, T. (2004). Heterotrophic microorganisms in air and biofilm samples from Roman catacombs, with special emphasis on actinobacteria and fungi. *International Biodeterioration & Biodegradation*, *54*(1), 27–37.

Saini, D. K., Pabbi, S., & Shukla, P. (2018). Cyanobacterial pigments: Perspectives and biotechnological approaches. *Food and Chemical Toxicology*, *120*, 616–624.

Salim, H., Kolpakov, P., Bonn, D., & Shahidzadeh, N. (2020). Self-Lifting NaCl Crystals. *Journal of Physical Chemistry Letters*, *11*(17), 7388–7393. https://doi.org/10.1021/acs.jpclett.0c01871

Salomffio, M. C. de F., Bauer, E., & Kazmierczak, C. de S. (2018). Drying parameters of rendering mortars. *Ambiente Construído*, *18*, 7–19.

Salvadori, O., & Municchia, A. C. (2016). The role of fungi and lichens in the biodeterioration of stone monuments. *The Open Conference Proceedings Journal*, *7*(1).

Sánchez-Antón, F., & Asencio-Martínez, A. D. (2007). Participation of Cyanophyceae in the biodeterioration of the stones of the Santo Domingo College in Orihuela, Alicante (SE Spain). *Algological Studies*, 95–108.

Santo, A. P., Cuzman, O. A., Petrocchi, D., Pinna, D., Salvatici, T., & Perito, B. (2021). Black on white: microbial growth darkens the external marble of florence cathedral. *Applied Sciences*, *11*(13), 6163.

Sato, M., & Hattanji, T. (2018). A laboratory experiment on salt weathering by humidity change: salt damage induced by deliquescence and hydration. *Progress in Earth and Planetary Science*, *5*(1). https://doi.org/10.1186/s40645-018-0241-2

Sbeinati, M. R., Darawcheh, R., & Mouty, M. (2005). The historical earthquakes of Syria: an analysis of large and moderate earthquakes from 1365 BC to 1900 AD. *Annals of Geophysics*.

Scheerer, S. (2008). *Microbial biodeterioration of outdoor stone monuments: Assessment methods and control strategies*. Cardiff University (United Kingdom).

Scheffler, G. A., & Plagge, R. (2010). Introduction of a drying coefficient for building materials. *ASHRAE Transactions*, *116*(pt 2).

Schröer, L., Boon, N., De Kock, T., & Cnudde, V. (2021). The capabilities of bacteria and archaea to alter natural building stones–A review. *International Biodeterioration & Biodegradation*, *165*, 105329.

Scrivano, S., & Gaggero, L. (2020). An experimental investigation into the salt-weathering susceptibility of building limestones. *Rock Mechanics and Rock Engineering*, *53*(12), 5329–5343. https://doi.org/10.1007/s00603-020-02208-x

Seaward, M. R. D. (1993). Lichens and sulphur dioxide air pollution: field studies. *Environmental Reviews*, *1*(2), 73–91. https://doi.org/10.1139/a93-007

Sena da Fonseca, B., Castela, A. S., Duarte, R. G., Neves, R., & Montemor, M. F. (2015).

Non-destructive and on site method to assess the air-permeability in dimension stones and its relationship with other transport-related properties. *Materials and Structures*, *48*(11), 3795–3809.

Sengun, N., Demirdag, S., Akbay, D., Ugur, I., Altindag, R., & Akbulut, A. (2014). Investigation of the relationships between capillary water absorption coefficients and other rock properties of some natural stones, V. *Global Stone Congress*, 22–25.

Siegesmund, S., & Dürrast, H. (2011). Physical and mechanical properties of rocks. In *Stone in architecture* (pp. 97–225). Springer.

Siegesmund, S., & Snethlage, R. (2011). *Stone in architecture: properties, durability*. Springer.

Singh, J. (2006). *Building Mycology: Management of decay and health in buildings*. Taylor & Francis.

Snethlage, R., & Sterflinger, K. (2011). Stone conservation. In *Stone in architecture* (pp. 411–544). Springer.

Souza-Egipsy, V., Wierzchos, J., García-Ramos, J. V., & Ascaso, C. (2002). Chemical and ultrastructural features of the lichen-volcanic/sedimentary rock interface in a semiarid region (Almeria, Spain). *The Lichenologist*, *34*(2), 155–167.

Stanaszek-Tomal, E. (2020). Environmental factors causing the development of microorganisms on the surfaces of national cultural monuments made of mineral building materials. *Coatings*, *10*(12), 1203.

Steiger, M. (2003). Salts and crusts. *The Effects of Air Pollution on the Built Environment*, 133–181.

Steiger, Michael. (2005). Crystal growth in porous materials - I: The crystallization pressure of large crystals. *Journal of Crystal Growth*, *282*(3–4), 455–469. https://doi.org/10.1016/j.jcrysgro.2005.05.007

Steiger, Michael, Charola, A. E., & Sterflinger, K. (2011). Weathering and deterioration. In *Stone in architecture* (pp. 227–316). Springer.

Stück, H., Siegesmund, S., & Rüdrich, J. (2011). Weathering behaviour and construction suitability of dimension stones from the Drei Gleichen area (Thuringia, Germany).

Environmental Earth Sciences, *63*(7), 1763–1786.

Suwannarach, N., Kumla, J., Watanabe, B., Matsui, K., & Lumyong, S. (2019). Characterization of melanin and optimal conditions for pigment production by an endophytic fungus, Spissiomyces endophytica SDBR-CMU319. *PLoS One*, *14*(9), e0222187.

Theodoridou, M., & Török, ā. (2019). In situ investigation of stone heritage sites for conservation purposes: a case study of the Székesfehérvár Ruin Garden in Hungary. *Progress in Earth and Planetary Science*, *6*(1), 1–14.

Thomachot-Schneider, C., Vázquez, P., Gommeaux, M., Lelarge, N., Conreux, A., Drothière, X., Mouhoubi, K., & Bodnar, J.-L. (2019). Thermal response of building stones contaminated with salts. *Construction and Building Materials*, *226*, 331–344.

Togkalidou, T., Karoglou, M., Bakolas, A., Giakoumaki, A., & Moropoulou, A. (2013). Correlation of water vapor permeability with microstructure characteristics of building materials using robust chemometrics. *Transport in Porous Media*, *99*(2), 273–295.

Tomaselli, L., Lamenti, G., Bosco, M., & Tiano, P. (2000). Biodiversity of photosynthetic micro-organisms dwelling on stone monuments. *International Biodeterioration and Biodegradation*, *46*(3), 251–258. https://doi.org/10.1016/S0964-8305(00)00078-0

Torfs, K., Van Grieken, V., Zezza, F., Garcia, N., & Macri, F. (1997). The cathedral of Bari, Italy: evaluation of environmental effects on stone decay phenomena. *Studies in Conservation*, *42*(4), 193–206.

Török, ā. (2003). Surface strength and mineralogy of weathering crusts on limestone buildings in Budapest. *Building and Environment*, *38*(9–10), 1185–1192.

Torraca, G. (1982). *Porous building materials: Materials science for architectural conservation*.

Tsilimantou, E., Delegou, E. T., Nikitakos, I. A., Ioannidis, C., & Moropoulou, A. (2020). GIS and BIM as integrated digital environments for modeling and monitoring of historic buildings. *Applied Sciences*, *10*(3), 1078.

Tsuji, T., Tokuyama, H., Costa Pisani, P., & Moore, G. (2008). Effective stress and pore pressure in the Nankai accretionary prism off the Muroto Peninsula, southwestern Japan. *Journal of Geophysical Research: Solid Earth*, *113*(B11).

Van Hees, R. P. J., Koek, J. A. G., De Clercq, H., De Witte, E., Binda, L., & Baronio, G. (1996). Evaluation of the performance of surface treatments for the conservation of brick masonry. *8th= Eighth International Congress on Deterioration and Conservation of Stone, Berlin, 30 Sept.-4 Oct. 1996: Proceedings*, 1695–1715.

Vandevoorde, D., Pamplona, M., Schalm, O., Vanhellemont, Y., Cnudde, V., & Verhaeven, E. (2009). Contact sponge method: Performance of a promising tool for measuring the initial water absorption. *Journal of Cultural Heritage*, *10*(1), 41–47.

Vaniman, D. T., Bish, D. L., Chipera, S. J., Fialips, C. I., Carey, J. W., & Feldman, W. G. (2004). Magnesium sulphate salts and the history of water on Mars. *Nature*, *431*(7009), 663–665. https://doi.org/10.1038/nature02973

Vasanelli, E., Calia, A., Masieri, M., & Baldi, G. (2019). Stone consolidation with SiO2 nanoparticles: Effects on a high porosity limestone. *Construction and Building Materials*, *219*, 154–163.

Vasanelli, E., Sileo, M., Calia, A., & Aiello, M. A. (2013). Non-destructive techniques to assess mechanical and physical properties of soft calcarenitic stones. *Procedia Chemistry*, *8*, 35–44.

Vázquez, P., Alonso, F. J., Carrizo, L., Molina, E., Cultrone, G., Blanco, M., & Zamora, I. (2013). Evaluation of the petrophysical properties of sedimentary building stones in order to establish quality criteria. *Construction and Building Materials*, *41*, 868–878.

Vazquez, P., Sartor, L., & Thomachot-Schneider, C. (2018). Influence of substrate and temperature on the crystallization of KNO3 droplets studied by infrared thermography. *Progress in Earth and Planetary Science*, *5*(1). https://doi.org/10.1186/s40645-018-0229-y

Vergès-Belmin, V. (2011). *ICOMOS-ISCS: Illustrated glossary on stone deterioration patterns= Glosario ilustrado de formas de deterioro de la piedra* (Vol. 15). Icomos.

Verrecchia, E. P., Dumont, J.-L., & Rolko, K. E. (1990). Do fungi building limestones exist in semi-arid regions? *The Science of Nature*, *77*(12), 584–586.

Viles, H. A., Camuffo, D., Fitz, S., Fitzner, B., O., L., R.A., L., P.N.V., M., Sabbioni, C., & Warscheid, T. (1997). What is the State of Our Knowledge of the Mechanisms of Deterioration and How Good Are Our Estimates of Rates of Deterioration? In *Saving*

our architectural heritage. Conservation of Historic Stone Structures (pp. 95–112).

Wakefield, R. D., & Jones, M. S. (1998). An introduction to stone colonizing micro-organisms and biodeterioration of building stone. *Quarterly Journal of Engineering Geology and Hydrogeology*, *31*(4), 301–313.

Wang, H., Sun, S. Z., Yang, H., Gao, H., Xiao, Y., & Hu, H. (2011). The influence of pore structure on P-& S-wave velocities in complex carbonate reservoirs with secondary storage space. *Petroleum Science*, *8*(4), 394–405.

Wang, L. K., Ivanov, V., Tay, J.-H., & Hung, Y.-T. (2010). *Environmental biotechnology* (Vol. 10). Springer Science & Business Media.

Warscheid, T., & Leisen, H. (2011). Microbiological studies on stone deterioration and development of conservation measures at Angkor Wat. *Biocolonization of Stone: Control and Preventive Methods, Proceedings from the MCI Workshop Series*, *2*, 1–18.

Wasserman, I., & Bentur, A. (2005). The efficiency of surface treatments on enhancement of the durability of limestone cladding stones. *Materials and Structures*, *38*(1), 99–105.

Wedekind, W., Doncel, R. A. L., Marié, B., & Salvadori, O. (2016). First investigations of the weathering and deterioration of rock cut monuments in Myra, Lycia (Turkey). *Science and Art: A Future for Stone*, 197.

Xie, Z., Duan, Z., Zhao, Z., Li, R., Zhou, B., Yang, D., & Hu, Y. (2021). Nano-materials enhanced protectants for natural stone surfaces. *Heritage Science*, *9*(1), 1–13.

Yu, S., & Oguchi, C. T. (2010). Role of pore size distribution in salt uptake, damage, and predicting salt susceptibility of eight types of Japanese building stones. *Engineering Geology*, *115*(3–4), 226–236. https://doi.org/10.1016/j.enggeo.2009.05.007

Zanardini, E., May, E., Purdy, K. J., & Murrell, J. C. (2019). Nutrient cycling potential within microbial communities on culturally important stoneworks. *Environmental Microbiology Reports*, *11*(2), 147–154.

Zezza, F., & Macrì, F. (1995). Marine aerosol and stone decay. *Science of the Total Environment*, *167*(1–3), 123–143.

Zhang, Y., Zhang, Y., & Huang, J. (2022). Experimental study on capillary water absorption of sandstones from different grotto heritage sites in China. *Heritage Science*, *10*(1), 1–

DOI: 10.15774/PPKE.BTK.2024.021

17.

Zhou, X., Lu, H., Zhao, F., & Yu, G. (2020). Atmospheric water harvesting: a review of material and structural designs. *ACS Materials Letters*, *2*(7), 671–684.

Zimmer, J., Meyer, W., Boscardin, M.-L., & Bandelli, A. (2011). *Krak des Chevaliers in Syrien: Archäologie und Bauforschung 2003 bis 2007*. Dt. Burgenvereinigung.

DOI: 10.15774/PPKE.BTK.2024.021

Table of figures

DOI: 10.15774/PPKE.BTK.2024.021

DOI: 10.15774/PPKE.BTK.2024.021

DOI: 10.15774/PPKE.BTK.2024.021

DOI: 10.15774/PPKE.BTK.2024.021

DOI: 10.15774/PPKE.BTK.2024.021

DOI: 10.15774/PPKE.BTK.2024.021

DOI: 10.15774/PPKE.BTK.2024.021

DOI: 10.15774/PPKE.BTK.2024.021

DOI: 10.15774/PPKE.BTK.2024.021

Table of tables

DOI: 10.15774/PPKE.BTK.2024.021

DOI: 10.15774/PPKE.BTK.2024.021

Table of Equations

DOI: 10.15774/PPKE.BTK.2024.021

Appendix 1 Decay types at Crac des Chevaliers

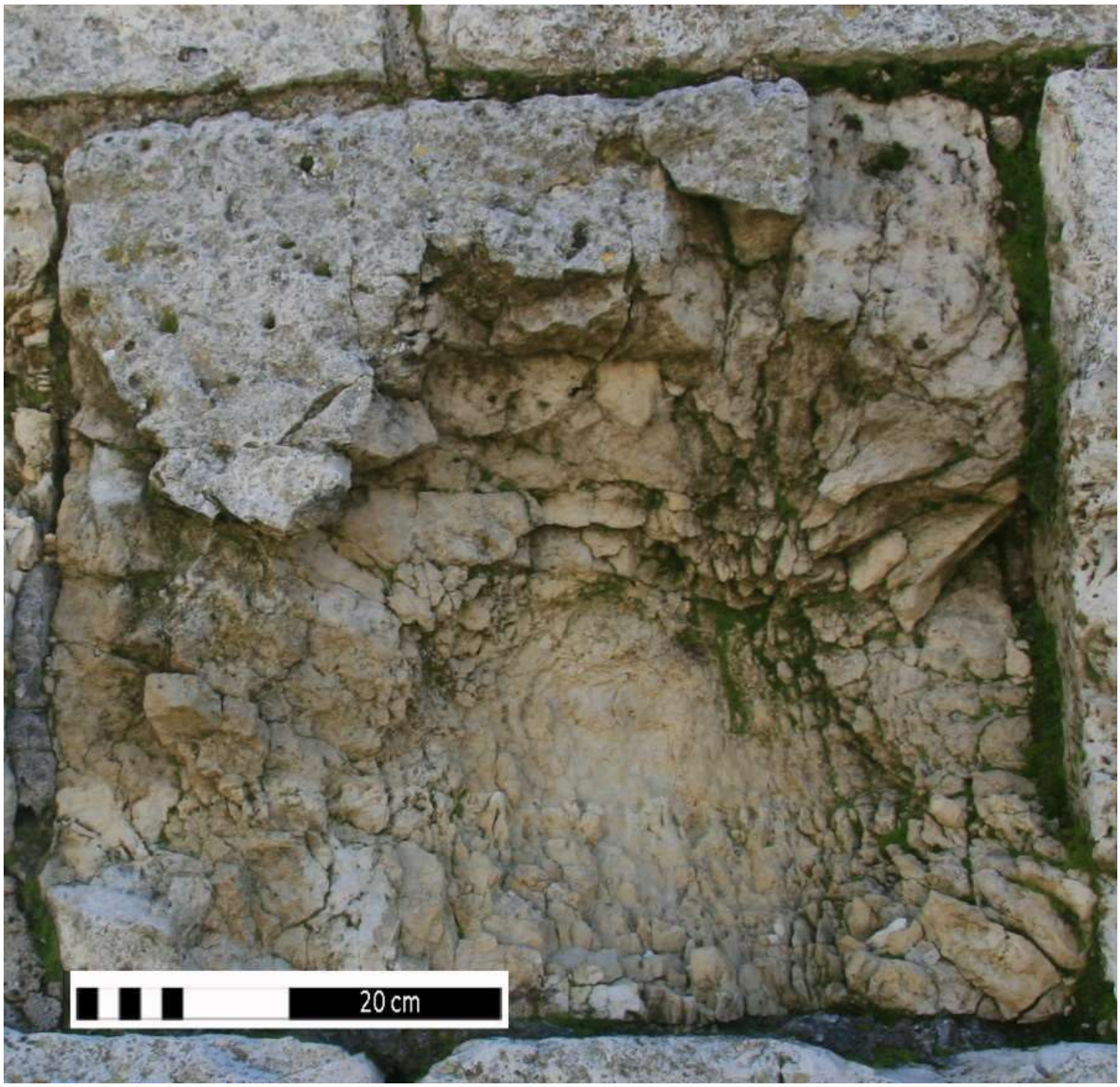

Figure 1

Fragmentation:

- There are types of fragmented stones, either the stone entirely or partially fragmented.
- The fragmentation is caused by the shots.
- The size of each single fragment from the stone ranges [0.5-10 cm (width) and 1-10cm (depth)].

DOI: 10.15774/PPKE.BTK.2024.021

Figure 2

Powdering:

- It mainly exists in stones exposed to a direct bullet at the castle.
- The diameter of the hole, which caused by the bullet, is around 15 cm while its depth around 5 cm from the stone surface.

DOI: 10.15774/PPKE.BTK.2024.021

Figure 3

Loss in stone material

- It mainly exists in stones exposed missiles fragmentation.
- The thickness of the lost material ranges (0.5 – 1.5 cm.).

DOI: 10.15774/PPKE.BTK.2024.021

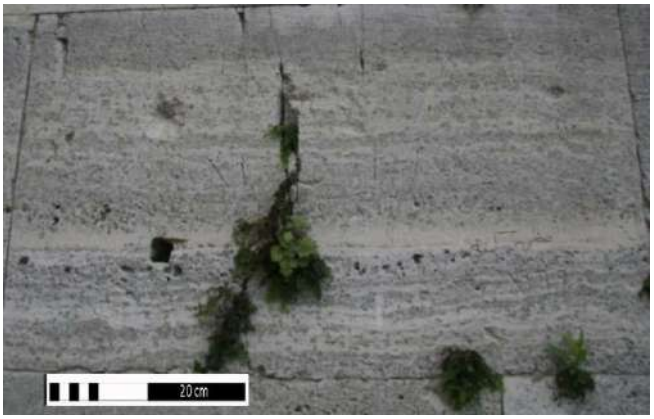

Figure 4

Higher plants:

- Two major types of higher plants that are growing on the castle walls are the shrubs and herbaceous species.
- The herbaceous species can be found either between stone joints, where the mortar was lost or inside the cracks of the stone.
- The shrubs invade some walls at the castle. They grow strongly and threat the stability of the wall. The black arrows, in the photo, refer to a huge crack in the wall.

DOI: 10.15774/PPKE.BTK.2024.021

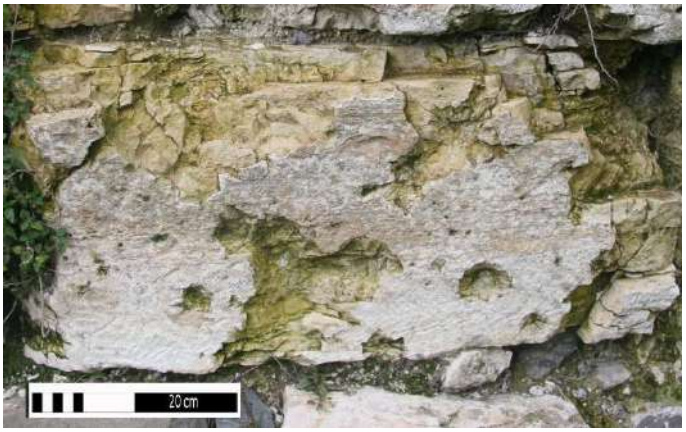

Figure 5

Green algae colonization:

- They flourish at indoor stones, which are damped enough by either water infiltration or rising damp from the ground.
- They also colonize the outdoor stones which affected by bullets and missiles fragmentations (specifically in the powdering or fragmented area).
- They appear on the stone surface in variable thickness which ranges from a moisturized green layer with no thickness, to a 1cm thick layer in some stones.

DOI: 10.15774/PPKE.BTK.2024.021

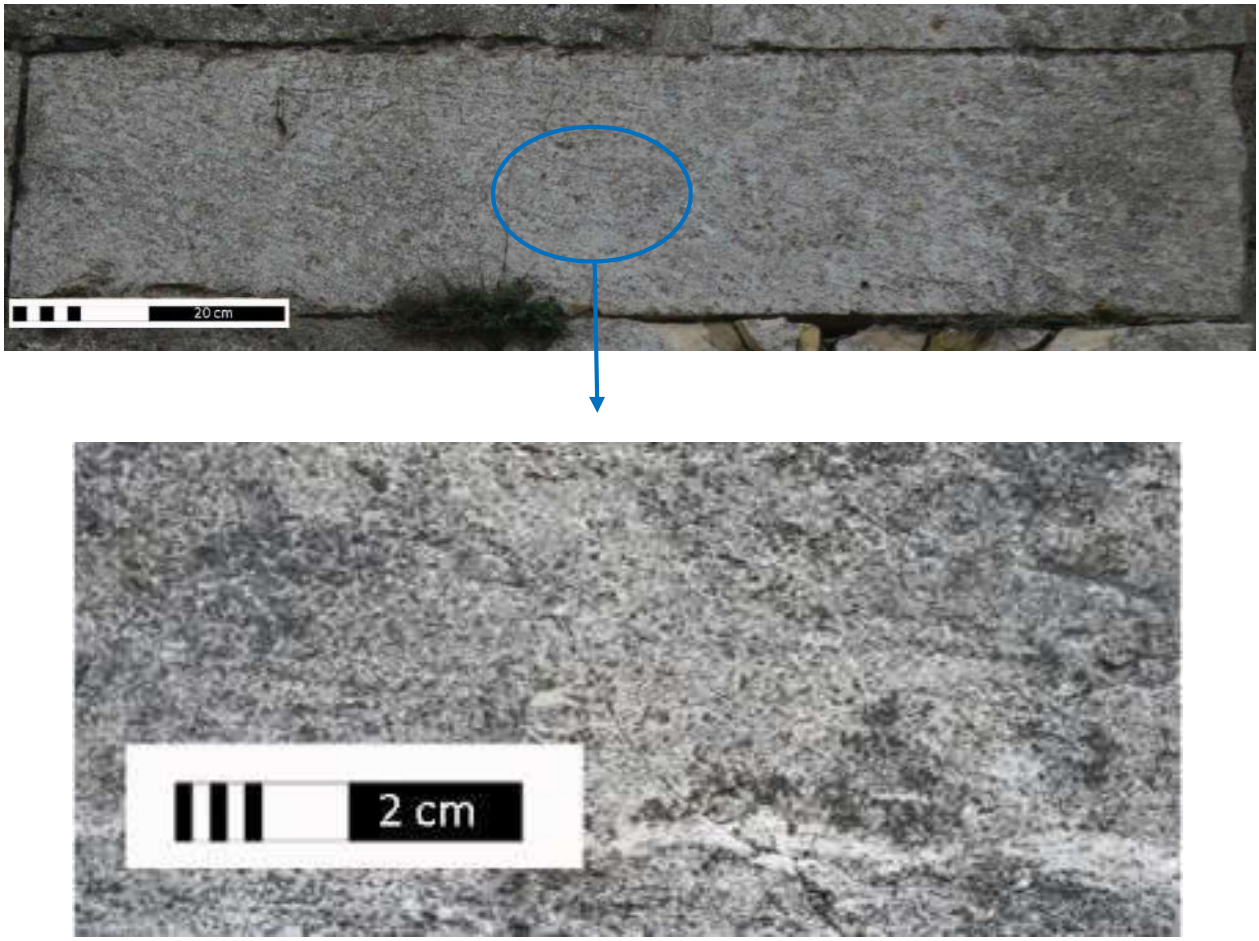

Figure 6

Deposition of grey microorganisms:

- It is an accumulation of dead microorganisms that previously colonized the stone surface
- The thickness of the deposited layer, whose colour is grey, is not visible to the naked eye in most of cases.
- This layer dominates the external west and north façades at the castle, where the moisturized stones can be dried in summertime leading to the death of the microorganisms on it.

DOI: 10.15774/PPKE.BTK.2024.021

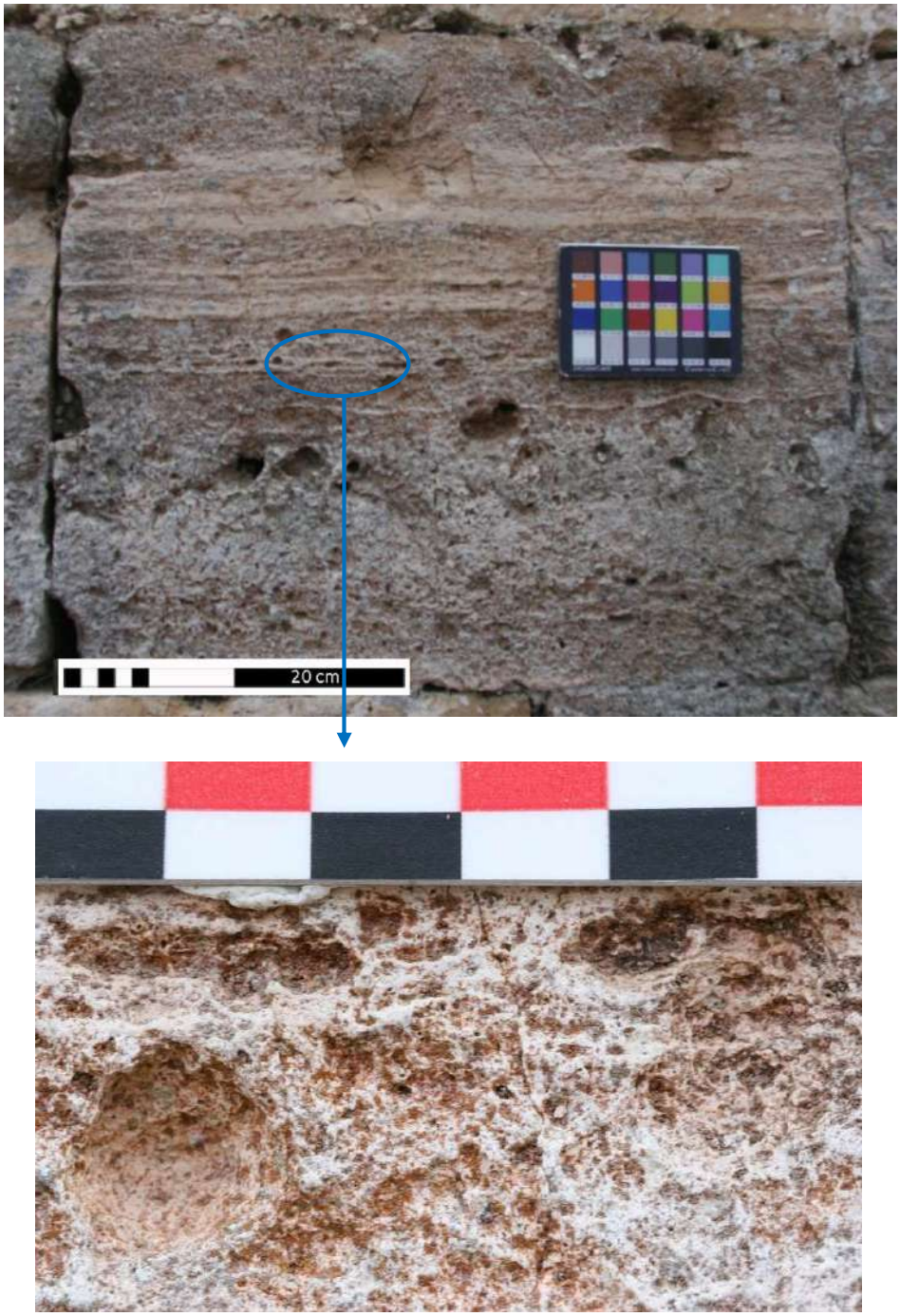

Figure 7

Red-orange algae colonization:

- This kind of biological colonization gives an orange- brown appearance to the stone surface.
- They flourish in stones that have continuous dampness. Even they can be recognized in summertime at some places at the castle.
- Their thickness on stone surface is not visible by the naked eye.

DOI: 10.15774/PPKE.BTK.2024.021

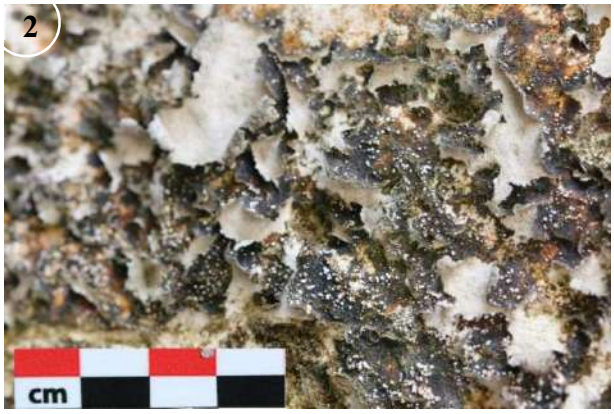

Other species of biological colonisations:

This kind of microorganisms can be found at Building (4) in northern pillars where the rainwater leaks from the roof.

The colonization is colored orange, green, and black. It forms a thin layer with a thickness of less than 0.5 mm, and that layer is peeled off from the stone surface in some areas, with a small amount of stone material attached to it.

Figure 8

DOI: 10.15774/PPKE.BTK.2024.021

Other species of biological colonisations:

This kind of microorganisms can be found at Building (4) in northern pillars where the rainwater leaks from the roof.

The colonization is brown in colour and has the appearance of moistened sand.

The thickness of the colonization is about 0.5mm.

Figure 9

DOI: 10.15774/PPKE.BTK.2024.021

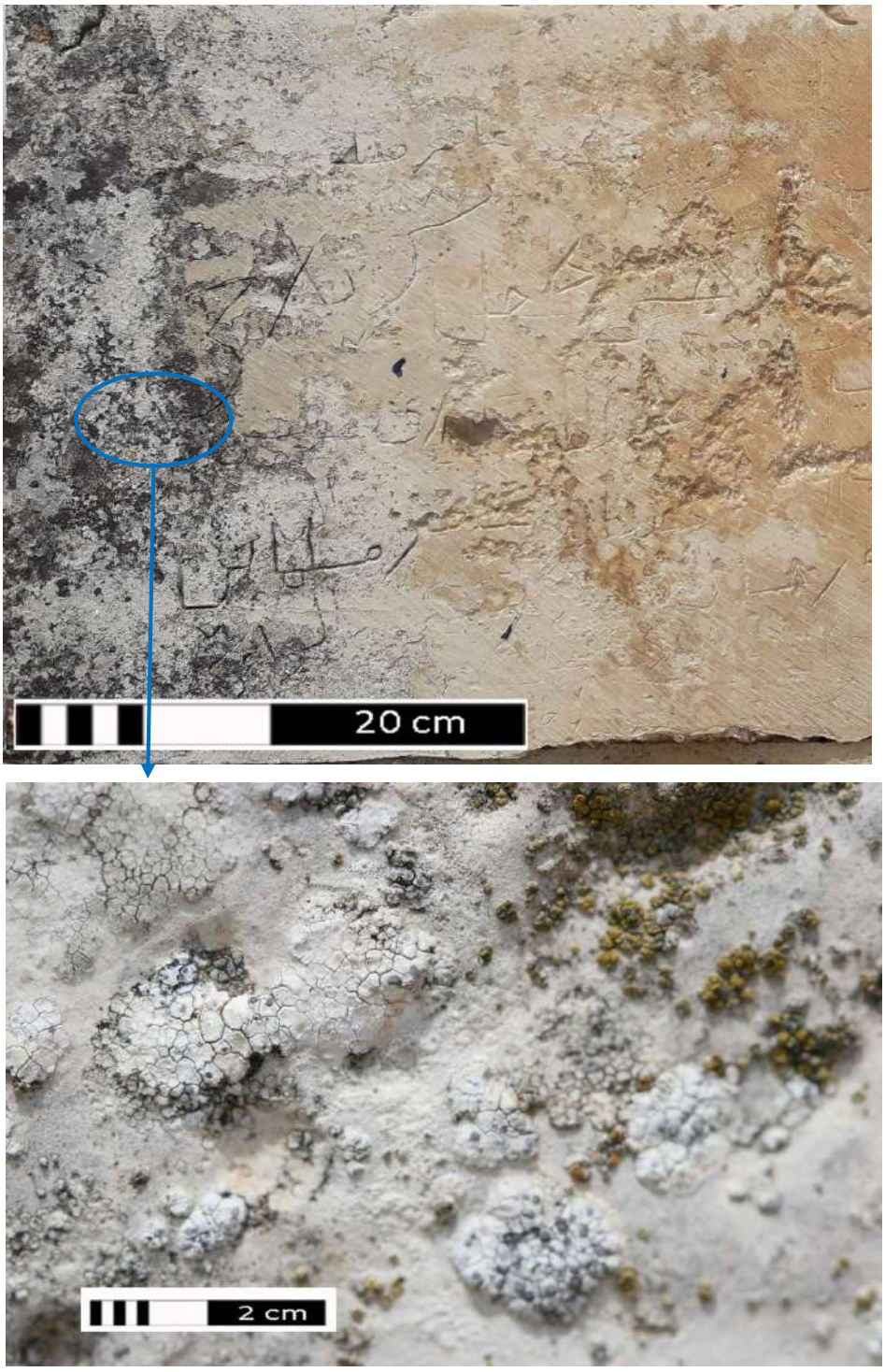

Figure 10

Accumulation of black and white microorganisms:

- This kind of biological colonization flourish in the western section of the external south façade of Building (46).
- Its thickness is about few millimetres (1-3mm).

DOI: 10.15774/PPKE.BTK.2024.021

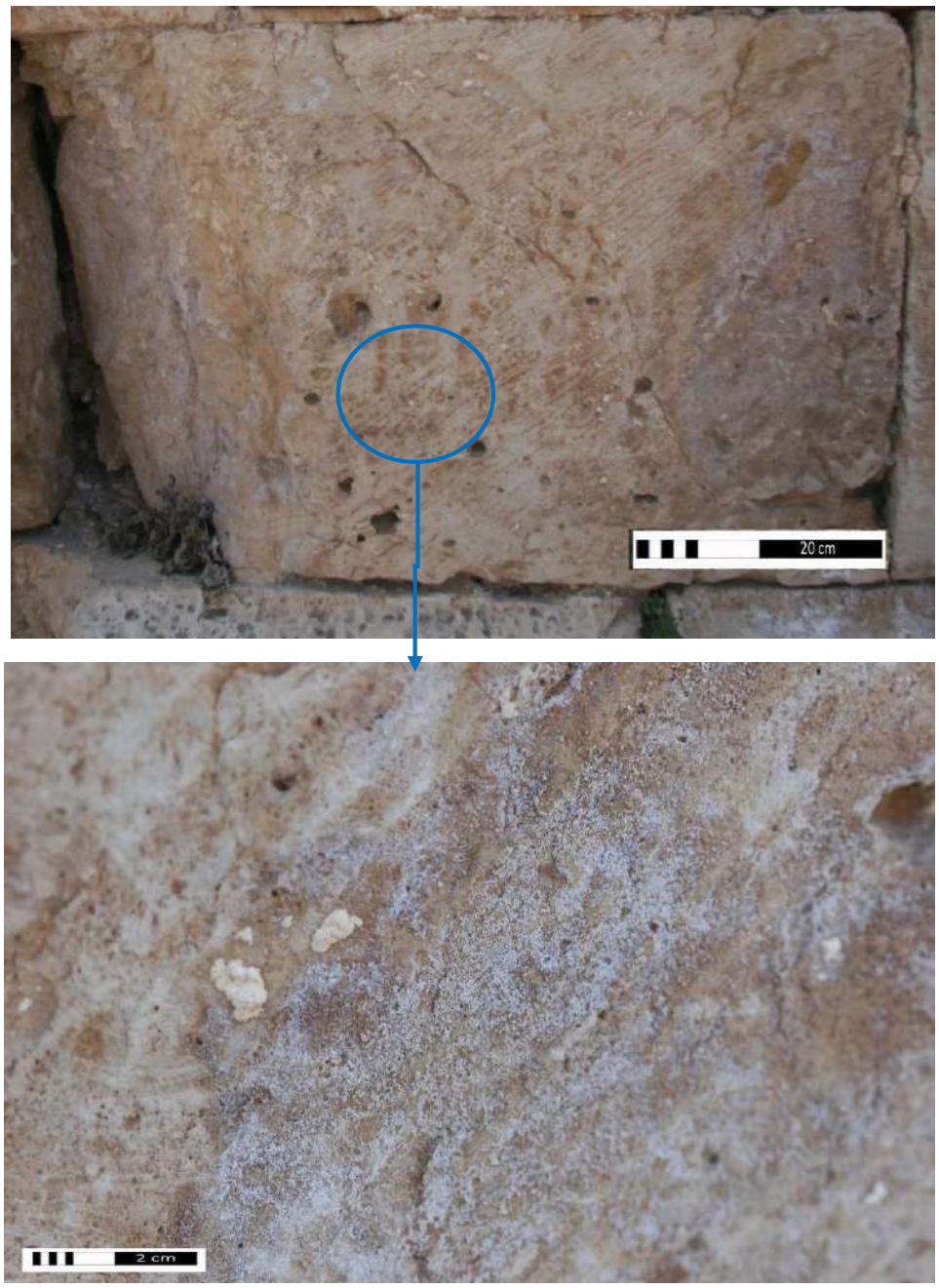

Figure 11

Salt efflorescence:

- The salts at the castle normally crystallize on the stone surface in very fine thickness (less than 0.5 mm).
- The salts layer can be distinguished at the stones that are located at both the external south and east façades.
- The white salts layer clearly appears at the discoloured stones with orange.

DOI: 10.15774/PPKE.BTK.2024.021

Figure 12

Scaling and Salt sub-efflorescence:

- The thickness of exfoliated layer on the stone surface is maximum about 0.5 cm
- The exfoliation at the castle normally co- occurs on the stones with discolouration with orange.
- On some stones appear traces of salt crystallization under the exfoliated layer.

DOI: 10.15774/PPKE.BTK.2024.021

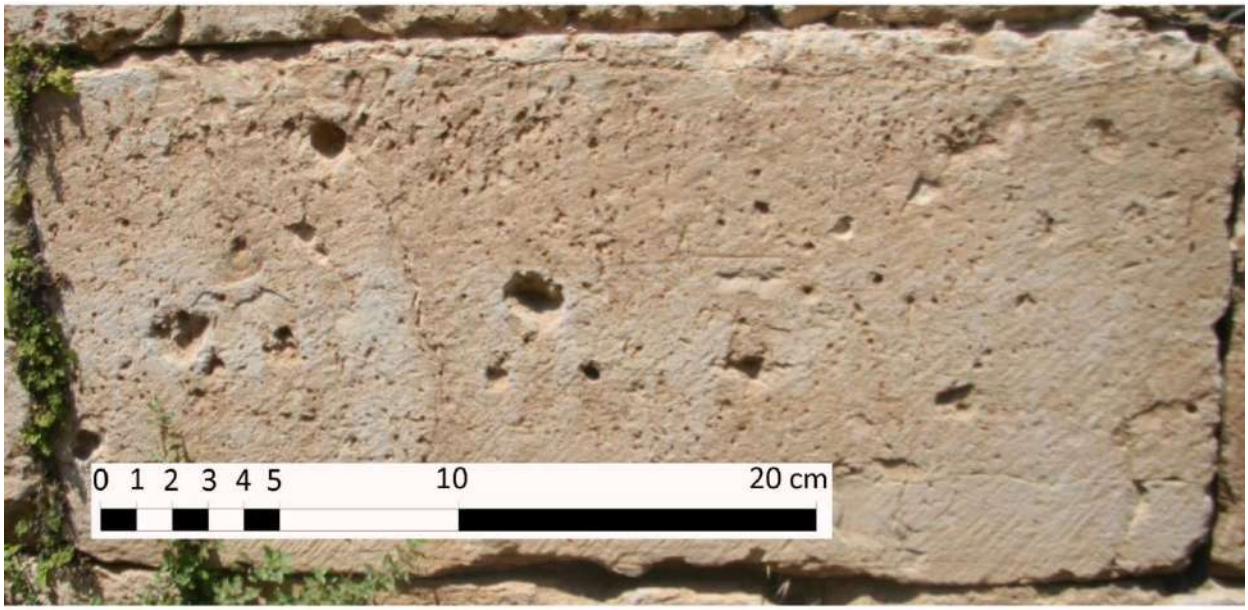

Figure 13

Discoloration with orange:

- It is an alteration in stone colour (normally from white to orange).
- This alteration generally spread in the external east and southern facades at the castle.

DOI: 10.15774/PPKE.BTK.2024.021

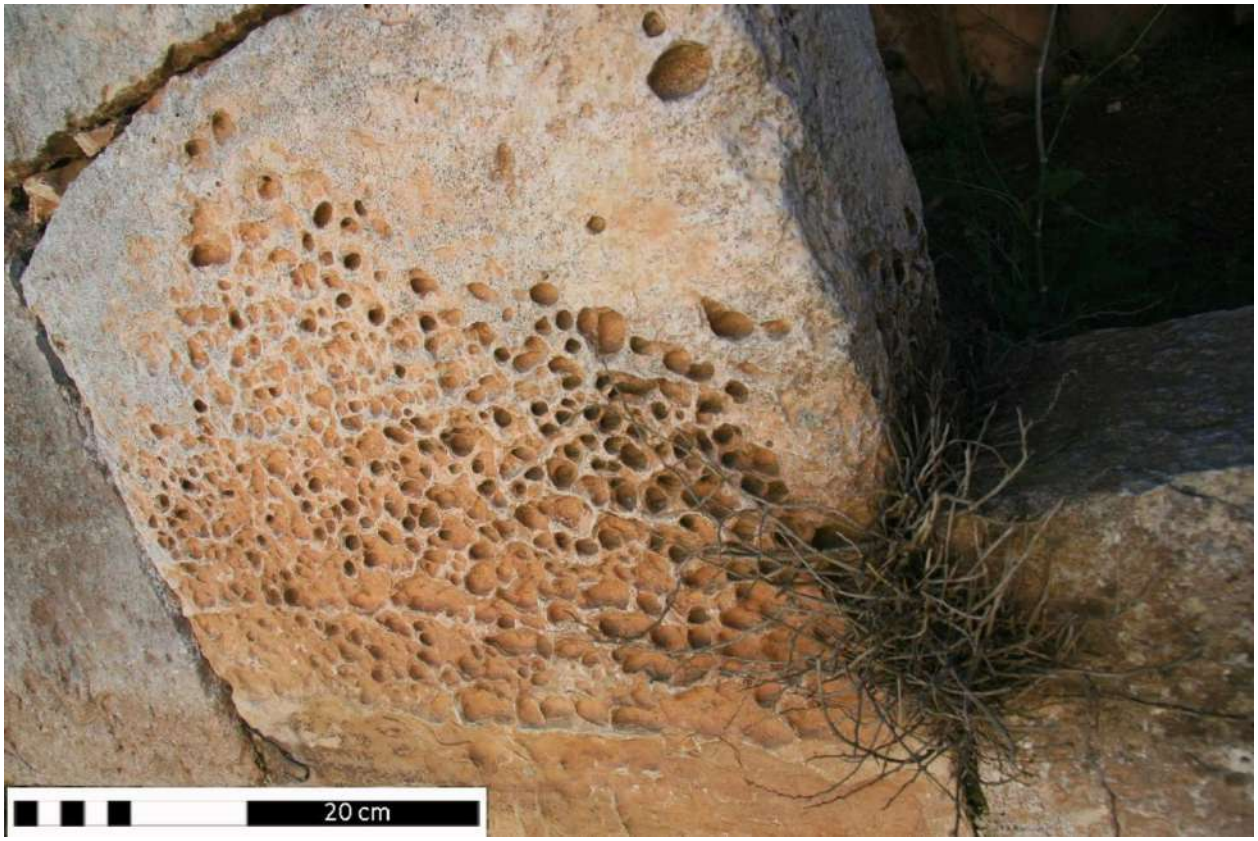

Figure 14

Pitting:

- It is a chemical erosion (acidic erosion by carbonic acid) which is caused by the physiological processes of higher plants.
- The thickness of the eroded area on the stone surface ranges from less than 0.5 mm - 0.5 cm. Whereas, the circle shape of this erosion has a diameter range of 1 mm - 1 cm.

DOI: 10.15774/PPKE.BTK.2024.021

Figure 15

Erosion:

- The eroded stones characterised by smooth surface and rounded corners.
- The stone lost approximately 1 mm- 1 cm from its surface.
- This type of deterioration is a typical case in Building (35).

DOI: 10.15774/PPKE.BTK.2024.021

Figure 16

Fracture:

- Fracture divides the stone into two separated parts.
- The thickness of the fracture ranges 0.5 mm - 2 cm.

DOI: 10.15774/PPKE.BTK.2024.021

Figure 17

Star crack:

- It is a network of cracks that are originated from one point (centre).
- The thickness of each crack is around 0.5- 10 mm.
- That point is created by mechanical damage that might be resulted from bombing effect or growth of higher plant.

DOI: 10.15774/PPKE.BTK.2024.021

Figure 18

Hair and minor crack:

- The sizes of these cracks range 0.5 mm to 2 cm.
- The cracks and fissures are not caused only by missiles and exploding effects, whereas some of them have existed before the war.
- These type of cracks do not cause separation of the of stone parts.

DOI: 10.15774/PPKE.BTK.2024.021

Figure 19

Splitting:

- Those parts are fragmented and weakly attached to the mother stone.
- The sizes of splitting parts are variable (between 2- 10 cm in depth and 1-15 cm in wide).
- In some stone, splitting parts appear in white and grey colours.
- This case found is typical in building (35).

DOI: 10.15774/PPKE.BTK.2024.021

Figure 20

Graffitti:

- Paint marker pen or sharp tools were used for writing.

DOI: 10.15774/PPKE.BTK.2024.021

Figure 21

Deposition of orange material

- In sheltered stones, this orange material concentrates on areas which exposed to shut bullets.
- This material can be removed easily by hand.

DOI: 10.15774/PPKE.BTK.2024.021

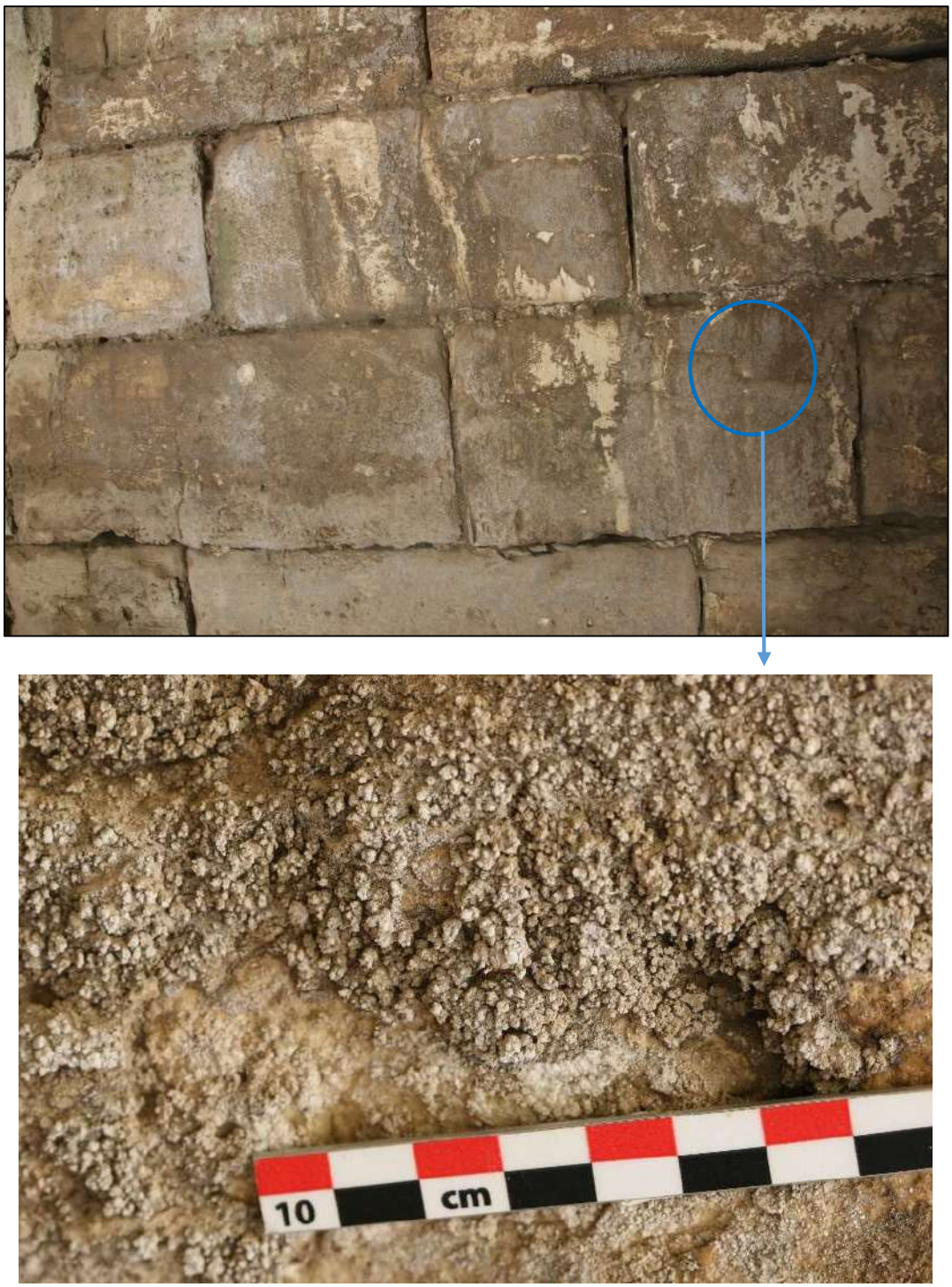

Figure 22

Encrustation:

- This orange material deposits on the stone surfaces inside Building (38).
- Its thickness ranges 2-5 mm.
- This material cannot be removed easily by hand rather it can be removed by a scraper

DOI: 10.15774/PPKE.BTK.2024.021

Appendix 2 The locations of tested stones by Rilem tube and Schmidt hammer tests and the results of the both tests

The location of tested stone	The Photo of tested stone	Name	Rilem tube results	Schmidt hammer results				
			Absorption curve	Measurements number	Rebound value			
					Min. value	Max. value	Average	Standard deviation
		HPS_0_1	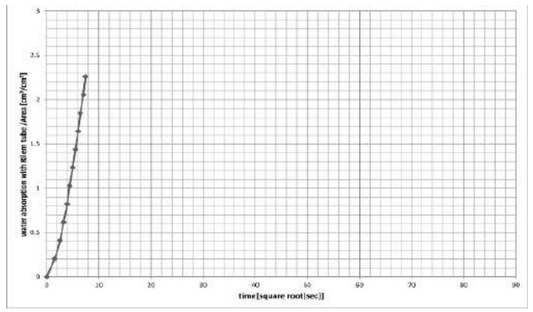	29	21.4	37.7	30.1	3.8
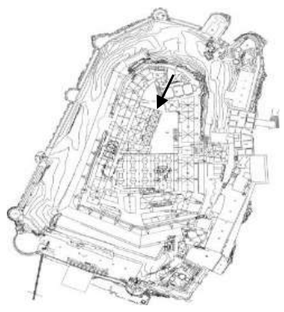		HPS_0_2	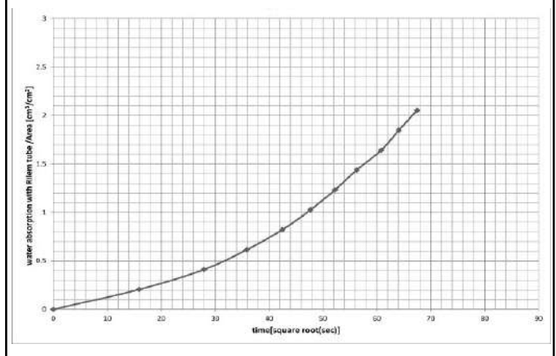	23	25.4	41.8	32.6	3.7
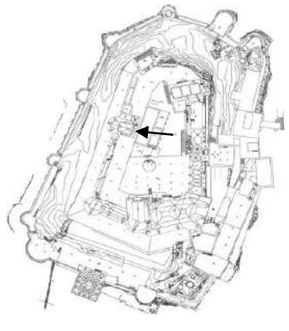		HPS_s	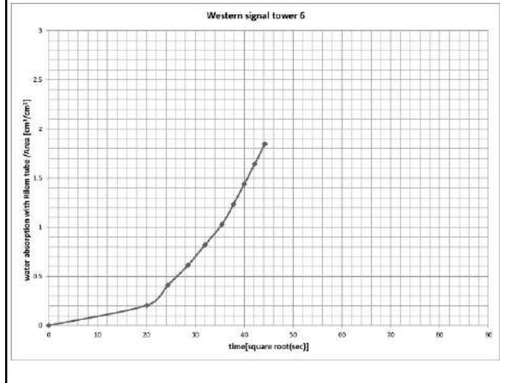	14	33.6	38.7	34.5	5.6

DOI: 10.15774/PPKE.BTK.2024.021

The location of tested stone	The Photo of tested stone	Name	Rilem tube results	Schmidt hammer results				
			Absorption curve	Measurements number	Rebound value			
					Min. value	Max. value	Average	Standard deviation
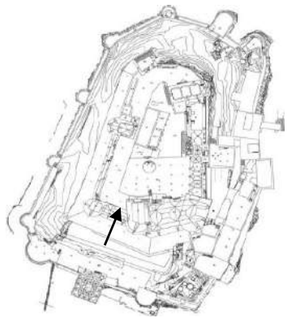		HPS_D	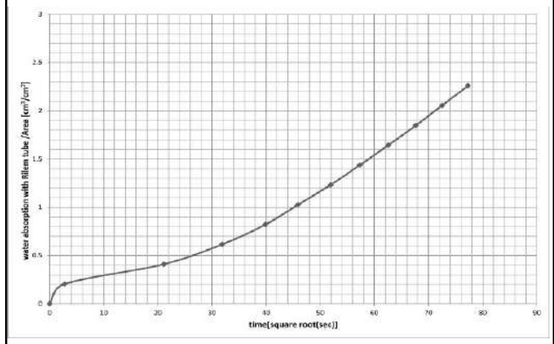	32	23.4	49.0	33.6	6.5
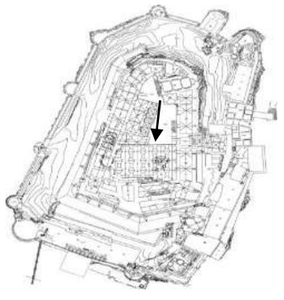		HPS_MC	_____	28	25.4	52.1	38.4	6.8

DOI: 10.15774/PPKE.BTK.2024.021

The location of tested stone	The Photo of tested stone	Name	Rilem tube results	Schmidt hammer results				
			Absorption curve	Measurements	Rebound			
					Min. value	Max. value	Average	Standard deviation
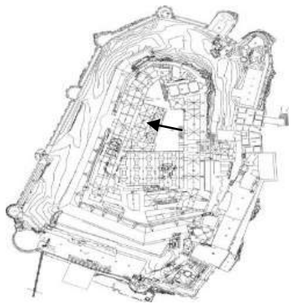		HDS_0	_____	33	27.5	48.0	39.5	5.4
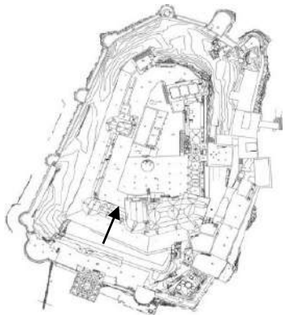		HDS_D_1	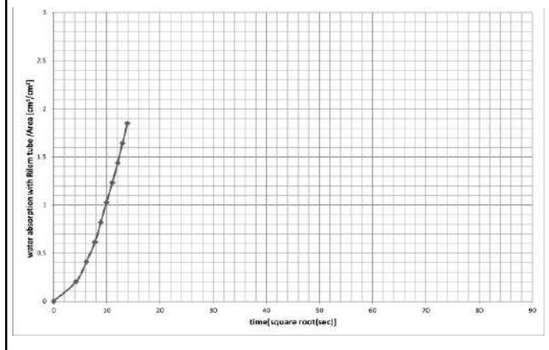	27	27.5	48.0	36.4	4.9

DOI: 10.15774/PPKE.BTK.2024.021

The location of tested stone	The Photo of tested stone	Name	Rilem tube results	Schmidt hammer results				
			Absorption curve	Measurements number	Rebound value			
					Min. value	Max. value	Average	Standard deviation
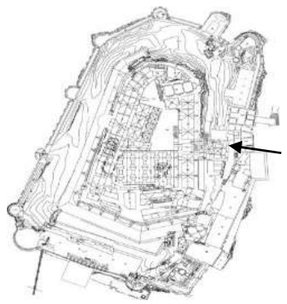		HDS_D_2	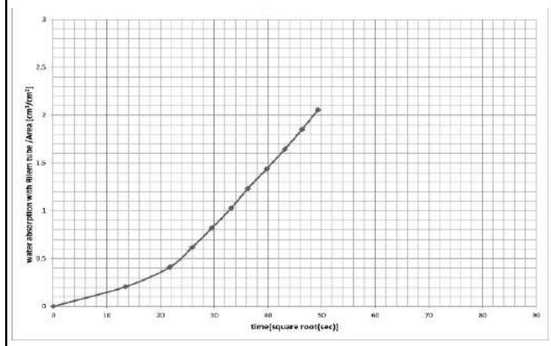	29	24.4	45.9	32.6	4.8
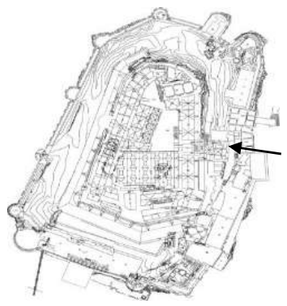		HDS_D_3	_____	31	31.5	64.5	48.5	8.9
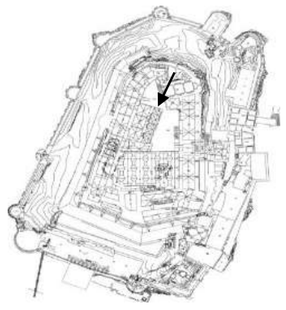		HDS_D_4	_____	25	14	30	20.6	4.2

DOI: 10.15774/PPKE.BTK.2024.021

The location of tested stone	The Photo of tested stone	Name	Rilem tube results	Schmidt hammer results				
			Absorption curve	Measurements number	Rebound value			
					Min. value	Max. value	Average	Standard deviation
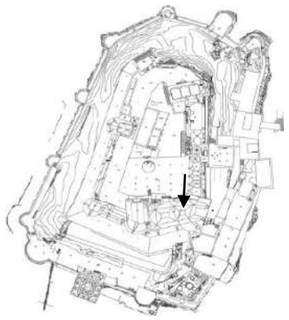		HDS_E	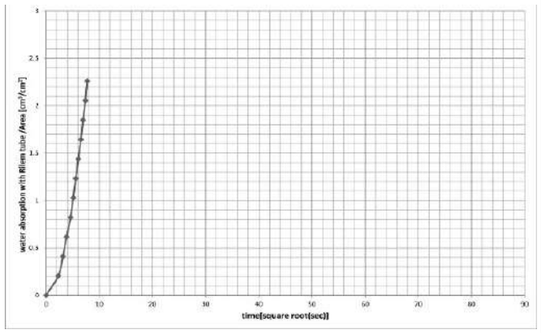	19	19.4	31.5	24.7	4
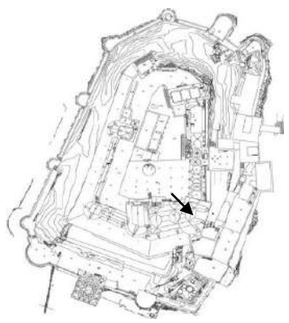		HDS_EF	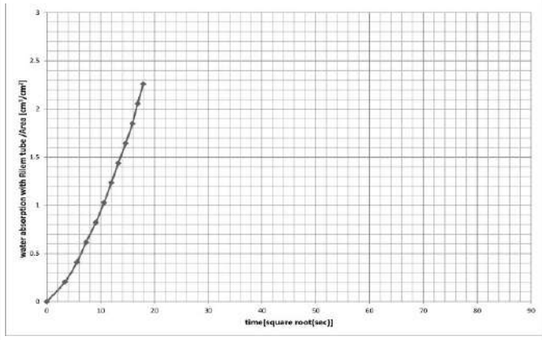	27	18.8	39.7	27.7	5.4
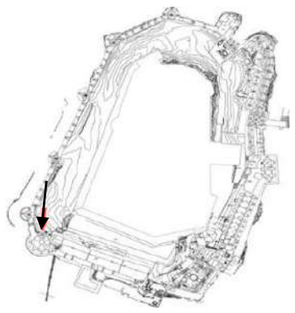		HDS_FMC	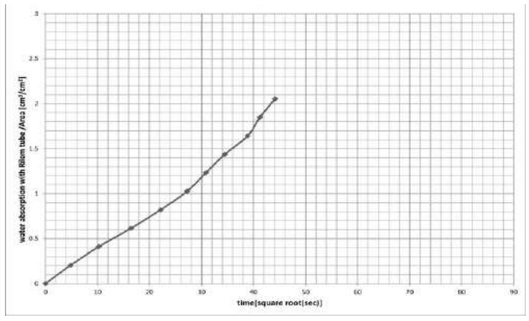	20	16.8	48.0	32.5	10.8

DOI: 10.15774/PPKE.BTK.2024.021

The location of tested stone	The Photo of tested stone	Name	Rilem tube results	Schmidt hammer results				
			Absorption curve	Measurements number	Rebound value			
					Min. value	Max. value	Average	Standard deviation
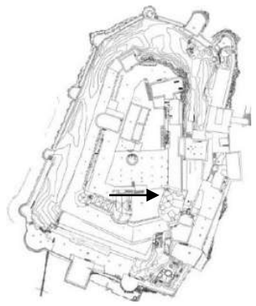		HDS_MC_1	_____	38	39.7	56.2	45.8	4
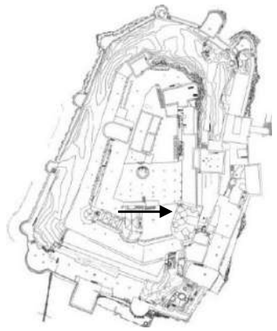		HDS_MC_2	_____	23	37.7	56.2	45.3	4.8
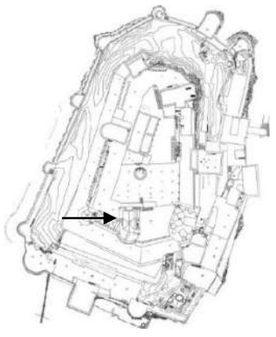		HDS_MC_3	_____	31	27.4	50.0	37.8	4.9

DOI: 10.15774/PPKE.BTK.2024.021

The location of tested stone	The Photo of tested stone	Name	Rilem tube results	Schmidt hammer results				
			Absorption curve	Measurements number	Rebound value			
					Min. value	Max. value	Average	Standard deviation
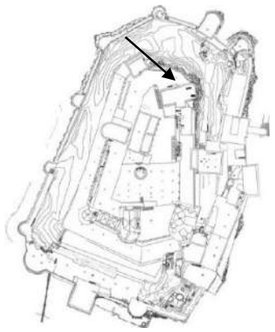	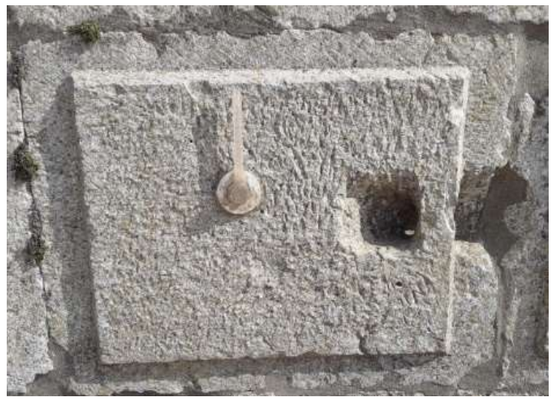	HDS_MC_4	_____	31	41.8	52.1	46.8	2.7
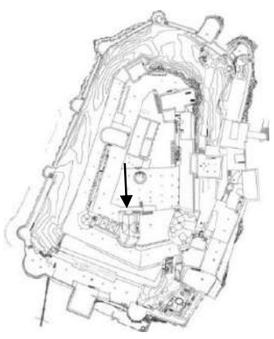		**HDS_MC_5**	_____	**29**	**27.5**	**50**	**41**	**6.1**
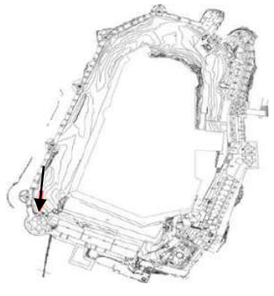		HDS_MC_6	_____	29	34.1	56.3	47.5	6.1

DOI: 10.15774/PPKE.BTK.2024.021

The location of tested stone	The Photo of tested stone	Name	Rilem tube results	Schmidt hammer results				
			Absorption curve	Measurements number	Rebound value			
					Min. value	Max. value	Average	Standard deviation
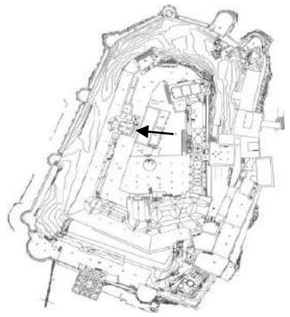		HDS_DS	_____	23	41.8	52.1	47.9	2.4
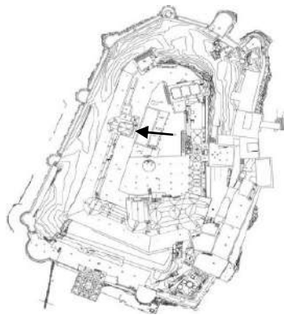		HDS_S	_____	28	28	49	40.6	1.6

DOI: 10.15774/PPKE.BTK.2024.021

The location of tested stone	The Photo of tested stone	Name	Rilem tube results	Schmidt hammer results				
			Absorption curve	Measurements number	Rebound value			
					Min. value	Max. value	Average	Standard deviation
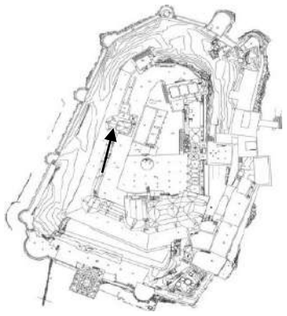		LS_S_1	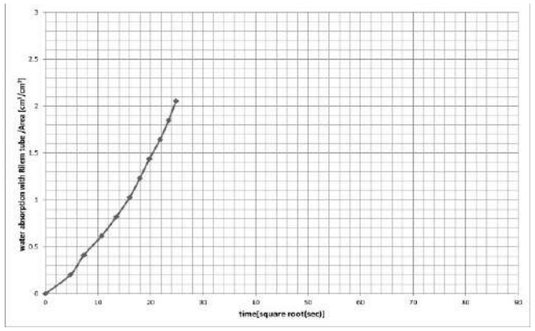	42	25.4	46.9	34.9	4.6
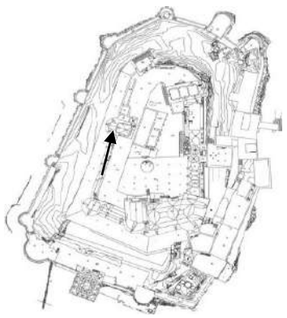		**LS_S_2**	_____	28	30	46	38.6	4.6
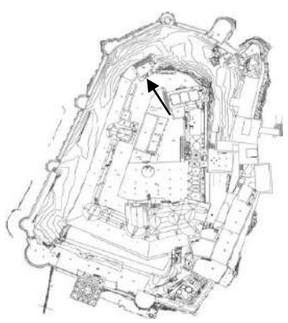		**LS_D**	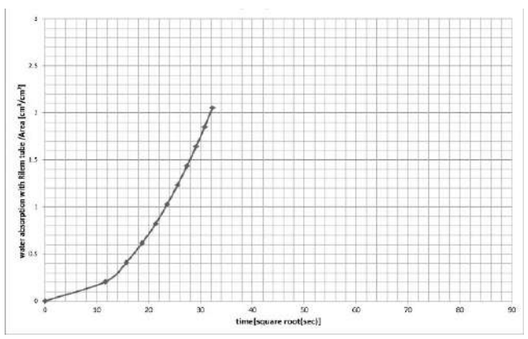	42	35.6	54.2	42.2	4.4

DOI: 10.15774/PPKE.BTK.2024.021

The location of tested stone	The Photo of tested stone	Name	Rilem tube results	Schmidt hammer results				
			Absorption curve	Measurements number	Rebound value			
					Min. value	Max. value	Average	Standard deviation
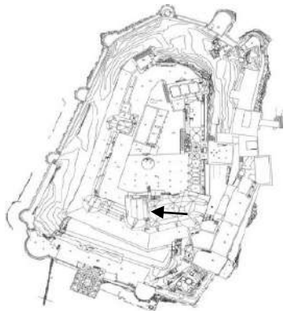		LS_DS	_____	30	34.5	61.0	46.8	5.5
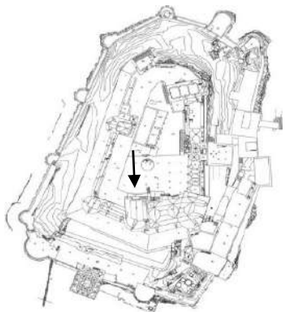		LS_MC_1	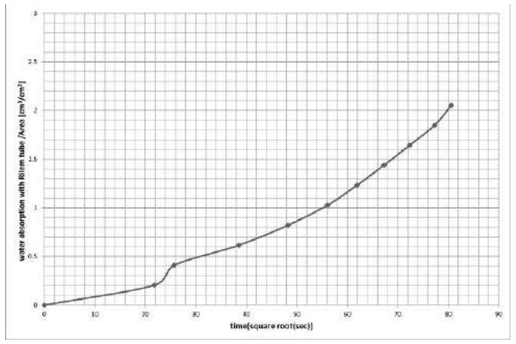	43	27.5	56.2	41.3	5.3
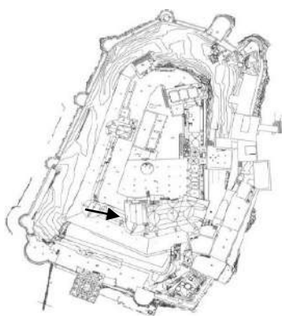		LS_MC_2	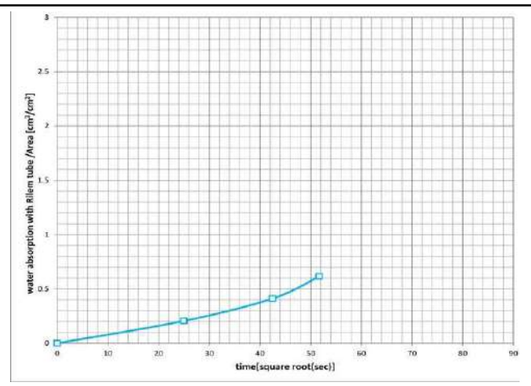	40.0	31.5	56.2	44.4	5.2

DOI: 10.15774/PPKE.BTK.2024.021

The location of tested stone	The Photo of tested stone	Name	Rilem tube results	Schmidt hammer results				
			Absorption curve	Measurements number	Rebound value			
					Min. value	Max. value	Average	Standard deviation
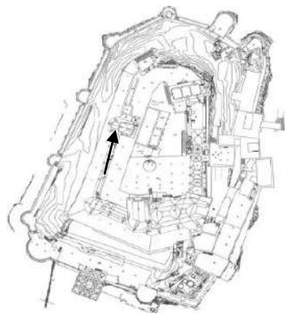		LS_MC_3	_____	38	35.6	54.2	43.6	3.9
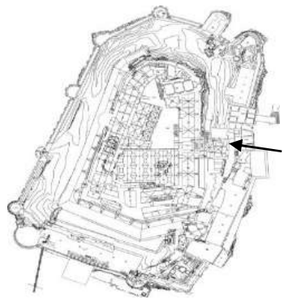		NBS_0_1	_____	26	33.6	45.9	38.1	3.4
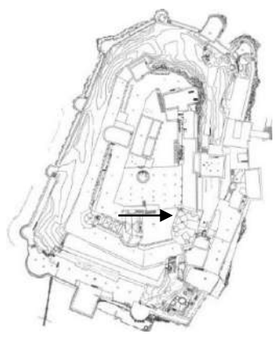		**NBS_0_2**	_____	23	35.6	53.1	42.6	4.9

DOI: 10.15774/PPKE.BTK.2024.021

The location of tested stone	The Photo of tested stone	Name	Rilem tube results	Schmidt hammer results				
			Absorption curve	Measurements number	Rebound value			
					Min. value	Max. value	Average	Standard deviation
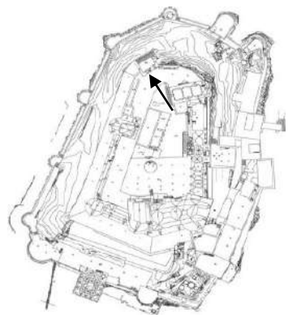		NBS_MC	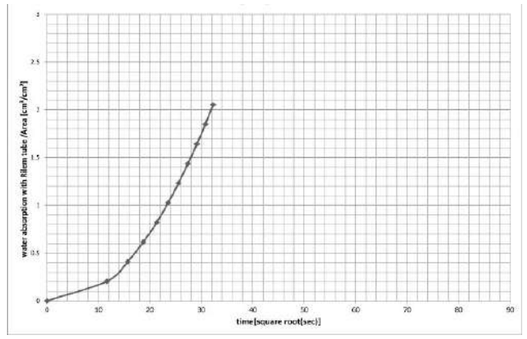	28	33.6	50	42.4	4.6
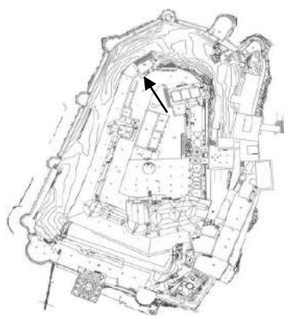		NBS_D	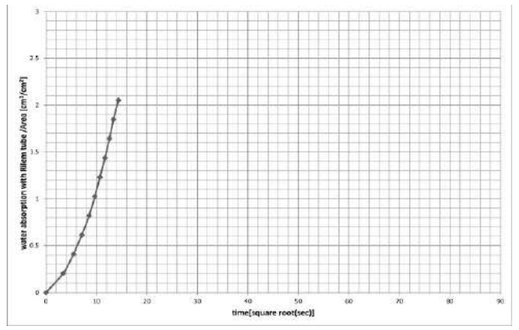	28	33.6	50	42.4	4.6
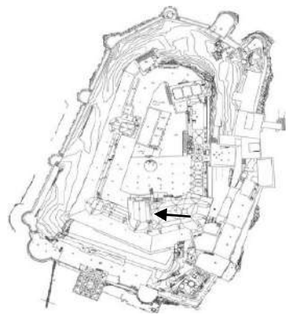		NBS_S	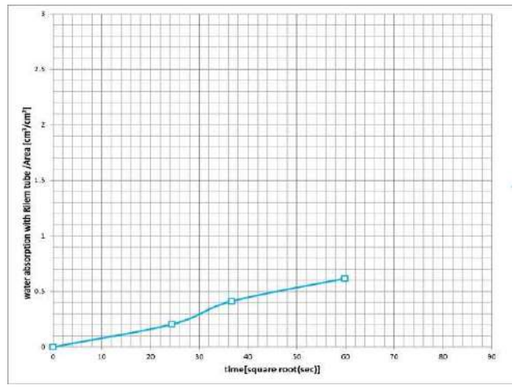	29	31.5	51.1	40.5	4.4

DOI: 10.15774/PPKE.BTK.2024.021

Appendix 3 The locations of the specimens that has been taken from the

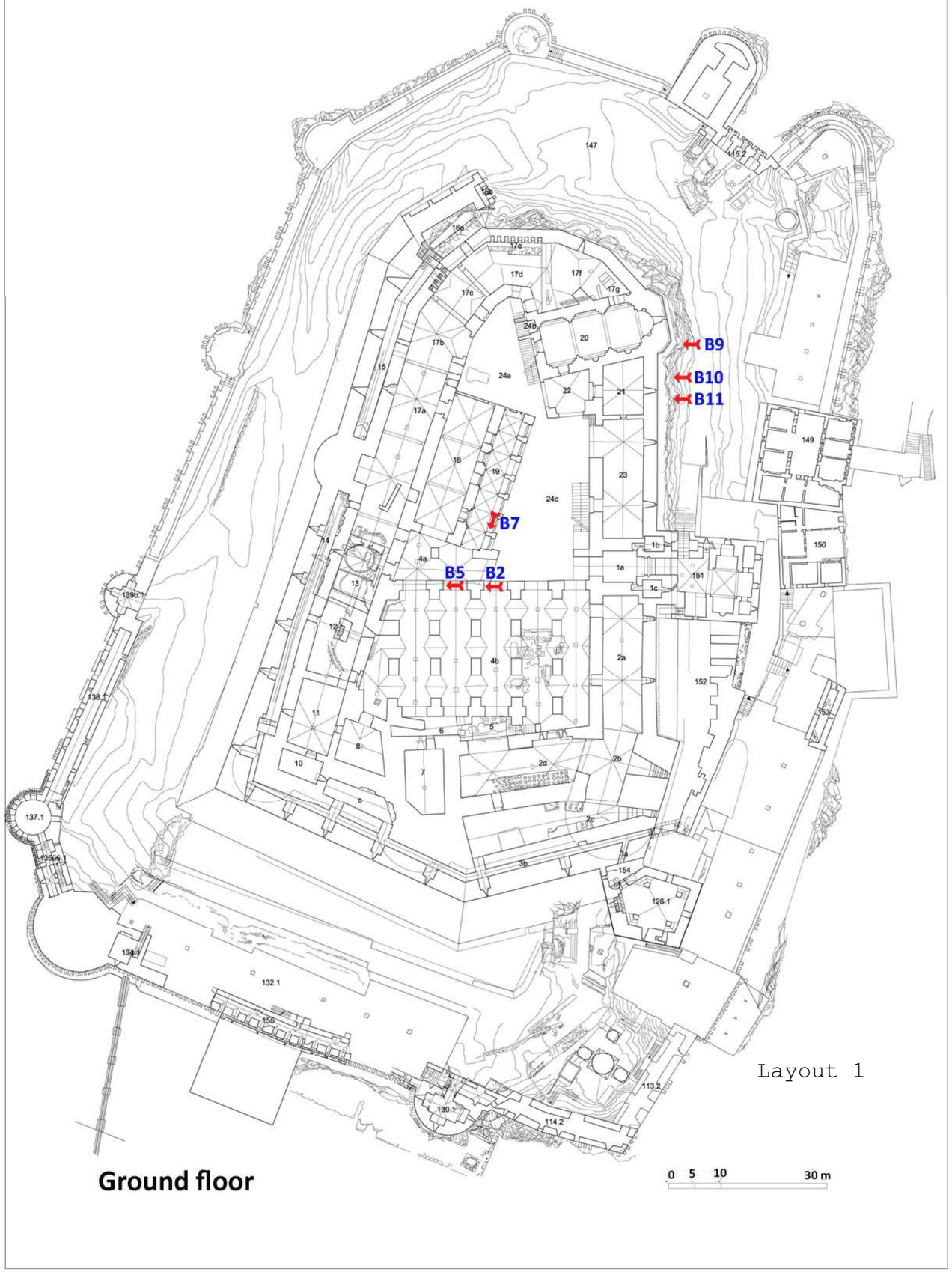

Layout 1

DOI: 10.15774/PPKE.BTK.2024.021

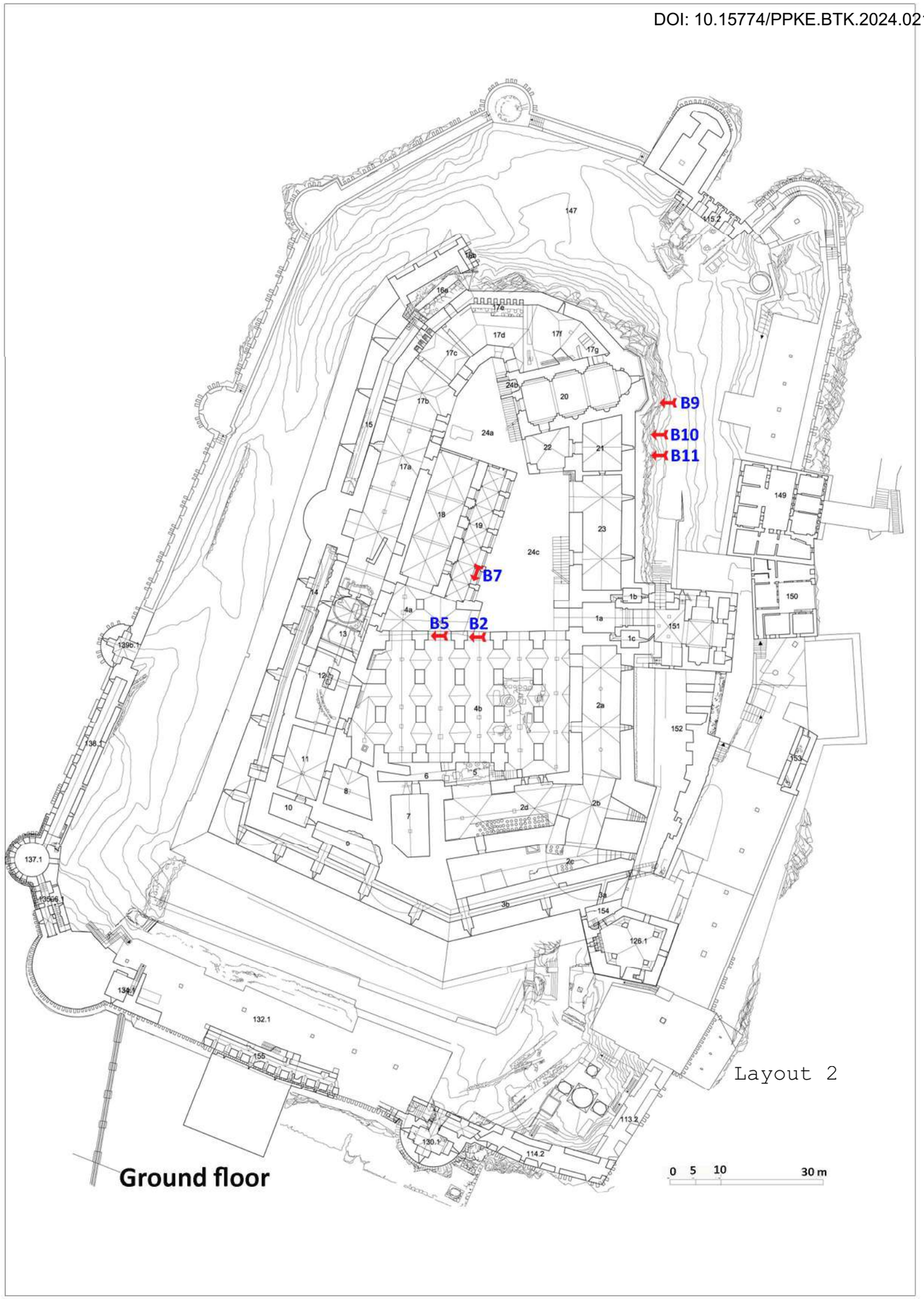

Layout 2

B10

B11

DOI: 10.15774/PPKE.BTK.2024.021

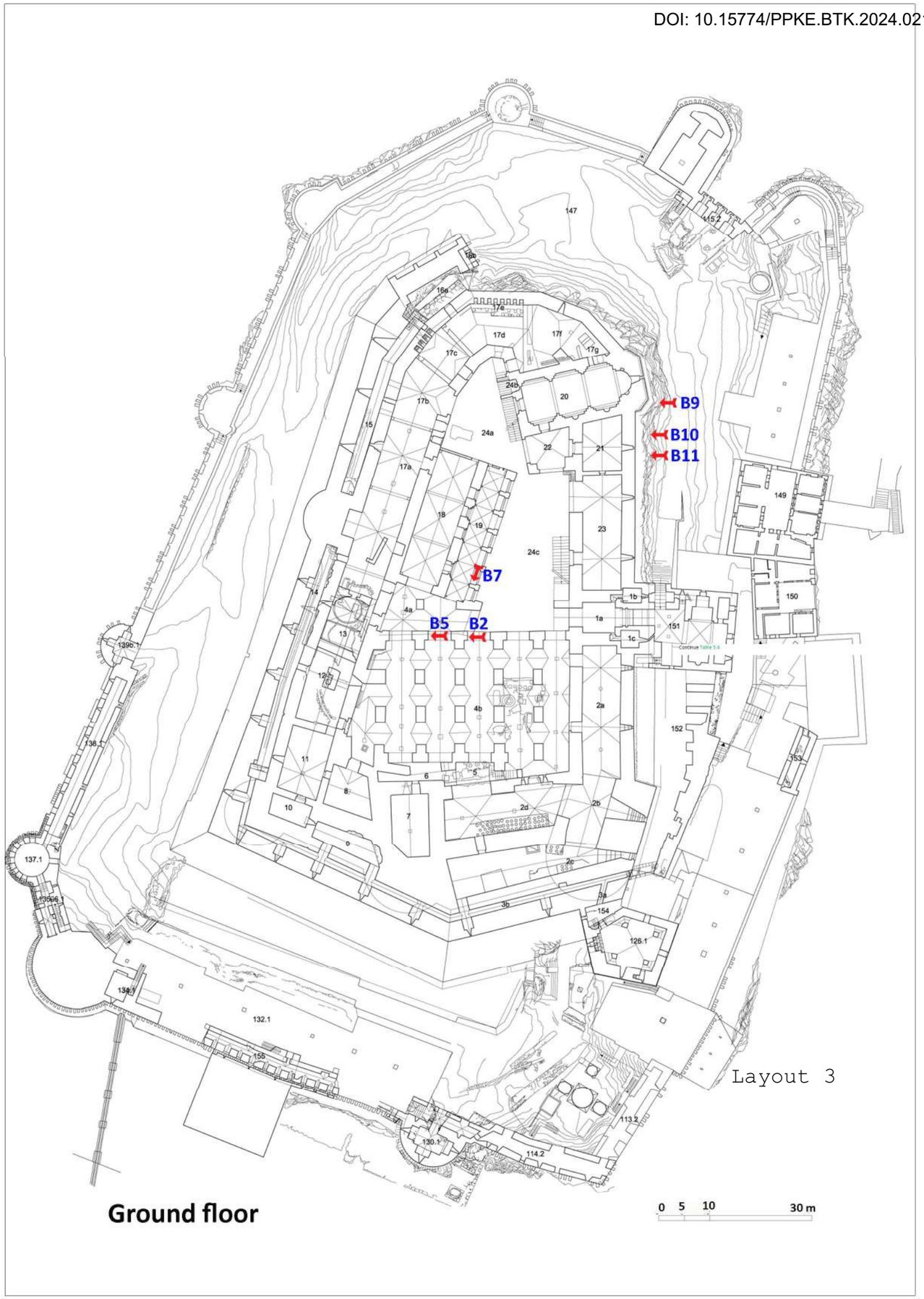

Layout 3

B9

DOI: 10.15774/PPKE.BTK.2024.021

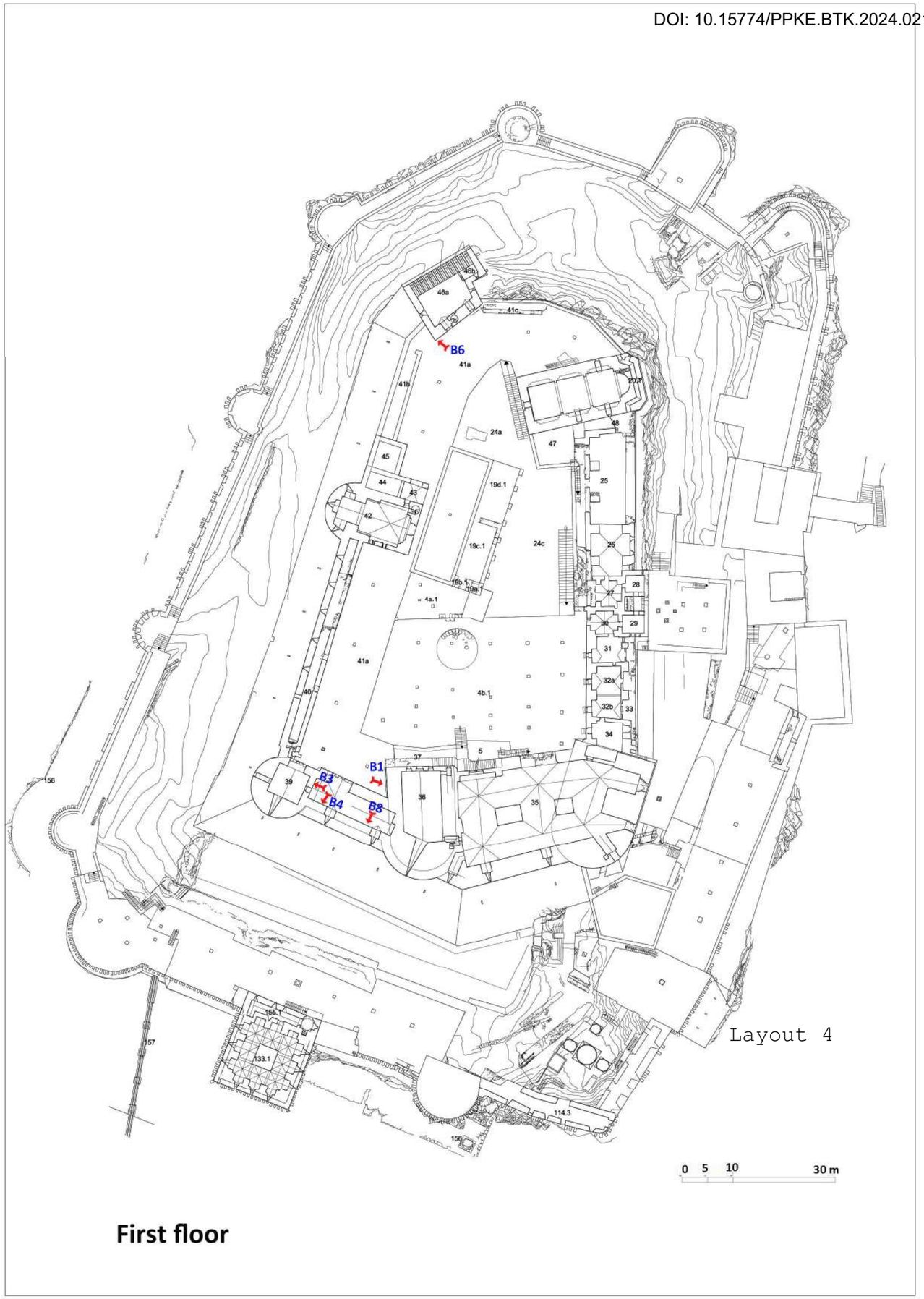

Layout 4

First floor

DOI: 10.15774/PPKE.BTK.2024.021

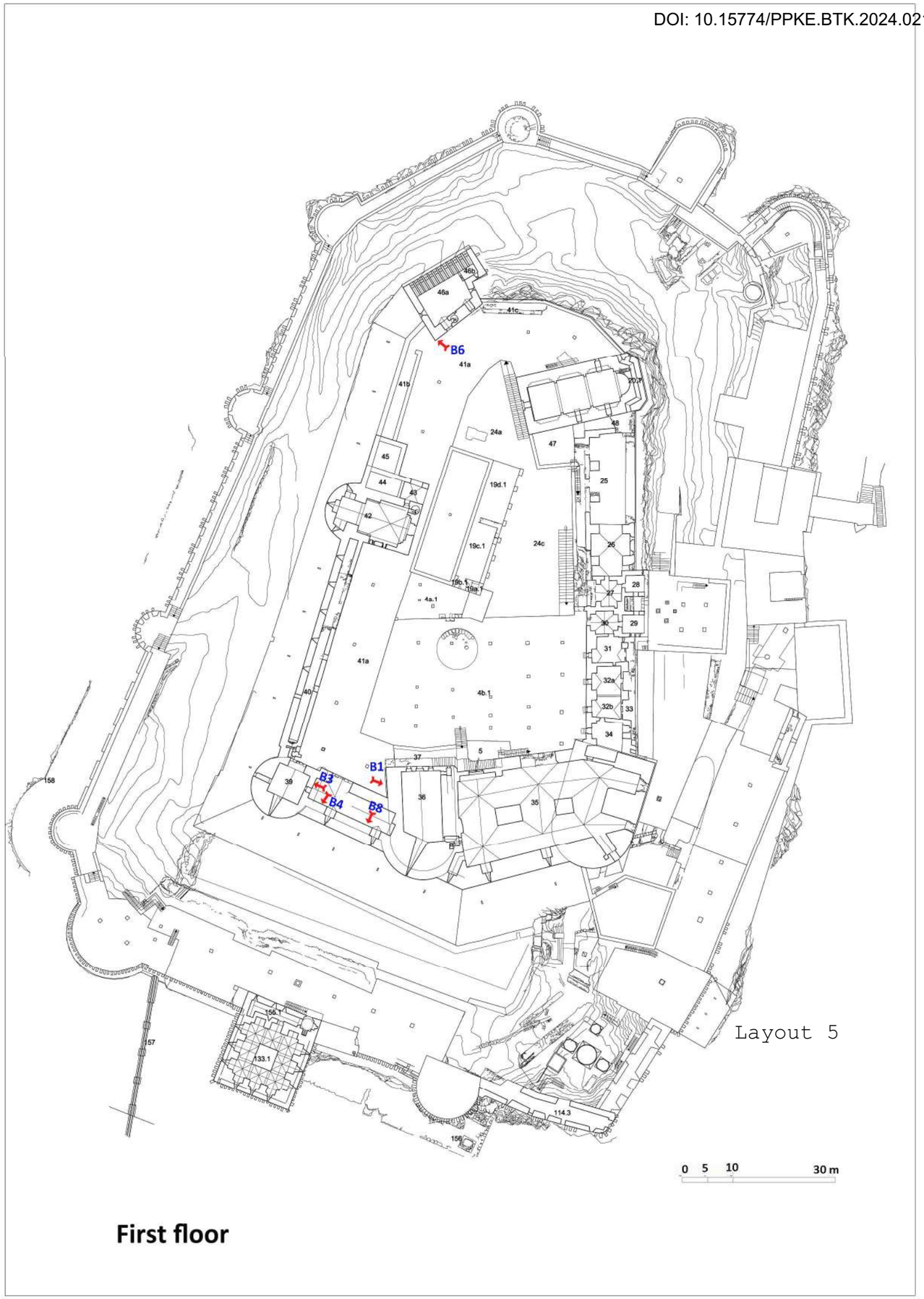

Layout 5

First floor

DOI: 10.15774/PPKE.BTK.2024.021

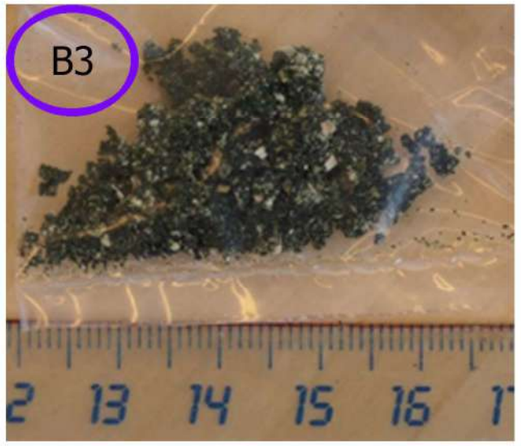

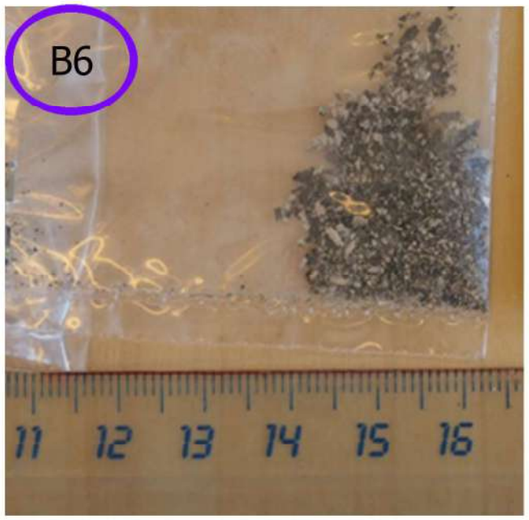

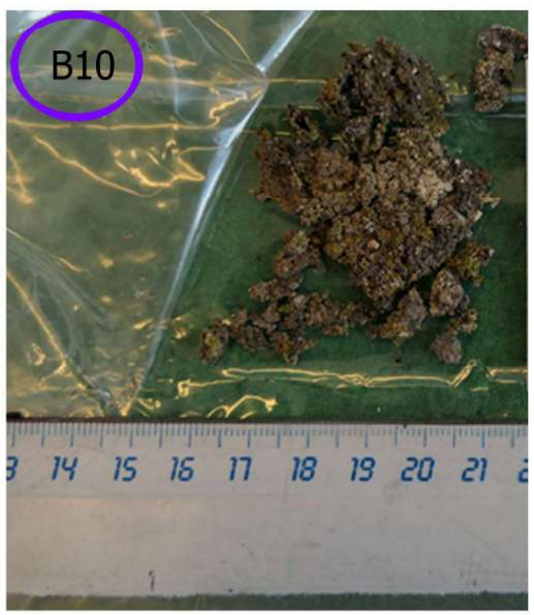

DOI: 10.15774/PPKE.BTK.2024.021

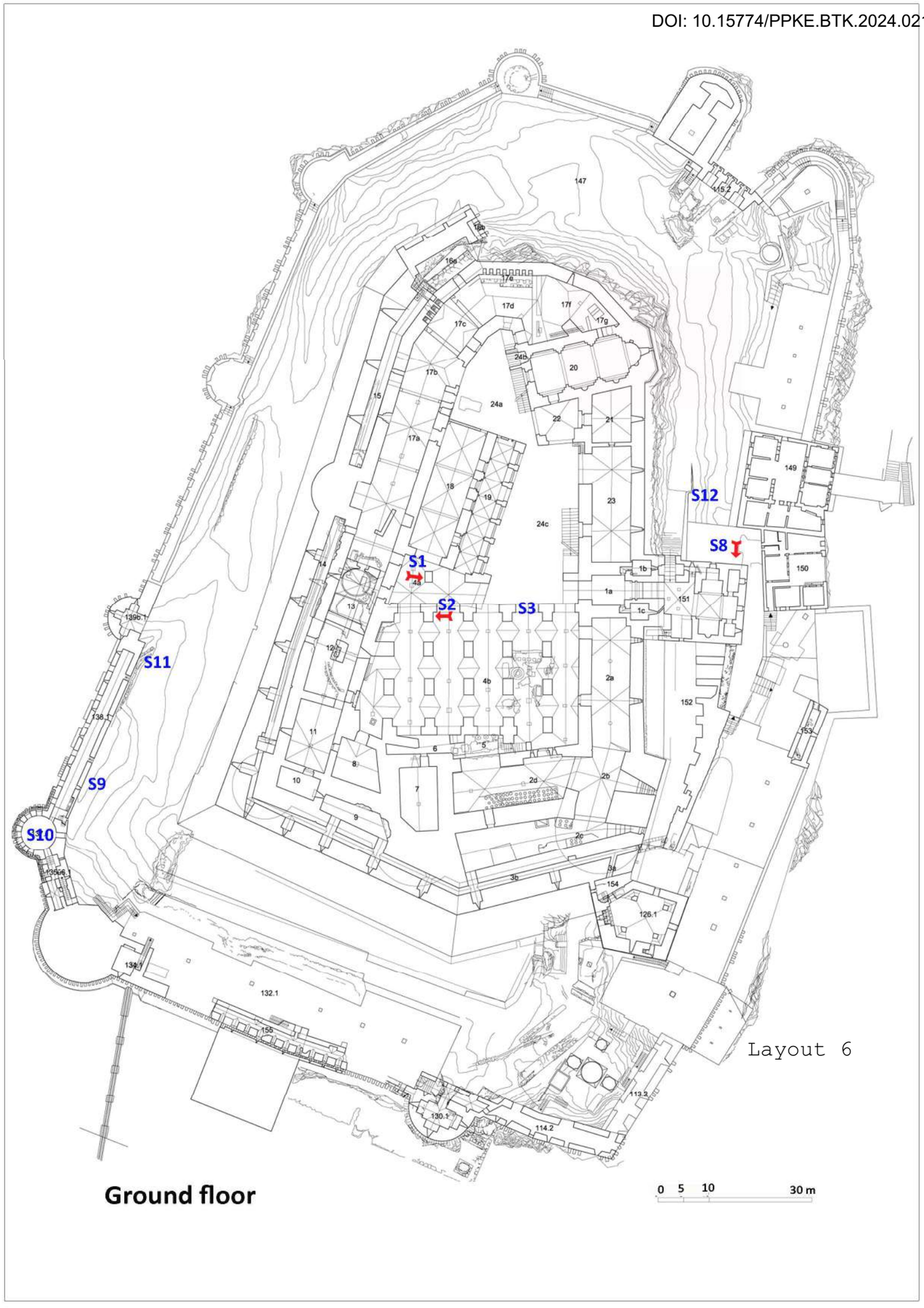

Layout 6

DOI: 10.15774/PPKE.BTK.2024.021

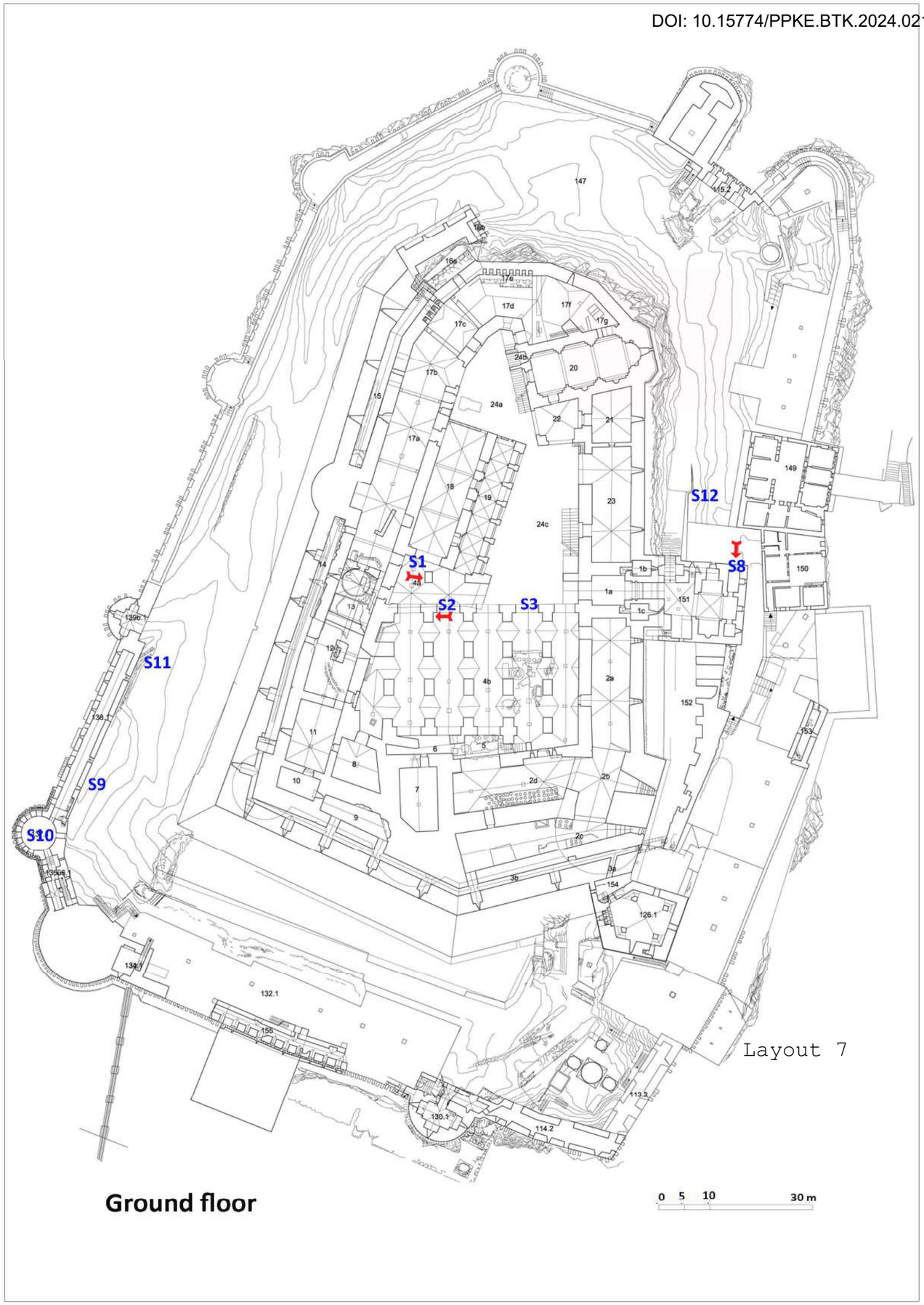

Layout 7

DOI: 10.15774/PPKE.BTK.2024.021

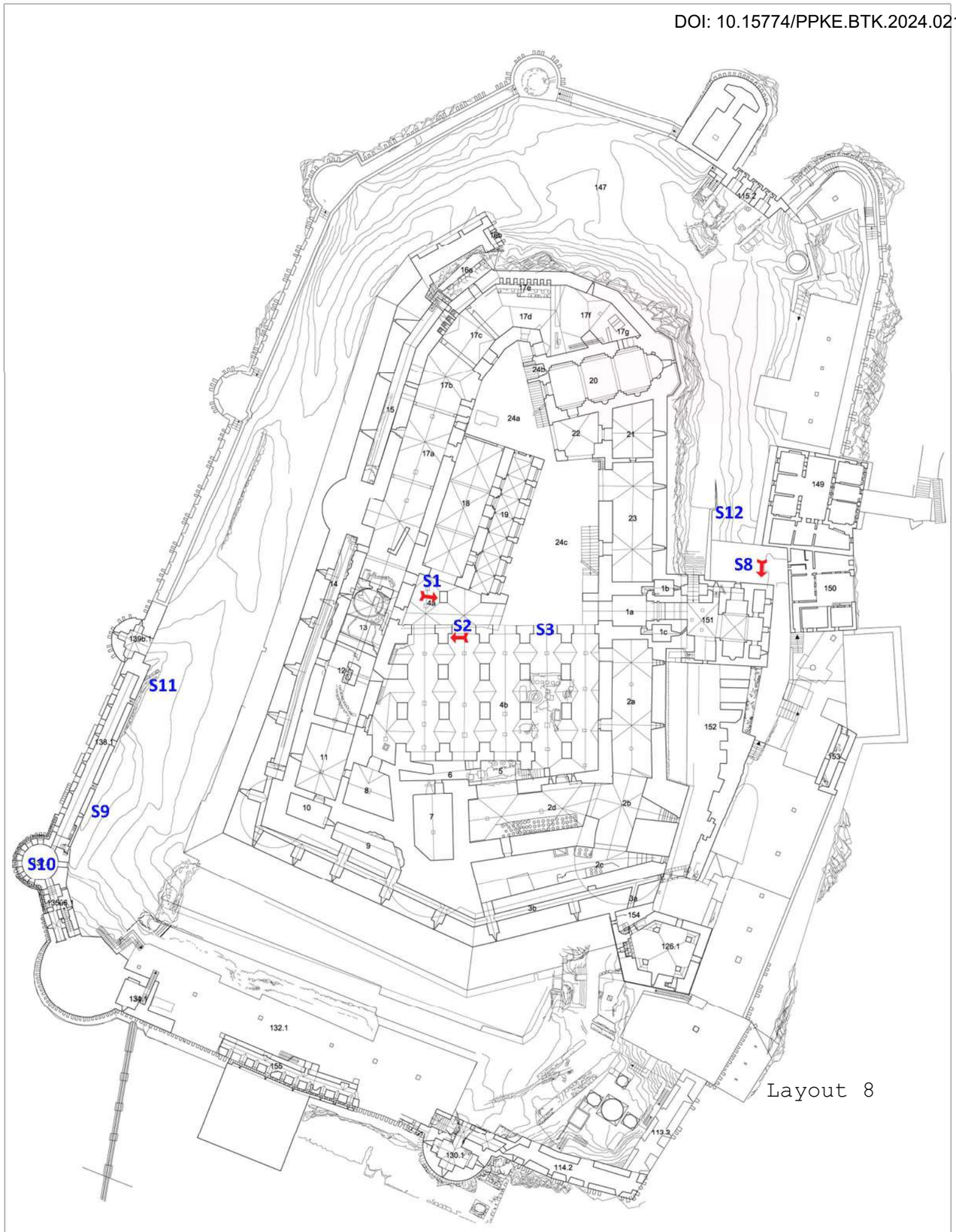

Ground floor

Layout 8

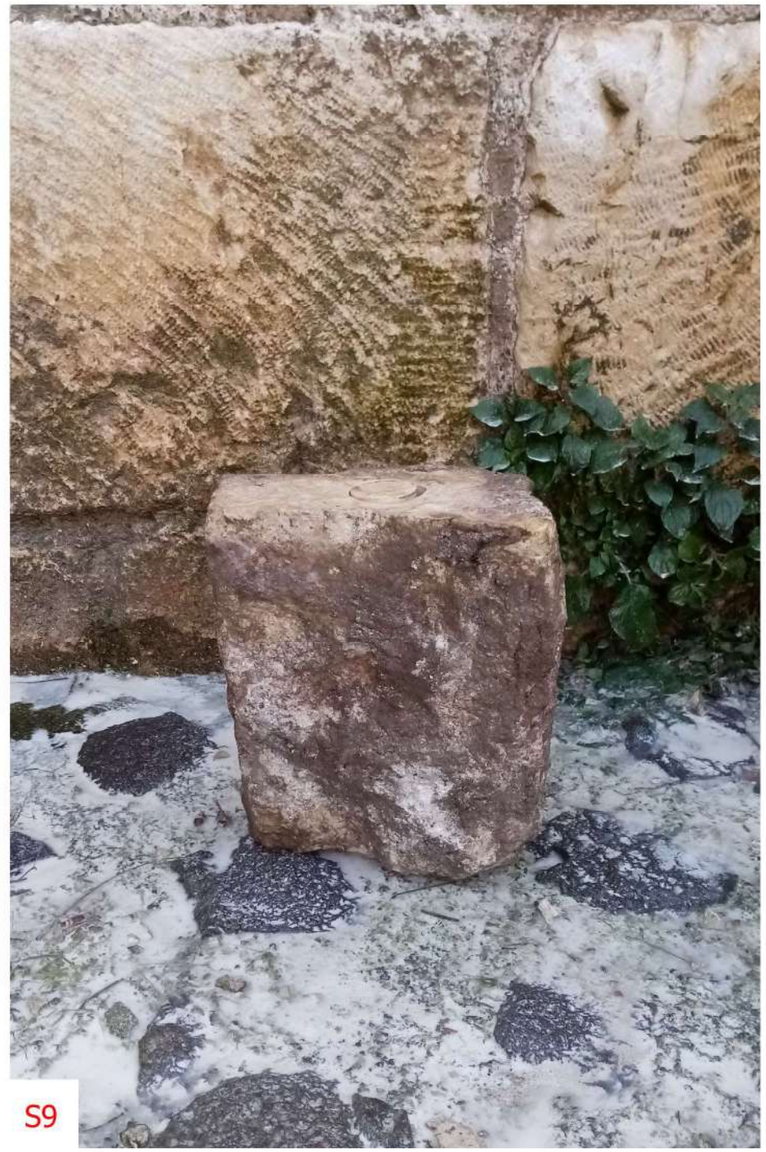

DOI: 10.15774/PPKE.BTK.2024.021

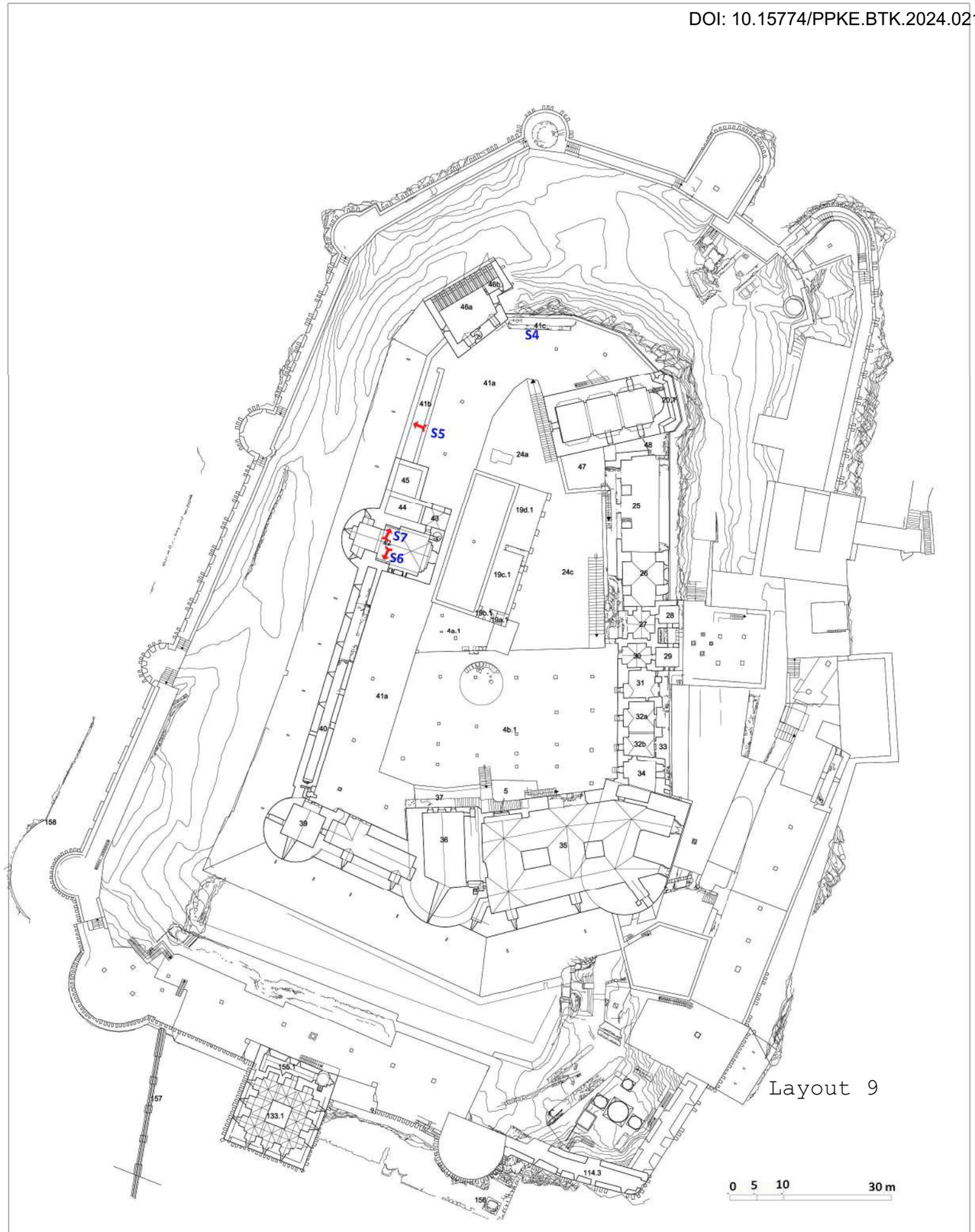

First floor

DOI: 10.15774/PPKE.BTK.2024.021

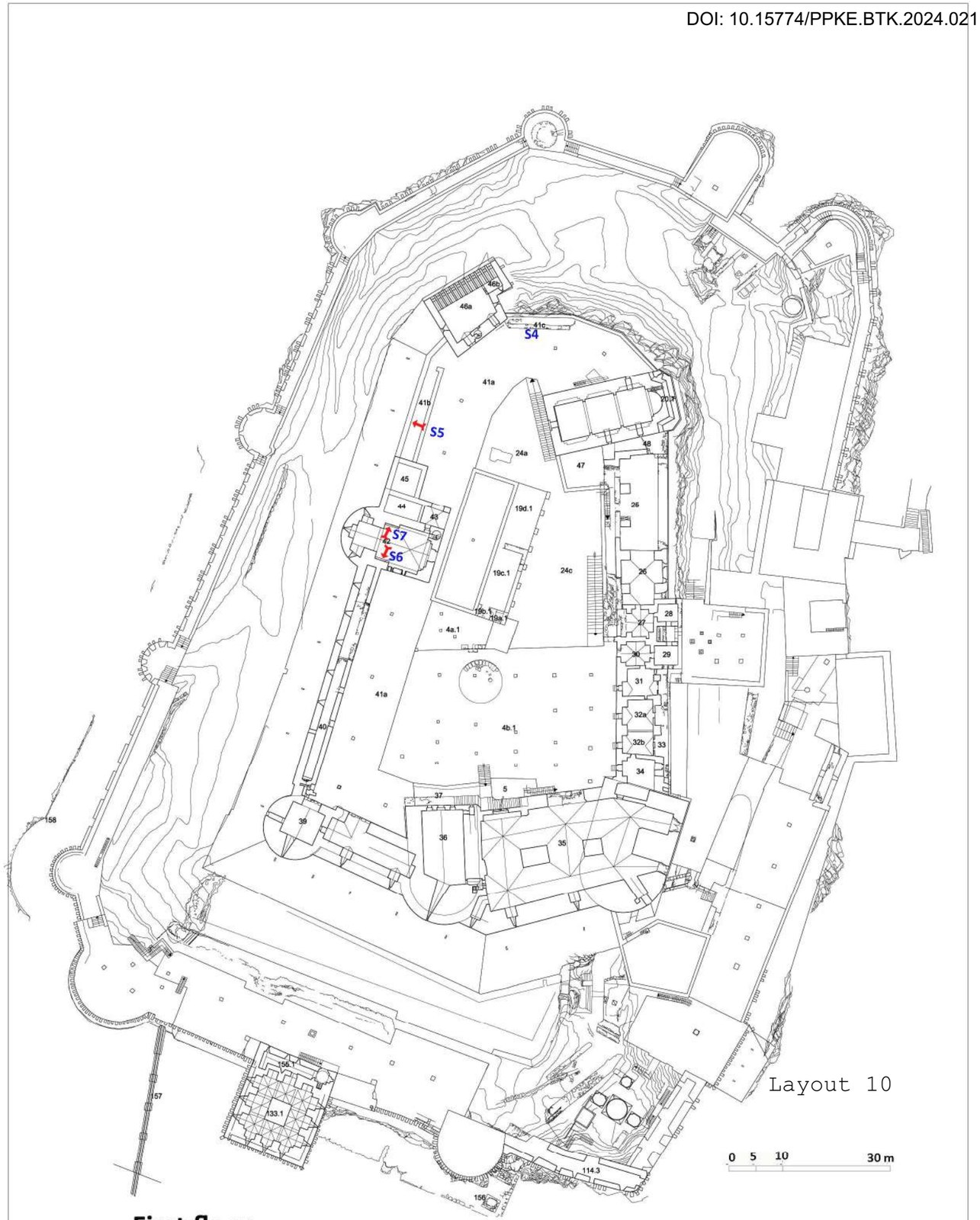

First floor

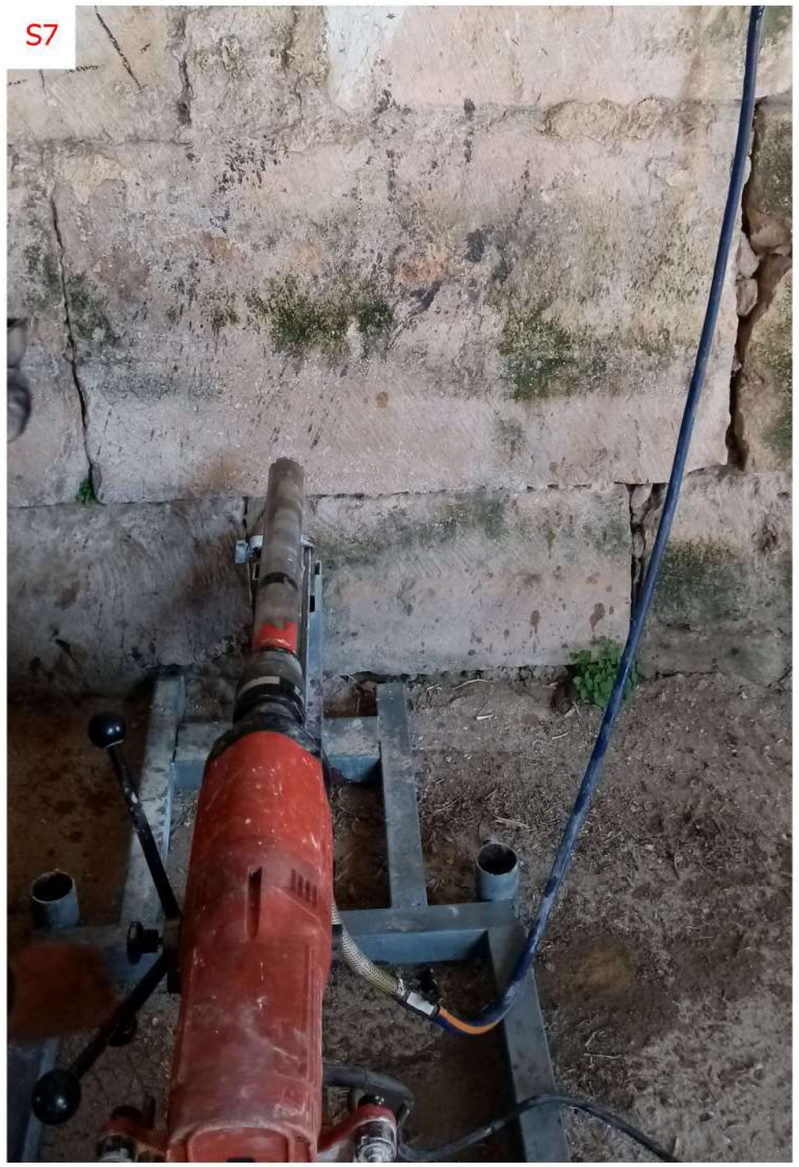

DOI: 10.15774/PPKE.BTK.2024.021

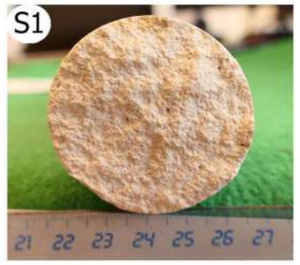

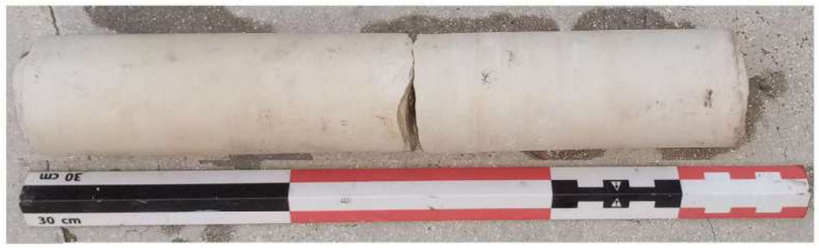

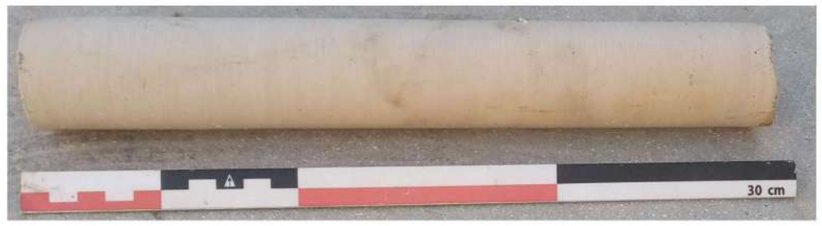

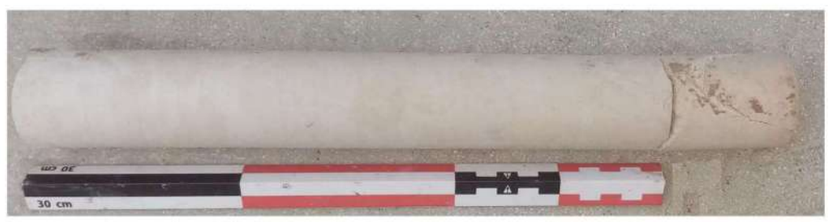

DOI: 10.15774/PPKE.BTK.2024.021

Appendix 4 The thermoanalytical results / (DTA/TG/ DTG) Curves:

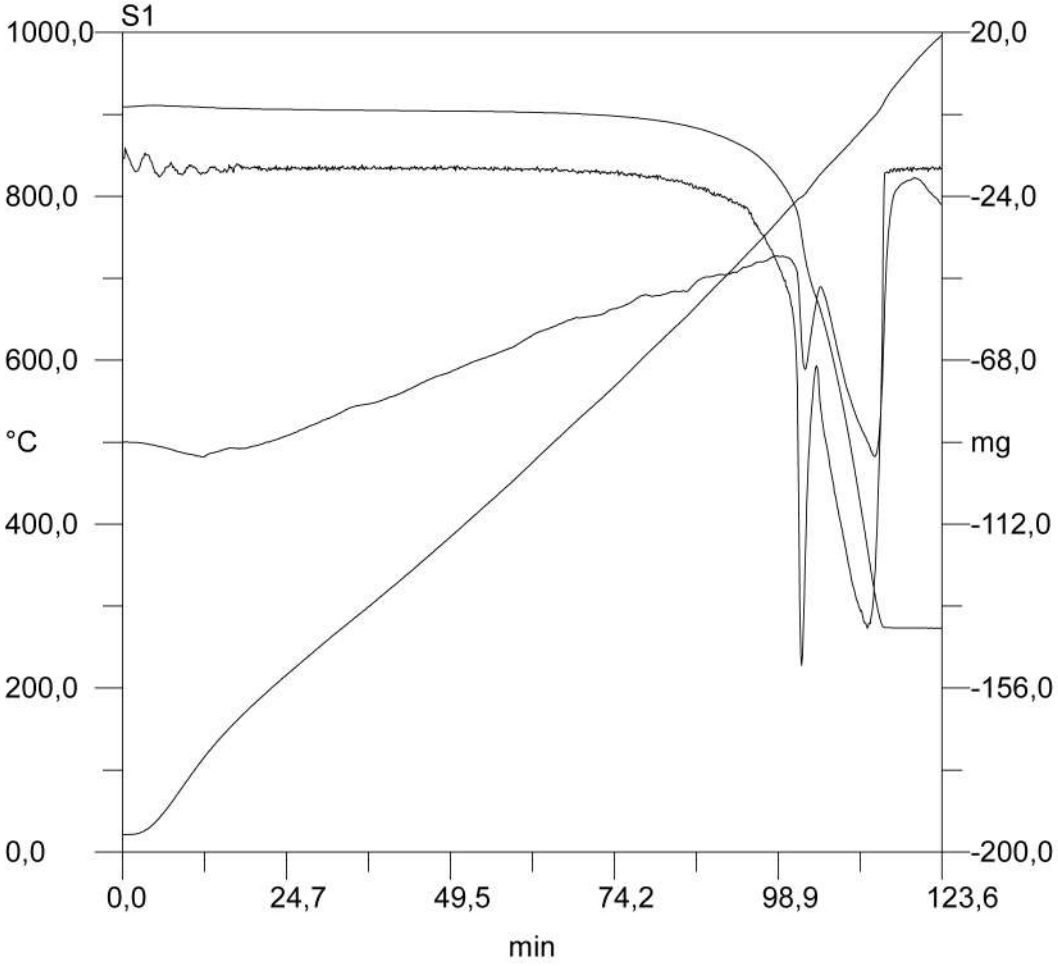

1 TG lépcsõ
T1: 619,9 °C
T2: 730,3 °C
Idõ1: 80,9 min
Idõ2: 94,5 min
Minta: 300,4 mg
Maradék: 289,12 mg
TG: 7,64 mg
TG%: 2,54%

2 TG lépcsõ
T1: 730,3 °C
T2: 818,1 °C
Idõ1: 94,5 min
Idõ2: 104,5 min
Minta: 300,4 mg
Maradék: 250,34 mg
TG: 38,78 mg
TG%: 12,91%

3 TG lépcsõ
T1: 818,1 °C
T2: 925,6 °C
Idõ1: 104,5 min
Idõ2: 115,8 min
Minta: 300,4 mg
Maradék: 160,6 mg
TG: 89,74 mg
TG%: 29,87%

4 TG lépcsõ
T1: 21,3 °C
T2: 985,2 °C
Idõ1: 1,3 min
Idõ2: 122,2 min
Minta: 300,4 mg
Maradék: 160,49 mg
TG: 139,97 mg
TG%: 46,59%

Paraméterek
Fájlnév: 21019K.der
Neve: S1
Minta
Ref. anyag:
Atmoszféra:
Tégely:
Kályha: 2
Dátum: 04-22-2021
Max. idõ: 123,6 min
Hõm. max.: 1000,0 °C
DTA e.m.d.: 20,0 °C
M. tömege: 300,4 mg
TG e.m.d.: 200,0 mg
Megjegyzés:

DOI: 10.15774/PPKE.BTK.2024.021

Contuniue Appendix 4 The thermoanalytical results / (DTA/TG/ DTG) Curves:

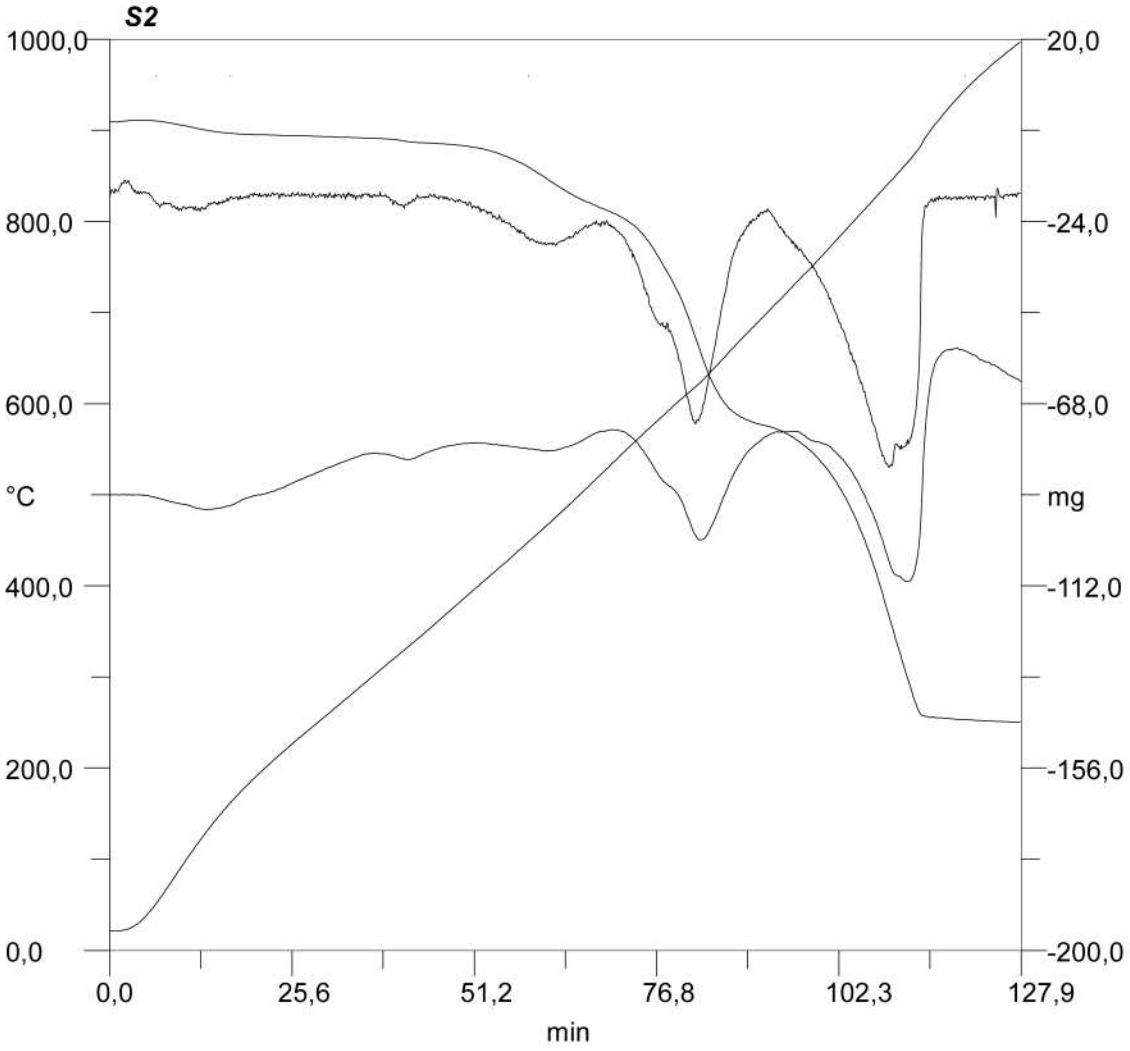

TG lépcső
T1: 396,1 °C
T2: 530,2 °C
Idő1: 51,3 min
Idő2: 70,1 min
Minta: 300,8 mg
Maradék: 279,33
TG: 15,32 mg
TG%: 5,09%

TG lépcső
T1: 530,2 °C
T2: 698,3 °C
Idő1: 70,1 min
Idő2: 92,2 min
Minta: 300,8 m
Maradék: 227,4
TG: 51,89 mg
TG%: 17,25%

Fájlnév: 22050K.der
Neve: S2
Minta:
Ref. anyag:
Atmoszféra:
Tégely:
Kályha: 2
Dátum: 03-24-2022
Max. idő: 127,9 min
Hőm. max.: 1000,0 °C
DTA e.m.d.: 20,0 °C
MDTG e.m.d.: 4,0
M. súlya: 300,8 mg
TG e.m.d.: 200,0 mg
Megjegyzés:

TG lépcső
T1: 698,3 °C
T2: 904,1 °C
Idő1: 92,2 min
Idő2: 115,8 min
Minta: 300,8 mg
Maradék: 157,17
TG: 70,27 mg
TG%: 23,36%

TG lépcső
T1: 21,3 °C
T2: 991,9 °C
Idő1: 0,5 min
Idő2: 127,1 min
Minta: 300,8 mg
Maradék: 155,92 mg
TG: 144,86 mg
TG%: 48,16%

DOI: 10.15774/PPKE.BTK.2024.021

Contuniue Appendix 4 The thermoanalytical results / (DTA/TG/ DTG) Curves:

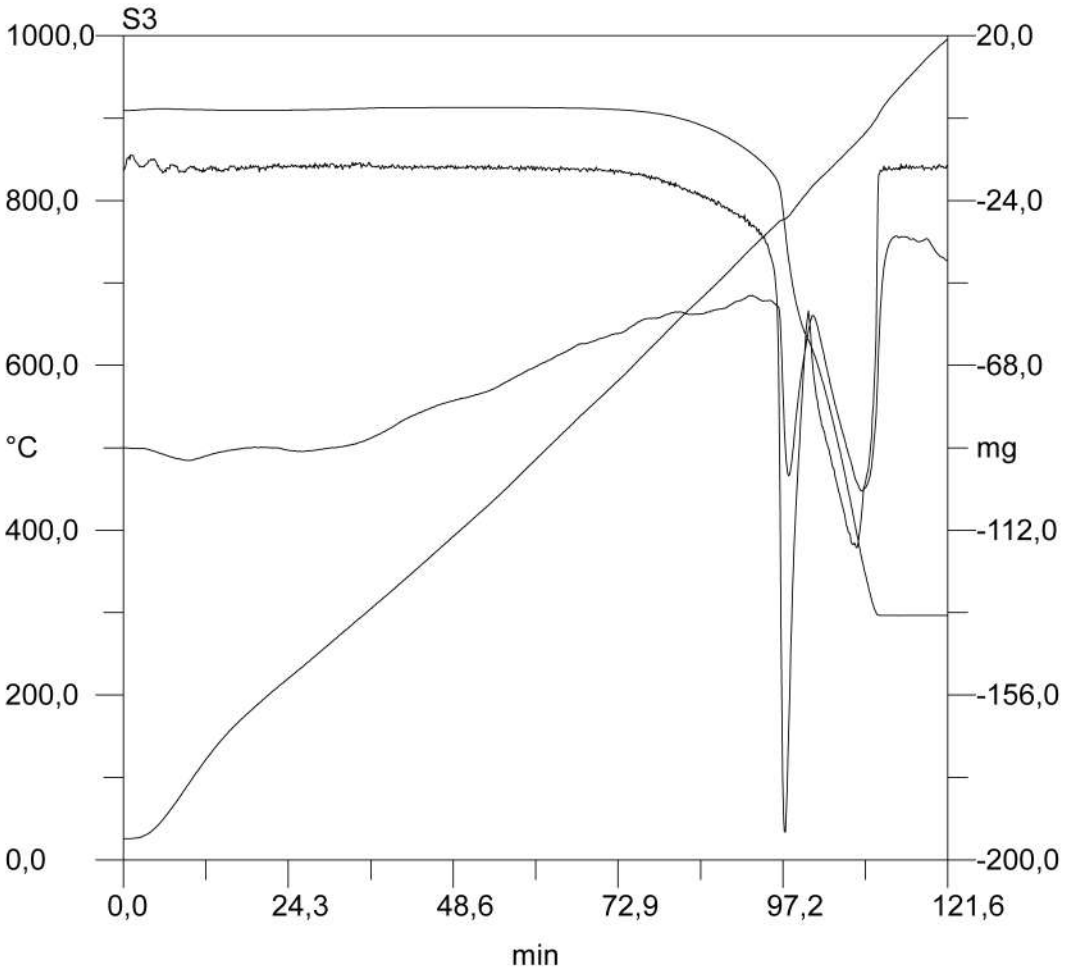

1 TG lépcsõ
T1: 584 °C
T2: 756,8 °C
Idõ1: 73,4 min
Idõ2: 94,6 min
Minta: 300,3 mg
Maradék: 286,0 mg
TG: 14,53 mg
TG%: 4,84%

2 TG lépcsõ
T1: 756,8 °C
T2: 811,5 °C
Idõ1: 94,6 min
Idõ2: 101,1 min
Minta: 300,3 mg
Maradék: 238,93 mg
TG: 47,08 mg
TG%: 15,68%

3 TG lépcsõ
T1: 811,5 °C
T2: 919 °C
Idõ1: 101,1 min
Idõ2: 112,7 min
Minta: 300,3 mg
Maradék: 165,54 mg
TG: 73,39 mg
TG%: 24,44%

4 TG lépcsõ
T1: 26,1 °C
T2: 988,5 °C
Idõ1: 1,6 min
Idõ2: 120,6 min
Minta: 300,3 mg
Maradék: 165,55 mg
TG: 134,83 mg
TG%: 44,9%

Paraméterek
Fájlnév: 21022K.der
Neve: S3
Minta
Ref. anyag:
Atmoszféra:
Tégely:
Kályha: 1
Dátum: 04-28-2021
Max. idõ: 121,6 min
Hõm. max.: 1000,0 °C
DTA e.m.d.: 20,0 °C
M. tömege: 300,3 mg
TG e.m.d.: 200,0 mg
Megjegyzés:

DOI: 10.15774/PPKE.BTK.2024.021

Contuniue Appendix 4 The thermoanalytical results / (DTA/TG/ DTG) Curves:

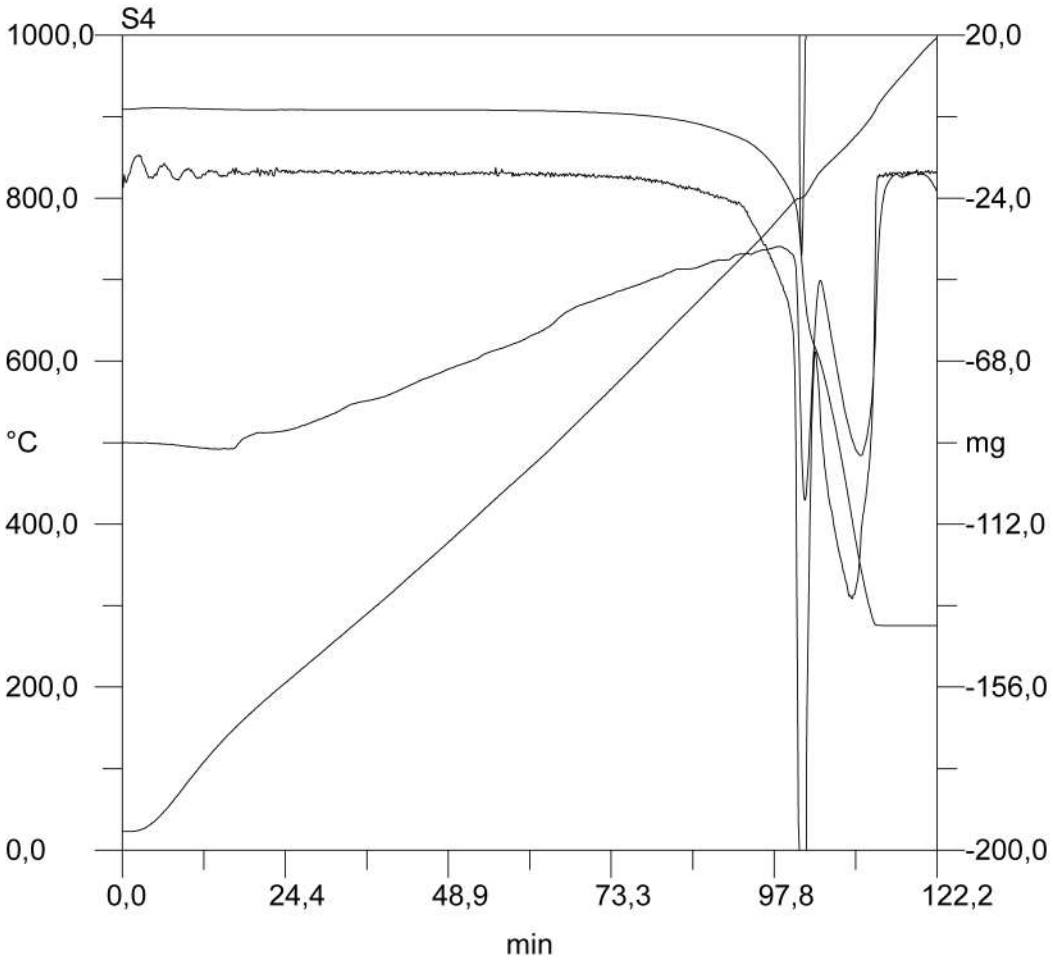

1 TG lépcsõ
T1: 603 °C
T2: 726 °C
Idõ1: 78 min
Idõ2: 92,9 min
Minta: 300,9 mg
Maradék: 293,04 mg
TG: 6,25 mg
TG%: 2,08%

2 TG lépcsõ
T1: 726 °C
T2: 823,3 °C
Idõ1: 92,9 min
Idõ2: 104 min
Minta: 300,9 mg
Maradék: 236,66 mg
TG: 56,38 mg
TG%: 18,74%

3 TG lépcsõ
T1: 823,3 °C
T2: 932,4 °C
Idõ1: 104 min
Idõ2: 115,1 min
Minta: 300,9 mg
Maradék: 161,49 mg
TG: 75,17 mg
TG%: 24,98%

4 TG lépcsõ
T1: 23,5 °C
T2: 989,2 °C
Idõ1: 2,2 min
Idõ2: 121,3 min
Minta: 300,9 mg
Maradék: 161,49 mg
TG: 139,57 mg
TG%: 46,38%

Paraméterek
Fájlnév: 21015K.der
Neve: S4
Minta
Ref. anyag:
Atmoszféra:
Tégely:
Kályha: 2
Dátum: 03-22-2021
Max. idõ: 122,2 min
Hõm. max.: 1000,0 °C
DTA e.m.d.: 20,0 °C
M. tömege: 300,9 mg
TG e.m.d.: 200,0 mg
Megjegyzés:

DOI: 10.15774/PPKE.BTK.2024.021

Contuniue Appendix 4 The thermoanalytical results / (DTA/TG/ DTG) Curves:

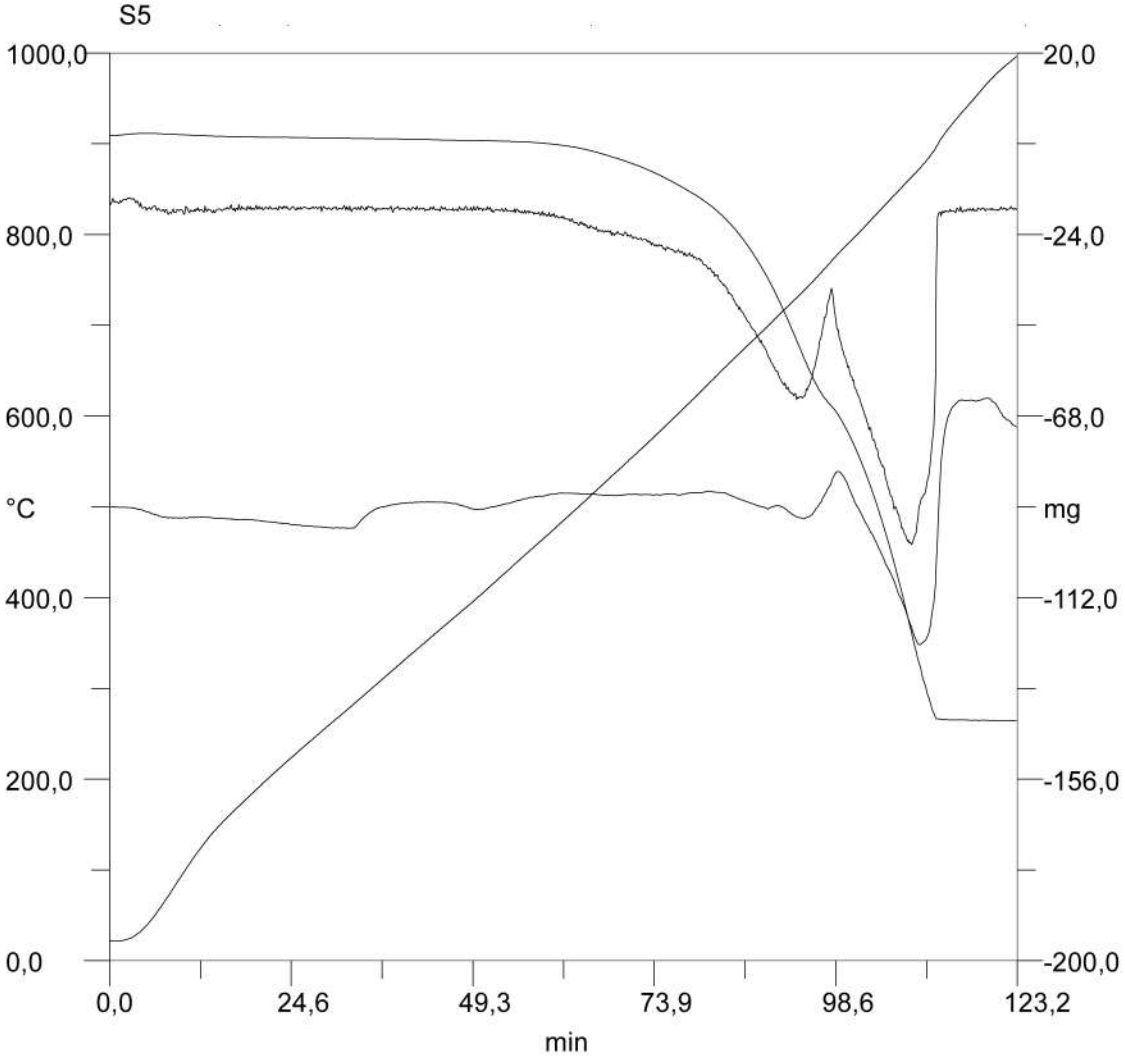

TG lépcső
T1: 492,7 °C
T2: 768 °C
Idő1: 62,8 min
Idő2: 97,9 min
Minta: 300,8 mg
Maradék: 235,73
TG: 62,39 mg
TG%: 20,74%

TG lépcső
T1: 21,7 °C
T2: 991,7 °C
Idő1: 0,8 min
Idő2: 122,6 min
Minta: 300,8 mg
Maradék: 158,97
TG: 141,85 mg
TG%: 47,16%

TG lépcső
T1: 773 °C
T2: 918,7 °C
Idő1: 98,4 min
Idő2: 114,2 min
Minta: 300,8 mg
Maradék: 159,2 m
TG: 75,54 mg
TG%: 25,11%

Fájlnév: 22051K.der
Neve: S5
Minta:
Ref. anyag:
Atmoszféra:
Tégely:
Kályha: 1
Dátum: 03-25-2022
Max. idő: 123,2 min
Hőm. max.: 1000,0 °C
DTA e.m.d.: 20,0 °C
MDTG e.m.d.: 4,0
M. súlya: 300,8 mg
TG e.m.d.: 200,0 mg
Megjegyzés:

DOI: 10.15774/PPKE.BTK.2024.021

Contuniue Appendix 4 The thermoanalytical results / (DTA/TG/ DTG) Curves:

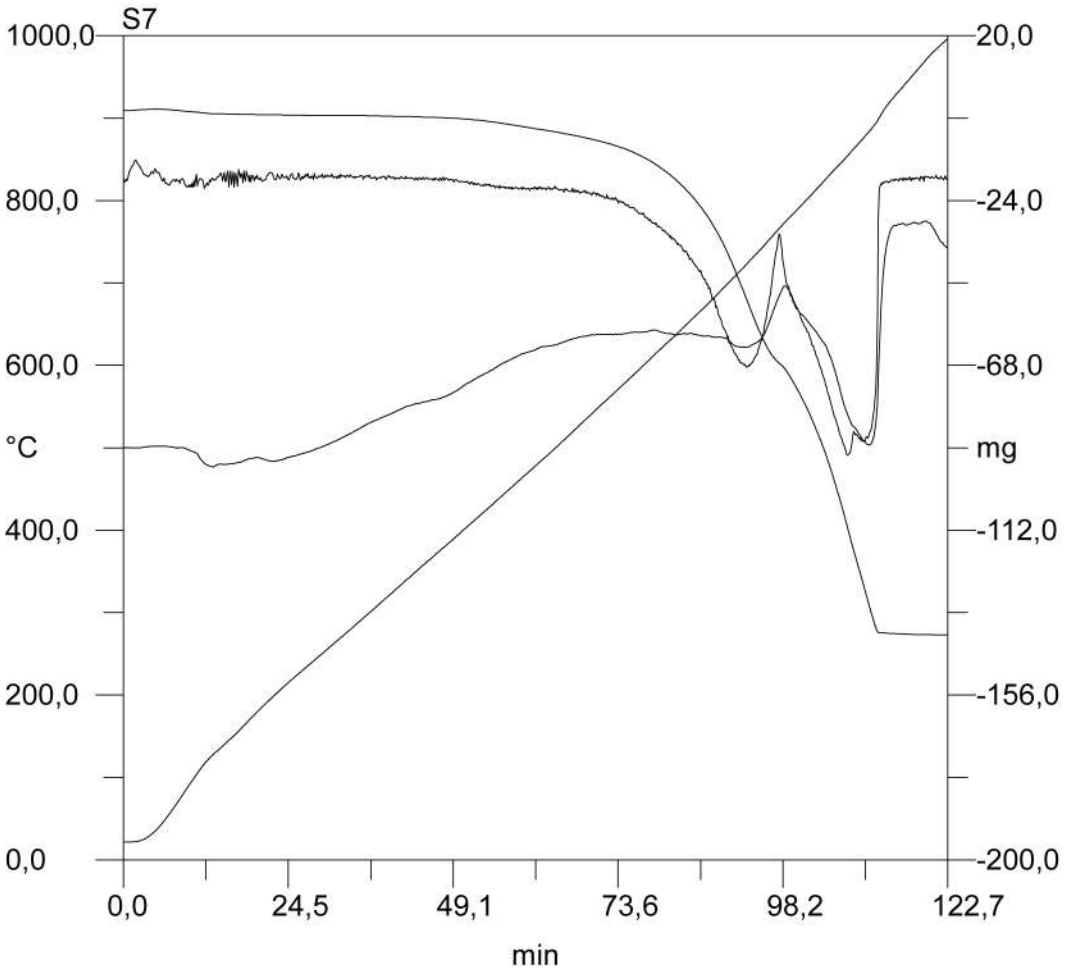

1 TG lépcsõ	2 TG lépcsõ	3 TG lépcsõ
T1: 385,2 °C	T1: 544,4 °C	T1: 765,9 °C
T2: 496,3 °C	T2: 765,9 °C	T2: 917 °C
Idõ1: 48,7 min	Idõ1: 70,3 min	Idõ1: 97,7 min
Idõ2: 64 min	Idõ2: 97,7 min	Idõ2: 114 min
Minta: 300,9 mg	Minta: 300,9 mg	Minta: 300,9 mg
Maradék: 295,35 mg	Maradék: 233,53 mg	Maradék: 161,38 mg
TG: 3,57 mg	TG: 59,56 mg	TG: 72,16 mg
TG%: 1,19%	TG%: 19,79%	TG%: 23,98%

4 TG lépcsõ	5 TG lépcsõ	6 TG lépcsõ
T1: 765,9 °C	T1: 865,2 °C	T1: 24,4 °C
T2: 865,2 °C	T2: 917 °C	T2: 988,8 °C
Idõ1: 97,7 min	Idõ1: 109,1 min	Idõ1: 3 min
Idõ2: 109,1 min	Idõ2: 114 min	Idõ2: 121,8 min
Minta: 300,9 mg	Minta: 300,9 mg	Minta: 300,9 mg
Maradék: 181,84 mg	Maradék: 161,38 mg	Maradék: 160,95 mg
TG: 51,69 mg	TG: 20,47 mg	TG: 140,23 mg
TG%: 17,18%	TG%: 6,8%	TG%: 46,6%

Paraméterek	
Fájlnév:	21016K.der
Neve:	S7
Minta	
Ref. anyag:	
Atmoszféra:	
Tégely:	
Kályha:	1
Dátum:	03-23-2021
Max. idõ:	122,7 min
Hõm. max.:	1000,0 °C
DTA e.m.d.:	20,0 °C
M. tömege:	300,9 mg
TG e.m.d.:	200,0 mg
Megjegyzés:	

DOI: 10.15774/PPKE.BTK.2024.021

Contuniue Appendix 4 The thermoanalytical results / (DTA/TG/ DTG) Curves:

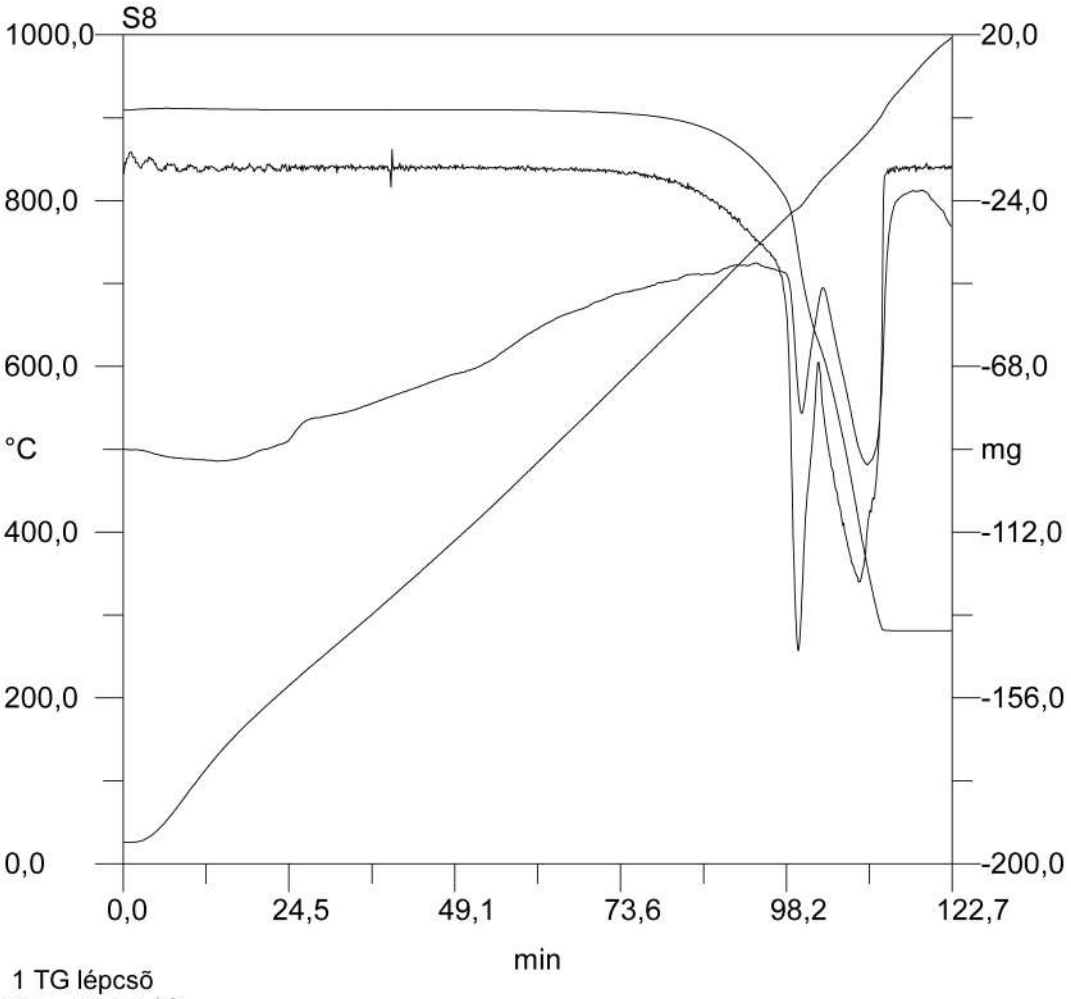

1 TG lépcsõ
T1: 599,2 °C
T2: 761,5 °C
Idõ1: 75,9 min
Idõ2: 96 min
Minta: 300,5 mg
Maradék: 282,56 mg
TG: 16,85 mg
TG%: 5,61%

2 TG lépcsõ
T1: 761,5 °C
T2: 821 °C
Idõ1: 96 min
Idõ2: 103,1 min
Minta: 300,5 mg
Maradék: 238,77 mg
TG: 43,79 mg
TG%: 14,57%

3 TG lépcsõ
T1: 821 °C
T2: 928 °C
Idõ1: 103,1 min
Idõ2: 114,5 min
Minta: 300,5 mg
Maradék: 162,33 mg
TG: 76,44 mg
TG%: 25,44%

4 TG lépcsõ
T1: 25,9 °C
T2: 988,9 °C
Idõ1: 1,6 min
Idõ2: 121,5 min
Minta: 300,5 mg
Maradék: 162,3 mg
TG: 138,32 mg
TG%: 46,03%

Paraméterek
Fájlnév: 21017K.der
Neve: S8
Minta
Ref. anyag:
Atmoszféra:
Tégely:
Kályha: 2
Dátum: 03-23-2021
Max. idõ: 122,7 min
Hõm. max.: 1000,0 °C
DTA e.m.d.: 20,0 °C
M. tömege: 300,5 mg
TG e.m.d.: 200,0 mg
Megjegyzés:

DOI: 10.15774/PPKE.BTK.2024.021

Contuniue Appendix 4 The thermoanalytical results / (DTA/TG/ DTG) Curves:

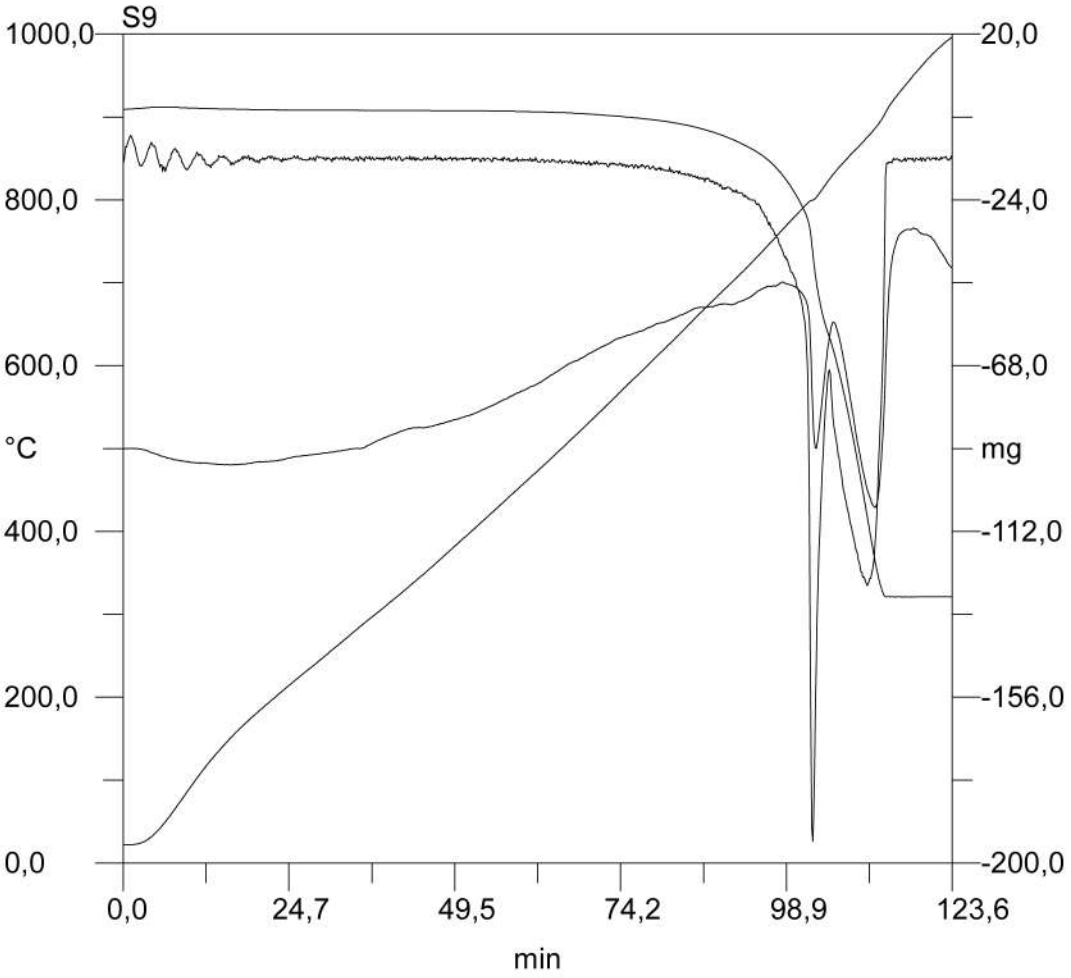

1 TG lépcsõ
T1: 625,3 °C
T2: 729,4 °C
Idõ1: 81,5 min
Idõ2: 94,5 min
Minta: 300,3 mg
Maradék: 289,21 mg
TG: 7,78 mg
TG%: 2,59%

2 TG lépcsõ
T1: 729,4 °C
T2: 823,5 °C
Idõ1: 94,5 min
Idõ2: 105,3 min
Minta: 300,3 mg
Maradék: 240,48 mg
TG: 48,73 mg
TG%: 16,23%

3 TG lépcsõ
T1: 823,5 °C
T2: 921,6 °C
Idõ1: 105,3 min
Idõ2: 115,1 min
Minta: 300,3 mg
Maradék: 170,9 mg
TG: 69,58 mg
TG%: 23,17%

4 TG lépcsõ
T1: 22,1 °C
T2: 988,1 °C
Idõ1: 1,6 min
Idõ2: 122,5 min
Minta: 300,3 mg
Maradék: 170,96 mg
TG: 129,48 mg
TG%: 43,12%

Paraméterek
Fájlnév: 21018K.der
Neve: S9
Minta
Ref. anyag:
Atmoszféra:
Tégely:
Kályha: 1
Dátum: 04-06-2021
Max. idõ: 123,6 min
Hõm. max.: 1000,0 °C
DTA e.m.d.: 20,0 °C
M. tömege: 300,3 mg
TG e.m.d.: 200,0 mg
Megjegyzés:

DOI: 10.15774/PPKE.BTK.2024.021

Contuniue Appendix 4 The thermoanalytical results / (DTA/TG/ DTG)

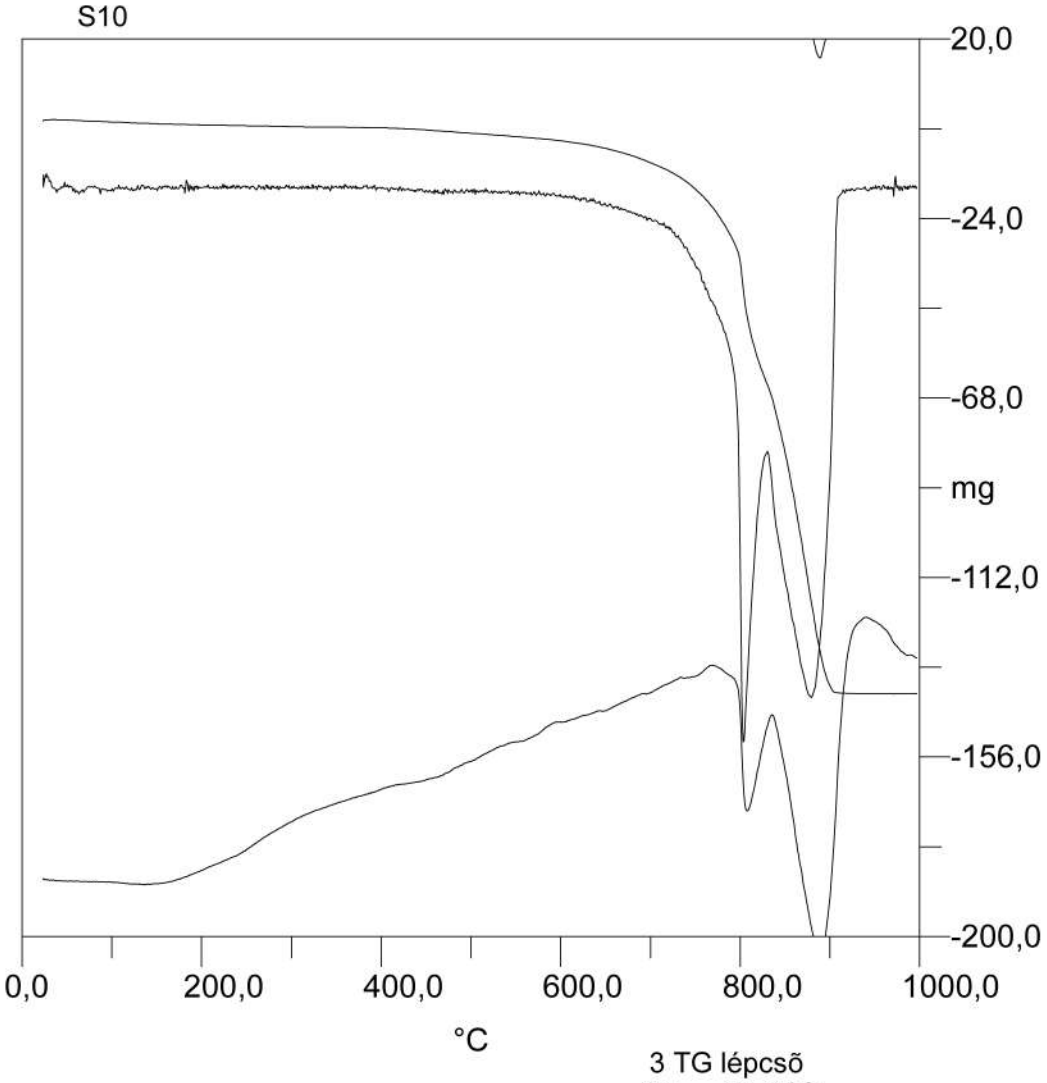

1 TG lépcsõ
T1: 593 °C
T2: 830,4 °C
Idõ1: 80,8 min
Idõ2: 109,2 min
Minta: 300,2 mg
Maradék: 235,42 mg
TG: 60,02 mg
TG%: 19,99%

2 TG lépcsõ
T1: 830,4 °C
T2: 932,9 °C
Idõ1: 109,2 min
Idõ2: 119,7 min
Minta: 300,2 mg
Maradék: 159,73 mg
TG: 75,69 mg
TG%: 25,21%

3 TG lépcsõ
T1: 36,7 °C
T2: 990,9 °C
Idõ1: 5,1 min
Idõ2: 127,5 min
Minta: 300,2 mg
Maradék: 159,71 mg
TG: 140,72 mg
TG%: 46,88%

Paraméterek
Fájlnév: 21023K.der
Neve: S10
Minta
Ref. anyag:
Atmoszféra:
Tégely:
Kályha: 2
Dátum: 05-04-2021
Max. idõ: 128,4 min
Hõm. max.: 1000,0 °C
DTA e.m.d.: 37,44 °C
M. tömege: 300,2 mg
TG e.m.d.: 200,0 mg
Megjegyzés:

DOI: 10.15774/PPKE.BTK.2024.021

Appendix 5 The photos of stone specimens under salt ageing test.

DOI: 10.15774/PPKE.BTK.2024.021

Continue Appendix 5 The photos of stone specimens under salt ageing test.

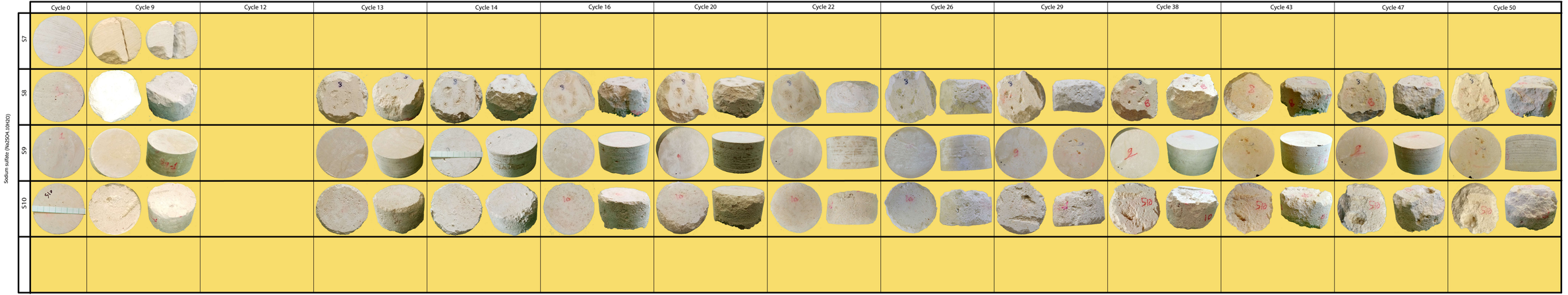

Continue Appendix 3 The photos of stone specimens under salt ageing test.

DOI: 10.15774/PPKE.BTK.2024.021

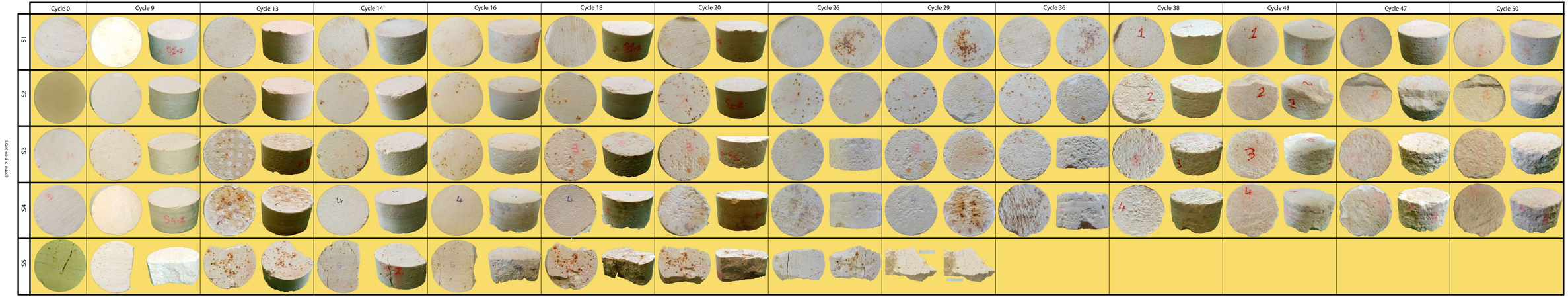

Continue Appendix 5 The photos of stone specimens under salt ageing test.

DOI: 10.15774/PPKE.BTK.2024.021

DOI: 10.15774/PPKE.BTK.2024.021

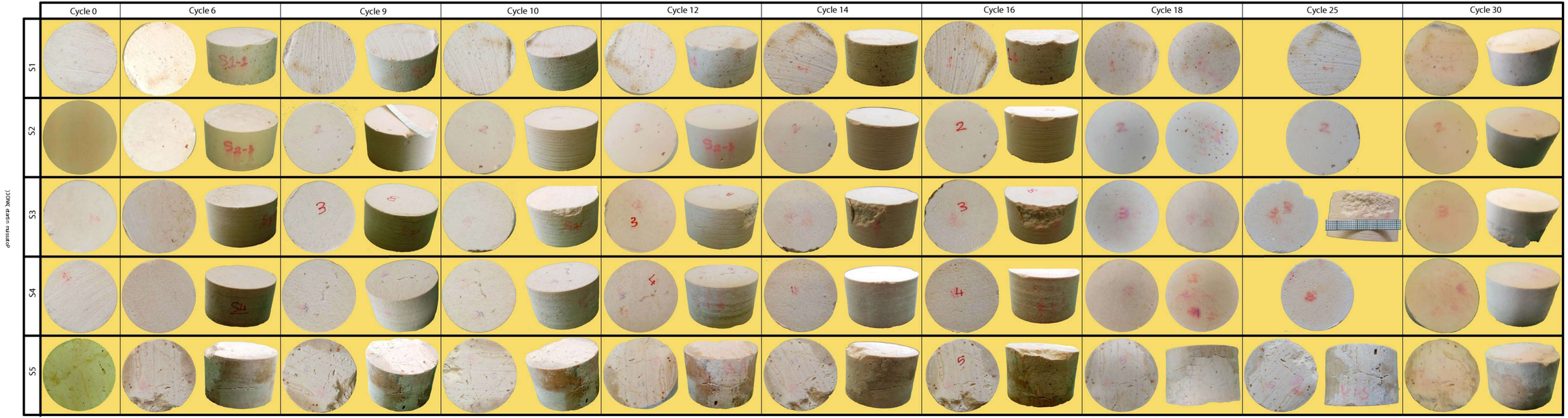

DOI: 10.15774/PPKE.BTK.2024.021

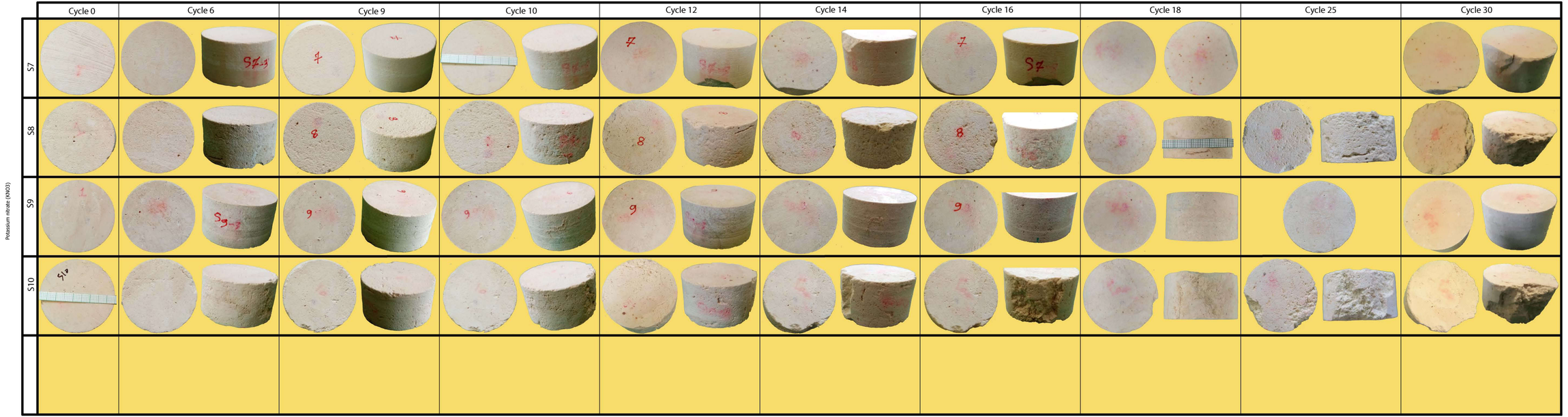

DOI: 10.15774/PPKE.BTK.2024.021

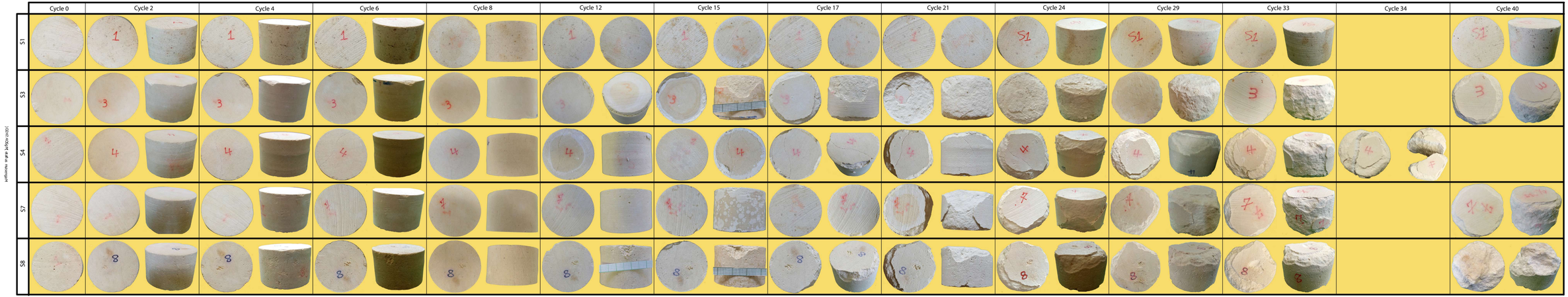

[2021-09-24 Tue] Hamuthermo

Continue Appendix 5 The photos of stone specimens under salt ageing test.

DOI: 10.15774/PPKE.BTK.2024.021

Magnesium sulfate ($MgSO_4.7H_2O$)

	Cycle 0	Cycle 2	Cycle 4	Cycle 6	Cycle 8	Cycle 12	Cycle 15	Cycle 17	Cycle 21	Cycle 24	Cycle 29	Cycle 33	Cycle 34	Cycle 40
S9	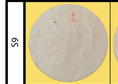					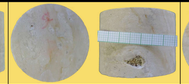								
S10	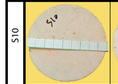													

5 cm

DOI: 10.15774/PPKE.BTK.2024.021

Appendix 6 Crac des Chevaliers Plan- Level 1

HISTORY MODIFICATION

Code of plan |	Description |	Date |

COMPLETE PLAN \|

LOCATION

Syria, Crac des Chevaliers

Data of location \|

PROJECT NFO \|

Project Name \|

Syro-Hungarian Archaeological Mission SHAM \|

Logo \|

Project Director \|

Directorate-General of Antiquities & Museums DGAM \|

Name \| Hazem Hanna
Phone \| +963 947534935
Email \| hazem-hanna@hotmail.com

Name \| Naima Mahartam
Phone \| +963 947530379
Email \| @hotmail.com

Pázmány Péter Catholic University \|

Name \| Dr. Balázs Major
Phone \| +36204396561
+963968225859
Email \| balazsmajor@hotmail.com

Name \| Zsolt Vágner
Phone \| +36205996568
Email \| vagnerzsolt@gmail.com

Project Partner \|

Budapest Universtiy of Technology and Economics \|

Name \| Dr. Zsolt Vasáros
Entitled to \| É1 01-1247/15
Phone \| +36-1/365-1444
Email \| narmer@narmer.hu

LEGEND

Inner Castle: 1 - 51
Outer Castle : 100 - 158

PLAN INFOS

Type of plan \|

Codification Survey

Scale \|

Layout \|

Codification Plan Level 1

Drawn by \| Carla Chlela
Assisted by \| Rahaf Orabi
Checked by \| Hazem Hanna
Accepted by \| Lina Qutayfan

Date \|

20191016

Code of plan \| **SYR_20191016_Crac_Codification_1 .pdf**

Software \| AutoCAD

Number of plan \|

F001

Scale bar \| 0,5m - 5cm
1:100-1:10
1:50-1:5
1:25
1:20-1:2

DOI: 10.15774/PPKE.BTK.2024.021

Continue Appendix 6 Crac des Chevaliers plan- level 2

HISTORY MODIFICATION

Code of plan |	Description |	Date |

COMPLETE PLAN \|

LOCATION

Syria, Crac des Chevaliers

Data of location \|

PROJECT NFO \|

Project Name \|

Syro-Hungarian Archaeological Mission SHAM \|

Logo \|

Project Director \|

Directorate-General of Antiquities & Museums DGAM \|

Name \| Hazem Hanna
Phone \| +963 947534935
Email \| hazem-hanna@hotmail.com

Name \| Naima Mahartam
Phone \| +963 947530379
Email \| @hotmail.com

Pázmány Péter Catholic University \|

Name \| Dr. Balázs Major
Phone \| +36204396561
+963968225859
Email \| balazsmajor@hotmail.com

Name \| Zsolt Vágner
Phone \| +36205996568
Email \| vagnerzsolt@gmail.com

Project Partner \|

Budapest Universtiy of Technology and Economics \|

Name \| Dr. Zsolt Vasáros
Entitled to \| É1 01-1247/15
Phone \| +36-1/365-1444
Email \| narmer@narmer.hu

LEGEND

Inner Castle: 1 - 51
Outer Castle : 100 - 158

PLAN INFOS

Type of plan \|

Codification Survey

Scale \|

Layout \|

Codification Plan Level 2

Drawn by \| Carla Chlela
Assisted by \| Rahaf Orabi
Checked by \| Hazem Hanna
Accepted by \| Lina Qutayfan

Date \|

20191016

Code of plan \| **SYR_20191016_Crac_Codification_2 .pdf**

Software \| AutoCAD

Number of plan \|

F002

Scale bar \| 0,5m - 5cm
1:100-1:10
1:50-1:5
1:25
1:20-1:2

DOI: 10.15774/PPKE.BTK.2024.021

Continue Appendix 6 Crac des Chevaliers plan- level 3

HISTORY MODIFICATION

Code of plan |	Description |	Date |

COMPLETE PLAN \|

LOCATION

Syria, Crac des Chevaliers

Data of location \|

PROJECT NFO \|

Project Name \|

Syro-Hungarian Archaeological Mission SHAM \|

Logo \|

Project Director \|

Directorate-General of Antiquities & Museums DGAM \|

Name \| Hazem Hanna
Phone \| +963 947534935
Email \| hazem-hanna@hotmail.com

Name \| Naima Mahartam
Phone \| +963 947530379
Email \| @hotmail.com

Logo \|

Pázmány Péter Catholic University \|

Name \| Dr. Balázs Major
Phone \| +36204396561
+963968225859
Email \| balazsmajor@hotmail.com

Name \| Zsolt Vágner
Phone \| +36205996568
Email \| vagnerzsolt@gmail.com

Project Partner \|

Budapest Universtiy of Technology and Economics \|

Logo \|

Name \| Dr. Zsolt Vasáros
Entitled to \| É1 01-1247/15
Phone \| +36-1/365-1444
Email \| narmer@narmer.hu

LEGEND

Inner Castle: 1 - 51
Outer Castle : 100 - 158

PLAN INFOS

Type of plan \| Codification Survey

Scale \|

Layout \| **Codification Plan Level 3**

Drawn by \| Carla Chlela
Assisted by \| Rahaf Orabi
Checked by \| Hazem Hanna
Accepted by \| Lina Qutayfan

Date \| **20191016**

Code of plan \| **SYR_20191016_Crac_Codification_3 .pdf**

Software \| AutoCAD

Number of plan \| **F003**

Scale bar \|
0,5m - 5cm
1:100-1:10
1:50-1:5
1:25
1:20-1:2

DOI: 10.15774/PPKE.BTK.2024.021

Continue Appendix 6 Crac des Chevaliers plan- level 4

HISTORY MODIFICATION

Code of plan |	Description |	Date |

COMPLETE PLAN \|

LOCATION

Syria, Crac des Chevaliers

Data of location \|

PROJECT NFO \|

Project Name \|

Syro-Hungarian Archaeological Mission SHAM \|

Logo \|

Project Director \|

Directorate-General of Antiquities & Museums DGAM \|

Name \| Hazem Hanna
Phone \| +963 947534935
Email \| hazem-hanna@hotmail.com

Name \| Naima Mahartam
Phone \| +963 947530379
Email \| @hotmail.com

Logo \|

Directorate General of Antiquities and Museums of the Syrian Arab Republic

Pázmány Péter Catholic University \|

Name \| Dr. Balázs Major
Phone \| +36204396561
+963968225859
Email \| balazsmajor@hotmail.com

Name \| Zsolt Vágner
Phone \| +36205996568
Email \| vagnerzsolt@gmail.com

Pázmány Péter Catholic University
Faculty of Humanities and Social Studies

Project Partner \|

Budapest Universtiy of Technology and Economics \|

Name \| Dr. Zsolt Vasáros
Entitled to \| É1 01-1247/15
Phone \| +36-1/365-1444
Email \| narmer@narmer.hu

Logo \|

LEGEND

Inner Castle: 1 - 51
Outer Castle : 100 - 158

PLAN INFOS

Type of plan \|

Codification Survey

Scale \|

Layout \|

Codification Plan Level 4

Drawn by \| Carla Chlela
Assisted by \| Rahaf Orabi
Checked by \| Hazem Hanna
Accepted by \| Lina Qutayfan

Date \|

20191016

Code of plan \| **SYR_20191016_Crac_Codification_4 .pdf**

Software \| AutoCAD

Number of plan \|

F004

Scale bar \|
0,5m - 5cm
1:100-1:10
1:50-1:5
1:25
1:20-1:2

DOI: 10.15774/PPKE.BTK.2024.021

Appendix 7 The freezing- thaw cycles during winter days in Crac des Chevaliers